NASA SP-228

ANALYTIC METHODS IN AIRCRAFT AERODYNAMICS

N70-21351
(ACCESSION NUMBER)
N70-21382
(THRU)

A symposium held at
AMES RESEARCH CENTER
Moffett Field, California
October 28–30, 1969

NATIONAL AERONAUTICS AND SPACE ADMINISTRATION

REPRODUCED BY
U.S. DEPARTMENT OF COMMERCE
NATIONAL TECHNICAL INFORMATION SERVICE
SPRINGFIELD, VA. 22161

736

ERRATA

NASA Special Publication SP-228

ANALYTIC METHODS IN AIRCRAFT AERODYNAMICS

1970

In Paper No. 19 entitled "Finite-Difference Analysis of the Compressible Turbulent Boundary Layer on a Blunt Swept Slab With Leading-Edge Blowing" by James L. Hunt, Dennis M. Bushnell, and Ivan E. Beckwith, the following pages should be corrected:

Page 429, equation (26): The density ρ in the second equation of the set should be replaced by the mean density $\bar{\rho}$.

Page 430, lines 8 and 9 of third paragraph: In sentence beginning "Consequently, the comparison . . .," the expression "a direct evaluation" should be changed to read "an indirect evaluation."

Page 434, line 3: Reference 20 should be reference 21.

Page 450, reference 14: The author's name is misspelled. The correct spelling is Glushko.

Page 458, figures 7(a) and (b): In the ordinate labels, ΔL should be replaced by ΔY.

Page 459, figure 8: The horizontal lines adjacent to $\dot{q}_1$ and $\dot{q}_4$ should be extended into surfaces $A_{\dot{q},1}$ and $A_{\dot{q},4}$, respectively, and arrowheads applied to indicate a heat flux to the right through these surfaces.

Page 470: Figures 20 and 21 should be replaced by the attached figures.

NASA-Langley, 1970

Reproduced by
NATIONAL TECHNICAL
INFORMATION SERVICE
Springfield, Va. 22151

Issued 10-12-70

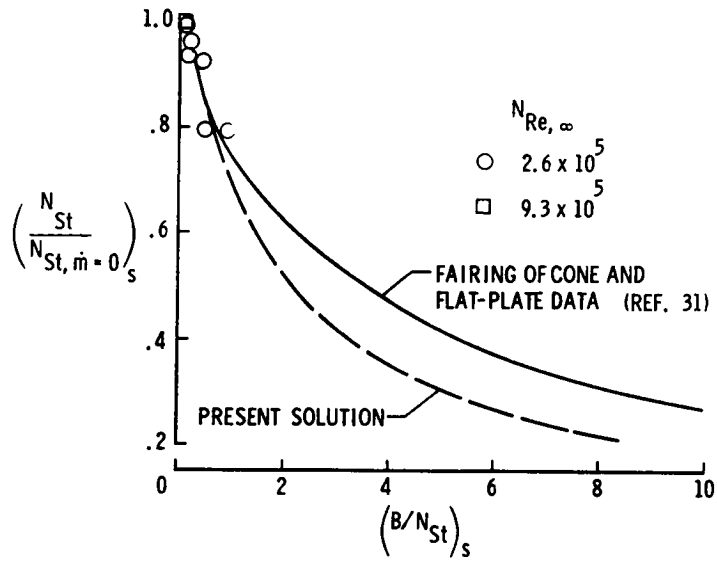

Figure 20.- Effect of blowing in the stagnation region $x/d \approx 0.1$.

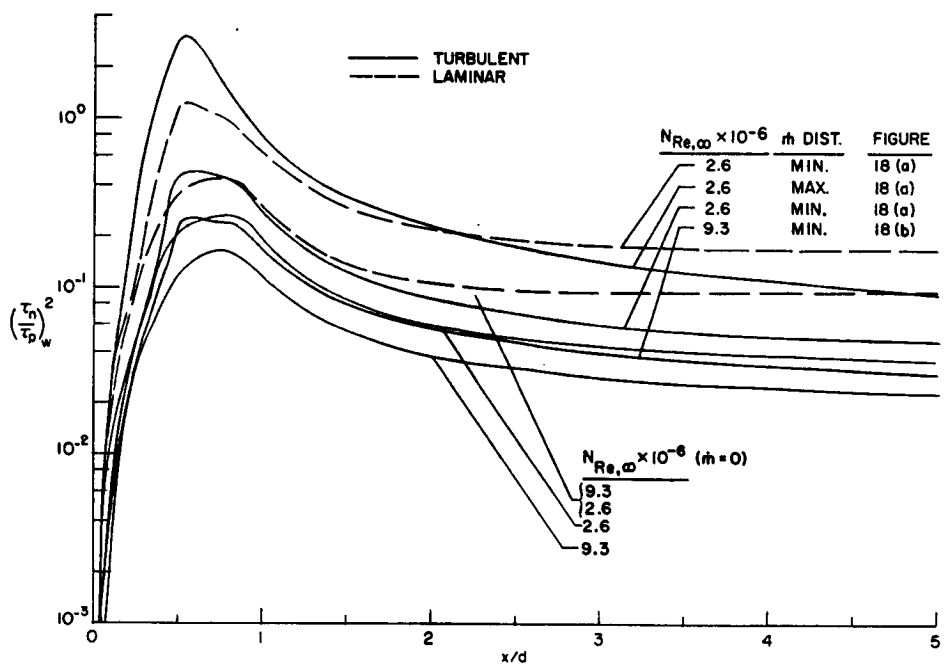

Figure 21.- Chordwise distribution of small-cross-flow parameter from theory. Invariant-turbulence model with $(l/\delta)_{max} = 0.05$ used for turbulent computations.

RECEIVED

OCT 16 1970

INPUT SECTION
CLEARINGHOUSE

NASA SP-228

ANALYTIC METHODS IN AIRCRAFT AERODYNAMICS

A symposium held at
Ames Research Center
Moffett Field, California
October 28-30, 1969

Scientific and Technical Information Division
OFFICE OF TECHNOLOGY UTILIZATION 1970
NATIONAL AERONAUTICS AND SPACE ADMINISTRATION
Washington, D.C.

For sale by the Clearinghouse for Federal Scientific and Technical Information
Springfield, Virginia 22151 – Price $

PRECEDING PAGE BLANK NOT FILMED.

PREFACE

A NASA Symposium on Analytic Methods in Aircraft Aerodynamics was held at the Ames Research Center on October 28-30, 1969. The symposium was divided into the following sessions:

I. PRESSURE AND FORCES ON BASIC SHAPES

II. FLOW FIELDS

III. BOUNDARY LAYERS AND SHOCK—BOUNDARY-LAYER INTERACTIONS

IV. INTERNAL AERODYNAMICS

V. CONFIGURATION AERODYNAMICS

Contributions were made by representatives from Ames, Lewis, and Langley Research Centers, as well as by representatives of the Aerophysics Research Corporation, Air Vehicle Corporation, Applied Theory, Inc., Grumman Aerospace Corporation, Nielsen Engineering & Research, Inc., Princeton University, Rutgers University, Stanford University, University of California, and U.S. Army Aeronautical Research Laboratory.

General discussions of some of the papers, taken from transcript, are also included.

CONTENTS

PREFACE iii

I. PRESSURES AND FORCES ON BASIC SHAPES

Session Chairman – Victor L. Peterson, Ames Research Center

1. SOME RECENT DEVELOPMENTS IN SUBSONIC LIFTING-SURFACE THEORY 1
Siegfried Wagner, Ames Research Center

2. THE USE OF FINITE ELEMENT METHODS FOR PREDICTING THE AERODYNAMICS OF WING-BODY COMBINATIONS 37
Ralph L. Carmichael, Charles R. Castellano, Ames Research Center; and Chuan F. Chen, Rutgers University

3. CALCULATIVE TECHNIQUES FOR TRANSONIC FLOWS 53
John R. Spreiter, Stanford University; Steven S. Stahara and William H. Frey, Nielsen Engineering and Research, Inc.

4. PROCEDURES FOR DESIGNING SUPERSONIC BODIES OF REVOLUTION FROM PRESCRIBED SURFACE PRESSURE DISTRIBUTIONS 75
Raymond L. Barger, Langley Research Center

5. EMPIRICAL METHOD FOR ESTIMATING PRESSURES ON ELLIPTIC CONES 85
George E. Kaattari, Ames Research Center

6. IMPROVEMENT OF WING-BODY INTERFERENCE THEORY FOR HYPERSONIC SPEEDS 101
William C. Pitts, Ames Research Center

II. FLOW FIELDS

Session Chairmen – Robert L. Trimpi and Harry L. Runyan, Jr., Langley Research Center

7. THEORETICAL STUDIES OF VORTEX FLOW ON SLENDER WING-BODY COMBINATIONS 113
E. S. Levinsky and M. H. Y. Wei, Air Vehicle Corporation; and Ralph L. Maki, Ames Research Center

Preceding page blank

8. METHODS FOR CALCULATING NONLINEAR CONICAL FLOWS 131
Jerry C. South, Jr., and E. B. Klunker, Langley Research Center

9. APPLICATION OF THREE-DIMENSIONAL METHOD OF CHARACTERISTICS TO NONCIRCULAR BODIES AT ANGLE OF ATTACK 159
John V. Rakich, Ames Research Center

10. TIME-DEPENDENT NUMERICAL METHOD FOR TREATING COMPLICATED BLUNT-BODY FLOW FIELDS 177
Richard W. Barnwell, Langley Research Center

11. AN ANALYSIS OF COANDA JET FLOWS 197
M. H. Y. Wei, Air Vehicle Corporation; and
Victor R. Corsiglia, Ames Research Center

12. A NEW METHOD FOR CALCULATING NEAR AND FAR FIELD PRESSURE ABOUT ARBITRARY CONFIGURATIONS 215
Frank A. Woodward, Aerophysics Research Corporation;
Lynn W. Hunton and Anthony R. Gross, Ames Research Center

13. PROPAGATION OF SONIC BOOM THROUGH A STRATIFIED ATMOSPHERE 229
Wallace D. Hayes, Princeton University; and
Harry L. Runyan, Jr., Langley Research Center

14. AN ANALYSIS OF FINITE-DIFFERENCE TECHNIQUES APPLIED TO EQUATIONS GOVERNING CONVECTIVE TRANSFER 245
Harvard Lomax, Ames Research Center

15. A NUMERICAL METHOD FOR COMPUTING THREE-DIMENSIONAL VISCOUS SUPERSONIC FLOW FIELDS ABOUT SLENDER BODIES 265
L. Walitt and J. G. Trulio, Applied Theory, Inc.; and
L. S. King, Ames Research Center

16. EXACT SOLUTION FOR RADIATION OF SOUND FROM A SEMI-INFINITE CIRCULAR DUCT WITH APPLICATION TO FAN AND COMPRESSOR NOISE 323
Donald L. Lansing, Langley Research Center

17. A CRITICAL EVALUATION OF PANEL FLUTTER AERODYNAMICS 335
Peter A. Gaspers, Jr., Ames Research Center

III. BOUNDARY LAYERS AND SHOCK-BOUNDARY LAYER INTERACTIONS

Session Chairman – Alfred Gessow, NASA Headquarters

18. RECENT ADVANCES IN RESEARCH ON COMPRESSIBLE TURBULENT BOUNDARY LAYERS 355
Ivan E. Beckwith, Langley Research Center

19. FINITE-DIFFERENCE ANALYSIS OF THE COMPRESSIBLE TURBULENT BOUNDARY LAYER ON A BLUNT SWEPT SLAB WITH LEADING-EDGE BLOWING 417
James L. Hunt, Dennis M. Bushnell, and Ivan E. Beckwith, Langley Research Center

20. METHODS OF ANALYZING PROPELLER AND ROTOR BOUNDARY LAYERS WITH CROSS FLOW. 473
W. J. McCroskey, U.S. Army Aeronautical Research Laboratory; and H. A. Dwyer, University of California at Davis

21. A CRITICAL EVALUATION OF ANALYTIC METHODS FOR PREDICTING LAMINAR-BOUNDARY-LAYER SHOCK-WAVE INTERACTION 515
John D. Murphy, Ames Research Center

22. A METHOD FOR ANALYZING THE INTERACTION OF AN OBLIQUE SHOCK WAVE AND A BOUNDARY LAYER 541
William C. Rose, Ames Research Center

IV. INTERNAL AERODYNAMICS

Session Chairman – Edward W. Perkins, Ames Research Center

23. OPTIMIZATION OF SUPERSONIC INLETS USING THE METHOD OF CHARACTERISTICS 569
Bernhard H. Anderson, Lewis Research Center

24. PREDICTION OF SUPERSONIC AND HYPERSONIC INLET FLOW FIELDS 583
Norman E. Sorensen, Eldon A. Latham, and Shelby J. Morris, Ames Research Center

25. A NEW METHOD FOR ANALYSIS OF TRANSONIC FLOW 597
Theodore Katsanis, Lewis Research Center

26. PREDICTION OF HEAT-TRANSFER CHARACTERISTICS FOR EJECTOR EXHAUST NOZZLES 623
Francis C. Chenoweth and Arthur Lieberman, Lewis Research Center

V. CONFIGURATION AERODYNAMICS

Session Chairman – Bradford H. Wick, Ames Research Center

27. A UNIFIED SYSTEM OF SUPERSONIC AERODYNAMIC ANALYSIS 639
Harry W. Carlson and Roy V. Harris, Jr., Langley Research Center

28. POTENTIAL FLOW SOLUTIONS FOR INLETS OF VTOL LIFT FANS AND ENGINES 659
Norbert O. Stockman, Lewis Research Center

29. ANALYSIS OF THE FLOW FIELD OF A JET IN A SUBSONIC CROSSWIND 683
Richard J. Margason, Langley Research Center

30. THEORETICAL INVESTIGATION OF DUCTED FAN INTERFERENCE FOR TRANSPORT-TYPE AIRCRAFT 703
S. B. Spangler, M. R. Mendenhall, and M. F. E. Dillenius, Nielsen Engineering and Research, Inc.

31. THE ANALYSIS OF PROPELLER-WING FLOW INTERACTION 721
Antony Jameson, Grumman Aircraft Engineering Corp.

SOME RECENT DEVELOPMENTS IN SUBSONIC LIFTING-SURFACE THEORY

By Siegfried Wagner*

Ames Research Center

N70-21352

SUMMARY

The objective of the present paper is to develop a general procedure that allows some flexibility in the choice of the spanwise control-point locations employed in Multhopp-Truckenbrodt type lifting-surface theories. In these theories the spanwise distribution of control points where the boundary conditions are fulfilled is fixed and prescribed. This constraint is very disadvantageous when the theory is applied to wings with a discontinuity in the spanwise angle-of-attack distribution (e.g., flapped wings, wings with tip tanks). The present procedure allows one to prescribe two arbitrary control-point locations for each semispan and distributes the rest of the control points in an optimal manner.

INTRODUCTION

The most difficult and laborious part of existing lifting-surface theories is the numerical solution of the singular integral equation that relates the pressure distribution on the wing to the induced downwash velocity. In the following study only true lifting-surface theories are discussed; that means methods in which the wing is represented by a continuous singularity sheet and is not approximately replaced by any system of discrete singularities. Only these true lifting-surface theories will ultimately produce the best description of the physical flow.

There are various approaches to solving the singular integral equation of lifting-surface theory, as for instance, discussed by Landahl and Stark (ref. 1). The emphasis of the existing methods is on the two main problems: finding the functions that represent the unknown pressure distribution functions best and developing quadrature formulas that compute the integrals as accurately as possible within an acceptable computation time. For instance, in the kernel-function procedure of Watkins et al. (ref. 2), the spanwise variation of the pressure is approximated by a power series which allows arbitrary spanwise locations of the control points (where the tangential flow condition is fulfilled). The disadvantage of the kernel-function procedure (ref. 2) is that it provides no general optimization of the spanwise control-point locations. In the methods developed by Multhopp (ref. 3) and Truckenbrodt (ref. 4) the spanwise variation of the pressure is expressed by Multhopp's (ref. 5) well-known development of the Lagrangian interpolation formula. This

*NRC-NASA Resident Research Associate

procedure provides an optimal distribution of spanwise control-point locations, but does not allow the choice of any arbitrary locations. The latter constraint is very detrimental for wings with a discontinuity in the spanwise angle-of-attack distribution. Such discontinuities occur, for instance, on wings with deflected flaps or with tip tanks and on wing-body combinations (see fig. 1). In these cases the accuracy in fulfilling the boundary conditions could be increased if some control points could be put at and close to the discontinuity of the angle-of-attack function.

The objective of the current study is to develop a general procedure that allows some flexibility in the spanwise location of the control points so that they can be positioned in an optimal manner for the particular wing configuration being studied. In the current investigation the procedure of reference 6, which is an extension and an improvement of the original theories of Multhopp (ref. 3) and Truckenbrodt (ref. 4), is modified to optimize the spanwise control-point locations for wings with discontinuities in the spanwise angle-of-attack distribution.

NOMENCLATURE

A	aspect ratio, $\frac{b^2}{S}$
b	wing span, 2s
$c(\eta)$	local streamwise chord
$c_\ell(\eta)$	local lift coefficient
$c_m(\eta)$	local pitching-moment coefficient about local quarter chord
$c_n(\eta)$	spanwise pressure distribution functions
C_L	lift coefficient, $\frac{\text{lift}}{q_\infty S}$
ΔC_p	incremental pressure coefficient, $\frac{\Delta p}{q_\infty}$
c_r	root chord
$f_n(\eta)$	dimensionless spanwise pressure distribution functions, $\frac{c_n(\eta)c(\eta)}{2b}$
$g(\xi,\eta,\eta')$	$\sum_{n=0}^{N} H_n(\xi,\eta,\eta')f_n(\eta')$
$h_n(X)$	chordwise pressure distribution functions

$H_n(X,Y)$	influence functions
$K_n(\xi_p,\eta_\nu,\eta')$	$H_n(\xi_p,\eta_\nu,\eta_\nu) - H_n(\xi_p,\eta_\nu,\eta')$
M	Mach number or number of spanwise control sections
N	N + 1 equals number of chordwise control points
Δp	lifting pressure, $p_{lower} - p_{upper}$
q_∞	dynamic pressure
s	wing semispan
S	total wing area
x,y,x',y'	Cartesian coordinates (see fig. 2)
X	$\frac{x - x_{\ell e}}{c}$
Y	$\frac{y - y'}{c}$
β	Prandtl-Glauert compressibility factor, $(1 - M^2)^{1/2}$
θ	trigonometric variable for spanwise quadrature
ξ,η,ζ	Cartesian coordinates made dimensionless with respect to $\frac{b}{2}$
ξ_p,η_ν	coordinates of the control points

Subscripts

ac	aerodynamic center
exp	experiment
ℓe	leading edge
te	trailing edge
th	theory

INTEGRAL EQUATION OF LIFTING-SURFACE THEORY FOR CALCULATING

THE PRESSURE DISTRIBUTION OF WINGS

When the tangential flow condition along the surface of the wing is fulfilled, the following singular integral equation of lifting-surface theory is obtained:

$$\alpha(\xi,\eta) = -\frac{1}{8\pi} \fint_{-1}^{+1} \int_{\xi_{\ell e}}^{\xi_{te}} \frac{\Delta C_p(\xi',\eta')}{(\eta - \eta')^2} \left\{ 1 + \frac{\xi - \xi'}{[(\xi - \xi')^2 + \beta^2(\eta - \eta')^2]^{1/2}} \right\} d\xi' \, d\eta' \tag{1}$$

This integral contains a strong singularity at $\eta \to \eta'$ and has to be defined by (see ref. 6):

$$\fint_{-1}^{+1} \frac{g(\xi,\eta,\eta')}{(\eta - \eta')^2} d\eta' = \lim_{\varepsilon \to 0} \left[\fint_{-1}^{+1} \frac{g(\xi,\eta,\eta')}{(\eta - \eta')^2} d\eta' - \frac{2}{\varepsilon} g(\xi,\eta,\eta) \right] \qquad (\xi_{\ell e} < \xi \leqq \xi_{te}) \tag{2a}$$

$$\fint_{-1}^{+1} \frac{g(\xi,\eta,\eta')}{(\eta - \eta')^2} d\eta' = \fint_{-1}^{+1} \frac{g(\xi,\eta,\eta')}{(\eta - \eta')^2} d\eta' \qquad (\xi = \xi_{\ell e}) \tag{2b}$$

where

$$\fint_{-1}^{+1} \ldots d\eta' = \int_{-1}^{\eta-\varepsilon} \ldots d\eta' + \int_{\eta+\varepsilon}^{+1} \ldots d\eta' \tag{3a}$$

and

$$\fint_a^y \frac{d\eta}{(y - \eta)^{i+1/2}} = \frac{(-1)^i 2^i}{2i - 1} \left(\frac{\partial}{\partial y}\right)^i \int_a^y \frac{d\eta}{(y - \eta)^{1/2}} = \frac{-2}{(2i - 1)(y - a)^{i-1/2}}$$

$$(a < y, \quad i = 1, 2, \ldots) \tag{3b}$$

The wing geometry and coordinate system used are illustrated in figure 2.

If it is assumed that the pressure distribution can be represented by a linear combination of chordwise and spanwise pressure modes (see refs. 2, 3, 4, and 6)

$$\Delta C_p(\xi,\eta) = \frac{2b}{c(\eta)} \sum_{n=0}^{N} h_n(\xi) f_n(\eta) \tag{4}$$

the integration of equation (1) in the chordwise direction can be separated from integration in the spanwise direction:

$$\alpha(\xi,\eta) = -\frac{1}{2\pi} \sum_{n=0}^{N} \fint_{-1}^{+1} \frac{H_n(\xi,\eta,\eta')}{(\eta - \eta')^2} f_n(\eta') d\eta' \tag{5a}$$

$$H_n(\xi,\eta,\eta') = H_n(X,Y) = \int_0^1 h_n(X') \left\{ 1 + \frac{X - X'}{[(X - X')^2 + Y^2]^{1/2}} \right\} dX' \tag{5b}$$

where

$$X = \frac{b}{2c(\eta')} [\xi - \xi_{\ell e}(\eta')] \ , \quad X' = \frac{b}{2c(\eta')} [\xi' - \xi_{\ell e}(\eta')] \ , \quad Y = \frac{b\beta}{2c(\eta')} (\eta - \eta') \tag{6}$$

Following the usual assumptions in three-dimensional lifting-surface theories (see ref. 1), the chordwise pressure modes $h_n(\xi)$ are prescribed by utilizing the pressure distribution functions of two-dimensional thin-airfoil theory (see ref. 6):

$$h_n(X) = \frac{1}{\pi} \left(\frac{1 - X}{X} \right)^{1/2} \left[\frac{T_n(1 - 2X) + T_{n+1}(1 - 2X)}{1 - X} \right] \tag{7}$$

The functions T_n are Chebyshev polynomials of the first kind with the argument $1 - 2X$. The chordwise pressure modes $h_n(X)$ of equation (7) are illustrated in figure 3. They satisfy the proper boundary conditions in each term; namely, they go to infinity as the square root of the distance from the leading edge, and they go to zero like the square root of the distance from the trailing edge. The pressure modes are smooth and continuous except at

the leading edge and can only be used to represent a smooth and continuous pressure distribution in the chordwise direction. It should be noted that the pressure modes of equation (7) cannot describe any pressure peaks that occur, for instance, along the hinge line of wings with deflected flaps.

SOLUTION OF THE INTEGRAL EQUATION OF LIFTING-SURFACE THEORY

Distribution of Control Points

Because of the great amount of computation, the tangential flow condition cannot be fulfilled along the whole surface of the wing but only at a restricted number of points, which are called control points. In the present study, $N + 1 = 5$ chordwise control points are used at each of the $M = 19$ spanwise control sections. The chordwise positions of the control points are the same as in reference 6, namely,

$$X_p = \frac{b}{2c(\eta_\nu)} [\xi_p(\eta_\nu) - \xi_{\ell e}(\eta_\nu)] = \frac{p}{N} \qquad (p = 0, 1, \ldots, N) \tag{8}$$

It is the objective of the present study to calculate optimal spanwise positions η_ν of the control points for wings with discontinuous angle-of-attack functions (see fig. 1). A wing with deflected flaps is selected as an example to discuss the problems and the proposed solutions. For such a configuration the function $\Delta\alpha(\eta)$ is constant within the region of the deflected flap (the flap deflection angle, δ) and is zero elsewhere. To fulfill the boundary conditions accurately, a control point is located at each step of the function $\Delta\alpha(\eta)$, that is, at both edges of the flap. In addition, at the edges of the flaps $\Delta\alpha(\eta)$ is defined to be half the flap deflection angle, $\delta/2$. For further discussion only the symmetric case is considered. Two spanwise positions of the control points have been defined on each semispan of the wing so far. It is intended to optimize the spanwise positions of the rest of the control points in the following paragraphs.

Because of the assumptions in the previous section regarding the pressure distribution, the original integral equation of lifting-surface theory (see eq. (1)) was transformed into a system of integral equations (5). The spanwise pressure modes $f_n(\eta)$ remained the only unknowns of the system of integral equations. To solve this system of integral equations the unknown pressure modes $f_n(\eta)$ are approximated by the following Fourier polynomial:

$$f_n(\eta') = 2 \sum_{\mu=1}^{M} a_{n\mu} \sin \mu\theta' \tag{9}$$

where

$$a_{n\mu} = \frac{1}{\pi} \int_0^\pi f_n(\theta') \sin \mu\theta' \, d\theta' \tag{10}$$

and

$$\eta' = \cos \theta' \tag{11}$$

If the spanwise angle-of-attack distribution is smooth and continuous, the integral of equation (10) can be evaluated by the following Chebyshev-Gauss quadrature (see ref. 7):

$$\int_{-1}^{+1} f(\eta)(1 - \eta^2)^{-1/2}\, d\eta = \int_0^{\pi} f(\theta)d\theta = \frac{\pi}{M + 1}\left[\sum_{m=1}^{M} f(\theta_m) + \frac{f(0) + f(\pi)}{2}\right] \tag{12a}$$

where

$$\theta_m = \frac{\pi m}{M + 1} \qquad (m = 1, 2, \ldots, M) \tag{12b}$$

Hence

$$a_{n\mu} = \frac{1}{M + 1}\sum_{m=1}^{M} f_n(\theta_m)\sin \mu\theta_m \tag{13}$$

If equation (13) is put into equation (9), Multhopp's well-known version of the Lagrangian interpolation formula is obtained:

$$f_n(\theta') = \frac{2}{M + 1}\sum_{m=1}^{M} f_n(\theta_m) \sum_{\mu=1}^{M} \sin \mu\theta_m \sin \mu\theta' \tag{14}$$

In many procedures (e.g., refs. 3 through 6), the spanwise locations of the control points are identical with the so-called Gaussian nodes

$$\eta_m = \cos \theta_m\,, \quad \theta_m = \frac{m\pi}{M + 1}\,, \quad (m = 1, 2, \ldots, M) \tag{15}$$

which result from optimizing the integration stations η_k of the Hermite quadrature (see ref. 7).

$$\int_a^b w(\eta)f(\eta)\,d\eta = \sum_{k=1}^{m} A_k f(\eta_k) + \sum_{k=1}^{m} B_k f'(\eta_k) \tag{16}$$

It is well-known that the Hermite formula reduces to the Gaussian quadrature (for which all coefficients B_k are zero) if the integration stations η_k are identical with the Gaussian nodes. These Gaussian nodes are the zeros of the orthogonal polynomials over the integration interval (a,b) with respect to the weight function $w(\eta)$ which has to be nonnegative in (a,b). If $w(\eta)$ changes sign in (a,b), there is no assurance that the zeros of the orthogonal polynomials will be real or, if so, that they will lie inside (a,b). Since the B_k are forced to be zero in the Gaussian quadrature rule, this procedure retains the same precision as the Hermite quadrature but uses half as many terms.

So far no preassigned abscissas have been discussed. However, in some applications (e.g., the wing with flaps), it is desirable to prescribe some abscissas to be involved in a quadrature formula. In this case the Gaussian nodes are determined as the zeros of the orthogonal polynomials over the integration interval with respect to the modified weight function

$$\overline{w}(\eta) = w(\eta)\nu(\eta) \tag{17}$$

where

$$\nu(\eta) = \prod_{i=1}^{r} (\eta - \eta_i) \tag{18}$$

is an arbitrary polynomial, whose zeros η_i are the preassigned abscissas. For instance, the weight function of the first integral in equation (12a) is $w(\eta) = (1 - \eta^2)^{-1/2}$. The orthogonal polynomials in (-1,+1) with respect to $w(\eta)$ are the Chebyshev polynomials of first kind $T_n(\eta) = \cos(n \arccos \eta)$. If both end points $\eta = -1$ and $\eta = +1$ are prescribed as integration stations, $\nu(\eta)$ is equal to $(\eta^2 - 1)$. The modified weight function is then

$$\overline{w}(\eta) = (1 - \eta^2)^{1/2} \tag{19}$$

The orthogonal polynomials in (-1,+1) with respect to the weight function of equation (19) are the Chebyshev polynomials of second kind

$$S_n(\eta) = \frac{\sin[(n + 1)\arccos \eta]}{\sin(\arccos \eta)} \tag{20}$$

whose zeros are given in equation (15). No problem occurs when the end points of the integration interval are prescribed, since $\overline{w}(\eta)$ does not change the sign in (-1,+1). However, for general wing-flap configurations being discussed here, two additional preassigned abscissas, namely the edges of the flap, η_3, η_4, are needed between the edges of each semispan. Therefore, the new modified weight function

$$\overline{w}(\eta) = (1 - \eta^2)^{1/2}(\eta^2 - \eta_3{}^2)(\eta^2 - \eta_4{}^2) \tag{21}$$

usually changes sign within (-1,+1). For that reason there is no assurance that the Gaussian nodes are located in (-1,+1) or are real as mentioned before.

To guarantee acceptable locations of the Gaussian nodes for any flap configuration (location of preassigned abscissas), the Gaussian quadrature rule has to be modified, according to personal communication with Messrs. David C. Galant and William P. Jones of the Research Computation Analysis Section, Ames Research Center:

$$\int_{-1}^{+1} f(\eta)(1 - \eta^2)^{-1/2} d\eta = \sum_{j=1}^{2} G_j f'(\eta_{j+2}) + \sum_{j=3}^{M-2} G_j f(\eta_j) + \sum_{j=M-1}^{M} G_j f'(\eta_{j-2}) \tag{22}$$

where $\eta_3 = -\eta_{M-2}$ and $\eta_4 = -\eta_{M-3}$ are the spanwise locations of the outboard and inboard edges of the flap, respectively. Mr. Galant was kind enough to write two computer subroutines which calculate the Gaussian nodes η_j ($j = 5, 6, \ldots, M - 4$) and weights G_j ($j = 1, 2, \ldots, M$) for any symmetric flap-wing configuration.

The spanwise locations η_ν ($\nu = 3, 4, \ldots, M - 2$) of the control points are identical with the two preassigned abscissas of each semispan η_j ($j = 3, 4, M - 3, M - 2$), and with the Gaussian nodes η_j ($j = 5, 6, \ldots, M - 4$), as illustrated in figure 4. Since the integral of equation (10) is evaluated by the quadrature rule of equation (22) the spanwise pressure modes $f_n(\eta)$ are now approximated by

$$f_n(\eta') = \sum_{\mu=1}^{M} \left[\sum_{j=1}^{2} R_{j\mu} f_n'(\eta_{j+2}) + \sum_{j=3}^{M-2} R_{j\mu} f_n(\eta_j) + \sum_{j=M-1}^{M} R_{j\mu} f_n'(\eta_{j-2}) \right] \sin \mu\theta' \tag{23}$$

where

$$R_{j\mu} = \frac{2}{\pi} G_j \sin \mu\theta_{j+2} \qquad (j = 1, 2) \tag{24a}$$

$$R_{j\mu} = \frac{2}{\pi} [G_j \sin \mu\theta_j - G_{j-2}\mu \cos \mu\theta_j / \sin \theta_j] \qquad (j = 3, 4) \tag{24b}$$

$$R_{j\mu} = \frac{2}{\pi} G_j \sin \mu\theta_j \qquad (j = 4, 5, \ldots, M - 4) \tag{24c}$$

$$R_{j\mu} = \frac{2}{\pi} [G_j \sin \mu\theta_j - G_{j+2}\mu \cos \mu\theta_j / \sin \theta_j] \qquad (j = M - 3, M - 2) \tag{24d}$$

$$R_{j\mu} = \frac{2}{\pi} G_j \sin \mu\theta_{j-2} \qquad (j = M - 1, M) \tag{24e}$$

If the unknown pressure modes $f_n(\eta)$ of equation (5a) are replaced by the approximation polynomials of equation (23), the system of integral equations (5a) is transformed into a system of linear equations, the unknowns of which are the values of the pressure modes $f_n(\eta_j)$, $j = 3, 4, \ldots, M - 2$, and of the first derivatives $f_n'(\eta_j)$, $j = 3, 4, M - 3, M - 2$. The number of control sections η_ν ($\nu = 1, 2, \ldots, M$) has to be equal to the number of unknown values of each pressure mode f_n, $n = 0, 1, \ldots, N$. Since the value of the first derivative $f_n'(\eta_j)$, $j = 3, 4, M - 3, M - 2$, of each pressure mode is also used in equation (23), the tangential flow condition has to be fulfilled at two additional control sections η_ν ($\nu = 1, 2, M - 1, M$) of each semispan besides the already defined control sections η_ν ($\nu = 3, 4, \ldots, M - 2$) which are identical with the preassigned abscissas and the Gaussian nodes (see fig. 4). These four additional control-point locations are usually chosen close to four of the Gaussian nodes to minimize the error when the pressure modes are approximated by the trigonometric approximation polynomial of equation (23).

Integration in Chordwise Direction

Since the chordwise pressure modes are prescribed by equation (7), the chordwise integration of the integral equation (1) is identical with the computation of the influence functions $H_n(X,Y)$ of equation (5b) that depend on the geometry of the wing planform and the Mach number only. The influence functions are evaluated by the same Gaussian quadrature formula used in reference 6 (eq. (11)).

Integration in Spanwise Direction

Transforming equation (5a) into a more convenient form (see ref. 6) and fulfilling the tangential flow condition at the $(N + 1)M$ control points (ξ_p,η_ν), one gets the following system of integral equations for the unknown spanwise pressure modes $f_n(\eta)$, $n = 0, 1, \ldots, N$:

$$\alpha(\xi_p,\eta_\nu) = \frac{1}{2\pi}\sum_{n=0}^{N} \lim_{\varepsilon\to 0}\left\{H_n(\xi_p,\eta_\nu,\eta_\nu)\left[\frac{2}{\varepsilon} f_n(\eta_\nu) - \fint_{-1}^{+1} \frac{f_n(\eta)d\eta}{(\eta_\nu - \eta)^2}\right] + I_{np}(\eta_\nu)\right\}$$

$$(\nu = 1, 2, \ldots, M) \tag{25a}$$

$$I_{np}(\eta_\nu) = \fint_{-1}^{+1} \frac{K_n(\xi_p,\eta_\nu,\eta)}{(\eta_\nu - \eta)^2} f_n(\eta)d\eta \qquad (p = 1, 2, \ldots N) \tag{25b}$$

$$I_{np}(\eta_\nu) = \int_{-1}^{+1} \frac{K_n(\xi_p,\eta_\nu,\eta)}{(\eta_\nu - \eta)^2} f_n(\eta)d\eta \qquad (p = 0) \tag{25c}$$

where

$$K_n(\xi_p,\eta_\nu,\eta) = H_n(\xi_p,\eta_\nu,\eta_\nu) - H_n(\xi_p,\eta_\nu,\eta) \tag{26}$$

To solve this system of integral equations, the technique developed in reference 6 is applied. However, instead of introducing the interpolation polynomial of equation (14), the unknown spanwise pressure modes are now approximated by the polynomial with preassigned abscissas of equation (23). This formula can be used to evaluate the first integral of equation (25a) analytically:

$$\frac{1}{2\pi}\lim_{\varepsilon\to 0}\left[\frac{2}{\varepsilon}f_n(\eta_\nu) - \fint_{-1}^{+1}\frac{f_n(\eta)d\eta}{(\eta_\nu - \eta)^2}\right] = \sum_{m=3}^{M-2} b_{\nu m}f_{nm} + \sum_{m=1}^{2} b_{\nu m}f'_{nm+2} + \sum_{m=M-1}^{M} b_{\nu m}f'_{nm-2} \tag{27}$$

where f_{nm} and f'_{nm} are equal to the values and first derivates, respectively, of the spanwise pressure modes at the locations $\eta_m = \cos\theta_m$, which are identical with the preassigned abscissas and the Gaussian nodes of equation (23). The quadrature coefficients $b_{\nu m}$ are defined by equations (A5) of the appendix.

The integrals $I_{np}(\eta_\nu)$ of equations (25b) and (25c) can be evaluated immediately using results of reference 6:

$$I_{np}(\eta_\nu) = 2\pi\left[A_{np_{\nu\nu}}f_{n\nu} + \sum_{m=1}^{M}\left(B_{np_{\nu m}} + C_{np_{\nu m}}\right)f_{nm}\right] \tag{28}$$

The coefficients $A_{np_{\nu\nu}}$, $B_{np_{\nu m}}$, and $C_{np_{\nu m}}$ are defined by equations (27),(29), and (30) of reference 6. Only one thing has to be changed: the coefficients $s_m(\eta_i)$ and $s_m(\eta_j)$ are not defined anymore by equation (32) of reference 6, but by equations (A6) of the present paper. In addition, it should be remarked that $f_{n\nu}$ has to be replaced by equation (A7) if the spanwise control-point location is not identical with one of preassigned abscissas or Gaussian nodes.

From all the results, the following set of linear equations for the $(N + 1)M$ unknowns f_{nm} and f'_{nm} is obtained:

$$\alpha(\xi_p,\eta_\nu) = \sum_{n=0}^{N}\sum_{m=1}^{M}\left(b_{\nu m}H_{np_{\nu\nu}} + D_{np_{\nu m}}\right)p_{nm} \tag{29}$$

$$(\nu = 1, 2, \ldots, M;\ p = 0, 1, \ldots, N)$$

where

$$p_{nm} = f'_{nm+2} \text{ , if } m = 1, 2, \text{ and } p_{nm} = f'_{nm-2} \text{ , if } m = M - 1, M$$

$$p_{nm} = f_{nm} \text{ , if } m = 3, 4, \ldots, M - 2$$

$$D_{np_{\nu m}} = \delta_{\nu m} A_{np_{\nu m}} + B_{np_{\nu m}} + C_{np_{\nu m}}$$

$\delta_{\nu m}$ = Kronecker symbol: $\delta_{\nu m} = 0$ for $\nu \neq m$ and $\delta_{\nu m} = 1$ for $\nu = m$

RESULTS

To check the accuracy of the present theory, the loading was calculated for a delta wing (see fig. 5) by the theory of reference 6 and the present method. The results were compared with measurements.

First, a plain wing with a continuous angle-of-attack distribution was investigated. In the present method the preassigned abscissas were identical with those which will be used for the flap-wing configuration. The plots of f_{nm}, obtained from the system of linear equations, equation (29), depended too much on the location of the additional control points, which have to be used besides the Gaussian nodes and preassigned abscissas. However, when these results of equation (29) were put into equation (A7) and $f_n(\eta)$ was then plotted by evaluating equation (A7), the curves became stable as long as the additional control points were close to Gaussian nodes. The only disadvantage of this procedure is that the curves oscillate a little around the accurate curve if the pressure modes have a kink. But this is a well-known feature of trigonometric interpolation polynomials.

In figure 5 the spanwise pressure modes are plotted as computed by the theory of reference 6 (original theory) and by the present method (extended theory). Besides those small oscillations discussed in the preceding paragraph, the results of both methods agree very well with measurements of reference 8. The values in predicting the lift differ from measurements only -1.1 and -1.3 percent in the original and extended theory, respectively. Even x_{ac}/c_r is predicted with an error of only -0.6 and -1.7 percent, respectively.

The next question that arises is: How do those oscillations of the pressure modes predicted by the present method affect the pressure distribution? Figure 6 is a sketch of a theoretically predicted pressure distribution on a delta wing. Because of the difficulties in plotting the pressure accurately near the tips of the actual wing, a dimensionless reference area is used to compare the theoretical pressure distributions with the measured one (see fig. 7). Figure 7 shows that the differences between the original theory of reference 6 and the present extended one are negligible. The agreement between the measurement and the theories is very good except near the leading edge and near the wing tips. But near the leading edge, a difference between theory and

measurement is inevitable since in potential flow theory the pressure goes to infinity like the square root of the distance from the leading edge, whereas the physical pressure is finite. It was mentioned in reference 8 that even at an angle of attack of 4.2°, an onset of stall was observed near the tips of the wing. This could be the reason for the differences between measurements and theory in regions near the wing tips.

The results obtained so far indicate that the concept of the present method seems to be sound. Therefore, the new method is now applied to a wing with a discontinuous angle-of-attack distribution for which the present method was actually developed. The discontinuity in the angle-of-attack distribution is caused by symmetrically deflected flaps. Now the differences between the original theory of reference 6 and the present extended method are remarkable as shown in figure 8. The comparison of both theories with measurements of reference 9 proves that the extended theory predicts the loading more accurately than the original theory. The errors in calculating the lift are -31.5 and 0.2 percent in the original and extended theory, respectively. The aerodynamic center is predicted with an error or -2.0 and -3.2 percent, respectively. The error of the original theory in computing x_{ac}/c_r is, incidentally, smaller than that of the present method since the large error in predicting the lift was compensated by a similar error in computing the pitching moment.

Figure 8 contains some additional interesting results. While the pressure mode f_0, which is proportional to the lift distribution, dominates in comparison to the higher modes f_n ($n = 1, 2, \ldots$) of plain wings (see fig. 5), this is not true in case of a flap-wing configuration (see fig. 8). The pressure modes are converging toward zero very rapidly with increasing numbers of n for the plain wing (f_4 is not plotted in fig. 5 because it is practically zero). In figure 8 (wing with flaps) the absolute values of f_1, f_2, and f_3 in most parts of the wing are larger than f_0. Only f_4 is smaller than f_0. The reason for this behavior of the pressure modes could be that smooth chordwise pressure modes (see eq. (7) and fig. 3) have been used which cannot represent the pressure peak near the hinge line of the flaps. Perhaps, even with proper chordwise pressure modes, more spanwise and chordwise pressure modes are needed for wings with flaps to represent the pressure distribution accurately enough. To answer these questions, chordwise pressure modes that can properly represent the pressure peak near hinge lines of flaps should be added. They should be incorporated anyway because the presently used chordwise pressure modes cannot even approximately represent any pressure distribution of wings with deflected flaps. Suggestions for such pressure modes can already be found in references 10 and 11. In addition, more wings with deflected flaps should be investigated and compared with measurements. In fact, the whole concept of linear lifting-surface theory allows only the treatment of low cambered wings. But a flap deflection angle of 59° is far beyond that limit. It could be that the theory is fortunately applicable to high flap deflection angles or agrees just incidentally well with measurements for the wing configuration being investigated. It should also be noted that the present study is just one possibility for optimizing the control-point locations for arbitrary flap-wing configurations. There could easily be other and better methods.

CONCLUSIONS

A general procedure has been developed to allow the choice of spanwise control-point locations in Multhopp-Truckenbrodt type lifting-surface theories. In these methods the spanwise distribution of the control points has been fixed and prescribed so far. However, this constraint can cause inaccuracies in fulfilling the boundary conditions, if the theories are applied to wings with a discontinuity in the spanwise angle-of-attack distribution (e.g., flapped wings, wings with tip tanks and wing-body configurations). Therefore, a procedure has been developed which allows the location of two spanwise control points at arbitrary positions of each semispan. The rest of the spanwise control points are then distributed in an optimal manner.

An original method (ref. 6) which is an extension and an improvement of Multhopp's (ref. 3) and Truckenbrodt's (ref. 4) theories was extended with respect to the flexibility in the choice of the control-point locations. The original and extended methods were then used to calculate the loading of a delta wing with and without flaps. Comparison with measurements showed that both theories quite accurately predicted the loading of a plain wing without flaps. On the other hand only the extended method predicted accurately the lift and aerodynamic center of a flapped wing.

APPENDIX

CALCULATION OF QUADRATURE COEFFICIENTS

$$I_1 = \lim_{\varepsilon \to 0} \left[\frac{2}{\varepsilon} f_n(\eta_\nu) - \fint_{-1}^{+1} \frac{f_n(\eta) d\eta}{(\eta_\nu - \eta)^2} \right] = \oint_0^\pi \frac{(df_n/d\eta) \sin\theta \, d\theta}{\cos\theta_\nu - \cos\theta} \tag{A1}$$

Introducing equation (23) and differentiating with respect to η yields:

$$I_1 = \sum_{\mu=1}^{M} \left[\sum_{j=1}^{2} R_{j\mu} f_n'(\eta_{j+2}) + \sum_{j=M-1}^{M} R_{j\mu} f_n'(\eta_{j-2}) + \sum_{j=3}^{M-2} R_{j\mu} f_n(\eta_j) \right] \mu \oint_0^\pi \frac{\cos\mu\theta \, d\theta}{\cos\theta - \cos\theta_\nu} \tag{A2}$$

The integral can be solved analytically:

$$\oint_0^\pi \frac{\cos\mu\theta \, d\theta}{\cos\theta - \cos\theta_\nu} = \pi \frac{\sin\mu\theta_\nu}{\sin\theta_\nu} \tag{A3}$$

The relationships of equations (24) transform I_1 into

$$I_1 = \sum_{j=1}^{2} f_n'(\eta_{j+2}) b_{\nu j} + \sum_{j=M-1}^{M} f_n'(\eta_{j-2}) b_{\nu j} + \sum_{j=3}^{M-2} f_n(\eta_j) b_{\nu j} \tag{A4}$$

where

$$b_{\nu j} = \frac{G_j \bar{b}_{\nu j}}{\sin\theta_\nu} \qquad (j = 1, 2, M - 1, M \text{ and } 5, 6, \ldots, M - 4) \tag{A5a}$$

$$b_{\nu j} = \frac{G_j \bar{b}_{\nu j} - G_{j-2} c_{\nu j} / \sin\theta_j}{\sin\theta_\nu} \qquad (j = 3, 4) \tag{A5b}$$

$$b_{\nu j} = \frac{G_j \bar{b}_{\nu j} - G_{j+2} c_{\nu j} / \sin\theta_j}{\sin\theta_\nu} \qquad (j = M - 3, M - 2) \tag{A5c}$$

The coefficients $\bar{b}_{\nu j}$ and $c_{\nu j}$ are sums over μ and can be evaluated in closed form:

$$\bar{b}_{\nu j} = 2\sum_{\mu=1}^{M} \mu \sin \mu\theta_\nu \sin \mu\theta_j$$

$$= \frac{1}{2}\left\{ M\left[M + \frac{2(\sin M\theta_\nu \sin \theta_\nu - \cos M\theta_\nu \cos \theta_\nu)\sin M\theta_\nu}{\sin \theta_\nu}\right] + \left(\frac{\sin M\theta_\nu}{\sin \theta_\nu}\right)^2 \right\} \quad \text{if } \theta_\nu = \theta_j$$

$$= M\left[\sin M\theta_\nu \sin M\theta_j + \frac{(\sin M\theta_\nu \cos M\theta_j \sin \theta_j - \cos M\theta_\nu \sin M\theta_j \sin \theta_\nu)}{\cos \theta_j - \cos \theta_\nu}\right]$$

$$+ \frac{(1 - \cos \theta_\nu \cos \theta_j)\sin M\theta_\nu \sin M\theta_j - \sin \theta_\nu \sin \theta_j (1 - \cos M\theta_\nu \cos M\theta_j)}{(\cos \theta_j - \cos \theta_\nu)^2} \quad \text{if } \theta_\nu \neq \theta_j$$

$$c_{\nu j} = 2\sum_{\mu=1}^{M} \mu^2 \sin \mu\theta_\nu \cos \mu\theta_j$$

$$= M^2\left[\sin M\theta_\nu \cos M\theta_\nu + \frac{(2 \sin^2 M\theta_\nu - 1)\cos \theta_\nu}{2 \sin \theta_\nu}\right] + \frac{M \sin M\theta_\nu \cos M\theta_\nu}{\sin^2 \theta_\nu}$$

$$- \frac{\sin^2 M\theta_\nu \cos \theta_\nu}{2 \sin^3 \theta_\nu} \quad \text{if } \theta_\nu = \theta_j$$

$$c_{\nu j} = M^2 \sin M\theta_\nu \cos M\theta_j - \frac{M^2(\cos M\theta_\nu \cos M\theta_j \sin \theta_\nu + \sin M\theta_\nu \sin M\theta_j \sin \theta_j)}{\cos \theta_j - \cos \theta_\nu}$$

$$+ \frac{2M[(1 - \cos \theta_\nu \cos \theta_j)\sin M\theta_\nu \cos M\theta_j - \sin M\theta_j \cos M\theta_\nu \sin \theta_j \sin \theta_\nu]}{(\cos \theta_j - \cos \theta_\nu)^2}$$

$$+ \frac{\begin{pmatrix} (\cos M\theta_\nu \cos M\theta_j - 1)\sin \theta_\nu(2 - \cos \theta_j \cos \theta_\nu - \cos^2 \theta_j) \\ + \sin M\theta_\nu \sin M\theta_j \sin \theta_j(2 - \cos \theta_j \cos \theta_\nu - \cos^2 \theta_\nu) \end{pmatrix}}{(\cos \theta_j - \cos \theta_\nu)^3} \quad \text{if} \quad \theta_\nu \neq \theta_j$$

If equations (24) are put into equation (23), the summations over μ can be evaluated in closed form:

$$\bar{s}_m(\theta) = 2 \sum_{\mu=1}^{M} \sin \mu\theta_m \sin \mu\theta$$

$$= M + \sin^2 M\theta_m - \frac{\sin M\theta_m \cos M\theta_m \cos \theta_m}{\sin \theta_m} \quad \text{if} \quad \theta = \theta_m$$

$$= \sin M\theta_m \sin M\theta + \frac{(\sin M\theta_m \cos M\theta \sin \theta - \sin M\theta \cos M\theta_m \sin \theta_m)}{\cos \theta - \cos \theta_m}$$

$$\text{if} \quad \theta \neq \theta_m$$

$$r_m(\theta) = 2 \sum_{\mu=1}^{M} \mu \cos \mu\theta_m \sin \mu\theta$$

$$= \sin M\theta_m \cos M\theta_m(M + 0.5/\sin^2 \theta_m) + \frac{M(\sin^2 M\theta_m - 0.5)\cos \theta_m}{\sin \theta_m} \quad \text{if} \quad \theta = \theta_m$$

$$= M\left[\sin M\theta \cos M\theta_m + \frac{(\cos M\theta \cos M\theta_m \sin \theta + \sin M\theta \sin M\theta_m \sin \theta_m)}{\cos \theta - \cos \theta_m}\right]$$

$$+ \frac{(1 - \cos \theta \cos \theta_m)\sin M\theta \cos M\theta_m - \cos M\theta \sin M\theta_m \sin \theta \sin \theta_m}{(\cos \theta - \cos \theta_m)^2}$$

where θ is equal to arc cos η_i or arc cos η_j. Thus, the coefficients $s_m(\eta_i)$ or $s_m(\eta_j)$ are obtained from:

$$s_m(\eta) = \frac{1}{\pi} G_m \bar{s}_m(\theta) \qquad (m = 1, 2, M - 1, M, \text{ and } 5, 6, \ldots, M - 4) \tag{A6a}$$

$$s_m(\eta) = \frac{1}{\pi} \left[G_m \bar{s}_m(\theta) - \frac{G_{m-2} r_m(\theta)}{\sin \theta_m} \right] \qquad (m = 3, 4) \tag{A6b}$$

$$s_m(\eta) = \frac{1}{\pi} \left[G_m \bar{s}_m(\theta) - \frac{G_{m+2} r_m(\theta)}{\sin \theta_m} \right] \qquad (m = M - 3, M - 2) \tag{A6c}$$

Hence,

$$f_n(\eta) = f_n(\text{arc cos } \eta) = \sum_{m=1}^{2} s_m(\eta) f'_{nm+2} + \sum_{m=M-1}^{M} s_m(\eta) f'_{nm-2} + \sum_{m=3}^{M-2} s_m(\eta) f_{nm} \tag{A7}$$

REFERENCES

1. Landahl, M. T.; and Stark, V. J. E.: Numerical Lifting-Surface Theory - Problems and Progress. Preprint 68-72, AIAA, 1968.

2. Watkins, C. E.; Woolston, D. S.; and Cunningham, H. G.: A Systematic Kernel Function Procedure for Determining Aerodynamic Forces on Oscillating or Steady Finite Wings at Subsonic Speeds. NASA TR R-48, 1959.

3. Multhopp, H.: Methods for Calculating the Lift Distribution of Wings (Subsonic Lifting-Surface Theory). A.R.C. Rep. and Mem. 2884, 1955.

4. Truckenbrodt, E.: Tragflaechentheorie bei inkompressibler Stroemung. WGL Jahrbuch, 1953, pp. 40-65.

5. Multhopp, H.: Die Berechnung der Auftriebsverteilung von Tragfluegeln. Luft.-Forschung, vol. 15, 1938, pp. 153-169.

6. Wagner, S.: On the Singularity Method of Subsonic Lifting-Surface Theory. Preprint 69-37, AIAA, 1969.

7. Hildebrand, F. B.: Introduction to Numerical Analysis. McGraw-Hill Book Co., Inc., New York, 1956.

8. Graham, D.: Chordwise and Spanwise Loadings Measured at Low Speeds on a Large Triangular Wing Having an Aspect Ratio of 2 and a Thin, Subsonic-Type Airfoil Section. NACA RM A50A04a, 1950.

9. Kelly, M. W.; and Tolhurst, W. H.: The Use of Area Suction to Increase the Effectiveness of a Trailing-Edge Flap on a Triangular Wing of Aspect Ratio 2. NACA RM A54A25, 1954.

10. Landahl, M.: Pressure-Loading Functions for Oscillating Wings With Control Surfaces. AIAA J., vol. 6, no. 2, 1968, pp. 345-348.

11. Crespo, A. N.; and Cunningham, H. J.: On the Calculation of the Three-Dimensional Pressure Distribution on Wings With Control Surfaces, Based on the Integral Equation for Subsonic Flow. NASA TN D-5419, 1969.

EXAMPLES FOR SPANWISE ANGLE-OF-ATTACK DISTRIBUTIONS WITH DISCONTINUITIES

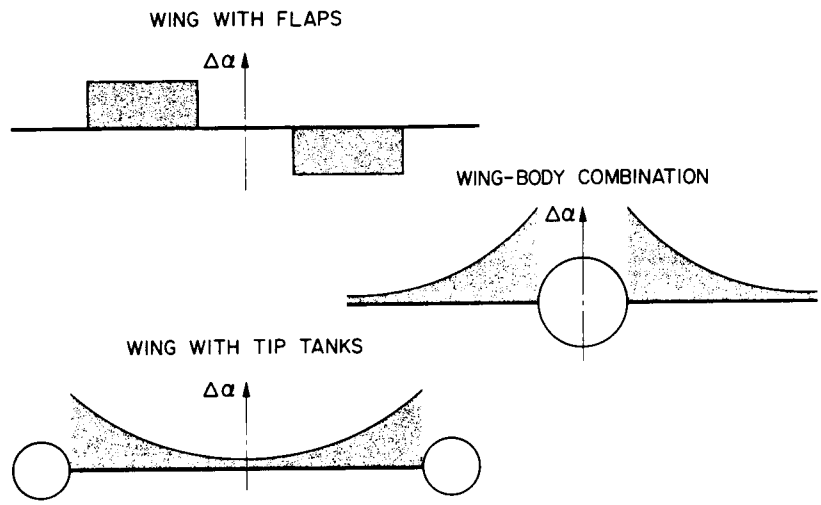

Figure 1

WING GEOMETRY AND COORDINATE SYSTEM

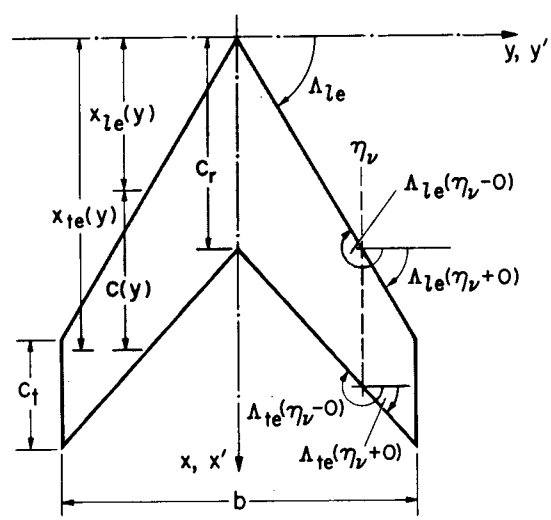

Figure 2

CHORDWISE PRESSURE DISTRIBUTION FUNCTIONS

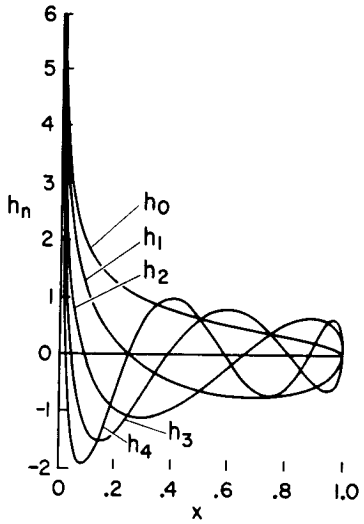

Figure 3

SPANWISE CONTROL-POINT LOCATIONS

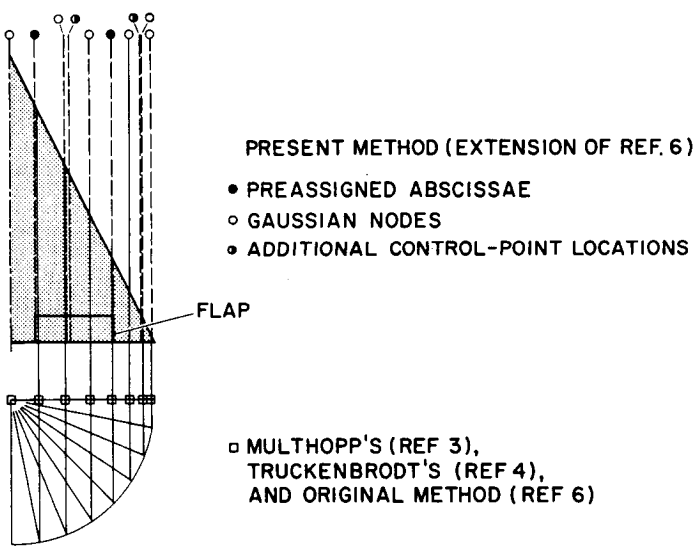

Figure 4

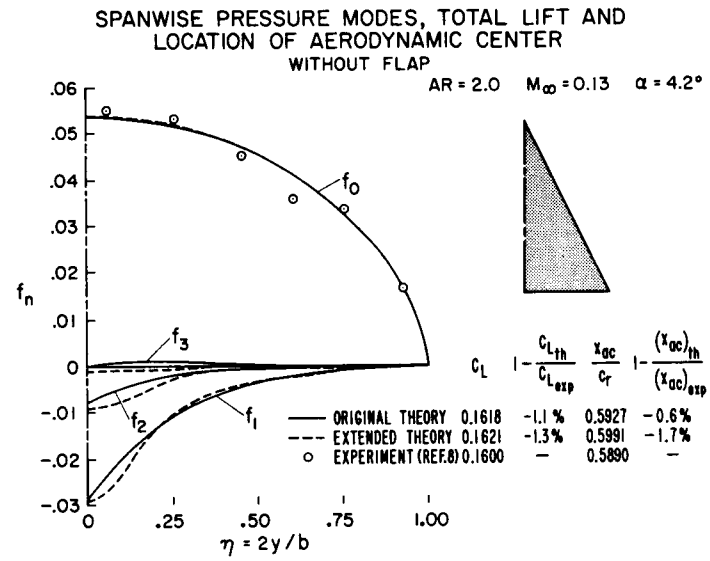

Figure 5

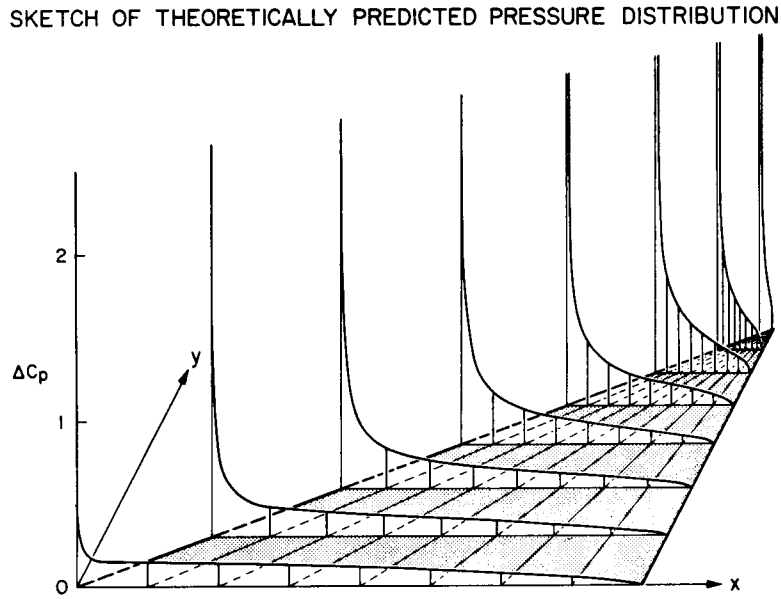

Figure 6

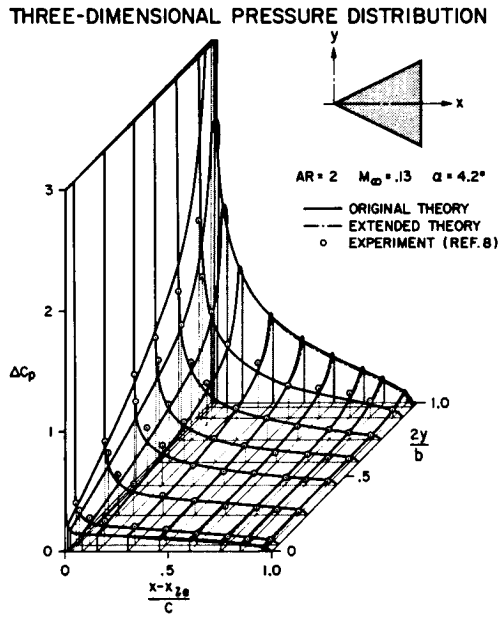

Figure 7

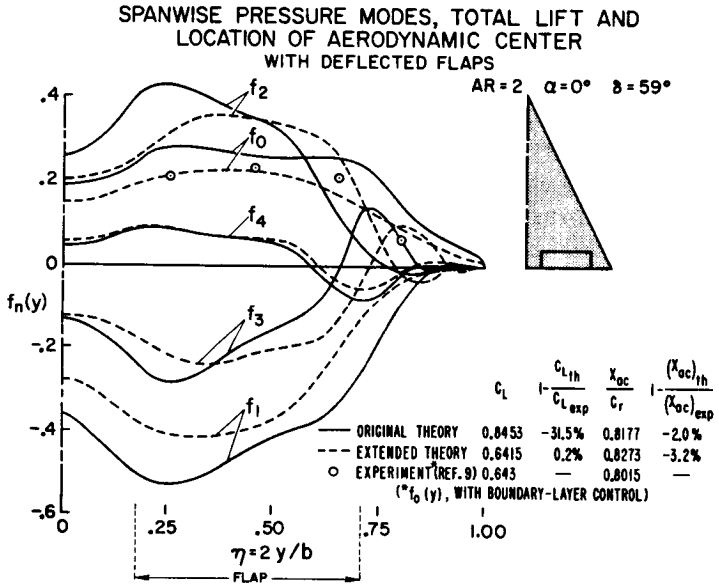

Figure 8

DISCUSSION

WILLIAM P. RODDEN, Consulting Engineer: I'd like to ask Dr. Wagner and John Lamar, if he is here from Langley, why we need two more modifications of Multhopp's method. The vortex lattice method and the doublet lattice method for the oscillatory case have been demonstrated in the last few years to be tremendously simple and versatile in terms of the arbitrary types of configurations that can be handled. They also seem to have as much accuracy as is available from any other method, and they provide solutions when you are not in a position to guess at the pressure functions, the basic functions needed by Multhopp and Truckenbrodt.

WAGNER: Well, this question is not very easy to answer, because it is true that the vortex lattice methods accurately predict in many cases most of the data a design engineer wants to know. But there are always some cases where we need a better approximation of the physical flow by a lifting surface theory. For instance, if you are going to calculate the leading-edge suction force, it is very difficult to do this with a vortex lattice method because the pressure distribution is not continuous.

I haven't been working so much with vortex lattice methods, so I can only answer this question as far as I have gotten answers from communication with other people. I have learned that these vortex lattice methods are quite sensitive to the selection of the control-point locations and box sizes. There are some cases where, if you have not selected these control points or box sizes properly, the answers might not be very good.

JOSEPH P. GIESING, Douglas Aircraft Company: You mentioned difficulty in calculating the induced drag distribution by the vortex lattice method. We used the basic approach where you just use Prandtl's basic $F = \rho V X \Gamma$. We get very excellent agreement with, say, Garner's results, so we don't need really to calculate the leading-edge suction.

Also, as far as the optimum control point problem (for the lattice method) is concerned, we believe we have this one worked out. We use one specific set of control point rules, obtained from two-dimensional analysis, and this has given us accurate results in all cases that we have tried for very complicated configurations.

WAGNER: Well, if you have gotten good results, I don't have any objections. Maybe it is really better to use those vortex lattice methods. If this is true, why not? Then you can leave all these methods, which are very complicated, such as this lifting-surface method. I don't have any objections against that.

ATLEE M. CUNNINGHAM, JR., General Dynamics, Fort Worth Division: I'd like to say something in support of your method versus the vortex lattice and doublet lattice methods. Although these collocation type methods are more complex, once you get the associated problems worked out, in the end I feel that these types of methods will give some solutions more efficiently.

As an example, you could take a configuration where you might require 64 doublet lattice panels to obtain nearly the same solution that you would get with six control points through the use of a collocation method. So my contention is that although the doublet lattice and vortex panel methods now allow us to treat more complex cases, in the end I believe we will be able to arrive at more efficient solutions once we understand more about these assumed pressure modes and so forth that are required.

I would like to know if you looked at the effect of choosing these off Gaussian chords, that is, what the effect is on trying to account for the spanwise singularity?

WAGNER: I didn't quite understand what you mean. What the effect of the spanwise singularity is, when we are doing what?

CUNNINGHAM: When you are taking these slightly off Gaussian control points.

WAGNER: Oh, I see. I have done this before, going off of these Gaussian control points, and what you usually get is very violent oscillation. So if you go away from those Gaussian nodes, you cannot guarantee results, because they depend on the control-point location, and of course this result is not good to use because you don't know whether you get results from the wing configuration or from the location of the control points.

CUNNINGHAM: I have been working with this control surface problem and I have derived a pressure function which also accounts for the chordwise singularity as well as the spanwise variation and I find it works quite well using the standard control points (the control points of Hsu, which spanwise are the same as your spanwise points).

WAGNER: Now, you are talking about chordwise.

CUNNINGHAM: No, I was talking about the spanwise points, the Gaussian points as you had derived. I found that the chordwise points were more critical, and that the solution is very sensitive to where these are located.

WAGNER: Well, in my case, I am using as chordwise control points one at the leading edge, one at the trailing edge; then I am distributing the points between the leading edge and trailing edge equidistantly.

But I have heard from other people - I was talking to some gentlemen at Lockheed - and they indicated it would probably be better to distribute the chordwise location of the control points by the same procedure as we are using for the spanwise locations. But it is advisable to have a control point at the leading edge and at the trailing edge, because there is a paper which was presented by Dr. Jordan[1] and it indicates that if you are taking more and more chordwise control points, then the Multhopp procedure

---

[1]Jordan, P. F.: Remarks on Applied Subsonic Lifting Surface Theory. Wissenschaftliche Gesellschaft für Luft-und Raumfahrt, Jahrbuch 1967, pp. 192-210.

might diverge if you don't take at the same time more spanwise control points and if you are not using the correction for the logarithmic singularities, whereas if you are using a control point at the leading edge and at the trailing edge you can prevent this divergence.

GEORGE R. BARTÉ, JR., General Electric Company: I'd like to add just a brief historical footnote. In earlier conversations - for the benefit of those attendees here, I had spent a little time with Dr. Wagner, and at the time the question of who came up with what method first was discussed briefly. It turns out that both in England and in Germany, Truckenbrodt and Multhopp arrived independently at very similar approaches to the question of calculating wing lift distributions.

In Germany at that time, Multhopp, then with Fockewulf and now with the General Electric Company, prefers to reserve some of his advanced work for later publication on the presumption it gives certain advantages in a competitive industry.

EDITOR'S COMMENT

Following the first paper of the Symposium by Siegfried N. Wagner, Joseph P. Giesing of Douglas Aircraft Company asked for time to present some prepared comments (with figures). He was given ten minutes in which to present a short progress report on the doublet lattice approach in subsonic lifting surface theory. The doublet lattice method is an unsteady extension to the vortex lattice method and is very simple, since it does not require loading functions. However, it does have important limitations and should be applied with special care and knowledge, as emphasized by the comments which follow the prepared slides and written remarks of Giesing.

PREPARED FIGURES AND REMARKS OF JOSEPH P. GIESING, Douglas Aircraft Company

FIGURE 1

Figure 1 compares the spanwise lift-curve-slope distribution across a wing-fuselage combination as calculated by Douglas (nonplanar) (ref. 1), Douglas (planar) (ref. 2), and Woodward (ref. 3). Lifting surface panels were placed both on the wing and fuselage for the Douglas (nonplanar) and Woodward methods. The control point on each box in the Woodward method was selected as the 85-percent point on the basis of two-dimensional calculations. Woodward, in reference 3, incorrectly suggests the 95-percent point. The control point for the Douglas methods, both planar and nonplanar, is at the 75-percent point of each box. The Douglas nonplanar method and the Woodward method agree. Slight disagreement between these and the Douglas planar method is observed however. The Douglas planar method uses an image system within the fuselage instead of lifting surface elements on the fuselage surface. The image system eliminates the wing root singularity (the flow is infinite at the terminus of a lifting surface) and thus is probably more accurate than the Douglas nonplanar or the Woodward methods for this case.

FIGURE 2

Figure 2 compares the static stability derivatives as calculated by Douglas (nonplanar) (ref. 1) and Belotserkovskii (ref. 4), for annular wings of various diameter to length ratios.

FIGURE 3

Dynamic stability derivatives for annular wings of various diameter to length ratios are given in figure 3. The oscillatory aerodynamic method was evaluated at low values of reduced frequency for these calculations (see ref. 5).

FIGURE 4

Figure 4 presents calculation for a wing with and without pylons. In steady flow a comparison is made between the Douglas nonplanar method and the

method of Blackwell, reference 6. Also shown are calculations done for the wing oscillating in pitch (about its apex) at a reduced frequency of 0.5.

FIGURE 5

The pressure distributions as calculated by the Douglas nonplanar method and the method of Zwaan, reference 7, are compared with Experiment. The T-tail is oscillating in yaw at a frequency of 0.55.

FIGURE 6

The induced drag distribution is not calculated in the usual way by the Douglas method. Instead of determining the leading-edge suction along with the normal force drag, the Douglas vortex-doublet lattice method uses the fundamental Kutta-Joukowski law. The upwash at each bound vortex is determined and multiplied by the vortex strength to obtain the local contribution to the induced drag.

Figure 6 compares the spanwise induced drag distribution as calculated by Douglas and by Garner, reference 8. The agreement is very good except at the wing tips where Garner's results seem to be ambiguous. The numbers N in Garner's calculation represent the number of chordwise loading functions used.

It may be remarked that the spanwise distribution of induced drag is very sensitive to the spanwise loading. Small changes in span load cause large variations in the induced drag distribution. The total induced drag is, however, not as sensitive.

FIGURE 7

A comparison of induced drag distribution for a variable sweep configuration as calculated by Wagner, reference 9, and Douglas is given in figure 7. The distributions do not agree nearly as well as in the hyperbolic wing case.

REFERENCES

1. Kalman, T. P.; Rodden, W. P.; Giesing, J. P.: Aerodynamic Influence Coefficients by the Doublet Lattice Method for Interfering Nonplanar Lifting Surfaces Oscillating in a Subsonic Flow. Rep. DAC-67977, McDonnell Douglas Aircraft Co., October 1969.

2. Giesing, J. P.: Lifting Surface Theory for Wing-Fuselage Combinations. Rep. DAC-67212, McDonnell Douglas Aircraft Co., Aug. 1, 1968.

3. Woodward, F. A.: A Unified Approach to the Analysis and Design of Wing-Body Combinations at Subsonic and Supersonic Speeds. J. Aircraft, vol. 5, no. 6, November-December 1968.

4. Belotserkovskii, S. M.: The Theory of Thin Wings in Subsonic Flow. Plenum Press, N. Y., 1967.

5. Rodden, W. P.; and Giesing, J. P.: Application of Oscillatory Aerodynamic Theory for Estimation of Dynamic Stability Derivatives. Paper 5630, McDonnell Douglas Aircraft Co.

6. Blackwell, J. A., Jr.: A Finite Step Method for Calculation of Theoretical Load Distributions for Arbitrary Lifting-Surface Arrangements at Subsonic Speeds. NASA TN D-5335, 1969.

7. Zwaan, R. J.: Application of a Method for Estimating Experimental Pressure Distributions to an Oscillating T-Tail. Rep. TR 68048L, National Aerospace Laboratory NLR, The Netherlands, Jan. 1968.

8. Garner, H. C.; Hewitt, B. L.; Labrujere, T. E.: Comparison of Three Methods for the Evaluation of Subsonic Lifting-Surface Theory. NLR TN G. 65, June 1968.

9. Wagner, S.: On the Singularity Method of Subsonic Lifting Surface Theory. Paper 69-37, AIAA, Jan. 1969.

LIFT DISTRIBUTION ON A WING FUSELAGE COMBINATION

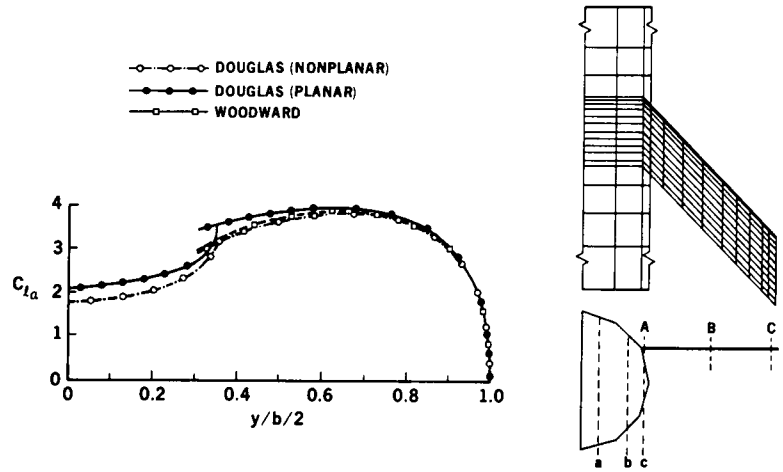

Figure 1

STATIC STABILITY DERIVATIVES FOR ANNULAR WINGS

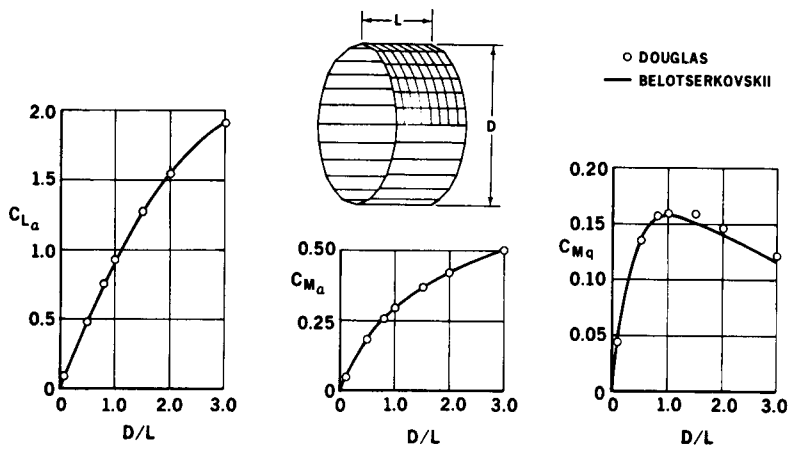

Figure 2

DYNAMIC STABILITY DERIVATIVES FOR ANNULAR WINGS

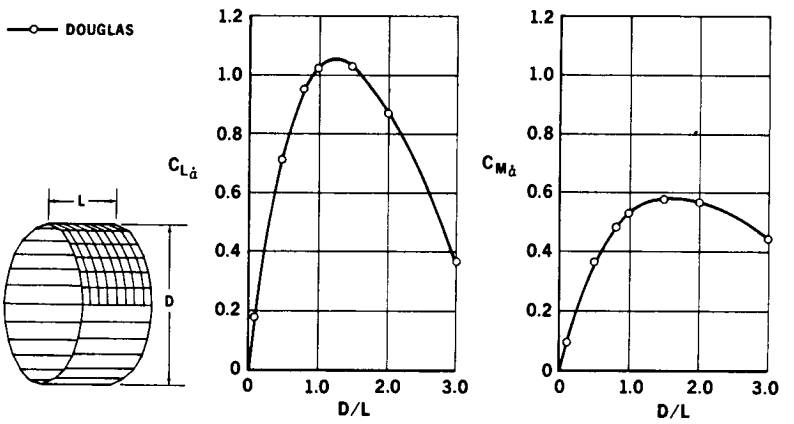

Figure 3

LIFT DISTRIBUTION ON A WING WITH PYLON

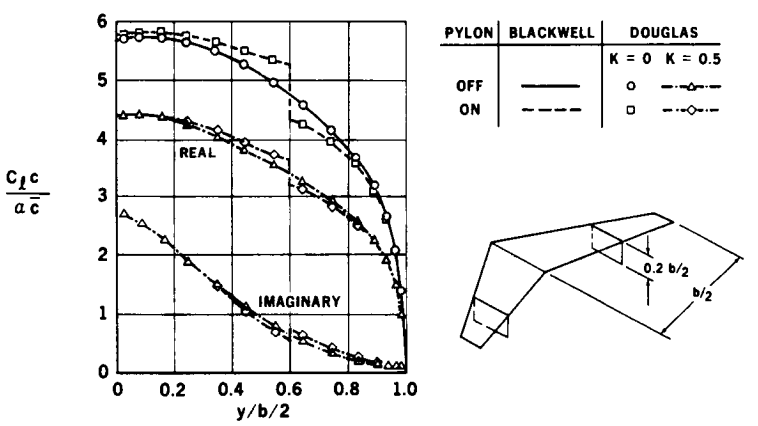

Figure 4

PRESSURES ON A T-TAIL OSCILLATING IN YAW

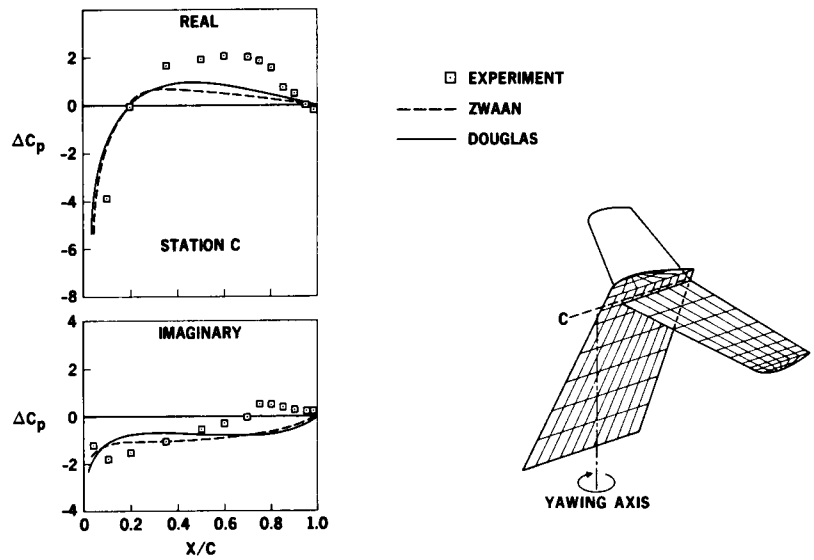

Figure 5

INDUCED DRAG DISTRIBUTION

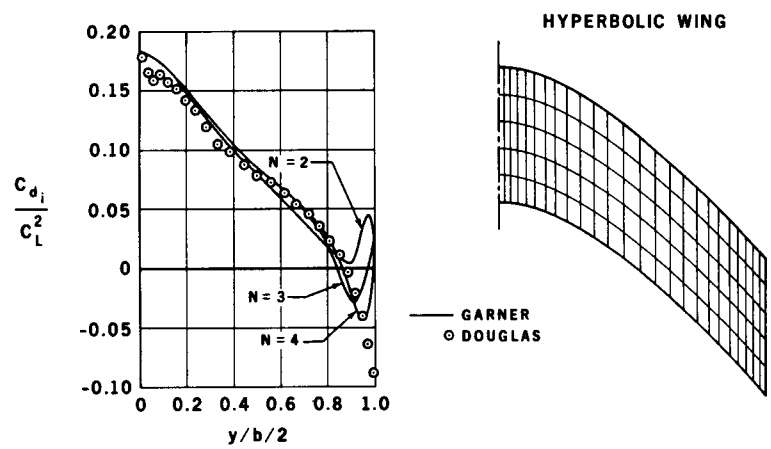

Figure 6

INDUCED DRAG DISTRIBUTION

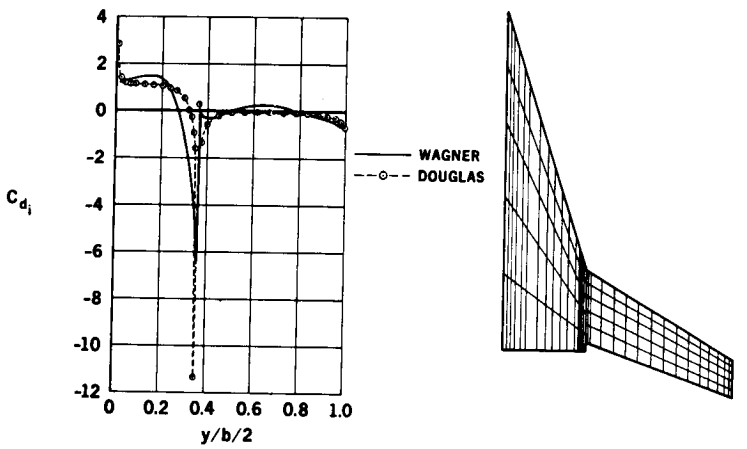

Figure 7

DISCUSSION

JACK N. NIELSEN, Nielsen Engineering and Research Inc.: From what I understood you to say earlier, you indicated that the induced drag you calculate was just as accurate as the induced drag that Siegfried Wagner gets using his method. I don't know Garner's results with which you compared. Well, do they treat the leading-edge singularity accurately?

GIESING: Will you show the second to the last slide? Garner showed a conversion study with various numbers of terms. As you see, n, n_2, n_3, n_4, that's his conversion study. Garner was putting more chordwise variables to determine his spanwise --

NIELSEN: The number of chordwise stations is the thing that is important. You see, the problem is you have to get the strength of the leading-edge singularity accurately. Depending on how far your nearest control point is from the leading edge, you get more or less leading-edge suction.

GIESING: Right.

NIELSEN: Therefore, I think that the accuracy of your method basically depends on how many chordwise panels you put on the wing, but that's not the case in Wagner's work because he uses the Munk stagger theorem to get the strength of the leading-edge singularity. So it seems to me there is a basic advantage to his method.

GIESING: Well, Wagner uses the coefficients of the terms in the chordwise series to get the leading-edge suction. That's right.

We do not pretend to get the leading-edge suction at all. We do not get it. We use the basic Kutta-Joukowski law.

NIELSEN: The strength depends on how close you get your control point to the leading edge.

GIESING: So does the upwash.

ROBERT T. STANCIL, LTV Aerospace Corp.: That also means that your answer requires full leading-edge suction.

GIESING: Full leading-edge suction? Yes.

STANCIL: It means that you cannot correlate some percentage of leading-edge suction or assume no leading-edge suction, is that right?

GIESING: Well, we haven't even thought about it, but on the face of it, no, you can't.

STANCIL: I think in the real world you never do achieve full leading-edge suction, but it is significant to know approximately how much or whether there is some peak in it that you would not expect to get in the real world.

GIESING: I agree.

SIEGFRIED WAGNER: First of all, I would like to say that both of these methods, the vortex lattice methods and the lifting-surface type methods, have their significance and are very important. For instance, I have no doubt that your methods are very well applicable to wing design, and they predict the lift and the pitching moment reasonably well. Also, these methods are applicable to more complicated configurations to which the lifting-surface method, the continuous distribution of vorticity, is not yet applicable. But the basic approach of the lifting-surface theory will probably ultimately give you the best answer because your method depends on the panel size or the position of the control points, and I have no doubt that you can arrange these variables so that you always get fine answers. But there might be questions in a very small region of the flow field where we have to know the flow field very accurately, for instance, near the leading edge or near slots of deflected flaps, and so on. Therefore, we need a better answer, and for this reason I am working on these lifting-surface theories to develop them to a point where they can be used as easily as the vortex lattice methods, but we are far away from this point.

Therefore, I am not going to say that I am replacing all your methods. I see the significance and importance of your methods. I think the lifting-surface methods as such are also very important to be studied, and it is important to continue their development to where they can be as easily handled as your methods.

THE USE OF FINITE ELEMENT METHODS FOR PREDICTING THE AERODYNAMICS OF WING-BODY COMBINATIONS

By Ralph L. Carmichael and Charles R. Castellano
Ames Research Center

and

Chuan F. Chen
Rutgers University

2

N70-21353

SUMMARY

The method of finite elements is a procedure for solving linear partial differential equations by the superposition of a large number of elementary solutions in such a way as to approximate the exact boundary conditions. Computer programs based upon this method are able to predict the subsonic and supersonic aerodynamic characteristics of wing-body combinations with very few restrictions on geometry. Comparisons between finite element solutions and established benchmark solutions indicate that the approximations involved introduce negligible amounts of error.

INTRODUCTION

The principal objective of this paper is to summarize the principles of the method of finite elements for solving problems in the external aerodynamics of complex configurations in subsonic and supersonic flow. The method of finite elements is a procedure for solving linear partial differential equations with complicated boundary conditions by superposing a large number of elementary solutions in such a way as to approximate the exact boundary conditions.

The secondary objective is to describe the computer programs developed by the NASA which enable one to estimate the aerodynamic characteristics of wing-body combinations. The ultimate objective of this work is to prepare a collection of procedures of sufficient generality to handle the actual geometrical description of flight vehicles, although the current programs require a somewhat idealized configuration.

SYMBOLS

$\mathcal{A}R$ aspect ratio

b span

Preceding page blank

C local chord

C_{av} average chord of wing, $\frac{\text{area}}{\text{span}}$

C_{D_i} induced drag

C_L lift coefficient

C_{L_α} $\frac{dC_L}{d\alpha}$

C_l section lift coefficient

C_m pitching-moment coefficient

C_{m_α} $\frac{dC_m}{d\alpha}$

ΔC_p $\frac{\text{pressure on lower surface - pressure on upper}}{\text{dynamic pressure}}$

C_R root chord

M Mach number

q dynamic pressure

y distance coordinate in span direction

α angle of attack

β $\sqrt{M^2-1}$

Λ sweep angle

THEORY

Concept of the Method of Finite Elements - The Airship Problem

One of the first problems in aerodynamics to be studied by theoretical methods was that of the pressure distribution on an airship (fig. 1). Once the configuration was idealized to a body of revolution at zero angle of attack, it was found that the flow about the airship could be represented by a distribution of sources along the axis and that an integral equation could be written which related this source distribution to the geometry of the airship. For certain simple mathematical shapes, this integral equation could be solved, and from the resulting source distribution one could compute the

pressure loading on the airship. A typical solution (for a quadratic variation of radius) is shown in the lower left of figure 2. The general case remained intractable, however, because of the mathematical difficulties in treating complicated expressions and because airship dimensions were not specified by mathematical equations but by tables of coordinates from engineering drawings. Since the exact closed-form solution could not be obtained, various attempts at approximating the solution were tried, and the method of finite elements was one of the most successful of these approximations.

The essential concept of the method of finite elements is illustrated in the lower right of figure 2. Since the smooth curve representing the exact solution cannot, in general, be obtained, it is assumed that a simple function (dashed lines) closedly approximates the smooth function. (Note: a simple function is defined as one that assumes only a finite set of values.) This means that we are now representing the physical boundary of the airship by a finite number of sources of constant strength instead of a continuous source distribution.

The mathematical problem of the source distribution of constant strength can be solved in closed form in terms of elementary functions; hence the problem is to find the best choice of these finite values of the simple function in order to approximate the exact solution. This is done by establishing a set of control points on the body and requiring that the flow be tangent to the surface at each point. If there are N sources, then there are N control points and the problem can be formulated as the simultaneous solution of N linear algebraic equations in N unknowns. With computers, it is feasible for N to assume quite large values, although it has been our experience that values of 25 to 50 provide adequate accuracy.

Let us emphasize that the velocities induced by each of the individual constant source elements are exact solutions of the linearized equation of flow and hence the superposition of all of them is also an exact solution to the partial differential equation. The approximation that is made is in the boundary conditions; the flow is required to be tangent to the body only at the N control points and not at every point on the body surface.

Finite Element Concepts for Configuration Synthesis

The distribution of sources along a line simulates the flow about a body of revolution at zero angle of attack. For the representation of the flow about other shapes, there are other basic finite element solutions (fig. 3). In each case, there is a closed-form solution to the fundamental linearized equation of flow, either subsonic or supersonic. The line doublets, in conjunction with the line sources, simulate a body of revolution at angle of attack. The surface elements represent both thickness and lifting effects of wings. The surface thickness elements are wedges with swept leading and trailing edges. The surface lifting elements are thin surfaces which support a constant pressure differential across the surface. Such a surface is, by its nature, highly warped near the root and tip regions. The combination of surface thickness and lifting elements simulates the flow about a thin lifting wing of finite thickness.

Combination of Finite Elements to Represent a Wing-Body Combination

By use of the finite element solutions described above, we can describe components of airplane configurations. As stated previously, the line sources and doublets represent an isolated lifting body and the surface thickness and lifting elements represent an isolated lifting wing. If the elements representing these isolated components are placed in close proximity, as in a wing-body combination, the resultant flow about the body will penetrate the wing and vice versa; hence the boundary conditions will be violated. In order to represent a wing-body combination, it is necessary to use additional elements to satisfy the boundary conditions in the presence of interfering fields. One method for doing this is to locate surface lifting elements on the surface of the body (fig. 4) and adjust the pressure across the wing and body panels simultaneously to insure that there is no mass flow through the surface of the wing-body combination. If there are N finite elements, then we establish N control points on the configuration and require that the net velocity satisfy the boundary condition at each of these points. In general, the more elements used to represent a configuration, the greater the accuracy of the solution, and the practical upper limit on the number of elements is the maximum number of simultaneous linear algebraic equations that can be solved.

APPLICATION

Comparisons Between Finite Element Method and Exact Linear Theory

Since this procedure is an approximate method, it is desirable to study the magnitude of error introduced by the assumption of finite elements. To make such estimates, some comparisons are made between well-known established solutions and solutions obtained by finite elements. In supersonic flow, there are exact solutions to the linear theory for conical wings. In figure 5, the results of the finite element computing program are compared to exact linear theory (ref. 1) for both supersonic and subsonic leading-edged delta wings. The solid lines are the exact solution and the symbols are the program output. In figure 6, a comparison is made for a swept, constant-chord wing with subsonic leading and trailing edges. Here, the exact solution may be obtained by superposition of several conical fields (ref. 2). As in the previous case, the finite element procedure provides quite adequate approximations to the exact solutions.

In subsonic flow, in contrast to supersonic, there are no exact soltuions to which we may compare program results. For the purposes of making similar comparisons at subsonic speeds, we use the highly perfected lifting surface theories based on Multhopp's original idea (refs. 3 and 4). Figure 7 shows the results of one such comparison. The solutions labelled

"modified Multhopp" are from Lamar (ref. 4), and the finite element solutions are from our computing program. As can be seen the results are very close. These and other similar results indicate that the method of finite elements is very accurate for solving problems in subsonic and supersonic wing theory.

For wing-body combinations, there are yet fewer benchmark results with which to make studies of the accuracy of approximate methods. Some of these results and comparisons to finite element solutions may be found in reference 5. It is concluded in reference 5 that the finite element (or panel) method does not introduce significant errors into the calculation of wing-body interference at supersonic speeds.

Application to Complex Configuration

The method of finite elements is, therefore, as accurate as any existing linear theory procedure for calculating the aerodynamic characteristics of these simple shapes. It has the added virtue of being programmed for rapid solution on a digital computer. The great value of the method lies in its ability to generate solutions for complex configurations which can be solved in no other way, for example, the lifting body under the lifting wing, biplanes, ring-wings, and wing-body-tail configurations (fig. 8). Studies are now in progress to explore the application of linear theory to such configurations that rely on interference for the generation of desirable aerodynamic characteristics. The predicted results for the supersonic biplane are shown in figure 9. The infinite aspect ratio case was treated by Licher (ref. 6), and the results are duplicated by finite element theory. The finite aspect ratio solutions are not obtainable by other theories. Figure 10 illustrates the use of the program in predicting the characteristics of a configuration with multiple lifting surfaces. The experimental data are from the supersonic transport concept known as SCAT-17. In figure 11, the predicted and measured results for a ring-wing are compared (ref. 7). The small struts used to attach the ring-wing to the body must be considered to obtain proper correlation.

Computer Programs

The Ames Research Center of the NASA has undertaken the development and distribution of computer programs for predicting pressure distributions on wing-body combinations at subsonic and supersonic speeds. Some early versions of these programs are described in references 8 and 9. The latest version of these programs, commonly known at the "Ames Wing-Body Program" is now available for distribution. This version contains significant improvements over the program of reference 9. The execution time has been reduced by a factor of 10 to 20, and the input requirements have been greatly streamlined. Also, many of the restrictions on geometry have been eliminated and the subsonic surface elements derived by Woodward (ref. 10) have been incorporated, so that the complete wing-body interference problem can now be solved at subsonic as well as supersonic speeds. The development of these

programs is continuing at Ames, and the ultimate goal is a program that will handle the actual geometry of flight vehicles, including propulsion units, internal flow, exhaust plumes, separated flows, shock waves, and so forth.

CONCLUDING REMARKS

The method of finite elements has been shown to be an accurate and straightforward approach to the approximate solution of linear partial differential equations with complicated boundary conditions. Computer programs based on this method are now able to handle wing-body combinations with very few restrictions of geometry. With a reasonable amount of progress in both aerodynamic theory and computer technology, it will be possible to create computer programs that will predict the aerodynamic characteristics of complete flight vehicles. The development of these programs is a major element in the goal of aeronautical research and development, namely "providing all information required for a designer to go from paper designs to production with complete confidence of success" (ref. 11).

REFERENCES

1. Jones, Robert T.; and Cohen, Doris: High-Speed Wing Theory. Princeton University Press, 1960.

2. Cohen, Doris: Formulas for the Supersonic Loading, Lift, and Drag of Flat Swept-Back Wings With Leading Edges Behind the Mach Lines. NACA Rep. 1050, 1951.

3. Wagner, Siegfried: Some Recent Developments in Subsonic Lifting-Surface Theory. Paper presented to the NASA Symposium on Analytic Methods in Aircraft Aerodynamics, Oct. 28-30, 1969.

4. Lamar, John E.: A Modified Multhopp Approach for Predicting Lifting Pressures and Camber Slopes for Composite Planforms in Subsonic Flow. NASA TN D-4427, 1968.

5. Carmichael, Ralph L.: A Critical Evaluation of Methods for Computing Wing-Body Interference at Supersonic Speeds. Paper 68-08, 6th Congress International Council of the Aeronautical Sciences, Munich, West Germany, Sept. 9-13, 1968.

6. Licher, R. M.: Optimum Two-Dimensional Multiplanes in Supersonic Flow. Rep. SM18688, Douglas Aircraft Co., Jan. 1955.

7. Morris, Odell: Aerodynamic Characteristics in Pitch of Several Ring-Wing--Body Configurations at a Mach Number of 2.2. NASA TN D-1272, 1962.

8. Carmichael, Ralph L.; and Woodward, Frank A.: An Integrated Approach to the Analysis and Design of Wings and Wing-Body Combinations in Supersonic Flow. NASA TN D-3685, 1966.

9. Woodward, F. A.; Tinoco, E. N.; and Larsen, J. W.: Analysis and Design of Supersonic Wing-Body Combinations, Including Flow Properties in the Near Field. Part 1 - Theory and Application. NASA CR-73106, 1967.

10. Woodward, Frank A.: Analysis and Design of Wing-Body Combinations at Subsonic and Supersonic Speeds. J. Aircraft, vol. 5, no. 6, Nov.-Dec. 1968, pp. 528-534.

11. Harper, Charles W.: Prospects in Aeronautical Research and Development. J. Aircraft, vol. 5, no. 5, Sept.-Oct. 1968, pp. 417-426.

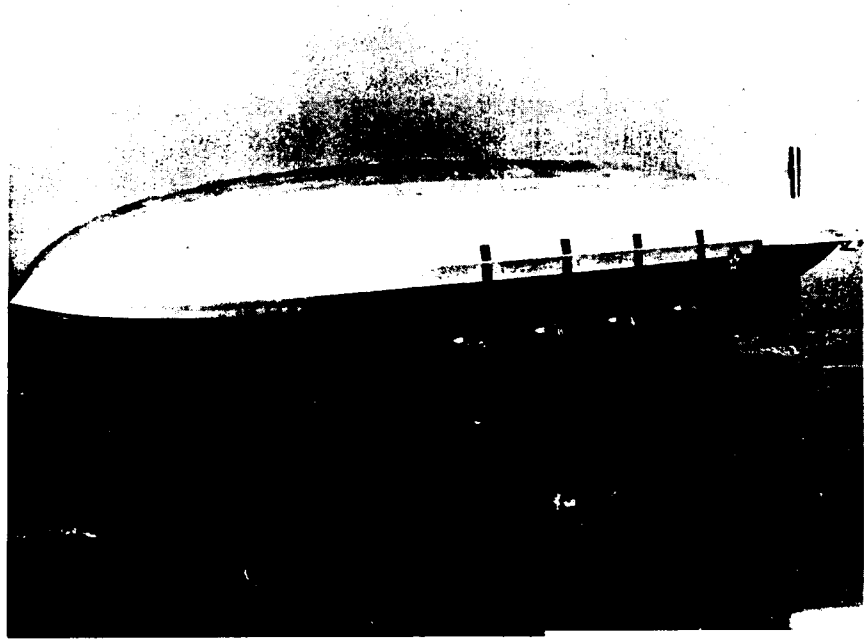

Figure 1

This page is reproduced at the back of the report by a different reproduction method to provide better detail.

SIMULATION OF AIRSHIP FLOW FIELD BY AXIAL SOURCE DISTRIBUTIONS

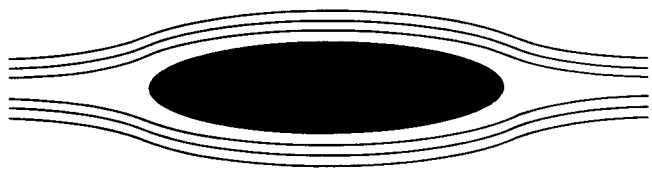

AXIAL SOURCE DISTRIBUTION

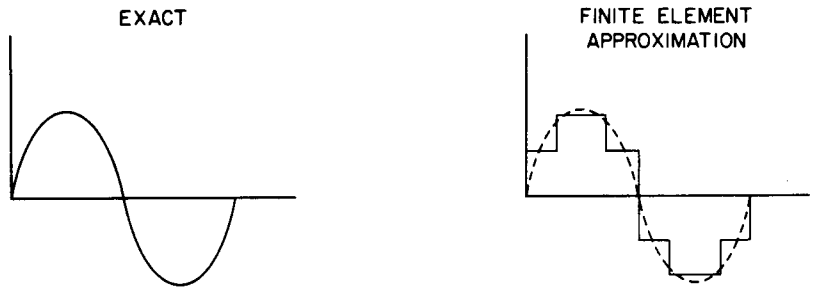

Figure 2

FINITE ELEMENT COMPONENTS FOR CONFIGURATION SYNTHESIS

- POINT ELEMENTS
  - SOURCE (SINK)
  - DOUBLET
- LINE ELEMENTS
  - SOURCE
  - DOUBLET
  - VORTEX
- SURFACE ELEMENTS
  - THICKNESS
  - LIFTING

Figure 3

COMBINATION OF FINITE ELEMENTS TO REPRESENT WING-BODY COMBINATION

- BODY THICKNESS BY LINE SOURCES
- BODY LIFT BY LINE DOUBLETS
- WING THICKNESS BY CONSTANT SOURCE PANELS
- WING LIFT BY CONSTANT PRESSURE PANELS
- WING-BODY INTERFERENCE BY CONSTANT PRESSURE PANELS

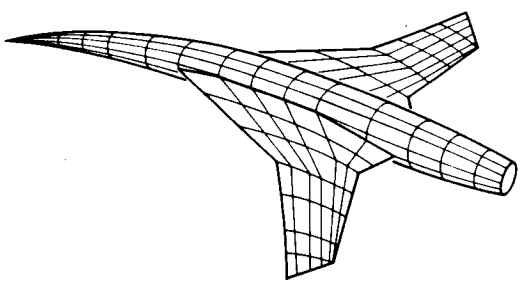

Figure 4

COMPARISON BETWEEN EXACT LINEAR THEORY AND PROGRAM RESULTS FOR DELTA WINGS

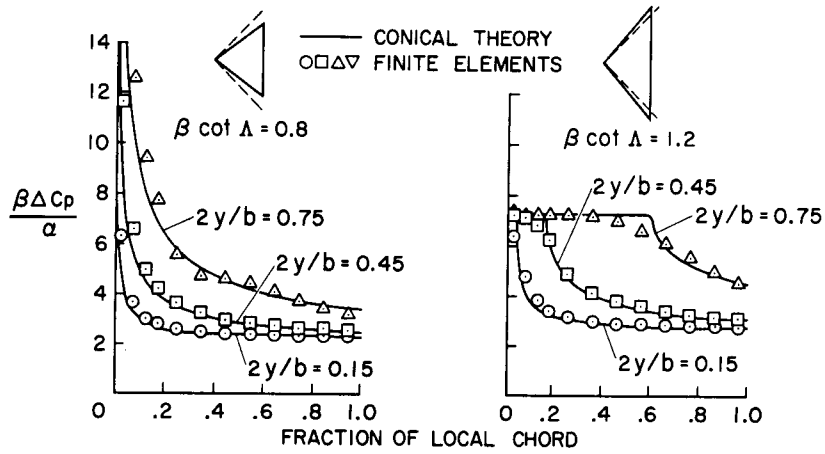

Figure 5

COMPARISON BETWEEN EXACT LINEAR THEORY AND PROGRAM RESULTS FOR A SWEPT WING

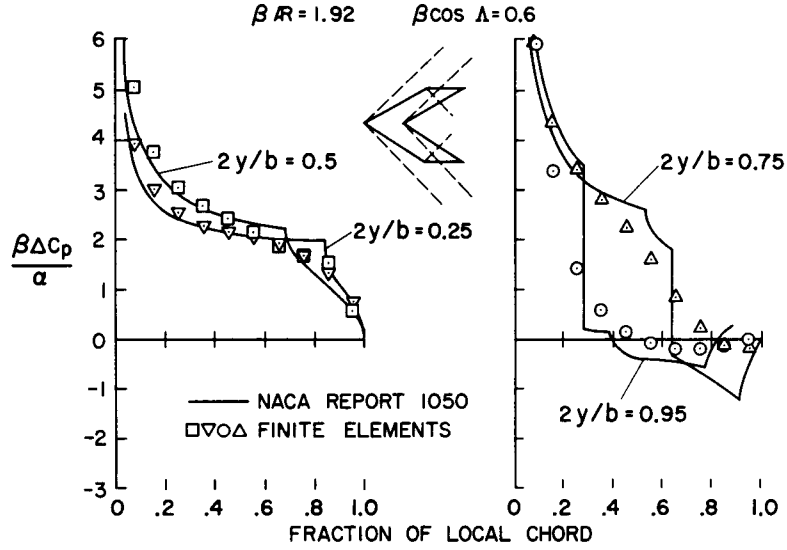

Figure 6

FINITE ELEMENT APPROACH TO LIFTING-SURFACE THEORY

M≈0

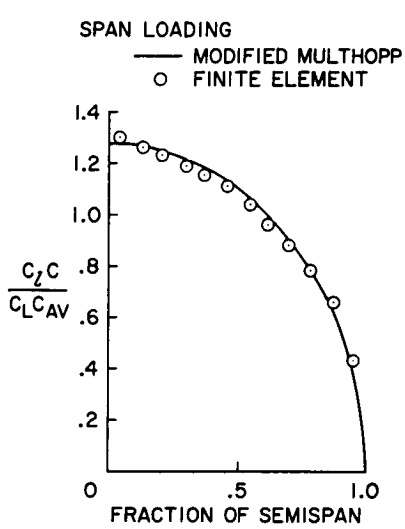

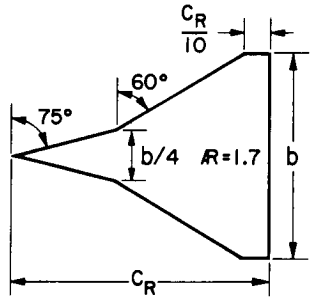

RESULTS

	MODIFIED MULTHOPP	FINITE ELEMENT (120 PANELS)
C_{L_α}	0.0364	0.0359
C_{D_i}/C_L^2	.187	.188
C_{m_α}	.0229	.0233

Figure 7

NONPLANAR INTERFERENCE CONFIGURATIONS

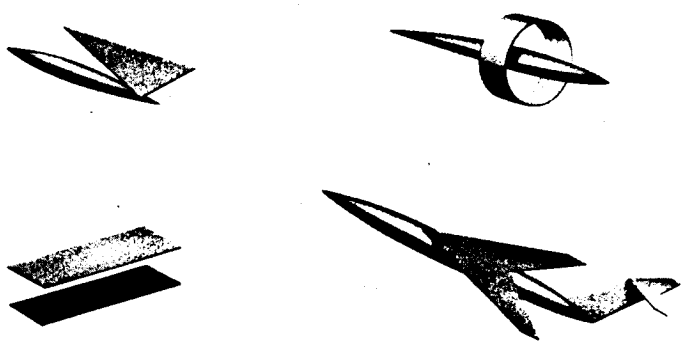

Figure 8

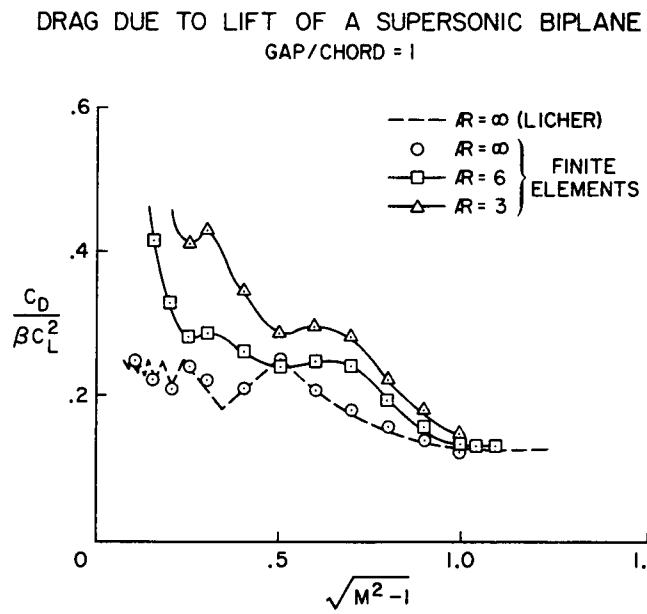

Figure 9

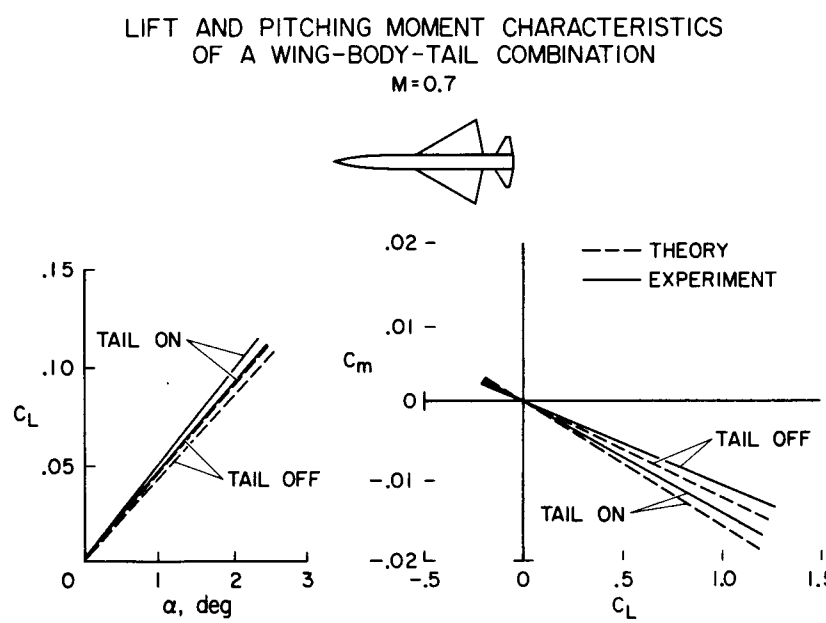

Figure 10

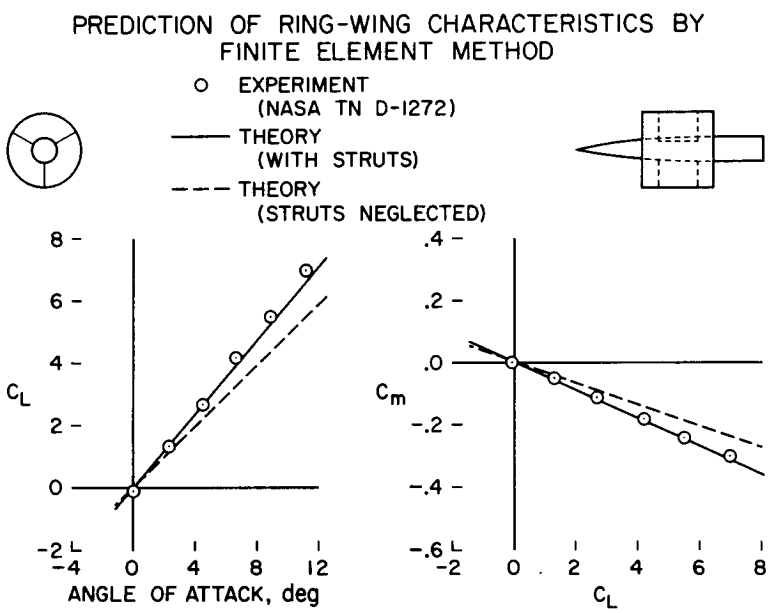
PREDICTION OF RING-WING CHARACTERISTICS BY
FINITE ELEMENT METHOD
EXPERIMENT
(NASA TN D-1272)
THEORY
(WITH STRUTS)
THEORY
(STRUTS NEGLECTED)
C_L
8
6
4
2
0
-2
-4
0
4
8
12
ANGLE OF ATTACK, deg
C_m
.4
.2
.0
-.2
-.4
-.6
-2
0
2
4
6
8
C_L

Figure 11

DISCUSSION

PETER B. S. LISSAMAN, Northrop Corporate Laboratory: The author kept on talking about subsonic. Does he mean subsonic or does he mean incompressible? If he means subsonic, how would he take into account compressibility?

CARMICHAEL: Well, let's say compressible within the limits of the Prandtl-Meyer transformation. There is no nonlinear treatment of the compressible flow equations, so this would be a small perturbation theory for compressible speeds.

THEODORE R. GOODMAN, Oceanics, Inc.: I have the distinct impression that a graduate student at Cornell University in the early '50s under Bill Sears solved the supersonic biplane with a finite aspect ratio rectangular planform, and if you would contact him I am sure he would tell you exactly how to get hold of that information.

WILLIAM J. EVANS, Grumman Aircraft: Ralph, is your limitation still one hundred wing panels?

CARMICHAEL: I haven't modified the program that I am running here, even though we now do have a larger machine. I see no reason why not, and I understand that some people who have gotten our program and modified it run up to 300 finite elements.

EVANS: Is there any indication of computer running time for those cases?

CARMICHAEL: The time is proportional to n^2, where n is the number of panels. We did say 150 panels in 4 minutes. If you used 600 panels, that is, 4 times as many, the time required would be 16 times as long. These are all on a 360, model 67, FORTRAN-H.

EVANS: Have you replaced the matrix inversion procedures?

CARMICHAEL: No, they are still single precision. That would be a limit if you used a very large number of panels. In fact, I am not aware of how the people who have run this up to 300 panels do the inversion.

It may still work. You know, these aerodynamic matrices are very well conditioned in the sense that the big, strong elements are on the diagonal, so you may be able to do single precision inversion up to 200 or 300.

JOSEPH P. GIESING, Douglas Aircraft: I don't want you to give all your secrets away at one time, but I would like to know, since you are using a small-perturbation compressible flow analysis, how do you handle pointed type bodies with your lifting surface elements?

How do you handle the nonplanar aspects of the elements that you place on the fuselage?

CARMICHAEL: Oh, yes, there is a real problem, that's right, if you try to put up to the nose.

GIESING: Or back by the tail.

CARMICHAEL: We solve this by avoiding that problem.

I know that is a real problem. We ran into that in the early days, trying to put the panels as you saw in that picture (fig. 4), right up to the nose, making a cone solution with panels. It violates the assumption that the panels are nominally parallel to the free stream.

GIESING: I just have one other comment. Using the recommended 0.95 does not give you the right answer in subsonic flow for this method.

We came up with another magic number, 0.85. We found that this worked exactly right in two dimensions for wings without camber.

CARMICHAEL: Okay. I hate to get into the nitty gritty of this thing, but the question of where you put that control point in the individual panel has been the subject of great grief and hand-wringing and all that stuff. Seventy-five percent was supposedly a magic number at one time, too.

SIEGFRIED WAGNER: I just wanted to say maybe the Multhopp-Truckenbrodt methods aren't bad.

CARMICHAEL: When we agree with it, we say well, that must be the right answer.

CALCULATIVE TECHNIQUES FOR TRANSONIC FLOWS

By John R. Spreiter
Stanford University

and

Stephen S. Stahara and William H. Frey
Nielsen Engineering and Research, Inc.

N70-21354

3

SUMMARY

A summary of old and new ideas and results is presented to show that a theory already exists that is capable of accounting for many of the properties of transonic flows, that the fundamental equations, although nonlinear, are amenable to solution by a number of methods, and that the full potential for developing calculative techniques for three-dimensional flows has not been explored. Further progress is definitely possible and some examples of new developments are provided.

INTRODUCTION

The desire to design aircraft capable of cruising efficiently at speeds as close to Mach 1 as possible without incurring excessive drag penalties and the development of military aircraft able to maneuver at transonic speeds are leading to a renewal of interest in transonic aerodynamics. Although nearly half a century has elapsed since NACA, predecessor to NASA, initiated its long line of studies of transonic flow by sponsoring a series of experimental investigations by Briggs, Hull, and Dryden (ref. 1), the development of techniques for transonic analysis has continued to be "a real challenge to technology," as noted in a recent survey of emerging technologies by Lamar (ref. 2). He went on to say: "The dominant nonlinear characteristics of mixed transonic flows have been far too complex for analysis, especially in the three dimensions of real vehicles."

In spite of, or perhaps because of, this state of affairs, it is the purpose of this paper to report on an effort to develop calculative techniques for predicting transonic aerodynamic characteristics of wing-body combinations. This investigation is currently in progress at Nielsen Engineering and Research, Inc., under the sponsorship of Ames Research Center. While this goal may seem unduly optimistic in view of Lamar's assessment of the field and although the contract has been under way for only six months so that our specific advances to date are modest, we are confident that much progress can be made and will present a summary of existing knowledge and some new results to support this view.

Preceding page blank

DISCUSSION

First of all, it should be recognized that considerable progress was achieved in the analysis of transonic flow in the decade and a half following World War II (see Spreiter, refs. 3 and 4; Guderley, ref. 5; and Ferrari and Tricomi, ref. 6, for significant summaries). Most important was the establishment of the basic concept that there is a major body of transonic flow problems that can be analyzed adequately within the framework of steady inviscid flow theory rather than the more general, and far more difficult, framework of unsteady viscous compressible flow theory. For these problems the basic equations are therefore those associated with Euler's equation of motion rather than with the Navier-Stokes' equations. Furthermore, the general concern with efficient flight of streamlined objects permits the assumptions of small disturbances and irrotational flow for transonic speeds, just as in most aerodynamic analyses of subsonic and supersonic flows. Although the familiar Prandtl-Glauert equation of linearized compressible flow theory shown on the bottom left of figure 1 is also based on similar assumptions, its well-known degeneracy at free-stream Mach number M_∞ equal to 1 led Oswatitsch and Wieghardt (ref. 7), Busemann and Guderley (ref. 8), Guderley (refs. 9 and 10), and von Kármán (refs. 11 and 12) to develop a new nonlinear theory of small disturbance flow with M_∞ near or equal to unity. Although the basic differential equation for the perturbation velocity potential ϕ has been written in several slightly different forms, the form presented on the bottom right of figure 1 was shown (Spreiter, ref. 13) to be generally advantageous because it (a) provides greater accuracy, (b) is no more difficult to solve, and (c) is applicable not only to transonic flows, but also to subsonic and supersonic flows as well. This equation thus provides a basis for a unified flow theory for all Mach numbers from 0 to that supersonic Mach number (at least 2 or 3) at which linearized supersonic flow theory must be supplanted by the nonlinear theory of hypersonic flow.

In spite of the seemingly simple form of the differential equation for transonic flow, the presence of the term involving $\phi_x\phi_{xx}$ introduces great complications. These difficulties arise not primarily from the nonlinearity that this term introduces, but rather from the change of the basic character of the differential equation from elliptic to hyperbolic type as the sign of $1 - M_\infty^2 - M_\infty^2(\gamma + 1)(\phi_x/U_\infty)$ changes from positive to negative. Since no general mathematical theory exists for such equations, aerodynamicists and applied mathematicians working in transonic flow theory have had to develop their own methods. Several of the more successful and generally applicable of these are listed on figure 2 together with pertinent comments.

Listed first is the hodograph method, since it is the most firmly founded mathematically and has provided most of the exact solutions with which the results of approximate theories can be compared. The key step in this method, summaries of which are given by Guderley (ref. 5) and Ferrari and Tricomi (ref. 6), is the linearization without approximation of the transonic flow equation by interchange of the dependent and independent variables through use of either of two classical transformations of compressible flow theory, the Molenbroek transformation or the Legendre transformation. The differential

equation that results in either case can then be transformed simply, by introducing new normalizing variables, to a linear equation of mixed elliptic-hyperbolic type named after Tricomi for his pioneering mathematical studies of its properties begun approximately 50 years ago. Solutions for a number of problems of aerodynamic interest have been determined in this way by superposition of more elementary solutions found by application of either analytical or numerical techniques. In all except certain special applications, however, the analysis must proceed in an indirect manner because the shape of the body cannot be prescribed in advance but must be found as part of the solution. Although many valuable results have been obtained in this way, the fundamental restriction of the hodograph method to two-dimensional planar flows precludes its further consideration in the present study directed toward wing-body combinations.

The integral equation method is an approximate method based on consideration of a nonlinear integral equation derived from the differential equation for transonic flow through application of Green's theorem. It originates from a series of papers of Oswatitsch (refs. 14 and 15), Gullstrand (refs. 16-19), Spreiter and Alksne (ref. 20), and Spreiter, Alksne, and Hyett (ref. 21). More recently, reviews of this method have been given by Zierep (ref. 22) and by Ferrari and Tricomi (ref. 6). Although the initial steps of the integral equation method are analytic, the calculations proceed directly toward the solution for a body of specified shape through a combination of numerical and iterative procedures. At present, the method has been developed for planar flow past nonlifting airfoils for $M_\infty < 1$, and the results for such cases appear to be the most satisfactory of those provided by any of the methods listed on figure 2. The method is potentially more versatile than these results indicate, and discussions of preliminary aspects of extensions to other cases may be found in the references cited above. Precise details for such cases remain to be developed, however.

The parabolic method stems from the daring proposal by Oswatitsch and Keune (ref. 23) that the nonlinear term in the transonic flow equation could be approximated satisfactorily for flows with $M_\infty = 1$ past slender bodies of revolution by replacing $\phi_x\phi_{xx}$ by $K\phi_x$, where K is a constant. The method derives its name from the parabolic type of the resulting approximate differential equation for ϕ which has the form of the equation of heat conduction. This procedure was subsequently applied to planar flows past thin airfoils, and extended to other Mach numbers by the simple expedient of retaining the term $(1 - M_\infty^2)\phi_{xx}$. Reviews of these developments have been given by Maeder (ref. 24) and Hosokawa (ref. 25), the two leading contributors. Although the procedures are direct and simple, the results lack accuracy generally and must be judged to be the least satisfactory of those provided by any of the methods listed on figure 2.

The local linearization method which grew out of the parabolic method of Oswatitsch and Keune is yet another approximate method for solving the transonic flow equation. This method has been applied to planar flow past thin airfoils and to axisymmetric flow past slender bodies (Spreiter and Alksne, refs. 26 and 27) for the Mach number ranges $M_\infty \approx 1$, $M_\infty \leq M_{cr,l}$ and $M_\infty \geq M_{cr,u}$, where $M_{cr,l}$ and $M_{cr,u}$ refer to the lower and upper critical

Mach numbers that bound the transonic range. It has also been applied by Alksne and Spreiter (ref. 28) to flows with $M_\infty \approx 1$ past nonlifting wings of finite span having simple planform and airfoil shapes. In addition to being the most versatile of all the methods presently available for predicting aerodynamic properties of thin wings and slender bodies at transonic speeds, the local linearization method has consistently displaced accuracy comparable with the best theoretical and experimental results. For these reasons, this method has been selected for further study as holding the greatest promise for successful extension to wing-body combinations. Briefly, the basic idea underlying the method is that of linearizing the transonic flow equation by replacing either ϕ_x or ϕ_{xx} in the nonlinear term by a constant λ, solving the simplified equation, and then introducing different values for λ for different points in the flow. This procedure might be considered equivalent, in some sense, to replacing the original nonlinear partial differential equation by a different linear partial differential equation at each point. Results obtained by such a procedure depend, of course, on the choice of λ and must be assembled to determine the final results. This step is accomplished by putting the results into such a form that a first-order nonlinear ordinary differential equation is obtained for the streamwise perturbation velocity component $u = \phi_x$ after λ is replaced by the quantity it originally represented. In many cases, this equation is of sufficiently simple form that it can be integrated analytically and the solution expressed in closed form. In other cases, the integration must be performed numerically, but the equation is of such a form that standard methods can be applied.

The parametric differentiation method of Rubbert and Landahl (ref. 29) is a recent addition to the list of procedures for obtaining satisfactory approximate solutions of the transonic flow equation. The difficulties associated with the nonlinearity of the basic equation are avoided by considering the linear problem governing the rate of change of the flow velocity with respect to the airfoil thickness ratio parameter and integrating solutions of this problem over the thickness ratio. This procedure is equivalent to summing a series of perturbations in airfoil thickness and has the advantage, shared with the local linearization method, of moving all the nonlinearity to a first-order ordinary differential equation where it causes little difficulty. The method has been applied to planar flow past nonlifting airfoils, and the results are either identical to or very nearly the same as those of the local linearization method. There is obviously considerable merit to this method, and further study to extend the range of cases for which it is explicitly applicable is clearly warranted. The close relationship between the results of the parametric differentiation and local linearization methods, in spite of the seemingly different nature of the approximations involved, is also provocative; further investigation of the reasons for this may be anticipated to lead to a better understanding of the mathematical foundations of both methods. For the present, however, we will continue to apply the method of local linearization, knowing that it is likely that many of the results so obtained might also be effectively reproduced by suitable extensions of the parametric differentiation method.

Solution of the transonic flow equation by completely numerical procedures is included in the list of methods not so much because of the

demonstrated ability of such procedures to yield useful results, but because of the promise that this approach holds with the continued improvement of electronic computing capability. Although a number of groups are developing these methods, progress has been slow, and very few details or results for transonic flows have been published to date. It is clear, however, that the completely numerical solution of transonic flow problems is not only expensive but probably limited to two-dimensional flows with the present generation of computers. For these reasons, we have not considered it profitable at this time to seek solutions for transonic flow about wing-body combinations by application of completely numerical techniques.

The first and simplest transonic flow problem to which the local linearization method was applied was flow with $M_\infty = 1$ past thin nonlifting airfoils having a finite angle at the leading edge. The variation of the pressure coefficient $C_p = (p - p_\infty)/(\rho_\infty U^2/2)$, or its transonic similarity counterpart $\overline{C}_p$, along the surface of such an airfoil is found to be given by the expression at the top of figure 3, in which Z represents the ordinates of the airfoil surface and x^* represents the x-coordinate of the point on the airfoil surface at which the flow accelerates through the speed of sound. Although x^* is known a priori to be at the shoulder of a single- or double-wedge airfoil (see, e.g., ref. 5), the location of the sonic point on a continuously curved profile must be found as part of the solution. It is, according to the method of local linearization, at the point x at which the second equation shown on figure 3 is satisfied. In the original presentation of these results, Spreiter and Alksne (ref. 26) applied the theory to a family of airfoils tested by Michel, Marchaud, and Le Gallo (refs. 30 and 31) having thickness ratios τ from 6 to 12 percent and positions of maximum thickness from 30 to 70 percent of the chord. The ordinates of the airfoils with maximum thickness at 30-, 40-, and 50-percent chord are proportional to

$$1 - (x/c) - [1 - (x/c)]^n$$

where $n = 6.05$, 3.38, and 2, respectively. In the original comparisons, the integrations were performed analytically, but it was necessary to approximate the exponent 6.05 by 6, and 3.38 by either 3 or 3.5, in order to carry out the indicated integrations. Even with this simplification, the final expressions are so lengthy that even substituting numbers into them to obtain specific results is a laborious task. Nevertheless, the comparisons, such as that shown on figure 3 for airfoils with $n = 3.38$, served to demonstrate that the theoretical results are indeed both versatile and in good accord with experiment.

As the first step in the application of electronic computers to the method of local linearization, we have programmed the general equations shown on figure 3, and applied them to calculate the pressure distribution on the airfoil defined by the above expression with $n = 3.38$. The new results have been added to the plot in figure 3, and we note that they fall between the previous analytic results for $n = 3$ and 3.5 as they should. All three sets of theoretical results are also in satisfactory agreement with the experimental pressure distributions for all four airfoils tested except near the

trailing edge, where interactions between the boundary layer and the trailing shock waves disregarded in the theory are undoubtedly responsible for the discrepancies.

The pressure distributions shown on figure 3 are displayed in transonic similarity form so that the results appear in terms of $\bar{C}_p$ instead of C_p. This is done to facilitate comparison of a single theoretical curve with data for four affinely related airfoils having different thickness ratios. The corresponding results for C_p are presented in the left-hand part of figure 4 for a specific airfoil of the same family having a thickness ratio of 1/12. In addition to the results for $M_\infty = 1$, the theoretical pressure distributions indicated by the local linearization method for the lower and upper critical Mach numbers are also displayed. In the right-hand part of figure 4 are shown the variation with M_∞ of the minimum value of C_p for subsonic flow and the maximum value of C_p for supersonic flow. The intersections of these curves with the curve representing the variation of the critical pressure coefficient $C_{p_{cr}}$ with M_∞ defines the boundaries of the transonic range. Of particular interest is the remarkable width of the transonic range, which for this particular airfoil extends from $M_\infty = 0.75$ to 1.66. Moreover, this range would be even greater were the airfoil lifting.

Results for axisymmetric flow past a body of revolution having the same ordinates as the airfoil considered in figure 4 are presented in figure 5. In the left-hand part are shown the theoretical pressure distributions on the body surface for $M_\infty = 1$ and for the lower and upper critical Mach numbers. Also included for comparison are the experimental results for $M_\infty = 1$ for this body, as measured in the Ames 14-Foot Transonic Wind Tunnel by McDevitt and Taylor (ref. 32) and abridged for clarity of representation. As with previous comparisons with other bodies of revolution having simpler expressions for the ordinates (Spreiter and Alksne, ref. 27; and Spreiter, Smith, and Hyett, ref. 33), the results calculated using the local linearization method agree well with the experimental results over most of the body but disagree noticeably over the rear of the body. Comparison with the results presented in figure 4 shows that the magnitudes of the peak pressure coefficients are much smaller for axisymmetric flow past a body of revolution than for planar flow past an airfoil having the same profile. As a result, the transonic range is also much smaller and, as can be seen from the right-hand part of figure 5, extends from $M_\infty = 0.94$ to 1.29 for the present example.

With respect to the discrepancies between the theoretical and experimental results near the rear of the body, many would be inclined to dismiss further discussion by attributing the differences to shock-wave—boundary-layer interaction effects not included in the theory. While there is little doubt that such effects are important, we believe that the experimental results for the rear of this body are subject, in addition, to significant interference effects of the wind-tunnel walls. Although there is no explicit experimental evidence to support or refute this statement for the specific body considered in figure 5, the data on figure 6 for a closely related pair of bodies are definitely relevant. The plots on the left show pressure distributions measured at $M_\infty = 1$ on two bodies of revolution having ordinates proportional to $1 - (x/l) - [1 - (x/l)]^n$ and

diameter-length ratio D/l of 1/12. The results shown in the upper plot are for a parabolic-arc body, for which $n = 2$, and those in the lower plot are for a body with maximum thickness at 30 percent of its length, for which $n = 6$. Both wind-tunnel models were 6 inches in diameter, the same as that for which data are shown in figure 5. The data for these bodies obtained by Taylor and McDevitt (ref. 34) and McDevitt and Taylor (ref. 32) in the Ames 14-Foot Transonic Wind Tunnel with square test section are indicated by the open circles. The closed circles indicate the data obtained when the same actual models were subsequently tested under choking conditions in the Ames 12-Foot Pressure Wind Tunnel which has solid walls and a circular test section (Spreiter, ref. 4; and Spreiter, Smith, and Hyett, ref. 33). The principal points to observe are that both sets of experimental data are in essential agreement with each other and with theory over most of the body but that all three sets of results are widely divergent over the rear of the body.

The source of these differences has been discussed previously (Spreiter, ref. 4; Spreiter, Smith, and Hyett, ref. 33; and Berndt, ref. 35), but it is worth reviewing here because similar considerations are likely to be of importance in most comparisons of theoretical and experimental results for transonic flow past slender bodies or wing-body combinations. This can best be done by considering the diagram of figure 6 which shows the characteristic lines for an unbounded flow with $M_\infty = 1$ past a parabolic-arc body of revolution having a diameter-length ratio of 1/12. These results have been calculated by application of the transonic similarity rule for axisymmetric flow (Oswatitsch and Berndt, ref. 36) to a related diagram given by Oswatitsch (ref. 37) for a parabolic-arc body of revolution with a diameter-length ratio of 1/6. The position of the wall with respect to the model in the tests in the 12-foot pressure wind tunnel is as indicated, and the nearest part of the wall in the tests in the 14-foot transonic wind tunnel is 7/6 as far away. Although it was thought at the time of the tests in the 14-foot transonic wind tunnel that the 6-inch diameter of the models was sufficiently small to avoid significant effects of wind-tunnel-wall interference, figure 6 shows that this may not be the case because characteristics, or Mach waves, originating from the forepart of the body are indicated to be reflected from the walls onto the aft part of the body. It can be seen, moreover, that the most upstream reflected characteristic strikes the body at about $x/l = 0.6$ in the 12-foot wind tunnel test, and only slightly aft of that location in the 14-foot wind tunnel. The effect of the reflected waves striking the body is to make the pressure coefficients more negative in the 12-foot wind tunnel, because the outgoing characteristics represent expansion waves that reflect from the solid wall of the tunnel as rarefaction waves. The effects are amplified, moreover, because of the focusing characteristics of the reflected axisymmetric waves as they collapse down onto a part of the body that has a smaller circumference than that from which they originated. The sign of the corresponding effects in the 14-foot transonic wind tunnel is not so simple to ascertain, since the reflections from the partly open wall of that wind tunnel are very nearly equal in magnitude, but opposite in sign, to that of the reflections from the solid wall of the 12-foot wind tunnel. In addition to the direct effects of the reflected waves impinging on the rear of the body, there exists the distinct possibility of significant augmentation arising from the interaction of the boundary layer with a shock wave that may form adjacent to the body. The latter may form either because of coalescence of compression

waves reflecting from the body or because of boundary-layer separation resulting from the wall-induced steepening of the adverse pressure gradients. In either case, it is clear that considerable additional study will have to be made before it is possible to properly evaluate the significance of discrepancies between theoretical and experimental pressure distributions on the aft parts of bodies of revolution such as those illustrated in figures 5 and 6.

Perhaps one of the best-known properties of transonic flows is the transonic area rule of Whitcomb (ref. 38). It states that, near the speed of sound, the zero-lift drag rise of a slender wing-body combination (thin low-aspect-ratio wing, slender body) is primarily dependent on the axial distribution of cross-sectional area normal to the air stream. This rule, which was proposed on the basis of certain fundamental, yet elementary, statements regarding the nature of transonic flow fields and demonstrated experimentally, is closely related to the transonic equivalence rule which relates the flow around a slender body of arbitrary cross section to the flow around an "equivalent" nonlifting body of revolution having the same longitudinal distribution of cross-section area $S(x)$. The latter rule was first proposed for transonic flow past thin nonlifting wings by Oswatitsch (ref. 39) and later extended initially to lifting wings by Spreiter (ref. 3) and subsequently to slender bodies of arbitrary cross section, including wing-body combinations, by Heaslet and Spreiter (ref. 40). Figure 7, which is an extension to wing-body combinations of a rather similar figure presented by Spreiter (ref. 3) for thin wings, summarizes the theoretical essentials of both the equivalence and area rules. Most important is that the expression for the perturbation velocity potential ϕ in the vicinity of a slender body of arbitrary cross section is approximately of the form $\phi = \phi_2 + g(x)$ where ϕ_2 is the solution of Laplace's equation $\phi_{yy} + \phi_{zz} = 0$ for the given boundary conditions in the yz plane at each x station, and $g(x)$ is an additional contribution dependent upon M_∞ and $S(x)$ but not on the shape of the cross section. It is thus possible to determine $g(x)$ from the solution of the simpler problem of axisymmetric flow past the equivalent body. The equivalence rule, which is described in mathematical terms by

$$\phi = \phi_{2,\alpha} + \phi_{2,t} - \phi_{2,B} + \phi_B$$

in which each component of ϕ has the meaning indicated in figure 7, follows immediately by writing $\phi = \phi_2 + g(x)$ for the body of arbitrary cross section and subtracting the corresponding expression for the equivalent body.

The order of error in the transonic equivalence rule has been established by Heaslet and Spreiter (ref. 40) for thin wings of aspect ratio A, chord c, and thickness ratio τ. It was shown that the magnitude of the quantity $\phi/U_\infty c$ retained in the equivalence rule is $O(A\tau \ln A)$, whereas that of the quantities discarded in the derivation for $M_\infty = 1$ is $O(A^4\tau^2 \ln A)$. Since the magnitude of the quantities discarded in the derivation of the corresponding result in linearized subsonic and supersonic flow past slender bodies is $O(A^3\tau \ln A)$, it follows that the equivalence rule ought to be applicable to wings of greater aspect ratio at $M_\infty = 1$ than at any other Mach number.

Once the appropriate expression has been constructed for ϕ, the pressure distribution on or near the surface of slender bodies may be determined by use of the expression for C_p shown on figure 7. The results may, in turn, be integrated to obtain expressions or values for the total forces, including lift and drag, and moments on slender bodies or wing-body combinations of arbitrary cross section. Since the aerodynamic loading, lift, and all lateral forces and moments depend on differences in pressure between pairs of points at the same longitudinal station, these quantities depend solely on ϕ_2 and are therefore independent of M_∞. In particular we may note, as discussed by Spreiter (ref. 41) and Heaslet, Lomax, and Spreiter (ref. 42) even before the discovery of the transonic equivalence rule, that these quantities may be calculated quite adequately by linearized slender-body theory even though M_∞ may be unity.

It is evident that the transonic area rule of Whitcomb is closely related to the transonic equivalence rule. In a detailed examination of the relation between these two rules, Heaslet and Spreiter (ref. 40) derived the expression shown on the bottom of figure 7 between the drag D of a slender body of arbitrary cross section and the drag D_B of the equivalent body of revolution. Each of the integrals is a line integral along a curve that is situated in a plane perpendicular to the x-axis and that traverses the base of the body and any vortex wake which may be present. The difference $D - D_B$ is thus independent of M_∞ and is the same as given by linearized slender-body theory. If the arbitrary body is inclined at angle of attack α, the first integral provides a contribution to the drag that is proportional to α^2. This quantity is exactly the vortex drag associated with the production of lift. If attention is confined to nonlifting cases, several classes of shapes exist for which the contribution of the two remaining integrals cancel, and $D = D_B$ as proposed by Whitcomb. One important class includes shapes that taper to a point at the rear, since then both integrals vanish as the contour shrinks to a point. Another includes shapes that are cylindrical at the base, since then $\partial\phi_{2,t}/\partial n = \partial\phi_{2,B}/\partial n = 0$. Still another includes bodies for which the equivalent body and the original body have the same shape and surface slopes at the base, since then both integrals are carried out over the same contour, along which $\phi_{2,t} = \phi_{2B}$ and $\partial\phi_{2,t}/\partial n = \partial\phi_{2B}/\partial n$, and the integrals again cancel. These and many other cases for which the integrals cancel constitute the class of shapes for which the transonic area rule applies.

We now turn to two new applications of the transonic equivalence rule that are significant to the further development of calculative techniques for three-dimensional transonic flows. The first of these, summarized on figure 8, exploits the result that $\phi = \phi_2 + g(x) = (U_\infty/2\pi)(dS/dx)\ln r + g(x)$ in order to calculate the properties of the flow field at points removed from the body surface. The plot in the lower left shows the theoretical pressure distribution for $M_\infty = 1$ on the surface of a parabolic-arc body of revolution with a diameter-length ratio of 1/12, as indicated by the local linearization method and data from the experiments of Taylor and McDevitt (ref. 34) in the Ames 14-Foot Transonic Wind Tunnel. The two plots in the upper left show the corresponding comparisons of calculated and measured pressure distributions along lines parallel to the body axis but removed from it by distances of 4 and 8 times the maximum diameter D of the body. The plot on the right

shows the variation of C_p with distance measured laterally from the midpoint of the body axis. Except for the discrepancies near the rear of the body that have already been discussed in connection with the presentation of the same results for the surface pressure distribution in figure 5, the agreement between theory and experiment is generally satisfactory. This is particularly so when considered with respect to possible applications of the transonic equivalence rule to configurations having wings or related extremities of such size that they, rather than the body, provide the major contribution to C_p at lateral distances of the order of those for which results are shown in figure 8.

The second application, summarized in figure 9, is to flows with $M_\infty = 1$ past two different slender bodies with elliptical cross section having ratios a/b of major to minor axes of 1.5 and 3. The experimental data are those of McDevitt and Taylor (ref. 43) for the longitudinal variation of C_p at the extremities of the major and minor axes. The theoretical results have been determined by using the transonic equivalence rule to account for the differences between the elliptic bodies and the equivalent body of revolution and the local linearization method to provide the results for the equivalent body. The expression for $\phi_{2,t}$ required to describe the two-dimensional flow associated with the growing and shrinking of the elliptic cross sections is known (see for instance Nielsen, ref. 44) to be given by the relation shown on figure 9, where R.P. stands for the real part of the complex function that follows. As in the previous comparisons, the theoretical and experimental results are in good agreement except near the rear of the bodies, where at least part of the discrepancies must be attributed to the extraneous effects of the wind-tunnel walls.

CONCLUDING REMARKS

It is hoped that this summary of old and new ideas and results has served to show that a theory already exists that is capable of accounting for many of the properties of transonic flows, that the fundamental equations, although nonlinear, are amenable to solution by a number of methods, and that the possibilities for the development of calculative techniques for three-dimensional transonic flows are not nearly so bleak as indicated by the quotation in the opening paragraph. Further progress is definitely possible but will come only with determination and the expenditure of effort, and these have largely been lacking in this field during the past decade.

REFERENCES

1. Briggs, L. J.; Hull, J. F.; and Dryden, H. L.: Aerodynamic Characteristics of Airfoils at High Speeds. NACA TR 207, 1925.

2. Lamar, W. E.: Military Aircraft: Technology for the Next Generation. Astronautics and Aeronautics, vol. 7, 1969, pp. 68-78.

3. Spreiter, J. R.: Theoretical and Experimental Analysis of Transonic Flow Fields. NACA-University Conference on Aerodynamics, Construction, and Propulsion, vol. II, "Aerodynamics," 1954, pp. 18/1-18/17.

4. Spreiter, J. R.: Aerodynamics of Wings and Bodies at Transonic Speeds. J. Aero/Space Sci., vol. 26, no. 8, Aug. 1959, pp. 465-487.

5. Guderley, K. G.: Theory of Transonic Flow. Pergamon Press, Oxford, England, 1962.

6. Ferrari, C.; and Tricomi, F.: Transonic Aerodynamics. Academic Press, N. Y., 1968.

7. Oswatitsch, K.; and Wieghardt, K.: Theoretische Untersuchungen Über stationäre Potentialströmungen und Grenzschichten bei hohen Geschwindigkeiten. Lilienthal-Gesellschaft für Luftfahrt-forschung, Ber. 13/1, 1942, pp. 7-24 (also available as NACA TM 1189).

8. Busemann, A.; and Guderley, K. G.: The Problem of Drag at High Subsonic Speeds. Rep. and Trans. No. 184, British M.A.P., March 1947.

9. Guderley, K. G.: On the Transition from a Transonic Potential Flow to a Flow with Shocks. Tech. Rep. F-TR-2160-ND, AAF, Air Materiel Command, Wright Field, Aug. 1947.

10. Guderley, K. G.: Considerations of Structure of Mixed Subsonic-Supersonic Flow Patterns. Tech. Rep. F-TR-2168-ND, AAF, Air Materiel Command, Wright Field, Oct. 1947.

11. von Kármán, T.: Supersonic Aerodynamics - Principles and Applications. J. Aero. Sci., vol. 14, no. 7, July 1947, pp. 373-402, Discussion, pp. 403-409.

12. von Kármán, T.: The Similarity Law of Transonic Flow. J. Math. and Phys., vol. XXVI, no. 3, Oct. 1947, pp. 182-190.

13. Spreiter, J. R.: On the Application of Transonic Similarity Rules to Wings of Finite Span. NACA Rep. 1153, 1953. (Supersedes NACA TN 2726.)

14. Oswatitsch, K.: Die Geschwindigkeitsverteilung bei lokalen Überschallgebieten an flachen Profilen. ZAMM, Bd. 30, Nr. 1/2, Jan./Feb. 1950, pp. 17-24.

15. Oswatitsch, K.: Die Geschwindigkeitsverteilung an symmetrischen Profilen beim Auftreten lokaler Überschallgebiete. Acta Physica Austriaca, Bd. 4, Nr. 2/3, Dec. 1950, pp. 228-271.

16. Gullstrand, T. R.: The Flow Over Symmetrical Aerofoils without Incidence in the Lower Transonic Range. KTH Aero TN 20, Royal Inst. Tech., Stockholm, Sweden, 1951.

17. Gullstrand, T. R.: The Flow Over Symmetrical Aerofoils without Incidence at Sonic Speed. KTH Aero TN 24, Royal Inst. Tech., Stockholm, Sweden, 1952.

18. Gullstrand, T. R.: A Theoretical Discussion of Some Properties of Transonic Flow Over Two-Dimensional Symmetrical Aerofoils at Zero Lift with a Simple Method to Estimate the Flow Properties. KTH Aero TN 25, Royal Inst. Tech., Stockholm, Sweden, 1952.

19. Gullstrand, T. R.: The Flow Over Two-Dimensional Aerofoils at Incidence in the Transonic Speed Range. KTH Aero TN 27, Royal Inst. Tech., Stockholm, Sweden, 1952.

20. Spreiter, J. R.; and Alksne, A.: Theoretical Prediction of Pressure Distributions on Nonlifting Airfoils at High Subsonic Speeds. NACA Rep. 1217, 1955. (Supersedes NACA TN 3096.)

21. Spreiter, J. R.; Alksne, A. Y.; and Hyett, B. J.: Theoretical Pressure Distributions for Several Related Nonlifting Airfoils at High Subsonic Speeds. NACA TN 4148, 1958.

22. Zierep, Jürgen: Die Integralgleichungsmethode zur Berechnung schallnaher Strömungen. In Symposium Transsonicum, K. Oswatitsch, ed., Springer-Verlag, Berlin/Göttingen/Heidelberg, 1964, pp. 92-109.

23. Oswatitsch, K.; and Keune, F.: The Flow Around Bodies of Revolution at Mach Number 1. Proc. Conf. on High-Speed Aeronautics, Polytechnic Institute of Brooklyn, Brooklyn, N. Y., Jan. 20-22, 1955, pp. 113-131.

24. Maeder, P. F.: The Linear Approximation to the Transonic Small Disturbance Equation. In Symposium Transsonicum, K. Oswatitsch, ed., Springer-Verlag, Berlin/Göttingen/Heidelberg, 1964, pp. 112-125.

25. Hosokawa, Iwao: A Simplified Analysis for Transonic Flows Around Thin Bodies. In Symposium Transsonicum, K. Oswatitsch, ed., Springer-Verlag, Berlin/Göttingen/Heidelberg, 1964, pp. 184-199.

26. Spreiter, J. R.; and Alksne, A. Y.: Thin Airfoil Theory Based on Approximate Solution of the Transonic Flow Equation. NACA Rep. 1359, 1958. (Supersedes NACA TN 3970.)

27. Spreiter, J. R.; and Alksne, A. Y.: Slender Body Theory Based on Approximate Solution of the Transonic Flow Equation. NASA Rep. 2, 1959.

28. Alksne, A. Y.; and Spreiter, J. R.: Theoretical Pressure Distributions on Wings of Finite Span at Zero Incidence for Mach Numbers Near 1. NASA TR R-88, 1961.

29. Rubbert, P. E.; and Landahl, M. T.: Solution of the Transonic Airfoil Problem Through Parametric Differentiation. AIAA J., vol. 5, 1967, pp. 470-479.

30. Michel, R.; Marchaud, F.; and Le Gallo, J.: Étude des écoulements transsoniques autour des profils lenticulaires, a incidence nulle. O.N.E.R.A. Pub. No. 65, 1953.

31. Michel, R.; Marchaud, F.; and Le Gallo, J.: Influence de la position du maitre-couple sur les écoulements transsoniques autour de profils a pointes. O.N.E.R.A. Pub. No. 72, 1954.

32. McDevitt, J. B.; and Taylor, R. A.: Pressure Distributions at Transonic Speeds for Slender Bodies Having Various Axial Locations of Maximum Diameter. NACA TN 4280, 1958.

33. Spreiter, J. R.; Smith, D. W.; and Hyett, B. J.: A Study of the Simulation of Flow with Free-Stream Mach Number 1 in a Choked Wind Tunnel. NASA TR R-73, 1960.

34. Taylor, R. A.; and McDevitt, J. B.: Pressure Distributions at Transonic Speeds for Parabolic-Arc Bodies of Revolution Having Fineness Ratios of 10, 12, and 14. NACA TN 4234, 1958.

35. Berndt, S. B.: Theory of Wall Interference in Transonic Wind Tunnels. In Symposium Transsonicum, K. Oswatitsch, ed., Springer-Verlag, Berlin/Göttingen/Heidelberg, 1964, pp. 288-309.

36. Oswatitsch, K.; and Berndt, S. B.: Aerodynamic Similarity at Axisymmetric Transonic Flow Around Slender Bodies. KTH Aero TN 15, Royal Inst. Tech., Stockholm, Sweden, 1950.

37. Oswatitsch, K.: Die Berechnung wirbelfreier achsensymmetrischer Überschallfelder. Österreichisches Ingenieur-Archiv, Band X, Heft 4, 1956, pp. 359-382.

38. Whitcomb, R. T.: A Study of the Zero-Lift Drag-Rise Characteristics of Wing-Body Combinations Near the Speed of Sound. NACA Rep. 1273, 1956. (Supersedes NACA TM L52H08.)

39. Oswatitsch, K.: Die Theoretischen Arbeiten Über Schallnahe Strömungen am Flugtechnischen Instut der Kungl. Tekniska Hökskolan, Stockholm. Proc. Eighth Int. Cong. on Theo. and Appl. Mech., 1953.

40. Heaslet, M. A.; and Spreiter, J. R.: Three-Dimensional Transonic Flow Theory Applied to Slender Wings and Bodies. NACA Rep. 1318, 1957. (Supersedes NACA TN 3717.)

41. Spreiter, J. R.: The Aerodynamic Forces on Slender Plane- and Cruciform-Wing and Body Combinations. NACA Rep. 962, 1950. (Supersedes NACA TN's 1662 and 1897.)

42. Heaslet, M. A.; Lomax, H.; and Spreiter, J. R.: Linearized Compressible-Flow Theory for Sonic Flight Speeds. NACA Rep. 956, 1950. (Supersedes NACA TN 1824.)

43. McDevitt, J. B.; and Taylor, R. A.: Force and Pressure Measurements at Transonic Speeds for Several Bodies Having Elliptical Cross Sections. NACA TN 4362, 1958.

44. Nielsen, J. N.: Missile Aerodynamics. McGraw-Hill Book Co., New York, 1960, p. 30.

BASIC CONCEPTS

GOAL: TO CALCULATE PRESSURE DISTRIBUTION, AERODYNAMIC CHARACTERISTICS, AND FLOW FIELD OF WING-BODY COMBINATIONS AT TRANSONIC SPEEDS

EQUATIONS, EXACT AND APPROXIMATE

NAVIER-STOKES EQ. FOR UNSTEADY COMPRESSIBLE VISCOUS FLOW

ASSUME STEADY INVISCID FLOW

EULER EQ. OF STEADY COMPRESSIBLE FLOW

ASSUME SMALL DISTURBANCES AND IRROTATIONAL FLOW, $0 \leq M_\infty \leq \sim 3$

LINEARIZED THEORY

$$(1-M_\infty^2)\phi_{xx}+\phi_{yy}+\phi_{zz} = 0$$

TRANSONIC RANGE EXCLUDED

TRANSONIC THEORY

$$(1-M_\infty^2)\phi_{xx}+\phi_{yy}+\phi_{zz} = \frac{M_\infty^2(\gamma+1)}{U_\infty}\phi_x\phi_{xx}$$

UNIFIED THEORY FOR SUBSONIC, TRANSONIC, AND SUPERSONIC FLOW

Figure 1

PRINCIPAL METHODS OF SOLUTION

HODOGRAPH

EXACT, LIMITED TO PLANAR FLOW, INDIRECT, ANALYTIC OR NUMERICAL

INTEGRAL EQUATION

APPROXIMATE, DEVELOPED ONLY FOR $M_\infty < 1$ PLANAR FLOW BUT POTENTIALLY VERSATILE, DIRECT, NUMERICAL INTEGRATION

PARABOLIC METHOD FOR $M_\infty = 1$, AND EXTENSION FOR ALL M_∞

APPROXIMATE, PLANAR OR AXISYMMETRIC FLOW, DIRECT, SIMPLE, BUT NOT ACCURATE GENERALLY

LOCAL LINEARIZATION

APPROXIMATE, DEVELOPED FOR PLANAR, AXISYMMETRIC, OR NONLIFTING FINITE SPAN WING FLOWS WITH $M_\infty \approx 1$, $M_\infty \leq M_{cr,l}$, OR $M_\infty \geq M_{cr,u}$ AND POTENTIALLY MORE VERSATILE, DIRECT, RELATIVELY SIMPLE, ACCURATE

PARAMETRIC DIFFERENTIATION

NEW, PLANAR RESULTS SIMILAR TO THOSE OF LOCAL LINEARIZATION, DIRECT, PROMISING

COMPLETELY NUMERICAL

DEPENDS ON INCREASING CAPABILITIES OF ELECTRONIC COMPUTERS, EXPENSIVE, UNDER DEVELOPMENT FOR TWO DIMENSIONS AT PRESENT

Figure 2

APPLICATION TO PLANAR FLOW, $M_\infty = 1$

LOCAL LINEARIZATION PROVIDES

$$\bar{C}_p = \frac{\left[M_\infty^2(\gamma+1)\right]^{1/3}}{\tau^{2/3}} C_p = -2\left\{\frac{3}{\pi}\int_{x^*}^{x}\left[\frac{d}{dx_1}\int_0^{x_1}\frac{d(Z/\tau)/d\xi}{\sqrt{x_1-\xi}}\,d\xi\right]^2 dx_1\right\}^{1/3}$$

WHERE x^* IS VALUE OF x WHERE

$$\frac{d}{dx}\int_0^x \frac{d(Z/\tau)/d\xi}{\sqrt{x-\xi}}\,d\xi = 0$$

EXPERIMENT

$n = 3.38$, $\left(\frac{x}{c}\right)_{Z_{max}} = .40$

[MICHEL et al. 1954]

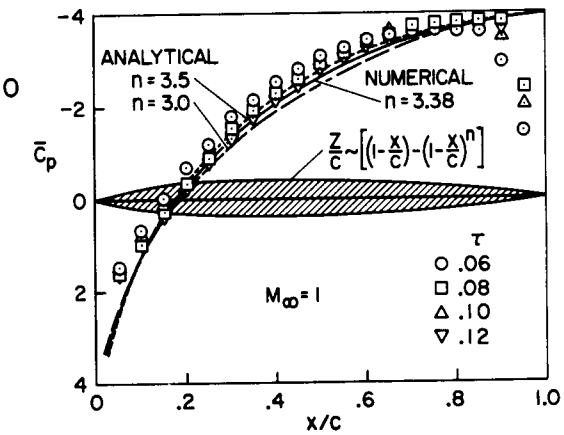

Figure 3

APPLICATION TO PLANAR FLOW

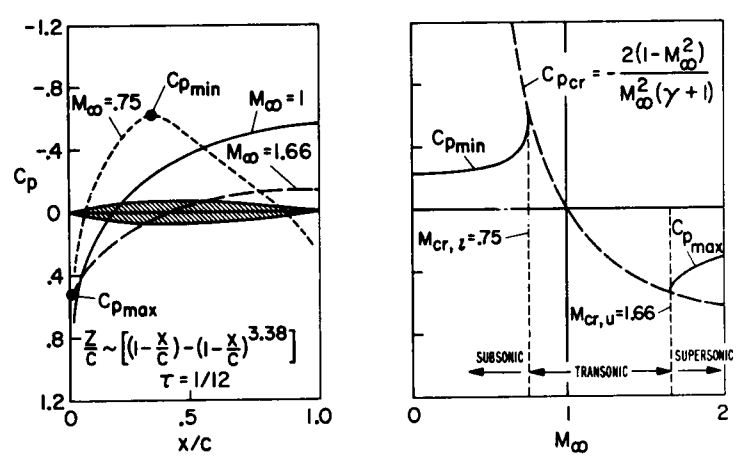

Figure 4

APPLICATION TO AXISYMMETRIC FLOW

o EXPERIMENT, 14' TRANSONIC WIND TUNNEL, $M_\infty = 1$
[McDEVITT AND TAYLOR, 1958]

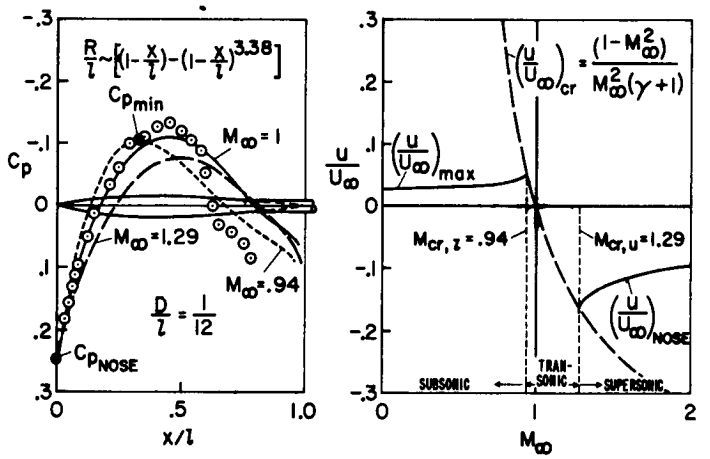

Figure 5

EFFECT OF WIND TUNNEL WALLS AND BOUNDARY LAYER ON PRESSURE DISTRIBUTION ON SLENDER BODIES OF REVOLUTION, $M_\infty = 1$

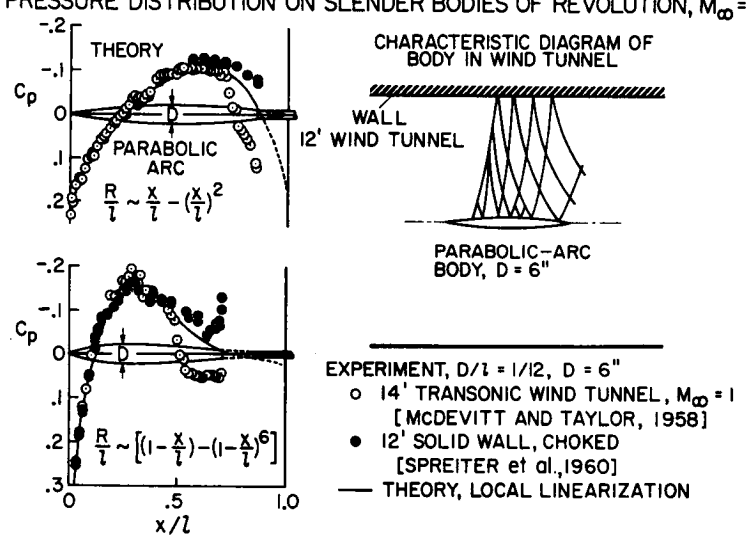

Figure 6

TRANSONIC EQUIVALENCE AND AREA RULES FOR SLENDER WING-BODY COMBINATIONS

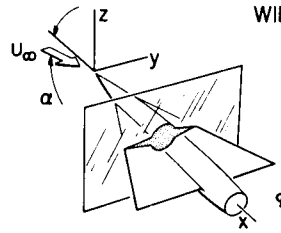

$$(1-M_\infty^2)\,\phi_{xx} + \phi_{yy} + \phi_{zz} = \frac{M_\infty^2(\gamma+1)}{U_\infty}\,\phi_x\,\phi_{xx}$$

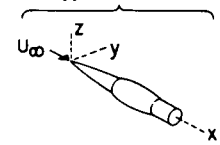

$$\phi_{yy} + \phi_{zz} = 0$$

$\phi =$

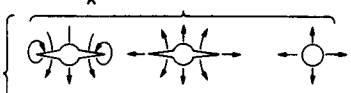

EQUIVALENT BODY WITH SAME S(x) AS WING-BODY

$$\underbrace{\phi_{2,a} + \phi_{2,t}}_{\phi_2} + \underbrace{-\phi_{2B} + \phi_B}_{g(x)\ \text{FOR SMALL}\ r}$$

$$C_p = -\frac{2}{U_\infty}(\phi_x + \alpha\phi_z) - \frac{1}{U_\infty^2}(\phi_y^2 + \phi_z^2)$$

AREA RULE FOR DRAG

$$D = D_B - \frac{\rho_\infty}{2}\left(\overbrace{\oint_c \phi\,\phi_{2,a}\frac{\partial\phi_{2,a}}{\partial n}ds_c}^{\text{VORTEX DRAG}} + \oint_c \phi\,\phi_{2,t}\frac{\partial\phi_{2,t}}{\partial n}ds_t - \oint_B \phi\,\phi_{2B}\frac{\partial\phi_{2B}}{\partial n}ds_B\right)$$

Figure 7

PRESSURE DISTRIBUTION IN FLOW FIELD OF A SLENDER BODY OF REVOLUTION, $M_\infty = 1$

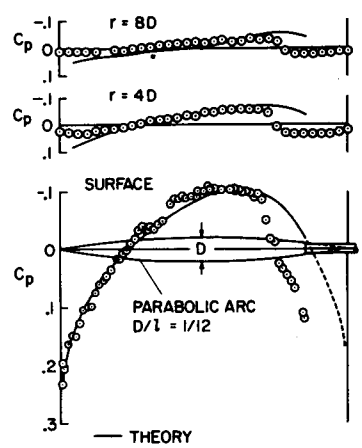

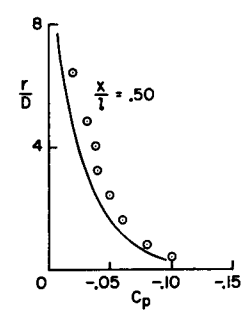

EXPERIMENT, 14' TRANSONIC WIND TUNNEL
D = 6" BODY
[TAYLOR AND McDEVITT, 1958]

— THEORY
SURFACE: LOCAL LINEARIZATION

FLOWFIELD: $\phi = \frac{U_\infty}{2\pi}\left(\frac{dS}{dx}\right)\ln r + g(x)$

PRESSURE: $C_p = -\frac{2}{U_\infty}\phi_x - \frac{1}{U_\infty^2}\phi_r^2$

Figure 8

PRESSURE DISTRIBUTION ON PARABOLIC-ARC BODY
WITH ELLIPTIC CROSS SECTION, $M_\infty = 1$

THEORY: —— $\theta = 0°$, --- $\theta = 90°$
LOCAL LINEARIZATION AND EQUIVALENCE RULE

$$\phi_{2,t} = \text{R.P.}\left[\frac{U_\infty S'(x)}{2\pi}\, \ln \frac{\sigma + \left(\sigma^2 - a^2 + b^2\right)^{\frac{1}{2}}}{2}\right]$$

$S = \pi ab, \quad \sigma = y + iz$

○● EXPERIMENT
14' WIND TUNNEL [McDEVITT AND TAYLOR, 1958]

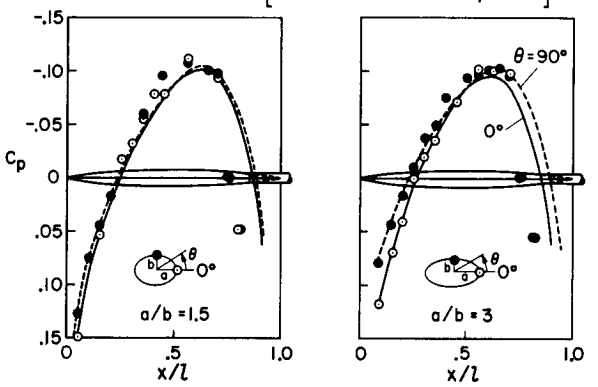

Figure 9

DISCUSSION

NORMAN MALMUTH, North American Rockwell Science Center: I was wondering, Dr. Spreiter, whether you cared to comment on the relative advantages of unsteady and steady difference methods compared to the integral equation method, which you briefly mentioned.

SPREITER: No, I don't think I could make any very good comments on that.

MALMUTH: I have another question about the applicability of your technique of local linearization to flows with a shock. Have you given any attention to this recently?

SPREITER: Not yet. So far our concern has been to develop programs which will let us do quickly what we already know; and we are using them to explore more configurations to get a firmer feeling of where we can go and where we cannot.

MALMUTH: My last question is on the equivalence rule. Can you extend it to larger incidence angles beyond its original limitation of small angle of attack compared to thickness ratio?

SPREITER: I don't know that the restriction you quote applies all of the time, since you can actually apply the equivalence rule to a wing with no thickness, ideally, a lifting flat plate, and it works perfectly well. I think in some of these instances one lacks a full definition of the boundaries of applicability. There are various ways in which these theories are applicable; and one must be a little careful when in possession of a demonstration or proof that it is true under certain circumstances not to regard that as a necessary condition, but more as a sufficient condition.

JAN RAAT, General Dynamics/Convair: I would like to draw attention to still another approximate method to attack the transonic potential equation. One can rewrite the equation in the form $(1 - M^2)\phi_{xx} + \phi_{yy} = 0$ and then assume M to be a function of x alone. This simplification has also been made by Rubbert and Landahl. However, at this stage one does not have to go into parametric differentiation. The simplified equation can be handled by operational techniques so that the problem reduces to a nonlinear ordinary differential equation, which can then be treated by the WKBJ method for slowly varying functions. We have done some work along these lines at Convair and we have obtained encouraging results for symmetric bodies at zero incidence.

SPREITER: Actually I could have extended my list by several more schemes. What you are describing sounds quite similar to the method that Julian Cole and Royce developed at one time in which they replaced $\phi_x\phi_{xx}$ term with $x(\phi_{xx})$. They then applied the method to a body of revolution having, I believe, a parabolic arc profile.

Mrs. Alksne and I inspected that method at the time; and what we found was that it would indeed give a good result for a parabolic arc body of

revolution and also, as I recall, a parabolic arc airfoil. But as we tested it by going to other bodies, with maximum thickness fore and aft of the midpoint, its success deteriorated very badly.

I think these are all closely related concepts of approximation, and don't regard them so much as competing with each other as supplementing. Ultimately, we may have a better theory than any of them.

RAAT: As far as accuracy is concerned, I think operational methods and Rubbert and Landahl's technique produce about the same results. In either case, one starts out with the crucial assumption of the local Mach number M being a function of x alone. From then on it essentially is a matter of applying different tools to the same problem.

I agree with you that the various approximation schemes that have been employed, usually lead to surprisingly similar results.

SPREITER: Yes, and perhaps this would be even more clear if one had a better insight into similar ideas. Heaslet, for example, in the Japan National Congress of Applied Mechanics in 1959, which probably is very unknown since it was only published in the proceedings volume in Japan, has a very provocative development which leads to the same results as the local linearization method. In his development, he starts with a reciprocity theorem, a nonlinear one, and relates the transonic flow to another flow in the reverse direction about the same object. He then makes a plausible approximation, and lo and behold, the familiar results emerge. I think it is a very interesting situation where you have several approaches that seem rather different in the beginning, but end up with either identically or very closely the same results.

PROCEDURES FOR DESIGNING SUPERSONIC BODIES OF REVOLUTION FROM PRESCRIBED SURFACE PRESSURE DISTRIBUTIONS

By Raymond L. Barger

NASA Langley Research Center

N70-21355

SUMMARY

An iterative procedure for designing a body from a prescribed surface pressure coefficient distribution is described. The method of successive approximation was preferred over a possible analytic inversion procedure because any slight deviation from exactness in computing the body shape, made in order to obtain an analytic solution, would cause a greatly amplified error in the final pressure distribution. The present method also facilitates comparing design and off-design performance. Results calculated for a static pressure probe designed by this method indicated that it could be effectively used over a range of Mach numbers including the design Mach number.

INTRODUCTION

There are a number of problems involving bodies of revolution at supersonic speeds for which it would be advantageous to relate the body design directly to a desired surface pressure distribution. Such problems arise, for example, in the design of fuselages for experimental wing-body combinations, in pressure-sensor design, and in the design of certain specialized types of projectiles.

It does not appear to be possible to obtain a direct analytic solution for the body shape in terms of the pressure distribution, except by using a theory that is so approximate that the results are essentially useless. However, an iterative method that appears to work well (provided, of course, that the prescribed pressure distribution is a reasonable one) is described herein.

It is apparent that in prescribing a surface pressure distribution there must be some limitation on the initial positive portion in order that the condition of shock attachment be satisfied. It is also necessary to place some constraints on both the area and the slope of the negative portion in order to obtain a body with a reasonable base area and in order to prevent a sudden necking down or "wasping" of the body shape. Any such sudden or large reduction in body radius would cause premature flow separation on the resultant body and might result in the calculation of a negative radius, in which case the procedure would fail to converge. In other cases the procedure would converge, so these

Preceding page blank

constraints are not critical with regard to convergence; however, if one prescribes a completely absurd pressure distribution, the resulting shape will be unsatisfactory in some way.

SYMBOLS

C_p	body surface pressure coefficient
l	body length
M	Mach number
R	body radius
S	body cross-sectional area
t,x	axial coordinates
U	tabulated function
u,v	dimensionless axial and radial disturbance velocities, respectively
$\beta = \sqrt{M^2 - 1}$	
Δ	denotes increment in indicated quantity

Subscripts:

n	denotes nth iteration
∞	free stream

Superscript:

'	denotes derivative in axial direction

GENERAL PROCEDURE

The general procedure is summarized first, and some of the steps are described subsequently in more detail. The general procedure includes the following six steps:

(1) An initial body shape is assumed. (The convergence of the procedure is not at all sensitive to this initial guess; the program as written simply uses a parabolic shape.)

(2) Its pressure coefficient distribution is calculated. (This calculation is described subsequently.)

(3) The error is computed – that is, the values of C_p for the body are subtracted from the desired values of C_p.

(4) The body slope distribution is changed in such a way that the error in step (3) is reduced. (This step is also discussed subsequently.)

(5) The new slope function is integrated to obtain an improved body shape – that is, a body that has a pressure distribution nearer to the desired distribution.

(6) The improved shape is introduced into the program as the input for the next iteration.

This procedure is repeated until the error is reduced to a negligible value.

PRESSURE CALCULATION

Step (2) of the general procedure requires some further discussion. The basic expression used in this pressure calculation is Lighthill's approximate solution of the linear equation for the nondimensional axial velocity (ref. 1, p. 455)

$$u(x) = -\frac{1}{2\pi}\int_0^x U\left[\frac{x - t}{\beta R(t)}\right]\frac{dS'(t)}{\beta R(t)}$$

in which β has the constant free-stream value. This expression is modified in the analysis of reference 2, which makes use of an approach somewhat similar to local linearization to obtain the following equation (given here in the present notation):

$$u(x) = -\frac{1}{2\pi}\int_0^x U\left[\frac{x - t}{\beta(t)R(t)}\right]\frac{[1 + u(t)]dS'(t)}{\beta(t)R(t)}$$

This equation contains the local β instead of the free-stream value, and a factor of $1 + u$ has been inserted. This new factor is a result of using the exact boundary condition in Lighthill's original derivation instead of the slender-body approximation.

It is seen that, whereas the basic Lighthill expression is simply a formula for u, the modified expression is an integral equation for u. Furthermore, it is highly nonlinear because u is involved not only on the left-hand side of the equation and explicitly under the integral but also in each β. An approximate solution to this equation was

obtained in reference 2 by the method of parametric differentiation, with the body thickness ratio used as the parameter.

Inasmuch as parametric differentiation is a complicated procedure, both theoretically and computationally, that method was not used in the present analysis. Instead, the integral equation was solved by successive approximation, as indicated by

$$u_{n+1} = -\frac{1}{2\pi}\int_0^x U\left(\frac{x - t}{\beta_n R}\right)\frac{(1 + u_n)dS'(t)}{\beta_n R}$$

where the functions u, β_n, and R have the local values, as in the preceding equation. For convenience, u_0 is taken to be identically zero. This iterative procedure has the advantages that it converges rapidly, it is a natural method for machine calculation, and it yields essentially the exact solution of the integral equation (whereas the parametric differentiation solution is approximate). The solution of this equation for u is the basis of the pressure calculation, because after u has been calculated, v is obtained from the exact boundary condition:

$$v(x) = \left[1 + u(x)\right]R'(x)$$

Then C_p can be computed in terms of u and v by using the exact expression for $C_p(u,v)$ (ref. 3, eq. (9.9)).

Since the design procedure relies on performing a pressure calculation and then reducing the error in it, the accuracy of this calculation is a crucial consideration for the method. Figures 1 to 3 show some comparisons of computations on known shapes for which accurate solutions are available just to give an indication of the accuracy of this pressure calculation method.

It is convenient to use cone calculations to compare theories because exact solutions are available and because, for such comparisons, it is easy to observe the variation of the pressure coefficient with Mach number. In figure 1, results obtained by the present theory are compared with some results presented in reference 1 (p. 468) for a cone with a half-angle of 15°. The data for the exact solution are from reference 4. The Broderick second-order theory is an expansion in powers of the square of some parameter such as the tangent of the cone semivertex angle. Thus the second-order theory includes terms up to the fourth power in this parameter, whereas the first-order theory includes terms no higher than second degree. For the curve labeled "Linear Equation Solved Exactly," the linear solution for u was used together with the exact boundary condition and the exact pressure coefficient formula. It is seen that even the second-order theory is applicable only over a small Mach number range, whereas the present theory is accurate over

an extensive range, the only exception being the region within a few tenths of the minimum Mach number – that is, the Mach number for which the shock detaches.

Figure 2 shows a comparison of results obtained by the present theory with some data given in reference 5 for a cone with a half-angle of 20°. The Van Dyke second-order theory is somewhat more accurate than the Broderick second-order theory in figure 1; however, it begins to diverge significantly for the higher Mach numbers. Again the present theory is inaccurate only within a few tenths of the detachment Mach number. The significance of the weakness of the theory in this region as far as the overall design problem is concerned is that if one is designing for a very low supersonic Mach number, it is expedient to check in a table of pressure coefficient versus cone half-angle and Mach number to make sure that the value of C_p prescribed at the nose corresponds to a cone half-angle well within the attachment capability for the design Mach number.

In order to illustrate the application of the direct pressure calculation to nonconical bodies, figure 3 shows some results for a parabolic body at two free-stream Mach numbers. The Lighthill first-order theory is somewhat more accurate than a strict linear theory. The agreement of the present theory with the method of characteristics is very good at $M_\infty = 2$, with just small deviations at $M_\infty = 4$.

These comparisons in figures 1 to 3 indicate that the accuracy of the pressure calculation is good.

BODY SLOPE CORRECTION

Step (4) of the general procedure corrects the body slope so as to reduce the error in the distribution of C_p.

The change in C_p at a point x due to a change in R' at point t (for $x \geqq t$) is given by the following expression (modification of equation given in ref. 1, p. 453):

$$\Delta C_p(x) = \frac{2\Delta R'(t)\left[1 + u(t)\right]}{\beta(t)} U\left[\frac{x - t}{\beta(t)R(t)}\right]$$

Here U is the same tabulated function used in step (2), the pressure calculation. In general, changes are to be made in C_p and in R' at all points. Consequently this calculation can become quite involved. However, it can be shown by an argument utilizing the fact that $U = 1$ when $t = x$ that the following simple equation is an approximate expression for $\Delta C_p(x)$:

$$\Delta C_p(x) = \frac{2\Delta R'(x)\left[1 + u(x)\right]}{\beta(x)}$$

This simplification does represent a rough approximation, but it is used here to relate incremental quantities; furthermore, the error does not have to be eliminated on any one iteration but just reduced significantly. In this equation the function $\Delta C_p(x)$ is simply the error in $C_p(x)$ obtained from step (3) of the general procedure. The equation is easily solved for $\Delta R'$ to obtain the new slope distribution for the new body shape:

$$R'_{n+1} = R'_n + \Delta R'$$

SAMPLE APPLICATION

The procedure converges rapidly. Four iterations appear to be adequate even for the worst cases. Machine time on the Control Data 6600 computer system is about 2 minutes for the entire program.

Figure 4 shows the results for one sample application, the design of a static pressure probe. The problem is to design a sensor that will read the free-stream pressure over a range of Mach numbers.

The sequence of calculations is as follows: The program input was represented by the solid curve – the design distribution of C_p for a free-stream Mach number of 2.5. With this input the body shape shown in the figure was computed. Then direct pressure calculations were made for the shape at the off-design Mach numbers, with the results indicated by the dashed lines.

It is seen that, if an orifice is located at about the 55-percent station, the probe should read the free-stream pressure over a considerable range of Mach numbers. It is interesting that although the detailed body shape is determined by the single design Mach number, in certain applications like this one it is possible to obtain a result that is useful over a range of Mach numbers.

CONCLUDING REMARKS

A rapidly converging iterative procedure for designing a supersonic body of revolution from a prescribed surface pressure distribution has been developed. The method facilitates comparison of design and off-design performance. Results calculated for a static pressure probe designed by this method indicated that it could be effectively used over a range of Mach numbers including the design Mach number.

REFERENCES

1. Lighthill, M. J.: Higher Approximations. General Theory of High Speed Aerodynamics. Vol. VI of High Speed Aerodynamics and Jet Propulsion, sec. E, W. R. Sears, ed., Princeton Univ. Press, 1954, pp. 345-489.

2. Kacprzynski, J. J.; and Landahl, M. T.: Recent Developments in the Supersonic Flow Over Axisymmetric Bodies With Continuous or Discontinuous Slope. AIAA Paper No. 67-5, Jan. 1967.

3. Liepmann, H. W.; and Roshko, A.: Elements of Gasdynamics. John Wiley & Sons, Inc., c.1957.

4. Sims, Joseph L.: Tables for Supersonic Flow Around Right Circular Cones at Zero Angle of Attack. NASA SP-3004, 1964.

5. Van Dyke, Milton D.: First- and Second-Order Theory of Supersonic Flow Past Bodies of Revolution. J. Aeron. Sci., vol. 18, no. 3, Mar. 1951, pp. 161-178.

COMPARISON OF SOLUTIONS FOR PRESSURE ON A CONE

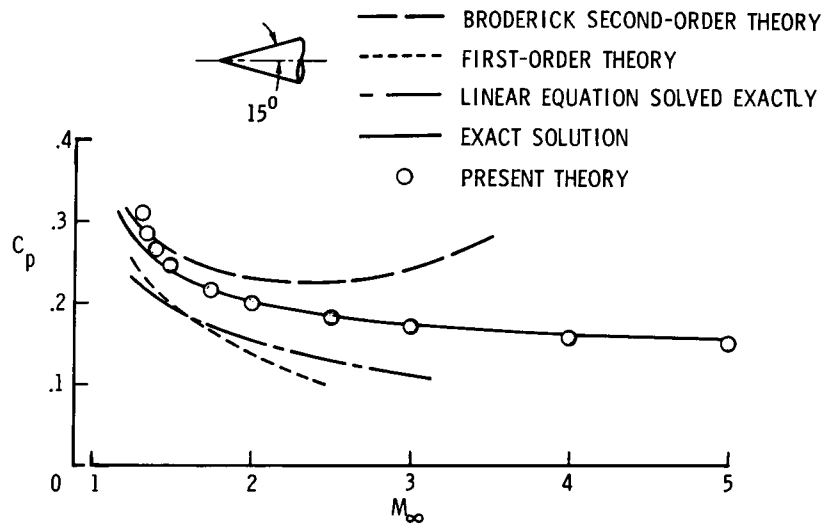

Figure 1

COMPARISON OF SOLUTIONS FOR PRESSURE ON A CONE

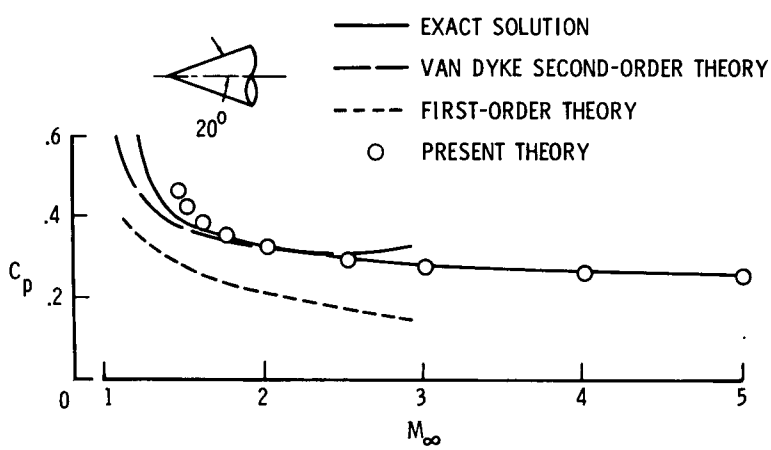

Figure 2

COMPUTED C_p DISTRIBUTION FOR PARABOLIC BODY
FINENESS RATIO, 7

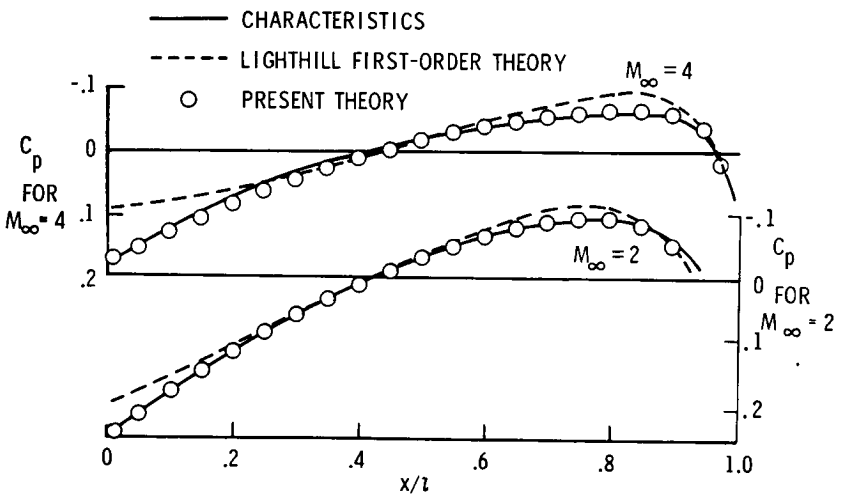

Figure 3

EXAMPLE CASE OF APPLICATION OF METHOD

PRESSURE-SENSOR DESIGN

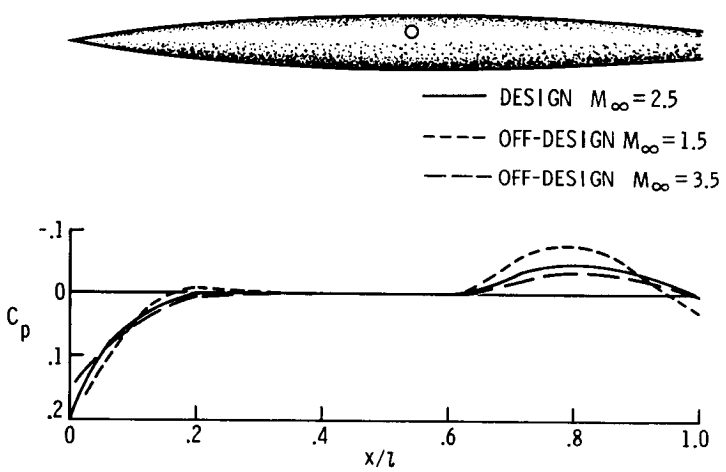

Figure 4

DISCUSSION

THEODORE R. GOODMAN, Oceanics, Inc.: Last spring I attended the Canadian Aeronautical Institute in a joint meeting with the AIAA in Ottawa, and a paper was presented which used exactly the same six-step procedure but in designing incompressible bodies, and I think that the two papers together cover the complete Mach number range. You might be interested to look it up.

BARGER: I am glad you mentioned the subsonic calculation. I have been working on a similar problem for the subsonic case in an effort to include the compressibility.

If you use the von Kármán source distribution formula, similar to this Lighthill formula in the supersonic case, again using the local value of β, and solve the resultant integral equation by iteration or successive approximation, then you obtain a pressure calculation which is considerably more accurate than a similar strictly linear type of computation, especially for blunt bodies where, as you know, near the nose you have real problems in the compressible case. But you get a very accurate calculation for the direct pressure calculation. I haven't been able to perform the inversion as yet.

WALLACE D. HAYES, Princeton University: In the supersonic case the problem is hyperbolic in the sense that there is no upstream influence, and you do not seem to take advantage of this property in your method. Your method is the same method that would be appropriate for the subsonic case. If you were worried, which I guess you aren't, about computational efficiency, it seems to me you should take this into account. Perhaps yours uses so little machine time it's not worthwhile.

BARGER: To some extent, this is taken into account in the calculation, and it has a lot to do with the rapid conversion of the method, and it seems to be the reason that as yet I haven't been able to do it for the subsonic case; but that is really a matter of time, a matter of debugging the program. But it is taken into account in the machine program. I just failed to mention it.

EMPIRICAL METHOD FOR ESTIMATING PRESSURES ON ELLIPTIC CONES

By George E. Kaattari

Ames Research Center

N70-21356

SUMMARY

A method is presented for estimating the pressure distribution over elliptical cones at supersonic Mach numbers at angle of attack. The method is based on an empirical correlation between experimental pressures in the symmetry planes of elliptic cones and the pressures given by two-dimensional shock theory. The method is applicable for cones whose ellipticity ratios b/a range from 1 to 6, and whose maximum semiapex angles are less than 30° at Mach numbers greater than 2. Results given by the method are shown to agree well with experimental values.

INTRODUCTION

There is currently considerable interest in flow solutions for cones at supersonic speeds. Exact solutions are difficult to obtain, particularly for elliptic cones at angle of attack. Engineering estimates of pressure distributions can be made by the tangent-cone method or by Newtonian theory. However, these methods are reliable only for large angle cones of low ellipticity.

The following analysis will describe the development of a method for predicting pressure distributions on elliptic cones at supersonic Mach numbers. The method is based primarily on unique correlations between pressures in the symmetry planes of elliptic cones and pressures given by two-dimensional shock-expansion theory.

NOTATION

A^*	normalized base area coordinate (fig. 3)
a	cone base vertical semiaxis
b	cone base horizontal semiaxis
c_p	pressure coefficient
$c_{p_{A^*}}$	pressure coefficient at A^*

$c_{p_{cc}}$	circular-cone pressure coefficient, $\alpha = 0$
c_{p_w}	two-dimensional or wedge pressure coefficient
c_{p_0}	cone pressure coefficient at $A^* = 0$, $\alpha = 0$
c_{p_1}	cone pressure coefficient at $A^* = 1$, $\alpha = 0$
d	differential operator
k_1,k_2,k_3	interpolation constants
l	cone length
M_∞	free-stream Mach number
n_0	exponent of A^*, $\alpha = 0$
n_α	exponent of A^*, $\alpha \neq 0$
y	vertical coordinate from cone axis
z	horizontal coordinate from cone axis
α	angle of attack, deg
Δc_{p_0}	incremental cone pressure coefficient at $A^* = 0$ due to angle of attack
Δc_{p_1}	incremental cone pressure coefficient at $A^* = 1$ due to angle of attack
δ^*	correlation constant (fig. 5)
δ_{w0}	wedge angle, zero angle of attack
$\delta_{w\alpha}$	wedge surface angle at angle of attack
δ_y	cone semiapex angle in vertical plane
δ_z	cone semiapex angle in horizontal plane

ANALYSIS

Zero Angle of Attack

Typical correlations developed between experimental pressures (refs. 1-4) in the symmetry planes of elliptic cones and the corresponding two-dimensional or wedge pressures when the wedge angles are equal to the cone

semiapex angles are shown in figure 1. Linear correlations result at a given Mach number for a family of cones that have the same ratio of base area to length but differ in cross-section ellipticity. Specifically, the slope is only a function of Mach number and the ratio $\sqrt{ab}/l$. Circular cones are included because the pressures at this coordinate point may be readily determined from supersonic handbooks (e.g., ref. 5). If, in addition, the value of the slope at this point were also known, the correlation line would be completely defined. The pressures in the symmetry planes of any elliptic cone in the family could then be determined from the correlation line with the two-dimensional (wedge) pressure coefficient corresponding to the cone angle in the plane of symmetry and the free-stream Mach number.

Experimentally determined slopes, including those of figure 1 and certain theoretical values (ref. 6), were plotted on logarithmic scales as a function of the ratio of circular-cone pressure to wedge pressure. The general, linear correlation shown in figure 2 was found to result for the indicated wide range of cone geometries and Mach numbers. The slope of this correlation is closely represented by $\left(c_{p_{cc}}/c_{p_w}\right)^{1.6}$. The pressure correlation lines of figure 1 are now fully defined, and the pressures in the symmetry planes of any elliptic cone in the family become determinable. Next, we attack the problem of determining the circumferential pressure distribution between the planes of symmetry.

By apparent mass theory, the chord force of a cone depends only on its maximum cross section or base area. Experimental indications (ref. 1) are that the chord forces of elliptic cones of a given length and Mach number also depend on the base area and are almost independent of ellipticity ratio. Newtonian theory predicts the same result for cones in a restricted ellipticity ratio range. It is therefore assumed, with some confidence, that the chord-force coefficient of an elliptic cone can be considered equal to that of a circular cone of the same base area and length.

Figure 3 outlines the manner in which the correlations of figures 1 and 2 and the above assumption with regard to chord-force coefficient may be used to estimate the circumferential pressure distribution on an elliptic cone at zero angle of attack. A quadrant of an elliptic cross section is shown. The variable A^* represents the ratio of the area of the indicated sector to that of the whole quadrant. The merit of this variable is that when the pressure distribution is integrated with respect to A^* over the quadrant, the chord force or average pressure coefficient with respect to the base area results. The pressure distribution is now characterized by the known pressures c_{p_0} and c_{p_1} in the planes of symmetry and the area under the pressure distribution curve which, by the previously stated assumption, is numerically the chord-force coefficient of an equivalent area circular cone or the mean pressure $c_{p_{cc}}$.

It is now assumed that the pressure variation is a monotonic function of the argument A^* modified by a distorting exponent n_0 which remains to be determined. The simple derivation indicated in figure 3 relates the known

pressures, c_{p_0}, c_{p_1}, and $c_{p_{cc}}$ to the integrated, assumed pressure distribution which, in normalized form, is a function only of n_0. Numerical values for the pressure coefficients fix the value of $f(n_0)$ and in turn, n_0 (fig. 4). The pressure-distribution function may then be evaluated as a function of A^* from equation (2).

Effect of Angle of Attack

It was again possible to correlate the pressures in the vertical plane of symmetry of cones at angle of attack with two-dimensional wedge pressures by an extension to the procedure described for zero angle of attack. On the left-hand portion of figure 5 is a schematic representation of the correlation technique used. The wedge angle δ_{w0} is determined so that the corresponding two-dimensional pressure is equal to the known pressure on the cone in the vertical plane of symmetry at zero angle of attack. The ratio of the wedge angle δ_{w0} to the vertical semiapex angle δ_{y0} is assumed to be a constant δ^* insensitive to angle of attack. Thus, if the cone is at angle of attack α, the corresponding wedge angle $\delta_{w\alpha}$ to give the same pressure should be equal to $\delta^*(\delta_y + \alpha)$. The validity of this assumption was borne out by the good correlation between predicted and experimental pressures shown on the right-hand portion of figure 5 for the range of variables indicated.

Predicting the effect of angle of attack on the pressures on cones in the horizontal plane of symmetry is somewhat more involved than in the vertical plane. Figure 6 shows the Newtonian theory result that the change in the horizontal plane pressure Δc_{p_1} with angle of attack is equal to the negative value of the zero angle of attack pressure c_{p_1} times sine squared of the angle of attack. Also shown on the figure are values from a sophisticated theory of Babenko (ref. 7) for circular cones. A linear correlation fit to these data in the low angle-of-attack range (0° to 5°) is represented by the top line for a wide range of Mach numbers and cone apex angles. It was discovered, however, that the ordinate value $\Delta c_{p_1}/\sin^2 \alpha$ had to be multiplied by a hypersonic similarity parameter $M_\infty \sin \delta_z$ in order to bring into correlation the data of those cones whose value for $M_\infty \sin \delta_z$ was less than unity. The Newtonian or bottom line was considered to represent data at $\alpha = 90°$ since the horizontal plane pressure will then be close to zero by reason of the resulting large flow expansion, that is, $\Delta c_{p_1} = -c_{p_1}$.

A technique for interpolating between the low-angle correlation (0°) expressed in the form $-\Delta c_{p_1}/c_{p_1} = (0.500 + 1.33c_{p_1})/c_{p_1} \sin^2 \alpha$ and the high-angle correlation (90°) expressed as $-\Delta c_{p_1}/c_{p_1} = \sin^2 \alpha$ was devised as follows: In figure 7 the line 0-1 has the slope $(0.500 + 1.33c_{p_1})/c_{p_1}$ and represents the low-angle correlation curve. The line 0-2 has the slope of unity (1) and represents the Newtonian and/or high-angle-of-attack correlation

curve. The solid curve represents a monotonic interpolation function of $\sin^2 \alpha$ which is tangent to the low- and high-angle correlation curves in the neighborhoods of their respective validity ($\sin^2 \alpha = 0$ and 1.0). The simplest monotonic interpolation function was found to be a series expression of three terms with the ordinate $\Delta c_{p_1}/c_{p_1}$ as the independent variable; that is,

$$\sin^2 \alpha = k_1\left(\frac{\Delta c_{p_1}}{c_{p_1}}\right) + k_2\left(\frac{\Delta c_{p_1}}{c_{p_1}}\right)^2 + k_3\left(\frac{\Delta c_{p_1}}{c_{p_1}}\right)^3$$

In order to satisfy the known slopes and ordinates required of the interpolation function, the values of the coefficients k were found to be

$$k_1 = \frac{c_{p_1} M_\infty \sin \delta_z}{0.500 + 1.33c_{p_1}}, \qquad k_2 = -2(k_1 - 1), \qquad \text{and} \qquad k_3 = (k_1 - 1)$$

The term $M_\infty \sin \delta_z$ is included only when its value is less than unity. The above equation for $\sin^2 \alpha$ was evaluated for various numerical values of k_1 to tabulate $\sin^2 \alpha$ as a function of $\Delta c_{p_1}/c_{p_1}$. This tabulation was used to construct curves of $-\Delta c_{p_1}/c_{p_1}$ as a function of angle of attack for various values of k_1. These curves are presented in figure 8. Although figure 8 is based on circular-cone data, the results are assumed to be valid for elliptic cones as well.

The pressure in the horizontal and vertical planes of symmetry is shown now for a cone at angle of attack. Through symmetry, the spanwise derivative of the pressure distribution at the vertical plane of symmetry is necessarily zero. These end conditions are not sufficient constraints to define the pressure distribution reliably, so additional pressure information is necessary.

The pressure derivatives given by Babenko's data for circular cones in the horizontal plane of symmetry at angle of attack compared with the simple result of Newtonian theory are presented in figure 9. Surprisingly, a good, one-to-one correlation results. Again, while this correlation is based on circular-cone data, it is assumed to be valid for elliptic cones as well. With this correlation, an additional constraint to the pressure distribution curve is in hand.

It is convenient to treat the angle-of-attack pressures as increments to be added to the zero angle-of-attack pressures. Figure 10 is a normalized plot of circular-cone incremental pressures against A^*. It is again assumed that the distribution is a simple monotonic cosine function of the argument A^* raised to some power n_α. The relationship of n_α to the assumed pressure distribution is easily found by the differentiation indicated in the

figure. The Newtonian value of $\pi \sin^2 \delta_z \sin 2\alpha/\tan \delta_y$ is substituted for the end-point slope $(dc_p/dA^*)_1$, allowing n_α and thus the incremental pressure distribution to be evaluated.

In the case of elliptic cones, a modification to the Newtonian pressure derivative given is required. This correction takes into account the fact that an elliptic cone does not have a constant zero angle-of-attack reference pressure distribution and although the pressure derivative is zero at $A^* = 1$, it rapidly assumes a value other than zero at $A^* < 1$. It was found for a wide range of cone ellipticity ratios that a good approximation to the zero angle-of-attack pressure distribution was characterized by a curve whose pressure derivative in the vicinity of $A^* = 1$ is $2(c_{p_1} - c_{p_0})$. This value was added to the Newtonian value to give the effective derivative of the incremental pressure distribution at $A^* = 1$ or

$$(dc_p/dA^*)_1 = \pi \sin^2 \delta_z \sin 2\alpha/\tan \delta_y + 2(c_{p_1} - c_{p_0})$$

COMPARISON OF PREDICTED AND EXPERIMENTAL RESULTS

Zero Angle of Attack

The present method is compared in figure 11 with the tangent-cone method, Newtonian theory, and experiment (refs. 1-2). The pressures are plotted as a function of the normalized spanwise coordinate z/b. For cones of large ellipticity at Mach number 2, the present method agrees better with experiment than does the tangent-cone method or Newtonian theory. The superiority of the method is less pronounced with respect to the tangent-cone method for cones with b/a ratios close to unity as is to be expected.

Angle of Attack

The comparison of experimental (ref. 2) and predicted results for pressure distributions for two elliptic cones at Mach number 6 presented in figure 12 indicates good agreement. For cones of low ellipticity such as those shown, the tangent-cone method will give good results at small angles of attack. For highly elliptic cones at large angles of attack, the present method is expected to give better results than the Newtonian or tangent-cone methods.

In figure 13 the present method is compared with a recent line method of Bazzhin (ref. 8) and modified Newtonian theory for a $b/a = 3$, elliptic cone at $M_\infty = 7$ and angle of attack of 30°. The present method is in good agreement with the method of Bazzhin. The Newtonian theory predicts the maximum pressure well in this case, but the pressure distribution differs considerably from the other predictions.

CONCLUDING REMARKS

It has been shown by comparison with experiment that good estimates of pressure in the symmetry planes of elliptic cones can be made by utilizing a simple empirical correlation with two-dimensional or wedge pressures. These pressures, in conjunction with experimentally verified constant chord-force coefficients for a given cone family and Mach number, are sufficient information to enable good estimates to be made of pressure distributions for cones at zero angle of attack.

The effect of angle of attack on pressures in the symmetry planes of cones was also shown to correlate in a simple manner with wedge theory and with Newtonian theory.

REFERENCES

1. Jorgensen, Leland H.: Elliptic Cones Alone and With Wings. NACA Rep. 1376, 1958.

2. Zakkay, Victor; and Visich, Marian, Jr.: Experimental Pressure Distributions on Conical Elliptical Bodies at $M_\infty = 3.09$ and 6.0. Pibal Rep. 467, AFOSR TN 59-10, AD 208591, March 1959.

3. Chapkis, Robert L.: Hypersonic Flow Over an Elliptic Cone: Theory and Experiment. Guggenheim Aeron. Lab., Calif. Inst. Tech. Hypersonic Res. Proj. Memo. No. 49, May 1, 1959.

4. Ortloff, Charles R.: Hypersonic Approximation for the Inviscid Flow Over Conical Bodies Without Axial Symmetry and Comparison With Test at Mach 8. Pibal Rep. 728, AFOSR 1634, Jan. 1961.

5. Ames Research Staff: Equations, Tables, and Charts for Compressible Flow. NACA Rep. 1135, 1953.

6. Van Dyke, Milton D.: The Slender Elliptic Cone as a Model for Non-Linear Supersonic Flow Theory. J. Fluid Mech., vol. 1, no. 1, May 1956, pp. 1-15.

7. Babenko, K. I.; Voskresenskiy, G. P.; Lyubimov, A. N.; and Rusanov, V. V.: Three-Dimensional Flow of Ideal Gas Past Smooth Bodies. TT F-380, 1966, NASA, from Prostranstvennoye Obtekaniye Gladkikh tel Ideal'nym Gazon Izdatel'stvo Nauka, Moscow, 1964.

8. Bazzhin, A. P.; Trusova, O. N.; and Chelysheva, I. F.: Analysis of Perfect Gas Flow Around Elliptic Cones at High Angles of Attack. Izv. Akad, SSSR. Mekh. i Gaza (Moscow), no. 4, 1968, pp. 45-51.

EXAMPLE CORRELATION OF CONE AND WEDGE PRESSURES

$\alpha = 0°$, z PLANE

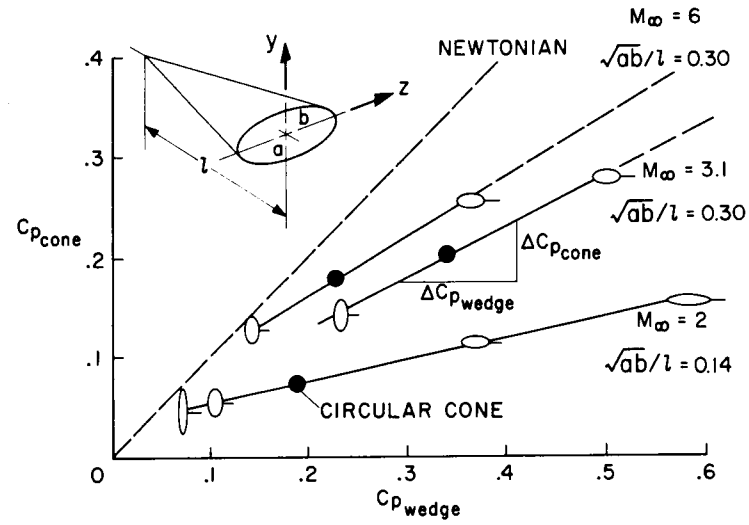

Figure 1

SLOPES OF CONE-WEDGE PRESSURE CORRELATION LINES

$\alpha = 0°$

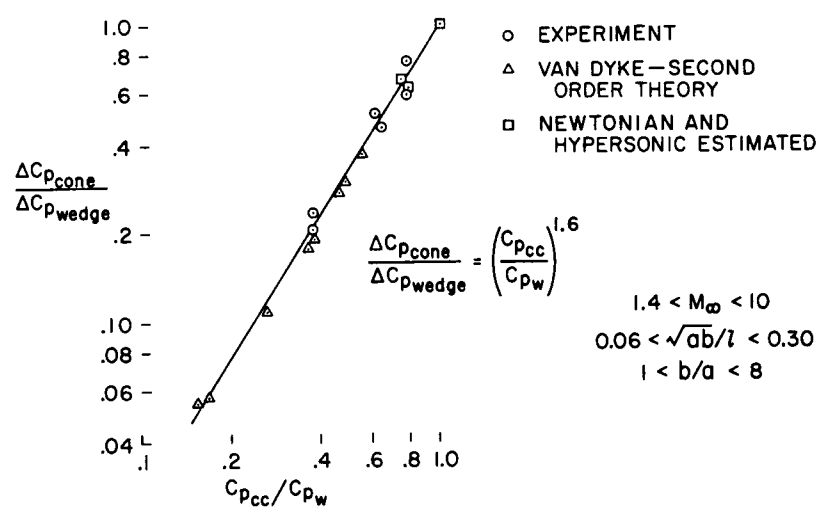

Figure 2

METHOD OF DETERMINING PRESSURE DISTRIBUTION

$\alpha = 0°$

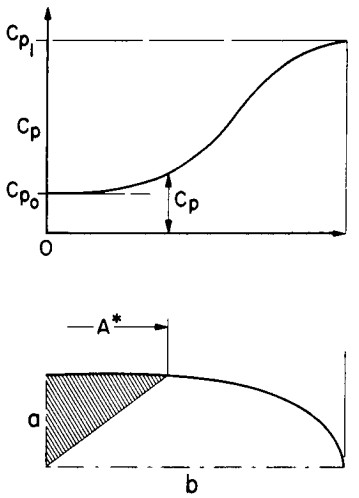

ASSUMPTIONS:

$$\int_0^1 C_p \, dA^* = C_{p_{cc}} \qquad (1)$$

$$\frac{C_{p_l} - C_p}{C_{p_l} - C_{p_o}} = \frac{1 + \cos \pi (A^*)^{n_o}}{2} \qquad (2)$$

$$\frac{C_{p_l} - C_{p_{cc}}}{C_{p_l} - C_{p_o}} = \int_0^1 \left[\frac{1 + \cos \pi (A^*)^{n_o}}{2}\right] dA^*$$

$$= f(n_o) \qquad (3)$$

Figure 3

THE FUNCTION $f(n_o)$

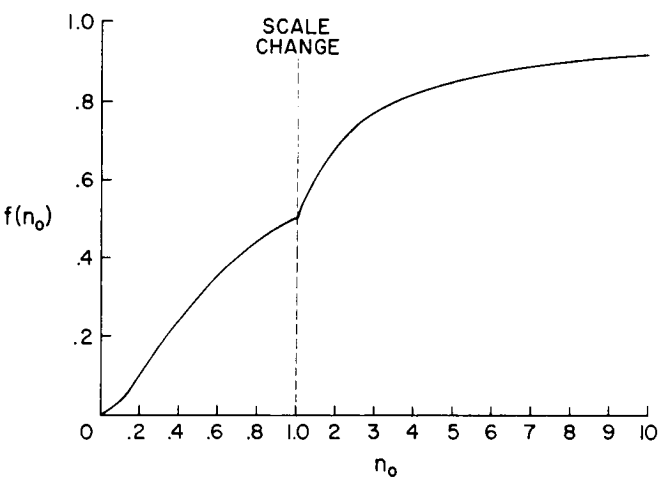

Figure 4

CALCULATED AND EXPERIMENTAL PRESSURES IN VERTICAL PLANE OF SYMMETRY

$\alpha \neq 0°$

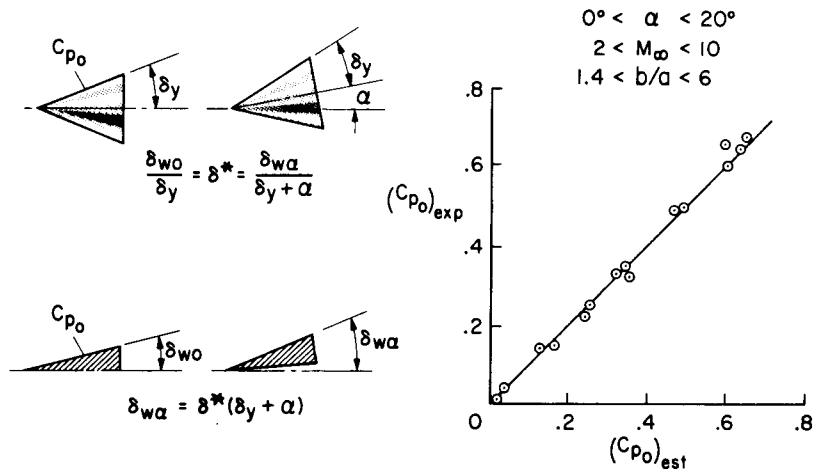

Figure 5

EFFECT OF ANGLE OF ATTACK ON PRESSURES IN HORIZONTAL PLANE OF SYMMETRY FOR CIRCULAR CONES

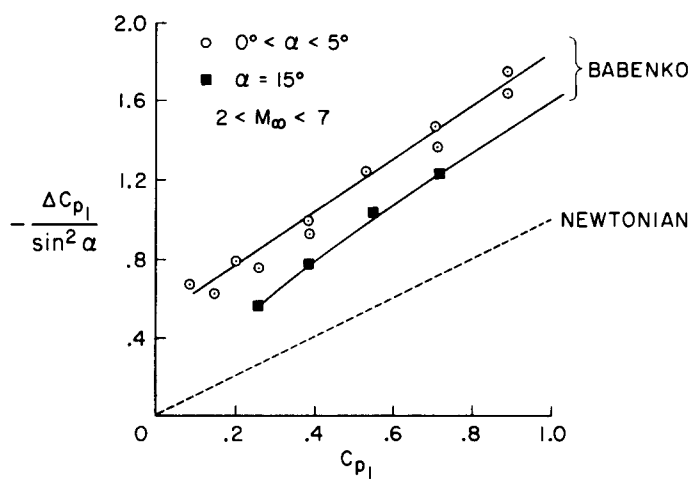

Figure 6

BASIS OF INTERPOLATION TECHNIQUE

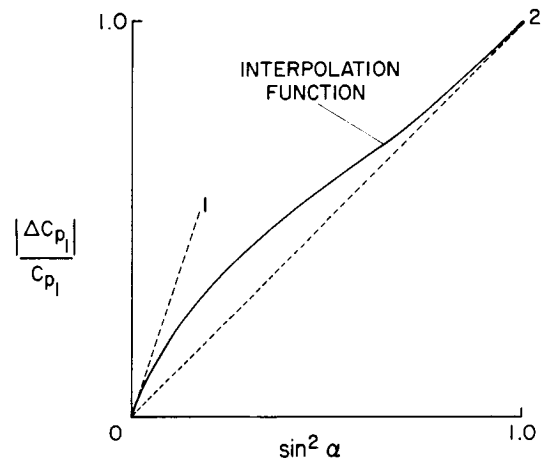

Figure 7

PRESSURE DECREMENT IN HORIZONTAL SYMMETRY PLANE

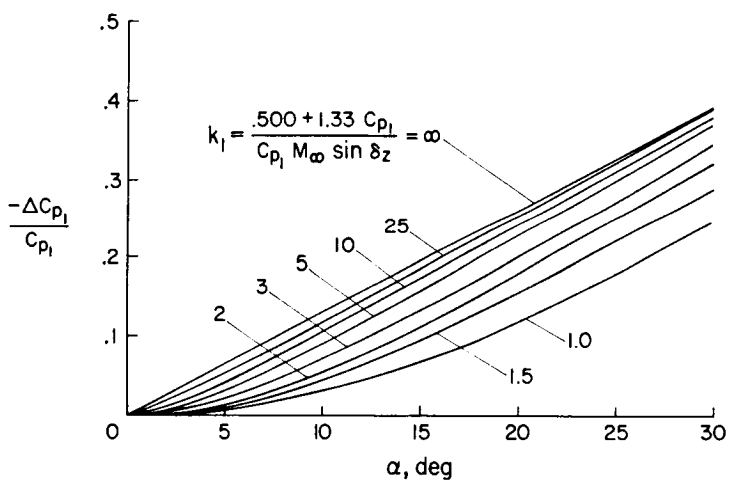

Figure 8

PRESSURE DERIVATIVES IN THE HORIZONTAL PLANE OF SYMMETRY FOR CIRCULAR CONES

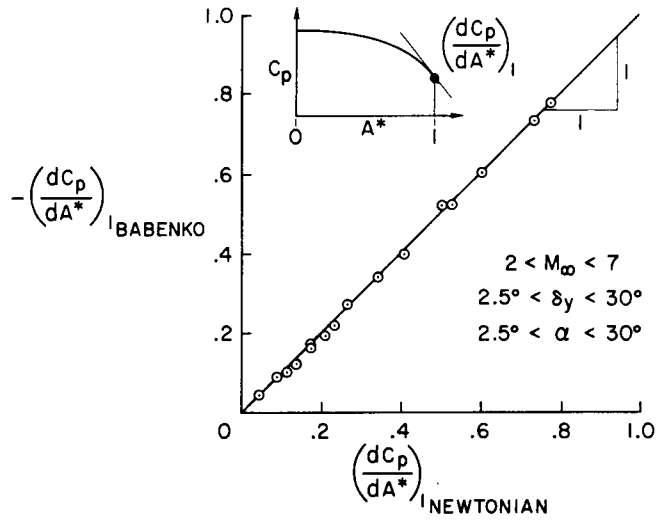

Figure 9

ESTIMATION OF PRESSURE DISTRIBUTION DUE TO ANGLE OF ATTACK

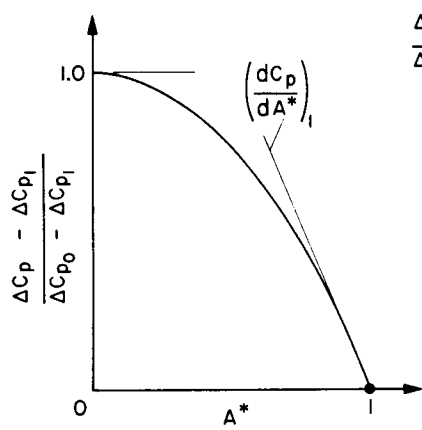

$$\frac{\Delta C_p - \Delta C_{p_1}}{\Delta C_{p_0} - \Delta C_{p_1}} = \cos\frac{\pi}{2}(A^*)^{n_a}$$

$$\left(\frac{dC_p}{dA^*}\right)_1 = -\frac{n\pi}{2}\left(\Delta C_{p_0} - \Delta C_{p_1}\right)$$

$$n = \frac{2\left(dC_p/dA^*\right)_1}{\pi\left(\Delta C_{p_1} - \Delta C_{p_0}\right)}$$

Figure 10

PREDICTED AND EXPERIMENTAL PRESSURES
$\alpha = 0°$

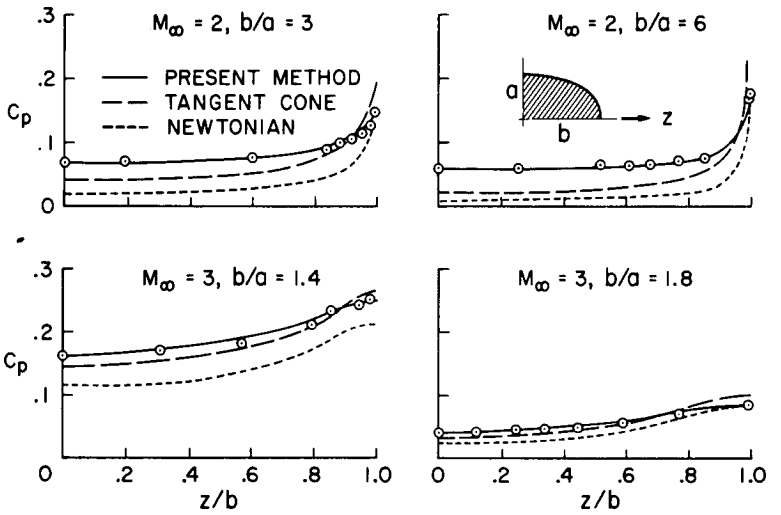

Figure 11

PREDICTED AND EXPERIMENTAL PRESSURE DISTRIBUTIONS
$M_\infty = 6$, $\alpha \neq 0°$
—— PREDICTED
△ □ EXPERIMENT

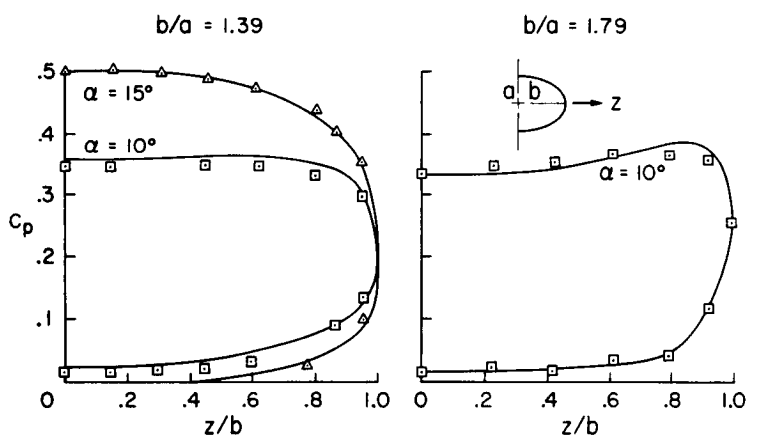

Figure 12

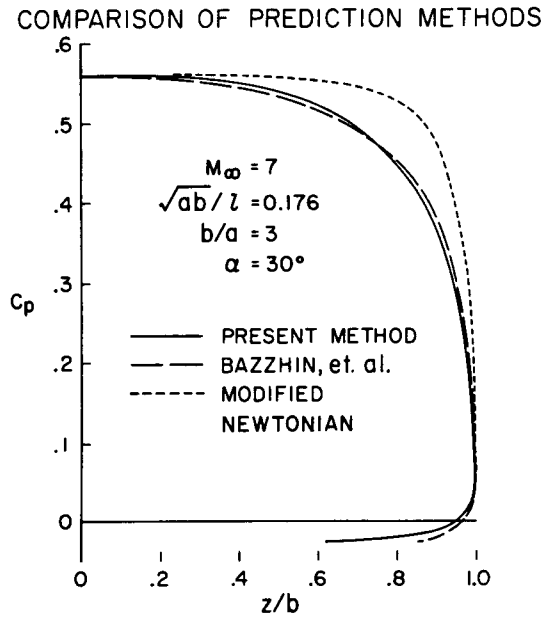
COMPARISON OF PREDICTION METHODS
$M_\infty = 7$
$\sqrt{ab}/l = 0.176$
$b/a = 3$
$\alpha = 30°$
PRESENT METHOD
BAZZHIN, et. al.
MODIFIED NEWTONIAN
C_p
z/b
.6
.5
.4
.3
.2
.1
0
0
.2
.4
.6
.8
1.0

Figure 13

DISCUSSION

ERNEST O. MARCHAND, ARO, Inc.: This is not in the form of a question but a comment that may be useful to some people here. There is a program, available upon request, by D. J. Jones (Aeronautical Report LR-507) of the National Aeronautical Establishment, Ottawa, Canada, that is capable of calculating elliptic cones at angle of attack. To my knowledge, this is the only readily available program. It runs very quickly for all the sharp cones. I think the 360-50 running time is only a minute and half.

This report seems to have gotten a rather limited distribution, and many people don't know about it. I thought it appropriate that I should bring it up.

LORNE C. DUNSWORTH, CCI Marquardt Corp.: I wonder if you would comment on the possibility of extending this technique to elliptic ogives at angle of attack. Is there a way to do it?

KAATTARI: I don't know. I have thought of it, but I don't know if it is possible. I couldn't say at this time. I'd be glad to try it.

It may be that one could use Prandtl-Meyer flow and start from the cone, but I don't know, it might be quite difficult. For the angle-of-attack case equal to zero it might be feasible, but for the angle-of-attack case it would be quite difficult.

IMPROVEMENT OF WING-BODY INTERFERENCE THEORY FOR HYPERSONIC SPEEDS

By William C. Pitts

Ames Research Center

N70-21357

SUMMARY

Calculated results from two theories are found to agree equally well with experimental data for the lift-curve slope and for the stability derivative for the Mach number range 5.3 to 10.7. The results agree despite the fact that one theory predicts a large effect of wing-body interference and the other neglects interference effects. Theoretical examination of load distributions on the body and wing, with and without interference effects, verifies that, for the example considered, the total force and moment is the same by both theories, but the load distributions are very different.

INTRODUCTION

The subject of wing-body interference has been extensively explored both theoretically and experimentally for the subsonic and supersonic speed ranges, but not very much has been done in the hypersonic speed range. In reference 1 an extensive comparison was made between theory and experiment for about 70 sets of data of widely different configurations for subsonic, transonic, and supersonic speeds up to Mach number 2. It was found that the lift-curve slope was predicted within 10 percent for all sets of data and that wing-body interference accounted for between 20 to 30 percent of the lift of the wing-body combinations. The purpose of the present program was to see if this large and favorable wing-body interference effect persisted to the hypersonic speed range.

6

TOTAL FORCE AND MOMENT

In lieu of an adequately established hypersonic Mach number theory, the supersonic theory of reference 1 was used as the first tool of the investigation. This theory was used to estimate the pitching moment and the lift-curve slope for a model that was tested at Ames (ref. 2). The model is shown in figure 1. The body has a fineness ratio 12 and a Sears-Haack nose. The wing has a delta planform with a 70° leading-edge sweep angle. The wing is 4 percent thick with flat surfaces; the bottom surface would pass through the body axis if extended.

Preceding page blank

In figure 2, experimental data for C_{L_α} and $\partial C_m/\partial C_L$ are compared with calculated results from two theories. Both of these quantities are predicted reasonably well by the theory of reference 1 (NACA Rep. 1307) within the Mach number range 5.3 to 10.7. This good agreement plus the fact that 25 percent of the lift is due to wing-body interference effects, according to the theory, suggests that wing-body interference is important at hypersonic speeds as well as at supersonic speeds. However, the tangent-cone, tangent-wedge method also predicts the experimental data well (except for $\partial C_m/\partial C_L$ at $M = 10.7$) and it includes no interference effects. Obviously, then, some compensating effects are present in one or both of these theories, and the question of the importance of wing-body interference is not resolved by this comparison.

THEORETICAL LOAD DISTRIBUTION

Correction Factors

To study this problem further the program was extended to look at the load distribution on the wing-body combination. The wing-body interference theory of reference 1 could not be used for this extension because it gives only the total force and moment. Instead, the linearized, quasi-cylindrical theory of Nielsen (ref. 3) was chosen for studying the load distribution. This theory has been demonstrated to be applicable at supersonic speeds by comparison with experiment (ref. 4) but several assumptions made in the theory must be examined before it can be applied to the hypersonic speed range. The first assumption is that the slender-body theory of Beskin properly predicts the body upwash. Other assumptions are that in the region of the wing the local dynamic pressure and the local Mach number are the same as in the free stream. These assumptions will now be examined in turn beginning with the body-upwash assumption.

The mechanics of body upwash are summarized in figure 3. Any body inclined at an angle α to a flowing gas will have a normal component of velocity V_N which streams around the body in the cross-flow plane. Then, according to the slender-body upwash theory of Beskin, the local angle of attack in the wing plane varies along the span as

$$\alpha_L = [1 + (a/r)^2]\alpha \tag{1}$$

where a is the body radius, and r is the radial coordinate. At the wing root, where $a/r = 1$, the wing is effectively flying at twice the angle of attack of the body. This then is the reason wing-body interference is favorable.

This upwash model has been found to be adequate at low supersonic Mach numbers but until recently its use in the hypersonic speed range has not been justified. Now the method-of-characteristics calculations by Rakich (ref. 5) have shown that upwash varies in a manner similar to the Beskin

equation except for an empirical factor σ.

$$\alpha_L = [1 + \sigma(a/r)^2]\alpha \tag{2}$$

This was found to be true for Mach numbers up to 10.7. The term in the brackets is then a factor that corrects the free-stream angle of attack to the local angle of attack.

The correction factors for Mach number and dynamic pressure will now be developed with the aid of figure 4. The sketch at the top of the figure shows a wing mounted on a cylindrical-body section. The theory of reference 3 will give the pressure distribution aft of the wing Mach wave. The method of reference 5 will give body-alone pressures forward of the wing. For this figure the subscript ∞ refers to free-stream conditions and the subscript L refers to conditions near the cylindrical part of the body. Calculations by the method of characteristics show that although flow parameters vary rapidly near the body nose they become virtually independent of axial distance in the subscript L region. For Mach numbers less than 2 the shock is relatively weak and the subscript L values are essentially equal to the subscript ∞ values. At hypersonic speeds they can differ significantly, and the pressure, p_2, cannot be calculated directly in terms of the free-stream conditions by simple theories. However, it can be calculated in terms of subscript L conditions because they are essentially free-stream conditions to the wing. The pressure coefficient according to linear theory is then

$$\frac{p_2 - p_L}{q_L} = \frac{2\alpha_L}{\beta_L} \tag{3}$$

The pressure coefficient can then be expressed in terms of free-stream conditions by simple algebraic manipulation of equation (3)

$$\frac{p_2 - p_\infty}{q_\infty} = \frac{2\alpha}{\beta_\infty}\left(\frac{\alpha_L}{\alpha}\frac{q_L}{q_\infty}\frac{\beta_\infty}{\beta_L}\right) + \frac{p_L - p_\infty}{q_\infty} \tag{4}$$

The second term of equation (4) is generally large in the body-nose region, and must be retained there, but calculations by the method of characteristics show that even for $M_\infty = 10.7$, this term approaches zero aft of the nose and can be neglected in the subscript L region. Thus the pressures on the winged region of the combination can be expressed in terms of free-stream conditions and three correction factors. The first is the upwash correction factor α_L/α given by equation (2). The other two factors, q_L/q_∞ and β_∞/β_L correct q and β to local values. The product of these three factors is called λ. Then the pressures on the winged region of the wing-body combination can be expressed in terms of the product of free-stream conditions and the total correction factor.

$$P = \frac{p_2 - p_\infty}{q_\infty} = \lambda\left(\frac{2\alpha}{\beta_\infty}\right) \tag{5}$$

Although λ and its components are virtually independent of axial distance they do depend on r. Calculations by the method of characteristics (ref. 5) show that the radial variation can be very closely approximated by the $\sigma(a/r)^2$ form of equation (2). The pressure distributions that will be presented later have had this correction factor incorporated into the calculations.

Figure 5 shows how these factors vary with Mach number at the wing-body juncture. Note that at Mach number 2 both β_L and q_L are essentially equal to free-stream values so that the assumption of this fact (for $M_\infty \leq 2$) in reference 3 was valid. Also the use of slender-body theory to estimate body upwash was valid in this Mach number range. As the Mach number is increased from 2, each of the individual correction factors diverges from the slender-body theory value. However, the effects of these divergences are compensating and, fortuitously, the net effect is that λ, as calculated by the method of characteristics, remains very nearly equal to the slender-body theory value for λ throughout the Mach range.

Calculated Loading

The effect of these correction factors is shown in figure 6. The figure shows the chordwise pressure distribution at the wing-body juncture for the model shown in figure 1. The pressure coefficient P and the axial distance x from the wing leading edge are presented in normalized forms $\beta P/\alpha$ and $x/\beta a$, where α is the free-stream angle of attack. All three curves were calculated using the quasi-cylindrical theory of reference 3. The only difference between the curves is the manner in which the correction factor is calculated. For the upper curve the method of characteristics was used to calculate λ. For the middle curve slender-body theory was used, and for the lower curve no correction was used for upwash, β_L or q_L. As would be expected from the results of figure 5, it makes little difference whether the method of characteristics or slender-body theory is used to calculate the correction factor. However, there is a large difference if no correction is used for local flow conditions.

Figure 7 shows the same thing for the entire wing. The $r/a = 1$, or wing-body juncture plane, shows the same pressure distribution as figure 6. The pressure distributions in the $r/a = 2$ and $r/a = 5$ planes are also shown. In all planes, the upper curve is the pressure coefficient with correction factor and the lower curve is the pressure coefficient for no correction factor. All along the wing leading edge the pressure is the same as that of an isolated flat plate inclined at the local angle of attack. At the wing root ($r/a = 1$) the pressure starts decreasing immediately in the chordwise direction. At $r/a = 2$ the pressure rises in front of the Mach wave from the wing root leading edge and then decreases behind the Mach wave. The rise is due to this wing element experiencing the influence of inboard elements which are flying at higher effective angles of attack. At $r/a = 5$ the wing is entirely in front of the Mach wave and the body upwash effect is small so that the pressure is nearly constant over the entire chord and the two curves are very nearly the same.

In contrast to the varying pressure level predicted by this theory, the tangent-wedge method predicts a uniform pressure over the entire wing, indicated by the three hash marks at the leading edges of the three radial stations. This is also the pressure level obtained if the interference theory pressure distribution is averaged over the entire wing. Thus the lift predicted on the wing is the same for both theories. The interference theory, however, predicts a larger nose-up moment on the wing than does the tangent-wedge method. This nose-up moment is compensated for by a nose-down moment contributed by interference pressures from the wing acting on the afterbody. This is shown by the pressure distribution on the body in figure 8. To simplify the isometric drawing the body is shown as a flat surface in the wing plane. In this view the Mach wave appears as a straight line rather than a helix around the cylindrical body. Because the cylindrical-body section generates no lifting pressure according to the theory of reference 3, this pressure is due entirely to interference on the body from the wing.

CONCLUDING REMARKS

In summary, two theories have been compared. One of them includes wing-body interference effects and the other does not. The two theories agree with each other and with experimental measurements of the total lift and pitching moment for the wing-body combination considered. They also agree on the amount of lift on the wing and on the body. However, they differ on the distribution of lift and hence on the moment acting on the wing and on the body. Fortuitously these differences cancel. The question still remains as to which, if either, of the two theories is correct. The answer to this question awaits experimental evidence from programs now in progress.

REFERENCES

1. Pitts, William C.; Nielsen, Jack N.; and Kaattari, George E: Lift and Center of Pressure of Wing-Body-Tail Combinations at Subsonic, Transonic, and Supersonic Speeds. NACA Rep. 1307, 1957.

2. Nelms, Walter P., Jr.; and Carmichael, Ralph L.: An Experimental and Theoretical Investigation of a Symmetrical and a Cambered Delta Wing Configuration at Mach Numbers From 2.0 to 10.6. NASA TN D-5272, 1969.

3. Nielsen, Jack N.: Quasi-Cylindrical Theory of Wing-Body Interference at Supersonic Speeds and Comparison With Experiment. NACA Rep. 1252, 1955.

4. Pitts, William C.; Nielsen, Jack N.; and Gionfriddo, Maurice P.: Comparison Between Theory and Experiment for Interference Pressure Field Between Wing and Body at Supersonic Speeds. NACA TN 3128, 1954.

5. Rakich, John V.; and Cleary, Joseph W.: Theoretical and Experimental Study of Supersonic Steady Flow Around Inclined Bodies of Revolution. Preprint 69-187, AIAA, 1969.

MODEL

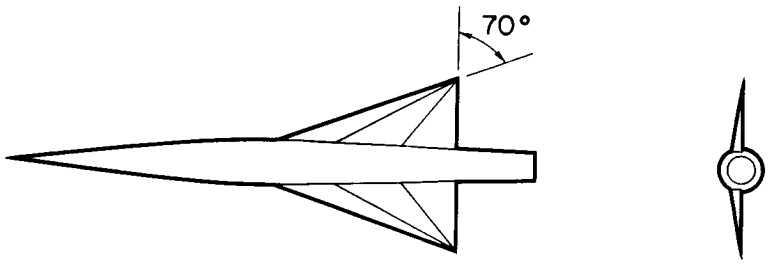

Figure 1

COMPARISON OF THEORY AND EXPERIMENT

$\alpha = 0°$

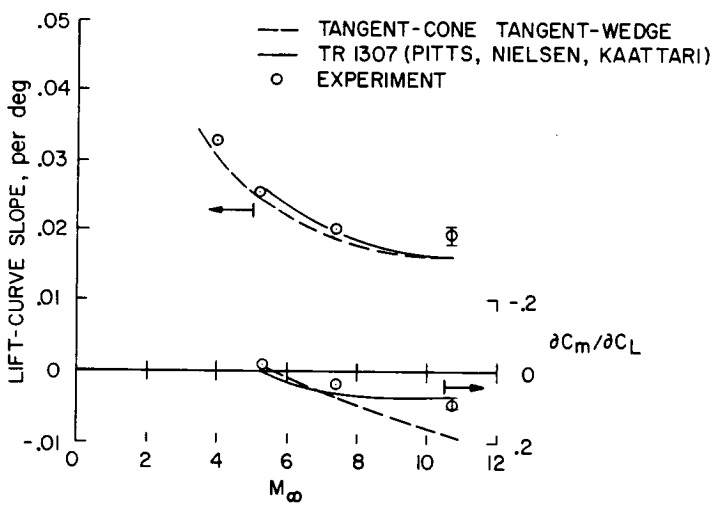

Figure 2

CORRECTION FACTOR FOR BODY UPWASH

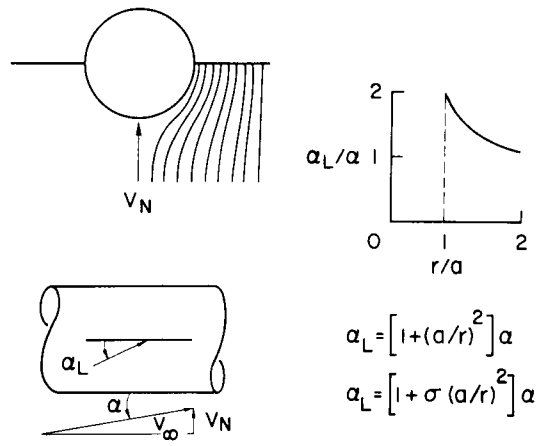

$$\alpha_L = \left[1+(a/r)^2\right]\alpha \quad \text{(SLENDER BODY)}$$

$$\alpha_L = \left[1+\sigma\,(a/r)^2\right]\alpha \quad \text{(σ FROM METHOD OF CHARACTERISTICS)}$$

Figure 3

CORRECTION FACTORS FOR MACH NUMBER AND DYNAMIC PRESSURE

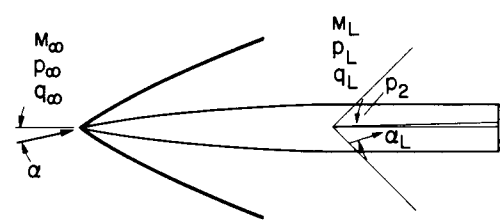

$$\frac{p_2-p_L}{q_L} = \frac{2}{\beta_L}\,\alpha_L$$

$$\frac{p_2-p_\infty}{q_\infty} = \frac{2}{\beta_\infty}\,\alpha\left(\frac{\alpha_L}{\alpha}\cdot\frac{q_L}{q_\infty}\cdot\frac{\beta_\infty}{\beta_L}\right) + \frac{p_L-p_\infty}{q_\infty}$$

$$\frac{p_2-p_\infty}{q_\infty} = \frac{2}{\beta_\infty}\,\alpha\lambda$$

Figure 4

VARIATION OF CORRECTION FACTORS WITH MACH NUMBER

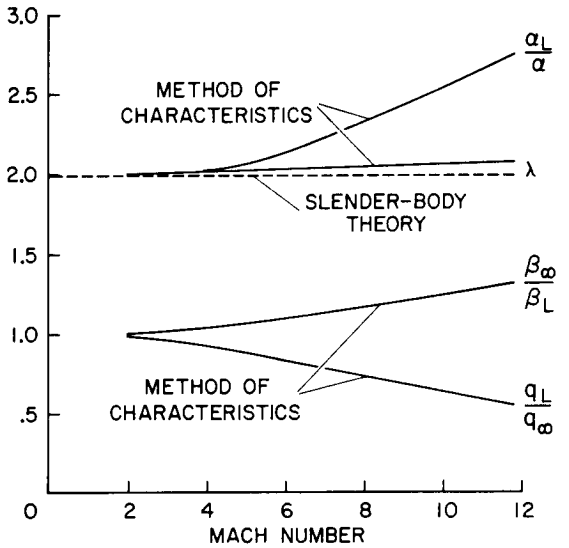

Figure 5

CHORDWISE PRESSURE DISTRIBUTION AT WING-BODY JUNCTURE
$M_\infty = 7.4$, $\Lambda_{L.E.} = 70°$

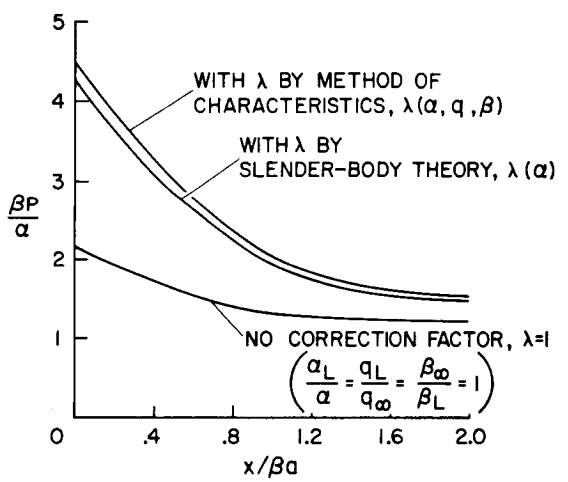

Figure 6

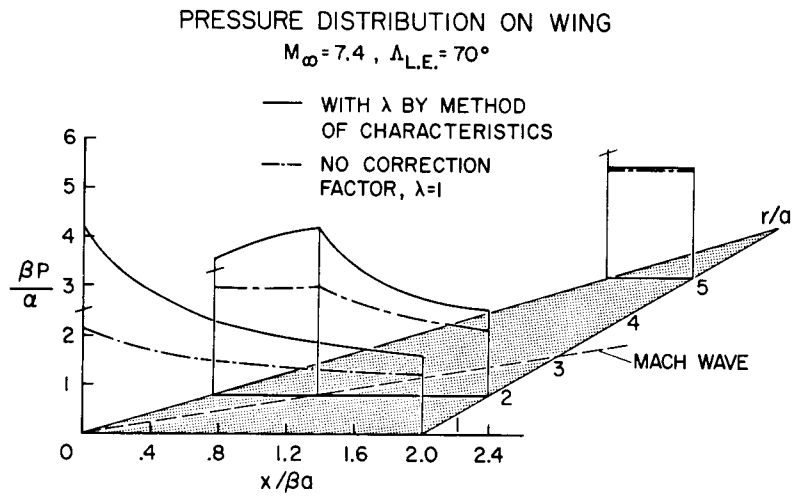

Figure 7

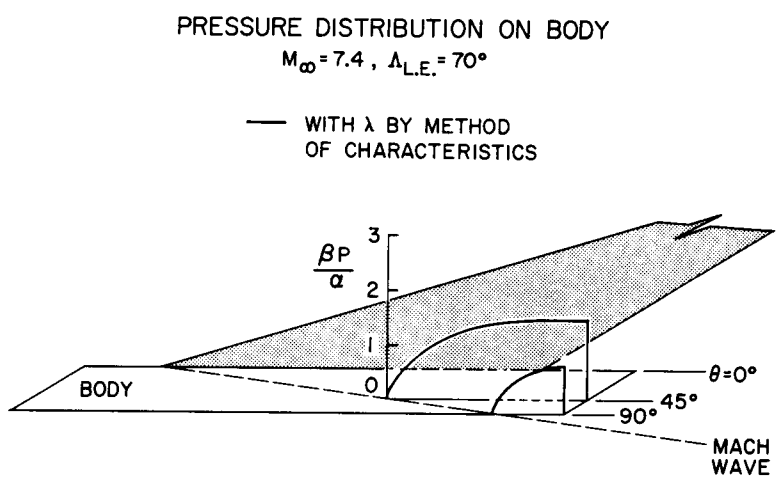

Figure 8

DISCUSSION

A. R. GEORGE, Cornell University: If these sigmas and lambdas were determined for this one shape that you showed, do you expect that you would get this close an equivalence between the slender body and the characteristics calculations in general?

PITTS: We are talking now about the cylindrical section of bodies. I don't think that the nose shape is going to have too much of an effect if you get far enough aft of the body shoulder.

THEORETICAL STUDIES OF VORTEX FLOW ON SLENDER WING-BODY COMBINATIONS

By E. S. Levinsky and M. H. Y. Wei
Air Vehicle Corporation

and

Ralph L. Maki
Ames Research Center

N70-21358

SUMMARY

An analytical procedure is presented for determining the nonlinear lift and pressure distribution on slender wing-bodies with leading-edge vortices. The theory is restricted to flows which satisfy the usual constraints imposed by slender-body theory.

Both conical and nonconical developments are presented. The theoretical results are evaluated by comparing with wind-tunnel force and pressure data. Both theory and test data show large increases in lift due to leading-edge vortices for even the smaller size strakes. Good correlation was obtained over the complete angle-of-attack range for cones with strakes of 50 percent of the body radius or greater. For these configurations the lift was approximately two times the linear theory value at angles of attack α equal to twice the strake semiapex angle δ. For cones with 25-percent and 10-percent strakes, good agreement was found except in the intermediate range $2 < \alpha/\delta < 4$.

Calculations for several nonconical configurations also agreed well with test data. Among the nonconical geometries considered were a cone with a filleted double-delta wing, a wing-body with a curved nose and strakes, and a conical body with variable incidence strakes.

7

INTRODUCTION

The present paper deals with the calculation of the nonlinear lift and pressure distribution on wing-bodies with leading-edge vortices. Such vortices are known to increase the lift at large angles of attack to several times that predicted by the usual linear analyses, thus invalidating the linear approach at large angles of attack. Both conical and nonconical theories are presented; however, the analysis is limited to configurations for which the usual slenderness assumptions apply.

A slender wing-body configuration with leading-edge vortices is shown in figure 1. The model, photographed in the Ames 7- by 10-Foot Wind Tunnel, is a blunted cone with small-span wings (strakes) at an angle of attack of

Preceding page blank

approximately 30°. The vortices are known to have a pronounced effect on lift and pressure distribution, hence the motivation for the present analysis. The well-known model for the leading-edge vortex consists of a feeding spiral sheet originating from the wing tip and winding inward into a central vortex core (see fig. 2). This model will be used in the subsequent analysis.

The general type of configuration geometry to be studied is also shown in figure 2. Effects of body cross section, relative strake-to-body size, strake dihedral, nose blunting, variable strake sweep angle, and variable strake incidence angle are included in the theory. Thus, the theory should be of use in evaluating the low-speed approach, landing, and control capabilities of recoverable booster or spacecraft configurations of high volumetric efficiency.

Several types of vortex flows have been observed for slender bodies and wing-bodies. For a body alone at a large angle of attack, two strong vortices are known to form on the leeward side (refs. 1 and 2) (see upper sketch in fig. 3). The separation point is determined by viscous effects for this case, and no complete theory which includes determination of the separation point has as yet been obtained. The present analysis deals with wing-body combinations for which the separation point is *fixed* at the wing leading edge (middle sketch in fig. 3). *A priori* knowledge of the separation point greatly simplifies the theory and enables an inviscid formulation to be used. It is conceivable that with very small span strakes the leading-edge vortex may influence the flow only locally in the region of the leading edge. In this case, body vortices could still occur as sketched in figure 3. Although the simultaneous occurrence of both body and strake vortices has not been confirmed visually, anomalous data obtained with small-span strakes can be explained by this hypothesis, as will be shown later.

Considerable research has been carried out on the leading-edge vortex for low aspect ratio wings and bodies as summarized in figure 4. The first successful analysis was carried out by Brown and Michael (ref. 3), who treated the conical flow past a flat delta wing. They used a simplified model for the vortex in which all the vorticity was lumped into the vortex cores. The vortex cores were joined to the wing tip by a cut. No feeding sheets were included. Their calculations gave the correct overall trend for the variation of lift with angle of attack. However, the vortex location was calculated to be too far outboard, and the overall lift was significantly overpredicted.

Mangler and Smith (ref. 4) improved the formulation by also including a feeding vortex sheet of a specified shape. This restriction was later removed by Smith (ref. 5) who considered a segmented vortex sheet and determined both its strength and position. The calculations by Smith (ref. 5) agreed remarkably well with test data. The present authors have generalized the conical Smith procedure to apply to bodies with small span strakes (ref. 6), and have also extended the formulation to nonconical flows.

SYMBOLS

a	vertical half-dimension of elliptical body; also, radius of circular body
b	horizontal half-dimension of elliptical body
C_L	lift coefficient based on planform area
$C_L(x)$	lift coefficient based on force and area ahead of station x
C_m	pitching-moment coefficient about apex based on body length and planform area
$C_m(x)$	pitching-moment coefficient about apex based on moment, length, and planform area ahead of station x
i	$\sqrt{-1}$
N	number of vortex sheet segments
n	inward normal to vortex sheet
p	static pressure ($\Delta p = p - p_\infty$)
q	free-stream dynamic pressure
R	Reynolds number
r	polar radius in physical plane
U	component of free-stream velocity along x
W	complex velocity potential
x,y,z	body-centered Cartesian coordinates
Z	complex variable $(y + iz)$
Z^*	complex variable in transformed crossflow plane
α	angle of attack
β	separation angle
Γ	vortex strength
δ	strake semiapex angle
η_o	parameter in transformation $Z^* = Z^*(Z)$

θ polar angle

ξ_o parameter in transformation $Z^* = Z^*(Z)$

$\Delta\Phi$ velocity potential jump across vortex sheet

Φ velocity potential

ϕ angle between r and tangent to sheet

σ distance along vortex sheet

Subscripts

m mean value

v isolated vortex core

Superscript

— complex conjugate

DISCUSSION

Conical Analysis

The usual slender-body approach is assumed in the analysis. The major steps in the theory have been outlined in figure 5. The governing differential equation is the Laplace equation in the crossflow plane $Z = y + iz$. The linear theory requires that the tangency condition be satisfied on the surface of the wing-body. A simple means for accomplishing this is to conformally map the wing-body into a vertical slit in the transformed Z^* plane. A generalized transformation for carrying this out is shown in figure 5, and applies to wing-bodies of elliptical cross section (b/a is the ratio of the major-to-minor axis) and of arbitrary dihedral angle. The quantities η_o and ξ_o are defined in reference 6.

In the nonlinear theory, additional boundary conditions, as listed in figure 5, must be satisfied to determine the strength and position of the vortex core and sheet. A typical six-segment sheet and vortex core are shown in figure 6. The core is joined to the end of the sheet by a cut. The Kutta condition, which states that the velocity is finite at the wing tip, provides a single algebraic expression for determining the unknown vortex strengths and positions. Two additional algebraic relations are provided by the zero force condition, which requires that the resultant force on the vortex and cut must vanish. The pressure and normal velocity boundary conditions, which state that both pressure and normal velocity must be continuous across the vortex sheet, are satisfied at the midpoint of each sheet segment. These provide 2N

additional algebraic relations making a total system of $2N + 3$ equations. The unknowns to be determined are the vortex core strength, the two vortex core position coordinates, the N vortex sheet strengths, and the N vortex sheet radius vectors.

The equations are nonlinear and must be solved by iteration. This is accomplished with a computer program based upon the iteration procedure originally developed by Smith (ref. 5). Sample results are presented in figures 7 through 9. Additional results may be found in reference 6.

The results in figure 7 are typical of calculations for bodies with strakes of exposed semispan equal to 50 percent of the body radius (50-percent strakes) or greater. The corresponding test data in this and subsequent figures were obtained in the Ames 7- by 10-Foot Wind Tunnel for models of different semiapex angle δ. Test conditions varied between a dynamic pressure of 50 psf and 75 psf. Good agreement between the nonlinear theory and test data was found over the entire angle-of-attack range shown (except when stall or vortex breakdown occurred, viz., at values of angle of attack $\alpha > 30°$).

Figure 8 shows a similar comparison with 10-percent strakes. Good agreement with test data is found up to $\alpha/\delta \simeq 2$ or 2.5. In the range $2.5 < \alpha/\delta < 4$, the theory was consistently below the test data. Beyond $\alpha/\delta = 4$, the theory becomes multivalued, and three possible theoretical solutions exist for the same α/δ. The lower nonlinear solution gives a weak leading-edge vortex lying close to the wing tip, whereas the upper solution contains a strong vortex located well above the wing. The middle nonlinear solution results in a vortex of intermediate strength. The test data, on the other hand, form a smooth transition between the theory at low α/δ and the upper theoretical solution at large α/δ. No experimental evidence of multiple lift values was found.

The failure of the theory in the range $2 < \alpha/\delta < 4$ may be due to the existence of body as well as leading-edge vortices, as postulated in the mixed case of figure 3. The estimated lift increment from body vortices has been added to the calculated nonlinear lift in figure 8 in order to check the magnitide of this correction.

It is of interest to examine the nonlinear analysis in the limit of vanishingly small strake size and to compare with test data for a cone. The separation angle β must now be varied parametrically, since as mentioned in the Introduction, β is no longer fixed by the strakes, but is determined by viscous effects. The resulting calculations are shown in figure 9 and indicate that the lift increases with decreasing separation angle. No nonlinear solutions were found for $\alpha/\delta < 2$, irrespective of the value β. This is in agreement with previous work by Bryson (ref. 2), who used the Brown and Michael model for a cone.

Nonconical Analysis

The nonlinear theory has been extended to nonconical configurations. In the nonconical theory, the tangential flow and Kutta conditions are

essentially unaltered from the conical theory. The remaining boundary conditions, however, are no longer algebraic as was the case for conical flow.

The zero force condition on the vortex and cut now becomes a first-order ordinary complex differential equation (see fig. 10), and is essentially the same as originally used by Bryson (ref. 2). The pressure continuity condition for a general nonconical vortex sheet becomes a quasilinear first-order partial differential equation. The general solution to this equation was obtained and is shown in figure 10. The continuity of normal velocity condition for a general vortex sheet is given by the third equation in figure 10. (Geometric definitions for some of the symbols in figure 10 may be found in figure 4.)

The system of algebraic and differential-integral equations describes an initial value problem starting from a given axial station. The system has been solved numerically by assuming the flow to be conical ahead of the initial station. Thus, the conical theory is used to generate initial data for the nonconical theory. Some sample results are presented in the following figures.

Calculated values of $C_L(x)$, $C_m(x)/C_L(x)$, and of a function proportional to vortex core strength up to station x are shown in figure 11 for a cone with a double-delta wing and fillet at $\alpha = 24°$. The theoretical results appear to approach the conical asymptotic values for $\delta = 18°$.

A comparison of the calculated C_L and C_m values with wind-tunnel data is shown in figure 12. A single theoretical point at $\alpha = 24°$ and the known linear theory slope at $\alpha = 0°$ were used in establishing the faired curve shown in figure 12.

The calculated upper surface spanwise pressure distribution for the same configuration is compared with test data in figure 13 at two axial stations. The theory agrees reasonably well with the test data for the filleted wing at both stations. Removing the wing fillet significantly affected the pressure at $x = 0.60$, directly behind the break in sweep, but had only a minor effect at the downstream station.

Additional comparisons of the nonconical theory with wind-tunnel test data are included in figures 14 through 16. Thus, figure 14 shows a comparison of the calculated values of C_L and C_m versus α with test data for a configuration consisting of a body with an ogive nose and curved 50-percent strakes. A comparison of upper surface pressure data at $\alpha = 24°$ is shown in figure 15 for the same configuration.

The nonconical theory was also used to calculate the effect of changing the strake incidence angle ε over the rear 45 percent of a conical wing-body (control effectiveness). The calculations for C_L versus α are compared with test data on figure 16.

CONCLUSION AND RECOMMENDATIONS

Analytical procedures have been developed for calculating the nonlinear lift and pressure distribution on conical and nonconical wing bodies with leading-edge vortices. Except for relatively small strakes in the range $2 < \alpha/\delta < 4$, agreement between both the conical and nonconical theories and subsonic test data was highly encouraging.

The nonlinear theory is at present limited to flows with lateral symmetry and to configurations which satisfy the geometric and Mach number constraints of slender-body theory. Removal of some of these restrictions would increase the usefulness and applicability of the theory. Thus, removal of the requirement for lateral symmetry would allow analysis of yawed flight and the evaluation of nonlinear lateral stability. The formulation of a companion theory for supersonic flows also appears to be highly desirable, since leading-edge vortices have been observed at Mach numbers well above one (ref. 7). Extension of the theory to include nonslender effects arising from the apex, trailing edge, step control deflections, etc., although needed from a practical standpoint, is considered very difficult to accomplish.

REFERENCES

1. Allen, H. J.; and Perkins, E. S.: A Study of Effects of Viscosity on Flow Over Slender Inclined Bodies of Revolution. NACA TR 1048, 1951.

2. Bryson, A. E.: Symmetric Vortex Separation on Circular Cylinders and Cones. J. Appl. Mech., vol. 26, no. 4, 1959.

3. Brown, C. E.; and Michael, W. H., Jr.: On Slender Delta Wings With Leading-Edge Separation. NACA TN 3430, 1955.

4. Mangler, K. W.; and Smith, J. H. B.: A Theory of the Flow Past a Slender Delta Wing With Leading-Edge Separation. Proc. Roy. Soc., A., vol. 251, 1959, pp. 200-217.

5. Smith, J. H. B.: Improved Calculations of Leading-Edge Separation From Slender Delta Wings. RAE Tech. Rep. 66070, March 1966.

6. Levinsky, E. S.; and Wei, M. H. Y.: Nonlinear Lift and Pressure Distribution of Slender Conical Bodies With Strakes at Low Speeds. NASA CR 1202, 1968.

7. Jorgensen, L. H.: Elliptic Cones Alone and With Wings at Supersonic Speeds. NACA TR 1376, 1958.

VORTEX FLOW VISUALIZATION

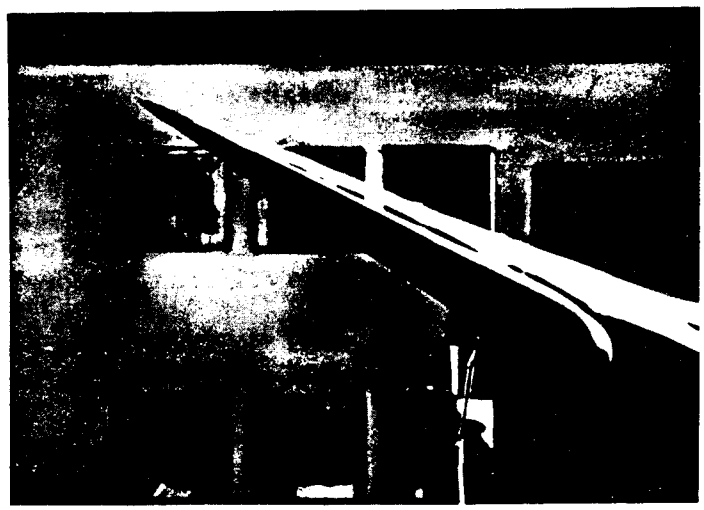

Figure 1

TYPICAL NONCONICAL SLENDER-BODY CONFIGURATION WITH VORTEX SHEET

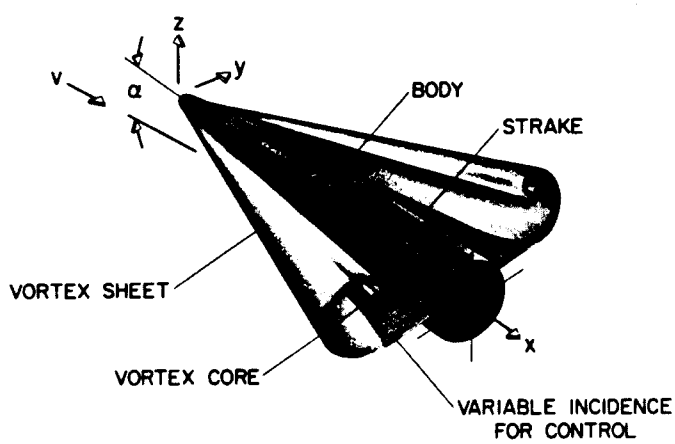

Figure 2

SOME VORTEX FLOWS

- BODY ALONE
  - SEPARATION POINT VARIABLE
  - DEPENDENT ON VISCOUS EFFECTS

- STRAKE / BODY
  (TREATED IN CURRENT ANALYSIS)
  - STRAKE VORTICES DOMINANT
  - SEPARATION FIXED BY SHARP L.E.

- MIXED

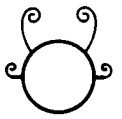

Figure 3

RELATION TO PREVIOUS WORK
INCOMPRESSIBLE FLOW

BROWN & MICHAEL 1955		ISOLATED VORTEX CORE NO FEEDING SHEET
MANGLER & SMITH 1959		ADDED FEEDING SHEET OF SPECIFIED SHAPE
SMITH 1966	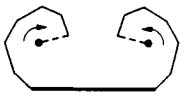	SEGMENTED FEEDING SHEET
CURRENT ANALYSIS 1968	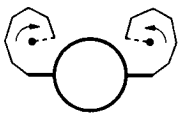	GENERALIZED TO STRAKE / BODY CONFIGURATIONS
1969		GENERALIZED TO NONCONICAL FLOW

Figure 4

CONICAL ANALYSIS

SLENDER-BODY THEORY

$$\frac{\partial^2 \Phi}{\partial y^2} + \frac{\partial^2 \Phi}{\partial z^2} = 0$$

- TANGENCY CONDITION (LINEAR THEORY)

  TRANSFORM STRAKE/BODIES (Z PLANE) INTO VERTICAL SLIT (Z^* PLANE)

$$Z^{*2} = \frac{1}{(b-a)^2}\left\{b\left[Z^2-(b^2-a^2)\right]^{1/2} - aZ - i(b-a)\eta_0\right\}^2 - \xi_0^2$$

- ADDITIONAL CONDITIONS (NONLINEAR THEORY)

  KUTTA CONDITION

  ZERO FORCE CONDITION

  PRESSURE CONTINUITY CONDITION

  NORMAL VELOCITY CONTINUITY CONDITION

Figure 5

NONCONICAL ANALYSIS SYMBOLS

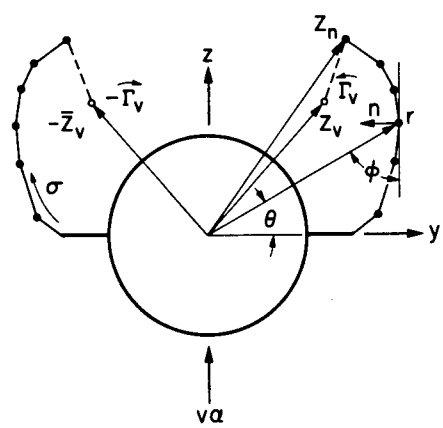

$\overline{W} = \Phi - i\psi$

$\Delta\Phi = \Phi$ JUMP ACROSS SHEET

m = MEAN VALUE ON SHEET

Figure 6

COMPARISON OF THEORY WITH SUBSONIC EXPERIMENT
CIRCULAR CONE, 50% STRAKES

SYMBOLS DENOTE DATA FOR
$6° \leq \delta \leq 12°$
$50 \leq q \leq 75$ psf
$1.4 \leq R \leq 1.6 \times 10^6$ (per ft)

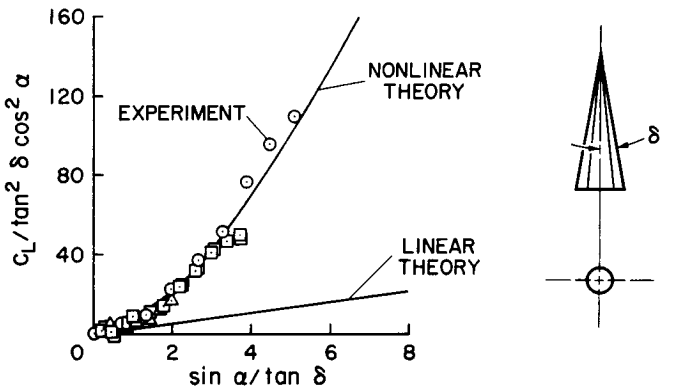

Figure 7

COMPARISON OF THEORY WITH SUBSONIC EXPERIMENT
CIRCULAR CONE, 10% STRAKES

SYMBOLS DENOTE DATA FOR
$4.4° \leq \delta \leq 11°$
$50 \leq q \leq 100$ psf
$1.4 \leq R \leq 1.8 \times 10^6$ (per ft)

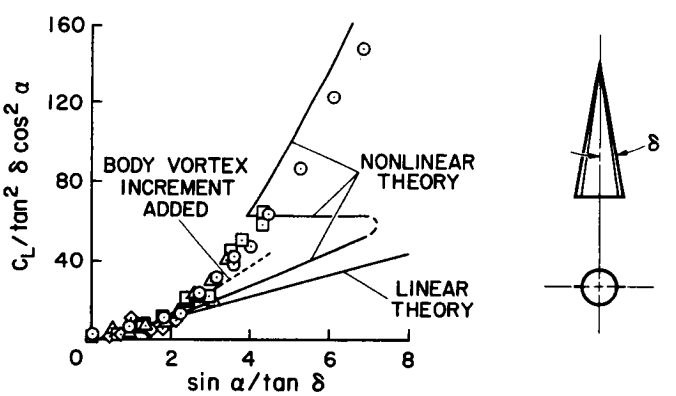

Figure 8

COMPARISON OF THEORY WITH SUBSONIC EXPERIMENT

CIRCULAR CONE WITHOUT STRAKES

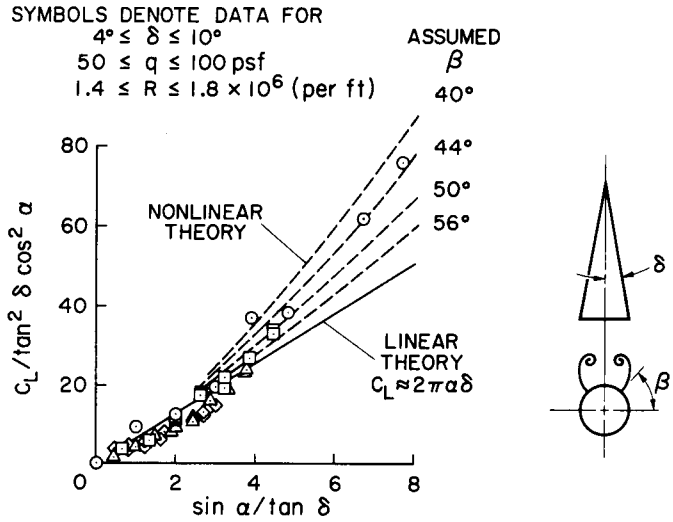

Figure 9

NONCONICAL ANALYSIS

- ZERO FORCE CONDITION (SAME AS BRYSON, 1959)

$$v\frac{d\Gamma_v}{dx}(Z_v - Z_m) = \Gamma_v\left[\frac{d\overline{W}}{d\overline{Z}} + \frac{\Gamma_v}{2\pi i}\left(\frac{1}{\overline{Z}-\overline{Z}_v}\right) - v\frac{d\overline{Z}_v}{dx}\right]_{Z=Z_v}$$

FORCE ON CUT FORCE ON VORTEX

- PRESSURE CONTINUITY CONDITION

$$\Delta\Phi = (\partial\Delta\Phi/\partial\sigma)\left[\sigma - \int_0^x \frac{(\partial\phi/\partial\sigma)_m}{v}\,dx\right]$$

- NORMAL VELOCITY CONTINUITY CONDITION

$$r(x,\theta) = \int_0^\theta r\cot\phi\,d\theta - \frac{1}{v}\int_0^x \frac{\partial\phi/\partial n}{\sin\phi}\,dx$$

- INITIAL VALUE PROBLEM

START WITH CONICAL SOLUTION

Figure 10

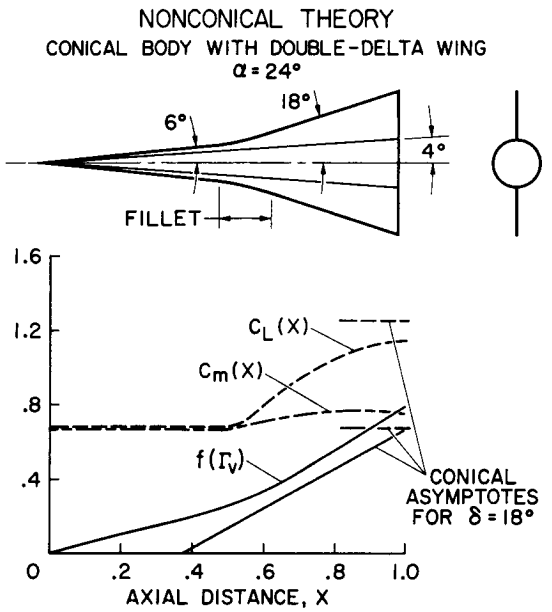

Figure 11

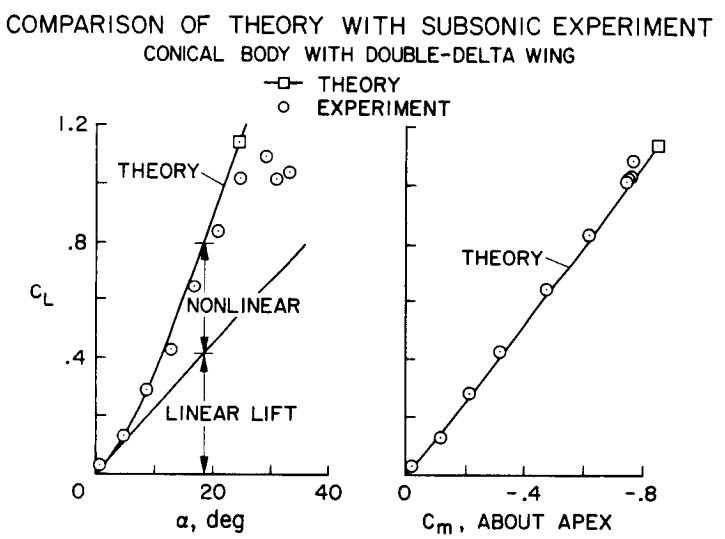

Figure 12

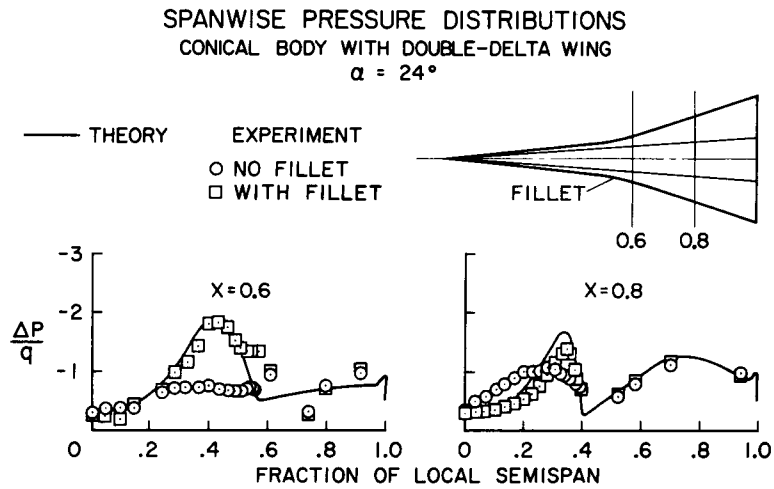

Figure 13

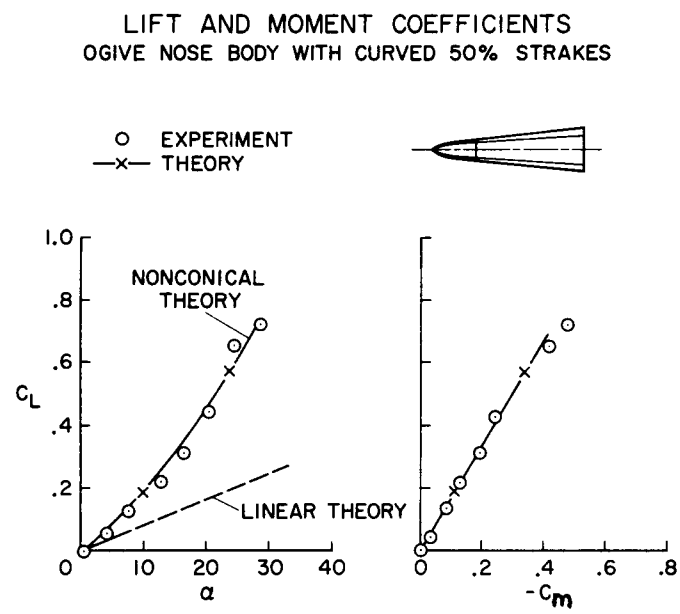

Figure 14

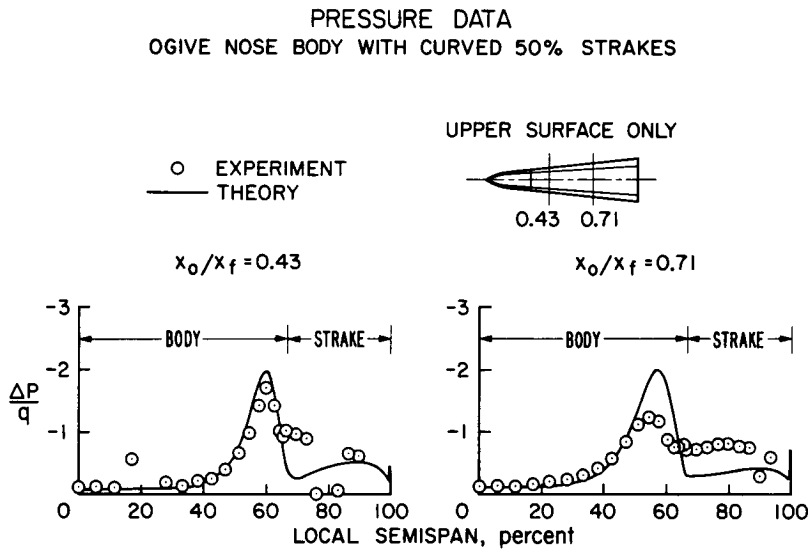

Figure 15

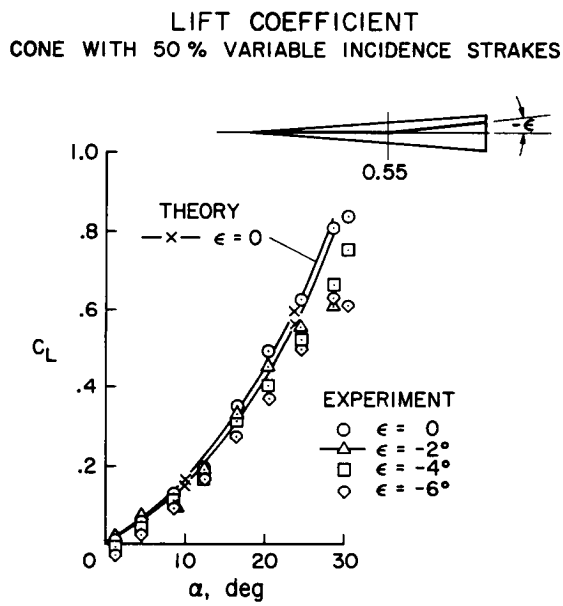

Figure 16

DISCUSSION

CAPT. DAVID FINKLEMAN, Air Force Academy: I'd like to hear your comments on the procedure due to Sacks, which introduces discrete vortices. Perhaps you classified this with empirical methods, but it need not necessarily be so. By increasing the number of vortices you arrive at a completely force-free vortex sheet, rather than one that is only force free in the mean, such as the Brown-Michael approach.

LEVINSKY: Well, I know there have been several methods. One I am familiar with is by Nielsen Engineering, where they had a large number of free vortices representing the sheet.

FINKLEMAN: I say this in particular because I know the Sacks approach seems to indicate good agreement for the same configurations you have examined. This was a NASA Contractor Report a couple of years ago. (A. H. Sacks, R. E. Lundberg, and C. W. Hanson, "A Theoretical Investigation of the Aerodynamics of Slender Wing-Body Combinations Exhibiting Leading-Edge Separation," NASA CR-719, March 1967)

LEVINSKY: If you take more turns of the vortex sheet than we have shown, eventually the force-free condition of the core and the cut should become less and less significant.

FINKLEMAN: Problems may arise with this method when one attempts to trace the wake behind, for instance, an arrow-shaped wing. If you have discrete vortices they are easy to follow, but with a sheet it is not quite clear how the wake could be followed.

LEVINSKY: We have used a slender-body approach. We are constrained to very small changes in the x direction of the configuration. If you go beyond the base of the body the vortices are no longer growing in strength, as they are in these cases. They become free. We are not talking about that kind of a case. The sheet would tear. You are not dealing with free vortices. This is a feeding sheet model.

FINKLEMAN: One other short question. You say you have handled cases at incidence. Am I correct in assuming that you are using the solutions to Laplace's equation for a shoulder or high-wing configuration as against one with only a mid-wing?

LEVINSKY: We have carried out a calculation with two degrees of incidence, and it is in the written version. As for mid-wing versus high wing, this is a wing displacement effect whereas the incidence effect was considered due to a change in wing slope only. The displacement effect was not included in our incidence calculations, just the slope effect.

We have compared our results with test data, and the comparison is reasonable.

FINKLEMAN: And then you always took the wing, you said, along the diameter?

LEVINSKY: Yes, we used a mid-wing configuration.

RAYMOND SEDNEY, Martin Company: Can you tell us the origin of this multiple-valued nature of the solution?

LEVINSKY: Yes, this occurred in the conical cases. With small strakes it turns out that you can get three different solutions which satisfy all of the boundary conditions. We have taken the Brown and Michael approach without any vortex sheet and found the same results. In other words, there appear to be three different strengths and three different positions for the vortex core and sheet which satisfy the force-free condition, the Kutta condition, etc. This is a consequence of the fact that there may be more than a single solution to a set of nonlinear equations.

ROBERT L. TRIMPI, NASA Langley Research Center: I may have missed it, but I don't think you told us what computer you were using.

LEVINSKY: We used a CDC-3600.

METHODS FOR CALCULATING NONLINEAR CONICAL FLOWS

By Jerry C. South, Jr., and E. B. Klunker

Langley Research Center

N70-21359

INTRODUCTION

In 1935 Busemann (ref. 1) introduced the concept of a general conical flow field as one in which the velocity vector is constant along any ray emanating from a common point in the flow. Solutions for such self-similar conical flows are of interest to the aerodynamicist for a number of reasons, among which two are: first, significant regions of the flow about many practical configurations are conical or nearly so (moreover, the supersonic flow past any pointed body with a shock wave attached at the apex is conical in the immediate neighborhood of the point) and, second, conical bodies and wings are the simplest class of three-dimensional shapes and thereby provide "bench-mark" cases for both experimental and theoretical studies in inviscid supersonic flow.

Two basic approaches are available for the numerical development of "exact"[1] nonlinear conical solutions:

(1) Distance-asymptotic methods, where approximate distributions of the flow variables and shock-wave shape are used near the apex as initial values for continuing the calculation downstream by some three-dimensional computation scheme. The calculation proceeds until conical similarity conditions are sufficiently satisfied.

(2) Methods which invoke the conical self-similarity and thereby reduce to two the number of independent variables are referred to simply as "conical" methods for brevity.

Both general approaches have their merits. The distance-asymptotic techniques develop the solution as a well-posed initial-boundary problem for equations of hyperbolic type, and convergence is "almost" guaranteed from both physical and theoretical considerations. However, to achieve a satisfactory solution in many problems where a fine mesh is needed, these methods require a large amount of computer storage and time. The conical methods reduce the problem to two dimensions but in the more difficult form of a free-boundary problem for equations of elliptic or mixed type. In fact, many of the conical methods are similar to methods used for solving the blunt-body problem.

The methods of references 2 to 7 are examples of the distance-asymptotic method. References 2, 3, and 4 consider circular cones at angle of attack, references 5 and 6

[1]Exact in the sense that the only approximation made is the reduction of the governing partial differential equations to ordinary differential equations or algebraic equations by using finite-difference expressions for the derivatives with respect to one or more of the coordinates.

Preceding page blank

8

include cones of elliptic cross section, and reference 7 presents calculations for the compression side of conical delta wings with shock wave attached not only at the apex but also along the swept leading edges.

Examples of conical methods appeared as early as 1929, when Busemann (ref. 8) constructed the axisymmetric conical flow by numerical-graphical construction in the hodograph. Reference 9 cites many of the approximate and exact conical methods documented up to about 1964; therefore, they are not all discussed in the present paper. Most recent conical methods are of the "inverse" type, in which an analytic function of two or more parameters is assumed for the conical shock wave and the governing partial differential equations are solved by marching inward until some body shape is obtained. Various inverse methods are reported in references 10 to 14. Unfortunately, these methods have not been successful for constructing solutions for body shapes which produce a shock wave requiring many parameters for an adequate description; only circular cross-section cones at incidence have been amenable, whereas solutions for elliptic cones have been obtained only painstakingly. It is apparently unfeasible to use the aforementioned inverse methods for elliptic cones at incidence. Other conical methods that have been used incorporate the method of relaxation in regions where the cross flow (velocity component normal to a conical ray) is subsonic and the governing differential equations are of the elliptic type; a two-dimensional method of characteristics is used in supersonic cross-flow regions where the equations are hyperbolic. Such approaches are developed in references 15 to 17 in which flat delta wings with attached leading-edge shocks are considered. It is not known if these methods can be easily coded for efficient machine calculation for nonflat conical wings, but it seems doubtful. Moreover, the results in reference 17 appear to be erroneous, as shown later in this paper.

The present paper concentrates attention on a method that is "direct" in the sense that the body shape is given and is one of the bounding coordinate surfaces; yet the shock wave is another bounding coordinate surface, and the governing differential equations are solved by integrating inward from the shock. Thus, in that respect, this method is like the inverse methods. The method has two distinguishing features: (a) the coordinate transformation which maps the region between the shock and body onto a rectangle and (b) the solution of the transformed problem by the method of "lines" or "straight lines," so-called by various authors. Neither feature is new, yet together they prove to be an efficient means of solving free-boundary problems such as the supersonic blunt-body problem or conical flows. The convenient device of transforming the shock and body surfaces into bounding coordinate surfaces is widely used in computational aerodynamics, for example, references 2 to 7 and 18 to 21. The basic idea of the method of lines is to discretize all but one of the independent variables in the partial differential equations so that a system of approximate, simultaneous, ordinary, differential-difference equations is obtained. The

approximate system can be solved numerically by an efficient routine such as a fourth-order Runge-Kutta method, and very good accuracy can be obtained with large steps in the direction of the continuous variable. The same purpose is achieved by the better-known (in the United States) method of integral relations (ref. 22). The difference between the two methods is that the method of integral relations, in its usual formulation (refs. 19, 23, and 24), requires new algebraic development for each higher approximation (i.e., more lines) and the equations grow more complex; whereas the method of lines system is written recursively with arbitrary number and spacing of lines.

The present method, including the transformation of the shock and body surfaces, is hereafter called the method of lines. In reference 25, the work of Telenin and his coworkers is cited, in which they used the method of lines for numerical solutions to the axisymmetric, supersonic blunt-body problem. That work was extended to the three-dimensional blunt-body problem and reported in reference 26.[2] More details of the preceding work are given in reference 27.

Makhin and Syagayev (ref. 28) recognized the difficulties associated with Syagayev's earlier inverse method (ref. 14) and applied the transformation discussed previously in which the body and shock become bounding coordinate surfaces. Their procedure was essentially the method of lines, although they used a first-order Euler method to integrate toward the body; to maintain accuracy, a small step size was used in the inward-marching direction (1/64th of the local shock-layer thickness). The modification allowed them to solve the direct elliptic-cone problem, which was intractable by the earlier inverse approach.

Bazzhin and Chelisheva (ref. 29) applied the method to conical bodies at large angles of attack where supersonic cross flow always occurs. Their procedure was quite similar to approaches to the blunt-body problem; they used the method of lines on the windward, high-pressure side of the conical body up to and beyond the region where the cross flow becomes supersonic. A conical, two-dimensional method of characteristics was used to continue the solutions in the supersonic cross-flow region. More results, with emphasis on the characteristics solutions, are given in reference 30. An interesting result in reference 30 was that in some instances it was possible to continue the characteristics solution through the leeward plane of symmetry of elliptic cones at large incidence; thus, symmetry conditions were violated and this indicated the impossibility of flow without embedded shocks in the general case. Neither reference 29 nor 30 suggests using the method of lines for the small-to-moderate incidences in which the cross flow is everywhere subsonic, nor was any mention given to the application in reference 28.

---

[2]The word "Attached" in the title of reference 26 is an obvious error in translation and should read "Detached."

During the progress of the present work, Jones (ref. 31) reported a method similar in many ways to the present procedure. He was apparently unaware of the work in the Soviet Union cited herein and did not refer to his method as a method of lines, although it is the same. Jones obtained solutions for circular and elliptic cones and a conical body with a four-parameter, smooth, cross-section contour having both concave and convex portions. The method was shown to be accurate and efficient, and he was able to experiment numerically with some of the more theoretical questions concerning conical flows such as the "lift-off" of the vortical singularity (refs. 32 and 33). He stated that the method was restricted to conical flows with subsonic cross flow, which is not found to be true in the present work.

The present paper outlines a method of lines for automatic computation of conical flows, including not only elliptic cross-section cones but also the compression side of conical delta wings with shock attached along the leading edge. In the latter problem, large regions of supersonic cross flow occur, yet the method is applicable there without modification.

SYMBOLS

a	semimajor axis of ellipse
b	semiminor axis of ellipse
C_p	pressure coefficient
i,j	indices indicating line number
M_∞	free-stream Mach number
N	number of lines
p	pressure
r	distance along ray
u,v,w	component of velocity in r-, η-, and ξ-direction, respectively
V_∞	free-stream velocity
v_c	component of velocity in plane ϕ = Constant

w_c	component of velocity normal to plane ϕ = Constant
$\bar{x}$	nondimensional spanwise coordinate
z	cylindrical coordinate in downstream direction
α	angle of attack
β	shock angle
γ	ratio of specific heats
ϵ	convergence criterion on normal velocity at conical surface
$\zeta = \frac{\eta}{\eta_s}$	
η	angle measured in plane normal to body from ray on surface to ray in field
η_s	value of η at shock
θ_o	conical apex angle of body in vertical plane of symmetry
Λ	sweep angle
ξ,τ	arc length along intersection of unit sphere with conical body
ρ	density
ϕ	polar angle in cylindrical coordinates (see fig. 2)

METHOD

Conical Coordinates

The equations governing supersonic, inviscid flow of an ideal gas are written in a body-oriented, orthogonal, conical coordinate system (r,η,ξ) as suggested in reference 34 where r is the distance along a conical ray, η is the angle measured from the body surface to the ray in a plane ξ = Constant, and ξ is a measure of the arc length along the intersection of the body surface with a sphere of radius r centered at the body apex. It should be noted that the body is the conical surface $\eta = 0$, and the contour along which

ξ is measured is a plane curve only in the special cases of a circular cone or a flat delta wing. This coordinate system has the advantage that the associated velocity components are the natural conical components (u,v,w); the v-component is zero at the surface $\eta = 0$ and the magnitude of the velocity component normal to a conical ray (hereafter called the "cross-flow" component) $\sqrt{v^2 + w^2}$ governs the type (elliptic or hyperbolic) of the partial differential equations for the conical flow. Furthermore, certain singularities appear where the cross-flow component vanishes $\left(\sqrt{v^2 + w^2} = 0\right)$, and it is extremely important that such points be recognized and interpreted correctly. In reference 35, for example, a cylindrical coordinate system was used, and the authors apparently assumed that a nodal singularity occurred where the two cylindrical components v_c, w_c vanished; they actually manufactured a singular node at that point and obtained an erroneous discontinuous solution for an elliptic cone at zero incidence. This is not to say that the use of cylindrical or other nonconical coordinates is wrong but rather that more care must be taken with them. Jones (ref. 31) used cylindrical coordinates with the method of lines, and he computed the same case as in reference 35 and obtained a valid continuous solution.

Transformation to a Rectangular Region

With the conical similarity $\left(\frac{\partial}{\partial r} = 0\right)$ the partial differential equations involve two independent variables, η and ξ, and the problem is solved on a spherical surface $r = 1$. To facilitate the formation of the boundary values at the shock wave, whose position must be determined as part of the solution, it is convenient to introduce the following change of variables:

$$\zeta = \frac{\eta}{\eta_s} \qquad \text{and} \qquad \tau = \xi \tag{1}$$

where $\eta = \eta_s(\xi)$ is the equation of the shock-wave contour on the spherical surface $r = 1$. The chain rule gives

$$\frac{\partial}{\partial \eta} = \frac{1}{\eta_s} \frac{\partial}{\partial \zeta} \tag{2a}$$

$$\frac{\partial}{\partial \xi} = -\frac{\zeta}{\eta_s} \frac{d\eta_s}{d\tau} \frac{\partial}{\partial \zeta} + \frac{\partial}{\partial \tau} \tag{2b}$$

so that the partial differential equations take the form

$$\frac{\partial p}{\partial \zeta} = P\left(p, \rho, u, v, w, \eta_s, \frac{\partial p}{\partial \tau}, \frac{\partial u}{\partial \tau}, \frac{\partial v}{\partial \tau}, \frac{\partial w}{\partial \tau}, \frac{d\eta_s}{d\tau}\right) \tag{3}$$

Similar forms hold for the three velocity components u, v, and w. The density is eliminated from the system as a differential variable by using the Bernoulli equation and its derivatives. It should be noted that the function η_s defining the unknown shock contour

and its derivative $d\eta_s/d\tau$ appear explicitly in the transformed equations. Likewise, because a body-oriented system is used, terms involving the body surface curvature also appear in the right-hand side of the equations, although they are not indicated in equation (3).

The problem is thus transformed to a rectangular region, where the cross-sectional contours of the shock wave and body surface are mapped onto the lines $\zeta = 1$ and $\zeta = 0$, respectively.

The Method of Lines

The region of interest in the ζ,τ plane is now divided by N lines parallel to the ζ-axis (N + 1 lines for delta wings with attached leading-edge shocks); it is not necessary that the strips be of equal width. For the elliptic cone, figure 1 illustrates the division in the physical ξ,η plane and the transformed ζ,τ plane for $N = 9$. At each strip boundary or line, the system of equations is reduced to ordinary differential-difference equations by replacing the derivatives $\partial/\partial\tau$ by finite differences or, say, by derivatives of polynomials in τ. One of the aims in the present work was generality with simplicity; hence, it was decided to use the derivative of a Lagrange interpolation polynomial to approximate $\partial/\partial\tau$. This use allowed experimentation with unequal line spacing, noncentral differencing, and arbitrary (within reason) number of lines to be included in the interpolation-difference formula. The current program uses an equal number of lines on either side of the line at which $\partial/\partial\tau$ is computed; therefore, central differencing is obtained when the line spacing is equal. The difference, or polynomial, approximations for $\partial/\partial\tau$ cause the differential equations along any line to be coupled to those along the other lines. There results a system of 4N simultaneous ordinary differential equations which are integrated by a fourth-order Runge-Kutta method.

Boundary Conditions

Shock-wave conditions.- The shock wave shape is unknown and must be determined in the solution. The flow variables are to satisfy the usual three-dimensional shock jump conditions at $\zeta = 1$.

Flow tangency at surface.- The condition of flow tangency at the surface must be satisfied, that is at $\zeta = 0$, the normal velocity component must be zero:

$$v(0,\tau) = 0 \tag{4}$$

Symmetry conditions.- So far, only problems with at least one plane of symmetry have been solved. Symmetry is accounted for in the formula for the τ derivatives by properly reflecting points (lines) about the symmetry plane. For the elliptic cone both

the windward ($i = 1$) and leeward ($i = N$) lines correspond to symmetry planes. For the compression side of delta wings, the line $i = 1$ is a symmetry plane.

Leading-edge shock conditions.- For the delta wings, the line $i = N + 1$ corresponds to the sharp leading edge, and the condition of shock attachment is enforced there. At that line the slope of the shock wave and the values of the flow variables can be determined directly from the shock conditions; hence, no differential equations need to be integrated along $i = N + 1$. In forming τ derivatives at lines near the leading edge, the number of points used in the derivative formulas is automatically reduced, if necessary, to retain an equal number of lines on either side of the line at which $\partial/\partial\tau$ is computed. For example, if a five-point formula is being used generally, with the derivative evaluated at the middle point, then the number of points in the formula is reduced to three at line $i = N$ to maintain an equal number of points on either side of this line.

Determination of the Shock Shape

The form of the shock-wave cross section is given by the unknown function $\eta = \eta_s(\tau)$. If η_s and $d\eta_s/d\tau$ were known, then all the information concerning the shock-wave geometry would be known, and the values of the functions p, ρ, u, v, and w at the shock wave ($\zeta = 1$) could be evaluated from the shock jump conditions. These values could be used to start the numerical integration at $\zeta = 1$ and proceed down to the body surface at $\zeta = 0$. Only the correct shock function η_s will cause the flow-tangency condition (eq. (4)) to be satisfied; thus, there must be a relation between the function $\eta_s(\tau)$ and the normal component at the surface $v(0,\tau)$. This is the basis, then, for determining the correct shock shape.

Newton iteration for shock shape.- The number of unknown values is equal to the number of normal components $v_i(0) = v(0,\tau_i)$. A Newton-type iteration procedure has been devised for adjusting $\eta_{s,i}$ to achieve $\max_i|v_i(0)| \leq \epsilon$, where ϵ is a prescribed accuracy criterion. The steps in the procedure are straightforward and easily automated and are given as follows:

(1) Assume an initial set of values $\eta_{s,i}$ $(i=1,\ldots,N)$ based on experience, approximate solutions, or previously computed cases with conditions close to those desired.

(2) Numerically differentiate the $\eta_{s,i}$ values with the formulas coded for obtaining τ derivatives.

(3) With $\eta_{s,i}$ and $d\eta_{s,i}/d\tau$ from steps (1) and (2), solve the shock jump conditions for p_i, ρ_i, u_i, v_i, and w_i $(i=1,\ldots,N)$.

(4) Use the results of step (3) for initial values to start a numerical integration of the system of 4N equations from $\zeta = 1$ to $\zeta = 0$, and evaluate the normal components at the surface $v_i(0)$.

(5) Test $\max_i |v_i(0)|$. If $\max_i |v_i(0)| \leq \epsilon$, then the shock shape is good and the problem is considered solved. Otherwise continue to the following perturbation cycle.

(6) Perturb each parameter $\eta_{s,j}$ independently and in order. That is, change $\eta_{s,j}$ to $\eta_{s,j}(1 + \delta)$, where δ is a small number $\left(\text{say, } 10^{-6}\right)$, and repeat steps (2) to (4). This results in small changes in each $v_i(0)$ due to the perturbation in $\eta_{s,j}$. Hence the jth column of an N by N matrix of influence coefficients or partial derivatives is generated with each perturbation.

(7) Solve the usual first-order linear system

$$\sum_{j=1}^{N} \left[\frac{\partial v_i(0)}{\partial \eta_{s,j}}\right] \Delta\eta_{s,j} = -v_i(0) \qquad (i=1,\ldots,N) \qquad (5)$$

to obtain the increments $\Delta\eta_{s,j}$ required to correct the shock shape and drive all $v_i(0) \rightarrow 0$.

(8) Use the new shock parameters $\eta_{s,j} + \Delta\eta_{s,j}$ to start a new cycle at step (2). Note that a complete cycle requires $N + 1$ integration runs: one "pivotal" run and N perturbation runs.

The shock-wave determination procedure of reference 31 differs somewhat from the present one in that the shock function is given by a trigonometric polynomial and the coefficients are chosen to minimize the sum of squares of the normal components at the surface. The computational scheme used herein appears to require more computation, but in the authors' experience it was the only one that was generally satisfactory.

Approximate starting shock shapes.- Usually a very good estimate of the shock shape is required for a successful calculation and convergence. The exceptions are circular cones at moderate relative incidences $\left(\frac{\alpha}{\theta_0} \lesssim 0.5\right)$ and delta wings at large supersonic Mach numbers $\left(M_\infty \gtrsim 3.0\right)$. For most other cases, however, considerable care must be exercised in choosing the initial shock shape to start the iterations previously described. A poor initial estimate can result in any of several program failures, such as negative pressures or vanishing denominators caused by excessive supersonic cross flow, which introduce characteristic-type singularities in the differential equations (i.e., when a ζ = Constant line is tangent to a conical characteristic). Moreover, as the number of lines is increased, the approximation to the elliptic-type partial differential equations improves, and the solutions tend to become sensitive to a small degree of "roughness" in the shock shape. A maximum number of lines (or a minimum $\Delta\tau$) is reached beyond which the numerical integration from the shock results in a singularity between the shock and body, even though the shock shape is a "good" one for a calculation with fewer lines. In the cases studied with this method so far, the maximum number of lines

has been about 19 or 20, but such a large number is seldom necessary except in severe cases of very flat elliptic cones $\left(\text{axis ratio } \frac{b}{a} \leqq 0.25\right)$.

In order to obtain a good initial estimate of the shock shape for such cases as elliptic cones at incidence, a "simpler" case was computed first and then the input parameters were changed gradually toward the desired configuration, a new converged shock shape being obtained with each change of input parameters (e.g., γ, M_∞, θ_o, α, and b/a). The history of the set of $\eta_{s,i}$ as a function of the set of input parameters was incorporated in an extrapolation procedure to predict the new shock shape for the new set of input parameters. Such a procedure was used in reference 31 and was also successful in the present work. The procedure is completely automated in the present program for circular and elliptic cones, and the variation of any of five different input parameters is allowed.

The initial approximation for the delta-wing shock shape could be estimated directly for any angle of attack α (up to that causing detachment from the leading edge), sweep angle Λ, and M_∞. The estimate used was an even function in τ which requires only an estimate of $\eta_{s,1}$ (the value of η_s in the plane of symmetry). The function is contrived to give $\eta_{s,N+1} = 0$ (the condition of attachment at the leading edge) and the correct value for $\left(d\eta_s/d\tau\right)_{N+1}$ which is calculated from the shock conditions. The function is

$$\eta_{s,i} \approx \left[1 - \left(\frac{\tau_i}{\tau_N}\right)^2\right]\left\{\eta_{s,1} - \left(\frac{\tau_i}{\tau_N}\right)^2\left[\eta_{s,1} + \frac{\tau_N}{2}\left(\frac{d\eta_s}{d\tau}\right)_{N+1}\right]\right\} \tag{6}$$

The value of $\eta_{s,1}$ used in equation (6) is a tangent-cone approximation, increased by a factor 1.2 to avoid the Mach wave condition for very thin wings at small α, as follows:

$$\eta_{s,1} \approx 1.2\left(\beta - \theta_o - \alpha\right) \tag{7a}$$

where (ref. 36)

$$\sin^2\beta = \frac{\gamma + 1}{2}\sin^2\left(\theta_o + \alpha\right) + \frac{1}{M_\infty^{\,2}} \tag{7b}$$

In a few instances, the value of $\eta_{s,1}$ was so far off that the required corrections $\Delta\eta_{s,i}$ were sizable, resulting in too much "roughness" in the shock shape; subsequent iterations would fail for reasons already described. However, it happens that in this event the first correction for $\eta_{s,1}$ is quite good so that restarting the iteration with this value in equation (6) has always been successful.

Extrapolation to Surface

At the surface, $\zeta = 0$, the derivatives $du/d\zeta$ and $dw/d\zeta$ are infinite because of the well-known vortical layer adjacent to the surface in conical flows (ref. 32). The derivatives $dp/d\zeta$ and $dv/d\zeta$ are finite, however, and this fact allows extrapolation of the functions p and v to the surface from $\zeta > 0$. In fact, it is only v_i that is extrapolated during the iteration runs in order to evaluate the magnitudes of $v_i(0)$ $(i=1,\ldots,N)$. When the convergence criterion is met, then the pressure p is also extrapolated to $\zeta = 0$. The surface entropy is a constant on the surface, and if the value is known, then the isentropic surface density can be calculated as a function of the extrapolated pressure and the surface entropy. The Bernoulli equation relates p, ρ, u, v, and w; since $v = 0$ at the surface and p and ρ are known, this gives one equation with two unknowns, u and w. The other equation needed for determining u and w is the differential equation

$$w(0,\tau) = \frac{\partial u}{\partial \tau}(0,\tau) \tag{8}$$

that is valid at the surface. Substitution of equation (8) into the Bernoulli equation gives a single nonlinear differential equation as follows:

$$\frac{2\gamma}{\gamma - 1}\frac{p_i}{\rho_i} + u_i^2 + \left(\frac{\partial u_i}{\partial \tau}\right)^2 = \text{Constant} \qquad (i=1,\ldots,N) \tag{9}$$

The usual formula is used for evaluating τ derivatives, and equation (9) is solved by Newton iteration. When convergence is achieved, equation (8) gives w_i; hence, the isentropic surface values are completely determined. This is essentially the same procedure as that of reference 31.

Computation of Surface Entropy

For the circular cone, the surface entropy is the value that occurs in the windward symmetry plane, line $i = 1$. For the elliptic cone with the free-stream velocity vector lying in the plane of the minor axis, the surface entropy is assumed to be the maximum value at the shock wave. When the free-stream vector is in the plane of the major axis, the surface entropy is piecewise constant; that is, it has the value of the windward symmetry plane on the surface segment where $w(0,\tau) < 0$ and the value of the leeward symmetry plane on the rest of the surface. The surface entropy for the delta wings with convex surfaces is the same as the leading-edge value. Other possible configurations are not covered in this paper.

RESULTS

Elliptic Cone

The present method was applied to the calculation of supersonic flow past an elliptic cone with $\gamma = 1.4$, $M_\infty = 5.8$, $\frac{b}{a} = 0.5$, and $\theta_o = 6.0^o$. The calculated shock shape and pressure distribution are shown in figure 2(a). The calculation was performed with $N = 17$ lines with unequal spacing; the density of lines in the region of large surface curvature was about double that elsewhere as shown by the dashed lines in the section view. The same problem was calculated with $N = 17$ and equal spacing and the results were of comparable accuracy; it is not yet clear if unequal spacing offers any advantage.

The calculated shock shape is shown for $\alpha = 6^o$, where the leeward side of the cone is alined with the free-stream vector. This angle of attack is difficult because at $M_\infty = 5.8$ the free-stream pressure is small, and pressures lower than the free-stream value are predicted on the leeward side as can be seen in the C_p plot. The abscissa of the C_p plot is the angle ϕ as shown in the section view. (The windward symmetry plane corresponds to $\phi = -90^o$.) The present results for the pressures are compared with the experiments of Chapkis (ref. 37), and the agreement is excellent except on the leeward side ($\phi > 0$) where a viscous buildup occurs to raise the level of the measured pressures. Typical of the inviscid calculations for both circular and elliptic cones, a pressure minimum occurs away from the leeward plane of symmetry when the relative incidence α/θ_o approaches unity.

Computation history.- The elliptic cone at $\alpha = 0^o$ was solved by starting from a circular cone $\left(\frac{b}{a} = 1\right)$ with semiangle equal to the desired semiangle (11.8^o) in the plane of the major axis of the ellipse $\left(\frac{b}{a} = 0.5\right)$. The axis ratio b/a was changed in increments of -0.1 until the desired configuration was obtained. The solutions for various angles of attack were then computed beginning with zero angle of attack. Table 1 gives the history of the automatic increase in α with the number of cycles (one cycle consists of $N + 1$ integration runs of the coupled 4N differential equations) required to converge the shock shape and print for each α. The convergence criterion for the normal velocity components was set at $\epsilon = 10^{-3}$, and the final value of $\max_i |v_i(0)|$ is also shown. Each integration from the shock to the body was made with 14 integration steps of variable size. The total central processing time required for these 16 cycles was about 14.5 minutes on a Control Data 6600 computer system. Thus each cycle required an average of about 56 seconds of central processing time.

Supersonic cross flow.- For $\alpha = 6^o$, a small region of supersonic cross flow occurs next to the surface ($0 \leqq \zeta \lesssim 0.12$) on the leeward side where the pressure drop is strongest ($10^o < \phi < 25^o$). Whenever supersonic cross flow occurs around circular or elliptic cones, convergence of the normal components $v_i(0)$ is more difficult at the lines in that

region. If the supersonic cross-flow region is not extensive, convergence is possible, as demonstrated by the present example.

Conical Delta Wings

Perhaps more appropriate to this compilation of papers are the wing-like bodies. The present method has been applied to the problem of conical delta wings with the shock wave attached at the sharp leading edges. In this problem the lower (compression) surface is independent of the upper (expansion) surface, and the two can be treated separately. The method of lines, as formulated herein, is only applicable to the compression side where the shock wave forms the outer boundary. Nevertheless, the compression-side results are valuable from both theoretical and practical standpoints. As mentioned earlier, the results from the present method provide a check for more complex three-dimensional calculation methods, and it will be seen that they corroborate results from other conical methods and experiment, too. Practically speaking, at large supersonic Mach numbers nearly all the aerodynamic-force contribution comes from the compression side.

In these problems the cross-flow component $\sqrt{v^2 + w^2}$ is supersonic at the leading edge and remains supersonic for some distance toward the wing center line. As stated before, the partial differential equations governing the conical flow are of the hyperbolic type in regions where the cross flow is supersonic, and a two-dimensional conical method of characteristics can be used to construct the exact flow in such regions. Maslen (ref. 15) was the first to describe this approach for conical delta wings, and it has been exploited extensively in reference 30 for the flow about elliptic cones at large angles of attack. A computer program using the conical method of characteristics has been developed at the Langley Research Center by C. W. Chiang[3] and Richard D. Wagner, Jr.; they supplied the results presented in this paper although the method has not yet been published.

Vincenti (ref. 38) proposed an approximate method which can also be used in regions of supersonic cross flow; it is analagous to the familiar shock-expansion method for two-dimensional and axisymmetric flows. The approximation reduces to a nonlinear ordinary differential equation that is numerically integrated along the surface in the spanwise direction from the leading edge inward to the cross-flow sonic point. Results obtained by Richard D. Wagner, Jr., by that method are presented and are referred to as a "conical shock expansion" method.

The supersonic cross flow in the delta-wing problems presents no difficulties for the method of lines; this is contrary to the case of the circular or elliptic cone at

---

[3]NRC-NASA Resident Research Associate on leave from the University of Denver.

incidence where convergence becomes more difficult when a region of supersonic cross flow occurs, as already mentioned.

Parabolic-arc cross section.- Reference 7 presents calculated results for a number of conical delta wings, with a three-dimensional implicit finite-difference scheme being used which is sometimes referred to as the "BVLR"[4] method or the "half-step" method. Delta wings with both flat and parabolic-arc cross sections were presented in the reference, and the results from reference 7 are compared herein with results from the present method and other methods. Planform and section views of a thin parabolic cross-section wing are shown in figure 2(b) with the calculated shock shape for $\alpha = 10^{\circ}$. The conditions for this problem are $M_{\infty} = 4$, $\Lambda = 50^{\circ}$, and $\theta_0 = 3^{\circ}$. The cross-flow sonic line is shown as a heavy dashed line in the section view, and the layout of the computational lines for $N = 9$ is depicted by the finer dashed lines which appear normal to the surface.

In the three wing problems of this paper, equal line spacing was used. Recall that this means equal $\Delta\tau$ increments where τ traces around the wing contour in the surface $r = 1$; thus, when projected onto the plane $z = 1$ in which the body cross section is prescribed, the lines appear to spread as the leading edge is approached. The solid curve for the shock represents the present results, whereas the squares represent Voskresenskii's results. The squares are not meant to coincide with the dashed lines; they were replotted from the continuous curves shown in reference 7 by using constant intervals in the spanwise ($\bar{x}$) direction. The replotting of those curves for the shock shape is probably not as accurate as the pressures because although Voskresenskii's shock appears to lie slightly inside the present result near the center line, shock pressures by both methods (not shown here) agree very well. The conical method of characteristics also gives a shock shape from the leading edge to the sonic line, and the results (not shown) coincide with the solid curve drawn through the present results.

On the right side of figure 2(b) the surface pressure coefficient is plotted against $\bar{x}$, a nondimensional spanwise coordinate; $\bar{x} = 0$ at the wing center line and $\bar{x} = 1$ at the leading edge. The vertical dashed lines indicate the spanwise location of the cross-flow sonic point[5] at the surface and, hence, the limit of applicability of both the conical method of characteristics (MOC) and the conical shock-expansion method. The method of lines, conical characteristics, and conical shock expansion agree very well in the supersonic cross-flow region. Voskresenskii's results are generally quite close to the present results with some small discrepancies. At the leading edge, where the pressure and other variables can be calculated accurately from the algebraic shock conditions, results

[4]After Babenko, Voskresenskii, Lyubimov, and Rusanov, the co-authors of reference 3.

[5]As the angle of attack is increased, the cross-flow sonic point moves toward the leading edge and reaches it just before leading-edge detachment occurs.

from all theories should agree exactly; yet Voskresenskii's result for the pressure is noticeably low. His pressure calculation just inboard of the leading edge rises slightly above that of the three conical methods, but then appears to agree well with the present results in the central subsonic cross-flow region. It appears, then, that a small error in the leading-edge boundary condition has little effect on the computation over the rest of the wing by Voskresenskii's three-dimensional, distance-asymptotic method.

Circular-arc cross section.- Reference 39 presents experimental data for various conical delta wings with attached leading-edge shocks; one of the models had a circular-arc cross section, a good test problem for the different computational methods. The conditions for this problem are $M_\infty = 8.1$, $\Lambda = 50^\circ$, and $\theta_0 = 6.54^\circ$. Figure 2(c) shows the shock shape calculated by three methods: the methods of lines and conical characteristics, and a three-dimensional method of characteristics (3D MOC) described in reference 40.[6] In reference 40, results are shown only for delta wings with a region of constant flow at the leading edge; that is, the outboard portion of the wing cross section is either flat or a wedge. Results were not shown for delta wings with curvature at the leading edge, such as the parabolic-arc or circular-arc cross-section wings, because difficulties were experienced with such wings. The source of these difficulties has not yet been located, but some preliminary results are shown in figure 2(c). The methods of lines and conical characteristics agree very closely for the portion of the shock wave bounding the supersonic cross flow, but the 3D MOC of reference 40 predicts a shock layer that is more than 20 percent too thin over most of the span.

For the problem of figure 2(c), the wing thickness and Mach number are both about twice the values used in the problem of figure 2(b); it can be seen that the cross-flow sonic line[7] leans closer to the wing center line. This behavior is caused mainly by the increase in M_∞ and is similar to that of the sonic line in the blunt-body problem (ref. 9).

The spanwise pressure distribution is also shown in figure 2(c), where the various theoretical results are compared with the data of reference 39. The hatched bands are used to represent the measurements for several different Reynolds numbers and stations downstream from the wing apex. The measured pressures are higher than the inviscid predictions over the entire surface; this is the expected hypersonic boundary-layer displacement effect, while boundary-layer—shock-wave interaction is most severe near the leading edge ($\bar{x} = 1$). A comparison (not shown) was made between results from the present method and the experimental data for $M_\infty = 5.08$, and the agreement was better because the viscous displacement and interaction effects were not as severe.

---

[6]Work supported by the NASA Langley Research Center under Contract NAS1-7850.
[7]Calculations were done with $N = 9$ and $N = 18$, and the results coincided. The $N = 18$ results were used to plot the cross-flow sonic line.

Two different results by the 3D MOC are shown. The long-dash—short-dash curve in figure 2(c) shows an earlier unpublished result that is clearly in error over the entire span. The authors of reference 40 modified the method and produced the more recent (but still preliminary) results represented by the triangles. These recent results are close to the other theories in the supersonic cross-flow region (although the corresponding shock shape is not in agreement, as already mentioned), but they depart from the method of lines results in the central region. When attempts were made to calculate farther downstream in hopes of improving the results, the calculation became unstable and diverged. Because of the failure of the method for this conical problem, the validity of any other results obtained by this method should be questioned. The point to be made is the necessity for rigorous checks on three-dimensional computational schemes; conical-flow problems provide excellent check cases because they are three dimensional but can be solved by two-dimensional methods.

Flat delta wing.- The classical problem of the flat delta wing is shown in figure 2(d). This problem has the interesting feature that flow properties are constant between the cross-flow sonic line and the leading edge; the sonic line is thus a singular line connecting a constant-property region to one of varying properties. The exact, inviscid pressure distribution should exhibit a "corner" or discontinuous slope at the cross-flow sonic point, and the shock wave should be planar from the leading edge to the sonic line. This weak singularity is not treated in any special way in the present method and the same is assumed true of reference 7.

Both methods produce nearly identical results as seen in figure 2(d). The open circles are used to show the actual location of the computational lines in the present method for $N = 12$; the results are surprisingly smooth around the sonic line. Although the assumed starting shock shape (eq. (6)) is analytic, the final converged shock points lie very close to a straight line between the leading edge and the cross-flow sonic line, as they should.

In the methods of references 17 and 40, the flow properties are set constant in the supersonic cross flow, and in reference 17, an effort was made to account for the weak singularities. Even so, the results of reference 17 (solid circles) appear to be in considerable disagreement with the other methods, particularly at the larger values of α; it seems reasonable to assume that the other methods are quite accurate. It is also noteworthy that although Babaev (ref. 17) attempted to account for the singularities, his results for the surface pressure distribution appear to be very smooth at the sonic point, without a corner. Results by the method of reference 40 (3D MOC) are shown on the C_p plot for $\alpha = 15^{\circ}$, and they are in fair agreement with the present results and those of reference 7.

Convergence history.- Figure 3 illustrates the convergence history for the flat delta wing problem used for figure 2(d). The surface pressure distribution obtained with each new pivotal shock shape, including the initial approximation given by equation (6), is shown. The key of the figure gives the maximum normal velocity magnitude at the end of each cycle and the approximate elapsed central-processing time for the Control Data 6600 computer system.

Convergence with increasing N.- Figure 4 is an illustration of the accuracy that can be achieved with smaller values of N. With only one line placed between the leading edge and the wing center line (N = 2), the accuracy is surprisingly good. More lines are used, however, to give better resolution of the spanwise distribution. The approximate central-processing time and number of cycles required to converge each case are shown in the key.

CONCLUDING REMARKS

The method of lines has proved to be an efficient, versatile procedure for constructing numerical solutions to conical-flow problems. The method has been applied to circular and elliptic cones at incidence and to the compression side of conical delta wings with attached leading-edge shocks. The results for surface pressures are in good agreement with experiment except where viscous effects become important, such as on the leeward side of the elliptic cone at relatively large incidence and near the leading edges of delta wings.

The method can be used for circular or elliptic cones at such incidences that small embedded regions of supersonic cross flow occur, but the convergence becomes more difficult. In the delta-wing problems, however, significant regions of supersonic cross flow occur, and the method is applicable with no difficulties.

Several other approaches for calculating conical flows were compared with the method of lines and were found to be in close agreement. One approach is a three-dimensional, implicit, finite-difference scheme that attains the conical solution asymptotically, whereas two others are strictly two-dimensional conical methods. These last two are applicable only in regions of supersonic cross flow, but they provide valuable corroboration for more general methods.

A three-dimensional method of characteristics was shown to fail for the problem of a delta wing with curvature at the leading edge. It appears that such conical-flow problems are excellent check cases for more general three-dimensional computational schemes because they are three-dimensional but can be solved by two-dimensional conical methods.

REFERENCES

1. Busemann, A.: Aerodynamic Lift at Supersonic Speeds. Ae. Techl. 1201, Rep. No. 2844, Brit. A.R.C., Feb. 3, 1937. (From Luftfahrtforschung, Bd. 12, Nr. 6, Oct. 3, 1935, pp. 210-220.
2. Moretti, Gino: Inviscid Flowfield About a Pointed Cone at an Angle of Attack. AIAA J., vol. 5, no. 4, Apr. 1967, pp. 789-791.
3. Babenko, K. I.; Voskresenskiy, G. P.; Lyubimov, A. N.; and Rusanov, V. V.: Three-Dimensional Flow of Ideal Gas Past Smooth Bodies. NASA TT F-380, 1966.
4. Rakich, John V.: A Method of Characteristics for Steady Three-Dimensional Supersonic Flow With Application to Inclined Bodies of Revolution. NASA TN D-5341, 1969.
5. Bebenko, K. I.; and Rusanov, V. V.: Difference Methods of Solving Three-Dimensional Problems in Gas Dynamics. NASA TT F-10,827, 1967.
6. Gonidou, René: Supersonic Flows Around Cones at Incidence. NASA TT F-11,473, 1968.
7. Voskresenskii, G. P.: Chislennoe Reshenie Zadachi Obtekaniia Proizvol'noi Poverkhnosti Treugul'nogo Kryla v Oblasti Szhatiia Sverkhzvukovym Potokom Gaza (Numerical Solution of the Problem of a Supersonic Gas Flow Past an Arbitrary Surface of a Delta Wing in the Compression Region). Izv. Akad. Nauk SSSR, Mekh. Zhidk. Gaza, no. 4, 1968, pp. 134-142.
8. Busemann, A.: Drücke auf kegelförmige Spitzen bei Bewegung mit Überschallgeschwindigkeit, Z. Angew. Math. Mech., Bd. 9, Heft 6, Dec. 1929, pp. 496-498.
9. Hayes, Wallace D.; and Probstein, Ronald F.: Hypersonic Flow Theory. Vol. I – Inviscid Flows. Second ed., Academic Press, 1966, pp. 526-536.
10. Briggs, Benjamin R.: The Numerical Calculation of Flow Past Conical Bodies Supporting Elliptic Conical Shock Waves at Finite Angles of Incidence. NASA TN D-340, 1960.
11. Mauger, F. E.: Steady Supersonic Flow Past Conical Bodies. A.R.D.E. Rep. (B)3/60, Brit. War Office, May 1960.
12. Stocker, P. M.; and Mauger, F. E.: Supersonic Flow Past Cones of General Cross-Section. J. Fluid Mech., vol. 13, pt. 3, July 1962, pp. 383-399.
13. Eastman, D. W.; and Omar, M. E.: Flow Fields About Highly Yawed Cones by the Inverse Method. AIAA J., vol. 3, no. 9, Sept. 1965, pp. 1782-1784.

14. Makhin, N. A.; and Syagaev, V. F.: Numerical Solution of the Problem of Supersonic Flow Past Conical Bodies at an Angle of Attack. Fluid Dyn., vol. 1, no. 1, Jan.-Feb. 1966, pp. 100-101.

15. Maslen, Stephen H.: Supersonic Conical Flow. NACA TN 2651, 1952.

16. Babayev, D. A.: Numerical Solution of the Problem of Flow Round the Upper Surface of a Triangular Wing by a Supersonic Stream. U.S.S.R. Comput. Math. Math. Phys., no. 2, 1963, pp. 296-308.

17. Babaev, D. A.: Numerical Solution of the Problem of Supersonic Flow Past the Lower Surface of a Delta Wing. AIAA J., vol. 1, no. 9, Sept. 1963, pp. 2224-2231.

18. Vaglio-Laurin, Roberto; and Ferri, Antonio: Theoretical Investigation of the Flow Field About Blunt-Nosed Bodies in Supersonic Flight. J. Aero/Space Sci., vol. 25, no. 12, Dec. 1958, pp. 761-770.

19. Belotserkovskiy, O. M.: Supersonic Gas Flow Around Blunt Bodies – Theoretical and Experimental Investigations. NASA TT F-453, 1967.

20. South, Jerry C., Jr.: Application of the Method of Integral Relations to Supersonic Nonequilibrium Flow Past Wedges and Cones. NASA TR R-205, 1964.

21. Sedney, Raymond; and Gerber, Nathan: Shock Curvature and Gradients at the Tip of Pointed Axisymmetric Bodies in Non-Equilibrium Flow. J. Fluid Mech., vol. 29, pt. 4, Sept. 27, 1967, pp. 765-779.

22. Dorodnitsyn, A. A.: General Method of Integral Relations and Its Application to Boundary Layer Theory. Vol. 3 of Advances in Aeronautical Sciences, Macmillan Co., 1962, pp. 207-219.

23. Chushkin, P. I.; and Shchennikov, V. V. (B. A. Woods, transl.): Calculation of Certain Conical Flows Without Axial Symmetry. Lib. Transl. No. 926, Brit. R.A.E., Dec. 1960.

24. Brook, John W.: The Method of Integral Relations for Conical Flow – Theoretical Analysis. Res. Mem. RM-193 (Contract No. AF 33(616)-6400), Grumman Aircraft Eng. Corp., Oct. 1961. (Available from DDC as AD 266 501.)

25. Roslyakov, G. S.; and Telenin, G. F.: Survey of Computational Work on Steady Axisymmetric Gas Flow Carried out at the Computational Center of Moscow State University. Numerical Methods in Gas Dynamics, G. S. Roslyakov and L. A. Chudov, eds., NASA TT F-360, Israel Program Sci. Transl., 1966, pp. 1-11. (Available from CFSTI, U.S. Dep. Com.)

26. Telenin, G. F.; and Tinyakov, G. P.: A Method of Calculating the Three-Dimensional Flow Past a Body With an Attached Shock Wave. Sov. Phys. – Doklady, vol. 9, no. 2, Aug. 1964, pp. 132-133.

27. Tiniakov, G. P.: Investigation of the Three-Dimensional Supersonic Flow Around Ellipsoids of Revolution. Lockheed Missiles & Space Co. Transl. (From Izv. Akad. Nauk SSSR, Otd. Tekhn. Nauk, Mekhan. i Mashinostr., no. 6, 1965, pp. 10-19.)

28. Makhin, N. A.; and Syagayev, V. F.: Numerical Solution of the Problem of Supersonic Flow at an Angle of Attack Past Conical Bodies. NASA TT F-10,481, 1966.

29. Bazzhin, A. P.; and Chelysheva, I. F.: Primenenie Metoda Priamykh k Raschetu Obtekaniia Konicheskikh Tel pri Bol'shikh Uglakh Ataki (Application of the Straight-Line Method in the Calculation of Flows Past Conical Bodies at Large Angles of Attack). Izv. Akad. Nauk SSSR, Mekh. Zhidk. Gaza, no. 3, 1967, pp. 119-123.

30. Bazzhin, A. P.; Trusova, O. N.; and Chelysheva, I. F.: Raschet Techenii Sovershennogo Gaza Okolo Ellipticheskikh Konusov pri Bol'shikh Uglakh Ataki (Calculation of Ideal-Gas Flows Around Elliptical Cones at Large Angles of Attack). Izv. Akad. Nauk SSSR, Mekh. Zhidk. Gaza, no. 4, 1968, pp. 45-51.

31. Jones, D. J.: Numerical Solutions of the Flow Field for Conical Bodies in a Supersonic Stream. Aeronaut. Rep. LR-507 (NRC No. 10361), Nat. Res. Counc. Can. (Ottawa), July 1968.

32. Ferri, Antonio: Supersonic Flow Around Circular Cones at Angles of Attack. NACA Rep. 1045, 1951. (Supersedes NACA TN 2236.)

33. Melnik, R. E.: Vortical Layers in Supersonic Conical Flow. Hypersonic Boundary Layers and Flow Fields, AGARD CP No. 30, 1968, pp. 26-1 – 26-20.

34. Scheuing, Richard A.; Brook, John W.; Mead, Harold R.; Melnik, Robert E.; Hayes, Wallace D.; Donaldson, Coleman duP.; Gray, K. Evan; and Sullivan, Roger D.: Theoretical Prediction of Pressures in Hypersonic Flow With Special Reference to Configurations Having Attached Leading-Edge Shock – Pt. I. Theoretical Investigation. ASD TR 61-60, Pt. I, U.S. Air Force, May 1962.

35. Babenko, K. I.: Investigation of a Three-Dimensional Supersonic Gas Flow Around Conic Bodies. Applied Mechanics, Henry Görtler and Peter Sorger, eds., Springer-Verlag, 1966, pp. 749-755.

36. Hord, Richard A.: An Approximate Solution for Axially Symmetric Flow Over a Cone With an Attached Shock Wave. NACA TN 3485, 1955.

37. Chapkis, Robert L.: Hypersonic Flow Over an Elliptic Cone: Theory and Experiment. J. Aerosp. Sci., vol. 28, no. 11, Nov. 1961, pp. 844-854.

38. Vincenti, Walter G.; and Fisher, Newman H., Jr.: Calculation of the Supersonic Pressure Distribution on a Single-Curved Tapered Wing in Regions Not Influenced by the Root or Tip. NACA TN 3499, 1955.

39. Mead, Harold R.; and Koch, Frank: Theoretical Prediction of Pressures in Hypersonic Flow With Special Reference to Configurations Having Attached Leading-Edge Shock – Pt. II. Experimental Pressure Measurements at Mach 5 and 8. ASD TR 61-60, Pt. II, U.S. Air Force, May 1962.

40. Beeman, E. R.; and Powers, S. A.: A Method for Determining the Complete Flow Field Around Conical Wings at Supersonic/Hypersonic Speeds. AIAA Pap. No. 69-646, June 1969.

TABLE 1

COMPUTATION HISTORY FOR AN ELLIPTIC CONE

$[\gamma = 1.4;\ M_\infty = 5.8;\ b/a = 0.5;\ \theta_0 = 6.0^0;\ N = 17]$

α	Cycles	$\max_i \lvert v_i(0) \rvert$
0.05	2	2.2×10^{-5}
1.0	2	9.9×10^{-5}
2.0	3	4.7×10^{-5}
3.0	2	3.7×10^{-5}
4.0	2	2.5×10^{-5}
5.0	2	1.6×10^{-4}
6.0	3	8.1×10^{-6}

LAYOUT OF COMPUTATIONAL LINES

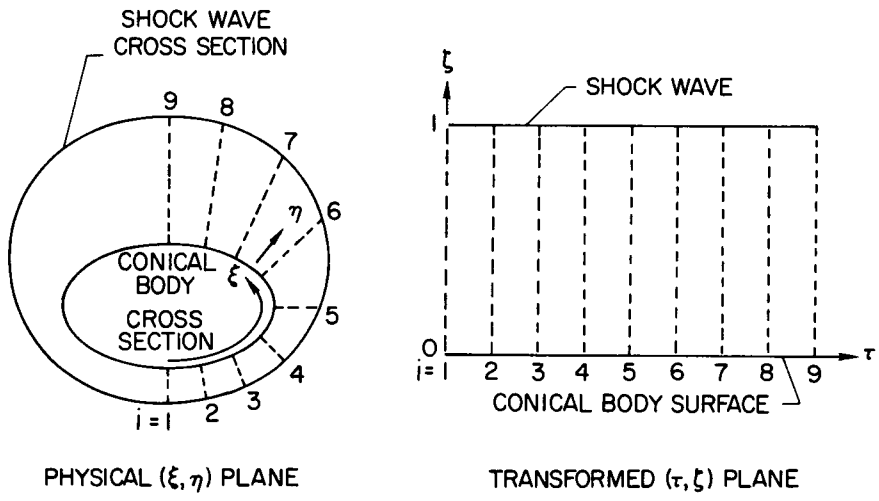

Figure 1

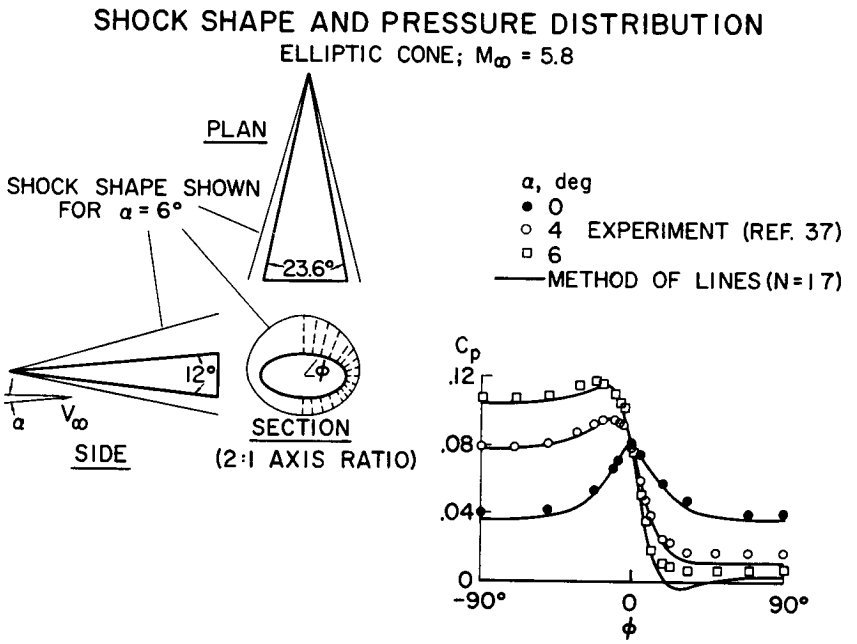

Figure 2(a)

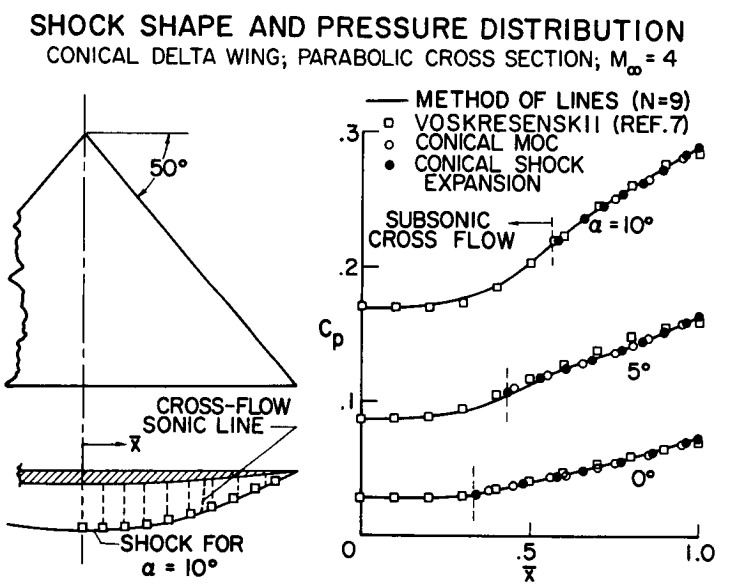

Figure 2(b)

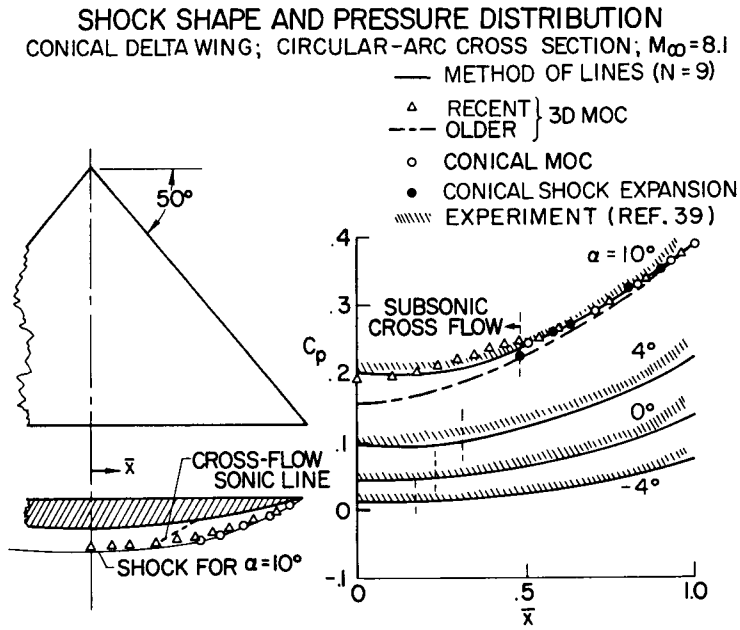

Figure 2(c)

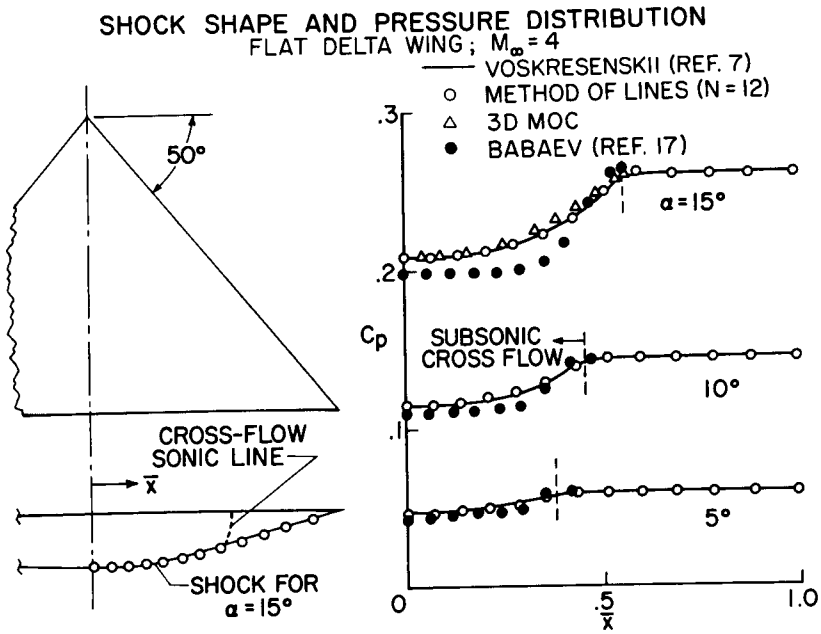

Figure 2(d)

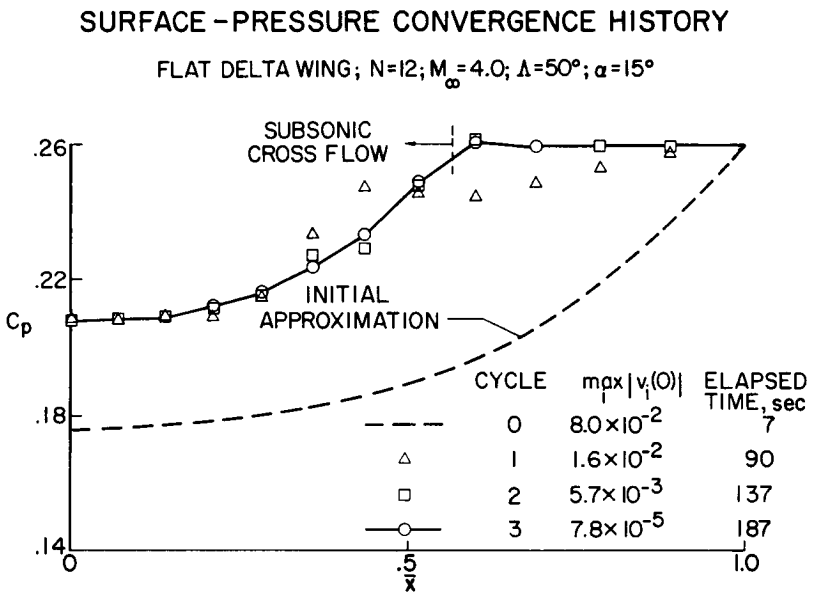

Figure 3

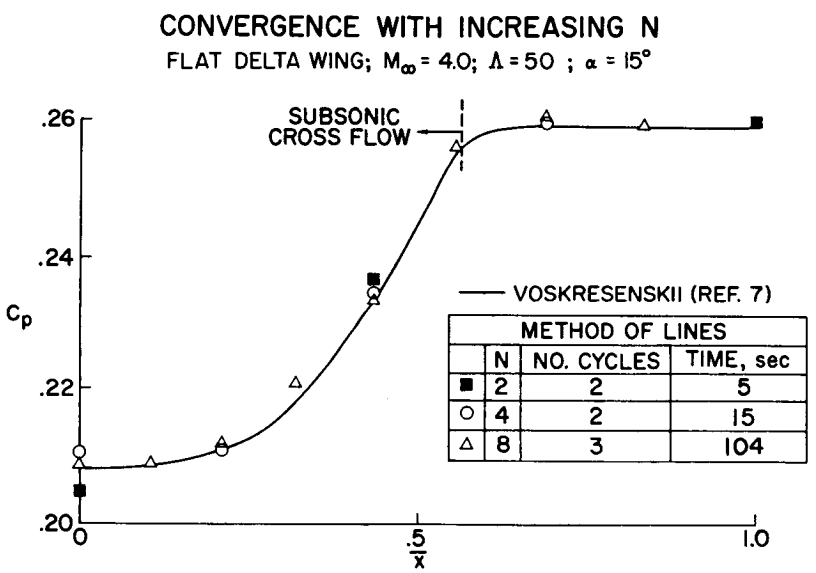

Figure 4

DISCUSSION

HARRY A. DWYER, University of California, Davis: I was just wondering how you located the shock position in the method of lines. How do you determine the shock location?

SOUTH: I must have done that pretty poorly on slide 3. Let us look at slide 3. [Information from slide 3 was incorporated in written version; therefore, this slide is reproduced at the end of this discussion.]

We specify the ordinates of the shock, and then we numerically differentiate the ordinates. Differentiating the ordinates we get the cross slopes of the shock wave, and this gives us all we need to satisfy the Rankine-Hugoniot jump conditions. This gives us the pressures and velocities behind the shock, so we can integrate the ordinary differential equations to the surface.

Now, when we get to the surface, the normal components are not zero, and we want to drive them to zero by selecting the right shock ordinates. In other words, the first guess for the shock location was wrong. I explained how we make a small perturbation on each ordinate and generate a matrix of influence coefficients. We invert it to obtain corrections for each one of the ordinates, and hence a new estimate for the shock location. We keep repeating the cycles until we have driven all the normal components at each line to zero.

WILBUR L. HANKEY, USAF Aerospace Research Laboratory: Have you looked at the leeside of a delta wing or a cone at high angle of attack, in which the vortical singularity was of any sufficient strength to lift off the surface? It would seem that with the method of lines you could get into trouble with the singularity.

SOUTH: Well, the vortical singularity... There was a comment earlier about a piece of work by D. J. Jones, of the National Research Council in Canada, and the method that Jones uses is almost identical with this. His work was published while we were still wrapping up the elliptic cone part and working on the wings, and he presented some results indicating the lift-off of the vortical singularity.

As far as I know, this is the only method that has actually given some results indicating the actual lift-off of the vortical singularity other than some work done by Gonidou with the BVLR method. This method, strangely, although it is very simple and very unsophisticated, seems to have little trouble with the nodal singularity on the leeside, at least before this "lift-off" occurs. I won't get into too much discussion of this. The method of lines seems to work better and easier than any other method as far as that feature is concerned.

We will never use this method for the leeside of wings. For one thing, we might work on the inviscid problem for years and finally succeed, but people wouldn't believe it anyway, because I think it is mainly viscous-dominated with vortical eddies at the leading edge. For another reason, there is no well-defined outer boundary on the leeside for the application of this method in its current formulation.

ROBERT FELDHUNE, U. S. Naval Ordnance Laboratory: Did you say that with your technique you do actually see the vortical singularity lift off the surface of the elliptical cones?

SOUTH: We have not done it, but Jones has, for circular cones, and you can look in his report and see it. He computed a low Mach number case, which was about a 1.8 Mach number, and a 12.5° half-angle cone, up to a relative incidence of 1.2 and beyond; that is, up to about 15° angle of attack and beyond.

The shock wave on the leeside was still not a Mach wave, and the normal component of velocity in the leeward plane of symmetry actually passed through zero above the surface and then went positive and then back to zero again. So there were two zeros in the normal component of velocity in that leeward plane. He states that his results indicate lift-off. We played with that briefly and we would always get into trouble. That seemed to be a limitation with our program. With his, it apparently wasn't a limitation.

SIDNEY A. POWERS, Northrop Corporation: Since we are doing the conical three-dimensional method of characteristics, I'll have to put in a commercial here.

In answer to Mr. Hankey, this method has been applied and does work on the expansion side. We run 4°, 8°, and 12° leeside solution for a 45° swept wing at Mach 3.

Now, our method follows streamlines, so we in essence bypass the vortical singularity problem that way.

We agree with Ralph Carmichael's comment this morning that one should have a good inviscid solution to give you something to base further judgments on. So we think that the leeside solutions are important. We have done some solutions with and without imbedded shock on the inside. [Mr. Carmichael's comment was made in paper no. 2 of this compilation.]

METHOD OF "LINES"

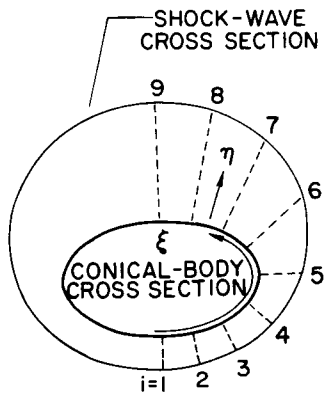

(1) WRITE GOVERNING EQS. IN FORM:

$$\frac{\partial p}{\partial \eta} = P\left\{p, \rho, u, v, w, \frac{\partial p}{\partial \xi}, \frac{\partial u}{\partial \xi}, \frac{\partial v}{\partial \xi}, \frac{\partial w}{\partial \xi}\right\}$$

$$\frac{\partial u}{\partial \eta} = U, \frac{\partial v}{\partial \eta} = V, \frac{\partial w}{\partial \eta} = W$$

(2) N LINES $\xi = \xi_i$ NORMAL TO BODY

(3) FINITE DIFFERENCES FOR $\frac{\partial}{\partial \xi}$

(4) ASSUME SHOCK SHAPE

(5) INTEGRATE FROM SHOCK TO BODY

(6) EVALUATE NORMAL COMPONENTS AT BODY

(7) ITERATE SHOCK SHAPE TO ACHIEVE $v_i = 0, \quad i = 1, \ldots, N$

Slide 3.

APPLICATION OF THE METHOD OF CHARACTERISTICS TO NONCIRCULAR BODIES AT ANGLE OF ATTACK

By John V. Rakich

Ames Research Center

N70-21360

SUMMARY

The generalized boundary conditions for bodies with noncircular cross sections are described, and numerical stability problems arising from these boundary conditions are discussed. Surface-pressure coefficients for a pointed elliptic cone at angle of attack are compared with experiment and with results of other theoretical methods. Flow-field results are presented for a nonconical wing-like body consisting of an elliptic cone forebody and an elliptic-wedge afterbody.

INTRODUCTION

A method of characteristics for three-dimensional flow was described in references 1 and 2. Although the method was developed in a general way, applications in those papers were limited to bodies of revolution. The main difference for bodies with noncircular cross sections is in the application of the boundary condition at the body surface. In the present paper the generalized boundary condition is described and tested on a wing-like body with elliptical cross sections.

Applications of the method of characteristics to noncircular bodies have been made previously by Moretti in reference 3. That method is one of first-order accuracy and was developed specifically for bodies with simple sections (flat and cylindrical surfaces in combination). The flow over a delta wing with supersonic leading edges was recently computed by Beeman and Powers (ref. 4) by a method of characteristics employing the distance-asymptotic technique. (Conical solutions may be considered analogous to the steady-state motion produced by a piston with an impulsive start.) A noncharacteristic method, developed in the Soviet Union, has been applied to elliptic cones in references 5 and 6. These also use the distance-asymptotic technique to get the conical solution. Numerous inverse methods have also been employed in the past for elliptic cones (e.g., ref. 7). In two recently reported methods (refs. 8 and 9), inverse methods have been successfully automated to find the shock shape consistent with the given body.

In the present study, flow over the nonconical wing-like body shown in figure 1 is calculated to test the proposed method. The elliptic-cone forebody solution is obtained by the distance-asymptotic technique. The forebody and afterbody solutions are obtained with the same computer program that maintains second-order accuracy in terms of mesh spacing.

9

PRINCIPAL SYMBOLS

a	speed of sound; local span
C_1^*, C_2^*	characteristic directions in Φ plane
C_p	pressure coefficient
M	Mach number
$\vec{N}$	body surface outer normal
p	pressure
s^*	projection of streamline on Φ plane
u,v,w	cylindrical velocity components
V	velocity magnitude, $\sqrt{u^2 + v^2 + w^2}$
x,r,Φ	cylindrical coordinates
$\hat{e}_x, \hat{e}_r, \hat{e}_\Phi$	unit vectors along x, r, Φ
α	angle of attack
β	$\sqrt{M^2 - 1}$
ε	surface upwash angle
θ	flow angle in Φ plane
ϕ	crossflow angle normal to Φ plane

THEORY

Differential Equations

The present description will begin directly with the compatibility equations derived and used in references 1 and 2. These are

$$\frac{\beta}{\rho V^2}\frac{\partial p}{\partial C_1^*} + \cos\phi\,\frac{\partial\theta}{\partial C_1^*} = \sin\mu^*\left[\left(F_1 - \frac{\cos\phi\sin\theta}{r}\right) + \beta\left(F_2 + \frac{\sin^2\phi\cos\theta}{r}\right)\right] \quad (1)$$

$$\frac{\beta}{\rho V^2}\frac{\partial p}{\partial C_2^*} - \cos\phi\,\frac{\partial\theta}{\partial C_2^*} = \sin\mu^*\left[\left(F_1 - \frac{\cos\phi\sin\theta}{r}\right) - \beta\left(F_2 + \frac{\sin^2\phi\cos\theta}{r}\right)\right] \quad (2)$$

$$\frac{\partial \phi}{\partial s^*} = - \frac{\sin \phi \sin \theta}{r\varepsilon_{11}^*} + F_3 \tag{3}$$

$$\frac{\partial \rho}{\partial s^*} = \frac{1}{a^2} \frac{\partial p}{\partial s^*} + F_4 \tag{4}$$

where C_1^* and C_2^* are projections of the Mach cone on the plane Φ = constant, s^* is the projection of the streamline on that plane, and ε_{11}^* is the direction cosine relating unit vectors $\hat{s}$ and $\hat{s}^*$ (see ref. 2). The F_i ($i = 1, \ldots, 4$) on the right-hand side of these equations contain the so-called cross derivatives which vanish for two-dimensional or axisymmetric flow but are always present in three-dimensional flow. The circumferential derivatives are evaluated by means of Fourier analysis, as described in reference 2. However, for the present calculations, the Fourier coefficients are multiplied by Lanczos' σ factors to damp high-frequency oscillations (see ref. 10).

In deriving equations (1) and (4), use was made of a cylindrical x, r, Φ coordinate frame (see fig. 1). The angles θ and ϕ are defined relative to the planes Φ = constant; θ is the flow direction measured in the plane; and ϕ is angle by which the velocity vector is turned out of the plane. In terms of velocity components, u, v, w, along the x, r, Φ directions, these angles are:

$$\theta = \tan^{-1} \frac{v}{u} \tag{5}$$

$$\phi = \tan^{-1} \frac{w}{(u^2 + v^2)^{1/2}} \tag{6}$$

For general body shapes the surface boundary condition will involve all three velocity components. This will introduce a coupling between flow angles θ and ϕ which does not occur for bodies with circular cross sections. While it is possible to simplify the boundary condition by using reference planes normal to the body surface, the basic equations would be more complex and the class of body shapes restricted. Therefore the basic cylindrical coordinate system was retained in spite of complications in the boundary condition. The general boundary condition is derived next.

Surface Boundary Condition

The boundary condition at the body surface may be written generally as

$$\vec{V} \cdot \vec{N} = 0 \tag{7}$$

Let the body be given by

$$g(x, r, \Phi) = r - f(x, \Phi) \tag{8}$$

Then the surface normal may be written

$$\hat{N} = \frac{-f_x\hat{e}_x + \hat{e}_r - (1/r)\ f_\Phi\hat{e}_\Phi}{\sqrt{1 + f_r^2 + (1/r^2)f_\Phi^2}} \tag{9}$$

where the subscripts indicate partial derivatives. The unit vector along the streamline direction may be written in terms of flow angles θ and ϕ as follows:

$$\hat{s} = \cos\phi\ \cos\theta\ \hat{e}_x + \cos\phi\ \sin\theta\ \hat{e}_r + \sin\phi\ \hat{e}_\Phi \tag{10}$$

Substituting equations (9) and (10) into equation (7), noting that $\vec{V} = V\hat{s}$, one can obtain the following expression for $\tan\theta$ (see ref. 2),

$$\tan\theta = \frac{f_x + (\tan\phi/r)f_\Phi\sqrt{1 + f_x^2 - [(\tan\phi/r)f_\Phi]^2}}{1 - [(\tan\phi/r)f_\Phi]^2} \tag{11}$$

COMPUTATIONAL PROCEDURE

The first effect of the generalized boundary condition is to change the procedure for computing the conditions at a typical body point (see fig. 2). Since $\tan\theta$ is not equal to the body slope $\partial f/\partial x$, the streamline projection s^* is not tangent to the body. Consequently, the integration of equation (3) requires interpolation for data at point D on the initial data line. This is the main change in program logic for noncircular bodies. For circular bodies, conditions at point A are employed without need for interpolation. To complete the calculation for point C on the body, equation (2) is applied on C_2^* using interpolated data at point B in the standard manner described in reference 2, equation (2) is replaced by the boundary condition equation (11), and equation (4) is replaced by a body entropy condition.

The body entropy condition mentioned here for the first time, requires additional comment. It is possible to employ equation (4) directly without explicitly introducing the entropy function. However, since the body entropy is usually known, the computation is simpler and more accurate if a surface

entropy condition is employed. This is especially true near conical singular points where density gradients are multivalued. For general conical flows it is always possible, in principle, to trace the stagnation streamlines from the body to the shock in order to determine the body entropy. However, detailed streamline tracing is a complication of questionable value in the light of experience with analogous blunt-body flows. Numerous studies have found that the stagnation entropy is very nearly equal to the maximum entropy on the shock. Therefore, as a practical expedient, the body entropy has been set equal to the maximum shock entropy in the present conical-flow calculations.

Numerical Stability

A stability analysis of the general nonlinear equations is too difficult to perform so one usually relies on a linear analysis. The stability condition for linear hyperbolic equations is the well-known Courant-Friedrichs-Lewy or C.F.L. condition. It states that the difference equations must include the domain of dependence of the differential equations. This means that the Mach line in figure 3 must lie above point A as shown. Although the C.F.L. condition is derived on the basis of linearized equations, and is rigorously shown to be only a necessary condition, it has been found to be sufficient in most practical applications. This was true for previous applications of the present method to bodies of revolution. However, the C.F.L. condition was not sufficient in present applications because of the coupling of the cross-flow angle through the boundary condition, equation (11).

Previous practice was to use a step slightly less than the C.F.L. condition. A value of 0.8 (C.F.L.) worked well for most applications. When this condition was applied to an elliptic-cone calculation, the computation became unstable as illustrated in figure 3. This figure shows the variation of ϕ with distance starting with flow conditions that depart only slightly from the conical solutions. For conical flow ϕ should be constant, but with a step size of 0.8 (C.F.L.), ϕ oscillates with increasing amplitude as x increases. When the step was reduced to 0.6 (C.F.L.), the amplitude was decreased but the computation still slightly unstable. Finally, with 0.4 (C.F.L.), it is seen that the oscillations are quickly damped, and the computation is stable.

RESULTS

Elliptic Cone

The present method-of-characteristics program has been used to obtain conical solutions by means of the distance-asymptotic technique. Starting with an approximate solution, the computation is carried downstream until variations of flow properties along conical rays decrease to a specified error. The maximum shock entropy is applied at the body as a boundary condition. The initial solution need not be accurate, but the relaxation process

tends to be slow if the initial solution is poor. Specialized conical methods have been developed (e.g., refs. 8 and 9) that are more efficient but more limited. These methods start with an assumed conical shock and march to the body. The process is repeated until the surface boundary condition is matched.

To test the present method, a 2:1 elliptic cone at $M = 5.8$ and 4° angle of attack was selected. Experimental results were available from reference 11 as well as theory from reference 9. The surface pressure distribution is shown in figure 4. The results of reference 9 agree better with experiment; the present method appears slightly low with the biggest difference occurring just to the leeward side of the leading edge. It is believed that the difference in theories is due to the coarser mesh employed in the present calculations. In reference 9, 17 planes were used and they were more densely spaced near the leading edge. The present calculations initially employed 13 planes and 6 points between the body and shock. The field was later refined to 11 points and 15 planes. Computing time was about 35 minutes on an IBM 7094, mod I computer.

A Wing-Like Body

To demonstrate the generality of the present method, a nonconical body, which has been studied for hypersonic transport missions (ref. 12), was selected. Flow computations have been performed for the delta-wing-like body shown in figure 5. This body is described as an elliptic-cone forebody with an elliptic wedge afterbody. This test body presents an especially difficult test because of the expansion corner at the junction between the cone and the wedge. This corner region was approximated with a small radius arc, so that the program could be applied directly without special treatment of the surface discontinuity. The approximating arc was made 0.01 of the nose length. About 35 steps were used in calculating across this arc segment.

Results of the circumferential pressure distribution at the start, midpoint, and the end of the arc are shown in figure 6. Note that the pressure on the leading edge $\Phi = 90°$ is unchanged, as it should be. Pressure on the windward and leeward sides, on the other hand, changes rapidly in this region. The symbols on the elliptic-cone curve ($x = 1.0$) show results of Kaattari's empirical method (ref. 13) and numerical results of South et al. (ref. 9). Agreement is good except for the region just leeward of the leading edge where the present predictions are slightly lower than those derived by the referenced methods.

The axial variation of the surface pressure is shown in figure 7. The pressure is constant on the elliptic cone, $x < 1$, and remains essentially constant for the leading edge $\Phi = 90°$. On the other planes, the pressure drops rapidly on the transition arc, $1 < x < 1.01$, and then rises for a short distance behind the corner. This type of pressure variation is typical of those observed for sphere-cones. An overexpansion usually occurs near regions where the body slope or curvature is discontinuous. Experiments with

blunted cones indicate that the boundary layer tends to smooth the discontinuous pressure gradients predicted by inviscid theory.

The two-dimensional pressure for a sharp expansion corner at $\Phi = 180°$ is also shown in figure 7. It is somewhat below the value obtained with the approximating arc segment. The present method should yield the two-dimensional value in the limit as Δx of the arc tends to zero.

The radial variation of pressure is shown in figure 8 for several x stations in the windward plane, $\Phi = 180°$. Moving from body to shock, $\eta = 0$ to 1, the pressure first overshoots and then relaxes to the elliptic-cone value. The overshoot results from numerical interpolation with a relatively coarse finite difference mesh (11 points were used between the body and shock). The pressure should be equal to the elliptic-cone value outside the initial Mach wave from the corner, and should be less than that value inside the Mach wave. The approximate location of the initial Mach wave is indicated by the small lines on the pressure curves. Previous experience with similar flows has shown that the pressure overshoot is decreased when the mesh is refined (see ref. 2).

Figures 9 and 10 show the axial and radial variations of flow angle θ. Figures 11 and 12 show similar curves for the crossflow angle ϕ. On the 90° and 180° planes, the flow angle θ is constant behind the corner as specified by the body shape. However, on intermediate planes, θ varies with distance in accordance with equation (11). The radial variations of the flow angles are qualitatively similar to those for the pressure described above. These angles approach the elliptic-cone value some distance off the body surface, but with some overshoot, as described in the discussion of pressure variations.

The sign reversal of the crossflow angle in figure 11 raises a question about the shape of streamlines on the wedge afterbody. To visualize better the streamline direction, an upwash angle measured on the body surface is introduced here. Let ε be the actual surface stream angle measured with respect to the meridional plane, Φ = constant, and defined as *positive* for an upwash. Then ε may be expressed as follows in terms of flow angles θ and ϕ, and body slopes f_x and f_ϕ:

$$\sin \varepsilon = \frac{(\cos \phi/r) f_\Phi (f_x \cos \theta - \sin \theta) - (1 + f_x^2) \sin \phi}{\sqrt{(1 + f_x^2)[1 + f_x^2 + (1/r^2) f_\Phi^2]}} \tag{12}$$

For a circular body, or, more generally, for $f_\Phi = 0$, equation (12) gives $\varepsilon = -\phi$. It is also noted here, for reference, that the conical crossflow velocity is given by

$$w_c = V \sin \varepsilon \tag{13}$$

The axial variation of ε is shown in figure 13 for the elliptic-cone elliptic-wedge body. The variation is similar to that shown for the cross-flow angle, ϕ, in figure 11. On the elliptic-cone forebody, ε is positive on the 75° plane and negative on the 105° plane. This indicates a flow away from the leading edge in the direction of decreasing pressure. A reversal of sign occurs at about $x = 1.01$ which seems unusual. A closer examination shows that this peculiar reversal is caused by the curvature of the reference line from which ε is measured. The reference line is the intersection of the plane Φ = constant with the body surface and is curved on the elliptic-wedge afterbody. The sketch in figure 13 shows the reference line for $\Phi = 105°$ (to the windward side of the leading edge). All the reference lines, except the $\Phi = 90°$ line, will approach the x axis at the trailing edge where the body closes.

CONCLUDING REMARKS

A three-dimensional method-of-characteristics program has been applied to noncircular bodies at angle of attack. Results for an elliptic cone were verified by experiments and by other available conical-flow solutions. Stability problems were encountered which were overcome by using a step size less than that allowed by the Courant-Friedrichs-Lewy condition. The C.F.L. condition gives the maximum allowable step for linear hyperbolic equations; it is a necessary but not a sufficient condition. Present results indicate that in nonlinear problems the maximum step can be appreciably less than the C.F.L. step. This illustrates a need for a more restrictive stability condition for complex, nonlinear flow-field calculations.

The present method was applied to a nonconical body with elliptic cross sections to demonstrate its generality. While the results appear reasonable and internally consistent, additional verification with experiment is essential.

While the present examples were all pointed bodies, the method is not so restricted. Flows over blunt-nosed bodies have also been calculated using a locally supersonic starting solution obtained from an inverse blunt-body method. Other problems which can be treated in a straightforward manner by the present method of characteristics include sharp wings with supersonic leading edges, and simple wing-body combinations. However, additional work is required to include the special leading-edge boundary condition for "supersonic" wings. For wings with subsonic leading edges, the leading-edge boundary condition is more difficult. At the present time, it is not clear how the problem of a subsonic leading edge is best solved numerically.

REFERENCES

1. Rakich, John V; and Cleary, Joseph W.: Theoretical and Experimental Study of Supersonic Steady Flow Around Inclined Bodies of Revolution. Preprint 69-187, AIAA, Jan. 1969.

2. Rakich, John V.: A Method of Characteristics for Three-Dimensional Supersonic Flow With Applications to Inclined Bodies of Revolution. NASA TN D-5341, 1969.

3. Moretti, G.: Three-Dimensional Supersonic Flow Computations. AIAA J., vol. 1, Sept. 1963, p. 2192.

4. Beeman, E. R.; and Powers, S. A.: A Method for Determining the Complete Flow Field Around Conical Wings at Supersonic/Hypersonic Speeds. Preprint 69-646, AIAA, June 1969.

5. Babenko, K. I.; and Rusanov, V. V.: Difference Methods of Solving Three-Dimensional Problems in Gas Dynamics. NASA TT F-10,827, 1967.

6. Gonidou, Rene: Supersonic Flow Around Cones at Incidence. NASA TT F-11,473, 1968.

7. Briggs, Benjamin R.: The Numerical Calculation of Flow Past Conical Bodies Supporting Elliptic Conical Shock Waves at Finite Angles of Incidence. NASA TN D-340, 1960.

8. Jones, D. J.: Numerical Solutions of the Flow Field for Conical Bodies in a Supersonic Stream. Natl. Res. Council Canada Aeron. Rep. LR507, July 1968.

9. South, J. C.; Klunker, E. B.; Wagner, R. D.; and Chiang, C. W.: Flow-Field Calculation for Conical Wings and Bodies. Methods for Calculating Conical Flows. NASA Symposium on Analytical Methods in Aircraft Aerodynamics, Oct. 28-30, 1969.

10. Hamming, Richard W.: Numerical Methods for Scientists and Engineers. McGraw-Hill Book Co., Inc., 1962.

11. Chapkis, Robert L.: Hypersonic Flow Over an Elliptic Cone: Theory and Experiment. Calif. Inst. Tech., Guggenheim Aeron. Lab. Memo. 49, May 1959.

12. Gregory, T. J.; Wilcox, D. E.; and Williams, L. J.: The Effects of Propulsion Systems-Airframe Interactions on Performance of Hypersonic Aircraft. Preprint 67-493, AIAA, July 1967.

13. Kaattari, George E.: Empirical Method for Estimating Pressures on Elliptic Cones. NASA Symposium on Analytical Methods in Aircraft Aerodynamics, Oct. 28-30, 1969.

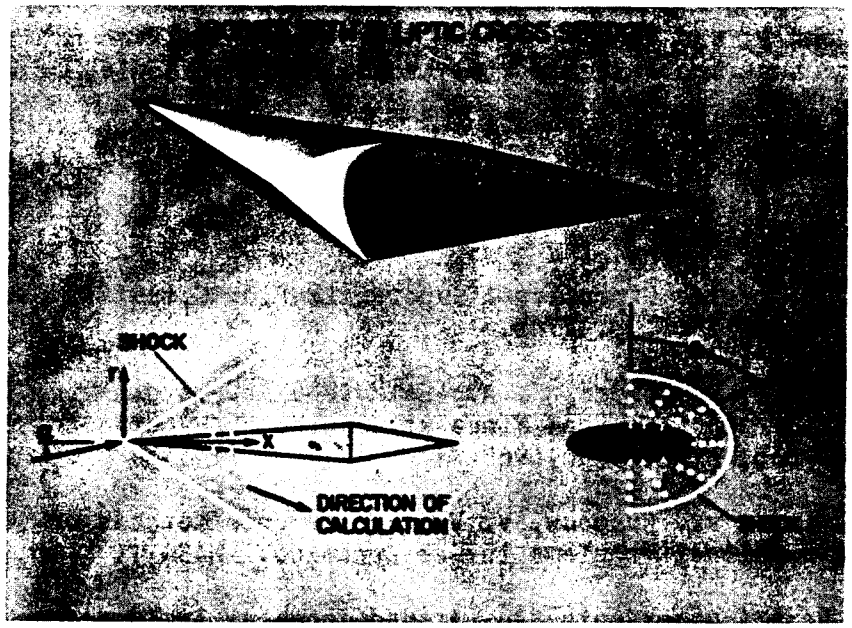

Figure 1

SURFACE BOUNDARY CONDITION

$$\tan\theta = \frac{\dfrac{\partial f}{\partial x} + \dfrac{\tan\phi}{r}\,\dfrac{\partial f}{\partial \Phi}\sqrt{1+\left(\dfrac{\partial f}{\partial x}\right)^2 - \left(\dfrac{\tan\phi}{r}\,\dfrac{\partial f}{\partial \Phi}\right)^2}}{1-\left(\dfrac{\tan\phi}{r}\,\dfrac{\partial f}{\partial \Phi}\right)^2}$$

$$\theta = \tan^{-1}\frac{v}{u} \qquad \phi = \tan^{-1}\frac{w}{\sqrt{u^2+v^2}}$$

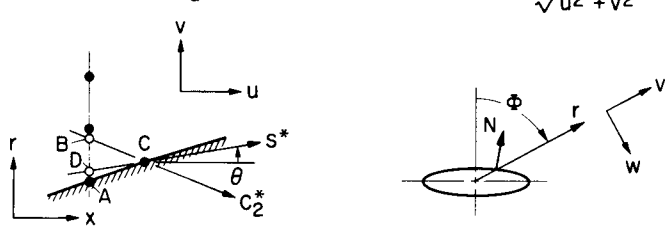

PLANE Φ = CONST

PLANE x = CONST

Figure 2

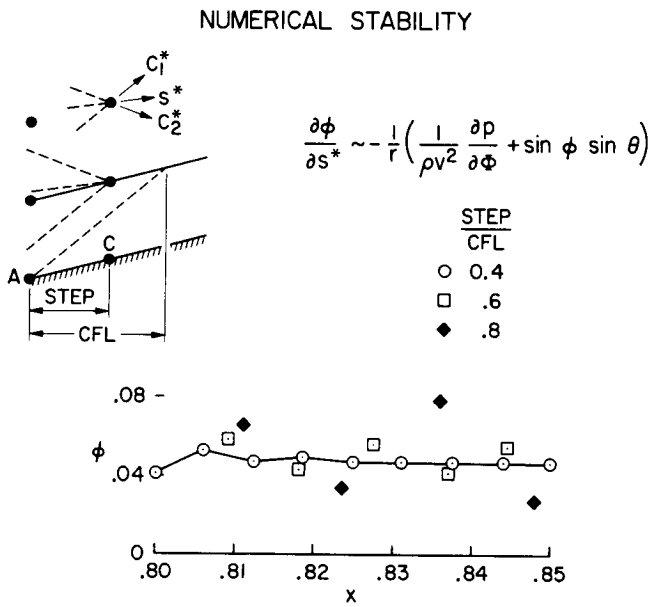

Figure 3

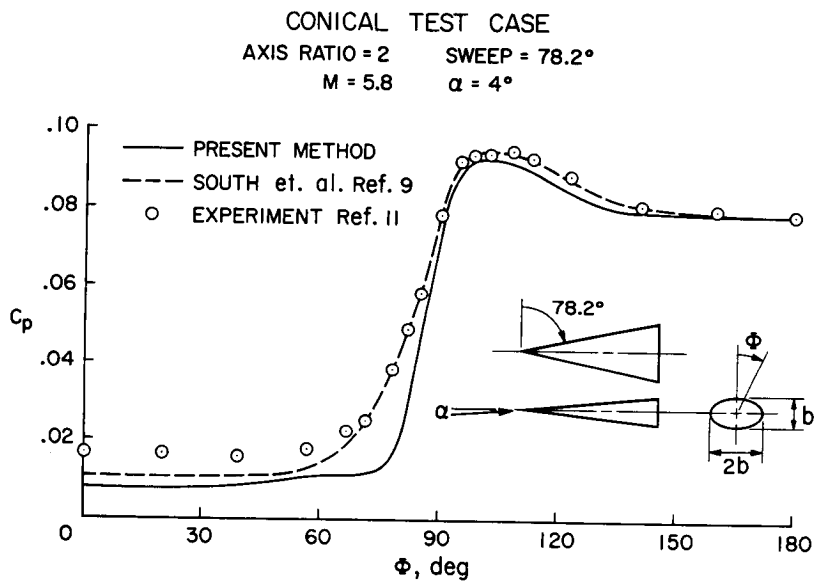

Figure 4

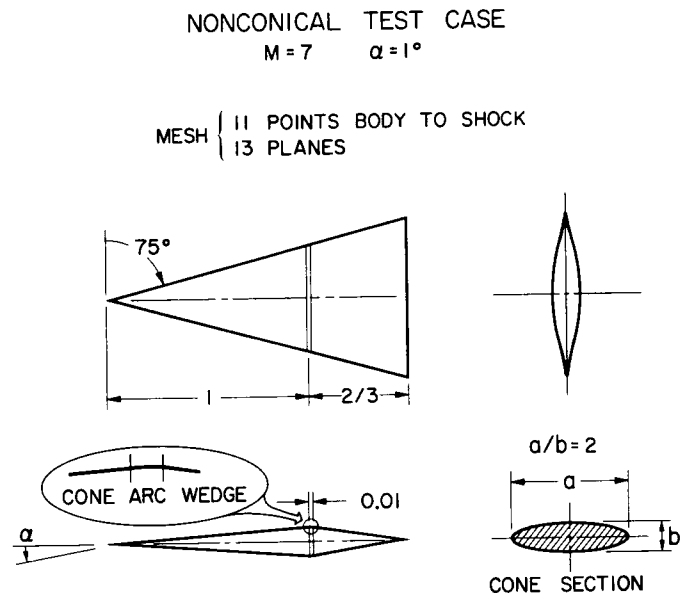

Figure 5

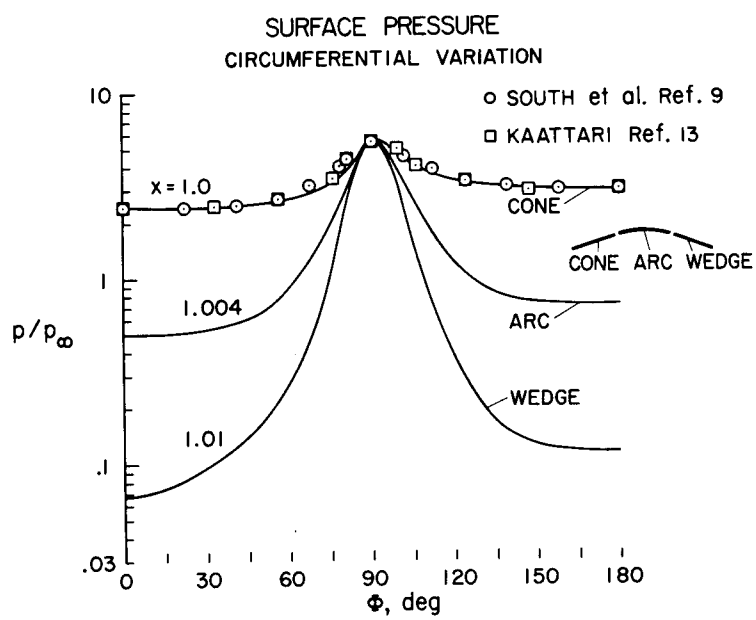

Figure 6

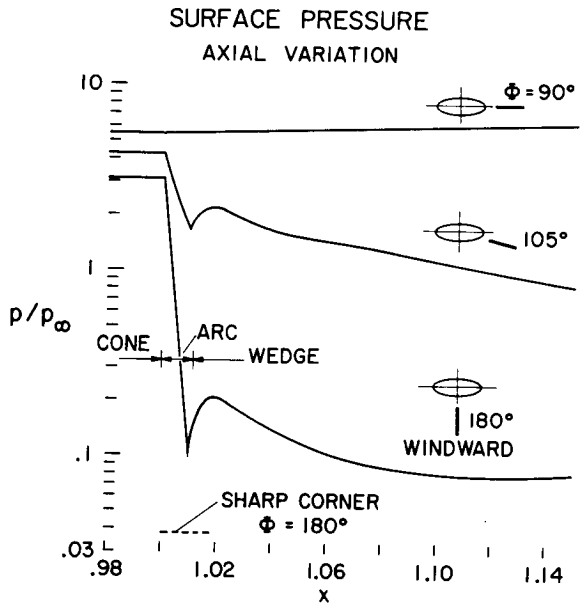

Figure 7

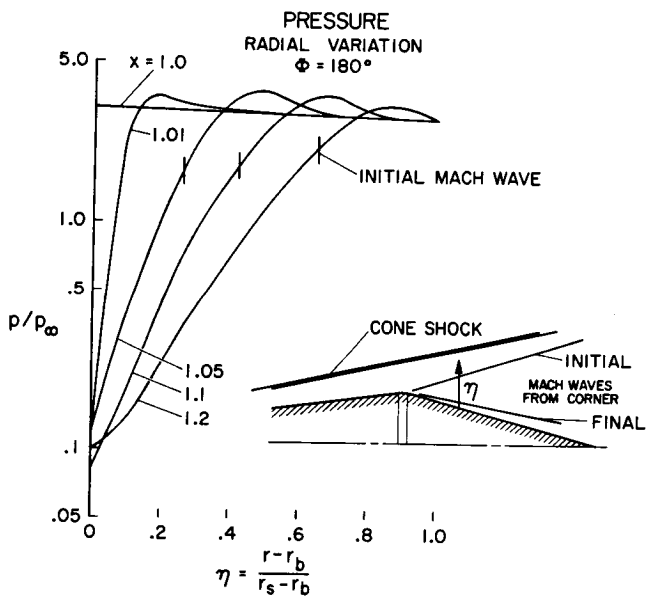

Figure 8

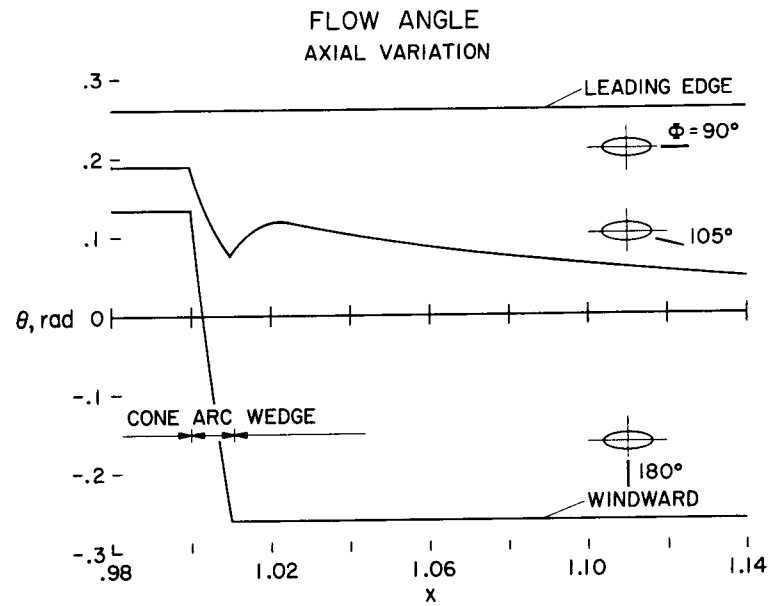

Figure 9

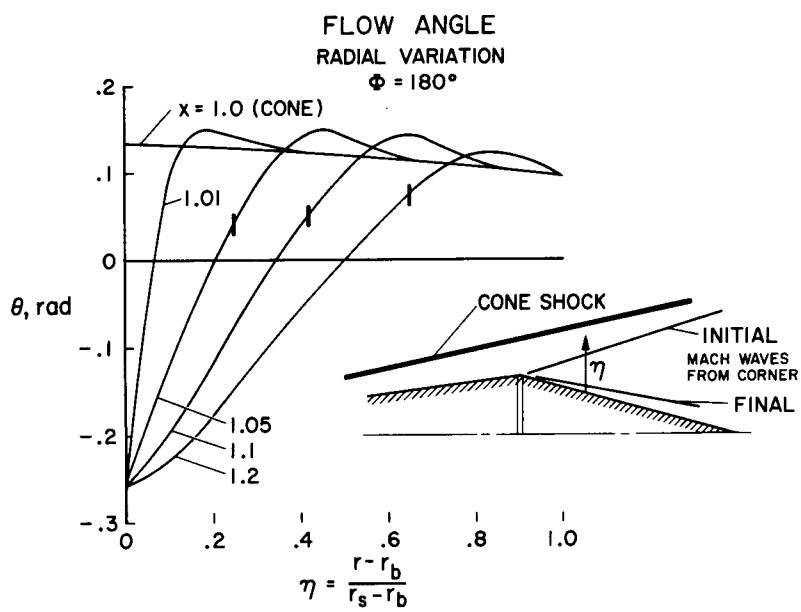

Figure 10

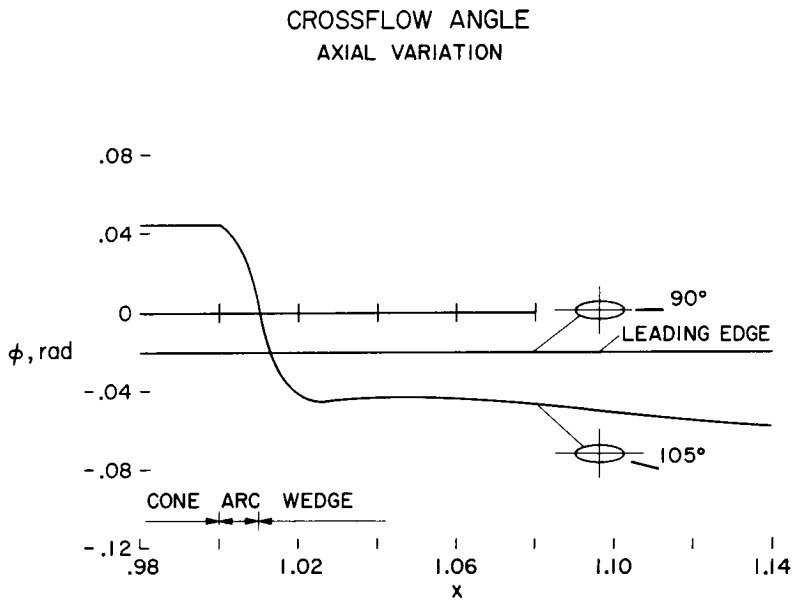

Figure 11

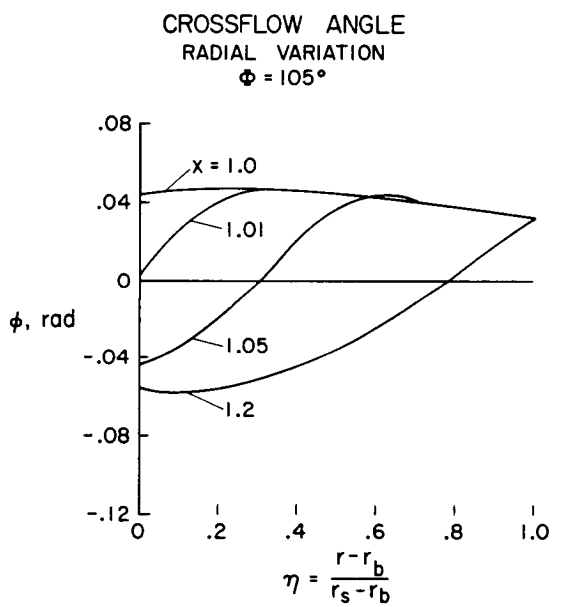

Figure 12

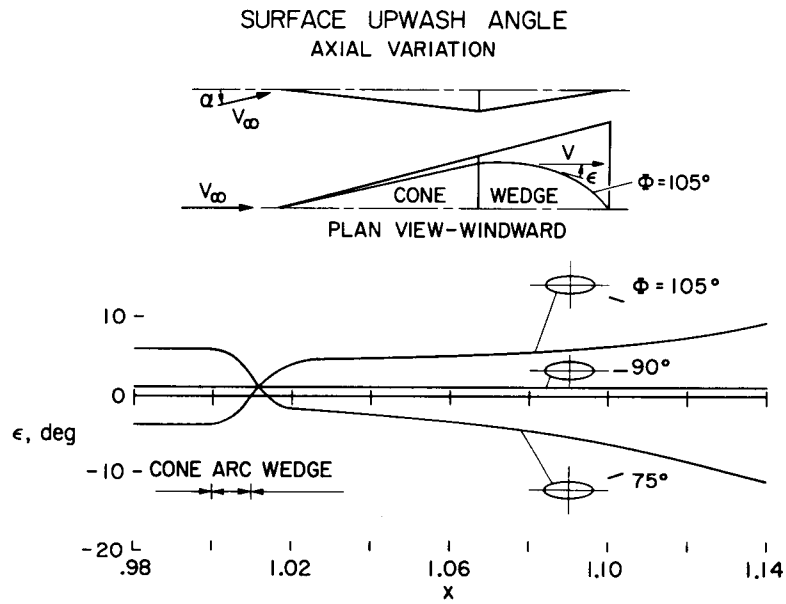
SURFACE UPWASH ANGLE
AXIAL VARIATION
α
V∞
V
ε
V∞
CONE
WEDGE
Φ=105°
PLAN VIEW-WINDWARD
Φ = 105°
10 -
-90°
0
ε, deg
-10 - CONE ARC WEDGE
75°
-20
.98
1.02
1.06
1.10
1.14
x

Figure 13

DISCUSSION

RAYMOND SEDNEY, Martin Company: I don't want to quibble at all with your excellent presentation, especially the part about the stability and the CFL condition, but I can't help but generalize from some experience in a completely different problem, and I just wonder if the fact that the CFL condition is violated so drastically might indicate it would be worthwhile to look into some more efficient grid scheme. Have you considered that at all?

RAKICH: Well, I'm not sure what you would mean by a more efficient grid scheme. I think a grid which employed body normal reference planes would probably be better from the stability criterion, because this is what we used before for bodies of revolution, and we didn't run into this type of instability problem. We tried to be general in using radial reference planes, and this coupled the crossflow angle and pressure too strongly and was really the cause of the instability. I don't know what other kind of a grid you might use, however.

GINO MORETTI, Polytechnic Institute of Brooklyn: Apropos of CFL rule, are you sure that the rule has been applied correctly in your work? If you work with finite differences instead of working with characteristics, then the elements which enter into the denominator of the expression which gives the allowed Δx depend essentially on crossflow values. It seems to me that you are using other velocity components, so probably you are using here a Δx which does not satisfy the CFL rule as it was originally written for multidimensional flow. I cannot make a precise comment, but I would like to put a question mark on the way you applied the CFL rule.

RAKICH: As I understand the rule, it just states that the domain of dependence of the difference equations must include that of the differential equations.

MORETTI: For the entire crossflow?

RAKICH: Yes, so it means you have to include points from reference planes at least beyond where the Mach lines would intersect the initial data surface.

MORETTI: I think that, on occasions, Δx may still be smaller than the one you use, and it may well depend on the grid.

So, no precise comment can be made, unless one provides a detailed analysis of the scheme which has been used.

RAKICH: Well, let me restate, then, what I said earlier. Can I have slide 3, please?

As I understand the CFL rule, it just says that we have to include points from our difference mesh just beyond the intersection of the actual Mach line with the initial data line. Of course, as you point out, this is just one plane, and the Mach lines we show here are the projections of the Mach cones

onto that reference plane. We imagine all the Mach cones lined up, and these make a Mach surface that crosses this reference plane.

Now, in the crossflow direction consider a similar projection of Mach cones onto the surface r = constant. All we have to do to satisfy the CFL condition is to use data from reference planes outside the intersection of these crossflow Mach lines with the initial data surface. Since the present Fourier method uses data from all the planes, $\Phi = 0$ to π, this has been satisfied.

MORETTI: How big is the speed in the crossflow? Is it supersonic?

RAKICH: In this case, no.

FRED R. DEJARNETTE, Virginia Polytechnic Institute: I believe you add some sort of smoothing function to your characteristics method, that is something like a second derivative term. Was that used in this characteristics program?

RAKICH: Yes, it was. This is not always used, but in certain cases it is. When the entropy layer on a blunted body is very thin, and also for conical flow, we find it helps out if we do employ that type of difference scheme for the streamwise calculation.

DEJARNETTE: I would like to add that possibly this has an effect on the stability criterion, because other people, using something like a Lax-Wendroff scheme, have found that they have to use something somewhat less than the CFL stability criterion in order to get stable solutions.

RAKICH: This is something that could be investigated, and I suppose I should.[1]

SIDNEY A. POWERS, Northrop Corp.: John, your slide 8 (fig. 11), where you show a crossflow angle of an axial variation, it looks a little bit strange. This angle ϕ is essentially the upwash angle, due normal to the leading edge. Is that correct? And yet you don't show any axial variation as you go downstream. Would you expect this crossflow angle or this upwash angle along the leading edge to change in this wedge region somewhat drastically actually, due to the influence of this fairly sharp corner up there?

RAKICH: No, I didn't expect a drastic change. We are talking about this line here on a 90° plane, right?

I didn't have any very strong feeling on whether it should or should not vary. It just turned out that it didn't. I guess it is because the pressure gradient is not changing much on the leading edge since the pressure is nearly a maximum there. If you recall slide 5 (fig. 6), the pressure was practically constant on that leading edge and dropped sharply to each side of the leading edge, but it was pretty much symmetrical.

---

[1]This question was studied after the conference and the smoothing function used does not affect the stability problem discussed in this paper.

TIME-DEPENDENT NUMERICAL METHOD FOR TREATING COMPLICATED BLUNT-BODY FLOW FIELDS

By Richard W. Barnwell

Langley Research Center

N70-21361

INTRODUCTION

Time-dependent methods have been used for several years to calculate numerical solutions for the flow fields about blunt bodies traveling at supersonic speeds in inviscid, compressible gases. The time-dependent method of characteristics has been used by Sauerwein (ref. 1) to treat this problem. However, time-dependent finite-difference methods provide a much more efficient means of making these calculations.

Several of the early finite-difference methods were based on the "artificial viscosity" technique, which treats shock waves as continuous compressions with steep gradients where the flow would otherwise be discontinuous. Artificial viscosity techniques of first-order accuracy in the mesh spacings have been developed by Bohachevsky and Rubin (ref. 2), Harlow (ref. 3), Gentry et al. (ref. 4), and others.

A finite-difference technique of second-order accuracy which treats embedded shock waves as continuous compressions has been developed by Lax and Wendroff (ref. 5). Burstein (ref. 6) and others have used this technique to solve the blunt-body problem.

Another approach to the blunt-body problem is to treat the bow shock wave as a discontinuity. Godunov et al. (ref. 7) have developed such a method which produces solutions of first-order accuracy. Masson et al. (ref. 8) have used this method to calculate flow fields about several complicated shapes. A method of second-order accuracy which treats the bow shock wave as a discontinuity has been developed by Moretti and Abbett (ref. 9).

The purpose of this paper is to describe a time-dependent numerical method similar to that of reference 9 which has been used to study some fairly complicated blunt-body flow fields. Examples of the types of complexities which have been treated are shown in figure 1. These complexities include embedded shock waves, sharp sonic corners on the body profile, and nonuniform free-stream properties upstream of the bow shock wave. All the results which are presented in this paper are for axisymmetric bodies at zero angle of attack. However, it should be noted that the techniques presented herein can be applied to more complicated flow fields.

SYMBOLS

$A_i, B_i, C_i, D_i, \tilde{A}_i, \overline{C}_i$	functions of flow properties, $i = 1, 2, 3, 4$
a	speed of sound
H	total enthalpy
M	Mach number
p	pressure
p_t	stagnation pressure
r	perpendicular distance from axis of symmetry
r_b	base radius
r_c	corner radius
r_n	nose radius
s	distance along surface from axis
s_c	distance along surface from axis to corner
t	time
t_o	initial time
t_1	specific time
u,v	velocity components normal to and tangent to body normal, respectively
V	magnitude of velocity
$\vec{V}$	velocity vector
X	distance along reference line from axis

X^*_{min}, X^*_{max} smallest and largest values of X associated with corner

Y nondimensional distance along body normal

y_b distance from body surface to reference line

α constant appearing in equation (4)

γ ratio of specific heats

δ distance from body to shock along body normal

ϵ percent deviation of free-stream velocity at distance $r = r_b$ from axis from center-line value

ρ density

ϕ angle between body normal and free-stream direction

Subscripts:

av average

℄ center line

I,II first and second bicharacteristics

∞ free stream

METHOD

In general, all time-dependent methods treat the blunt-body problem as an initial-value problem. This approach is possible because the governing equations for time-dependent flow, which are written as

$$\left.\begin{aligned} &\frac{\partial \rho}{\partial t} + \vec{\nabla} \cdot \left(\rho \vec{V}\right) = 0 \\ &\frac{\partial \vec{V}}{\partial t} + \left(\vec{V} \cdot \vec{\nabla}\right)\vec{V} + \frac{1}{\rho}\vec{\nabla} p = 0 \\ &\frac{\partial H}{\partial t} + \vec{V} \cdot \vec{\nabla} H - \frac{1}{\rho}\frac{\partial p}{\partial t} = 0 \end{aligned}\right\} \tag{1}$$

are hyperbolic everywhere in the flow field. The quantities ρ, $\vec{V}$, p, and H in equations (1) are the density, velocity vector, pressure, and total enthalpy, respectively. It should be noted that for steady flow, the governing equations are hyperbolic only where the flow is supersonic. Where the flow is subsonic, the governing equations are elliptic.

In general, the region of computation in the physical plane must enclose all of the region of subsonic flow. This requirement is necessary for the calculations to be stable, and it means that the sonic line must lie inside the downstream boundary of the region of computation. The upstream boundary of the region must lie on or beyond the bow shock wave. For axisymmetric flow fields, the region of computation can be terminated at the axis of symmetry.

Solutions for steady flow are obtained with time-dependent methods in the following manner. First, an approximate initial solution is assumed at $t = t_o$ in order to start the calculation. Next, the time-dependent equations are integrated from $t = t_o$ to $t = t_o + \Delta t$ in order to get the solution at $t = t_o + \Delta t$ for all the points in the region of computation. The time-dependent method of characteristics or one of several finite-difference methods can be used to integrate the time-dependent equations. This integration process is repeated to get the solutions at $t = t_o + 2\Delta t$, $t_o + 3\Delta t$, ... At each time interval, the solution just obtained is treated as the initial solution and the integration process is repeated to get the new solution. Steady results are obtained when the solutions at successive time intervals have converged sufficiently. Thus a solution is obtained for the steady blunt-body problem, which is a boundary-value problem with mixed governing equations, by treating a related initial-value problem, the unsteady blunt-body problem, with hyperbolic governing equations.

The region of computation and the coordinate system which are used in the present method are shown in figure 2. Due to the symmetry of the flow field, the lower boundary of the region of computation is located at the axis. The left boundary is located at the bow shock and moves with it as it adjusts to its steady position. The Y coordinate, which is measured along normals to the body surface, has values of 1 at the shock and 0 at the surface. The X coordinate is measured along a reference line which is located at a constant distance y_b from the body surface. This choice of the line along which X is measured provides a convenient means for rotating the coordinate system about sharp corners. The quantity δ is the distance from the body to the shock along the local body normal. The velocity components u and v are normal to and tangent to the body normal, respectively.

The present method is similar to that of reference 9 in that the bow shock wave is treated as a discontinuity, the time-dependent method of characteristics is used at the shock wave and body surface, and a time-dependent Lax-Wendroff finite-difference method is used between the shock and body. However, in the present treatment the characteristic compatibility relations are integrated along bicharacteristics rather than along

one-dimensional characteristics as in reference 9. Also, the governing equations for the finite-difference calculations are used in conservation form in this treatment, whereas in reference 9 they are used in expanded form.

When the governing equations are written in conservation form, the coefficients of the partial derivatives are not functions of the dependent variables. The equations of the present method are written as

$$\frac{\partial A_i}{\partial t} + \frac{\partial B_i}{\partial X} + \frac{1}{\delta}\frac{\partial C_i}{\partial Y} + D_i = 0 \qquad (i = 1, 2, 3, 4) \qquad (2)$$

where δ is a function of the independent variables X and t and the quantities A_i, B_i, C_i, and D_i are functions of the independent variables X, Y, and t and the dependent variables p, ρ, u, and v.

The present treatment employs an explicit two-step finite-difference method. The first step leads to a preliminary solution of first-order accuracy, and the second step provides a corrected solution of second-order accuracy. The equations for the preliminary and the corrected solutions are written as

$$\left(\tilde{A}_i\right)_{X,Y}^{t+\Delta t} = \left(A_i\right)_{av}^{t} + \Delta t\left(\frac{\partial A_i}{\partial t}\right)_{X,Y}^{t} \qquad (i = 1, 2, 3, 4) \qquad (3)$$

and

$$\left(A_i\right)_{X,Y}^{t+\Delta t} = \left(A_i\right)_{X,Y}^{t} + \frac{\Delta t}{2}\left[\left(\frac{\partial A_i}{\partial t}\right)_{X,Y}^{t} + \left(\frac{\partial \tilde{A}_i}{\partial t}\right)_{X,Y}^{t+\Delta t}\right] + \alpha\left[(\Delta X)^4\left(\frac{\partial^4 A_i}{\partial X^4}\right)_{X,Y}^{t} + (\Delta Y)^4\left(\frac{\partial^4 A_i}{\partial Y^4}\right)_{X,Y}^{t}\right]$$

$$(i = 1, 2, 3, 4) \qquad (4)$$

respectively. Numerical values for the partial derivatives $\partial A_i/\partial t$ and $\partial \tilde{A}_i/\partial t$ in equations (3) and (4) are determined from the finite-difference equations which are analogous to equations (2). These finite-difference equations are obtained by replacing the partial derivatives with respect to X and Y in equations (2) with central—finite-difference expressions. The quantities $\left(A_i\right)_{av}^{t}$ in equations (3) are the averages of the values of the quantities A_i at the points $(X + \Delta X,Y)$, $(X - \Delta X,Y)$, $(X,Y + \Delta Y)$, and $(X,Y - \Delta Y)$ at time t. The fourth-order terms in equations (4) are added to insure stability. A value of $\alpha = 1/32$ was used to determine the present results.

There are two advantages associated with the use of the conservation form of the governing equations. First, the use of this form permits stable calculations of flow fields containing embedded shock waves with no further consideration being given to the presence of these shocks. These embedded waves are represented by continuous compressions which extend over several mesh spacings. The flow-property profiles across these

compressions have steep gradients where the discontinuity would otherwise be. Second, the use of the conservation form results in improved solutions at grid points near a sharp corner where the flow is singular. Let X^*_{min} and X^*_{max} be the values of X associated with the normals to the upstream and downstream surfaces at the corner, respectively, as shown in figure 2. The second advantage is realized because the quantities C_i in equations (2) are proportional to Y for $X^*_{min} \leqq X \leqq X^*_{max}$ and can be written as

$$C_i = \overline{C}_i Y \qquad (i = 1, 2, 3, 4)$$

where the quantities $\overline{C}_i$ are functions of the dependent and independent variables. Therefore, the partial derivatives $\partial C_i/\partial Y$ are well-behaved near the corner, although the individual flow properties and the quantities $\overline{C}_i$ are singular there. It has been found that the quantities B_i are well-behaved near the corner and that the only complication which arises during the computation of the partial derivatives $\partial B_i/\partial X$ occurs for values of X where the curvature of the reference line changes discontinuously.

As stated previously, the time-dependent method of characteristics is used to determine the flow properties at grid points on the body surface. In general, three characteristic compatibility relations are used at each body point. The procedure which is used at a sharp corner is somewhat different. It should be noted that the present coordinate system maps the point at the corner onto the line $Y = 0$ and $X^*_{min} \leqq X \leqq X^*_{max}$. If the flow upstream of the corner is supersonic, the standard procedure is used for the point $Y = 0$ and $X = X^*_{min}$, but if the flow upstream of the corner is subsonic, the solution at this point is obtained by solving two characteristic compatibility relations and the condition $M = 1$ simultaneously. It has been found that the flow properties at the grid locations $Y = 0$ and $X^*_{min} < X \leqq X^*_{max}$ can be related to those at the point $Y = 0$ and $X = X^*_{min}$ by the transient analog to the Prandtl-Meyer solution.

Let s be the distance along the surface from the axis, and let $s = s_c$ at the sharp corner. The two compatability relations which are used to determine the sonic solution at the grid location $Y = 0$ and $X = X^*_{min}$ at some time $t = t_1$ are integrated along bicharacteristics which lie in the s-t surface. This surface is shown in figure 3. There are two alternate procedures which can be used. The first is to integrate the compatibility relations

$$\left(\frac{dp}{dt}\right)_I + \rho a\left(\frac{du}{dt}\right)_I = -\rho a^2\left(\frac{1}{\delta}\frac{\partial V}{\partial Y} + \frac{u}{r}\cos\phi\right) \tag{5}$$

and

$$\left(\frac{dp}{dt}\right)_{II} - a^2\left(\frac{d\rho}{dt}\right)_{II} = 0 \tag{6}$$

along the bicharacteristic with slope

$$\left(\frac{ds}{dt}\right)_I = u + a \tag{7}$$

and the bicharacteristic with slope

$$\left(\frac{ds}{dt}\right)_{II} = u \tag{8}$$

respectively. The quantity a in equations (5), (6), and (7) is the speed of sound, and the quantities r and ϕ in equation (5) are the perpendicular distance from the axis and the angle between the body normal and the free-stream direction, respectively. The second procedure consists of integrating equation (6) and the transient Bernoulli equation

$$\left(\frac{dH}{dt}\right)_{II} - \frac{1}{\rho}\frac{\partial p}{\partial t} = 0$$

along the bicharacteristic with the slope defined in equation (8). It has been found that results obtained with the two procedures are essentially the same.

RESULTS AND DISCUSSION

The present results for the flow past a flat-face cylinder for a ratio of specific heats of 1.4 and a free-stream Mach number of 2.81 are compared with the experimental results of Kendall (ref. 10) in figure 4. Kendall's results are shown as solid lines in the figure and the present results are shown as circles. The shock-wave and sonic-line shapes are shown on the left. The open circles are the present results for the shock-wave location, and the solid circles are the results for the sonic-line location. The pressure distribution is given at the right.

It should be noted that the grid used is fairly coarse. There are four grid spaces across the shock layer and nine along the shock (five of these subtend the face and four subtend the corner).

In figure 5, results are presented for the effect of nonuniform flow on the shock-wave and sonic-line shapes for a 60° blunted cone with a ratio of nose radius to base radius of 0.25. The ratio of specific heats is 1.4 and the free-stream Mach number at the center line is 10. The nonuniformity of the flow consists of a parabolic dependence of the free-stream velocity on the distance from the axis. The quantity ϵ is the percent deviation of the velocity at a distance $r = r_b$ from the axis from the center-line value. The free-stream pressure and total enthalpy are constant. This type of nonuniformity may be similar to the disturbed flow in some wind tunnels with strong viscous effects at the walls.

It is seen in figure 5 that the nonuniformity has a marked influence on the shock-wave and sonic-line shapes. The general trend is for the shock wave to move closer to the body in the stagnation region and farther from the body in the transonic and supersonic regions as ϵ is increased. The sonic point at the shock moves outward away from the axis as ϵ is increased. The present results indicate that the sonic point is positioned at the corner for $\epsilon = 0$ and 0.01 but that it is located upstream of the corner on the cone surface for $\epsilon = 0.03$. This displacement of the sonic point will be discussed subsequently.

The effect of this nonuniform flow on the pressure distribution for the 60° cone is shown in figure 6. The pressure p is nondimensionalized with the center-line value of $\rho_{\infty}V_{\infty}^{2}$, and it is plotted as a function of the distance from the axis along the surface.

It can be seen that for $\epsilon = 0.01$, the pressure in the vicinity of the corner is reduced by about 20 percent, and for $\epsilon = 0.03$, the pressure near the corner is reduced by about 50 percent. It should be noted that these severe pressure reductions are accompanied by equally severe reductions in the free-stream Mach number. At a distance $r = r_b$ from the axis the free-stream Mach number for $\epsilon = 0.01$ is reduced 16 percent from 10 to 8.4, and for $\epsilon = 0.03$, it is reduced 34 percent to 6.6.

It can be seen that the present results are irregular in the region just upstream of the corner. It has been found that this irregularity decreases as the grid is refined. This irregularity may exist because an average value of the curvature of the reference line is used at points where this quantity changes discontinuously.

The calculations for $\epsilon = 0.01$ are compared with the results of the method of integral relations of South in figure 6. It should be noted that these results have not been published previously. The basic method which South used is given in reference 11. The close agreement of the present results and those of the method of integral relations is encouraging in the absence of experimental data on the subject.

The Newtonian pressure distributions are also presented in figure 6. The standard Newtonian equation was used, but the radial dependence of the quantity $\rho_{\infty}V_{\infty}^{2}$ was included. For $\epsilon = 0$ and $\epsilon = 0.01$, the flow remains subsonic all along the face, and the present results differ from the Newtonian results as expected. As stated previously, the present results indicate that the sonic point is located on the cone surface upstream of the corner for $\epsilon = 0.03$. The present results for the pressure for $\epsilon = 0.03$ differ from the Newtonian results in the region where the flow is subsonic. However, in the region between the sonic point and the corner, the results of the two methods are in close agreement.

In general, there is a reluctance to accept solutions which indicate that the sonic point on the surface of a body in a symmetric inviscid flow field is located on a straight

segment of the surface. In fact, Shifrin (ref. 12) has proved that for symmetric, non-isentropic, inviscid plane flow such a solution cannot exist. However, it should be noted that this proof does not apply directly to the present cases for axisymmetric flow.

It is possible that the truncation error of the present method is responsible for the displacement of the sonic point upstream of the corner for $\epsilon = 0.03$ since this error is viscouslike in nature. However, it is also possible that the present results represent the inviscid flow correctly and that the displacement occurs because the dynamic pressure at points off the axis for $\epsilon = 0.03$ becomes too small to support subsonic flow at the surface all the way to the corner.

In figure 7 results are presented for the effect of Mach number on the shock-wave and sonic-line shapes for a 45° truncated cone with rounded corners. The cone is followed by a cylindrical afterbody.

At a Mach number of 2.8, the flow in the nose region is independent of the flow on the conical portion of the body since the sonic line at the first shoulder extends all the way from the body to the bow shock. The flow expands around the first shoulder and becomes supersonic. It then compresses on the conical portion of the body and becomes subsonic. At the second shoulder, it again expands to the supersonic state.

The regions of subsonic flow are connected for a Mach number of 2.6. However, a bubble of supersonic flow remains at the first shoulder. For a free-stream Mach number of 2.4, the subsonic zone in the vicinity of the conical portion of the body enlarges so that it extends all the way to the bow shock wave. There are two isolated regions of supersonic flow at this Mach number: one at the first shoulder and one at the shock wave.

For a Mach number of 2, the flow field upstream of the second shoulder is subsonic with the exception of the supersonic bubble at the first shoulder. At this Mach number, the entire subsonic region is affected by the presence of the conical surface.

The compression which occurs over the conical portion of the body starts as a continuous compression at the first shoulder. For higher Mach numbers, the compression fan probably merges to become a weak embedded shock wave which intersects the bow shock wave near the first inflection point. Experimental data (refs. 10 and 13) indicate that these embedded shock waves do form. On the basis of the present results, it cannot be determined whether or not this effect occurs since the present method smears embedded shock waves so that weak shocks cannot be distinguished from continuous compressions. It is clear that the continuous compression extends all the way to the bow shock wave for $M_{\infty} = 2$ because the flow is subsonic throughout the compression region.

Results which show the effect of Mach number on the pressure distributions for the truncated cone are presented in figure 8. The free-stream Mach numbers which are

treated include the four treated in figure 7 and infinity. The pressure is nondimensionalized with its stagnation-point value and is plotted as a function of distance along the surface from the axis.

It is seen in the figure that the results correlate quite well on the face and on the upstream portion of the first shoulder. On the rearward part of the shoulder, a Mach number effect appears which becomes very pronounced on the conical portion of the body. This effect is monotonic with the higher nondimensional pressures corresponding to the lower Mach numbers. Note that the curves representing the results for the lower Mach numbers converge as the second shoulder is approached. The curves between the junction of the first shoulder and the cone and the first point on the cone where calculations are made are dashed because the present results do not indicate what is happening there. Mach number effects are observed on the downstream portion of the second shoulder and the cylindrical afterbody, but they are small.

Some further applications of the present method are shown in figure 9. One of the problems to be treated is concerned with the blunt body at angle of attack. The bodies under consideration include those with sharp sonic corners since a means has been found to compute the cross flow at these corners. In principle, blunt bodies with no symmetry at all can be treated.

The second application involves the calculation of flow about delta wings with the shock attached only at the tip. It is hoped that the present techniques for treating sharp corners on blunt bodies can be extended to treat the flow at the sharp leading edges of these wings. It should be noted that for the cases of interest, the flow over these wings is always supersonic. Therefore, the governing equations for steady flow are hyperbolic everywhere in the flow field, and results for steady flow can be calculated directly using the distance from the tip rather than time as the marching variable. This procedure has been used by Moretti (ref. 14), Babenko et al. (ref. 15), and others to calculate supersonic flow past pointed bodies.

REFERENCES

1. Sauerwein, Harry: A General Numerical Method of Characteristics. AIAA Paper No. 65-25, Jan. 1965.

2. Bohachevsky, Ihor O.; and Rubin, Ephraim L.: A Direct Method for Computation of Nonequilibrium Flows With Detached Shock Waves. AIAA J., vol. 4, no. 4, Apr. 1966, pp. 600-607.

3. Harlow, Francis H.: The Particle-in-Cell Method for Numerical Solution of Problems in Fluid Dynamics. Vol. XV of Proceedings of Symposia in Applied Mathematics, Amer. Math. Soc., 1963, pp. 269-288.

4. Gentry, Richard A.; Martin, Robert E.; and Daly, Bart J.: An Eulerian Differencing Method for Unsteady Compressible Flow Problems. J. Comput. Phys., vol. 1, no. 1, Aug. 1966, pp. 87-118.

5. Lax, Peter D.; and Wendroff, Burton: Difference Schemes for Hyperbolic Equations With High Order of Accuracy. Commun. Pure Appl. Math., vol. XVII, no. 3, Aug. 1964, pp. 381-398.

6. Burstein, Samuel Z.: Finite-Difference Calculations for Hydrodynamic Flows Containing Discontinuities. J. Comput. Phys., vol. 1, no. 2, Nov. 1966, pp. 198-222.

7. Godunov, S. K.; Prokopov, G. P.; and Zabrodin, A. V.: A Difference Scheme for Two-Dimensional Non-Steady Problems of Gas Dynamics and Calculation of Stream Flow With a Detached Shock Wave. UCRL-Trans-1060/L/, Lawrence Radiat. Lab., Univ. of California, Mar. 26, 1965.

8. Masson, B. S.; Taylor, T. D.; and Foster, R. M.: Application of Godunov's Method to Blunt-Body Calculations. AIAA J., vol. 7, no. 4, Apr. 1969, pp. 694-698.

9. Moretti, Gino; and Abbett, Michael: A Time-Dependent Computational Method for Blunt Body Flows. AIAA J., vol. 4, no. 12, Dec. 1966, pp. 2136-2141.

10. Kendall, James M., Jr.: Experiments on Supersonic Blunt-Body Flows. Progr. Rep. No. 20-372 (Contract No. DA-04-495-Ord 18), Jet Propulsion Lab., California Inst. Technol., Feb. 27, 1959.

11. South, Jerry C., Jr.: Calculation of Axisymmetric Supersonic Flow Past Blunt Bodies With Sonic Corners, Including a Program Description and Listing. NASA TN D-4563, 1968.

12. Shifrin, E. G.: The Direct Problem of Plane Symmetrical Flow With Detached Shock Wave About a Smooth Convex Profile. Sov. Phys. – Doklady, vol. 12, no. 1, July 1967, pp. 4-6.

13. Hastings, S. M.; Persh, J.; and Redman, E. J.: Experimental Investigation of the Pressure Distribution on Axi-Symmetric Flat-Face Cone-Type Bodies at Supersonic and Hypersonic Speeds. NAVORD Rep. 5659, U.S. Navy, Oct. 1, 1957.

14. Moretti, Gino: Inviscid Flowfield About a Pointed Cone at an Angle of Attack. AIAA J., vol. 5, no. 4, Apr. 1967, pp. 789-791.

15. Babenko, K. I.; Voskresenskiy, G. P.; Lyubimov, A. N.; and Rusanov, V. V.: Three-Dimensional Flow of Ideal Gas Past Smooth Bodies. NASA TT F-380, 1966.

BLUNT-BODY FLOW-FIELD STUDY

TYPES OF COMPLICATIONS TREATED

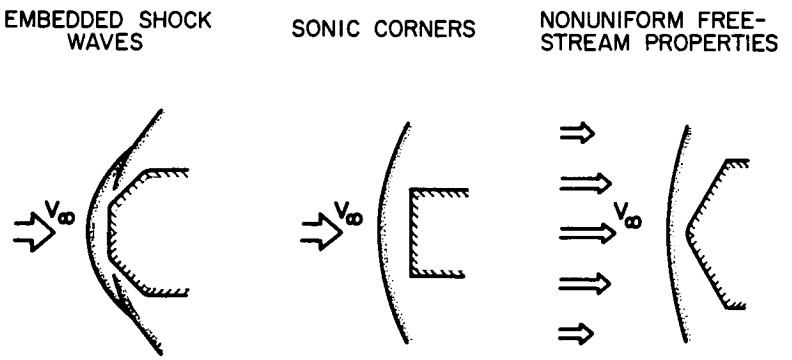

Figure 1

REGION OF COMPUTATION AND COORDINATE SYSTEM

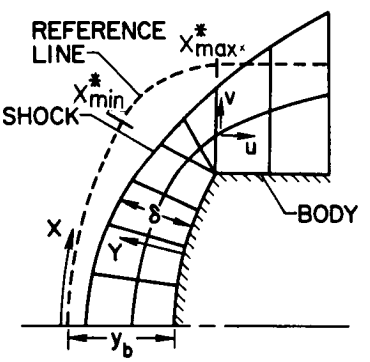

Figure 2

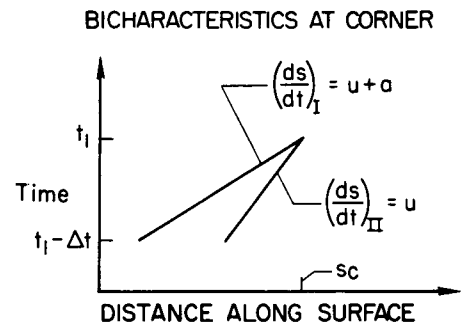

Figure 3

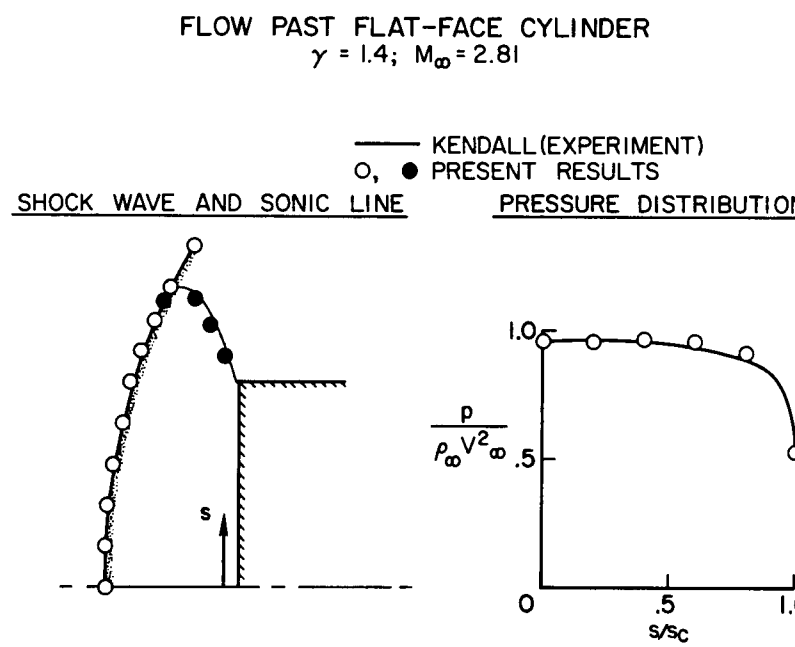

Figure 4

EFFECT OF NONUNIFORM FLOW ON SHOCK-WAVE AND SONIC-LINE SHAPES FOR BLUNTED CONE

$\gamma = 1.4;\ (M_\infty)_{℄} = 10$

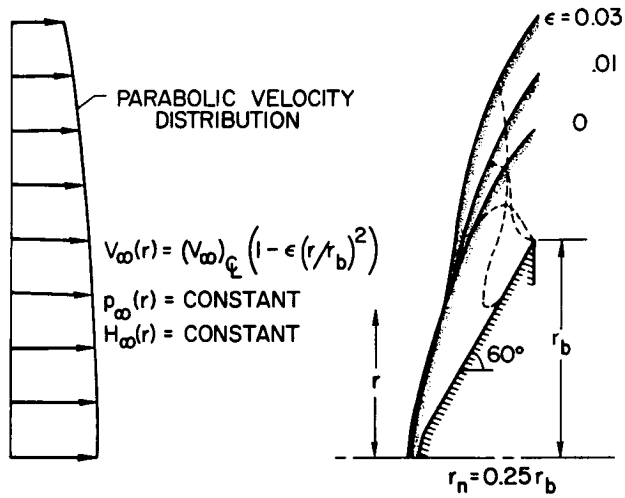

Figure 5

EFFECT OF NONUNIFORM FLOW ON PRESSURE DISTRIBUTION FOR BLUNTED CONE

$\gamma = 1.4;\ (M_\infty)_{℄} = 10$

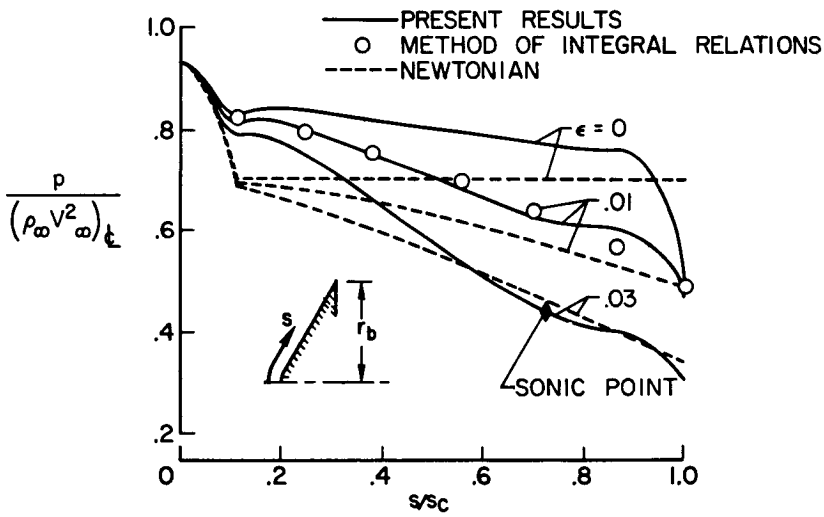

Figure 6

EFFECT OF MACH NUMBER ON SHOCK-WAVE AND SONIC-LINE SHAPES FOR TRUNCATED CONE

$\gamma = 1.4$

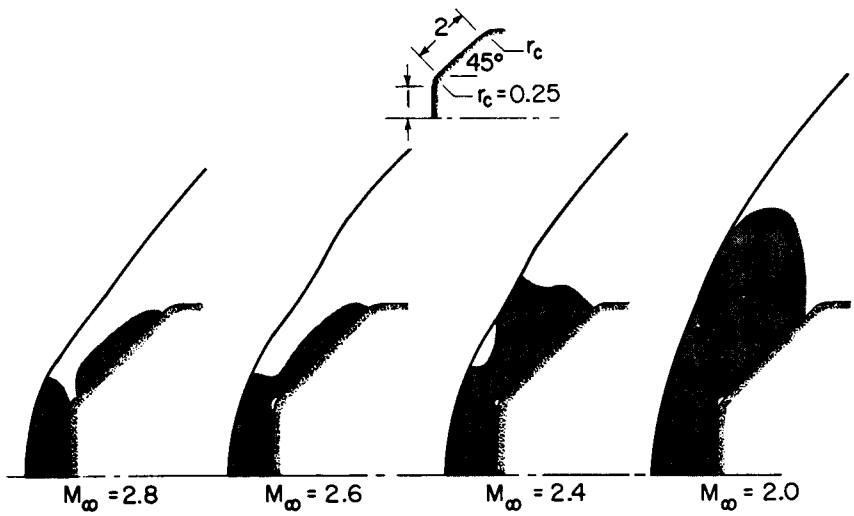

Figure 7

EFFECT OF MACH NUMBER ON PRESSURE DISTRIBUTION FOR TRUNCATED CONE

$\gamma = 1.4$

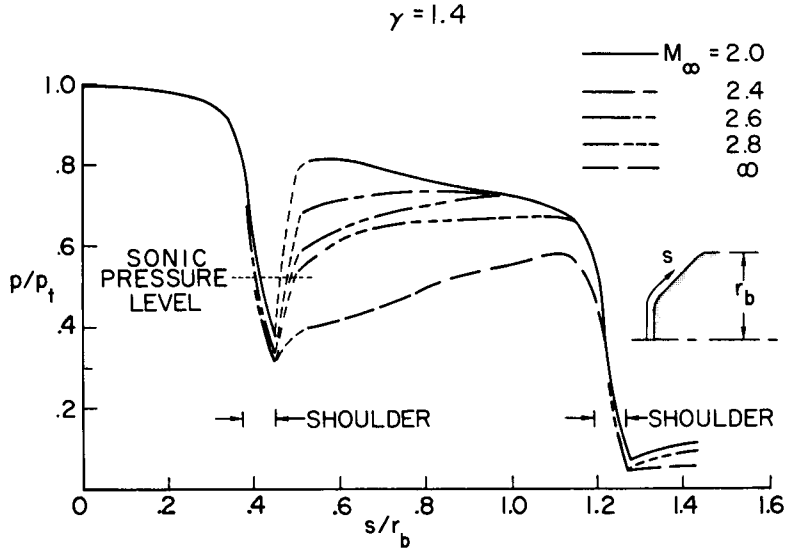

Figure 8

FUTURE EXTENSIONS

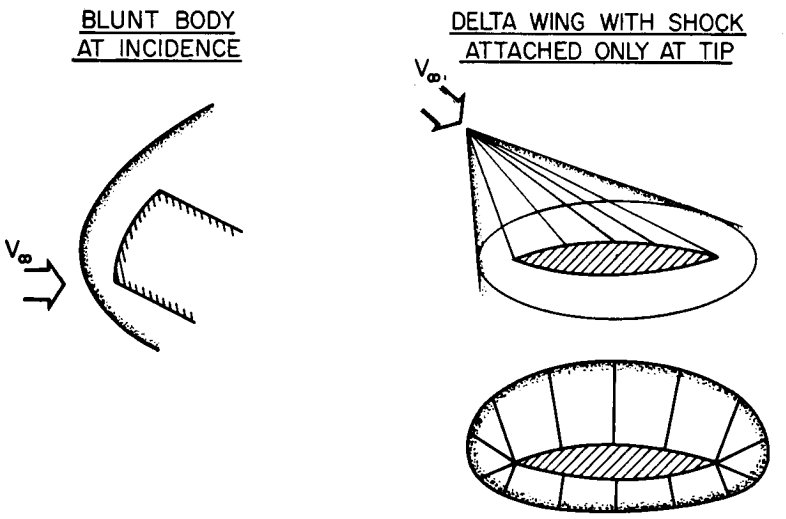

Figure 9

DISCUSSION

FERNANDO L. FERNANDEZ, The Aerospace Corp.: I had a question, just out of curiosity. You didn't show many results for high Mach number, free-stream flow. Is there any difficulty that might occur with these methods as one gets to high Mach numbers?

BARNWELL: The answer is no, there are no difficulties. In general, the results presented are for Mach numbers of interest in airplane work.

LEONARD WALITT, Applied Theory, Inc.: This, I assume, is an explicit method. Do you have any stability criterion you have to satisfy when you integrate your finite difference equations?

BARNWELL: Yes, I do. The stability criterion used is the von Neumann condition. A linearized stability analysis would tell you that the time step is 0.707 times that determined from the CFL condition. Our time step is a little bit smaller to be safe.

WALITT: Because of this, how close can you put your zones to define imbedded shock surfaces?

BARNWELL: I don't understand.

WALITT: Well, in the area of imbedded shock waves you would have to have zones pretty close together. You indicated the flow field was smeared over a shock.

BARNWELL: Yes, the imbedded shock is smeared. At the bow shock waves, I use the method of characteristics so there is no smearing there.

WALITT: I just have one other comment. Do you really believe that methods like this are practical for viscous three-dimensional, time-dependent flows? You indicated in your last slide that you did. I have to disagree with you.

BARNWELL: I would use techniques like this to calculate the subsonic region.

WALITT: I think you may have to develop a new kind of computer for calculating viscous, time-dependent flow fields in three spatial dimensions.

BARNWELL: Well, I don't agree.

GINO MORETTI, Polytechnic Institute of Brooklyn: I am not answering you, of course, but Dr. Walitt. I would like to mention a blunt-body time-dependent program which I did about 3 years ago for Sandia Corporation, and which has been used since then by Sandia and a large number of other industries. Nobody has complained that they need to buy a new computer. The ones who use the CDC-6600 can perform the computation in 6 minutes.

Now, since I have the microphone let me tell you that I like your presentation, but I do not believe that the equations which you used take care of imbedded shocks.

ROBERT CHARLES GUNNESS, JR., Boeing Company: I understand that some of the Lax-Wendroff type methods experience difficulties when the sonic line is crossed. Was this a problem?

BARNWELL: Yes, I did have trouble with stability. My problem did not arise at the sonic line but rather at the stagnation streamline. At both places the eigenvalues of the amplification matrix go to zero and neutral stability can occur. I had to put in a fourth order damping term to insure stability in the vicinity of the stagnation streamline.

GUNNESS: Will this appear in the paper?

BARNWELL: Yes.

EARLL MURMAN, Boeing Scientific Research Laboratories: Could you explain again why you chose the time-dependent method of characteristics for handling the boundary condition at the body, and do you think it is better than other methods for handling the boundary condition? I haven't seen the method before.

BARNWELL: I used it because it worked. Dr. Moretti has used this procedure before and has published several papers in which it is used.

MURMAN: Did Moretti use it for a solid body or did he just use it for shock waves?

BARNWELL: No, he used it at the body surface also.

One difference in his technique and mine is that he uses a one-dimensional characteristic and I use a bicharacteristic for the line along which the compatibility relation is integrated.

MORETTI: Yes, and no. In 4 years I changed my mind many times. However, as a general rule, if the numerical scheme reflects the physical nature of the problem, then it is bound to work.

AN ANALYSIS OF COANDA JET FLOWS

By M. H. Y. Wei
Air Vehicle Corporation

and

Victor R. Corsiglia
Ames Research Center

N70-21362

SUMMARY

This work concerns the second-order theory of a static laminar Coanda jet flow around a circular cylinder with external flow entrainment. It is assumed that the jet is very thin in comparison with the cylinder radius; hence the matched asymptotic theory for high Reynolds number proposed by Van Dyke is used. Accordingly, the second-order theory is being formulated including the effects due to curvature and entrainment. The objective of this research is to predict the laminar separation point. Preliminary results indicate that the curvature and entrainment effects tend to promote separation.

INTRODUCTION

It is well-known that jets, particularly two-dimensional jets, show a strong tendency to become attached to nearby solid surfaces. This phenomenon is usually associated with Coanda (fig. 1) who discovered the effect in his numerous experiments (refs. 1 and 2). An outline of the computational scheme appears in figure 2. Some applications are noted in figure 3 (e.g., cyclic circulation control of rotors, and jet flap wings). For laminar flow, the effect is also used with fluidic amplifiers.

For a better understanding of the effect, a comparison between the free jet and wall jet is made in figure 4. Here a free jet emerging from a slot[1] of a finite width h is shown. Downstream of the slot, the flow at the edge of the jet mixes with the surrounding air so that the width of the jet increases and the jet velocity decreases. If we replace the x-axis with a solid surface, the free jet becomes a wall jet. The velocity profile of the wall jet consists of an inner boundary layer for $y < y_m$ and an outer free jet layer for $y > y_m$. Furthermore, if the pressure in the jet is slightly lower than the ambient pressure, the free jet will not deflect due to symmetry. However, for a wall jet, the pressure differences will cause

[1]The transition length from a parabolic velocity profile for the nozzle flow to the jet flow velocity profile is assumed to be small (of the order of $Re^{-2/3}$).

Preceding page blank

the jet to deflect toward the wall. Particularly for a wall jet along a curved surface, the centrifugal force tends to make the jet pressure slightly lower than the ambient pressure and the jet will become strongly attached to the wall.

It is realized that the complexity of the problem makes analysis of this effect in a free stream very difficult. To gain fundamental understanding of the problem, the wall jet around a simple curved surface without any external flow should first be examined. The objective of this work is to develop a theory for Coanda jet flow around a circular cylinder for predicting the variation of wall shear, the approximate separation point, and the external mass entrainment. The authors are grateful to Prof. Libby for his stimulating discussions concerning this objective.

SYMBOLS

See also figure 5.

f	dimensionless similarity function defined in Glauert's solution
f_{1_∞}	normalization constant in Glauert's solution
h	slot width, ft
p	pressure, lb/ft^2
R	cylinder radius, ft
Re	Reynolds number, dimensionless
u, v	tangential and radial velocities, ft/sec (u_D, u_c defined in fig. 10)
x, y	rectangular coordinates, ft (y_m defined in fig. 4)
Y	normalized y-coordinates, $Y = \frac{y\sqrt{Re}}{R}$
δ	jet thickness, ft
η	defined as $\frac{Y}{\theta^{3/4}}$, dimensionless
θ	angular coordinate, rad
ν	kinematic viscosity, ft^2/sec
ρ	density, $slugs/ft^3$

EQUATIONS AND ASSUMPTIONS

As shown in figure 6, the equations to be considered are the incompressible Navier-Stokes equations in cylindrical coordinates. According to

the Prandtl boundary-layer theory, the terms in the equations can be grouped into different orders (i.e., the first, second, and higher orders). It is noted that the equations are invariant by translation in the θ coordinate.

Assumptions made for this analysis are:

1. Thin jet - the thickness of jet is small compared with cylinder radius.

2. Laminar flow - the Reynolds number of the flow based upon the cylinder radius is in the order of 3×10^4 or less.

3. Incompressible flow.

METHOD OF SOLUTION

For viscous flow at high Reynolds number, Professor Van Dyke at Stanford University has developed a matched asymptotic expansion theory (refs. 3 and 4). The problem is, then, to apply his method systematically to the Navier-Stokes equations. Accordingly, as shown in figure 7, we define an inner and an outer expansion for the tangential velocity. The outer equations take account of the external entrainment flow. The equations are Laplace equations subject to matching boundary conditions calculated from the inner equations. The inner equations are boundary-layer equations. The normal coordinate y is stretched by a factor equal to the square root of the Reynolds number.

FIRST-ORDER INNER SOLUTION

The first-order inner equations are determined to be Glauert's wall-jet equations (ref. 5) in which the jet is assumed to flow along a flat wall without any normal and tangential pressure gradient. The velocity distribution of Glauert's solution across the jet is shown in figure 8. Because of the homogeneous boundary conditions, Glauert's solution contains an undetermined normalization constant. This constant, as shown in reference 6, can be determined by the product of jet momentum and jet volume flow. After the constant is determined, a unique relation between the jet thickness and the θ coordinate is obtained:

$$\theta = \left(\frac{h}{R}\right)^2 \frac{Re}{18} \tag{1}$$

The streamlines of Glauert's solution, as shown in figure 9, indicate that the entrainment flow is perpendicular to the main jet flow. This imposes a boundary condition for the determination of the first-order outer solution, which must properly describe the upstream entrainment flow. The boundary condition at $y = 0$ for the outer first-order stream function is

$$\psi^{(1)}\left(\frac{y}{R}, \theta\right)_{y=0} = 4f_{1\infty}\theta^{1/4} \quad \text{for} \quad \theta > 0 \tag{2}$$

$$= 0 \quad \text{for} \quad \theta < 0$$

which yields a sink distribution of

$$V^{(1)}\left(\frac{y}{R}, \theta\right)_{y=0} = -f_{1\infty}|\theta^3| \quad \text{for} \quad \theta > 0 \tag{3}$$

$$= 0 \quad \text{for} \quad \theta < 0$$

along the cylinder surface.

SECOND-ORDER CORRECTIONS

There is no separation from the first-order inner solution. Second-order inner solutions are needed to predict separation. It has been shown in references 3 and 4 that the second-order inner correction may be split into two parts, namely, curvature and displacement as noted in figure 10. Due to curvature, a normal pressure gradient is generated by the centrifugal force of the flow. This introduces a tangential pressure gradient in the tangential momentum equation. However, this term cancels with the other second-order terms in the tangential momentum equation. In addition, the changing of the arc length between the y coordinates also introduces a viscous shear term $\nu y(\partial^2 u/\partial y^2)$ into the momentum equation.

To find the second-order inner correction due to entrainment, one must solve the first-order outer equation. The outer equation is given by the Laplace equation, and the solution must satisfy the boundary conditions, equation (2) or (3); a sink distribution is thus required along the cylinder surface. The solution can be found by the use of Poisson's formula for a circle (ref. 7). The outer stream function is seen to be bounded at large values of y. From the Poisson's integral, it is found that the external entrainment flow induces a tangential velocity $u_D^{(1)}$ at the outer edge of the boundary layer.

$$u_D^{(1)} = \frac{0.504}{\theta} + \frac{0.25}{\theta^{3/4}} + 0.109 - 0.043\theta - 0.0007\theta^3 \ . \ . \ . \tag{4}$$

This series expansion is an approximation for Poisson's solution at $y = R$ for $\theta < 2\pi$.

The equations to account for the curvature effect are shown in figure 11. The boundary conditions are homogeneous, but the equations are nonhomogeneous. The solution to the second-order curvature equations is shown

in figure 12 and indicates that the curvature effect tends to decrease the velocity near the wall and increase the velocity in the outer part of the layer.

To obtain the curvature effect, a resultant velocity profile can be formed by adding the second-order curvature correction to Glauert's wall-jet solution. It is found that the velocity profile (fig. 13) becomes flatter with increasing θ coordinate, indicating decrease in wall shear as θ increases.

The equations to take account of the displacement effect are shown in figure 14. The tangential velocity at the outer edge of the boundary layer is given by equation (4). The solutions of the second-order displacement equations corresponding to the first two terms in the series expansion (eq. (4)) are shown in figure 15. The displacement effect decreases the wall shear and tends to promote separation. A plot of the resultant velocity profile including the first six terms in the series expansion is shown in figure 16 indicating a significant reduction in wall shear.

UNIQUENESS OF THE SECOND-ORDER THEORY

The above solutions of the problem are not unique. There may exist a set of infinite discrete eigensolutions, each of which satisfies the homogeneous boundary conditions and exhibits exponential decay at infinity (refs. 8 and 9). However, in the second-order inner equations, there is an eigenfunction with eigenvalue equal to zero. This solution decays with the θ coordinate at the same rate as Glauert's solution; hence, one cannot simply dismiss it by invoking the principle of minimum singularity (ref. 10). Thus in the formulation of the second-order theory, the need for deriving a unique condition to include the eigensolution becomes apparent. When the constant associated with the eigensolution is determined, there is a possibility that the wall shear predicted by the theory will be significantly changed. Presently we are trying to find a condition for determining the constant. Lindow and Greber (ref. 11) noted similar results in their study of the similarity solution of the second-order wall-jet equation.

CONCLUSIONS

Based upon the work completed to date, the preliminary conclusions of this brief progress report may be summarized as follows (fig. 17):

1. The first-order solution is similar and gives no separation (this is the Glauert wall jet).

2. The curvature effect allows separation. However, the separation angle seems unreasonably large if the unknown constant is taken to be equal to zero.

3. The displacement effect decreases wall shear significantly, promoting separation.

4. The theory needs experimental verification. Tests in oil to observe the laminar separation angle are planned.

REFERENCES

1. Metral, A.: Sur un Phenomene de Deviation des Veines Fluides et ses Applications. Coanda Effect, Cabinet Technique due Ministere de l'Air (1938).

2. Metral, A.; and Zerner, F.: L'Effect Coanda, Publication Scientifiques et Techniques du Minister de l'Air, No. 218 (1948).

3. Van Dyke, M. D.: Higher Approximations in Boundary Layer Theory. Part 1. General Analysis. J. Fluid Mech., vol. 14, 1962, pp. 161-177.

4. Van Dyke, M. D.: Higher Approximation in Boundary Layer Theory. Part 2. Application to Leading Edges. J. Fluid Mech., vol. 14, 1962, pp. 481-495.

5. Glauert, M. B.: The Wall Jet. J. Fluid Mech., Aug. 1956, pp. 161-177.

6. Parks, E. K.; and Petersen, R. E.: Analysis of a Coanda Type Flow. AIAA, vol. 6, no. 1, Jan. 1968.

7. Morse, Philip M.; and Feshbeah, Herman: Methods of Theoretical Physics. McGraw-Hill, 1953, pp. 370-374.

8. Libby, P. A.; and Fox, H.: Some Perturbation Solutions in Laminar Boundary-Layer Theory. Part 1. The Momentum Equation. J. Fluid Mech., vol. 17, 1963, pp. 433-449.

9. Stewartson, K.: On Asymptotic Expansions in the Theory of Boundary Layers. J. Math. and Phys., vol. 36, 1957, pp. 173-191.

10. Van Dyke, M. D.: Perturbation Method in Fluid Mechanics. Academic, New York & London (1964), pp. 131-132.

11. Lindow, B. G.; and Greber, I.: Similarity Solution of a Laminar, Incompressible Jet Flowing Along a Curved Surface. AIAA, vol. 6, no. 7, July 1968.

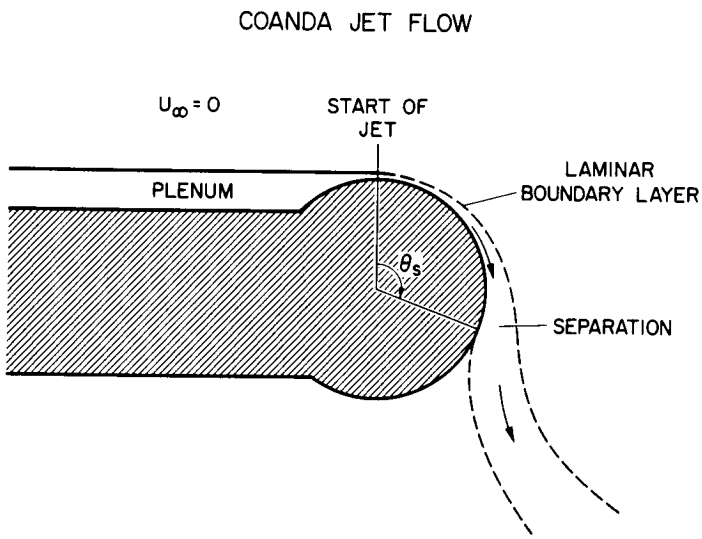

Figure 1

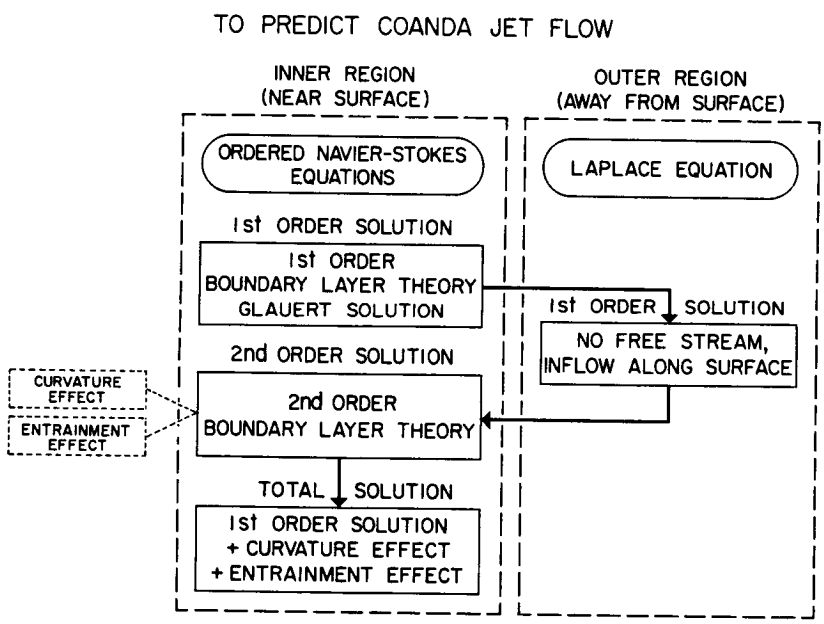

Figure 2

COANDA JET THEORY

- APPLICATIONS
  - CIRCULATION CONTROL, JET DEFLECTION — TURBULENT FLOW
  - FLUIDIC CONTROLS — LAMINAR FLOW
- OBJECTIVE
  - DEVELOP A THEORY TO PREDICT COANDA JET FLOW SEPARATION
- APPROACH
  - FIRST PHASE — CONSIDER ONLY LAMINAR FLOW WITHOUT FREE STREAM ON A CIRCULAR CYLINDER
  - LATER PHASES — EXTEND THEORY TO INCLUDE TURBULENT FLOW, FREE STREAM, AND OTHER GEOMETRIES

Figure 3

TWO-DIMENSIONAL FREE JET

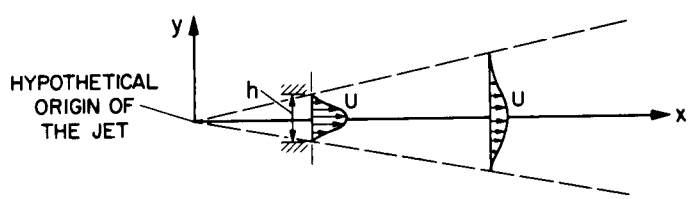

TWO-DIMENSIONAL WALL JET

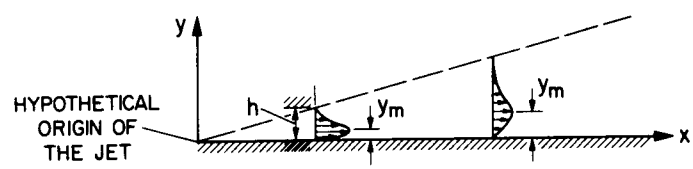

Figure 4

NOTATION

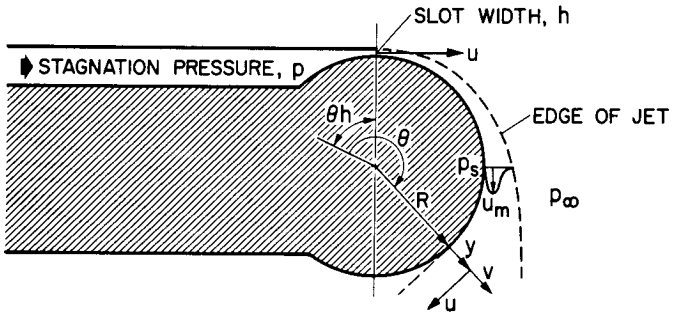

u.....TANGENTIAL VELOCITY
v.....RADIAL VELOCITY
θ, y.....TANGENTIAL AND RADIAL COORDINATES
p_∞.....AMBIENT PRESSURE
p_s.....SURFACE PRESSURE AT THE CYLINDER

Figure 5

NAVIER - STOKES EQUATIONS

- CONTINUITY

$$\underbrace{\left(\frac{\partial u}{\partial \theta}+\frac{\partial v}{\partial y}\right)}_{\text{1st ORDER}}+\underbrace{\left(v+y\frac{\partial v}{\partial y}\right)}_{\text{2nd ORDER}}=0$$

- TANGENTIAL MOMENTUM

$$\underbrace{\left(v\frac{\partial u}{\partial y}+\frac{u}{R+y}\frac{\partial u}{\partial \theta}-\nu\frac{\partial^2 u}{\partial y^2}\right)}_{\text{1st ORDER}}+\underbrace{\left(\frac{1}{R+y}\frac{\partial (P/\rho)}{\partial \theta}+\frac{vu}{R+y}-\frac{\nu}{R+y}\frac{\partial u}{\partial y}\right)}_{\text{2nd ORDER}}+$$

$$\underbrace{\nu\left(\frac{u}{(R+y)^2}-\frac{1}{(R+y)^2}\frac{\partial^2 u}{\partial \theta^2}+\frac{2}{(R+y)^2}\frac{\partial v}{\partial \theta}\right)}_{\text{HIGHER ORDER}}=0$$

- NORMAL MOMENTUM

$$\underbrace{\left(\frac{u^2}{R+y}-\frac{\partial P/\rho}{\partial y}\right)}_{\text{1st ORDER}}-\underbrace{\left(v\frac{\partial v}{\partial y}+\frac{u}{R+y}\frac{\partial v}{\partial \theta}-\nu\frac{\partial^2 v}{\partial y^2}\right)}_{\text{2nd ORDER}}+$$

$$\underbrace{\nu\left(\frac{1}{R+y}\frac{\partial v}{\partial y}-\frac{v}{(R+y)^2}+\frac{1}{(R+y)^2}\frac{\partial^2 v}{\partial \theta^2}\;\frac{2}{(R+y)^2}\frac{\partial u}{\partial \theta}\right)}_{\text{HIGHER ORDER}}=0$$

ν = KINEMATIC VISCOSITY ρ = DENSITY

Figure 6

- ASSUMPTIONS
  - THIN JET ($\frac{\delta}{R} < 1$) – BOUNDARY LAYER ANALYSIS IS APPLICABLE
  - LAMINAR FLOW ($Re = \frac{RU}{\nu} < 3 \times 10^4$)
  - INCOMPRESSIBLE FLOW

- METHOD OF SOLUTIONS
  - OUTER REGION (VALID FOR y LARGE)
    LAPLACE EQUATION
  - INNER REGION (VALID FOR y SMALL)
    NAVIER - STOKES EQUATIONS

- EXPANSIONS
  - OUTER EXPANSION

$$u = \frac{1}{\sqrt{Re}} \tilde{u}^{(1)}\left(\frac{y}{R}, \theta\right) + \frac{1}{Re} \tilde{u}^{(2)}\left(\frac{y}{R}, \theta\right) + \cdots$$

  - INNER EXPANSION

$$u = u^{(0)}\left(\frac{y}{R}\sqrt{Re}, \theta\right) + \frac{1}{\sqrt{Re}} u^{(1)}\left(\frac{y}{R}\sqrt{Re}, \theta\right) + \cdots$$

Figure 7

FIRST-ORDER INNER SOLUTION
GLAUERT WALL JET

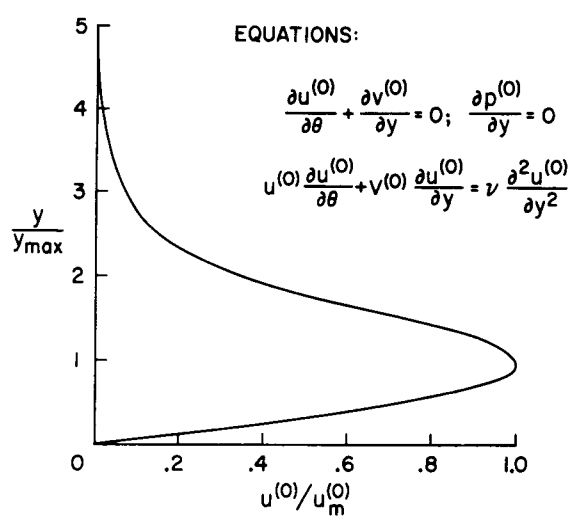

Figure 8

FIRST-ORDER INNER STREAMLINES FOR WALL JET

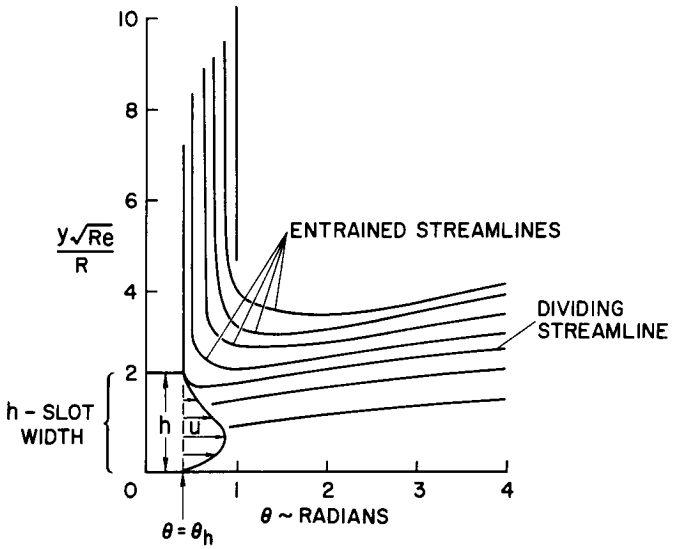

Figure 9

SECOND-ORDER CORRECTIONS $u^{(1)} = u_C^{(1)} + u_D^{(1)}$

- CURVATURE EFFECTS: $(u_C^{(1)})$
  - CHANGING ARC LENGTH BETWEEN y COORDINATES
  - NORMAL MOMENTUM EQUATION IS INCLUDED
  - INDUCED TANGENTIAL PRESSURE GRADIENT TERMS DROP OUT
- DISPLACEMENT EFFECT: $(u_D^{(1)})$
  - UPSTREAM ENTRAINMENT:

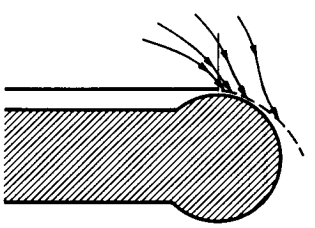

NONZERO TANGENTIAL VELOCITY AT OUTER EDGE OF JET

Figure 10

SECOND-ORDER CURVATURE EQUATIONS

$u_C^{(1)}$

- CONTINUITY

$$\frac{\partial u_C^{(1)}}{\partial \theta} + \frac{\partial v_C^{(1)}}{\partial Y} + V^{(0)} + Y\,\frac{\partial v^{(0)}}{\partial Y} = 0$$

- TANGENTIAL MOMENTUM

$$u^{(0)}\,\frac{\partial u_C^{(1)}}{\partial \theta} + u_C^{(1)}\frac{\partial u^{(0)}}{\partial \theta} + V^{(0)}\,\frac{\partial u_C^{(1)}}{\partial Y} + V^{(1)}\,\frac{\partial u^{(0)}}{\partial Y} - \frac{\partial^2 u_C^{(1)}}{\partial Y^2} =$$

$$-\frac{\partial p^{(1)}}{\partial \theta} + \frac{\partial}{\partial Y}\,Y\,\frac{\partial u^{(0)}}{\partial Y} - V^{(0)}\,\frac{\partial}{\partial Y}\,Y u^{(0)}$$

- NORMAL MOMENTUM

$$\frac{\partial p^{(1)}}{\partial Y} = \left(u^{(0)}\right)^2$$

$$Y = \sqrt{Re}\;y/R$$

Figure 11

VELOCITY CORRECTIONS DUE TO CURVATURE

$u_C^{(1)}$

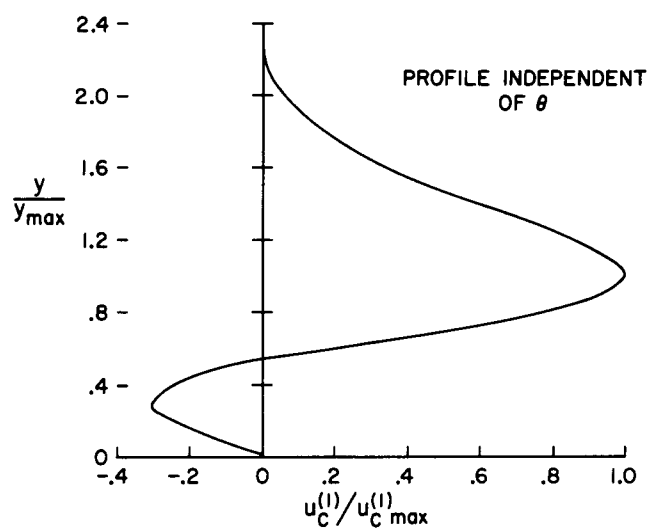

Figure 12

TO OBTAIN CURVATURE EFFECT

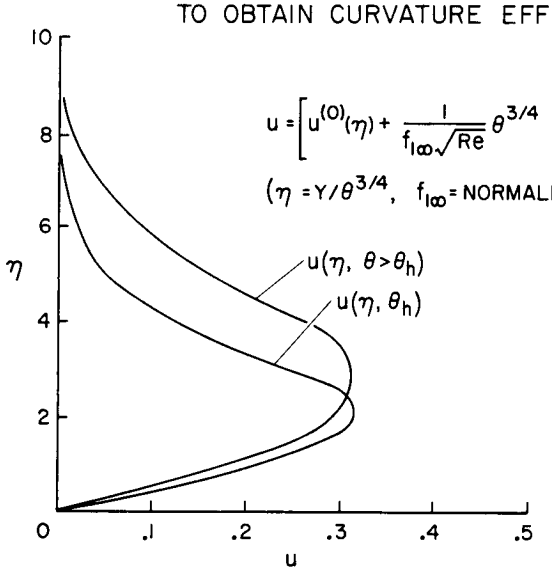

Figure 13

SECOND-ORDER DISPLACEMENT EFFECT
$u_D^{(1)}$

- OBTAIN INFLOW VELOCITY DISTRIBUTION AT OUTER EDGE OF JET BY SOLVING OUTER FLOW EQUATION

$$u_D^{(1)}(\infty, \theta) = 0.504/\theta + 0.25/\theta^{3/4} + 0.109 - 0.043\theta \ldots\ldots$$

- SOLVE

$$\frac{\partial u_D^{(1)}}{\partial \theta} + \frac{\partial v_D^{(1)}}{\partial Y} = 0$$

$$\frac{\partial}{\partial \theta}\left(u_D^{(1)}\, u^{(0)}\right) + v^{(0)}\frac{\partial u_D^{(1)}}{\partial Y} + v_D^{(1)}\frac{\partial u^{(0)}}{\partial Y} = \frac{\partial^2 u_D^{(1)}}{\partial Y^2}$$

- BOUNDARY CONDITIONS

$$u_D^{(1)}(0, \theta) = 0 \qquad v_D^{(1)}(0, \theta) = 0$$

$$u_D^{(1)}(\infty, \theta) = 0.504/\theta + 0.25/\theta^{3/4} + 0.109 - 0.043\theta \ldots\ldots$$

Figure 14

VELOCITY CORRECTIONS DUE TO DISPLACEMENT

$$U_D^{(1)} = \left(f_1(\eta)/\theta + f_2(\eta)/\theta^{3/4} + f_3(\eta) + \ldots\right)$$

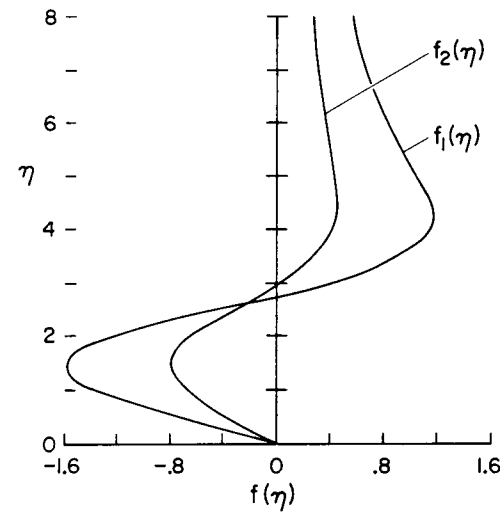

Figure 15

RESULTANT VELOCITY PROFILE (u)

$$U = 4\left\{f^{(0)}(\eta) + \frac{1}{\sqrt{Re}\, f_{1\infty}} f^{(1)}(\eta, \theta)\right\}/\theta^{1/2}$$

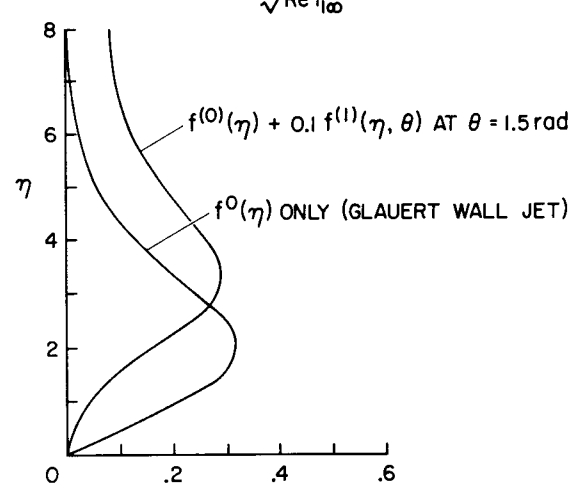

Figure 16

SEPARATION POINT

- FIRST-ORDER SOLUTION IS SIMILAR, i e NO SEPARATION
- CURVATURE EFFECT ALLOWS SEPARATION, HOWEVER, SEPARATION ANGLE SEEMS UNREASONABLY LARGE
- DISPLACEMENT EFFECT DECREASES WALL SHEAR SIGNIFICANTLY, PROMOTING SEPARATION
- EXPERIMENTAL VERIFICATION TESTS IN OIL

Figure 17

DISCUSSION

STANLEY G. RUBIN, Polytechnic Institute of Brooklyn: I just want to ask you a question about the entrained streamline that you show on Slide 9 and a little bit on Slide 10. It indicates that the streamline flow has negative slope and all streamlines go away from the origin of the jet.

Now, a while ago I had a short note on a free jet expansion.

WEI: Yes.

RUBIN: In that particular case a turnaround occurs indicating a sink-like action of the potential flow. I'm just curious as to this effect in your case.

WEI: Yes, that's right. I tried to find the solution first for the plane wall jet. It did turn around, very similar to Rubin's work on the free jet. However, on a cylinder, you will find that the stream function for entrainment flow is bonded at infinity. Now, Rubin's solution for the plane free jet is not bonded, and it is over here that we are going to get a difference between the slopes of the entrainment streamlines.

Furthermore, on the cylinder surface you will find that the inflow velocity distribution has a reversal of slope. (Drawing on board.) The inflow velocity is very large near the jet origin, directing from left to right. This inflow velocity diminishes to zero tentatively assumed at here and grows in reverse direction over the rest of surface. Of course, at the reversal point, the tangential velocity is equal to zero and the radial velocity is not equal to zero. It seems to me that this kind of entrainment flow is very reasonable because you would expect that some place near the point of reversal the jet peels off from the cylinder surface.

RUBIN: Down there, but I am really concerned with where the flow approaches the origin.

WEI: Yes, what you are concerned with, kind of going like that. (Drawing on board)

RUBIN: That's only on a free jet?

WEI: This is correct. When you get into wall jet on cylinder, you will find that the slope of the entrainment flow is different from the plane free jet.

RUBIN: Let me just ask one additional question. Since your initial solution and all your subsequent solutions are based on similarity, have you investigated what the effect of the initial conditions would be, and the possibility of having eigensolutions dependent on the initial conditions?

WEI: Yes, there are eigensolutions. If the eigenvalues for the eigensolutions are not equal to zero, you can invoke Van Dyke's minimum singularity principle that the eigensolutions belong to higher orders. Howeven, as I mentioned, there is an eigensolution with zero eigenvalue. This solution decays at the same rate as the wall-jet solution. That is why I said that I found a solution which ended with an undetermined constant. I still don't know how to determine the constant associated with the eigensolution.

RUBIN: That's the solution you were referring to?

WEI: Yes, that's right, a solution corresponding to zero eigenvalue. For the plane free jet, there is no eigensolution with zero eigenvalue.

RUBIN: I don't know if you are familiar with this, but do you know of Professor Libby's work on this subject?

W. J. McCROSKEY, Army Aeronautical Laboratory: I am also hung up on some of the details of the entrainment. Is it not correct that you have assumed that all of the entrainment in the outer flow is radially inward?

WEI: Yes.

McCROSKEY: This is an assumption which, in the first place, I wonder how good an assumption this is, on what basis you can make that, and secondly, if you make this assumption it sort of looks to me like you would get into trouble. There must be some kind of singularity or very funny behavior just upstream of $\theta = \beta_h$.

WEI: Yes, that's correct. The method assumes a radially inward inflow on the cylinder surface. Professor Van Dyke has worked out several other cases for the entrainment effect. One is the round jet. For the round jet, the zero-order solution shows that the entrainment flow is perpendicular to the jet flow. He used this as a boundary condition to calculate the outer solution. From the inner and outer solutions he constructed a composite stream function which is valid for all regions. The round jet has an exact solution. The exact solution was then used to check the composite solution. It turned out very close. So this is one indication that the method of matched asymptotic expansion seems to be very fruitful in treating this kind of problem. Of course, there are other illustrative examples. All I know is that they check very well with the exact solutions.

Referring to your second question, the velocities are indeed all singular at the jet origin. The entrainment effect introduces singular solutions of higher order than the wall-jet solution.

McCROSKEY: You're just throwing away all the regions upstream of this, in terms of the entrainment source.

WEI: Oh, you mean what is the upstream boundary condition on the stream function?

McCROSKEY: You have some entrainment from upstream.

WEI: The boundary condition is that the stream function is equal to zero for the θ-coordinate less than zero. This is for a plane wall jet, allowing some entrainment from upstream. For the cylinder, we only have to consider the boundary condition on the θ-coordinate between zero and 2π.

A NEW METHOD FOR CALCULATING NEAR AND FAR FIELD PRESSURE ABOUT ARBITRARY CONFIGURATIONS

By Frank A. Woodward
Aerophysics Research Corporation

Lynn W. Hunton and Anthony R. Gross
Ames Research Center

12

N70-21363

SUMMARY

A new method of calculating pressure signatures and associated shock wave patterns in the near and far field about arbitrary wing-body combinations is described herein and illustrated with several examples.

The principal difference between this method and the currently accepted theory of G. B. Whitham is shown to be in the aerodynamic representation used. Both methods use a linear distribution of singularities to represent a body of revolution, but the new method includes additional planar singularity distributions on the surfaces of wing-body combinations to improve the aerodynamic representation in the near field. In the far field, this spatial distribution of singularities gives the same result as Whitham's equivalent body of revolution in each azimuthal plane.

Examples of pressure signatures are presented only for bodies of revolution pending completion of the wing-body analysis computer program. Good correlation between theory and experiment is shown by these examples. The new method is expected to overcome some of the present limitations of the Whitham theory and to provide improved near field pressure signature estimates for arbitrary wing-body configurations.

INTRODUCTION

Calculations of the pressure signature and shock wave pattern in the field surrounding arbitrary airplane configurations at supersonic speed have been based for a number of years almost exclusively on a theory presented by G. B. Whitham in 1952 (ref. 1). Whitham's theory depends on the smooth slender-body assumption in which the airplane volume and lift are represented by separate equivalent line source singularity distributions along the body axis. The predictions of this theory have been verified by extensive wind-tunnel and flight-test measurements and are generally accepted as a basis for estimating sonic boom overpressures.

Recent studies (ref. 2) have indicated a number of limitations to the Whitham theory in areas of current interest, for example, in the analysis of

(a) Nonslender configurations
(b) Vertical displacement of wing (high wing, dihedral)
(c) Flow field definition very near the vehicle
(d) High Mach numbers

In an attempt to alleviate these deficiences, the method described here has been formulated for calculating pressures and velocities to first order throughout the entire flow field about arbitrary wing-body configurations. The method will be illustrated by several examples.

NOMENCLATURE

C_p	pressure coefficient
F	first-order correction function (Whitham)
k	$(\gamma + 1)M_\infty^4/\sqrt{2}\ \beta_\infty^{3/2}$
K	total number of singularities
M	Mach number
N	first-order correction function (present method)
r	radial coordinate
S	singularity strength
u	dimensionless perturbation velocity in x direction
v	dimensionless perturbation velocity in y direction
x,y,z	Cartesian coordinates
x_o	origin of first-order singularity
α	flow inclination angle
β	$\sqrt{M^2 - 1}$
γ	ratio of specific heat for air
δ	cone half-angle
μ	Mach angle
θ	cylindrical coordinate

Subscripts

∞	free-stream condition
j	singularity type
k	singularity number
r	radial direction

ANALYSIS

The procedure presented herein is based on a recently developed distributed singularity method described by R. L. Carmichael (ref. 3). The configuration is represented by a large number of aerodynamic singularities distributed along the body axis and on panels located on the wing and body surfaces. The panel subdivision of a typical wing-body combination is illustrated on figure 1. The six different types of singularities used in the analysis to simulate volume, camber, incidence, and interference effects are listed on the figure. Since the assumptions underlying this method and the procedures used in determining the potential functions and velocity components are described in reference 3, these details will not be repeated here. Compared with the Whitham theory, the method introduces two important analytical advantages. First, the spatial distribution of singularities gives an improved aerodynamic representation in the near field while retaining the correct asymptotic form in the far field. Second, the surface pressures, forces, and moments acting on the configuration are obtained automatically in addition to the pressure signatures in the field, thus greatly facilitating the overall aerodynamic analysis.

The first step in the pressure signature calculations is the determination of the characteristic lines in the field. Linearized theory gives the result that the disturbance field from each singularity is contained within the Mach cone from the singularity origin since the disturbances are assumed to have zero strength and to propagate into the field at the speed of sound of the fluid at rest. The slope of the characteristic lines of an outgoing wave in this "zero order" flow field is given by

$$\frac{dx}{dr} = \cot \mu_\infty = \beta_\infty$$

where μ_∞ is the Mach angle of the undisturbed flow.

The theory of characteristics gives the exact slope of the outgoing characteristic lines as

$$\frac{dx}{dr} = \cot(\mu + \alpha) = \frac{\cot \mu - \tan \alpha}{1 + \cot \mu \tan \alpha}$$

where μ is the local Mach angle, and α is the local inclination of the flow measured from the free-stream direction. Following Whitham, a first-order approximation to the slope of the characteristics may be obtained by expanding the exact equation for small values of βv_r, where $\beta = \cot \mu$ and $v_r = \tan \alpha$ (ratio of the radial to free-stream velocities). If, in addition, a linear relationship is assumed between the axial velocity ratio u and the local Mach number M, such that

$$M \approx M_\infty\left[1 + \left(1 + \frac{\gamma - 1}{2} M_\infty^2\right)u\right]$$

and

$$\beta \approx \beta_\infty + \frac{M_\infty^2}{\beta_\infty}\left(1 + \frac{\gamma - 1}{2} M_\infty^2\right)u$$

then,

$$\frac{dx}{dr} \approx \beta_\infty + \frac{\gamma + 1}{2}\frac{M_\infty^4}{\beta_\infty} u - M_\infty^2(v_r + \beta_\infty u)$$

This approximation to the slope is accurate only if βv_r is small. An alternate form of this equation is obtained, valid for higher Mach numbers, if the exact equation is inverted and expanded for small values of v_r/β. Then,

$$\frac{dr}{dx} \approx \frac{1}{\beta_\infty} - \frac{\gamma + 1}{2}\frac{M_\infty^4}{\beta_\infty^3} u + \frac{M_\infty^2}{\beta_\infty^2}(v_r + \beta_\infty u)$$

The first equation is referred to as the low Mach number expansion; the second, as the high Mach number expansion. The Whitham theory always uses the low Mach number expansion. This may introduce significant errors if the theory is applied at high Mach numbers. The present theory, on the other hand, may use either the low or the high Mach number expansion.

The equations of the first-order characteristic lines are obtained by integrating the slope equations outward from the body surface along the zero order characteristics using the linear theory expressions for u and v_r. The integration is performed in planes of constant θ for each of the singularities used in the representation, as illustrated on figure 2.

The low Mach number expansion gives an axial shift Δx to the zero order characteristic line, while the high Mach number expansion gives a corresponding radial shift Δr. Because of the nature of the line integrals being evaluated, it is found that $\Delta x = -\beta_\infty \Delta r$. For convenience in interpreting the results, an equivalent axial shift $\Delta x'$ can be defined in the high Mach number case in terms of Δr and the local slope of the characteristic line. In compression regions, Δx is always greater than $\Delta x'$, as indicated on the figure.

In the Whitham theory, the axial shift is given by the simple functional relationship

$$\Delta x = -k(M_\infty)\sqrt{r}\ F(x_o,\theta)$$

where the F function depends only on the equivalent area distribution in azimuthal planes. The present theory does not permit this convenient separation of variables. Instead, the axial shift is expressed in terms of six near field N-functions, one for each of the six types of singularities. For example,

$$\Delta x = \sum_{j=1}^{6} \sum_{k=1}^{K_j} N_{jk}(M_\infty, r, x_o, \theta) S_k$$

where N_{jk} is the axial shift calculated for the kth singularity of type j, S_k is the strength of the kth singularity, and K_j is the total number of singularities of type j used in the representation.

The first term of the asymptotic expansion of the N functions for large radial distance can be expressed exactly in the form of the Whitham F function. Thus, either theory will give the same results in the far field for a given distribution of singularities.

The pressure signatures in the field are now constructed by relocating the linear theory pressures along the first-order characteristic lines rather than the zero order Mach lines. The procedure is illustrated on figure 3 for a 15° half-angle cone at Mach 3. The zero order pressure signature for r = 0.5 rises rapidly from zero at the Mach line and reaches its surface value on the cone. The first-order pressure signature is obtained by applying the appropriate axial shift $\Delta x(x_o,r)$ to the zero order signature for each point on the curve. The forward distortion of the signature indicates a compression region containing overlapping characteristic lines. The envelope of the characteristics defines a limit cone corresponding to the most forward extent of the pressure signature.

The forward curvature of the signature between the Mach line and the limit line introduces a physically unrealistic solution. Instead, a shock wave will occur in this region which will provide a discontinuous pressure rise from zero to a value on the upper limb of the pressure curve. The shock wave is located by applying the principle that the shock wave bisects the angle formed between the upstream and downstream characteristic lines at that point. Within the approximations of the theory, this is equivalent to locating the shock wave so that the area under the distorted pressure signature is preserved, as indicated on the figure.

EXAMPLES

The shock wave angle for a 15° cone is presented as a function of Mach number in figure 4. The results of the present first-order near field theory are compared with Whitham's first-order far field theory and a recently published second-order far field theory given by Caughey (ref. 4). The present theory is seen to agree well with the Ames Research Center Cone Tables (ref. 5) over the entire Mach number range. It should be noted that the present theory is limited to Mach numbers below Mach tangency, or 3.86 in this example.

The effect of distance on the form of the pressure signature produced by a 15° half-angle cone-cylinder at Mach 1.7 is shown on figure 5. The compression waves from the cone move forward to form the front shock, as previously described. The expansion fan from the shoulder extends rapidly out into the field, modifying the pressure signature significantly as it overtakes the compression region. The near field signature represents an intermediate stage in this process resulting in a relatively flat-topped initial pressure distribution. The far field signature is first formed when the first expansion wave from the shoulder reaches the shock. This results in a typical N-wave pressure distribution which persists for all greater distances away from the body. The expansion wave is terminated by a weak rear shock wave in this example, followed by a trailing region of negative pressure. The far field pressure signature is not complete until all the characteristic lines emanating behind the shoulder are absorbed into the rear shock. At this point, the front and rear shocks become equal in strength, and the pressure behind the rear shock returns to the free-stream value.

A comparison of the theory with experiment for a 12.75° half-angle cone-cylinder at a distance of 80 cone lengths is given on figure 6 for $M = 1.69$. The present method is seen to give an accurate representation of the signature, especially in the expansion region between the shocks.

In figure 7, results are shown for a blunt-nosed body of revolution. Although the present method of analysis is restricted to bodies with nose angles that lie within the Mach cone, the pressure signatures of blunt bodies can be approximated by adding a conical extension to the nose that lies just inside the Mach cone and is tangent to the body surface. In this example the pressure signature is calculated at a distance of 10 nose lengths at $M = 2.01$. The pressures in the expansion region agree well with experiment, but the theory overestimates the pressure jump across the front shock. Because of the extreme pressure gradient behind the nose in this example, a small error in shock wave location can cause a large error in the pressure jump.

CONCLUDING REMARKS

A new method for calculating the pressure signatures around a wing-body combination in the near and far field has been developed and programmed for the digital computer. When complete the new method is expected to overcome some of the present limitations of the Whitham theory and provide improved near field pressure signature estimates for arbitrary configurations. Examples of pressure signatures calculated for bodies of revolution show good agreement between theory and experiment.

REFERENCES

1. Whitham, G. B.: The Flow Pattern of a Supersonic Projectile. Commun. Pure Appl. Math., vol. 5, 1952, pp. 301-348.

2. Hunton, Lynn W.: Current Research in Sonic Boom. Second Conference on Sonic Boom Research. NASA SP-180, 1968, pp. 57-66.

3. Carmichael, Ralph L.; Castellano, Charles R.; and Chen, Chuan F.: The Use of Finite Element Methods for Predicting the Aerodynamics of Wing-Body Combinations. NASA Symposium on Analytic Methods in Aircraft Aerodynamics, October 28-30, 1969.

4. Caughey, David A.: Second Order Wave Structure in Supersonic Flows. NASA CR-1438, September 1969.

5. Ames Research Staff: Equations, Tables, and Charts for Compressible Flow. NACA Rep. 1135, 1953.

AERODYNAMIC REPRESENTATION

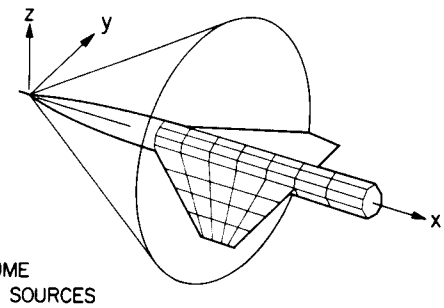

BODY VOLUME
- LINEAR SOURCES
- QUADRATIC SOURCES

BODY CAMBER AND INCIDENCE
- LINEAR DOUBLETS
- QUADRATIC DOUBLETS

WING THICKNESS
- CONSTANT SOURCE PANELS

WING CAMBER, INCIDENCE AND WING-BODY INTERFERENCE
- CONSTANT PRESSURE PANELS

Figure 1

LOCATION OF APPROXIMATE CHARACTERISTICS

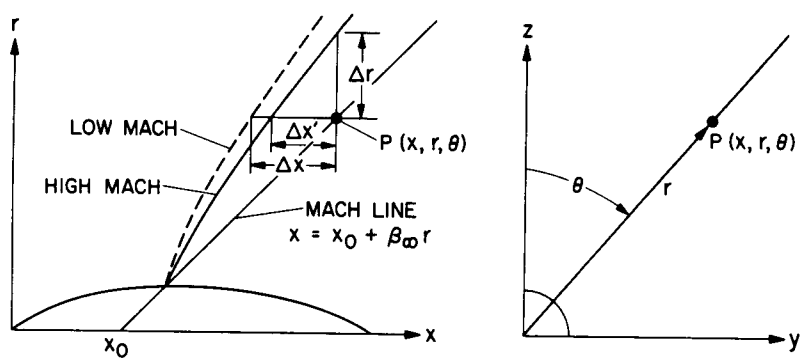

$$x = x_0 + \beta_\infty r - \Delta x \qquad \text{LOW MACH}$$

$$r = \frac{x - x_0}{\beta_\infty} + \Delta r \qquad \text{HIGH MACH}$$

Figure 2

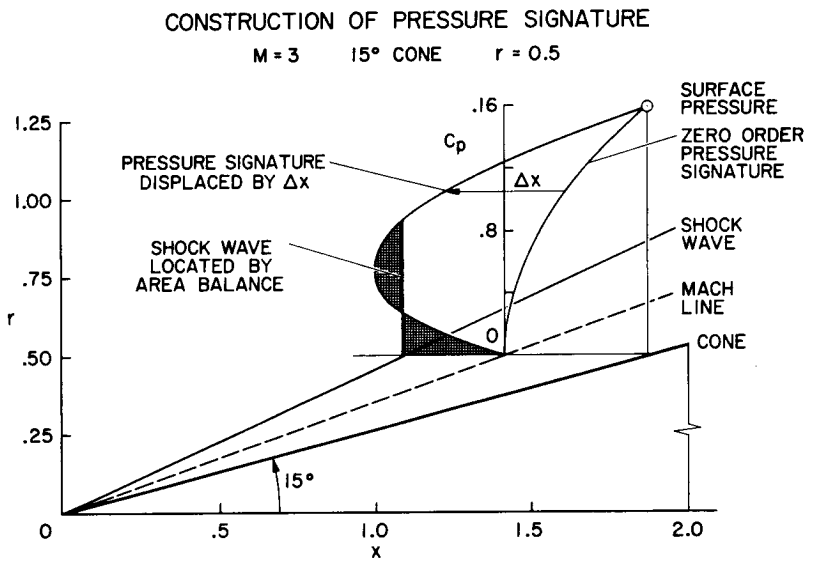

Figure 3

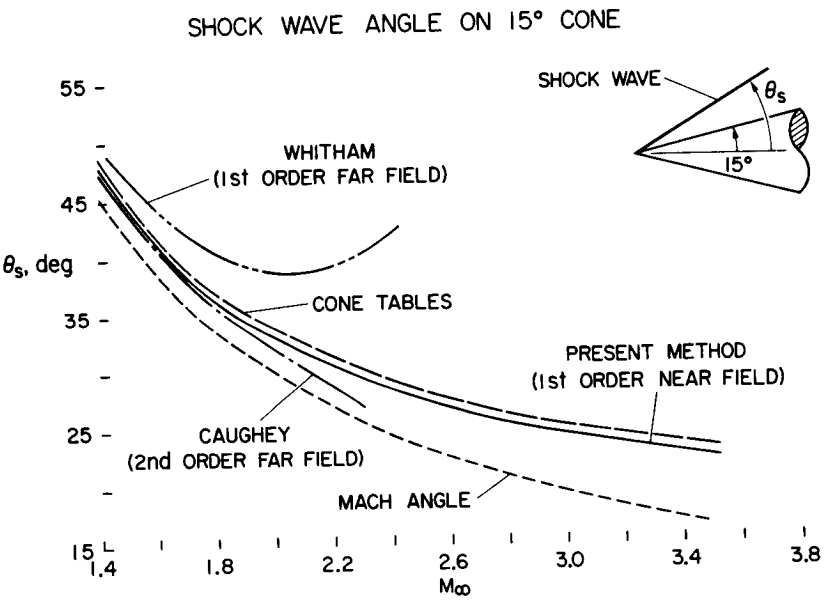

Figure 4

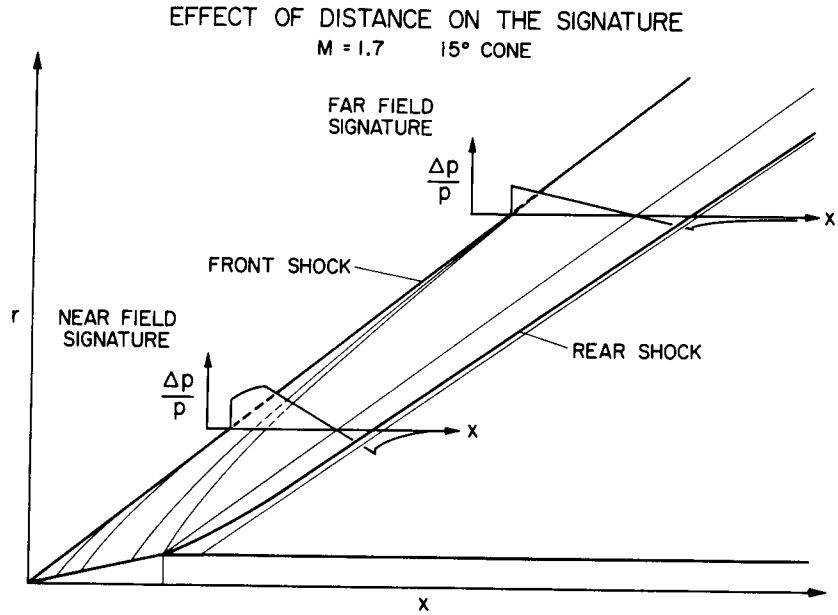

Figure 5

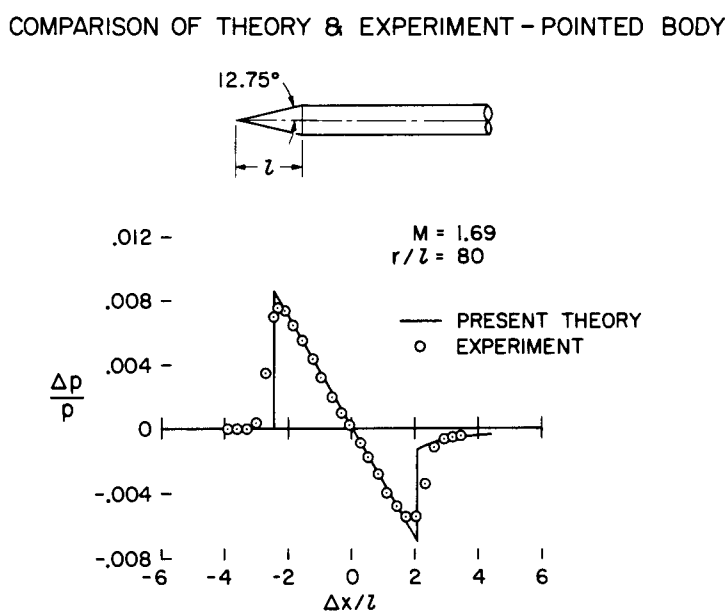

Figure 6

COMPARISON OF THEORY & EXPERIMENT - BLUNT BODY

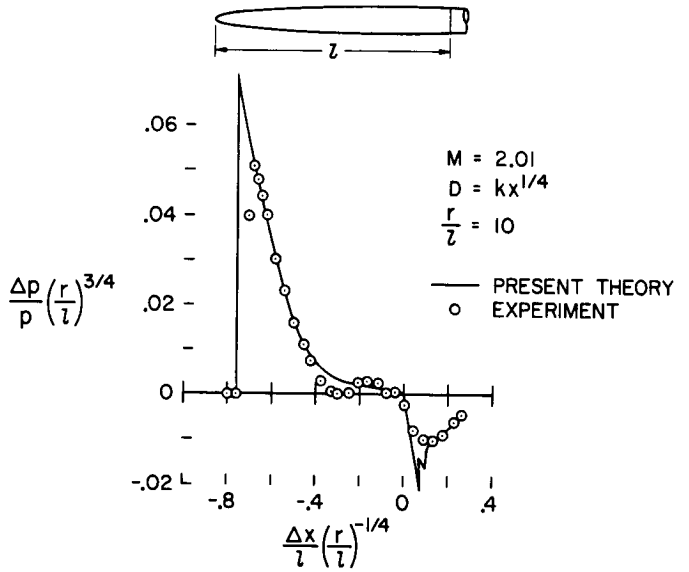

Figure 7

DISCUSSION

A. R. GEORGE, Cornell University: I'm not sure I understand. Does your theory use an expansion of the exact characteristics for large βv_r?

WOODWARD: Well, we have this option and have found in the studies done so far that above about a Mach number of 2 that the high Mach number expansion seems to give an improvement in the location of the characteristic lines.

GEORGE: This would only be valid in the near field because certainly v_r decreases as you move out.

WOODWARD: This is right, but we feel that the far-field shock location is dependent on its path through the near field. We are trying to improve the approximation in the near field to better understand the far-field signature.

GEORGE: How, do you switch from one to the other?

WOODWARD: No, the method is valid all the way out into the far field. In fact, it will give you the Whitham theory in the far field as the first term of the expansion in the normal way. It is a continuous solution all the way out.

GEORGE: One other question. For large βv_r I wouldn't expect the area balance-shock relation to hold. Have you done any work on that? As far as I know, it has never been worked out.

WOODWARD: That's right. We have had some difficulties with it, but at the moment we are basing our shock location on the area balance technique. This is one area in which we probably will be doing more work.

HARRY W. CARLSON, NASA Langley Research Center: Frank, as you know, the Whitham approach has been quite useful for airplane configuration work because you can take a quite complex airplane and reduce it to an equivalent body of revolution, get the F function and then calculate the signature from this. We have observed that it gives good results for moderate supersonic speeds, but there is some deterioration for higher supersonic speeds, say at Mach 3 and above, and particularly in the near field.

Now, have you given any thought to using the approach you have for finding the slope of these characteristic lines, to use these as a correction to the Whitham method, employing the same technique for describing the F function, but using this as a way of finding a new aging factor or a new way of calculating the advance of one characteristic relative to another?

WOODWARD: Yes, we have. As a matter of fact in the development of our displacement functions we have taken the far field limit of the disturbance from each one of the singularities, and this, in a sense, is the Whitham F function. As a matter of fact, they all show the v_r behavior that is characteristic of the far field solution. So with that in mind, I think that it

will be possible to tie this together and come up with a simple program for calculating the far field F functions, perhaps correcting them slightly, too, as you mentioned.

CARLSON: Yes, I think that this is a good approach because I believe the development of a system such as you have outlined here for handling complete airplane configurations is going to be very complex, and perhaps a long time off, but provisions for correction to the method of Whitham would be one that we could start employing almost immediately.

ROBERT L. TRIMPI, NASA Langley Research Center: I missed it, but where do you switch over from your high Mach number to your low Mach number approximation?

WOODWARD: Well, it depends on the magnitude of the product of β times the radial velocity. At the present stage of development it is really a choice that you make at the start of your calculations whether you use one or the other, but it can be checked by evaluating the magnitude of this product.

PROPAGATION OF SONIC BOOM THROUGH A STRATIFIED ATMOSPHERE

By Wallace D. Hayes
Princeton University

and

Harry L. Runyan, Jr.
Langley Research Center

N70-21364

SUMMARY

A method for predicting the sonic-boom signature due to a maneuvering aircraft has been presented. This method includes the effects of a variable, stratified atmosphere. The method is based on geometric acoustic principles and accounts for the use of a nonlinearity to account for the weak shock field. The analytical results have been compared with experimental data and excellent agreement has been shown, particularly with regard to signature length.

INTRODUCTION

Sonic booms have become of prime importance in the design and operation of supersonic aircraft. A need has been felt for a comprehensive analysis and algorithm, realized in a practicable computer program, which would provide more realistic calculations for sonic-boom signatures in the atmosphere. This paper will present a broad outline of such an analysis; the details of a full analysis, including the computer program, are given in reference 1.

Earlier algorithms for sonic boom have used various simplifying assumptions. A basic aim of the present algorithm has been to avoid these assumptions as far as possible and thus provide a more general treatment of the problem. Thus, the present algorithm includes the following features:

(1) The inclusion of maneuvering aircraft in calculation of a sonic-boom pressure

(2) An appropriate ray-tube-area calculation based on linear geometric acoustics

(3) Results in the form of complete signatures, without far-field assumptions, obtained through the use of an "age" variable in the calculation of nonlinear effects

Preceding page blank

The present procedure assumes a horizontally stratified atmosphere with horizontal winds. This limiting assumption is of great practical interest and considerably simplifies the calculation. However, the effects of wind turbulence have not been considered.

The analysis is largely a rational synthesis of existing theories described in the literature and includes some new theoretical development. A principal new theoretical development is in the calculation of ray-tube area. The analysis is also new in the careful piecing together of a number of calculations, principally in the relation of the wave system and rays issuing from the aircraft stratified atmosphere with winds. This relation requires the consideration of a Galilean transformation connecting a local coordinate system with the fixed coordinate system.

Figure 1 illustrates the geometry of the problem. At any given instant, $t = t_1$, and aircraft is in one position, and associated with the aircraft is a shock-wave system, which near the aircraft is approximately conical and which extends down to the ground; an observer senses the shock wave as a loud noise. The shock wave, however, was created at an earlier time, $t = t_0$, and the disturbances travel approximately along rays. The key to the present method is the correct linear analysis of propagation in the atmosphere by using the method of geometric acoustics, analogous to geometric optics. Therefore, the following analysis can be divided into a number of topics, including (1) ray tracing, (2) Blokhintsev invariant, (3) determination of the ray-tube areas, (4) flow near the aircraft, (5) definition of an age variable, (6) determination of shock shape and magnitude, and, finally (7) a comparison of theory and experiment.

SYMBOLS

A	horizontal component of area of ray tube
$\bar{A}$	area vector of ray tube normal to rays
A_n	area of ray tube normal to rays
a	speed of sound
a_o	initial speed of sound
$\bar{c}$	ray velocity
c_n	velocity of propagation of wave normal to wave front (eq. (1))

$c_o = \frac{c_n}{\cos \theta}$

F	integral defined by equation (9)
F_i	integral defined by equation (9)
I_1, I_2, I_3	integrals defined in equation (8)
$\bar{i}$	horizontal unit vector
M	Mach number
$\bar{n}$	unit vector normal to wave front
$\bar{n}'$	horizontal component of $\bar{n}$
p	pressure
q	perturbation velocity
r	radius
$\bar{r}$	radius vector
$\bar{r}'$	horizontal component of $\bar{r}$
S	area distribution of equivalent body of revolution (primes refer to derivatives)

$S_o = \int_{-\infty} (V_E) d\xi_1(\xi)$

s	backward facing distance from normal to wave front
T	temperature
t	time
t_a	time along aircraft trajectory

t_0	time of initiation of disturbance
t_1	time at which disturbances form a shock
$u(z)$	horizontal wind velocity as a function of altitude
$\bar{u}$	wind vector velocity
u_t	horizontal wind component in x_1,y_1 coordinate system
u_{t_o}	initial horizontal wind velocity component in x,y coordinate system
u_x,u_y	horizontal wind velocity component
V	aircraft velocity
V_E	parameter defined by equation (7)
x,y,z	fixed coordinate system; east, north, and above ground, respectively
$x_1,y_1,-z_1$	coordinate system alined with wave normal
$\beta = \sqrt{m^2 - 1}$	
γ	ratio of specific heats
γ_o	aircraft climb angle
θ	angle from horizon of ray
θ_o	initial angle from horizon of ray
μ	Mach angle, $\sin^{-1}\frac{1}{M}$
ν	heading angles
ξ	linear phase

ξ_1	actual phase
ρ	air density
ρ_o	initial air density
Φ	velocity potential
Φ_x	derivative of velocity potential with respect to x
ϕ	azimuth angle (see fig. 2)
ϕ_r	azimuth angle of wave normal relative to aircraft
τ	age variable defined by equation (11)

DISCUSSION

Ray Tracing

The first three topics are concerned with linear geometric acoustics. Ray tracing is tracing of the waves as they propagate through the stratified atmosphere. In geometric acoustics, the signal essentially follows wave fronts as given by

$$c_n = a + \bar{n} \cdot \bar{u} \tag{1}$$

and as illustrated in the following sketch:

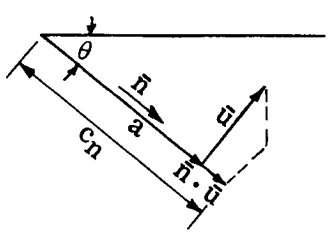

where a is the speed of sound, θ is the angle from the horizon of the ray, $\bar{n}$ is the unit vector normal to the wave front, and $\bar{u}$ is the wind vector velocity.

The ray velocity may then be given by

$$\frac{d\bar{r}}{dt} = \bar{c} = a\bar{n} + \bar{u} \tag{2}$$

Equation (2) could be integrated for the rays if the value of $\bar{n}$ was known, but this value, in general, is not known. An expression relating $\bar{n}$ to the changes in the speed of sound and the wind velocity is

$$\frac{d\bar{n}}{dt} = \nabla a + (\nabla\bar{u}) \cdot \bar{n} - \bar{n}\left[\bar{n} \cdot \nabla a + \bar{n} \cdot (\nabla\bar{u}) \cdot \bar{n}\right] \tag{3}$$

The simultaneous solution of equations (2) and (3) is required, and these equations constitute a fifth-order system.

In the present method, if a stratified atmosphere is assumed, so that the wind is horizontal and the temperatures and density are also known in stratified layers, then equation (3) can be reduced to a form of Snell's law of geometrical optics. For use herein, Snell's law then appears as

$$\frac{\bar{n}'}{c_n} = \frac{\bar{i}\cos\theta}{c_n} = \text{Constant along each ray} \tag{4}$$

where $\bar{n}'$ is the horizontal component of $\bar{n}$.

The ray equations, obtained from the simultaneous solution of equations (2) and (4), then appear as

$$\left.\begin{aligned} \frac{dx}{d(-z)} &= \frac{a\cos\theta\sin\nu - u_x}{a\sin\theta} \\ \frac{dy}{d(-z)} &= \frac{a\cos\theta\cos\nu - u_y}{a\sin\theta} \\ \frac{dt}{d(-z)} &= \frac{1}{a\sin\theta} \end{aligned}\right\} \tag{5}$$

where u_x and u_y are the horizontal wind components and ν is the heading angle. The vertical distance z has been chosen as the independent parameter in place of t, since most of the input data are known as a function of altitude. These equations may be solved by quadrature, and in this quadrature Snell's law can be applied.

Now, one remark on the minus sign in front of the wind velocity components, u_x and u_y. It has been said that "the north wind doth blow and we shall have snow." There is a meteorological convention that a wind that blows in the direction of south is called a north wind, so u_y is positive for a north wind and that is the only reason a minus sign is used on these components.

Blokhintsev Invariant

In the preceding section, the path of the acoustic waves was traced, but none of the important parameters, such as the pressure variation down the rays, have been related. For a stationary atmosphere, Rayleigh derived an invariant as given below

$$\left(\frac{\rho q^2}{2} + \frac{\Delta p^2}{2\rho a^2}\right) A_n a$$

or

$$\rho q^2 A_n a$$

where ρ is the air density, q is the perturbation velocity, A_n is the area of the ray tube normal to the rays, and a is the speed of sound. For a moving atmosphere, Blokhintsev derived an analogous invariant expression

$$\frac{\rho q^2 c_n}{a} \bar{c} \cdot \bar{A} = \rho q^2 A c_n \sin \theta \tag{6}$$

where A is the horizontal component of the area of the ray tube. Using the horizontal component of the area is more natural, since the problem is defined in terms of a horizontally stratified atmosphere.

Finally, for later use, a new invariant parameter V_E is introduced and defined as

$$\left.\begin{aligned} V_E{}^2 &= \frac{1}{c_o}\left(\rho q^2 A c_n \sin \theta\right) \\ \text{or} \qquad & \\ V_E &= \frac{q}{a}\left(\rho a^2 A \sin \theta \cos \theta\right)^{1/2} \end{aligned}\right\} \tag{7}$$

Ray-Tube Area

In equation (7), the ray-tube area is of fundamental importance, and an expression for the area must be determined. In figure 2 is depicted a two-parameter family of rays required to define a ray-tube area. One parameter is the azimuth angle ϕ which is measured with respect to the aircraft path in the direction the ray is considered to go. The other is the time t measured by a clock on the aircraft at the instant the ray is emitted. The precise definition of this ray-tube area may be given in terms of a Jacobian taken at constant altitude, so that it is a Jacobian of the horizontal coordinates x and y, taken with respect to the two ray-tube parameters, t and ϕ. The final expression for ray-tube area for a maneuvering aircraft is given as

$$
\begin{aligned}
A = {} & \left[\left(1 + \frac{\sin \gamma_o}{\sin \mu \sin \theta_o}\right)\left(I_2 - u_{t_o} I_1\right) - \frac{V \sin \phi \cos \mu \cos \gamma_o}{\cos \theta_o} I_1\right] \frac{\partial c_o}{\partial \phi} \\
& - \left[\left(1 + \frac{\sin \gamma_o}{\sin \mu \sin \theta_o}\right)\left(I_3 - u_{t_o} I_2\right) - \frac{V \sin \phi \cos \mu \cos \gamma_o}{\cos \theta_o} I_2\right] \frac{\partial \nu}{\partial \phi} \\
& + \left(\frac{\partial c_o}{\partial t_a} \frac{\partial \nu}{\partial \phi} - \frac{\partial c_o}{\partial \phi} \frac{\partial \nu}{\partial t_a}\right)\left(I_1 I_3 - I_2^2\right)
\end{aligned}
\tag{8}
$$

where

$$
I_1(-z) = \int_{-z_o} \frac{\cos^3 \theta \, d(-z)}{a^2 \sin^3 \theta}
$$

$$
I_2(-z) = \int_{-z_o} \frac{u_t \cos^3 \theta \, d(-z)}{a^2 \sin^3 \theta}
$$

$$
I_3(-z) = \int_{-z_o} \left(\frac{u_t^2 \cos^3 \theta}{a^2 \sin^3 \theta} + \frac{\cos \theta}{\sin \theta}\right) d(-z)
$$

and where γ_o represents the aircraft climb angle (γ in ref. 1), $c_o = \frac{c_n}{\cos \theta}$, and $\mu = \sin^{-1}\left(\frac{1}{M}\right)$.

If the aircraft were in straight and level flight, then locally, at least, the ray-tube area would simply be proportional to the distance away from the flight path, so the

ray-tube area would be expected to have terms that are proportional to a quadrature, an integral taken from the aircraft downward. But now, because of maneuvering in which the state of the aircraft changes as t_a changes, the orientation of these two rays at a later time may be different from the orientation of the two rays at an earlier time.

After quite a bit of algebra, a ray-tube area in the form of equation (8) is derived in terms of the three quadratures I_1, I_2, and I_3. These are taken from the aircraft position downward toward the ground. The terms in the first two lines of equation (8) are linear in the quadrature, and no terms which depend upon the maneuver are present. In the third line, there is a term with derivatives with respect to t_a and a factor which is quadratic in the quadrature; these third-line terms are required for the maneuver calculations.

The path of a ray as it propagates through the variable atmosphere and how its pertinent quantities will change during the travel of the acoustic wave have been discussed. The next section is concerned with connecting this system of rays to the aircraft.

Flow Near the Aircraft

The initial conditions must be obtained from a study of the flow near the aircraft which is a well-established theory. The velocity potential for a body of revolution may be given as

$$\Phi = -\frac{1}{2\pi}\int_{-\infty} \frac{S'(x_o)dx_o}{\left[(x - x_o)^2 - \beta^2(y - y_o)^2 - \beta^2(z - z_o)^2\right]^{1/2}}$$

where x_o, y_o, and z_o denote the source points and x, y, and z denote the field points. The denominator may be factored into two terms, one term proportional to the distance from the flight path and a second term, containing a parameter proportional to the shape of the body of revolution, which has historically been termed the "F" function. The velocity is obtained from

$$-\Phi_x = \frac{1}{M^2}\frac{q}{a} = \frac{1}{(2\beta r)^{1/2}} F_i(x - \beta r, \phi_r) = \frac{1}{M^2 r^{1/2}} F(x - \beta r, \phi_r) \tag{9}$$

where

$$F_1(x - \beta r, \phi_r) = \frac{1}{2\pi}\int_{-\infty}^{x-\beta r} \frac{S''(x_1, \phi_r)dx_1}{(x - \beta r - x_1)^{1/2}}$$

which is analogous to the Whitham "F" function. In this expression, S is the cross-sectional area for a body of revolution, but for a body with lifting surfaces, for instance, it is an effective cross-sectional area, as discussed in reference 1.

Through the perturbation velocity q/a, V_E and F can now be related. In equation (7), V_E is given in terms of q/a, and F is related to q/a in equation (9). After the necessary algebra, the relation between V_E and F is given as

$$V_E = \left(\frac{\rho_o a_o^2 \cos \mu \cos^2 \theta_o}{\sin \mu}\right)^{1/2} F \tag{10}$$

Age Variable

The analysis thus far has been linear; now the nonlinear aspects must be introduced so that a realistic shock-wave structure can be obtained. For this an age variable, given in equation (11), will be introduced.

The propagation velocity, equal to $\bar{c} = a\bar{n} + \bar{u}$ in the undisturbed fluid, is changed by $(\Delta a + q)\bar{n}$, where Δa is the perturbation in the speed of sound. This quantity is defined by

$$\Delta a = \frac{\gamma - 1}{2} \frac{\Delta p}{\rho a} = \frac{\gamma - 1}{2} q$$

so that the change in propagation velocity is simply $\frac{(\gamma + 1)q\bar{n}}{2}$.

If the phase were expressed as distance s measured backwards normal to the wave fronts, the signal would experience a phase shift arising from the change in propagation velocity given by

$$\frac{ds}{dt} = -\frac{\gamma + 1}{2} q$$

where t is time along the ray defined in equation (5).

In treating the phase, distinction must be made between the actual phase variable and the linear-theory phase variable. The nonlinear effect is basically the difference between the two. The actual phase is termed ξ_1 and the linear phase is ξ. The local distance phase s is related with ξ_1 by $ds = c_n \, d\xi_1$. The expression for the change in propagation velocity in terms of ξ_1 becomes

$$\frac{d\xi_1}{dt} = -\frac{\gamma + 1}{2} \frac{q}{c_n} = -\frac{\gamma + 1}{2} \frac{q}{c_o \cos \theta}$$

This equation describes the phase shift for a particular point on the signal. The point on the signal found at ξ according to the linear theory is actually found at ξ_1, which is a function of ξ and t.

The perturbation velocity q can be expressed in terms of V_E by using equation (7) to obtain

$$\frac{d\xi_1}{dt} = -\frac{\gamma + 1}{2c_o} \frac{V_E}{\cos\theta(\rho A \sin\theta \cos\theta)^{1/2}}$$

The variable t may be replaced by -z by using equation (5). To transform the equation for the phase shift to a canonical form, the age variable τ is introduced; this age variable is defined by

$$\tau = \frac{\gamma + 1}{2c_o} \int_{-z} \frac{d(-z)}{a \sin\theta \cos\theta(\rho A \sin\theta \cos\theta)^{1/2}} \tag{11}$$

The phase shift is then governed by

$$\frac{d\xi_1}{d\tau} = -V_E\left(\xi_1, \tau\right) \tag{12}$$

in the canonical form desired.

With the basic assumption that the linear results for the ray-tube area and Blokhintsev invariance still hold with only the phase shifted, the following relationship holds:

$$V_E\left(\xi_1, \tau\right) = V_E(\xi) \tag{13}$$

where $V_E(\xi)$ is the linear solution (independent of t or τ because of the invariance). Here the actual phase ξ_1 satisfies equation (12) at constant ξ and also the initial condition $\xi_1 = \xi$ at $\tau = 0$. The solution of equation (12) is then

$$\xi_1 = \xi - \tau V_E(\xi) \tag{14}$$

The linear phase ξ is a function of ξ_1 and τ, which may become multivalued in ξ_1. When τ is multivalued, equations (13) and (14) must be modified to take into account the presence of shock waves.

In a uniform atmosphere, τ is proportional to the distance to the one-half power, whereas in an actual layered atmosphere, τ is given by a convergent instead of divergent

integral. (See eq. (11).) Now, the fact that τ is given by a convergent integral means that it has a definite upper bound, and thus the signal never gets older than a certain age. This means that the signal freezes and approaches an asymptotic shape. No matter how far the signal progresses, it never gets any more distorted than this asymptotic distortion.

Sonic-Boom Signatures

The analysis is now complete and the resultant shock wave or sonic-boom signature can be defined. In figure 3 is shown a progression of curves needed in developing the signature. The top curve, $V_E(\xi)$, is obtained by use of equation (10) from a knowledge of the F function and is plotted against ξ. Utilizing the transformation of equation (14), the curve appears as indicated in the second curve, which is essentially a shift in phase and is multivalued. Because the compression parts of the signal move faster than the speed of sound relative to the medium, the resultant signal is distorted. The high-pressure parts of the signal move toward the head of the wave and the low-pressure parts move toward the rear of the wave.

Eventually this curve will fold over. This folding over will indicate that at a given point in the signal three different values can be obtained, and this, of course, is physical nonsense. Actually, what happens is that a shock wave appears, and this shock wave may be shown to appear where equal areas occur; that is, by using the equal-area rule, the location and strength of the shock can be obtained. A convenient method of locating the equal areas is shown in the third curve of figure 3, which is essentially the integration of V_E. By using the crossing of the upper branch of the curve, the location of the shock wave is obtained, and the final signature is shown on the bottom curve.

RESULTS

The foregoing analysis has been applied to a specific aircraft, and the results are shown in figure 4. Two examples are given, one for the aircraft flying at $M = 1.4$ at 35 000 feet, and the second for $M = 3.0$ at 70 000$^+$ feet. The shaded area represents the experimental results and the dashed curve represents the analytical results. Two different atmospheric inputs were used in this analysis, one was a uniform atmosphere to which was applied a standard correction factor which approximated the effects of a standard atmosphere; the second input was the standard atmosphere. For both inputs, good correlation with experimental data, with regard to the magnitude of the pressure, was shown; however, the standard-atmosphere input gave much better agreement with regard to signature length. This method has also been used for maneuvering aircraft by Haefeli, as reported in reference 2.

CONCLUDING REMARKS

A method for predicting the sonic-boom signature due to a maneuvering aircraft has been presented. This method includes the effects of a variable, stratified atmosphere. The method is based on geometric acoustic principles and accounts for the use of a non-linearity to account for the weak shock field. The analytical results have been compared with experimental data and excellent agreement has been shown, particularly with regard to signature length.

REFERENCES

1. Hayes, Wallace D.; Haefeli, Rudolph C.; and Kulsrud, H. E.: Sonic Boom Propagation in a Stratified Atmosphere, With Computer Program. NASA CR-1299, 1969.
2. Haefeli, Rudolph C.: Sonic Boom Propagation From Maneuvering Aircraft. AIAA Pap. No. 69-1134, Oct. 1969.

PROBLEM DEFINITION

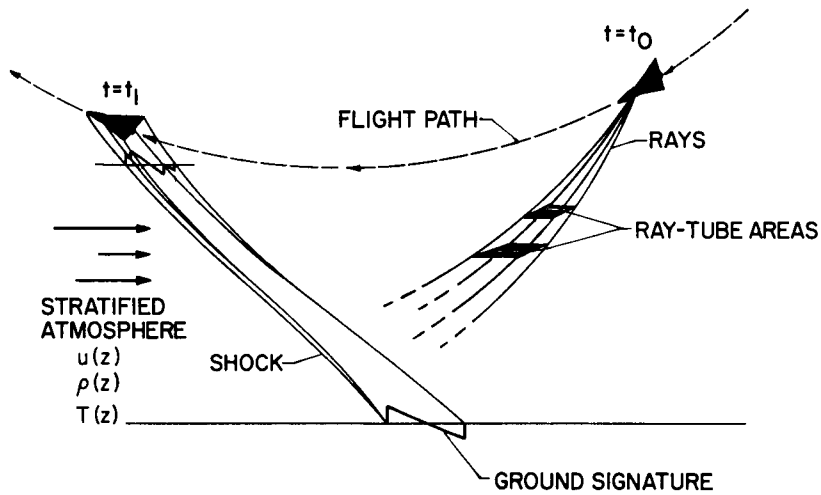

Figure 1

RAY-TUBE AREA

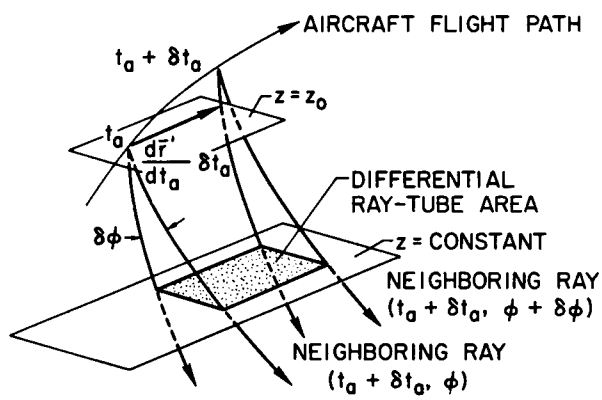

$$A(t_a, \phi, z) = \frac{1}{c_0} \begin{vmatrix} \frac{\partial x_1}{\partial t_a} & \frac{\partial y_1}{\partial t_a} \\ \frac{\partial x_1}{\partial \phi} & \frac{\partial y_1}{\partial \phi} \end{vmatrix}$$

Figure 2

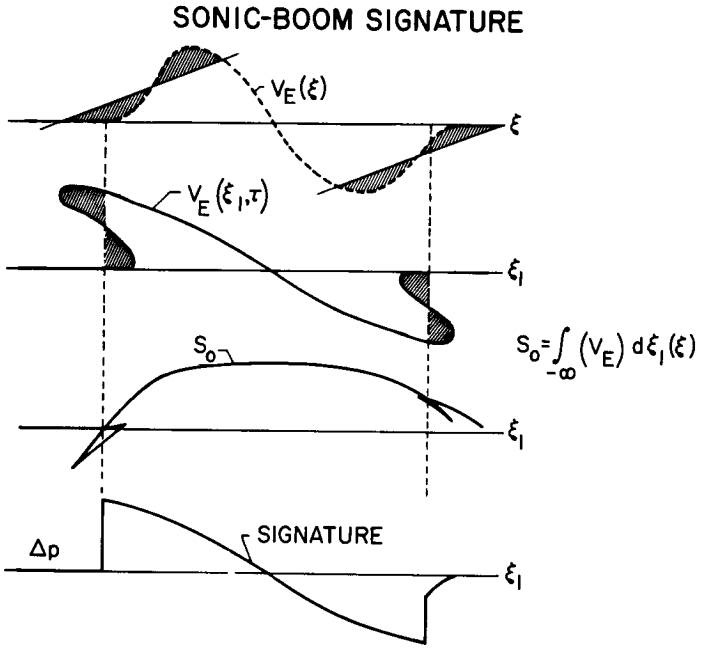

Figure 3

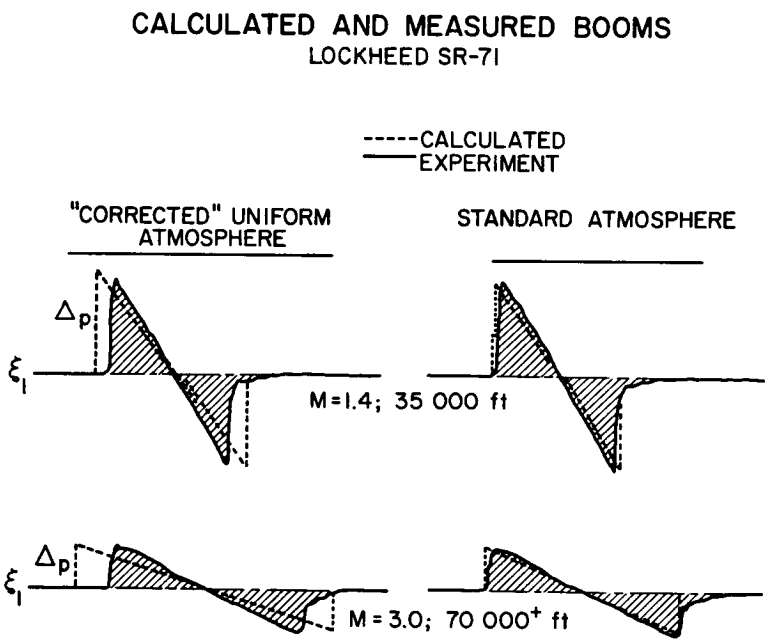

Figure 4

DISCUSSION

ALFRED GESSOW, NASA, Washington: Applying this method to a practical case, to what extent is the maximum overpressure affected by a nonuniform atmosphere as compared with a uniform atmosphere?

HAYES: Well, if you take a uniform atmosphere you get completely the wrong results, so these have to be corrected, and they are usually corrected by putting in the corrected acoustic impedance. In the atmosphere which is at a constant temperature, which is the simplest case, the correction factor is simply the square root of the pressure ratio.

Now, if you compare the uniform atmosphere method with this method for a constant-temperature atmosphere, what you would come up with is that the area under the lobe would be the same with both methods, and so, since the uniform atmosphere method would give you too large a signal range to the N wave, it would give you too low a value for the overpressure by a small amount. The differences are not very great.

GESSOW: I guess what was in back of my question was someone's suggestion that since there is quite a difference in temperature distribution in the atmosphere, one might take advantage of this and fly a path, in the practical case, so as to minimize the boom signature. However, if these effects are not that great, then such a scheme may not be too practical.

HAYES: Yes, I don't think we can get away from the boom that easily.

LORNE C. DUNSWORTH, CCI Marquardt Corp.: Is the ground reflection factor essentially 2?

HAYES: Well, the theory will give you 2. In practice various people use 1.9 or something like this. As far as I know there is no theoretical reason to use 1.9 instead of 2 so the justification for using 1.9 instead of 2 is purely empirical, I don't like it, but this is the way I am trained. I don't like things empirical.

AN ANALYSIS OF FINITE-DIFFERENCE TECHNIQUES APPLIED TO EQUATIONS GOVERNING CONVECTIVE TRANSFER

By Harvard Lomax

Ames Research Center

N70-21365

SUMMARY

A study is presented of fixed-mesh, finite-difference techniques as they apply to the numerical calculation of hyperbolic partial differential equations. Effects on diffusion or dissipation and dispersion are considered.

INTRODUCTION

A survey of the presentations made at this conference points clearly to the fact that the development of numerical wind tunnels for practical airplane shapes is emerging as a reality. One aspect of this development is the possibility of constructing finite-difference techniques that can, by means of a computer, proceed directly from the basic partial differential equations and boundary conditions to the solution for the entire flow field. The technical journals contain many papers giving results of such solutions for a variety of techniques. We have investigated some of these methods to see if there was in some sense a "best" one to use for a given aerodynamic problem posed in the Eulerian system. The purpose here is to review briefly some of the results of this investigation.

PROBLEM DEFINITION

One can ask: What is the best way to numerically analyze a set of differential equations? If we seek to attach any generality to the answer, some testing procedures must be constructed that are representative enough to serve as a common denominator for the various techniques that can be posed. Tests for ordinary differential equations are comparatively easy to construct. For example, the numerical integration of $u' \equiv du/dt = \sigma u + e^{\mu t}$ by any given differencing technique enables one to classify that technique with respect to all others when applied to the coupled set

$$\vec{u}' = [A]\vec{u} + \vec{f}(t) \tag{1}$$

where the elements of [A] are constants. Here, by classify, we mean specifically to predict in a solution: (1) the accuracy given to the driving eigenvalues of [A]; and (2) the bound on the parasitic eigenvalues.

The situation is much more complicated in the case of partial differential equations. In such cases it appears to be necessary to prescribe more about the physical nature of the problem being solved before attempting to analyze, let alone optimize, a numerical method that might be applied to it. The following is an attempt to describe some broad classes of problems that occur in the study of the partial differential equations governing fluid dynamics, each class having peculiarities which make the "best" choice of numerical procedure peculiar to it.

Initial and Boundary Conditions

One categorization of fluid flow problems applies to the type of restraints imposed on the various surfaces of contact. Three quite different sets of conditions arise. One leads to the study of transient phenomena in which, by definition, the initial and boundary conditions play about equally important roles. These are probably the hardest problems of all from the numerical viewpoint, and they are not discussed directly in this report. Another leads to the study of periodic phenomena in which the initial conditions prevail throughout the complete time history of the solution. A certain class of these problems leads to the least numerical difficulties and is given the most attention in the following discussion. Finally, another set leads to the study of steady-state problems in which, by definition, the final solution is independent of the initial conditions or any transient behavior, and depends, therefore, only on the boundary condition. These problems lead to interesting numerical concepts that are often discussed under the name "relaxation," but, for want of space, will not be considered here.

Each of the above categories is most efficiently analyzed by a different numerical procedure; the reason being most effectively illustrated by examining equation (1). Its solution can be written in the form

$$u = \sum \vec{C} e^{\sigma_j t} + \text{P.S.} \tag{2}$$

where $\sum \vec{C} e^{\sigma_j t}$ is the complementary solution, which is independent of $\vec{f}(t)$, and P.S. refers to the particular solution. In the transient case both solutions must be resolved with equal accuracy; hence, its relative difficulty. The periodic cases considered in the following are those in which $\vec{f}(t)$ is zero so that the particular solution disappears. In actual practice this represents a great simplification in the numerical adaptation of the boundary conditions. Finally, the steady-state cases (as defined in the above) are those for which $\vec{f}$ is independent of t and the final solution is identical to the particular solution which is

$$u = [A]^{-1}\vec{f} \tag{3}$$

In this case the complementary solution disappears and all the eigenvalues σ_j are parasitic.

Genuine and Weak Solutions

Most of the analysis of numerical methods applies to linear equations. Since the actual partial differential equations of interest in fluid flow are generally not linear, the qualification is generally made that they can be considered to be locally linear; and, in that sense, they can be relied upon to respond in a predictable way to a given differencing scheme. The usual procedure is to choose a numerical method that has a given order of accuracy on the basis of a local Taylor series expansion and, furthermore, satisfies some stability requirement in the linearized framework. With the added realization that one must also satisfy a dispersion requirement (discussed in the next section) this approach is usually practicable and is widely accepted when the dependent variables describing the flow field are everywhere continuous.

In most regions of a fluid flow the variables are continuous and the mathematical solution in those regions is referred to by Lax (ref. 1) as genuine. However, if supersonic flows occur, shocks appear and surfaces along which the dependent variables are discontinuous must be admitted. Lax refers to the mathematical description of such phenomena as weak solutions. Quite different numerical methods are recommended depending upon whether or not the desired solution is purely genuine. Both cases are considered but, at this point, the problem of calculating flows with shocks is considered in more detail.

If a weak[1] solution exists in the region of numerical calculation two possibilities arise: in one, the location of the discontinuity is in some way determined and the differencing formulas are never permitted to use values on both sides at once; in the other, the differencing formulas are allowed to cross the discontinuities (thereby locating them automatically) but in such a way as to limit the resulting errors. Only the latter is considered below.

Figure 1 shows what can be expected if one tries to represent a discontinuity by a set of continuous functions. One period of a periodic step wave is shown together with its representation by 3 to 11 harmonics from a Fourier series. The gross representation of the step wave is clear, but the local errors, caused by the omission of high-frequency terms, can be a sizable percentage of the jump at the discontinuity. Furthermore, the local error is not limited to the location of the jump, but is spread over the entire step, about equally for the number of harmonics shown. Examples of how particular differencing schemes calculate a moving periodic step wave are given later.

Dissipation and Dispersion

Consider the equation

$$\frac{\partial u}{\partial t} = a_1 \frac{\partial u}{\partial x} + a_2 \frac{\partial^2 u}{\partial x^2} + a_3 \frac{\partial^3 u}{\partial x^3} \tag{4}$$

[1]The term "weak", rather than "shock", is used because the formulas given by Lax provide the strength and location of any discontinuous solution of which the Rankine-Hugoniot is only one.

If at $t = 0$ the initial condition $u = e^{i\omega x}$ is imposed, the oscillatory solution

$$u = \exp\left\{-a_2\omega^2 t + i\omega\left[x + \left(a_1 - a_3\omega^2\right)t\right]\right\} \tag{5}$$

results. If a_3 is zero, the term a_1 is the speed of convection of u or the wave speed. It is also, in such a case, the slope dx/dt of the characteristic in the xt plane. Clearly, from a glance at equation (5), a_2 controls the damping of the solution. In heat conduction problems a_2 is referred to as the diffusion coefficient. In the Navier-Stokes equations, when multiplying terms in which u represents a velocity, it is referred to as the coefficient of viscosity. The term a_3 is a measure of dispersion or phase shift. When a_3 is not zero, the wave speed is $\left(a_1 - a_3\omega^2\right)$ which differs for each ω, that is to say, for each initial frequency.

If a_2 in equation (4) is zero, the equation is said to be conservative for u. Let the real part of equation (5) be the solution and let u^2 be representative of the "energy" of the system. If a_2 is zero, the "energy" is conserved and

$$\int_0^{2\pi/\omega} u^2 \, dx = \frac{\pi}{\omega} \tag{6}$$

regardless of t.

Of course conservation laws are extremely important to the physicist. In fact the partial differential equations for fluid dynamics represent the conservation of mass, momentum, and energy. Because of this, most modern numerical techniques used to solve conservative systems are constructed so that the *difference* equations are also conservative. That is to say, some summation (i.e., numerical integration) of certain components over the space mesh is forced to be invariant with the timewise calculation. The point to be made here is that such techniques control the gross effects of terms such as that containing a_2 in equation (4) -- that is, they are numerically stable and nondissipative; but they have no such control on terms such as that containing a_3. This we see at once because the integral in equation (6) is not only invariant with t but also with a_3. In short, conservative differencing methods tend to force all of their numerical error into dispersion.

THE SIMPLEST REPRESENTATIVE CONVECTION EQUATION

The simplest partial differential equation containing convective phenomena is

$$\frac{\partial u}{\partial t} = -c\,\frac{\partial u}{\partial x} \tag{7}$$

It has been used as a representative equation by many authors and is

sufficiently profound to display many of the difficulties involved in the numerical calculation of fluid flow. If c is a constant and periodic boundary conditions are imposed, any initial variation of u is transmitted in time as a wave with velocity c in the x-direction (see eq. (5)). In the following we consider two kinds of such waves: one, simple harmonic waves moving from left to right as time proceeds (the direction is given to fix the phase shift); and the other, a step wave whose harmonic analysis is shown in figure 1.

If c in equation (7) is set equal to u, a nonlinear equation results which is often used (ref. 1) as a model that is representative of the nonlinear, shock-like phenomena contained in fluid flow problems. In the following it is used to analyze a single, nonperiodic, weak solution moving from left to right as time proceeds.

TIME-CONTINUOUS METHODS

There are two distinct approaches to the numerical calculation of equation (7) in conventional fixed-step meshes. The choice of one or the other depends mostly on whether or not the conditions are such that a weak or "shock-like" solution is contained in the answer. In this part we survey methods that are appropriate for problems whose solutions are entirely genuine.

If the right side (space derivatives) of equation (7) is replaced by some discrete differencing scheme but the left side (time derivative) is allowed to remain continuous, the equation reduces to a set of coupled ordinary differential equations identical to equation (1). If c is a constant, the solution to these equations is given by equation (2) in which P.S. is zero if the boundary conditions are periodic. We note that the solution is critically dependent upon the eigenvalues σ_j.

Consider the following simple differencing scheme for the right side of equation (7)

$$\left(\frac{\partial u}{\partial x}\right)_j \approx \frac{1}{2\Delta x}\left[-(1 + \beta)u_{j-1} + 2\beta u_j + (1 - \beta)u_{j+1}\right] \tag{8}$$

If the constant β is taken to be -1, 0, or +1, equation (8) represents a forward, central, or backward differencing scheme, respectively. The *order* of the error term is the same for all nonzero β, but the eigenvalue structure of [A] is drastically altered by various choices of β in the region indicated. In fact, the real parts of the σ_j can be positive, negative, or zero, depending on the value chosen for β. All of this takes place without any regard for the physical nature of the problem.

However, the situation is clarified if we ask not what is the error introduced by replacing $\partial u/\partial x$ in equation (7) with equation (8), but what is the exact equation solved by the difference-differential combination? This latter equation turns out to be

$$\frac{\partial u}{\partial t} = -c\,\frac{\partial u}{\partial x} + \frac{c\beta\Delta x}{2}\,\frac{\partial^2 u}{\partial x^2} - \frac{c\Delta x^2}{6}\,\frac{\partial^3 u}{\partial x^3} + \ldots \tag{9}$$

It is easy to show that all even derivatives in this equation are multiplied by β and all odd ones are independent of β. Comparing with our previous discussion of equation (4), we see that any nonzero choice of β introduces a dissipation or diffusion term into the equation actually being solved, a term that is completely alien to the nature of the physical situation modeled by the original equation (7).

We have now arrived at an important point. If β is set equal to zero and equation (8) replaces the space derivative in equation (7), a numerical technique has been constructed that guarantees the conservation of "energy" in the sense discussed in equations (4) through (6). Combined with an appropriate timewise numerical integration, the method is stable and nondiffusive. It is apparent, however, that a wave of frequency ω which travels in the x-direction with the speed c in an exact solution, will travel with a speed approximately equal to $c[1 - (\omega^2\Delta x^2)/6]$ in the numerical computations. The entire error in the space differencing appears in dispersion. In the simple problem being considered all central differencing schemes for $\partial u/\partial x$ are conservative, the higher the order, the less the error in dispersion.

In order to illustrate the above discussion it is necessary to discuss the error brought about by the numerical integration of the time variable in the intermediate, time-continuous form that arises after the spare derivatives are made discrete. One of the principal reasons for approaching the problem from this point of view is that this kind of integration (i.e., the numerical solution of coupled ordinary differential equations) has been so thoroughly analyzed. Application of methods such as the Runge-Kutta (or any other explicit, one-root method) to equation (1) reduces that expression to a set of difference equations the solution of which, after n time steps of Δt, can be written

$$\vec{u}_n = \sum \vec{c}(\lambda_j)^n + \text{P.S.} \tag{10}$$

where each λ_j is related to a corresponding σ_j in equation (2) by a polynomial of the form

$$\lambda_j = 1 + b_1(\sigma_j\Delta t) + b_2(\sigma_j\Delta t)^2 + \ldots + b_k(\sigma_j\Delta t)^k \tag{11}$$

The b_k depend on the particular method, and for maximum accuracy are made to be $1/k!$ in which case λ_j is equal to a truncated Taylor series expansion of $e^{\sigma_j\Delta t}$.

Here we need only consider the time-continuous form of equation (7) in which some central differencing scheme has been used for $\partial u/\partial x$ and periodic boundary conditions applied. In such a case all the σ_j are imaginary, and a

fourth-order Runge-Kutta method provides the relationship between λ_j and $\bar{\sigma}_j\Delta t$ shown in figure 2 (note that $\sigma_j = i\bar{\sigma}_j$). It is clear from inspecting equation (10) that the time integration introduces no dissipation for $|\lambda_j| = 1$, and is unstable for $|\lambda_j| > 1$. If $|\lambda_j| < 1$, dissipation is introduced by an amount depending upon how much less than one it is. If we study figure 2 with these remarks in mind, we arrive at the following conclusions regarding the effect of applying the fourth-order Runge-Kutta method to the problem posed:

1. For small enough Δt there is practically no dissipation (< 1 percent after 700 steps if $\bar{\sigma}\Delta t \leq 0.3$).

2. Any frequency such that $\bar{\sigma}\Delta t \approx 2.6$ is heavily damped.

3. For a spectrum of frequencies such that $\bar{\sigma}_{max}\Delta t \approx 2.6$, the method acts as a low-pass filter, heavily damping the high frequencies without affecting the low ones.

Finally, before the illustrations are presented, something should be said about the ratio of step sizes $\Delta t/\Delta x$. In classical studies of the numerical solution of equations similar to equation (7), considerable importance is attached to the term $\nu \equiv c\Delta t/\Delta x$, which is often referred to as the Courant number. The condition is often imposed that ν must be less than or equal to one. Physically we must recognize that a "domain of dependence" exists in hyperbolic partial differential equations and the above condition is based on that concept. In the following, ν will be presented as high as 2.5 with quite acceptable results. This comes about, however, because the Runge-Kutta type methods used for the time integration are sequences of predictor-corrector formulas and the value of ν is not connected to the characteristic cones in the usual way. Actually, in no case presented did the numerical method violate the principle involved in the "domain of dependence."

Figure 3 shows the effect of dispersion caused by a three-point central differencing of $\partial u/\partial x$ in equation (7), c being a constant. The exact solution

$$u = \sin 6\pi(x - ct)$$

is shown by the solid line between $x = 0$ and 1.0 after 200 and 500 time steps had been integrated using a fourth-order Runge-Kutta method. In the x differencing 50 x points (excluding the last point) were used so $\Delta x = 1/50$. Since Δt was chosen such that $c\Delta t/\Delta x = 1$, $6\pi c\Delta t = 6\pi/50 \approx 0.38$. This is representative of $\bar{\sigma}\Delta t = 0.38$ in figure 2, so practically no damping can be expected over several hundred time steps, and this is in fact verified. The dispersion, however, is quite evident.

Figure 4 shows how the dispersion can be minimized by increasing the order of the x-wise central differencing scheme, and figure 5 shows how dissipation can be brought about by increasing the time step so that $\bar{\sigma}\Delta t$ in figure 2 falls in an area for which $|\lambda_j|$ is significantly less than one.

Figures 6 through 8 show the effect of analyzing equation (7) by the Runge-Kutta method when the boundary conditions are periodic and the initial condition is a step wave. Figure 6 shows the results after t has been increased from 0 to 40 using, again, 50 equally spaced x points. In this case equation (8) was used for the x derivative and β was taken to be 0.0, 0.1, and 0.2 for the three cases shown. The effect of adding "artificial viscosity" in this fashion is evident and typical. Figure 7 shows the first 5 time steps in a method which puts no damping in the $\partial u/\partial x$ approximation (by choosing β in eq. (8) to be zero), but does put damping on the higher frequencies in the composition of the time dependency, by fixing Δt at a value such that $\sigma_{max}\Delta t$ in figure 2 is around 2.5. Figure 1 shows what happens when all of the high-frequency terms above the limits 3 through 11 are removed. Figure 7 illustrates the initial phase of their gradual removal. Figure 8 shows how such low-pass filtering methods resolve a periodic step wave after the same elapsed time as was used for the results presented in figure 6 for methods that damped all frequencies.

FIXED-MESH APPROXIMATIONS TO THE METHOD OF CHARACTERISTICS

If a problem contains both a genuine and a weak solution, the "best" numerical procedure would compute both solutions with a given accuracy as if the other were not present. A popular procedure for doing just that in two-dimensional and axisymmetric flows is the well-known method of characteristics. In two-dimensional, linearized flow-field analysis, the equispaced, fixed-mesh, second-order differencing scheme of Lax-Wendroff is identical to the method of characteristics when a parameter similar to the Courant number is set equal to one. In higher dimensional and nonlinear cases, such a correspondence does not exist. Nevertheless, the published results of a large number of investigators have shown that this method (or a variant of it) gives acceptable results under the more stringent conditions.

Almost all second-order fixed-mesh difference schemes in popular use (e.g., refs. 2 through 8) for calculating flows with embedded shocks are identical to the Lax-Wendroff method when applied to the very simple linear form given by equation (7). When applied to higher order or nonlinear equations, however, they have individual differences. Some of these methods were tested under common conditions, and the one recommended here, both from the point of view of accuracy in resolving a genuine as well as a weak solution, and simplicity in programming, is that presented by MacCormack (ref. 8). As applied to equation (7) it can be written in several predictor-corrector forms, one of which is

$$\left.\begin{aligned} \tilde{u}_j^{n+1} &= u_j^n - \frac{c\Delta t}{\Delta x}\left(u_{j+1}^n - u_j^n\right) \\ u_j^{n+1} &= \frac{1}{2}\left[\tilde{u}_j^{n+1} + u_j^n - \frac{c\Delta t}{\Delta x}\left(\tilde{u}_j^{n+1} - \tilde{u}_{j-1}^{n+1}\right)\right] \end{aligned}\right\} \tag{12}$$

When applied to the solution of the periodic wave shown in figure 3, equations (12) gave the results shown in figure 9. Again 50 x points were used. Various values of the ratio $c\Delta t/\Delta x$ were chosen and all five cases were run for the same total time, which was identical to that for the 200 time step case in figure 3. The low Courant numbers show nearly the same dispersion as in figure 3 and considerably more dissipation. The higher Courant numbers show very little dispersion or dissipation because here the method is approaching the method of characteristics which is exact.

The results of applying equations (12) to the periodic step wave are shown in figure 10 and are typical of the Lax-Wendroff methods for linear problems when the mesh points do not lie along the characteristics as time proceeds.

The important nonlinear case in which equation (7) is replaced by

$$\frac{\partial u}{\partial t} = - \frac{\partial (u^2/2)}{\partial x} \tag{13}$$

is illustrated in figure 11. The figures show how a discontinuity (or "shock") moves from left to right started by setting $u = 1.0$ on the upper level and $u = 0.0$ on the lower one. The upper two figures illustrate the behavior for time-continuous methods with damping entered through both the x and the t derivative as explained previously. The lower figure shows the results for MacCormack's method.

On the basis of these (and similar) tests MacCormack's version of the Lax-Wendroff method was used to analyze the conical flow field about a triangular wing mounted on a cone. A Mach number was chosen such that the wing edges were sonic, and the combination was placed at angle of attack. Both the compression and expansion sides (which, of course, are independent of one another) were computed. A typical result for the pressure distribution along the body and wing surface and vertically through the shock layer is shown in figure 12. Further preliminary details are presented in reference 9.

REFERENCES

1. Lax, P. D.: Weak Solutions of Nonlinear Hyperbolic Equations and Their Numerical Computation. Commun. Pure Appl. Math., vol. 7, 1954, pp. 159-193.

2. Richtmyer, Robert D.: A Survey of Difference Methods for Non-Steady Fluid Dynamics. National Center for Atmospheric Research Technical Note 63-2, Aug. 1962.

3. Lax, P. D.; and Wendroff, B.: Difference Schemes for Hyperbolic Equations With High Order of Accuracy. Commun. Pure Appl. Math., vol. 17, 1964, pp. 381-398.

4. Burstein, S. Z.: Numerical Methods in Multidimensional Shocked Flows. AIAA J., vol. 2, 1964, pp. 2111-2117.

5. Emery, A. F.: An Evaluation of Several Differencing Methods for Inviscid Fluid Flow Problems. J. Comp. Phys., vol. 2, 1968, pp. 306-331.

6. Fromm, J. E.: A Method for Reducing Dispersion in Convective Difference Schemes. J. Comp. Phys., vol. 3, 1968, pp. 176-189.

7. Lapidus, A.: A Detached Shock Calculation by Second-Order Finite Differences. J. Comp. Phys., vol. 2, 1967, pp. 154-177.

8. MacCormack, R. W.: The Effect of Viscosity in Hypervelocity Impact Cratering. Preprint 69-354, AIAA, Jan. 1969.

9. Kutler, P.: Application of Selected Finite Difference Techniques to the Solution of Conical Flow Problems. Ph.D. thesis, Iowa State University, 1969.

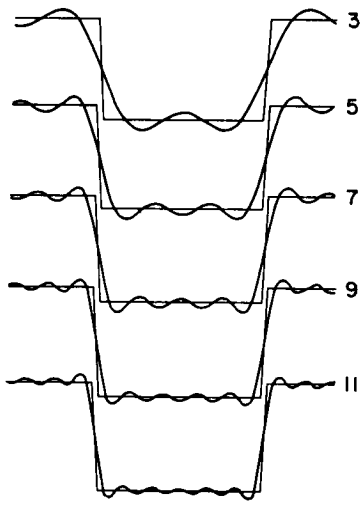

Figure 1.- Harmonic representation of a step.

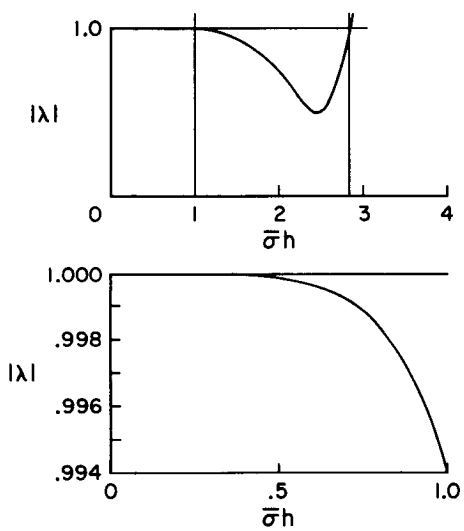

Figure 2.- The absolute value of the numerical root λ versus the product of the step size, h, and the absolute value of the time continuous root, $\bar{\sigma} \equiv |i\sigma|$, for the fourth-order Runge-Kutta method.

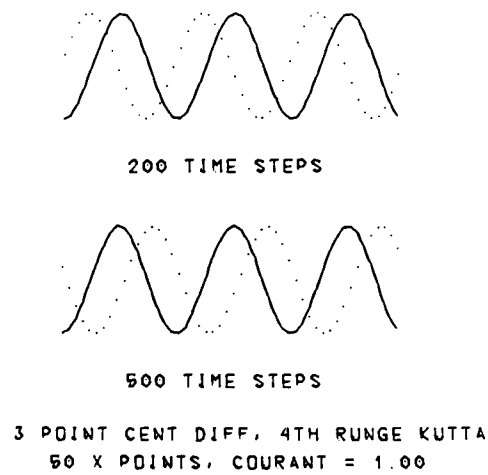

Figure 3.- Pure dispersion in a time-continuous method; solid line, exact method; dots, numerical.

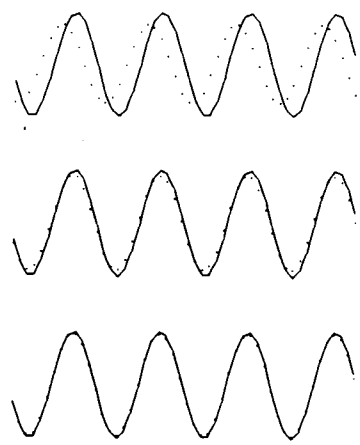

Figure 4.- Fourth-order Runge-Kutta time integration of a periodic harmonic wave defined by 50 x points. Top: $\nu \equiv c\Delta t/\Delta x = 2.5$, 3-point central difference. Center: $\nu = 2.0$, 5-point central difference. Bottom: $\nu = 1.6$, 7-point central difference.

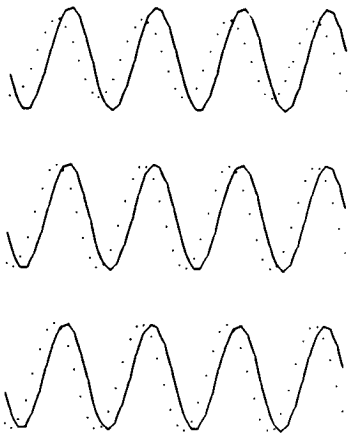

Figure 5.- Fourth-order Runge-Kutta time integration of periodic harmonic wave defined by 50 x points. All cases represent 3-point central difference. Top: $\nu = 2.5$. Center: $\nu = 1.6$. Bottom: $\nu = 0.8$.

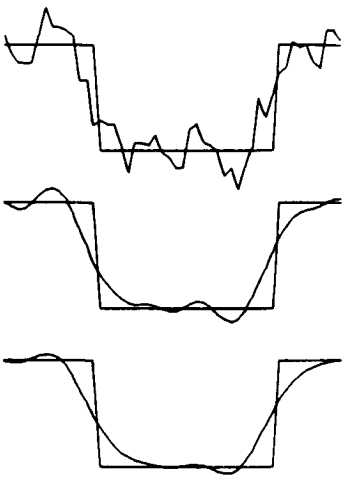

Figure 6.- Fourth-order Runge-Kutta time integration of periodic step wave defined by 50 x points. Results given for $\nu = 1.0$ after $t = 40\ c\Delta x$. Beta in equation (8) is 0.0 for top, 0.1 for center, and 0.2 for bottom.

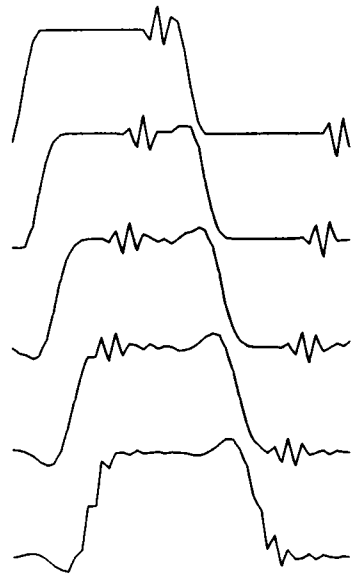

Figure 7.- Fourth-order Runge-Kutta time integration of periodic step wave defined by 50 x points using 3-point central differencing scheme and $\nu = 2.5$. Results shown after 1, 2, 3, 4, and 5 steps, top through bottom, respectively.

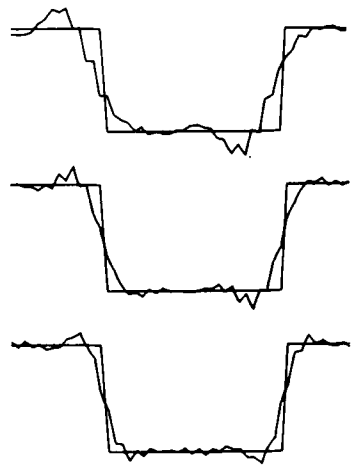

Figure 8.- Fourth-order Runge-Kutta time integration of periodic step wave defined by 50 x points. Top: $\nu = 2.5$, 3-point central differencing. Center: $\nu = 2.0$, 5-point central differencing. Bottom: $\nu = 1.6$, 7-point central differencing.

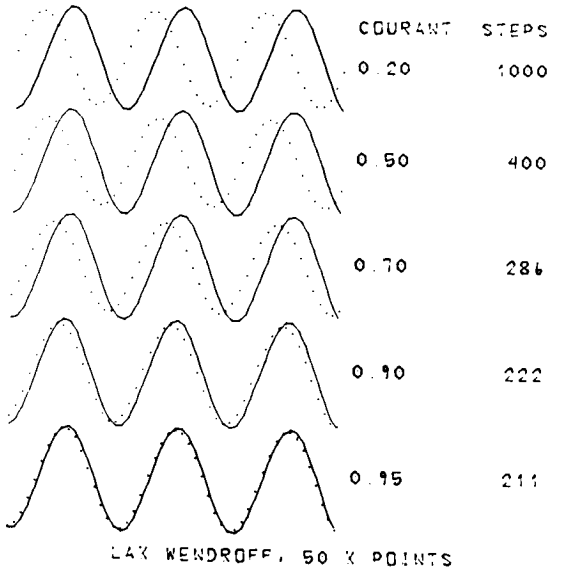

Figure 9.- Lax-Wendroff solution of periodic harmonic wave defined by 50 x points.

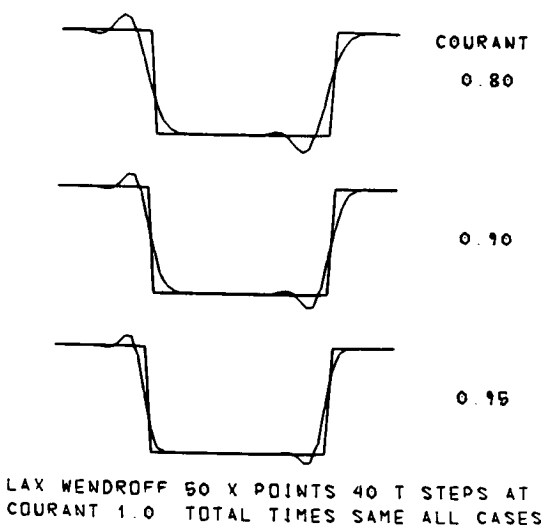

Figure 10.- Lax-Wendroff solution of periodic step wave defined by 50 x points.

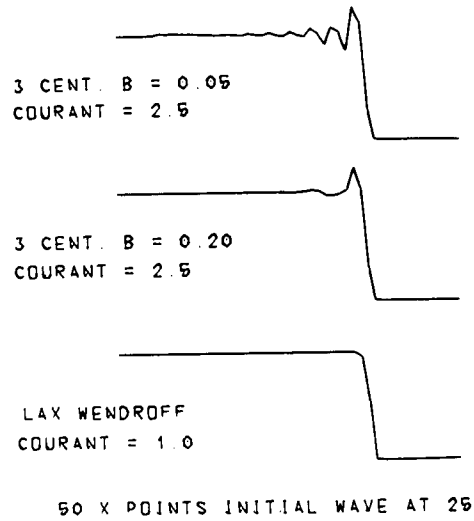

Figure 11.- Solutions of nonlinear equation (13). Top and central represent fourth-order Runge-Kutta integrations with various forms of damping. Bottom represents MacCormack's version of the Lax-Wendroff method.

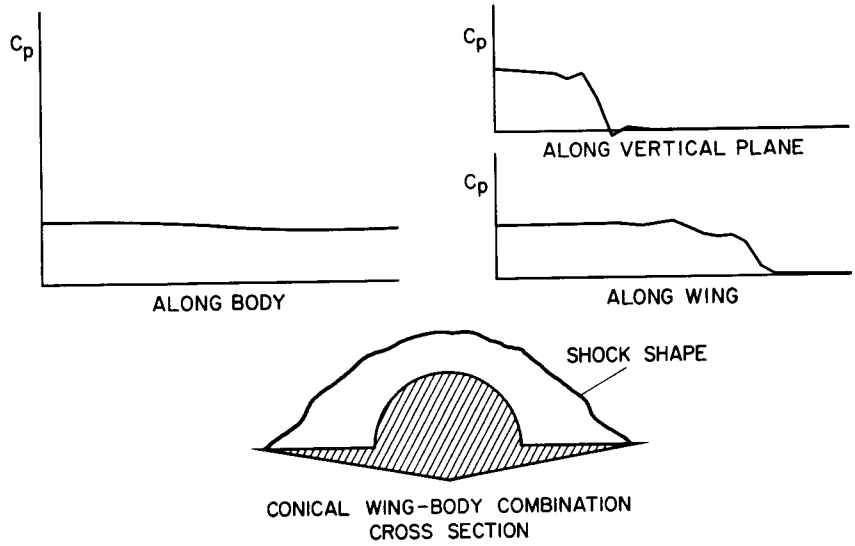

Figure 12.- Development of flow about a conical wing-body combination using MacCormack's method. Solution shown not fully converged.

DISCUSSION

RAYMOND SEDNEY, Martin Company: I hate to in any sense detract from the interesting material you presented, but I want to raise a strong objection to the rather provocative opening statement about numerical wind tunnels being on the verge of appearing. I can find statements like that going back to 1948 - or a little earlier than that - when there was a tremendous breakthrough on computing machines, and people really expected this.

I personally think it is rather dangerous to make statements like that because I feel the government wastes a great deal of money supporting work where the sales pitch is exactly that: you know, we are going to replace wind tunnels with computing machines.

So I would like to ask you a question. Do you visualize this happening in the next one year, or ten years or a hundred years?

LOMAX: That's too loaded a question, but I think that each year I can see significant progress in this area, and I think that we can cut back on wind-tunnel tests and rely more and more heavily in certain well understood areas on the methods that are being developed, and as they get more and more sophisticated they can go hand in hand.

When you bring in viscosity and turbulence and all this sort of thing, of course, I can't answer; perhaps that's a hundred years. But when you bring in the Eulerian forms of the equations, and other computations such as are presented in the other papers, you begin to get a feeling that yes, there is something more immediate that can be relied upon.

SIDNEY A. POWERS, Northrop Corp.: This is a tremendously fascinating piece of work, Mr. Lomax. I would just like to ask what is the difference in the Langley or the Ames method that made it so smooth? Could you describe the finite difference method you said you developed here that made it so smooth?

LOMAX: The details of the method are outlined in the written version. I have picked here a case (I didn't do it deliberately; actually I chose some cards at random when I had the camera working) where the shocks were exceptionally sharp. This is the best you can expect, one reason being that in this case the shock structure is rather uniform. If you have a problem where you have a rather weak shock in the presence of a strong one and try to use the same differences in every direction for both, you get a smearing of the weaker one. I do say that we did analyze a lot of these numerical methods, and this one was picked because it did give us the sharpest resolution we could find. As I say, the details are in the written version.

PETER B. S. LISSAMAN, Northrop Corp.: I would like to make a few comments which were suggested by a previous comment. First, I'd like to say this was a very entertaining and illuminating paper.

I am still interested in your remarks about electronic wind tunnels because I think that they are rather a long way away. It seems to me, as somebody who has spent a lot of sleepless nights and even some sleepless days, over trying to design wings, that the only interesting problem in wings are when the flow shows compressible regions, which is the cruise state of the airplane, or when it shows highly viscous separated regions, which is the landing state for the airplane. In fact, we are forced these days, almost, to make all our airplanes into biplanes, only we choose to pack the one wing inside the other one, and get it out with a lot of trouble when we want to land the airplane.

Now, I am very interested in all these incompressible techniques that are being developed, and I think I made some remarks yesterday which didn't sound the way I meant them to sound. I think that is the way we have to go to start, but I do believe that possibly we have to devote more attention to rather rough and crude numerical techniques toward tackling the very difficult problems, the problems of imbedded supersonic regions or imbedded viscous regions. If we could do that to within even 15 percent, then we could use the computer as a very valuable preliminary design tool.

I am thinking about, specifically, for example, a wing, perhaps of a subsonic airplane. You start to notice some shock pattern there in a wind tunnel, and then you ask your design engineer, "If I try to waist the fuselage or do something or maybe droop the leading edge a little bit, how would that help us?" The fact is that none of our computing methods, at least that I know of, can give us any indication about what we can do there.

Now, I will admit it is a formidable problem. As you say, it may be a hundred years away, but I think maybe that is all the more reason for us to address ourselves to some of those hard, messy problems at which we are forced to make approximations than to spend too much time toward refining known, regular, analytic techniques.

I would like to point out that this is in no way directed toward the talk that you have given. In fact, I just used the comment as an excuse to stand up and say this.

EARLL MURMAN, Boeing Scientific Research Laboratories: There was a research paper published in "Mathematics and Computations" in the July 1969 issue authored by Abarbanel and Zwas, who did a shock wave calculation using the Lax-Wendroff technique, similar to what you have shown today, only they used what they called an iterative technique of guessing Lax-Wendroff solutions and iterating. They ended up with a very sharp profile such as the one you showed that MacCormack produced. Would you care to comment, if you are familiar with this paper, how the iterative use of Lax-Wendroff technique damps the oscillation that is usually shown with shock wave?

LOMAX: I am not, right offhand, familiar with the paper. The particular method which you saw here tends to damp the oscillations because it takes first one side to evaluate the space derivative and advance the solution and then, if you like, iterates or, if you like, corrects as in a predictor-corrector sequence, takes the other side for the same derivative to make the second advance. Then it repeats the cycle.

MacCormack's method actually holds true when you have three-dimensional problems in which case you use all four sides in a cycle. In this way, in each individual advance, he is sampling only one side and hopefully not crossing the shock. I believe that is one secret of his success.

GINO MORETTI, Polytechnic Institute of Brooklyn: I am a little more familiar than you, probably, with that paper. A friend of mine at Sandia Corporation made some experiments on that technique, and found a very great dispersion. What you saw in the published paper seems to be a squeezed figure. In looking at the figure very closely, it seemed to me that about 20 points were used to cover the shock transition. This is not any better than what one obtains by using the old-fashioned Lax scheme. I didn't spend too much time analyzing this paper, but offhand it seems to me that what they achieved with this iterative Lax-Wendroff technique is to put a lot of additional viscosity which was not present in the original scheme.

I would like to make another comment about the MacCormack technique. I became aware of it a few days ago, and I played a little bit with it. Now, in simple, nonlinear problems where we know the exact solution it came out that not only the order of magnitude but even the numerical value of the errors coincide almost perfectly with the modified version of the Lax-Wendroff technique, which I have used many times.

Now, that is very interesting, because I must confess that my way of using the Lax-Wendroff scheme is much more complicated than the MacCormack scheme as far as programming is concerned, so I am now planning to switch to MacCormack's technique systematically. However, I wouldn't say that MacCormack's scheme allows you to go through a shock, because I think that if you go through a shock you do something against physics, and there is no mathematical gimmick which can do that.

LOMAX: You can go through a shock with the method of characteristics. MacCormack's method tries its best to do that. It fails insofar as it can't do it exactly.

I didn't bring this out, but one of the big advantages of MacCormack's method is its simplicity in programming and its low storage space.

MORETTI: Yes, I agree very much with you, and I even believe that such a scheme could be adopted using centered differences all the time, which is a trifle simpler than in MacCormack's version. I tried these centered differences on one problem with no deterioration of the results.

One great advantage is that one can handle viscous flows, probably, with no coding difficulty, whereas when I tried to use my original scheme for a viscous flow the coding became cumbersome.

And if I can add a word of optimism from the East Coast to what you said, I am sure that within two or three years we will be much better off with this electronic wind tunnel, so, Ray, don't be worried. It took time and money to to develop conventional wind tunnels and the same happens for these numerical techniques, but we are definitively making progress.

LOMAX: Apparently, the phrase numerical wind tunnel is a good one to use to bring out discussion.

FRED R. DEJARNETTE, Virginia Polytechnic Institute: I notice the shock waves looked very good and sharp, particularly compared to the basic Lax scheme. However, the basic Lax scheme when applied to just a basic Prandtl-Meyer expansion smears out expansions tremendously. I was wondering how the expansions in the MacCormack technique compared, say, to just basic Prandtl-Meyer expansions.

LOMAX: The written version again, I think that will help. The Lax method is very dissipative and dispersive if used off design, and I definitely recommend that you do not use the Lax method unless you really know what you are doing. The Lax-Wendroff is second order, and therefore it is much less dissipative. It does have troubles when you come to discontinuities in the slope, as any second order method will, and some of the wiggles you saw in the film were evidence of this. Aside from this difficulty we have used the method on expansion fans and have gotten very good results.

A NUMERICAL METHOD FOR COMPUTING THREE-DIMENSIONAL VISCOUS SUPERSONIC FLOW FIELDS ABOUT SLENDER BODIES

L. Walitt and J. G. Trulio
Applied Theory, Inc.

and

L. S. King
Ames Research Center

N70-21366

SUMMARY

A numerical method has been developed for calculating steady, three-dimensional, viscous, compressible flow fields about slender bodies at angle of attack. The method is based on the equivalence principle and on a two-dimensional, time-dependent numerical technique for solving the Navier-Stokes equations. The equivalence principle relates the axial coordinate of the three-dimensional problem to the time coordinate; thus, the steady three-dimensional problem becomes directly analogous to the two-dimensional problem of a cylinder (not necessarily circular) expanding with time. The basic features of both the numerical technique for two-dimensional, time-dependent flow and the equivalence principle as applied to this problem are presented.

Since the equivalence principle assumes axial velocities everywhere near the axial component of the free-stream velocity, the no-slip condition at the body surface in the axial direction cannot be applied. The flow field, including separation and body vortex development, is then predicted with a model incorporating a viscous crossflow with an inviscid axial flow. An analysis of the errors introduced by this approximation is presented.

Numerical calculations were made and compared with experimental results for an ogive-cylinder and an airplane fuselage configuration. Flow conditions were $M_\infty = 1.98$, $R_\infty = 4.68\times10^6$/ft, and $\alpha = 10°$ for the ogive-cylinder and $M_\infty = 2.50$, $R_\infty = 9.1\times10^6$/ft, and $\alpha = 15°$ for the fuselage configuration. Results are presented as static pressure distributions on the body surface, velocity vector plots, and contour maps in the flow field at selected axial locations. Good agreement between theory and experiment was obtained; maximum deviations of numerical surface pressures from corresponding experimental values were no more than 6 percent of free-stream dynamic pressure for both problems. However, some differences were noted. Boundary-layer separation and body vortex positions differed from experimental locations on the ogive-cylinder, and the shock induced by the fuselage canopy was predicted at a slightly different location. These differences are considered attributable to neglect of axial viscous effects, exclusion of turbulence phenomena, and the approximations introduced by the equivalence principle in describing the inviscid axial flow.

INTRODUCTION

For highly maneuverable advanced aircraft as exemplified in figure 1, the prediction of flow-field characteristics for nonsimple geometries at high angles of attack and high flight Mach numbers transcends the capabilities of linear theories. The need thus exists for an analytical or numerical method for providing an accurate, detailed description of the vehicle flow field for determining both fuselage configuration and inlet-airframe integration effects.

Prediction of the three-dimensional flow field about a slender body immersed in a supersonic airstream presents a formidable mathematical problem to which no exact solution has been obtained, either analytically or numerically. Successful numerical methods using the method of characteristics and the equivalence principle have been developed for three-dimensional, steady, inviscid flow fields. The work of Gallo and Rakich (ref. 1) is representative of the characteristics approach while the development by Van Dyke (ref. 2) of the theory introduced by Hayes (ref. 3) is representative of an approach that uses the equivalence principle.

In this research program the equivalence principle was applied to convert time-dependent viscous, compressible flow calculations in two space dimensions to steady motion of a viscous, compressible fluid in three space dimensions. The two-dimensional flow calculations were obtained by numerically solving the time-dependent compressible Navier-Stokes equations. In this paper the numerical technique is described in detail and results of its application to an ogive-cylinder body and to a fuselage forebody are presented.

SYMBOLS

a	Lagrangian coordinate
a	radius
A	surface area
A_1	abscissa of center of smaller circle of fuselage cross section
A_5	abscissa of center of canopy circle
B_1	ordinate of center of smaller circle of fuselage cross section
$B_2(z')$	ordinate of axis of the body with respect to the horizontal reference line
$B_2'(z')$	slope of axis of the body with respect to horizontal reference line

B_5	ordinate of center of canopy circle
$B(x,y,z)$	surface of the body
C	local sound speed
C_D	drag coefficient, $\frac{\text{drag force}}{q_\infty A_c}$
C_L	lift coefficient, $\frac{\text{lift force}}{q_\infty A_c}$
C_p	pressure coefficient, $\frac{P - P_\infty}{q_\infty}$
c_p	specific heat at constant pressure
c_v	specific heat at constant volume
d	diameter
$\underline{d}$	displacement vector
E	specific internal energy
f_2	bounded oscillating function used to determine discretization error
H	stagnation enthalpy
ℓ_x, ℓ_y, ℓ_z	direction cosines of the normal to the body's surface in the x, y, and z directions, respectively
m	mass
M	Mach number
$\underline{M}$	momentum vector
$\lvert\Delta M\rvert$	absolute error in Mach number
n_x, n_y, n_z	direction cosines of the normal to a shock surface in the x, y, and z directions, respectively
N	cycle number
N	mesh point density
P	pressure
P_s	stagnation pressure

$\lvert\Delta P\rvert$	absolute error in pressure
P_p	pitot pressure
q	dynamic pressure, $q = (1/2)\rho U^2$
R	Reynolds number
R_1	radius of smaller circle of fuselage cross section
R_2	radius of larger arc of fuselage cross section
R_3	radius of canopy circle
$\underline{R}(j,k)$	position vector of a mesh point about a fuselage cross section
$\underline{R}'(j,k)$	position vector of a mesh point about a circular cross section
S	entropy
$S(x,y,t)$	surface describing system of shock waves about a body
t	time
Δt	time step
T	temperature
u	velocity component in x direction
U	one-dimensional velocity, $U(a,t)$
$\underline{U}$	velocity vector
v	velocity component in the y direction
v	specific volume
V	volume
w	velocity component in the z direction
W	work rate
x	coordinate normal to plane consisting of the body axis and the perpendicular to that axis
x'	coordinate normal to the plane consisting of the horizontal reference line and the perpendicular to that line
X	Lagrangian coordinate, $X = X(a,t)$

y coordinate normal to body axis

y' coordinate normal to the horizontal reference line

z coordinate along the body axis

z' coordinate along the horizontal reference line

α free-stream angle of attack with respect to body axis

α_e local angle of attack with respect to a horizontal reference line, $\tan^{-1}\left(\frac{\text{velocity in } y' \text{ direction}}{\text{velocity in } z' \text{ direction}}\right)$

β sideslip angle, $\tan^{-1}\left(\frac{\text{velocity in } x' \text{ direction}}{\text{velocity in } z' \text{ direction}}\right)$

γ ratio of specific heats, $\frac{c_p}{c_v}$

ε discretization error in a property (eq. (29))

ρ density

τ maximum slope of surface of body with respect to the free-stream flow direction

$(\ )_s$ stagnation condition

$(\ )_s$ property downstream of a shock

$(\ )_\infty$ free-stream condition

$(\ )_o$ Lagrangian coordinate at time zero

$(\bar{\ })$ reduced variable

$(\ )_a$ actual variable

$(\ )_c$ variable associated with body cross section

FORMULATION OF EQUIVALENCE PRINCIPLE

The two-dimensional time-dependent equations of motion (independent variables x, y, t) can be transformed directly to steady-state three-dimensional (x, y, z) equations for slender bodies through the Hayes equivalence principle. The equivalence principle relates the steady-state flow field over a slender body to an equivalent time-dependent flow field in one less space dimension. In particular, steady three-dimensional flow about a

body can be reduced under certain conditions to two-dimensional time-dependent flow in a plane normal to the free-stream flow direction.

A simple example of the application of the equivalence principle is illustrated in figure 2, namely that of steady flow over an axisymmetric body at zero angle of attack. The steady-state two-dimensional axially symmetric flow field is analogous to time-dependent one-dimensional axially symmetric flow in a plane caused by an expanding cylinder. The cross-section plane of unsteady analogy moves downstream with free-stream velocity and the outline of the moving boundary is given by the trace of the original shape in the cross-section plane. At the station z (see fig. 2), the steady-state flow field in this plane is analogous to the flow field about the expanding cylinder at the time, $t = z/U_\infty$. To make the equivalence analogy valid, the normal velocity of the expanding cross section U_n, is given by the product of the free-stream velocity and the tangent to the surface. Far from the body, free-stream conditions are imposed (i.e., $P = P_\infty$, $\rho = \rho_\infty$, $u = v = 0$).

According to convention, the free-stream flow direction is chosen as the principal axis along which the linearization approximations for equivalence are made. However, for bodies at angle of attack as illustrated in figure 3, it is more convenient to choose the body axis as the principal axis. In planes normal to the body axis, the cross sections can usually be defined in terms of a few simple analytic expressions, which result in simpler, more accurate surface boundary conditions and facilitate the development of finite difference meshes about the cross sections. Because of this choice, free-stream crossflow will exist as an upstream boundary condition, but this choice of axis in no way affects the accuracy of the results.

It is convenient to discuss the equivalence principle in terms of flow about a slender body at angle of attack. Let the z axis coincide with the axis of the body, and let the cross section of the body lie in the x, y plane (see fig. 3). It is also assumed that the z component of the local velocity vector is approximately equal to the z component of the free-stream velocity vector, that is,

$$w = U_\infty \cos \alpha \tag{1}$$

Under this hypothesis, it follows that time-dependent flow in the x, y plane transforms to time-independent motion in x, y, z space according to the equations

$$z = U_\infty \cos \alpha t \tag{2}$$

$$y = y \tag{3}$$

$$x = x \tag{4}$$

This result - the equivalence principle - is derived for an inviscid fluid in appendix A.

In order for equations (2), (3), and (4) to represent a valid mapping between a flow field in x, y, t space and a flow field in x, y, z space,

the time-dependent solution in the x, y plane must be augmented by a three-dimensional boundary condition at the body surface

$$\ell_z U_\infty \cos \alpha + \ell_y v + \ell_x u = 0 \tag{5}$$

where ℓ_x, ℓ_y, ℓ_z are the direction cosines of the normal to the body surface in the x, y, and z directions, respectively. Equation (5) states that at the body, the component of the local velocity normal to the body surface is zero. The application of the boundary condition, equation (5), in the x, y plane implies that the body cross section varies in time and that the velocity normal to the surface is equal to $-\ell_z U_\infty \cos \alpha / \sqrt{\ell_y^2 + \ell_x^2}$. This normal velocity expression reduces to the product of the axial velocity ($U_\infty \cos \alpha$) and the local tangent to the surface.

A second boundary condition, a constraint on tangential flow at the body surface, must also be specified. Since the full time-dependent Navier-Stokes equations are solved in the x, y plane, a no-slip boundary condition is imposed at the surface of the body. We require that

$$v\ell_x - u\ell_y = 0 \tag{6}$$

It is seen in appendix A that the boundary condition, equations (5) and (6), are compatible with the assumptions inherent in the equivalence principle and permit a time-dependent viscous calculation to be made in the x, y plane. Thus, with the inclusion of boundary equations (5) and (6), a solution of the two-dimensional time-dependent Navier-Stokes equations can be applied directly to steady three-dimensional viscous flow.

The three-dimensional boundary layer on the body surface has been replaced by a two-dimensional boundary layer since the no-slip condition is imposed at the body surface only in the crossflow direction. This description of the flow field is poor in the boundary layer, but appears physically reasonable when either inertial forces predominate or crossflow viscous effects predominate in determining the flow field. Solving the Navier-Stokes equations in the crossflow plane provides a mechanism for effecting flow separation and subsequent development of spiral vortex sheets on the lee side of a body at angle of attack without recourse to empiricism. The extent that this model agrees with the physical situation must be carefully documented by comparisons with other methods and with experiment.

The computational procedure is then as follows. Initially we have a uniform flow field in the x, y plane with a velocity in the y direction equal in magnitude to $U_\infty \sin \alpha$. The slender-body cross section grows with time in the x, y plane. At discrete times solutions of the full time-dependent Navier-Stokes equations are obtained such that the cross-section surface boundary condition, equations (5) and (6), are satisfied; also, the flow far from the cross section is uniform with a crossflow velocity in the y direction equal to $U_\infty \sin \alpha$. The time-dependent solution in the x, y plane is then related to the steady-state three-dimensional flow field about the body through the transformation equations (2), (3), and (4).

DESCRIPTION OF THE NUMERICAL METHOD

The numerical method used to solve the time-dependent Navier-Stokes equations in two space dimensions is embodied in a computer code called "AFTON 2PE." The finite difference equations in the AFTON 2PE computer code are based on a physical model of the continuum. By a physical model of the continuum, it is meant that a framework be defined from which finite difference analogs of the full Navier-Stokes equations can be derived. The model utilized in this paper is described in some detail below. Since the Navier-Stokes equations are being used, this continuum model is not related to the particular phenomenon which is under study: once a physical model of the continuum is verified, its range of applicability extends to many flow situations.

In the conventional use of physical models, it is assumed that the partial differential form of the Navier-Stokes equations applies in general. A physical model is then postulated for the particular phenomenon to be studied and the equations are reduced to ordinary differential equations to obtain either an analytical or numerical solution. The Lees-Reeves (ref. 4) near-wake model is a good example of a conventional physical model. This model is concerned with the base flow and near-wake subregions shown in figure 4. To obtain a solution the boundary-layer approximations are used and pressure and velocity profiles in these regions are assumed. However, this solution is only valid in the base and near-wake regions; whereas, the entire flow field of figure 4 can be predicted with one numerical scheme utilizing a valid model of the continuum.

For illustrative purposes, the space-time continuum model employed in this research is presented in detail for the case of time-dependent one-dimensional flow of a compressible, inviscid fluid. This model was implied by a set of finite difference equations developed by von Neumann and Richtmyer (refs. 5 and 6). Trulio and Trigger (ref. 7) then derived the continuum model from a careful analysis of the von Neumann-Richtmyer equations.

Finite difference analogs of the continuity equation, momentum equation, the First Law of Thermodynamics will be derived in a Lagrangian coordinate system. Let a be the Lagrangian coordinate, and $X(a, t)$ be the Eulerian coordinate. That is, $X(a, t)$ gives the position at time t, of a fluid element that was originally at position a. Consider the Lagrangian coordinates a_1, a_2, and $a_{1/2}$ ($a_{1/2} = (1/2)(a_1 + a_2)$) shown in figure 5(a). Since the system is Lagrangian, the mass between the trajectories labeled a_1 and a_2 remains a constant. Let the one-dimensional space continuum be represented by a discrete set of zones, designated "thermodynamic" zones. At time zero, let the boundaries of these zones be spaced at a constant interval Δa along the X axis (see fig. 5(a)) and denoted by a_ℓ ($\ell = 0, 1, 2, 3, \ldots, L$). Let each of the thermodynamic zones be one unit high and one unit wide. Consider another set of zones designated "momentum" zones superimposed on the thermodynamic zones, such that each momentum zone surface always divides the mass of the thermodynamic zone which contains this surface in half. A schematic diagram showing a momentum zone and two thermodynamic zones at the time t is

shown in figure 5(b). The Eulerian coordinates which define the two thermodynamic zones are $X(a_{\ell-1}, t)$, $X(a_\ell, t)$, and $X(a_{\ell+1}, t)$, while the Eulerian coordinates of the momentum zone are $X(a_{\ell-(1/2)}, t)$ and $X(a_{\ell+(1/2)}, t)$.

The thermodynamic variables, such as internal energy, specific volume, and pressure, are assumed constant throughout a thermodynamic zone. The velocity is assumed constant throughout a momentum zone. Thus, thermodynamic variables are in effect centered at the momentum zone surfaces; that is, $P_\ell = P(a_{\ell-(1/2)}, t)$ denotes the pressure in the thermodynamic zone $X(a_{\ell-1}, t)$, $X(a_\ell, t)$ which effectively acts at $X(a_{\ell-(1/2)}, t)$ (see fig. 5(b)). Momentum zone variables are in effect centered at the thermodynamic zone surfaces; that is, $U_\ell = U(a_\ell, t)$ denotes the particle velocity in the momentum zone $X(a_{\ell-(1/2)}, t)$, $X(a_{\ell-(1/2)}, t)$ which effectively acts at $X(a_\ell, t)$.

Since an explicit formulation is the goal, the variables of motion are not only displaced spatially (as discussed above), but they are displaced in time as well. Let Δt denote the uniform time interval and t^n ($n = 0, 1, 2, \ldots, N$) denote the time after n uniform time intervals. The variables associated with thermodynamic zones are defined at integer times; that is, $P^n_{\ell-(1/2)} = P(a_{\ell-(1/2)}, t^n)$ denotes the pressure at the time t^n. The momentum zone variables are defined at half-integer times; that is, $U_\ell^{n-(1/2)} = U(a_\ell, t^{n-(1/2)})$ denotes the particle velocity at a time $t^{n-(1/2)}$, and the Eulerian coordinate position $X(a_\ell, t^{n-(1/2)})$.

Finite difference analogs of the continuity, momentum, and first law equations follow directly from the physical model of the continuum presented in figure 5(b). Since a Lagrangian coordinate system is employed, the zones of figure 5(b) will be displaced continuously from their initial positions; that is, $a_1, \ldots, a_L$ to coordinate positions $X(a_1, t), \ldots, X(a_L, t)$. Let us calculate the properties at the time, t^n, for the thermodynamic zone having Lagrangian coordinates $a_{\ell-1}, a_\ell$ and the momentum zone having Lagrangian coordinates $a_{\ell-(1/2)}, a_{\ell+(1/2)}$. The initial values for this calculation are $P^{n-1}_{\ell-(1/2)}, E^{n-1}_{\ell-(1/2)}, v^{n-1}_{\ell-(1/2)}, P^{n-1}_{\ell+(1/2)}, E^{n-1}_{\ell+(1/2)}, v^{n-1}_{\ell+(1/2)}$ for the thermodynamic zones and $X^n_{\ell-1}, X^n_\ell, X^n_{\ell+1}, U^{n-(1/2)}_{\ell-1}, U^{n-(1/2)}_\ell, U^{n-(1/2)}_{\ell+1}$ for the momentum zones. The objective is to update these variables by one time step in an explicit manner.

The finite difference analog to the conservation of mass is derived from the expression for the volume change of thermodynamic zone $a_{\ell-1}, a_\ell$.

$$V^n_{\ell-(1/2)} - V^{n-1}_{\ell-(1/2)} = \left[U_\ell^{n-(1/2)} - U_{\ell-1}^{n-(1/2)}\right]\Delta t \tag{7}$$

where

$V^{n-1}_{\ell-(1/2)}$ volume of zone $a_{\ell-1}, a_\ell$ at time t^{n-1}

$V^{n}_{\ell-(1/2)}$ volume of zone $a_{\ell-1}, a_\ell$ at time t^{n}

Based on equation (7), and the fact that the mass of material in the thermodynamic zone $a_{\ell-1}, a_\ell$ has the constant value $\rho_o \Delta a$, we find that

$$\rho_o \left[\frac{v^n_{\ell-(1/2)} - v^{n-1}_{\ell-(1/2)}}{\Delta t} \right] = \frac{U^{n-(1/2)}_\ell - U^{n-(1/2)}_{\ell-1}}{\Delta a} \tag{8}$$

where ρ_o is the density at time zero, and $v^n_{\ell-(1/2)}$ is the specific volume of material in the zone at time t^n (note that $(\rho_o \Delta a) v^n_{\ell-(1/2)} = V^n_{\ell-(1/2)}$).

For an inviscid, adiabatic fluid, the first law equation for a system in equilibrium is applicable:

$$\frac{DE}{Dt} = -P \frac{Dv}{Dt} \tag{9a}$$

The first law finite difference analog to equation (9a) is derived by first writing down a finite difference analog to the term -P(Dv/Dt) and then equating this to the rate of change of internal energy in the zone. Since the zone mass is constant and the pressure is homogeneous in a thermodynamic zone, the term -P(Dv/Dt) becomes

$$\left(-P \frac{\Delta V}{\Delta t}\right)_{\ell-(1/2)} = \frac{-(1/2)\left[P^n_{\ell-(1/2)} + P^{n-1}_{\ell-(1/2)}\right]\left[U^{n-(1/2)}_\ell - U^{n-(1/2)}_{\ell-1}\right]}{m_{\ell-(1/2)}} \tag{9b}$$

where

$$m_{\ell-(1/2)} = \rho_o \Delta a$$

On the basis of equation (9b), the finite difference first law equation becomes

$$\frac{\rho_o\left[E^n_{\ell-(1/2)} - E^{n-1}_{\ell-(1/2)}\right]}{\Delta t} = \frac{-(1/2)\left[P^n_{\ell-(1/2)} + P^{n-1}_{\ell-(1/2)}\right]\left[U^{n-(1/2)}_\ell - U^{n-(1/2)}_{\ell-1}\right]}{\Delta a} \tag{10}$$

where $E^{n-1}_{\ell-(1/2)}$ is the specific internal energy of thermodynamic zone $a_{\ell-1}$, a_ℓ.

The equation of state for a perfect gas is:

$$E = Pv(\gamma - 1) \tag{11}$$

Finally, the finite difference equation of motion for momentum zone $a_{\ell-(1/2)}$, $a_{\ell+(1/2)}$ becomes:

$$\frac{M_\ell^n - M_\ell^{n-1}}{\Delta t} = \left[P_{\ell-(1/2)}^{n-(1/2)} - P_{\ell+(1/2)}^{n-(1/2)}\right] \tag{12}$$

where

$$P_{\ell-(1/2)}^{n-(1/2)} = \frac{1}{2}\left[P_{\ell-(1/2)}^{n} + P_{\ell-(1/2)}^{n-1}\right]$$

$$P_{\ell+(1/2)}^{n-(1/2)} = \frac{1}{2}\left[P_{\ell+(1/2)}^{n} + P_{\ell+(1/2)}^{n-1}\right]$$

and M_ℓ^n defines the momentum in zone a_ℓ at time t^n.

Equations (8), (9), and (10), derived from the physical model presented in figure 5(b), are solved in the following manner. First, the specific volume, $v_{\ell-(1/2)}^n$, is calculated from equation (8). Then, the pressure $P_{\ell-(1/2)}^n$, and specific internal energy $E_{\ell-(1/2)}^n$ are calculated from equations (9), (10), and (11). The continuity and first law equations are then solved for specific volume and pressure in all thermodynamic zones. Based on the pressure field, equation (12) can be solved for the momentum M_ℓ^n. The particle velocity $U_\ell^{n+(1/2)}$ is found from the forward extrapolation formula

$$U_\ell^{n+(1/2)} = 2\,\frac{M_\ell^n}{m_\ell} - U_\ell^{n-(1/2)} \tag{13}$$

where

$$m_\ell = \rho_o\,\Delta a$$

Integration of the particle velocity $U_\ell^{n+(1/2)}$ with time establishes the new Eulerian position, X_ℓ^{n+1}. This can be done for all momentum zones. Thus, all the initial values cited above can be updated by one time step and the process repeated.

The success of this method coupled with the failure of other more recent numerical schemes to improve upon it, led Trulio and Trigger to a careful analysis of these finite difference equations in order to discover the reasons

for their success. They found that the finite difference equations possessed the same self-consistency property of form as the original differential equations from which they were derived, that is, the finite difference equations for momentum conservation and the first law implied an exact conservation of total energy (internal and kinetic) finite difference equation (ref. 7). In other words, the continuity, momentum, first law, and conservation of total energy relations are redundant by one. In most other numerical schemes if one tries to derive a conservation of total energy relation from finite difference analog of momentum conservation and the first law, error terms, usually assumed to be "second order," are produced. These numerical error terms are believed to be a primary source of the difficulties encountered in many other numerical schemes. Appendix B demonstrates the self-consistency property of the finite difference equations (8) to (13).

In addition to self-consistency of form, the numerical method has the following properties:

(a) Since the method is explicit, stability criteria must be met in order to obtain physically meaningful numerical results. In general, the time step must be small enough so that a sound signal cannot cross a zone in a time step (refs. 5 and 6).

(b) The numerical error has been correlated for this scheme. It has been found that the absolute error in a property is inversely proportional to the linear mesh point density to the three-halves power (ref. 8).

The physical model, from which equations (8) to (13) have been derived has been extended to two space dimensions (ref. 9). In that work, specific finite difference equations were formulated and their self-consistency properties demonstrated. Because they provide a base for the present calculation, a brief description of the derivation of these equations will be presented.

Consider two-dimensional flow of a viscous, compressible fluid in the x, y plane. As in the one-dimensional case, let us divide the continuum into two types of zones; namely, quadrilateral zones and momentum zones. See figure 6. The assumptions governing this analysis are as follows:

(a) All zones are polygons.

(b) The density, specific internal energy, pressure, stress tensor, and velocity derivatives are homogeneous in a quadrilateral zone.

(c) The velocity vector is homogeneous in a momentum zone.

(d) The zones have unit thickness normal to the plane of motion.

As in the one-dimensional case the continuity and first law equations are solved for each quadrilateral zone to determine the density, specific internal energy, and stress. When the stress tensor depends only on strain, the first law equation corresponds to that of thermodynamics. However, for a

stress-rate of strain dependence, the first law equation is a relationship involving internal energy, the specific internal energy being the difference between total and kinetic energy. Based on the stress tensors in each of the four quadrilateral zones which comprise a momentum zone (see fig. 6), the momentum equation is solved for each momentum zone. To accommodate the equivalence principle boundary conditions, the finite difference equations in AFTON 2PE are written in a generalized coordinate system where the four mesh points comprising a quadrilateral zone can move with arbitrary velocity. The numerical method is described in detail for a generalized coordinate system and an Eulerian coordinate system in two places (refs. 9 and 10).

All of the salient properties of the numerical method described in the one-dimensional example are preserved in two-dimensions and will also be preserved in three spatial dimensions; in that respect the numerical theory is internally consistent. The momentum and first law finite difference equations in two dimensions imply an exact finite difference equation for total energy. The stability criteria are the same as in the one-dimensional case. The one-dimensional correlation of absolute numerical error in a property extends directly to two dimensions. In two dimensions the absolute numerical error is inversely proportional to the area mesh point density to the three-quarters power (ref. 10).

ORDER OF ERROR OF THE NUMERICAL METHOD

In this section the order of error of the numerical method is determined. The numerical error is defined as the absolute difference between the actual value of a quantity and the value computed numerically. The error in this method stems from three sources, the equivalence principle, discretization errors, and neglect of axial viscous effects. The errors inherent in the equivalence principle lie in the neglect of velocity perturbations along the free-stream flow direction and have been deduced by Van Dyke (ref. 2). The discretization error is defined as the difference between the exact solution to the continuum motion equivalence principle equations for a given system, and the values of the flow variables computed from a finite difference approximation to these equations of motion; discretization error results basically from the substitution of a discrete set of points for the space-time continuum. The errors introduced when axial viscous effects and turbulence phenomena are neglected are manifested in the accuracy with which separation and vortex locations can be predicted. Since the determination of the accuracy of the method is of primary importance, all sources of error will be discussed at some length.

To deduce the order of error in the equivalence principle assumption, Van Dyke introduced what he termed "reduced" independent and dependent variables, and he redefined the functions describing the body and shock-wave surfaces. To obtain these reduced variables, consider a coordinate system where the z axis is alined with free-stream flow direction. Let the surface of the body be described by $B(x, y, z) = 0$, and let the complete system of shock waves be described by $S(x, y, z) = 0$. In this coordinate system the reduced variables are as follows:

$$\left.\begin{aligned} \bar{x} &= x/\tau \\ \bar{y} &= y/\tau \\ \bar{z} &= z \end{aligned}\right\} \tag{14}$$

$$\left.\begin{aligned} u &= U_\infty \tau \bar{u}(\bar{x},\bar{y},\bar{z}) \\ v &= U_\infty \tau \bar{v}(\bar{x},\bar{y},\bar{z}) \\ w &= U_\infty[1 + \tau^2 \bar{w}(\bar{x},\bar{y},\bar{z})] \end{aligned}\right\} \tag{15}$$

$$P = P_\infty \gamma M_\infty^2 \tau^2 \bar{P}(\bar{x},\bar{y},\bar{z}) \tag{16}$$

$$\rho = \rho_\infty \bar{\rho}(\bar{x},\bar{y},\bar{z}) \tag{17}$$

$$\left.\begin{aligned} B &= \bar{B}(\bar{x},\bar{y},\bar{z}) \\ S &= \bar{S}(\bar{x},\bar{y},\bar{z}) \end{aligned}\right\} \tag{18}$$

where τ is the maximum slope of the body surface with respect to the free-stream flow direction. This transformation of variables was introduced into the continuity, momentum, and first law equations. Reduced parameters were considered of order one or less and terms that contained τ^2 explicitly were discarded. A set of reduced equations, linear in $\bar{w}$ and derivatives with respect to $\bar{z}$, resulted. The boundary conditions for the reduced equations became:

At the body surface

$$\bar{u}\frac{\partial \bar{B}}{\partial \bar{x}} + \bar{v}\frac{\partial \bar{B}}{\partial \bar{y}} + \frac{\partial \bar{B}}{\partial \bar{z}} = 0 \quad \text{at} \quad \bar{B} = 0 \tag{19}$$

Far upstream of the body

$$\left.\begin{aligned} \bar{P} &\to \frac{1}{\gamma M_\infty^2 \tau^2} \\ \bar{\rho} &\to 1 \end{aligned}\right\} \quad \text{as} \quad \bar{z} \to -\infty \tag{20}$$

The parameters M_∞ and τ of the full problem enter the reduced problem only in the combination $M_\infty\tau$, which appears only in the upstream boundary condition on $\bar{P}$ (eq. (20)). Since $\bar{P}$ must be of order one or less for these equations to be valid, $M_\infty\tau$ must be of order one or greater for this theory to be consistent far upstream of the body. If this consistency condition is satisfied, the maximum error in a reduced variable must be of the order τ^2, because terms of order τ^2 have been omitted in the reduction. Since $M_\infty\tau$ is of order one, an error of order τ^2 implies that the error is also of order $1/M_\infty{}^2$, thus the theory becomes more accurate at high Mach numbers. At supersonic speeds and with $M_\infty\tau = O(1)$, this error is not negligible. Maximum errors

expected from the equivalence principle assumption for static pressure and local Mach number are derived below.

The absolute difference between the actual reduced pressure, $\bar{P}_a$, and the reduced pressure calculated from this theory, $\bar{P}$, is

$$\left|\bar{P}_a - \bar{P}\right| \approx \tau^2 \tag{21}$$

Combining equations (16) and (21) yields

$$\left|\bar{P}_a - \bar{P}\right| \approx \frac{\left|P_a - P\right|}{2q_\infty \tau^2} \approx \tau^2$$

where q_∞ is the free-stream dynamic pressure $((1/2)\rho_\infty U_\infty^2)$. Therefore, the absolute error in the pressure is as follows:

$$\left|P_a - P\right| \approx 2q_\infty \tau^4 \tag{22}$$

Since experimental and numerical local Mach numbers are compared in this research effort, it is important to determine the order of error in the Mach number. The Mach number M is defined as

$$M = \frac{(u^2 + v^2 + w^2)^{1/2}}{C} \tag{23}$$

where C is the local sound speed. From Bernoulli's equation, the local sound speed can be expressed in terms of the components of local velocity

$$C^2 = C_\infty^2 - \frac{\gamma - 1}{2}(u^2 + v^2 + w^2 - U_\infty^2) \tag{24}$$

where C_∞ is the free-stream sound speed. Introducing the reduced velocities $\bar{u}$, $\bar{v}$, and $\bar{w}$ from equations (15) into equations (23) and (24) yields the relation for the Mach number in terms of reduced velocities.

$$M = \frac{(1 + \tau^4\bar{w}^2 + 2\tau^2\bar{w} + \tau^2\bar{v}^2 + \tau^2\bar{u}^2)^{1/2}}{\left[M_\infty^{-2} - [(\gamma - 1)/2]\tau^2(\bar{w}^2\tau^2 + 2\bar{w} + \bar{v}^2 + \bar{w}^2)\right]^{1/2}} \tag{25}$$

Since $\bar{u}$, $\bar{v}$, and $\bar{w}$ are of order one, terms in τ^4 could be neglected in equation (25).

$$M \approx \left[\frac{1 + \tau^2(2\bar{w} + \bar{v}^2 + \bar{u}^2)}{M_\infty^{-2} - [(\gamma - 1)/2]\tau^2(2\bar{w} + \bar{v}^2 + \bar{u}^2)}\right]^{1/2} \tag{26}$$

Equation (26) can be linearized in terms of changes in $\bar{u}$, $\bar{v}$, and $\bar{w}$ by employing a first-order Taylor's expansion. Let M_a represent the actual

local Mach number and M represent the value computed by this numerical method. From a first-order Taylor's expansion

$$M_a \approx M + \left(\frac{\partial M}{\partial \bar{u}}\right)_{\bar{u}=\bar{v}=\bar{w}=1} \Delta\bar{u} + \left(\frac{\partial M}{\partial \bar{v}}\right)_{\bar{u}=\bar{v}=\bar{w}=1} \Delta\bar{v} + \left(\frac{\partial M}{\partial \bar{w}}\right)_{\bar{u}=\bar{v}=\bar{w}=1} \Delta\bar{w} \tag{27}$$

The coefficients of equation (27) can be determined by differentiation of equation (26) and evaluation of the derivatives at the values $\bar{u} = \bar{v} = \bar{w} = 1$, since barred quantities are assumed of order one. The final equation is as follows:

$$\frac{|\Delta M|}{M_\infty} \approx \frac{3}{2}\tau^4 \left[\frac{1 - 2(\gamma - 1)\tau^2 M_\infty^2}{1 + 4\tau^2}\right]^{1/2} \left|\frac{1 + (\gamma - 1)(1 + 2\tau^2)M_\infty^2}{1 + 4(\gamma - 1)\tau^2 M_\infty^4[(\gamma - 1)\tau^2 - 1]}\right| \tag{28}$$

where

$$|\Delta M| = |M_a - M|$$

If the reduced equations are rewritten in terms of the actual unbarred parameters, and the substitution $z = U_\infty t$ is made, the time-dependent equations of motion in two space dimensions result.

The discretization error in the above time-dependent equations of motion in two space dimensions is based on a general rule that relates the error to the density of mesh points employed in the numerical integration process. The derivation of this error rule can be found in reference 8; the relation is as follows:

$$\varepsilon = f_2 N^{-3/4} \tag{29}$$

where ε is the absolute discretization error in a given property, N is the two-dimensional mesh point density (i.e., number of zones per unit area of the x, y plane), and f_2 is a bounded oscillatory function. If the same problem is run with two different meshes, that is, a medium and fine mesh, the function f_2 can be evaluated from the values of a property and mesh point densities of the medium and fine meshes at the same point in space and time. For the case where the static pressure error is required,

$$f_2 = \frac{|P_f - P_m|}{\left|N_f^{-3/4} - N_m^{-3/4}\right|} \tag{30}$$

where P_f is the fine mesh pressure, P_m is the medium mesh pressure, N_m is the mesh point density of the medium mesh, and N_f is the mesh point density for the fine mesh.

The error introduced by neglecting axial viscous effects and turbulence phenomena is the most difficult of the three sources of error to evaluate. In fact, one of the primary objectives of the study was to determine how well the

flow field could be predicted with axial viscous effects neglected. No attempt was made to evaluate this error analytically. Instead, numerical results obtained with this method are compared with experimental data. These comparisons are discussed in some detail in succeeding sections concerned with the numerical results.

In this research effort the effects of mesh point density on the discretization error were not investigated; each problem of the program was run with only one mesh. Therefore, the order of error of the numerical method, which was established by comparing the numerical results with experimental ones, included all three sources of errors.

DESCRIPTION OF PROBLEMS SOLVED AND MESHES USED

The AFTON-2PE computer code, modified to accommodate the equivalence principle boundary conditions, was applied first to the flow field about an ogive-cylinder configuration and second to a fuselage geometry representative of an advanced tactical fighter plane. In both problems, air, represented as a gamma law gas ($\gamma = 1.4$), was considered and adiabatic flow was assumed throughout the flow field. For the ogive-cylinder problem the free-stream Mach number was 1.98, the angle of attack was 10° with respect to the axis of the body, and the free-stream Reynolds number was 4.68×10^6/ft. For the fuselage problem the free-stream Mach number was 2.5, the angle of attack was 15° with respect to the horizontal, and the free-stream Reynolds number was 9.1×10^6/ft. In this section the cross-sectional shapes for both problems are defined and the finite difference meshes generated about these cross sections are described.

The axisymmetric ogive-cylinder configuration is composed of an ogive which is three maximum cylinder diameters long and a cylinder 7.3 diameters long. This configuration is schematically illustrated in figure 7, where the equations which describe the variation of the radius of the body with axial distance are also indicated. In this problem the axis of the body, which is straight in this case, was chosen as the principal axis for the equivalence analogy between the steady and unsteady flows.

The fuselage had a drooped nose which resulted in a curved central axis of the body. This geometry is schematically illustrated in figure 8. The central axis of the body is composed of a straight portion, inclined 7-1/2° from the horizontal, and a curved portion which begins at a horizontal station of 15 inches (see fig. 8). To avoid introducing curvature effects into the equations of motion, the 7-1/2° reference line was chosen as the principal axis for the equivalence analogy. In this coordinate system, the angle of attack of 15° with respect to the horizontal becomes 7-1/2° with respect to the 7-1/2° reference line; hence α = 7-1/2°. The canopy, included in this problem, is indicated in the cross sections normal to the 7-1/2° reference line shown in figure 8.

The fuselage configuration has cross-sectional shapes normal to the 7-1/2° reference axis whose peripheries can be approximated by circular arcs and straight lines. In fact the fuselage cross section is circular to a

horizontal station of 9.44 inches from its nose, is asymmetric between horizontal stations 9.44 and 10.88, and includes a circular canopy between horizontal stations 10.88 and 30.68. The fuselage cross section at a horizontal station at the canopy location is shown schematically in figure 9. The parameters describing this periphery are also indicated in the figure. These parameters have been curve-fitted as functions of distance along the central axis of the fuselage.

A subroutine of the AFTON 2PE computer code has been developed for generating finite-difference meshes around an asymmetric half-body of a general fuselage-shaped cross section. This subroutine is based on previous work on finite-difference mesh development for a circular cylinder (ref. 10). The general cross-sectional shape of the half-body is assumed to consist of two circular arcs, two straight-line segments tangent to the circular arcs, and a circular canopy (see fig. 9). The procedure adopted in the calculation was as follows. The area of the half-body was computed and a half-circle of equivalent area was located with its center at the coordinate origin. The finite-difference mesh for this half-circle was calculated from a modified stream function and potential function from potential flow theory about a cylinder. The problem was to transform the cylinder mesh into a new mesh around the asymmetric half-body according to some suitable rule of transformation. In the subroutine developed, each half-circle mesh point (designated hereafter as an "unprimed" mesh point) was transformed into a half-body mesh point (designated hereafter as a "primed" mesh point) in the following manner. First, the periphery of the half-body shape was divided into as many equal arcs as the half-circle periphery. Then, surface vector displacements were obtained between corresponding unprimed points on the half-circle and primed points on the asymmetric half-body. Based on these surface vector displacements, unprimed mesh points in the flow field were displaced to their primed locations. Consider an unprimed mesh point in the flow field having a position vector $\underline{R}(j, k)$, where the integer k is associated with a potential-like line, and the integer j is associated with a streamline-like line. Let the surface vector displacement corresponding to the same k line be denoted as $\underline{d}(k)$. The position vector of the primed point $\underline{R}'(j, k)$ is determined from the following equation:

$$\underline{R}'(j,k) = \underline{R}(j,k) + \underline{d}(k)\left[\frac{a}{R(j,k)}\right]^2 \tag{31}$$

where a is the radius of the half-circle and $R(j, k)$ is the magnitude of the position vector $\underline{R}(j, k)$.

The finite-difference meshes for the ogive-cylinder were composed of 35 j lines and 90 k lines and continuously deformed with the radius of the body. The initial radius was 0.00046875 foot and the maximum radius was 0.046875 foot. Since the ogive-cylinder cross section is circular, only the equations of the mesh generating subroutine which pertained to the circular cylinder mesh points (unprimed mesh points) were used to continually calculate new meshes as the radius of the cross section changed. The finite-difference mesh in a cross-sectional plane normal to the body axis at a radius of 0.01 foot is shown in figure 10. The finite-difference mesh corresponding to the maximum radius (0.046875 ft) is indicated in figure 11.

The finite-difference meshes for the fuselage configuration were composed of 35 j lines and 99 k lines and continuously deformed as the body cross-sectional shape deformed. The mesh generating subroutine of the AFTON 2PE computer code continually calculated new meshes as the fuselage shape deformed. The finite-difference mesh in the cross-sectional plane normal to the central axis at a horizontal station 7 inches from the nose of the fuselage is shown in figure 12. At this station the fuselage cross section is circular. The finite-difference mesh corresponding to a horizontal station 25 inches from the fuselage nose is shown in figure 13. The canopy is also indicated in figure 13.

BOUNDARY CONDITIONS AND INITIAL CONDITIONS

In the x, y planes, the finite-difference meshes are bounded by an upstream boundary, a lateral boundary, and a boundary composed of the symmetry line of the cross section and the body cross section itself. The density and specific internal energy are given their free-stream values at the upstream boundary while the velocity of material normal to this boundary, v_∞, is evaluated from

$$v_\infty = U_\infty \sin \alpha \tag{32}$$

where α is the angle of attack with respect to the principal axis. Equations (5) and (6) are satisfied at the body's surface, while the fluid is allowed to slide without friction at the system's lateral boundary and symmetry lines. The downstream boundary condition was based on the method of characteristics. It was used previously in low-speed wake-flow calculations and gave a good approximation to the flow in this region. Reference 11 describes this downstream boundary condition in some detail.

The initial condition consisted of a uniform flow field in the x, y plane with $v_\infty = U_\infty \sin \alpha$ in which the body impulsively appeared at zero time. In both problems, the initial cross-sectional radius was approximately 1 percent of the maximum radius.

RESULTS OF OGIVE-CYLINDER PROBLEM

The ogive-cylinder problem was the first attempted in this study. This problem was a good test of the method in that vortices had been experimentally observed to occur on the leeward side of the body. The crossflow Mach number was 0.344 and the crossflow Reynolds number was 0.7625×10^5 based on the maximum diameter of the body. The problem was run 3406 cycles (i.e., time steps) on the UNIVAC 1108 computer, requiring approximately 10 hours of computer time. Solutions were obtained from the body's nose to an axial station 8.35 maximum cylinder diameters downstream. At this cross-sectional plane a well-developed pair of vortices were calculated. The problem duplicated the body geometry and free-stream conditions of a wind-tunnel test (ref. 12). In general, agreement between numerical and experimental data was good, providing evidence that the numerical method is applicable to bodies for which separation and the subsequent development of spiral vortex sheets occur.

To investigate the qualitative behavior of the flow field, it was convenient to exhibit the data in the form of vector plots of the velocities of the fluid particles; the tail of each vector corresponds to a mesh point. The sequence of events as one moves down the axis of the body is described by figures 14 to 17. In figure 14 the flow field is shown at a station 0.502 maximum cylinder diameters from the nose of the body. Although the finite-difference mesh is relatively coarse with respect to the radius of the body at this station, the bow shock is indicated as well as the expansion which occurs on the leeward side. In figure 15, at a station 2.99 maximum body diameters, where the ogive section ends, the bow shock is better defined. Figure 16 shows the flow field at a station of 4.92 maximum diameters, where separation first appears on the leeward side of the body. The spiral vortex sheets that develop on the leeward side of the body are indicated in figure 17. The formation of the bow shock, the leeward expansion, and subsequent development of the spiral vortex sheets are all in qualitative accord with experimental observations. The accuracy of these numerical results is considered below.

Numerical pressure distributions around the body are compared to experimental data at various axial stations in figure 18. As can be seen from the figure, quantitative agreement is achieved from the body nose to an axial station 4.92 diameters. At this station the numerical data indicate that separation had occurred on the leeward side of the body (see the velocity vector plot in fig. 16), whereas the experimental data showed leeward separation at a station approximately 6.00 diameters aft of the body's nose. As a result, the numerical pressure data on the leeward side of the body differed slightly from the experimental data between stations 4.92 and 6.00 diameters down the body axis. At stations greater than 6.00 diameters from the cylinder's nose, the experimental data also showed separated flow, and the numerical and experimental pressure coefficient data were in close agreement 7.63 diameters from the nose of the cylinder.

The circumferential positions of the separation points and vortex centers vary with axial location in a manner determined experimentally by measurements of pitot pressure at various body cross sections. Corresponding separation point and vortex center positions were also found from velocity plots of the numerical flow field. The calculated separation points and vortex centers were found to lie about 20° closer to the windward side than the corresponding experimental values as seen in figure 19. For example, in a crossflow plane 8.3 diameters down the body axis, the numerical separation point and vortex location were 109° and 137°, respectively, while the corresponding experimental values were 130° and 160°. The discrepancy between measured and calculated separation point and vortex center positions, while not very large, is perhaps the least satisfactory feature of the calculation. The difference is due to viscous effects of axial motion being neglected as well as to the exclusion of turbulence phenomena.

The flow field predicted numerically is laminar. However, the actual flow field is turbulent as a result of both axial and crossflow viscous effects. In the numerical method axial motion is treated as if the flow were inviscid. For laminar flow, separation would begin on the leeward side of the body at an axial station upstream of the station at which turbulent separation begins. Also, the separation point would be closer to the windward

side when the flow is laminar. From the pressure coefficient data for a circular cylinder (ref. 13), it was found that in turbulent flow at a Reynolds number of 6.7×10^5, separation occurred at 120°; in laminar flow at a Reynolds number of 1.85×10^5, separation occurred at 90°. Thus, the difference between the numerical and experimental separation positions is in qualitative agreement with the difference between laminar and turbulent separation positions. To obtain more realistic theoretical predictions, it will therefore be necessary to generalize the equivalence principle account for turbulent effects due to axial flow; it is felt that the principle, which was generalized for this program by including Newtonian viscosity in the crossflow equations, could be extended satisfactorily by the addition of eddy viscosity terms.

Based on the equivalence principle theory, an error analysis of the surface pressure results of figure 18 was made. The maximum slope of the ogive-cylinder body with respect to the free-stream flow direction was 28.92° which corresponds to a $\tau = 0.552$, and occurs on the windward side of the body at the nose. For this value of τ the hypersonic similarity parameter $M_\infty\tau$ is 1.09, which satisfies the consistency condition of the theory. Since consistency is satisfied, the maximum absolute error in the surface static pressures, $|\Delta P|$, that one should expect from this theory is about 19 percent of the free-stream dynamic pressure (see eq. (21)). The maximum absolute error in surface static pressure, or maximum difference between numerical and experimental pressures, for each of the cross sections of figure 18 is presented in table 1. Table 1 shows that the errors are very much less than the maximum error calculated from the equivalence principle theory of Van Dyke. It is believed that the static pressure errors in the vicinity of the body's nose would be of the order of 19 percent and would decay rapidly as τ decreased. For example, at the station 0.502 diameter, the parameter τ is 0.481, which results in a predicted absolute maximum error of 11 percent of free-stream dynamic pressure. Therefore, the numerical results are consistent with the equivalence principle theory of Van Dyke.

TABLE 1.- MAXIMUM SURFACE PRESSURE ERROR IN VARIOUS CROSS-SECTIONAL PLANES

Axial station, maximum cylinder diameter	$\lvert\Delta P\rvert/q$, percent
0.502	5
2.990	1
1.289	3
3.970	5
4.920	4
5.830	4
7.630	3

Drag and lift coefficients were determined on the basis of numerical pressure data only; shear stress effects were not included. To compute these coefficients, the pressure coefficients on the ogive-cylinder surface were numerically integrated to determine the lift and drag. Comparison of the numerical and experimental coefficients, as shown in figure 20, was found to be very satisfactory. The coefficients of total drag from the two sources proved to be almost identical functions of distance from the nose of the ogive. Differences in the lift coefficient curves began to be significant at

a distance of about 2.75 diameters from the nose of the ogive, increased to a maximum at about 4.5 diameters, and then decreased; the numerical lift coefficient was approximately 5.8 percent higher than that measured at about 4.5 diameters from the ogive nose, and about 2 percent higher at 8.35 diameters from the nose.

An overestimated lift coefficient is consistent with the fact that separation occurred earlier in the numerical flow field than in the experimental field. Lift coefficients are calculated from pressure forces on the surface of the body, as projected in a plane parallel to that of free-stream flow. Since the area of the appropriate projection is almost entirely derived from the body's long cylindrical surface, and separation takes place on that surface, separation that occurs too early increases the lift.

On the other hand, the drag coefficient should be relatively independent of the location of separation. Since the ogive becomes cylindrical at a station 3.0 diameters from its nose, the projected surface area normal to the direction of free-stream flow is very small for the long cylindrical surface aft of this station, and the corresponding pressure forces contribute very little to the total drag. Quantitative agreement in the pressure drag coefficients is therefore physically reasonable.

RESULTS OF FUSELAGE PROBLEM

For the fuselage problem the crossflow Mach number was 0.288 and the crossflow Reynolds number was 1.15×10^6/ft. Cross-section flows have been calculated in this problem in planes normal to the 7-1/2° reference line to a horizontal station 19.5 inches aft of the nose. At this station the curve bounding the body's surface represents an asymmetric fuselage configuration with a canopy. To reach this station the problem was run 2079 cycles (time steps) on the UNIVAC 1108 computer. This calculation required approximately 6 hours of computer time.

From velocity vector plots of the cross-sectional flow field, the qualitative behavior of the fuselage flow can be examined. The sequence of events as one moves downstream along the central axis of the fuselage is indicated in figures 21 to 25. The vectors in these figures correspond to the particle velocities of the flow at each mesh point of the finite difference mesh; the tail of each vector corresponds to the mesh point. Initially, a bow shock forms at the nose and an expansion fan, caused by the interaction between the expanding body and the crossflow, appears on the leeward side. This is indicated in figure 21 at a station 1.135 inches from the fuselage nose. This flow pattern continues as the fuselage cross section grows until it reaches the canopy which induces a shock wave in the flow field (see fig. 23). As the canopy radius reaches maximum (fig. 24) and starts to decrease, a rarefaction develops in the flow field above the canopy, leading to the formation of vortices (fig. 25).

The quantitative behavior of the predicted flow about the fuselage was ascertained by comparing the numerical results to experimental measurements.

The fuselage configuration of figure 6 was tested in the Ames 8- by 7-Foot Wind Tunnel. Static pressures were measured along the surface of the fuselage, and flow-field measurements with conical probes were made in cross-sectional planes normal to the horizontal reference line at a station 19.5 inches aft of the fuselage nose. The static-pressure instrumentation of the fuselage forebody surface is sketched in figure 26. The pressure taps were located in cross-sectional planes normal to the horizontal reference line. The point of intersection of the 7-1/2° reference line with this cross-sectional plane defined the axis from which pressure tap locations were measured along the periphery of the cross section. Pressure taps were located -90°, -60°, -30°, 0°, and +24° from this axis (see fig. 26). Thus, with respect to stations along the horizontal reference line, the instrumentation was located along the five planes indicated in figure 26.

Numerical and experimental distributions of surface pressure coefficients are compared in figure 27 along the five planes of figure 26. It is seen that excellent agreement has been achieved along the -90°, -60°, and -30° planes. The numerical and experimental pressure coefficients agree along the 0° plane until station 18. Along the 24° plane there is a discrepancy at station 15. These discrepancies can be attributed to two sources: (a) a canopy shock wave-axial boundary-layer interaction, which occurs experimentally but not numerically, and (b) a slightly different calculated canopy shock location which will be described in more detail in the discussion of the flow-field results. The canopy shock-axial boundary-layer interaction spreads the shock pressure rise over a greater distance than calculated.

As in the case of the ogive-cylinder problem, an error analysis was made of the surface static pressures. The maximum slope of the fuselage geometry with respect to the free-stream flow occurred on the windward side of the body at its nose (see fig. 8). Its value was 22°, which corresponds to $\tau = 0.400$ and $M_\infty \tau = 0.998$. Therefore, the consistency condition of the theory is satisfied. According to equation (22), the maximum absolute error then becomes 5 percent of the free-stream dynamic pressure. On the basis of the results of figure 27, the maximum error, $|\Delta P|/q_\infty$, in each of the planes was determined and the values are tabulated in table 2. It is seen from the table that the errors recorded are consistent with the maximum error calculated from the equivalence principle theory.

TABLE 2.- MAXIMUM SURFACE PRESSURE ERROR ALONG THE FIVE PLANES OF FIGURE 33

Plane, deg	$\lvert\Delta P\rvert/q_\infty$, percent
-90	2.0
-60	2.3
-30	3.4
0	5.6
24	5.8

At first glance, the relatively small errors of table 2 are surprising since the hypersonic equivalence principle is applied at supersonic speeds. One would expect only linearized supersonic theory to apply in this Mach number range. However, an analysis of the errors shows that linearized supersonic theory is only slightly more accurate for this fuselage. The error in

linearized supersonic theory is of order τ which results in a maximum error in static pressure of 4 percent of free-stream dynamic pressure. Thus, for a body with maximum slope, τ, great enough such that $M_\infty \tau = O(1)$, both the hypersonic equivalence principle and linearized supersonic theory give satisfactory results at supersonic speeds for $M_\infty > 2$.

Contour plots of the local pitot pressure ratio (P_p/P_{s_∞}), local sideslip angle (β), local Mach number (M), local angle of attack (α_e), and local total pressure ratio (P_s/P_{s_∞}) were generated from the numerical results and compared to corresponding contour plots from experimental data. The comparisons were made in a cross-sectional plane normal to the horizontal reference line at a station 19.5 inches from the fuselage apex. See figures 28 through 32.

The local pitot pressure, P_p, is effectively the stagnation pressure measured by a probe whose axis is parallel to the local flow direction. As in the case of the surface pressures the pitot pressure is measured directly; therefore, it provides a reliable measurement for comparison. The numerical pitot pressure was calculated from the Rankine-Hugoniot equations for a normal shock, where upstream of the shock the local Mach number and stagnation pressure were assumed to exist. The numerical and experimental pitot pressure ratios (P_p/P_{s_∞}) of figure 28 indicate good agreement in the lower quadrant of the flow field, where the two sets of P_p/P_{s_∞} contours are nearly coincident in the vicinity of the body. This quantitative agreement is in accord with the agreement obtained between surface static pressures on the -30° plane, which intersects the body in this region. In the upper quadrant of the flow field there is a discrepancy between the experimental and numerical contours. The numerical results indicate that the canopy shock intersects the fuselage surface above that point indicated by the experimental data. The increased downward distance of travel by the canopy shock in the experimental case accounts for the discrepancy in contours in the upper quadrant of the flow field. Although axial boundary-layer effects and discretization errors influence the canopy shock location, it is believed the equivalence principle approximation of neglecting the axial perturbation velocity is the primary cause of this discrepancy. The axial perturbation velocity is zero upstream of the body apex; thus the bow shock and windward flow field were calculated correctly. However, these perturbation velocities do exist in the vicinity of the canopy. The canopy shock is thus predicted imbedded in a flow field differing from the actual situation, and consequently, the location and strength of the canopy shock do not agree with experimental data.

The local sideslip angle, β, is measured in the cross-sectional plane normal to the horizontal reference line and is the flow inclination in the x', z' plane (see fig. 9). As in the case of the pitot pressures, the comparison of the experimental and numerical sideslip angle contours shown in figure 29 indicates that the predicted flow field in the lower quadrant is nearly correct. Furthermore, the predicted location of the canopy shock and the predicted flow-field contours in the upper quadrant deviate from experiment as in the pitot pressure comparisons.

Contours of constant Mach number and constant local angle of attack with respect to the horizontal reference line (see fig. 8) are presented in figures

30 and 31, respectively. It is seen from these figures that the numerical Mach number and angle-of-attack contours do not match the experimental contours even in the lower quadrant of the flow field. This discrepancy is not in accord with the surface static pressure comparison, pitot pressure comparison, and sideslip angle comparison discussed previously.

The reasons for this disagreement can be found in discretization errors in the numerical method, errors introduced by the equivalence principle assumption, and errors inherent in the experiment and data reduction process. The error in Mach number due to the equivalence principle has been determined previously (see eq. (28)). Equation (28), evaluated with $\tau = 0.40$ and $M_\infty = 2.5$, results in an absolute error of about 0.7 percent of the free-stream Mach number. This corresponds to an absolute Mach number error of about 0.02. Consider the experimental contour of figure 30 for a constant Mach number of 2.50. It is seen from figure 30 that this contour coincides with the numerical contour for a constant Mach number of 2.40, which results in an absolute Mach number difference of 0.10. Thus, the observed absolute difference in Mach number between the numerical and experimental results is five times the maximum error one would expect from the equivalence principle alone. Also, it is well known that Mach number and angle of attack are much more difficult to measure accurately than surface static pressures and pitot pressures. Therefore, one must conclude that the experiment and data reduction process are, at least in part, responsible for these discrepancies.

The calculated local total pressure recovery contours (P_s/P_{s_∞}) are shown in figure 32. The predicted total pressure recovery varies from 1.0 to 0.88 in the flow field, with recoveries near 1.0 throughout most of the flow region. This parameter is the most difficult to calculate accurately and to determine experimentally. Although the experimental data for this fuselage configuration are still preliminary, an error analysis indicates that the values of P_s/P_{s_∞} can be determined only within ±0.03. For a total pressure ratio bandwidth from 0.88 to 1.0, this error is too large to yield any significant contour data. Consequently, no experimental data are shown. Future refinement of the set of conical probe calibration data will hopefully reduce this error to a more meaningful level.

Numerical lift and drag coefficients for the fuselage problem are compared to corresponding lift and drag coefficients determined from inviscid, linearized supersonic theory for flow about an axisymmetric slender body at angle of attack (ref. 14). Linearized supersonic slender body theory was used because there were not enough pressure data to determine the lift and drag experimentally. The lift and drag coefficients from the numerical method were determined by numerical integration of the surface pressure coefficients over the surface and are based on a cross-sectional area corresponding to the maximum equivalent radius of the fuselage, $a_{max} = 3$ inches. As in the case of the ogive-cylinder problem, shear stress effects were not included. It is seen from figure 33 that the numerical drag coefficient distribution shows greater drag than the distribution from theory, due in part to the slenderness assumption of the theory. On the other hand, the numerical lift coefficient distribution nearly corresponds to that of linearized supersonic theory. This comparison does indicate that the lift and drag coefficients calculated by the numerical method of this paper, if not correct, are at least of the right order.

CONCLUSIONS

A numerical method has been developed for calculating three-dimensional flow fields about slender bodies at supersonic speeds. The primary advantage of the method is that detailed predictions may be obtained for realistic fuselage configurations at angle of attack. Secondly, boundary-layer separation and development of spiral vortex sheets are predicted by the method. Major sources of error in the method are neglect of the axial perturbation velocity, neglect of axial viscous effects, and exclusion of any turbulence phenomena.

The method can adequately predict the surface pressures and flow-field characteristics outside the boundary layer for bodies where the hypersonic similarity parameter, $M_\infty\tau$, is unity or greater and for free-stream Mach numbers of 2 and above. For the ogive-cylinder and fuselage problems, the surface static pressure distributions differed from corresponding experimental values by no more than 6 percent of the free-stream dynamic pressure. These deviations are contained within the predicted error bounds of the equivalence principle. From velocity vector plots and contour plots, the structure of the calculated flow field appeared correct, at least qualitatively. Contour plots of pitot pressures were of the same general shape as the experimental contours for the fuselage configuration, and good quantitative agreement was obtained in the lower quadrant of the flow field. Since the error inherent in the equivalence principle becomes smaller as the Mach number is increased and with the condition $M_\infty\tau = O(1)$ maintained, the accuracy of the numerical method will improve at higher Mach numbers. Additional comparisons between numerical results and experiment at higher Mach numbers would be desirable, however, to strengthen this conclusion.

The positions of boundary-layer separation points and vortex centers were not accurately predicted by the numerical method. Neglect of axial viscous effects and exclusion of any turbulence phenomena, which were observed experimentally, are considered responsible for these inaccuracies in the computed results. From the two problems which were run, it was not possible to determine the relative effects of viscosity in the axial and crossflow directions or to determine to what extent exclusion of turbulence affected the numerical results. Solution of another problem duplicating the body geometry and flight conditions of an experimental test at hypersonic speed and in the laminar flow regime would provide more understanding of the relationship between axial and crossflow viscous effects. At this flight condition differences between numerical and experimental results are attributable predominantly to neglect of axial viscous effects since errors in the equivalence principle are minimized and turbulence is not a consideration.

APPENDIX A

THE EQUIVALENCE PRINCIPLE

In this section the equivalence principle for steady, inviscid three-dimensional flow is derived. An Eulerian coordinate system fixed with respect to the body and having its z axis along the axis of the body is used throughout this section (see fig. 2).

The equations of motion for steady, inviscid three-dimensional flow about a body are:

Continuity

$$\frac{\partial}{\partial x}(\rho u) + \frac{\partial}{\partial y}(\rho v) + \frac{\partial}{\partial z}\left[\rho(U_\infty \cos\alpha + w)\right] = 0 \tag{A1}$$

Momentum

$$u\frac{\partial u}{\partial x} + v\frac{\partial u}{\partial y} + (w + U_\infty \cos\alpha)\frac{\partial u}{\partial z} = -\frac{1}{\rho}\frac{\partial P}{\partial x} \tag{A2a}$$

$$u\frac{\partial v}{\partial x} + v\frac{\partial v}{\partial y} + (w + U_\infty \cos\alpha)\frac{\partial v}{\partial z} = -\frac{1}{\rho}\frac{\partial P}{\partial y} \tag{A2b}$$

$$u\frac{\partial w}{\partial x} + v\frac{\partial w}{\partial y} + (w + U_\infty \cos\alpha)\frac{\partial w}{\partial z} = -\frac{1}{\rho}\frac{\partial P}{\partial z} \tag{A2c}$$

First law

$$u\frac{\partial E}{\partial x} + v\frac{\partial E}{\partial y} + (w + U_\infty \cos\alpha)\frac{\partial E}{\partial z} = -P\left[u\frac{\partial}{\partial x}\frac{1}{\rho} + v\frac{\partial}{\partial y}\frac{1}{\rho} + (w + U_\infty \cos\alpha)\frac{\partial}{\partial z}\frac{1}{\rho}\right] \tag{A3}$$

Boundary conditions at body

$$(U_\infty \cos\alpha + w)\ell_z + v\ell_y + u\ell_x = 0 \tag{A4a}$$

Boundary conditions at shock

$$\rho_\infty U_\infty(\cos\alpha n_z + \sin\alpha n_y) = \rho_s[(U_\infty \cos\alpha + w_s)n_z + v_s n_y + u_s n_x] \tag{A4b}$$

$$\rho_\infty + \rho_\infty U_\infty^2(\cos\alpha n_z + \sin\alpha n_y)^2 = P_s + \rho_s[(U_\infty \cos\alpha + w_s)n_z + v_s n_y + u_s n_x]^2 \tag{A4c}$$

$$\frac{\gamma}{\gamma - 1}\frac{P_\infty}{\rho_\infty} + \frac{1}{2}U_\infty^2(\cos\alpha n_z + \sin\alpha n_y)^2$$

$$= \frac{\gamma}{\gamma - 1}\frac{P_s}{\rho_s} + \frac{1}{2}[(U_\infty \cos\alpha + w_s)n_z + v_s n_y + u_s n_x]^2 \qquad \text{(A4d)}$$

where E is the internal energy per unit mass, P is the pressure, ρ is the density, U_∞ is the free-stream speed, w is perturbation velocity in the z direction, v is the velocity in the y direction, u is the velocity in the x direction, and ℓ_x, ℓ_y, and ℓ_z are the direction cosines of the body normal in the x, y, and z directions, respectively. The subscript s refers to properties downstream of the shock, and n_x, n_y, n_z are the direction cosines of the shock normal in the x, y, and z directions, respectively.

Boundary conditions far from body

$$z = -\infty : \quad w = 0 , \quad v = U_\infty \sin\alpha , \quad u = 0 \qquad \text{(A4e)}$$

Introducing the transformation equations

$$\left.\begin{aligned} z &= U_\infty \cos\alpha t \\ y &= y \\ x &= x \end{aligned}\right\} \qquad \text{(A5)}$$

and the slender body assumption

$$U_\infty >> w$$

into equations (A1) through (A4) yields

Continuity

$$\frac{\partial\rho}{\partial t} + \frac{\partial}{\partial x}(\rho u) + \frac{\partial}{\partial y}(\rho v) = 0 \qquad \text{(A6)}$$

Momentum

$$\frac{\partial w}{\partial t} + u\frac{\partial w}{\partial x} + v\frac{\partial w}{\partial y} = -\frac{1}{\rho}\frac{\partial P}{\partial t}\frac{1}{U_\infty \cos\alpha} \qquad \text{(A7a)}$$

$$\frac{\partial v}{\partial t} + u\frac{\partial v}{\partial x} + v\frac{\partial v}{\partial y} = -\frac{1}{\rho}\frac{\partial P}{\partial y} \qquad \text{(A7b)}$$

$$\frac{\partial u}{\partial t} + u\frac{\partial u}{\partial x} + v\frac{\partial u}{\partial y} = -\frac{1}{\rho}\frac{\partial P}{\partial x} \qquad \text{(A7c)}$$

First law

$$\frac{\partial E}{\partial t} + u\frac{\partial E}{\partial x} + v\frac{\partial E}{\partial y} = -P\left(\frac{\partial}{\partial t}\frac{1}{\rho} + u\frac{\partial}{\partial x}\frac{1}{\rho} + v\frac{\partial}{\partial y}\frac{1}{\rho}\right) \tag{A8}$$

Boundary conditions at body

$$\cos\alpha U_\infty \ell_z + u\ell_x + v\ell_y = 0 \tag{A9a}$$

Boundary conditions at shock

$$\rho_\infty U_\infty(-\cos\alpha\sin\beta + \sin\alpha\cos\beta) = \rho_s(v_s n_y + u_s n_x - U_\infty\cos\alpha\sin\beta) \tag{A9b}$$

$$P_\infty + \rho_\infty U_\infty(-\cos\alpha\sin\beta + \sin\alpha\cos\beta)^2 = P_s + \rho_s(v_s n_y + u_s n_x - U_\infty\cos\alpha\sin\beta)^2 \tag{A9c}$$

$$\frac{\gamma}{\gamma - 1}\frac{P_\infty}{\rho_\infty} + \frac{U_\infty(-\cos\alpha\sin\beta + \sin\alpha\cos\beta)^2}{2} = \frac{\gamma}{\gamma - 1}\frac{P_s}{\rho_s} + (v_s n_y + u_s n_x - U_\infty\cos\alpha\sin\beta)^2 \tag{A9d}$$

where β is the angle made by the shock surface with respect to the z axis in the y, z plane. Equations (A6), (A7b), (A7c), and (A8) are independent of w and, thus, represent the equations for time-dependent motion in the x, y plane. Therefore, the steady 3-D equations of motion have been transformed to a time-dependent 2-D set of equations. The 3-D shock boundary conditions also reduce to a nonsteady shock in the x, y plane moving with velocity proportional to $U_\infty\cos\alpha\sin\beta$. In summary, the necessary and sufficient conditions for the equivalence principle to be valid are:

1. The z component of the local velocity vector must be approximately equal to the z component of the free-stream velocity vector, and

2. The time-dependent solution in the x, y plane must satisfy the three-dimensional boundary condition equation (A9a) at the body surface.

The calculational procedure for inviscid flow is then as follows: First, equations (A6), (A7b), (A7c), (A8), and (A9a) are solved for v, u, P, and ρ. The perturbation velocity w may be subsequently obtained from the Bernoulli equation, which is

$$\frac{\gamma}{\gamma - 1}\frac{P}{\rho} + \frac{(w + U_\infty\cos\alpha)^2 + v^2 + u^2}{2} = \text{constant} \tag{A10}$$

Therefore, the equivalence between a steady three-dimensional flow and a time-dependent two-dimensional flow is proven.

If the conditions (1), (2) are satisfied, viscous effects can be included in the time-dependent calculations in the x, y plane without violating the equivalence principle assumptions. A no-slip boundary condition can be applied at the surface of the cross section in the x, y plane in conjunction with the equivalence principle boundary condition equation (A9a).

APPENDIX B

CONSERVATION OF TOTAL ENERGY

In this section the self-consistency property of form that the finite difference equations (8) to (13) possess is demonstrated. This demonstration proceeds in three steps. First, the finite difference kinetic energy equation is derived for the momentum zone $a_{\ell-(1/2)}, a_{\ell+(1/2)}$. Then the finite difference first law equation is derived for this momentum zone. Finally, these relations are added to determine the finite difference equation of total energy for the momentum zone $a_{\ell-1}, a_{\ell-(1/2)}$.

The kinetic energy equation for momentum zone $a_{\ell-(1/2)}, a_{\ell+(1/2)}$ can be derived from momentum equation (12) which is centered at the time $t^{n-(1/2)}$. Equation (12) can be written in terms of velocities by employing the forward extrapolation relation, equation (13):

$$\frac{1}{2} m_\ell \frac{U_\ell^{n+(1/2)} - U_\ell^{n-(3/2)}}{\Delta t} = \left[P_{\ell-(1/2)}^{n-(1/2)} - P_{\ell+(1/2)}^{n-(1/2)}\right] \tag{B1}$$

Multiplying equation (B1) by $U_\ell^{n-(1/2)}$ yields the kinetic energy equation for momentum zone $a_{\ell-(1/2)}, a_{\ell+(1/2)}$.

$$\frac{m_\ell}{\Delta t}\left[\frac{U_\ell^{n+(1/2)} U_\ell^{n-(1/2)}}{2} - \frac{U_\ell^{n-(1/2)} U_\ell^{n-(3/2)}}{2}\right] = U_\ell^{n-(1/2)}\left[P_{\ell-(1/2)}^{n-(1/2)} - P_{\ell+(1/2)}^{n-(1/2)}\right] \tag{B2}$$

The first law equation for momentum zone $a_{\ell-(1/2)}, a_{\ell+(1/2)}$ is derived as follows: the internal energy for this zone equals half the sum of the internal energies of thermodynamic zones $a_{\ell-1}, a_\ell$ and $a_\ell, a_{\ell+1}$ (see eqs. (9) and (10)). This division of internal energy comes directly from the relationship between thermodynamic and momentum zones specified when the physical model of figure 6 was postulated. The $-P(\Delta v/\Delta t)$ term for momentum zone $a_{\ell-(1/2)}, a_{\ell+(1/2)}$ comes from half the $-P(\Delta v/\Delta t)$ for thermodynamic zones $a_{\ell-1}, a_\ell$ and $a_\ell, a_{\ell+1}$. The first law equation for momentum zone $a_{\ell-(1/2)}, a_{\ell+(1/2)}$ becomes:

$$m_\ell \frac{(1/2)\left[E^n_{\ell-(1/2)} + E^n_{\ell+(1/2)}\right] - (1/2)\left[E^{n-1}_{\ell-(1/2)} + E^{n-1}_{\ell+(1/2)}\right]}{\Delta t}$$

$$= -\frac{1}{2}\left\{\frac{P^{n-1}_{\ell-(1/2)} + P^n_{\ell-(1/2)}}{2}\left[U^{n-(1/2)}_\ell - U^{n-(1/2)}_{\ell-1}\right]\right.$$

$$\left. + \frac{P^{n-1}_{\ell+(1/2)} + P^n_{\ell+(1/2)}}{2}\left[U^{n-(1/2)}_{\ell+1} - U^{n-(1/2)}_\ell\right]\right\} \quad \text{(B3)}$$

The finite difference equation for conservation of total energy for momentum zone $a_{\ell-(1/2)}, a_{\ell+(1/2)}$ results from the addition of equations (B2) and (B3).

$$m_\ell \frac{H^n_\ell - H^{n-1}_\ell}{\Delta t} = \left[W^{n-(1/2)}_{\ell-(1/2)} - W^{n-(1/2)}_{\ell-(1/2)}\right] \quad \text{(B4)}$$

where

$$H^n_\ell = \left[E^n_{\ell-(1/2)} + E^n_{\ell+(1/2)}\right]\frac{1}{2} + \frac{U^{n-(1/2)}_\ell U^{n+(1/2)}_\ell}{2}$$

$$W^{n-(1/2)}_{\ell-(1/2)} = \frac{P^n_{\ell-(1/2)} + P^{n-1}_{\ell-(1/2)}}{2}\,\frac{U^{n-(1/2)}_\ell + U^{n-(1/2)}_{\ell-1}}{2}$$

$$W^{n-(1/2)}_{\ell+(1/2)} = \frac{P^n_{\ell+(1/2)} + P^{n-1}_{\ell+(1/2)}}{2}\,\frac{U^{n-(1/2)}_{\ell+1} + U^{n-(1/2)}_\ell}{2}$$

Equation (B4), derived from finite difference analogs of the first law and momentum equations, is a reasonable finite difference expression for total energy conservation. The rate of work done on the surface, having the Lagrangian coordinate $a_{\ell-(1/2)}$ at time $t^{n-(1/2)}$, is the product of the time-averaged pressure in the thermodynamic zone $a_{\ell-1}, a_\ell$ and the space-averaged velocity between surfaces $a_{\ell-1}$ and a_ℓ. The internal energy of the momentum zone $a_{\ell-(1/2)}, a_{\ell+(1/2)}$ at time t^n, is half the internal energy of the two thermodynamic zones that contain it. Finally, the kinetic energy

of momentum zone $a_{\ell-(1/2)}$, $a_{\ell+(1/2)}$ at time t^n, is the product of the velocities at the surface a_ℓ, at times $t^{n-(1/2)}$ and $t^{n+(1/2)}$. It is believed that this self-consistency of form property, which the differential equations possess, and which the finite equations preserve, is the primary reason for their success in numerical calculation of one-dimensional time-dependent flow fields.

REFERENCES

1. Gallo, W. F.; and Rakich, C. V.: Investigation of Methods for Predicting Flow in the Shock Layer Over Bodies at Small Angles of Attack. NASA TN D-3926, 1967.

2. Van Dyke, M. D.: A Study of Hypersonic Small-Disturbance Theory. NACA Rep. 1194, 1954.

3. Hayes, W. D.: On Hypersonic Similitude. Quarterly Appl. Math., vol. 5, 1947, pp. 105-106.

4. Lees, L.; and Reeves, B. L.: Laminar Near Wake of Blunt Bodies in Hypersonic Flow. AIAA J., vol. 3, no. 11, 1965, pp. 2061-2074.

5. von Neumann, J.; and Richtmyer, R. D.: A Method for the Numerical Calculation of Hydrodynamic Shocks. J. Appl. Phys., vol. 21, no. 3, March 1950, p. 232.

6. Richtmyer, R. D.: Difference Methods for Initial Value Problems. Wiley (Interscience), New York, 1957.

7. Trulio, J. G.; and Trigger, K.: Numerical Solution of the One-Dimensional Hydrodynamic Equations. UCRL 2667, 1961.

8. Trulio, J. G.: Studies of Finite Difference Equations for Continuum Mechanics. WL-TDR-64-72, 1964.

9. Trulio, J.: Theory and Structure of the AFTON Codes. Tech. Rep. AFWL TR-66-19, 1966.

10. Walitt, L.: Numerical Studies of Supersonic Near-Wakes. Ph.D. Thesis, Univ. of California, Los Angeles, 1969.

11. Trulio, J. G.; Niles, W.; and Carr, W.: Calculations of Two-Dimensional Turbulent Flow Fields. NASA CR-430, 1966.

12. Jorgensen, L. H.; and Perkins, E. W.: Investigation of Some Wake Vortex Characteristics of an Inclined Ogive-Cylinder Body at Mach 1.98. NACA RM A55E31, 1955.

13. Schlichting, H.: Boundary Layer Theory. McGraw-Hill Book Co., Inc., 1955, p. 19.

14. Liepmann, H. W.; and Roshko, A.: Elements of Gas Dynamics. John Wiley and Sons, Inc., 1962, pp. 239-247.

FLOW FIELD IN FUSELAGE CROSS SECTION PLANE

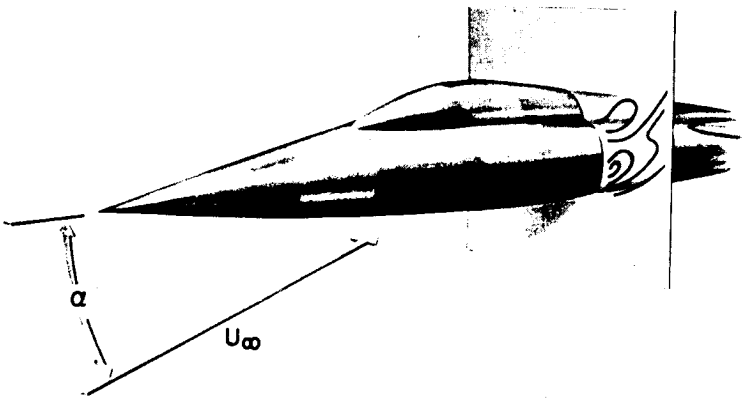

Figure 1

APPLICATION OF THE
EQUIVALENCE PRINCIPLE TO AN AXISYMMETRIC BODY

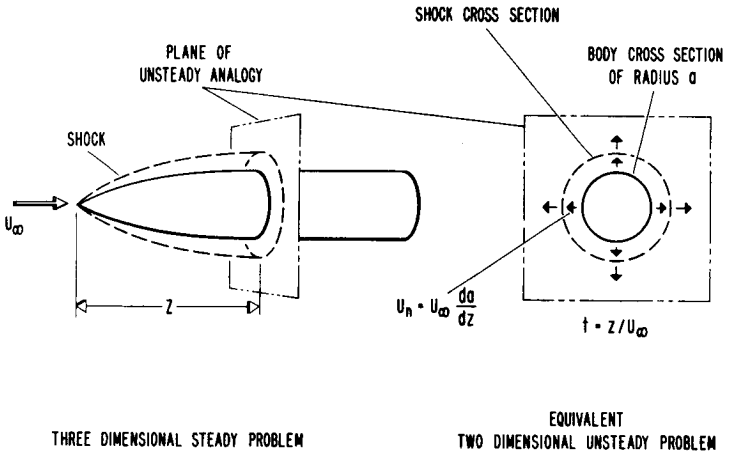

Figure 2

FLOW FIELD ABOUT AN AXISYMMETRIC BODY
AT ANGLE OF ATTACK

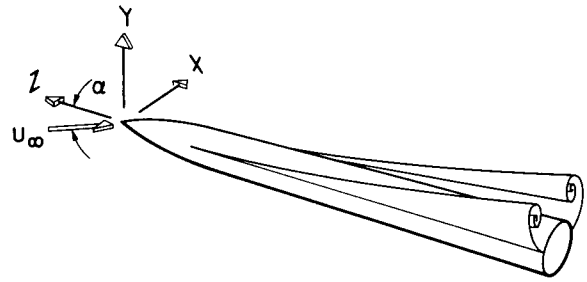

Figure 3

FLOW REGIONS ABOUT A BODY MOVING AT
SUPERSONIC VELOCITY

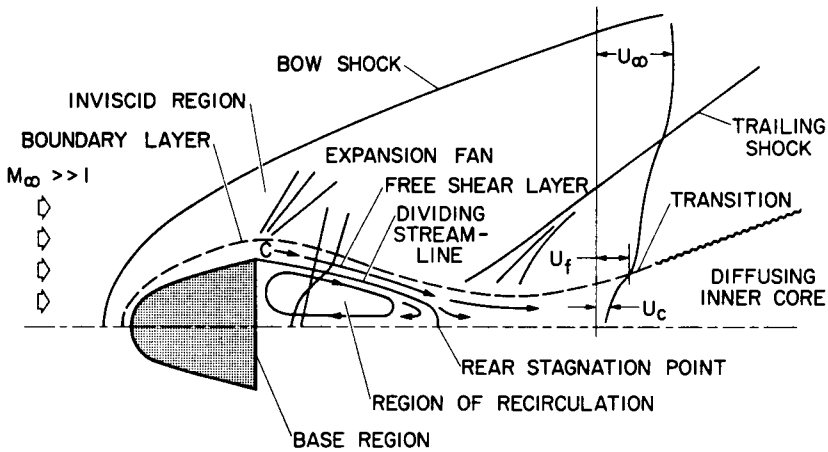

Figure 4

ONE-DIMENSIONAL, TIME-DEPENDENT MOTION
IN LAGRANGIAN COORDINATES

PARTICLE TRAJECTORIES IN A
LAGRANGIAN COORDINATE SYSTEM

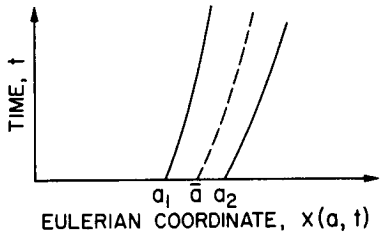

EULERIAN COORDINATE, $x(a, t)$

THERMODYNAMIC AND MOMENTUM ZONES FOR
ONE-DIMENSIONAL TIME-DEPENDENT MOTION

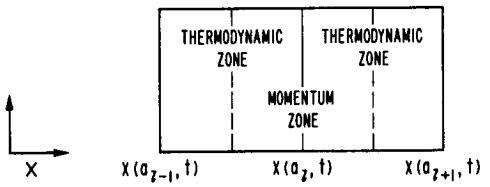

Figure 5

SCHEMATIC DIAGRAM OF A FINITE DIFFERENCE MESH

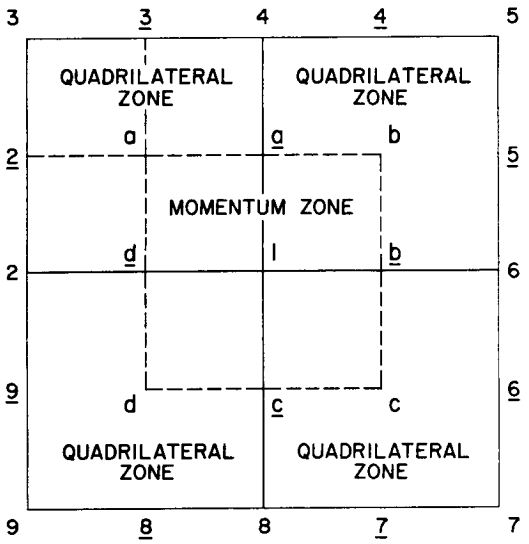

Figure 6

OGIVE-CYLINDER BODY GEOMETRY

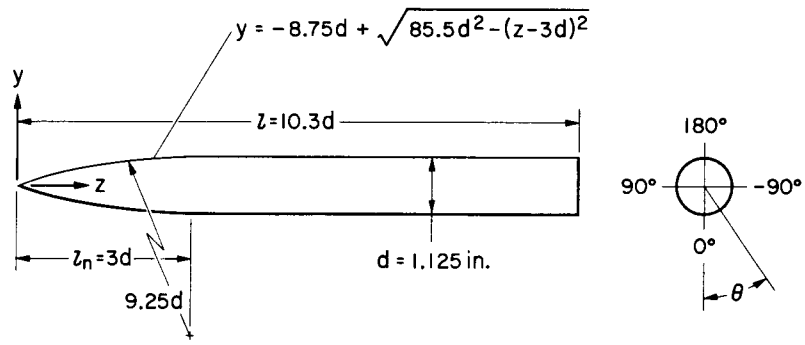

Figure 7

SCHEMATIC OF FUSELAGE CONFIGURATION

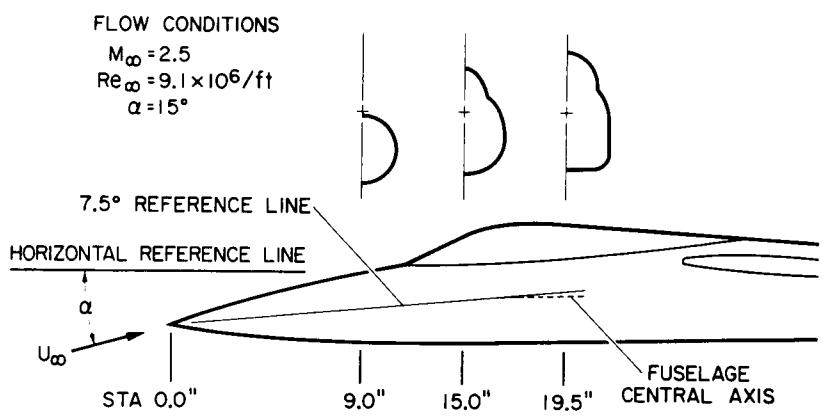

Figure 8

DEFINITION OF FUSELAGE CROSS-SECTIONAL PARAMETERS

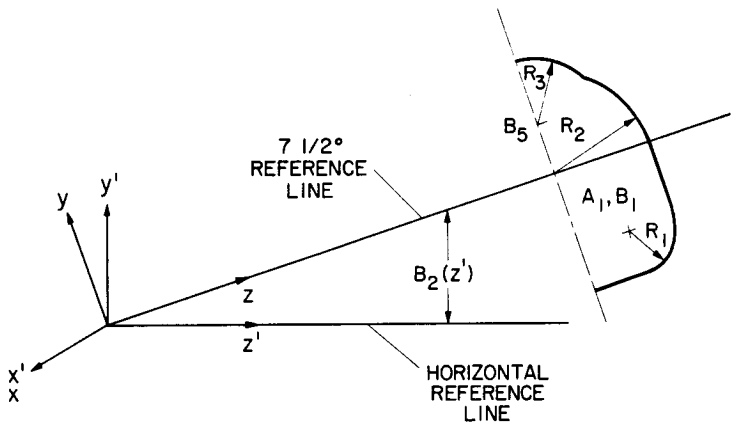

Figure 9

FINITE DIFFERENCE MESH FOR OGIVE-CYLINDER
RADIUS 0.01 ft

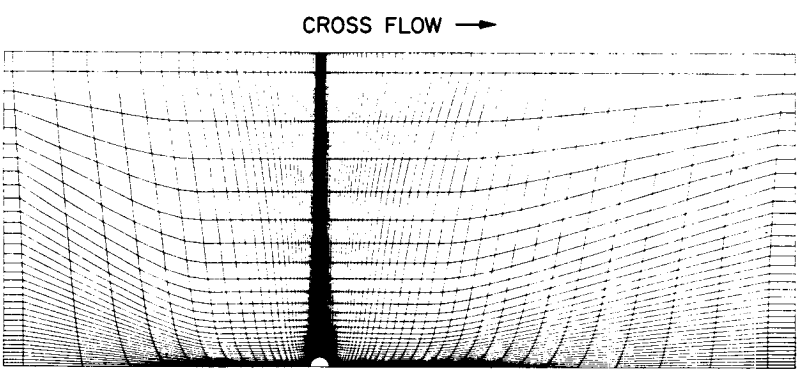

Figure 10

FINITE DIFFERENCE MESH FOR OGIVE-CYLINDER

RADIUS 0.046875 ft

CROSS FLOW →

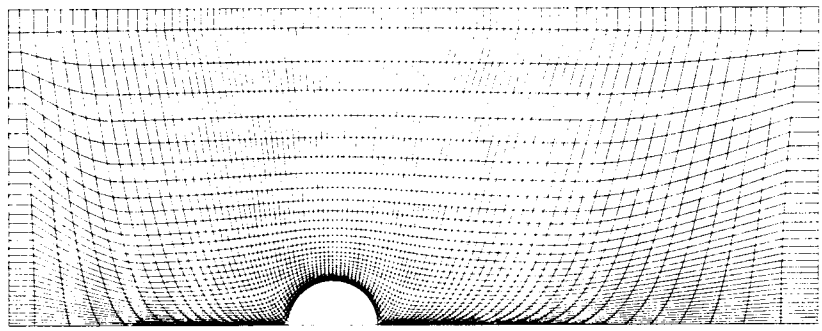

Figure 11

FINITE DIFFERENCE MESH AT STA 7.0

CROSS FLOW →

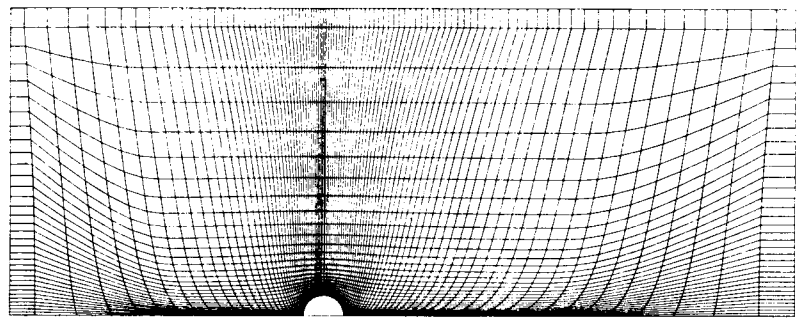

Figure 12

FINITE DIFFERENCE MESH AT STA 25.0

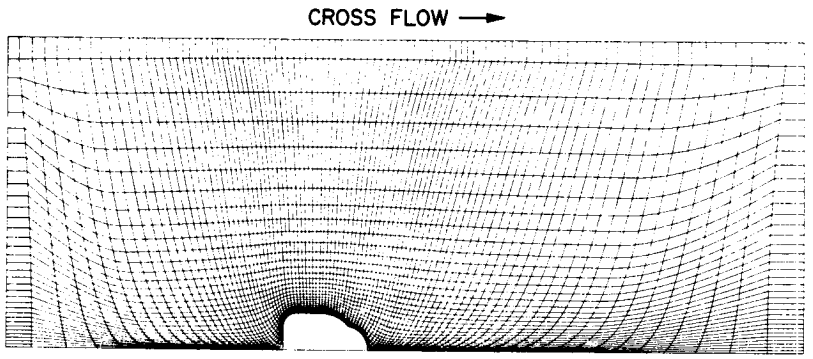

Figure 13

VELOCITY VECTOR PLOT OF FLOW FIELD
0.502 MAX BODY DIAMETERS FROM NOSE
RADIUS 0.0145 ft

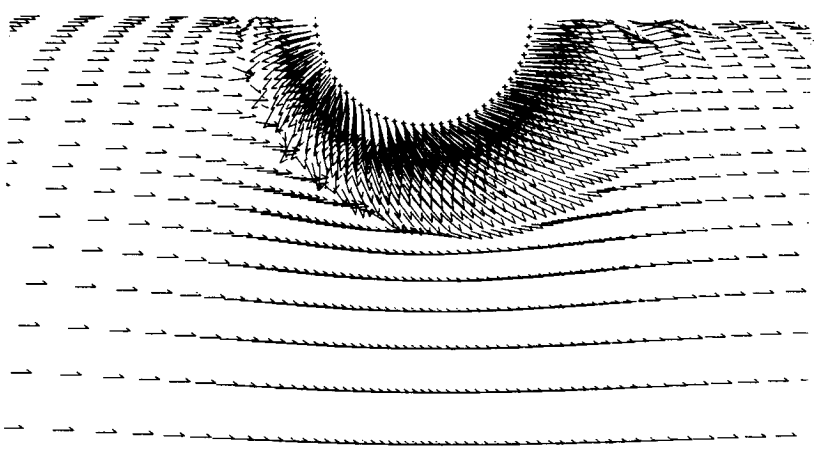

Figure 14

VELOCITY VECTOR PLOT OF FLOW FIELD
2.99 MAX BODY DIAMETERS FROM NOSE
RADIUS 0.046875 ft

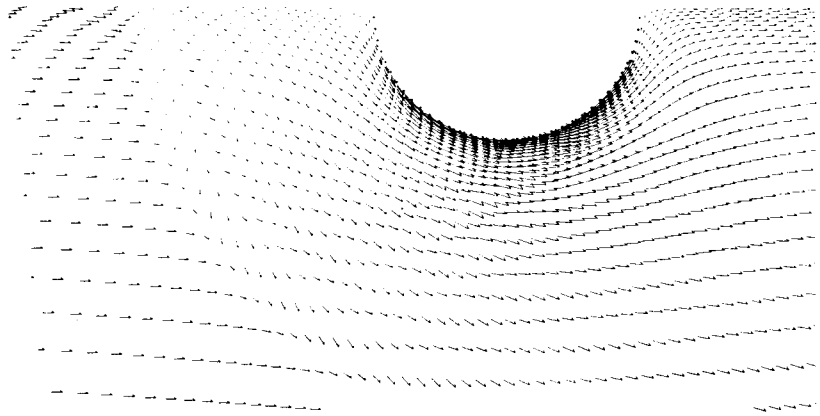

Figure 15

VELOCITY VECTOR PLOT OF FLOW FIELD
4.92 MAX BODY DIAMETERS FROM NOSE
RADIUS 0.046875 ft

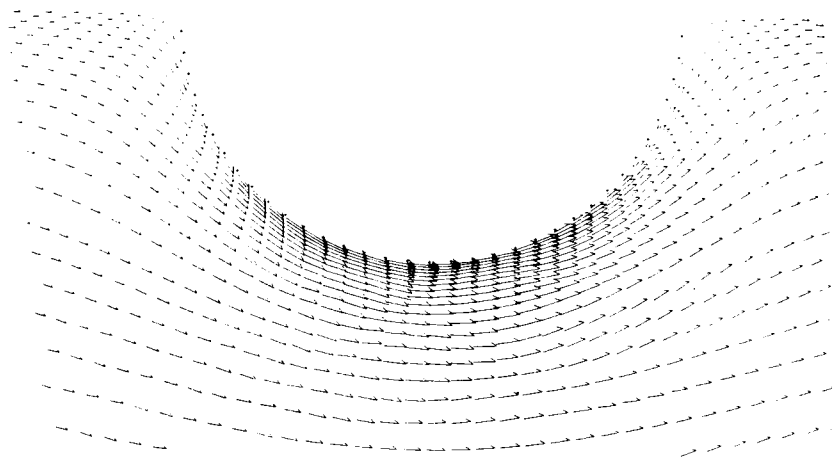

Figure 16

VELOCITY VECTOR PLOT OF FLOW FIELD
8.35 MAX BODY DIAMETERS FROM NOSE

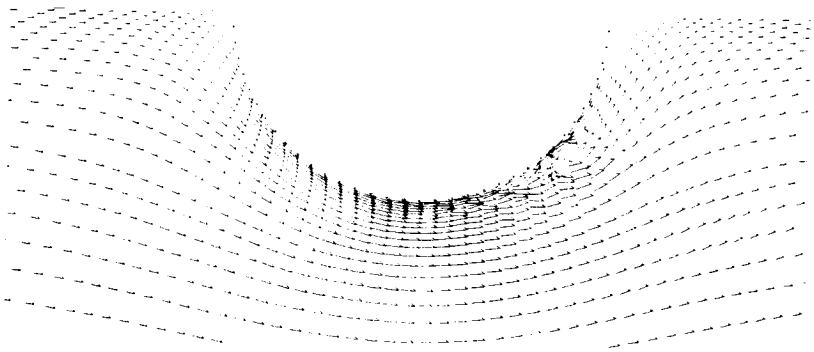

Figure 17

OGIVE-CYLINDER SURFACE PRESSURE DISTRIBUTION

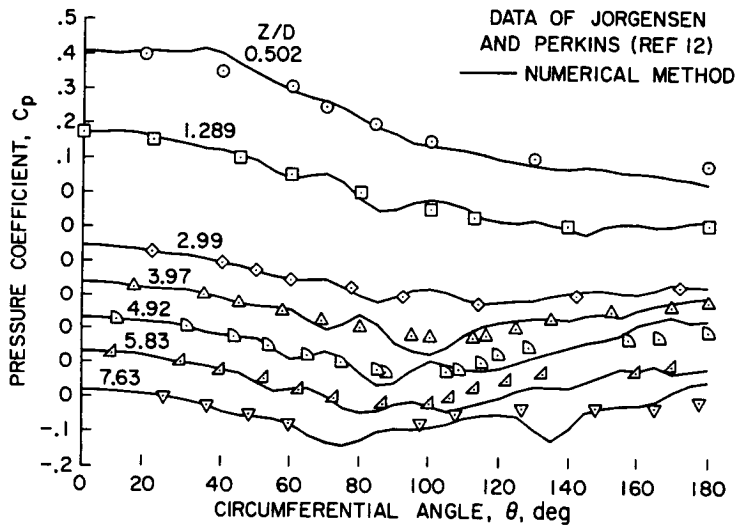

Figure 18

TRAJECTORIES OF SEPARATION AND VORTEX CENTER POINTS

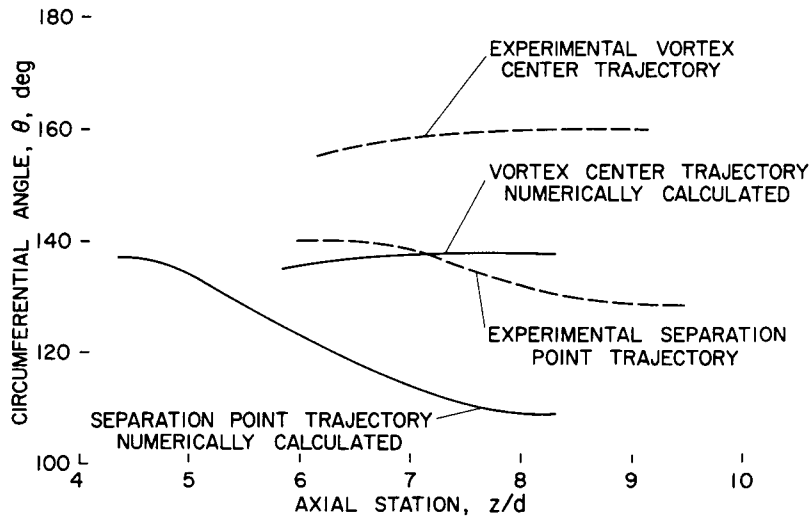

Figure 19

COMPARISON OF NUMERICAL AND EXPERIMENTAL LIFT AND DRAG COEFFICIENT DISTRIBUTIONS

OGIVE-CYLINDER BODY

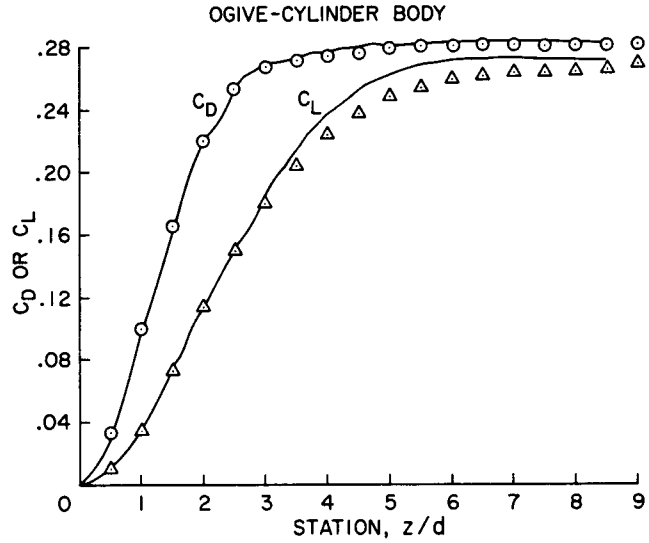

Figure 20

VELOCITY VECTOR PLOT AT STA 1.135

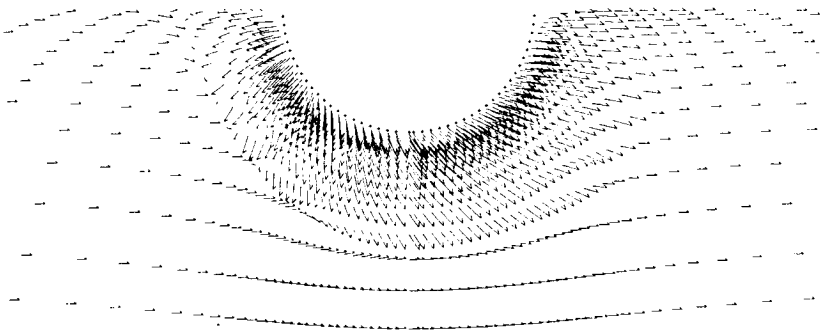

Figure 21

VELOCITY VECTOR PLOT AT STA 10.0

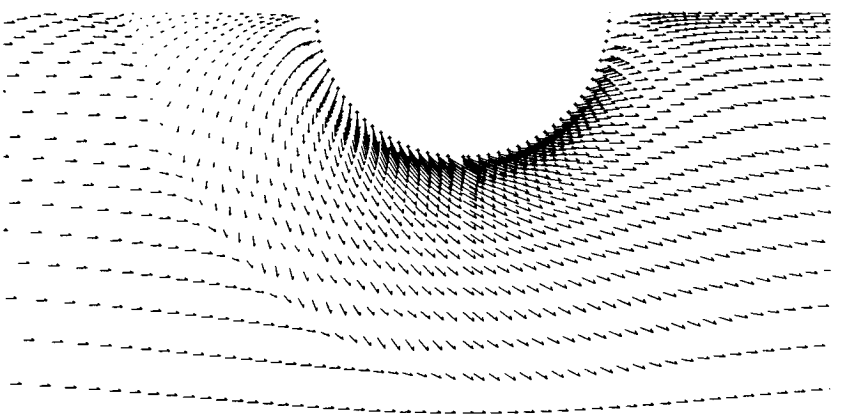

Figure 22

VELOCITY VECTOR PLOT AT STA 12.0

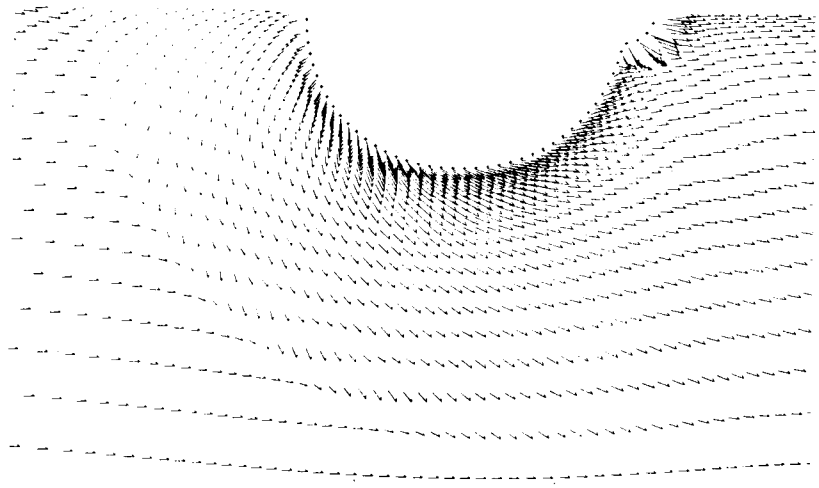

Figure 23

VELOCITY VECTOR PLOT AT STA 17.0

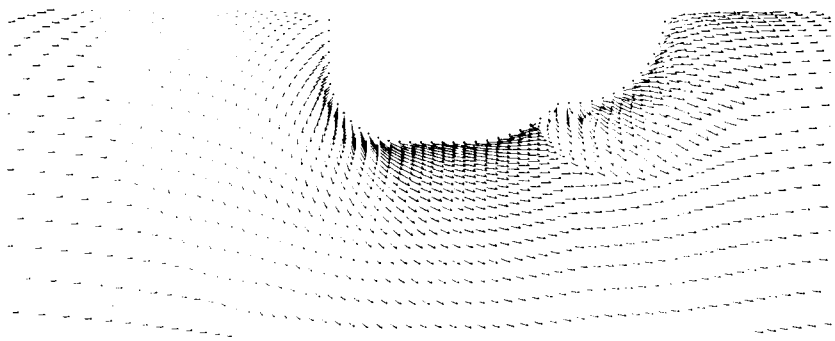

Figure 24

VELOCITY VECTOR PLOT AT STA 19.6

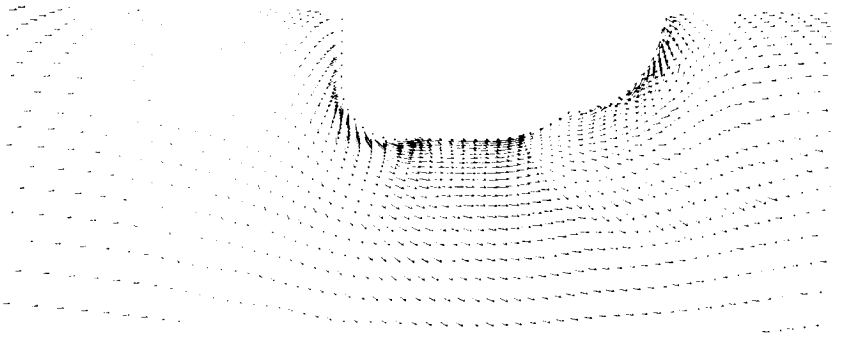

Figure 25

STATIC PRESSURE INSTRUMENTATION ON FUSELAGE FOREBODY

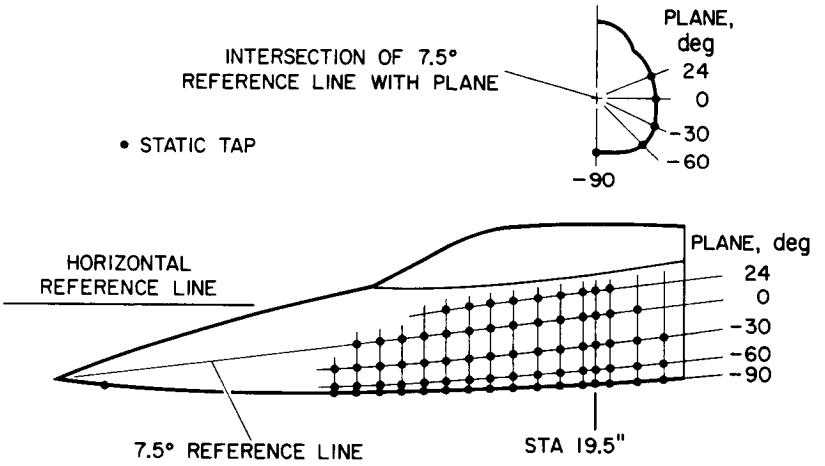

Figure 26

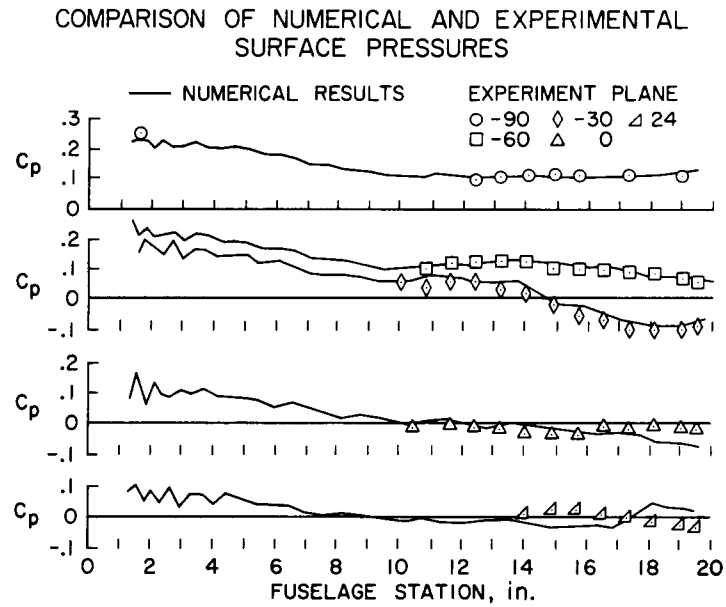

Figure 27

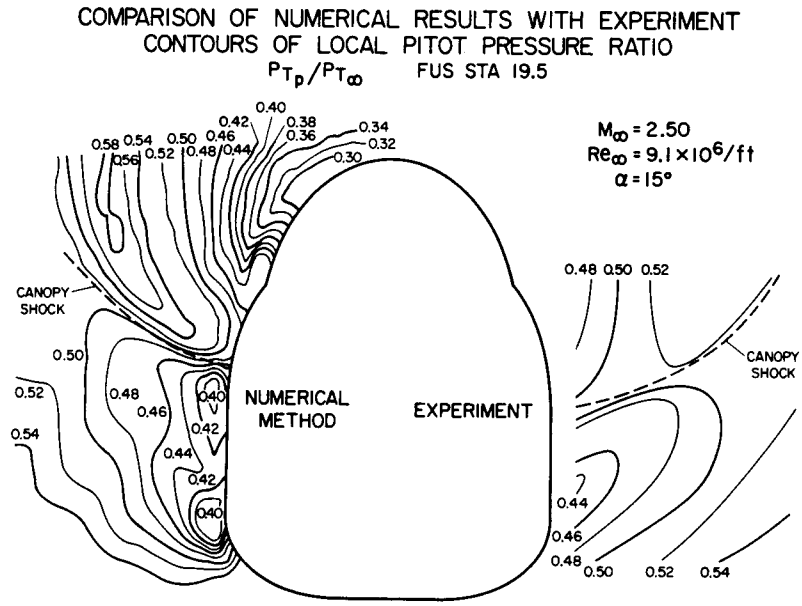

Figure 28

COMPARISON OF NUMERICAL RESULTS WITH EXPERIMENT
CONTOURS OF LOCAL SIDESLIP ANGLE, β
FUS STA 19.50

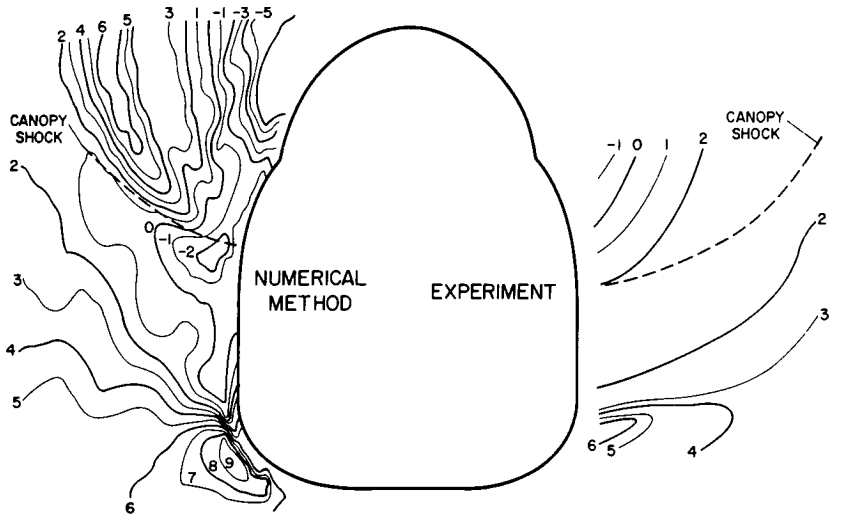

Figure 29

COMPARISON OF NUMERICAL RESULTS WITH EXPERIMENT
CONTOURS OF LOCAL MACH NUMBER, M
FUS STA 19.50

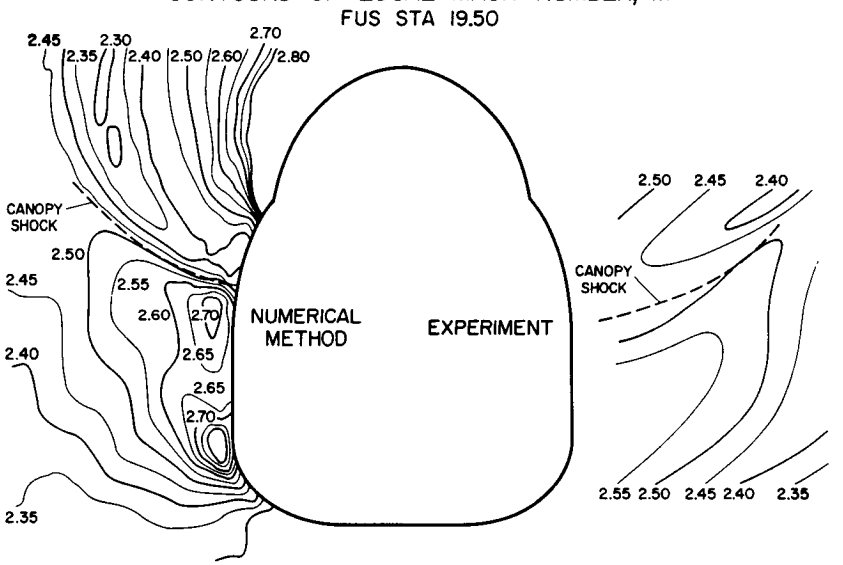

Figure 30

COMPARISON OF NUMERICAL RESULTS WITH EXPERIMENT
CONTOURS OF LOCAL ANGLE OF ATTACK, α_e
FUS STA 19.50

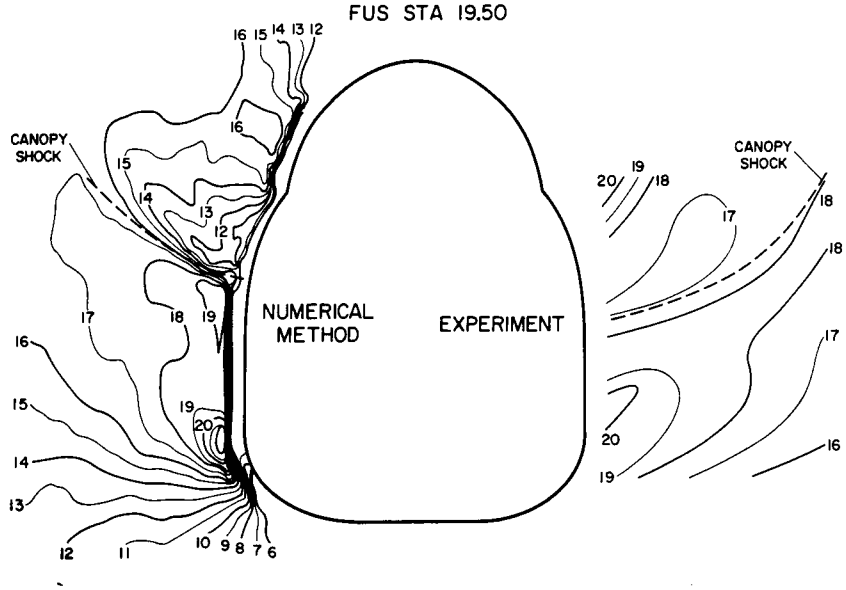

Figure 31

CONTOURS OF LOCAL TOTAL PRESSURE RATIO, p_s/p_{s_∞}
FUS STA 19.50

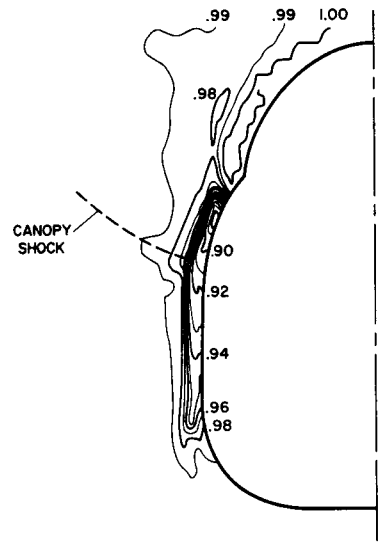

Figure 32

LIFT AND DRAG COEFFICIENT DISTRIBUTIONS
FUSELAGE CONFIGURATION

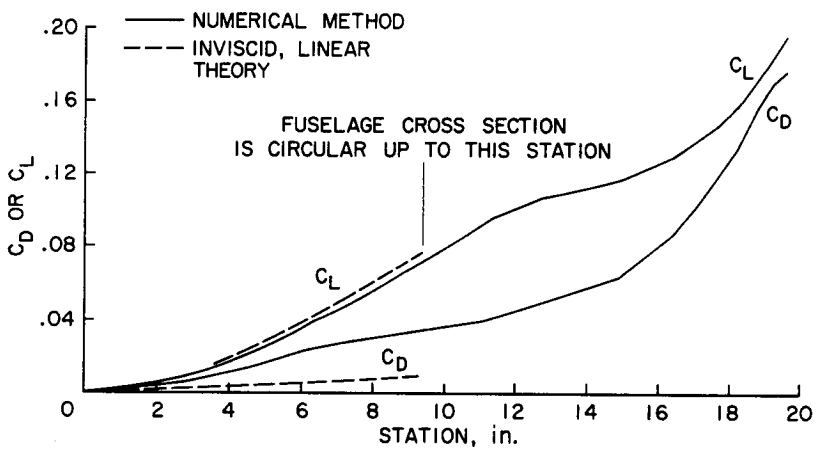

Figure 33

DISCUSSION

JAN RAAT, General Dynamics/Convair: Assuming that computing costs can be kept within reasonable limits - which is perhaps a bit optimistic at this time - numerical attacks on the hypersonic small-disturbance equations may hold some promise for unsteady flow fields, that is, flow problems in which the given body shape carries out a time-dependent motion. The equivalence principle holds true for unsteady flow. In that case one might consider a series of "planes of unsteady analogy" that follow each other at discrete time intervals.

WALLACE D. HAYES, Princeton University: I find myself in the somewhat peculiar position of trying to put down the equivalence principle, so I think a couple of remarks on what I think the proper role of the equivalence principle is are in order.

The equivalence principle was established primarily to establish a similitude, and as with most similitudes, the principal value is conceptual. It leads to an intuition and an understanding of the problem.

I believe that this type of approach to the problem of calculating supersonic flows is sound, and the way the equivalence principle fits in is that it will lead you to this particular approach.

The way the equivalence principle then ought to be applied is that it should be used strictly in the equations in the process of testing out numerical schemes to find out what will not work, what will work, what works very well. But when you actually set up a computational scheme for actual computations you should use the exact equations. They are not appreciably more complicated than the time-varying equations from the equivalence principle and you are not trying to establish a similitude. In considering x as though it were a time you are already using whatever you have acquired from the equivalence principle as leading to understanding.

WALITT: I wonder if Dr. Trulio would like to make a comment about that?

JOHN TRULIO, Applied Theory, Inc.: We used the equivalence principle in this way because to calculate three-dimensional flow directly would lead us to a very difficult implicit numerical problem. Here we are approximating (and making some error in the process) the exact statement of the problem that you feel we really should address. I think in the end the justification (for our procedure) has to lie in the comparison between actual data and the computed solution.

I would prefer myself to work toward the goal of transient three-dimensional numerical schemes (and we are) which make no approximation other than discretization assumptions, and which hopefully can be shown to lead to vanishing error to the limit of finer and finer meshes.

The work reported here is, in a sense, a digression from the main path we have followed, but I think it may be a useful one.

LARS E. ERICSSON, Lockheed Missiles and Space Co.: I think that when you try to expand this to the unsteady case you have to be very cautious. You have to make sure that you include the actual viscous flow effects, the boundary-layer collection on the leeward side with associated separation and free-body-vortex generation. I think some results obtained here at Ames by Tobak, Peterson, and others show, for instance, that at high angles of attack you can have free-body vortices on cone cylinder bodies, where the complete effect induced downstream by those vortices is determined by the relative crosswind at the conical nose section.

WALITT: I don't know what effect the crossflow at the nose section has on the lee vortices. However, when we start a problem, the calculations in the vicinity of the body nose are quite inaccurate, simply because we cannot afford to make the zoning fine enough at the nose of the body. Due to this coarse zoning, we have recorded oscillations in properties, such as the pressure, at the body nose. However, the oscillations dampen out and the answer approaches the correct answer at a station within a half diameter of the body's nose.

UNIDENTIFIED MEMBER FROM THE FLOOR: You have no way of including the effects of axial flow?

WALITT: Not exactly. However, we could include the turbulence effect. For example, in the ogive-cylinder problem, we did calculate flow separation and vortex formation. However, the separation point occurred about a diameter upstream from where the experimental separation point occurred. This deviation was a result of axial viscous effects and turbulence. The crossflow Reynolds number in the plane of calculation was laminar, whereas the actual axial Reynolds number was probably turbulent.

We believe we could, in a very empirical way, account for the axial turbulence effect. This can be done by adding crossflow eddy terms to the equations of motion. However, the effects of the axial viscous terms in the equations of motion would be more difficult to include.

JACK N. NIELSEN, Nielsen Engineering and Research, Inc.: I was wondering, were these data on the ogive-cylinder the Jorgensen and Perkins data?

WALITT: Yes.

NIELSEN: I know that they measured the position of the vortex core with the aid of the vapor stream technique and pitot tubes. Did you compare your vortex position with these experimental ones?

WALITT: Yes.

NIELSEN: Were they in good agreement?

WALITT: No. At each sectional plane, the centers of the numerically calculated vortices were about 20° closer to the windward side of the body than the centers of the experimentally determined vortices. The separation

also occurred earlier in the numerical calculations. The axial viscous terms and turbulence, which were not included in this method, account for this discrepancy. As I said before, both effects can be included in this method.

NIELSEN: Another comment, too. It seems to me that insofar as you are not getting separation, the question on the equivalence, whether the equivalence is applicable or not is exactly the same question as of whether the body is slender, in the sense of slender-body theory. Considering the body and the Mach number, it doesn't look like it is too slender, and therefore some of the points you made about that equivalence rule being applicable or not might be questionable.

WALITT: The deviations between the numerical and experimental data did conform to the maximum error predicted by Van Dyke for the equivalence principle at these flight conditions and for this geometry.

NIELSEN: Did he do it for viscous or inviscid?

WALITT: Inviscid, in the NACA paper he presented in 1954. However, it is possible to include crossflow viscous effects without violating any of the conditions of equivalence.

WILLIAM J. EVANS, Grumman Aircraft Engineering Corp.: For one thing, I notice that your pressure data does not go up over the canopy. Did you take data in that region?

WALITT: Yes, we have numerical data all over. The problem was the wind-tunnel test. They obtained data only on the five planes which I referred to in my talk. I would like to see another experiment run in conjunction with another numerical calculation. The experiment should be specifically designed for the numerical calculation, so that we could make a better evaluation of the numerical results.

ROBERT E. MELNIK, Grumman Aircraft Engineering Corp.: This question is directed more to Wally Hayes. I don't think anyone said, but I think the equivalence principle is basically a hypersonic thing. You are neglecting the streamwise perturbation and velocity. You can do this in the inviscid part of the flow field if the disturbances are small and the Mach number is high, and you can't do it at the boundary layer, so that for the Mach numbers you are doing it at, I think Wally was saying that it really doesn't apply to this case except in conceptual terms.

WALLACE D. HAYES, Princeton University: It applies only inviscidly.

MELNIK: Well, he made his calculations for Mach 2.5.

WALITT: The Mach number is important, but so is the hypersonic similarity parameter, $M_\infty \tau$, which in this case turned out to be 0.998. Van Dyke's theory predicts that the maximum error in a property is proportional to τ^2, where τ is the maximum slope of the body with respect to the free-stream flow direction. Since $M_\infty \tau$ is of the order one, the error is of the

order M_∞^{-2}. For this case the maximum static pressure error was 5 percent of the free-stream dynamic pressure. The static pressure errors we recorded were about 2 percent of free-stream dynamic pressure.

MELNIK: What you are saying is that hypersonic small disturbance theories apply to 15° angle of attack at Mach number 2.5.

WALITT: For this particular body and at this angle of attack it applies. The only way you can prove that is to measure the maximum slope of the body and determine the errors. For relatively thick bodies in the supersonic flight regime, the theory applies.

ELY S. LEVINSKY, Air Vehicle Corp.: First I would like to know if there is a viscous equivalence principle.

WALITT: No, not that I know of. What we have effectively done is included viscous crossflow effects without violating the equivalence principle theory.

LEVINSKY: If you were to continue this calculation downstream on your ogive-cylinder, would you find a change in the position of the vortex?

WALITT: Yes, it starts and the vortex center grows with distance --

LEVINSKY: And the boundary layer would be ageing somehow?

WALITT: Yes, the crossflow boundary layer would change.

LEVINSKY: Well, you probably haven't done this, but it would be of interest to look at these boundary-layer calculations that you make, say, for a cone, and compare with available solutions, for instance that by F. Moore for a cone, which is a three-dimensional boundary-layer calculation.

WALITT: We would have to redo the boundary-layer calculation. In other words, this method gives the pressures on the body and the flow field away from the body outside the boundary layer. In the area of the body itself, the calculations are not correct because axial effects are excluded. But you could take the calculated pressures and go back into a three-dimensional boundary-layer program and estimate what the boundary layer would be like as a second step.

LEVINSKY: I am trying to get at how we evaluate the separation point that you predict and the formation of the vortices.

WALITT: The extent to which the viscous crossflow determines separation determines the accuracy with which we can predict separation.

The only case tried was the ogive-cylinder body, and we predicted separation 1 diameter upstream of where it actually occurred. Now, both axial viscous effects and turbulence phenomena are the causes of the deviation. At this point we didn't know which effect is more important. However, with more research, we believe we can include these effects in the method.

LEVINSKY: Can you really predict separation if you only have two or three points inside the boundary layer, like you said?

WALITT: Yes. However, I don't think our separation point on the periphery of the body is very accurate. It might be plus or minus a couple of degrees on either side of the correct value, and the axial location might be a quarter of a diameter from the correct station. However, there is no reason to make it three mesh points. We did this because of economic factors. We could have made it ten, fifteen, or twenty points in the boundary layer and have gotten a closer prediction.

LEVINSKY: Just so we understand this, was the calculation made essentially at a crossflow Reynolds number of a million?

WALITT: The fuselage calculation was made at a crossflow Reynolds number of about a million per foot.

LEVINSKY: Because all the other calculations of this type that we have seen in the literature basically are much lower Reynolds numbers, this is a significant achievement.

WALITT: Well, it is a million per foot and the maximum body cross section is a half a foot, so it is 500,000.

LEVINSKY: This is still large compared to the other calculations which are on the order of a thousand.

WALITT: Yes, but in this particular case it was one million per foot. That is why we were only able to get three points in the boundary layer.

RAAT: It seems to me that the preceding discussions have left unclarified some of the details concerning the applicability of the unsteady analogy. It may be useful to recall that the equivalence principle is based on the hypersonic small-disturbance equations and this implies the double limit $M_\infty \to \infty$, $\tau \to 0$ (τ being a characteristic inclination of the streamlines with respect to the oncoming flow). Under these conditions the streamwise velocity perturbation is expected to be an order τ smaller than the lateral velocity perturbation. This makes it possible to set the streamwise velocity equal to its undisturbed value and to treat the lateral flow problem separately. Now, at the indicated Mach numbers of 1.98 and 2.50, one would not expect hypersonic small-disturbance theory to be very accurate even in the inviscid part of the shock layer. At such low supersonic Mach numbers it seems more realistic to assume that the inviscid streamwise and lateral velocity perturbations are of the same order of magnitude.

JERRY C. SOUTH, JR., Langley Research Center: My question is really out of ignorance; I have never done anything with Navier-Stokes equations, and I haven't ever used a dissipative difference scheme, but somebody showed a paper by McCormick to me last night that I believe was an inviscid calculation of the flow past a sharp-cornered, blunt body, and he had no physical viscosity; it was an inviscid flow model, yet there was an eddy around the corner, and it was apparently caused by the dissipation of his difference scheme.

My question is, if you have dissipative terms in your difference scheme, could you set your physical viscosity to zero and still get the eddy around the canopy?

WALITT: I don't think so. We tried a problem like that in another case. We at one time calculated a Karman vortex street about a cylinder at Mach 0.2 and Reynolds number 100, and in that particular problem we were interested in what would happen if we set the viscosity to zero. This was done and we obtained the potential flow solution around the cylinder.

We feel that there is a numerical viscosity as well as the dissipative viscosity; there is no question about it, but we feel that if the mesh is fine enough the numerical viscosity is small.

EXACT SOLUTION FOR RADIATION OF SOUND FROM A SEMI-INFINITE CIRCULAR DUCT WITH APPLICATION TO FAN AND COMPRESSOR NOISE

By Donald L. Lansing

Langley Research Center

N70-21367

INTRODUCTION

Calculating the rotational noise radiated from the compressor of a modern turbofan engine is currently a problem of great interest. At present there exist two approximate analytical procedures for treating this problem. One of these was developed under contract to NASA by M. V. Lowson while at Wyle Laboratories (ref. 1). The other was sketched out by J. M. Tyler and T. G. Sofrin of Pratt & Whitney Aircraft Division of United Aircraft Corporation in reference 2. This paper presents a third, an exact theory, which is compared with the two simpler approximate methods.

The three theoretical models used in the present investigation are shown in table I. The first model, developed by Lowson (ref. 1), consists of an unducted rotor or rotor-stator combination. This model predicts the free-space radiation properties of the noise source and hence may be described as a "source-only" model. This model has a minimum of mathematical and conceptual complications. However, it is not possible to add acoustic liners, to include shear flow through the duct, or to account for the modal structure of the sound within the duct without starting all over again with a new theory.

The second model, which was suggested by Tyler and Sofrin (ref. 2), consists of a hard-wall annular duct which is terminated at the open end by an infinite baffle. Tyler and Sofrin discussed the transmission of individual modes along the duct and their radiation from the open end; thereby, the general mathematical form was obtained for the sound field. However, they did not combine the duct modes to represent the noise sources within the compressor. The baffle is an artificial device included only for the purpose of calculating the radiation patterns in front of the duct. Furthermore, this model neglects any reflection or coupling phenomena which occur at the open end. In spite of these simplifications, the model is very attractive because it does incorporate a duct using tractable mathematics and can act as a stepping stone toward analytical studies of ducts containing acoustic treatment and nonuniform axial flow.

The third model, developed in this paper, consists of a semi-infinite circular duct with hard walls. One end is open to the free field, and this open end is unbaffled so as to resemble a sawed-off pipe. A uniform free-stream velocity parallel to the duct axis is assumed. This flow may be used to simulate the effect of a steady flight condition on the

Preceding page blank

radiated noise or, if one is concerned only with conditions within the duct, to simulate the effect of the inlet or exhaust flow on the noise transmission along the duct.

The contribution of the present paper is twofold. First, the ideas laid out by Tyler and Sofrin (ref. 2) have been synthesized so that now the duct modes are combined to represent thrust and torque forces on the rotating blades. The fact that there is an unambiguous mathematical procedure for summing hard-wall duct modes deserves mention since many questions seem to arise on the matter of how the sound energy should be distributed among the various modes. The second and main contribution of the present paper consists of generalizing the work of Levine and Schwinger (ref. 3), Carrier (ref. 4), and Vajnshtejn (ref. 5) on the transmission and radiation of single modes from an unbaffled circular pipe to include flow effects, high frequencies, and high circumferential and radial mode numbers. Furthermore, these individual mode results are combined together to represent thrust and torque forces on rotating blades. The coupling of the sound field within the duct to the external free field is treated rigorously within linearized acoustic theory so that a realistic assessment of the diffraction and reflection phenomena at the open end is possible. Thus, the model of the present paper provides an exact solution which is useful in appraising the validity of approximate methods.

SYMBOLS

$A_n(x,r;u,\lambda,\omega)$	function defined by equation (9)
a	duct radius
B	number of rotor blades
c	speed of sound
$\overline{F}$	force vector acting on fluid arising from thrust and torque on rotating blades
$F_{n,j}(r)$	spanwise loading function
$h(\alpha,\lambda,M)$	function defined by equation (11)
I_n,J_n,J_ν,K_n	Bessel functions
k	frequency parameter, ω/c

$\bar{k}$	nondimensional frequency parameter, $a\omega/c$ or $nB(a\Omega/c)$
l	distance of rotating blades from inlet
M	Mach number, U/c
M_t	tip Mach number
n,j	integers
p	perturbation pressure
Q	mass source term associated with blade thickness
S	source function
$S_n(u,\lambda,\omega)$	source spectrum
t	time
U	free-stream velocity, positive into duct
u,λ,α	transform variables
V	number of stator vanes
$\bar{v}$	perturbation velocity vector
x,r	cylindrical coordinates, x positive out of duct
$\gamma(\lambda) = \sqrt{\lambda^2 - (M\lambda - k)^2}$	
θ	angle around duct axis
μ_m	mth zero of $J'_\nu(x)$
ρ_o	ambient density
ψ	azimuth angle

Ω shaft speed

ω frequency

A prime with a symbol denotes differentiation with respect to argument.

THEORY

The governing differential equations for the mathematical formulation of the radiation problem are the linearized equations for the continuity of mass

$$\frac{1}{c^2}\frac{Dp}{Dt} + \rho_o \nabla \cdot \bar{v} = Q \tag{1}$$

and the conservation of momentum

$$\rho_o \frac{D\bar{v}}{Dt} = -\nabla p + \bar{F} \tag{2}$$

where

$$\frac{D}{Dt} = \frac{\partial}{\partial t} - U\frac{\partial}{\partial x}$$

These two equations may be combined into an inhomogeneous wave equation for the pressure as follows:

$$\nabla^2 p = \frac{1}{c^2}\frac{D^2 p}{Dt^2} + S \tag{3}$$

The source function S depends upon the gradient of $\bar{F}$ and $\frac{DQ}{Dt}$ as shown in the following equation:

$$S = \nabla \cdot \bar{F} - \frac{DQ}{Dt} \tag{4}$$

The mathematical problem is to find a solution of equations (1) and (2) for p and $\bar{v}$ which satisfies the following auxiliary conditions:

(1) There must be no flow through the duct wall.

(2) The radiation condition which requires the source within the duct to generate only outgoing waves at infinity must be satisfied.

(3) The perturbation pressure must be continuous everywhere in the free field as well as through the open end into the duct.

(4) The radiated energy generated by the source must be finite. This condition places a restriction on the behavior of p and $\bar{v}$ at the sharp rim at the open end.

This problem constitutes a mixed boundary-value problem which can be solved exactly by using a combination of separation of variables and complex variable methods. The quantities $\bar{F}$ and Q can be assumed known from the geometry and operation conditions of the compressor. Consequently, S is known throughout some region within the duct. By separating the variables where possible, the wave equation with its complicated source term S can be transformed to a more manageable problem which can be solved by using the Wiener-Hopf technique (ref. 6).

By using Fourier series around the duct axis, Fourier integrals for time and in the axial direction, and Hankel integrals in the radial direction, the source term $S(x,r,\theta,t)$ can be broken down into its spectrum $S_n(u,\lambda,\omega)$ as shown in the following equation:

$$S(x,r,\theta,t) = \frac{1}{(2\pi)^3} \sum_{n=-\infty}^{+\infty} e^{in\theta} \iint_{-\infty}^{+\infty} \int_0^{\infty} S_n(u,\lambda,\omega)\, J_n(ur)\, e^{-i(\lambda x+\omega t)} u\, du\, d\lambda\, d\omega \tag{5}$$

The spectrum can be evaluated directly from the source distribution by using

$$S_n(u,\lambda,\omega) = \iint_{-\infty}^{+\infty} \int_0^{2\pi} \int_0^{\infty} S(x,r,\theta,t)\, J_n(ur)\, e^{-in\theta}\, e^{i(i\lambda x+\omega t)} r\, dr\, d\theta\, dx\, dt \tag{6}$$

Similarly, the pressure can be represented in terms of its spectrum as indicated in the following equation:

$$p(x,r,\theta,t) = \frac{1}{(2\pi)^3} \sum_{n=-\infty}^{+\infty} e^{in\theta} \iint_{-\infty}^{+\infty} \int_0^{\infty} S_n(u,\lambda,\omega)\, A_n(x,r;u,\lambda,\omega)\, e^{-i\omega t} u\, du\, d\lambda\, d\omega \tag{7}$$

The unknown function $A_n(x,r;u,\lambda,\omega)$ must be determined so that $p(x,r,\theta,t)$ satisfies the wave equation (eq. (3)). The governing differential equation for $A_n(x,r;u,\lambda,\omega)$ is

$$\left[\frac{\partial^2}{\partial r^2} + \frac{1}{r}\frac{\partial}{\partial r} - \frac{n^2}{r^2} + \frac{\partial^2}{\partial x^2} - \left(M\frac{\partial}{\partial x} + ik\right)^2\right] A_n(x,r;u,\lambda,\omega) = J_n(ur)\, e^{-i\lambda x} \tag{8}$$

This is a Helmholtz type equation which has only two independent variables x,r rather than the four original variables x,r,θ,t. The important transformation accomplished is that the forcing function on the right-hand side of the equation is no longer a complicated function of space and time but is a comparatively simple function of just the right form for the rest of the mathematics.

The problem is now reduced to finding $A_n(x,r;u,\lambda,\omega)$. Once this has been accomplished, equations (6) and (7) make it possible to determine the pressure for any $S(x,r,\theta,t)$ distribution. The method used for finding $A_n(x,r;u,\lambda,\omega)$, which satisfies equation (8) and the auxiliary conditions, depends upon a knowledge of the analytical properties of the Fourier transform of $A_n(x,r;u,\lambda,\omega)$ in the complex transform plane. This method is referred to as the Wiener-Hopf technique. The final solution for $A_n(x,r;u,\lambda,\omega)$ is given by the following equation:

$$A_n(x,r;u,\lambda,\omega) = \frac{-J_n(ur)\, e^{-i\lambda x}}{u^2 + \gamma^2(\lambda)} + \frac{1}{2\pi}\int_{-\infty}^{+\infty} A_n(\alpha) \begin{Bmatrix} I_n(r\gamma(\alpha))\, K_n'(a\gamma(\alpha)) & (0 \leqq r \leqq a) \\ K_n(r\gamma(\alpha))\, I_n'(a\gamma(\alpha)) & (a \leqq r) \end{Bmatrix} e^{-i\alpha x}\, d\alpha \tag{9}$$

This solution is the sum of two terms. The first term accounts for the inhomogeneous term in the differential equation for $A_n(x,r;u,\lambda,\omega)$ and the second term takes care of the auxiliary conditions. The second term is a contour integral whose integrand has two forms; one within the duct, $0 \leqq r \leqq a$, and another outside the duct, $a \leqq r$. The function $A_n(\alpha)$, given by the equation

$$A_n(\alpha) = \frac{2i}{1 - M^2} \frac{u\, J_n'(ua)}{\left[u^2 + \gamma^2(\lambda)\right]\left(\lambda + \frac{k}{1 - M}\right) K_+^{(n)}(\lambda)} \frac{\gamma(\alpha)\, h(\alpha,\lambda,M)}{(\alpha - \lambda)\left(\alpha - \frac{k}{1 + M}\right) K_-^{(n)}(\alpha)} \tag{10}$$

where

$$h(\alpha,\lambda,M) = \begin{cases} \dfrac{M\alpha - k}{M\lambda - k} & (0 \leqq M < 1) \\ 1 & (-1 < M \leqq 0) \end{cases}$$

depends upon the transform variables in the source spectrum u, λ, ω and contains functions $K_+^{(n)}(\lambda)$ and $K_-^{(n)}(\alpha)$ which are themselves defined by contour integrals of the following type:

$$\log_e K_+^{(n)}(\lambda) = \frac{1}{2\pi i} \int_{-\infty}^{+\infty} \frac{\log_e \left[-2K_n'(a\gamma(\zeta))\, I_n'(a\gamma(\zeta))\right]}{\zeta - \lambda}\, d\zeta \tag{11}$$

Before proceeding to any results, it will probably be helpful to discuss briefly the nature of the source distributions which occur in fan and compressor noise problems and show the basic expression for the far-field pressures. The sketch shows several variables of the problem. For simplicity, the effects of mean flow are ignored. The sound generating mechanism is the thrust and torque forces acting on the rotating blades. These forces are periodic in nature and hence may be expanded in Fourier series. The individual terms in this Fourier series have the form $F_{n,j}(r)\, e^{i[(nB-jV)\theta - nB\Omega t]}$ where the function $F_{n,j}(r)$ depends upon the spanwise variation of the loading.

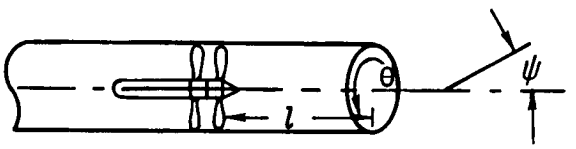

Each such source term contributes to the radiated noise field. The far-field pressure arising from one such source term as predicted by the present theory is an infinite series as shown in the following equation:

$$p = \sum_m \left\{ \underbrace{\left[\int_0^a r\, F_{n,j}(r)\, J_\nu\left(\frac{r}{a}\mu_m\right) dr\right]}_{\text{Loading factor}} \underbrace{\left[\frac{\left(\tan\frac{\psi}{2}\right)\left(\bar{k}\cos\psi + \sqrt{\bar{k}^2 - \mu_m^2}\right) J_\nu'(\bar{k}\sin\psi)}{\left(\mu_m^2 - \bar{k}^2\sin^2\psi\right) K_+^{(\nu)}(\bar{k}\cos\psi)}\right]}_{\text{Directivity factor}} \underbrace{e^{+i\frac{l}{a}\sqrt{\bar{k}^2 - \mu_m^2}}}_{\text{Propagation factor}} \right\} \tag{12}$$

where

$$\nu = nB - jV$$

Each term in the series arises from a single radial duct mode $J_\nu\left(\frac{r}{a}\mu_m\right)$ and consists of a loading factor which depends upon the spanwise distribution $F_{n,j}(r)$, a directivity factor which determines how the pressures vary with the azimuth angle ψ measured outward from the duct center line, and an important propagation factor which determines how efficiently a mode carries sound energy along the duct to the inlet. A mode for which

the square root is imaginary is said to be "below cutoff." The power of e is then a negative real number so that the sound pressures decrease rapidly with l. A mode for which the square root is real is said to be "above cutoff." The exponential function varies sinusoidally with l and represents a wave traveling along the duct. These duct modes are very efficient carriers of sound energy. Because of the large number of rotating blades and high tip speeds, compressors generally operate with many modes above cutoff. On the other hand, ducted propellers usually have far fewer blades so that at subsonic tip speeds they are operating entirely below cutoff.

RESULTS AND DISCUSSION

Some of the results obtained from the three radiation models applicable to the fan and compressor noise problem are presented. Recall that these models are the Lowson model based on the source alone, the Tyler and Sofrin model which uses a duct ending in an infinite baffle, and the present model which consists of an unbaffled duct.

Figure 1 shows the variation of the sound power due to thrust and torque forces on a blade element at 0.8 of the duct radius with the nondimensional frequency parameter $\bar{k}$. The radiated sound power is the total sound energy produced by the source and hence is an indication of its noise generating efficiency. For $nB - jV = 5$, ducted fans with subsonic tip velocities operate in the range $\bar{k} < 5$, whereas compressors are associated with $\bar{k} = 10$ to 28. It can be seen that results obtained from a synthesis of Tyler and Sofrin's ideas are in excellent agreement with the present theory over the entire frequency range. At certain values of $\bar{k}$, the present theory appears to have nearly vertical discontinuities. These spikes are actually very narrow resonances which occur at the natural acoustic frequencies of the duct cross modes. The Tyler and Sofrin model shows very abrupt increases in the radiated sound power at these frequencies but does not peak to indicate a resonance. However, both duct models indicate large sound pressures within the duct near resonance. The difference in the behavior in the free field is believed to arise from the fact that the Tyler and Sofrin model neglects the coupling of the internal and external acoustic fields through the open end. For the length-to-radius ratio used, the Lowson model and the two duct models differ by 10 to 20 dB (re unity) in the low $\bar{k}$ range. At higher frequencies the two duct models give results which are at least 5 dB below the source-only model. There are broad frequency ranges where the difference is as much as 20 dB. For the conditions shown here the Lowson model appears to greatly overestimate the radiated noise.

Figure 2 shows the effect of varying the number of stator vanes on radiated sound power. The number of rotor blades B is held fixed at 16. The tip Mach number M_t of the rotating blades is 0.6. For very low and very high numbers of stator vanes the

duct is operating below cutoff, hence the steep dropoff in sound power at either end of the graph. When the number of stator vanes is between 16 and 26 blades, both theories give essentially the same results. However, when the number of stator vanes is between 6 and 16, the sound power levels predicted by the present theory are as much as 10 to 15 dB less than those predicted by the Lowson model. The Tyler and Sofrin model gives results (not shown) which are indistinguishable from the present theory.

Figure 3 shows a comparison of sound directivity patterns calculated for the three models. Directivity patterns show how the radiated sound pressures vary as a function of azimuth angle ψ measured outward from the center line of the inlet. These patterns are polar plots of the far-field sound pressure levels in a plane through the duct axis. As indicated at the upper left of the figure, the origin of the directivity plot is taken at the center of the inlet of the duct. Horizontally to the left is directly ahead of the inlet, and vertically upward is at right angles to the inlet. The directivity pattern as predicted by the present theory consists of one main lobe at about 50° to the duct axis. The directivity pattern computed from the Tyler and Sofrin model is in good agreement with present theory except near right angles to the inlet where the Tyler and Sofrin model assumes a baffle. As mentioned earlier, radiation patterns behind the inlet cannot be predicted with this model. The results from the Lowson model are obviously all together different in size and number of lobes. In particular, sound pressures at right angles to the inlet appear to be greatly overestimated.

CONCLUDING REMARKS

This paper has outlined an analytical method for investigating the radiation of noise generated by rotating blades within a hard-wall circular duct. The method is based upon a rigorous solution of the wave equation plus boundary conditions and hence provides an exact set of calculations against which simpler theories can be compared. The method accounts for the diffraction effects at the end of the duct and is capable of giving the complete radiation pattern. Reflection effects of the inlet are also included. These effects appear to produce resonances in the radiated sound power at the frequencies of the acoustic modes. It has been found that the baffled duct model is in excellent agreement with the present method for both radiated sound power and directivity patterns in front of the inlet. However, it was found that the source-alone model did not agree well with the present method.

REFERENCES

1. Lowson, M. V.: Theoretical Studies of Compressor Noise. NASA CR-1287, 1969.
2. Tyler, J. M.; and Sofrin, T. G.: Axial Flow Compressor Noise Studies. SAE Trans., vol. 70, 1962, pp. 309-332.
3. Levine, Harold; and Schwinger, Julian: On the Radiation of Sound From an Unflanged Circular Pipe. Phys. Rev., vol. 73, no. 4, Second ser., Feb. 15, 1948, pp. 383-406.
4. Carrier, G. F.: Sound Transmission From a Tube With Flow. Quart. Appl. Math., vol. XIII, no. 4, Jan. 1956, pp. 457-561.
5. Vajnshtejn, L. A. (J. Shmoys, transl.): The Theory of Sound Waves in Open Tubes. Propagation in Semi-Infinite Waveguides, Res. Rep. No. EM-63 (Contract No. AF-19(122)-42), Inst. Math. Sci., New York Univ., Jan. 1954, pp. 87-116.
6. Noble, B.: Methods Based on the Wiener-Hopf Technique for the Solution of Partial Differential Equations. Pergamon Press, Inc., c.1958.

TABLE I

THEORETICAL MODELS FOR FAN AND COMPRESSOR NOISE RADIATION

INVESTIGATOR	MODEL DESCRIPTION	REMARKS
LOWSON (REF. 1)	SOURCE ONLY 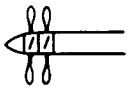	• MATHEMATICAL AND CONCEPTUAL SIMPLICITY • NO DUCT • ACOUSTIC LINERS AND SHEAR FLOW CANNOT BE INCLUDED
TYLER AND SOFRIN (REF. 2)	ANNULAR DUCT WITH BAFFLE 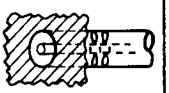	• ACOUSTIC LINERS AND SHEAR FLOW CAN BE ADDED SYSTEMATICALLY • USE OF BAFFLE IS QUESTIONABLE
LANSING (PRESENT PAPER)	CIRCULAR DUCT WITHOUT BAFFLE 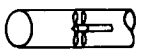	• EXACT TREATMENT OF REFLECTION AND DIFFRACTION EFFECTS OF INLET • DIFFICULT TO GENERALIZE

RADIATED SOUND POWER DUE TO THRUST AND TORQUE

TORQUE/THRUST = 0.75; nB - jV = 5; l/a = 1

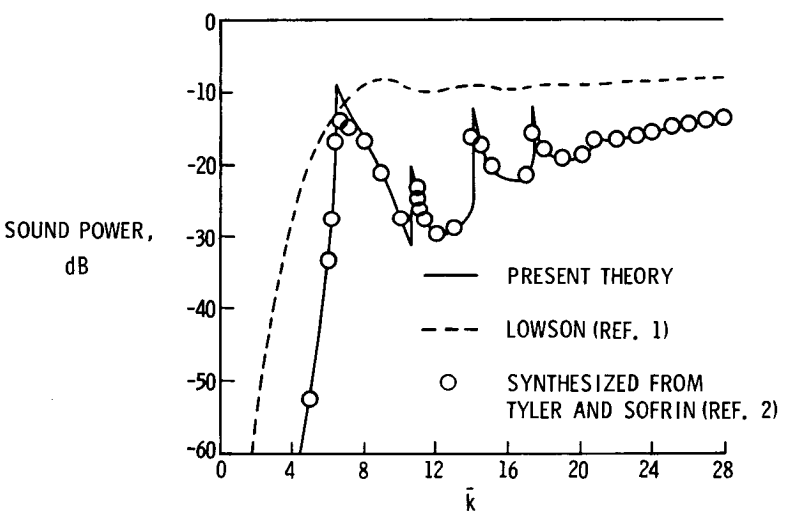

Figure 1

EFFECT OF STATOR VANE NUMBER ON SOUND POWER

TORQUE/THRUST = 0.75; B = 16; M_t = 0.6

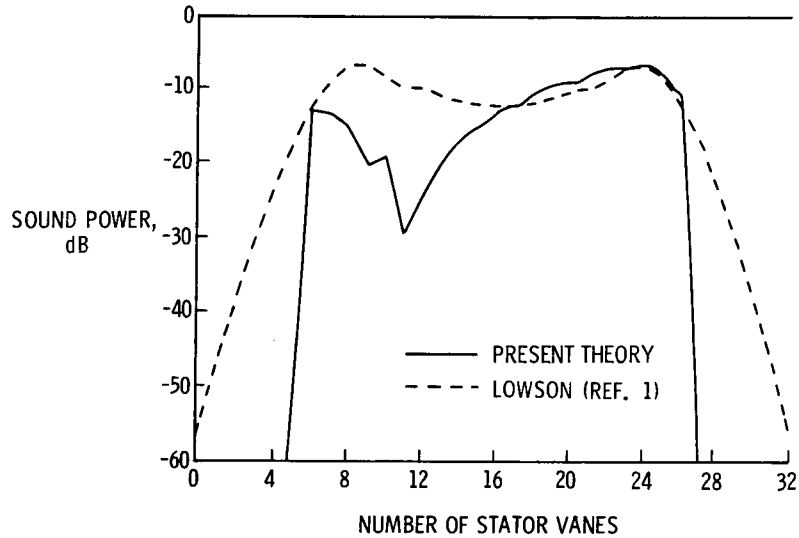

Figure 2

DIRECTIVITY PATTERNS DUE TO THRUST AND TORQUE

TORQUE/THRUST = 0.75; nB - jV = 5; $\bar{k}$=12

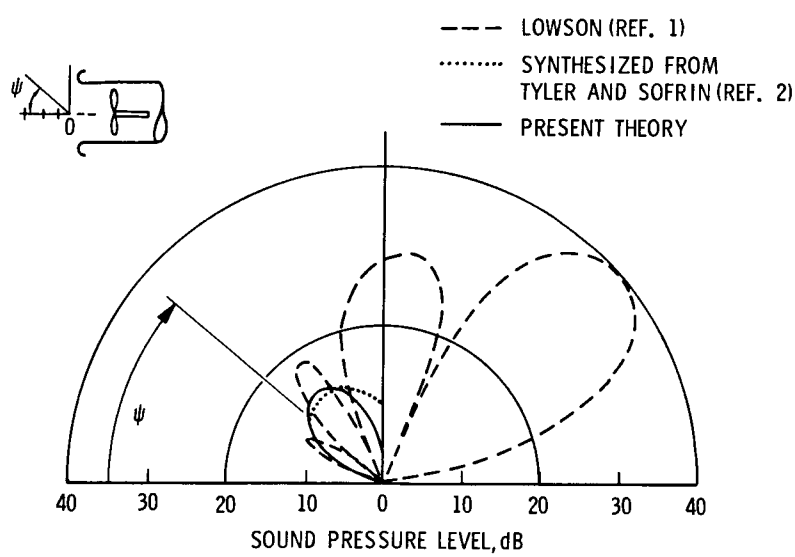

Figure 3

A CRITICAL EVALUATION OF PANEL FLUTTER AERODYNAMICS

By Peter A. Gaspers, Jr.

Ames Research Center

N70-21368

SUMMARY

Generalized forces based on Piston theory, quasi-steady theory, unsteady two-dimensional potential flow, and unsteady three-dimensional potential flow are compared. Curves are presented of typical generalized force components as functions of Mach number and length-to-width ratio. More comprehensive comparisons between Piston theory and unsteady three-dimensional theory in the form of the maximum difference of all off-diagonal components of a 6×6 matrix of generalized force components are presented as functions of Mach number, length-to-width ratio, and reduced frequency.

INTRODUCTION

In linear supersonic panel flutter analyses there are four aerodynamic theories in common use. These are the linear Piston theory, quasi-steady theory, unsteady two-dimensional potential flow, and unsteady three-dimensional potential flow. Usually the simplest theory is used that will yield acceptable results for the Mach number and length-to-width ratio of interest. However, no detailed comparison of the predictions (i.e., pressures or generalized forces) of the various theories is available, and at present the choice of a particular theory is usually based on order of magnitude considerations or on previous flutter results. Within the framework of linear aerodynamic theory the unsteady three-dimensional potential flow may be considered exact and the other theories approximate. In this paper generalized forces based on the approximate theories are compared with the exact three-dimensional results to provide a quantitative measure of their ranges of applicability.

17

SYMBOLS

a	panel length
a_j	Fourier coefficient (see eq. (25))
b	panel width
b_j	Fourier coefficient (see eq. (26))
B	wind-tunnel width

B_{jl}	$\Gamma_j \cos\left[\left(l + \frac{1}{2}\right)\frac{\pi}{L}\right] - KM$
c_j, d_j	see equation (29)
C_n	Galerkin expansion coefficient
$f_n(x)$	chordwise deflection mode
$g(y)$	spanwise deflection
i	imaginary unit, $\sqrt{-1}$
j	integer
K	$\frac{Mk}{\beta^2}$
k	$\frac{\omega a}{V}$
l,m,n	integers
M	Mach number
$p(x,y,t)$	dimensionless perturbation pressure, $p^* = qp$
$P_n(x,y)$	component of complex perturbation pressure
q	dynamic pressure, $\frac{\rho V^2}{2}$
Q_{mn}	generalized force component (see eq. (4))
R	see equation (18)
t	dimensionless time, $t^* = \left(\frac{a}{V}\right)t$
$u(x,y,t)$	transverse panel deflection
$u_n(x,y)$	nth mode shape
V	free-stream speed
W	downwash velocity (see eq. (9))
x,y	dimensionless rectangular coordinates, $x^* = ax$, $y^* = by$
β	$\sqrt{M^2 - 1}$
γ_l	$K\left\{M - \cos\left[\left(l + \frac{1}{2}\right)\frac{\pi}{L}\right]\right\}$

Γ_j	$\left[\left(\frac{j\pi a}{2\rho\beta b}\right)^2 + K^2\right]^{1/2}$
ε_j	see equation (24)
ζ	dimensionless rectangular coordinate
θ	see equation (27)
ξ	dimensionless rectangular coordinate
ρ	free-stream density
τ_1,τ_2	see equation (9) or (20)
$\phi(x,y,t)$	dimensionless velocity potential
$\Phi_n(x,y)$	component of complex velocity potential
ω	circular frequency

Superscript

*	dimensional quantity

ANALYSIS

The coordinate system and panel geometry are shown in figure 1. The analytical formulations of the various theories in terms of the perturbation pressure $p(x,y,t)$ and the transverse deflection $u(x,y,t)$ of the panel and derivations leading to expressions for the generalized forces are given below in dimensionless form. The relationships between dimensional and dimensionless variables are given in the list of symbols.

MODIFIED LINEAR PISTON THEORY (REF. 1)

The perturbation pressure is given by

$$p(x,y,t) = \frac{2}{\beta}\left(\frac{\partial u}{\partial x} + \frac{\partial u}{\partial t}\right)$$

The panel deflection is taken in the form

$$u(x,y,t) = \sum_{n=1}^{N} C_n u_n(x,y) e^{ikt} \tag{2}$$

where the u_n are specified functions. Hence, $p(x,y,t)$ has the form:

$$p(x,y,t) = \sum_{n=1}^{N} C_n P_n(x,y) e^{ikt} \tag{3}$$

The generalized force components Q_{mn} are defined by:

$$Q_{mn} = \int_0^1 \int_0^1 u_m(x,y) P_n(x,y) dx\, dy \tag{4}$$

we consider

$$u_m(x,y) = \sin m\pi x \sin \pi y$$

which are eigenfunctions for a plate with simply supported edges. A straightforward analysis yields:

$$\left.\begin{aligned} Q_{mn} &= \frac{1}{\beta}\left\{\frac{mn}{m^2 - n^2}\left[1 - (-1)^{m+n}\right]\right\} \qquad m \neq n \\ Q_{mm} &= i\,\frac{k}{2\beta} \end{aligned}\right\} \tag{5}$$

QUASI-STEADY THEORY (REF. 2)

The perturbation pressure is given by

$$p(x,y,t) = \frac{2}{\beta}\left[\frac{\partial u}{\partial x} + \left(\frac{M^2 - 2}{M^2 - 1}\right)\frac{\partial u}{\partial t}\right] \qquad u(0,y,t) = 0 \tag{6}$$

This differs from Piston theory only in the factor $(M^2 - 2)/(M^2 - 1)$, and the resulting generalized forces are

$$\left.\begin{aligned} Q_{mn} &= \frac{1}{\beta}\left\{\frac{mn}{m^2 - n^2}\left[1 - (-1)^{m+n}\right]\right\} \qquad m \neq n \\ Q_{mm} &= i\left(\frac{M^2 - 2}{M^2 - 1}\right)\frac{k}{2\beta} \end{aligned}\right\} \tag{7}$$

UNSTEADY TWO-DIMENSIONAL POTENTIAL FLOW (REF. 3)

The perturbation pressure is given by

$$p(x,y,t) = -2\left(\frac{\partial\phi}{\partial x} + \frac{\partial\phi}{\partial t}\right) \tag{8}$$

where the velocity potential $\phi(x,y,t)$ is given by:

$$\phi(x,y,t) = -\frac{1}{\pi\beta}\int_0^x \int_{\tau_1}^{\tau_2} \frac{W(\xi,y,t-\tau)d\tau\, d\xi}{\sqrt{(\tau-\tau_1)(\tau_2-\tau)}} \tag{9}$$

where

$$W(x,y,t) = \frac{\partial u}{\partial x} + \frac{\partial u}{\partial t}$$

$$\tau_1 = \frac{M(x-\xi)}{M+1} \qquad \tau_2 = \frac{M(x-\xi)}{M-1}$$

Let

$$u(x,y,t) = \sum_{n=1}^{N} C_n u_n(x,y)e^{ikt} \tag{10}$$

and make the transformation

$$\tau = \frac{1}{2}\left[(\tau_1-\tau_2)\cos\theta + \tau_1 + \tau_2\right]$$

yielding

$$\phi(x,y,t) = -\frac{e^{ikt}}{\pi\beta}\sum_{n=1}^{N} C_n \int_0^x \left(\frac{\partial u_n}{\partial\xi} + ik u_n\right)e^{-iMK(x-\xi)} \int_0^\pi e^{iK(x-\xi)\cos\theta}\, d\theta\, d\xi \tag{11}$$

Using

$$\int_0^\pi e^{iZ\cos\theta}\, d\theta = \pi J_0(Z)$$

(ref. 4) where $J_0(Z)$ is the Bessel function of the first kind of zero order results in

$$\phi(x,y,t) = \sum_{n=1}^{N} C_n \Phi_n(x,y) e^{ikt}$$

$$\Phi_n(x,y) = -\frac{1}{\beta}\int_0^x \left(\frac{\partial u_n}{\partial \xi} + ik u_n\right) e^{-iMK(x-\xi)} J_0[K(x-\xi)]d\xi \tag{12}$$

$$Q_{mn} = \int_0^1 \int_0^1 u_m(x,y) P_n(x,y) dx\, dy \tag{13}$$

$$P_n(x,y) = -2\left(\frac{\partial \Phi_n}{\partial x} + ik\Phi_n\right) \tag{14}$$

$$Q_{mn} = -2\int_0^1 \int_0^1 u_m \left(\frac{\partial \Phi_n}{\partial x} + ik\Phi_n\right) dx\, dy \tag{15}$$

integrating by parts and using

$$u_m(0,y) = u_m(1,y) = 0$$

results in

$$Q_{mn} = 2\int_0^1 \int_0^1 \left(\frac{\partial u_m}{\partial x} - ik u_m\right)\Phi_n\, dx\, dy \tag{16}$$

Following the method of references 5 and 6 the Bessel function is approximated by a sum of trigonometric functions in order to perform the integration for Φ_n:

$$J_0[K(x-\xi)] = \frac{1}{L}\sum_{l=0}^{L-1} e^{i(x-\xi)K\cos\left[\left(l+\frac{1}{2}\right)\frac{\pi}{L}\right]} \tag{17}$$

where L must be chosen to yield the desired accuracy. Let

$$u_m = \sin m\pi x \sin \pi y$$

Substituting into equations (12) and (16) and performing the integrations there result

$$Q_{mn} = \frac{mn}{\beta L}\sum_{l=0}^{L-1}\frac{1}{\gamma_l^2-n^2\pi^2}\left\{\frac{\pi^2(\gamma_l-k)^2}{\gamma_l^2-m^2\pi^2}\left[(-1)^m\cos\gamma_l - 1\right]\right.$$

$$\left. + \left[(-1)^{m+n} - 1\right]\left(\frac{n^2\pi^2-2k\gamma_l+k^2}{m^2-n^2}\right) - i\,\frac{\pi^2(\gamma_l-k)^2}{\gamma_l^2-m^2\pi^2}(-1)^m\sin\gamma_l\right\}$$

$$m \neq n \qquad (18)$$

$$Q_{mm} = \frac{1}{2\beta L}\sum_{l=0}^{L-1}\frac{1}{\gamma_l^2-m^2\pi^2}\left\{\frac{2m^2\pi^2(\gamma_l-k)^2}{\gamma_l^2-m^2\pi^2}\left[(-1)^m\cos\gamma_l - 1\right]\right.$$

$$\left. + i\left[-\frac{2m^2\pi^2(-1)^m(\gamma_l-k)^2}{\gamma_l^2-m^2\pi^2}\sin\gamma_l + m^2\pi^2\gamma_l - 2m^2\pi^2k + k^2\gamma_l\right]\right\} \qquad (19)$$

where

$$\gamma_l = K\left\{M - \cos\left[\left(l + \frac{1}{2}\right)\frac{\pi}{L}\right]\right\}$$

$$K = \frac{Mk}{\beta^2}$$

The derivation of the generalized force expressions given here closely parallels that of reference 7. The expressions for Q_{mn} contain removable singularities at $\gamma_l = m\pi$, and numerical accuracy will be impaired if γ_l is sufficiently close to $m\pi$. One method of avoiding this problem is to expand Q_{mn} in a Taylor series in γ_l about $m\pi$. Another method is to interpolate numerically in the vicinity of a singularity.

THREE-DIMENSIONAL UNSTEADY POTENTIAL FLOW (REF. 3)

$$p(x,y,t) = -2\left(\frac{\partial\phi}{\partial x} + \frac{\partial\phi}{\partial t}\right)$$

where

$$\phi(x,y,t) = -\frac{b}{2\pi a}\int_0^x\int_{\zeta_1}^{\zeta_2}\frac{W(\xi,\zeta,t-\tau_1) + W(\xi,\zeta,t-\tau_2)}{R}\,d\xi\,d\zeta \qquad (20)$$

$$W(x,y,t) = \frac{\partial u}{\partial x} + \frac{\partial u}{\partial t}$$

$$R = \left[(x - \xi)^2 - \frac{b^2\beta^2}{a^2}(y - \zeta)^2\right]^{1/2}$$

$$\zeta_1 = y - \frac{a(x - \xi)}{b\beta} \qquad \zeta_2 = y + \frac{a(x - \xi)}{b\beta}$$

$$\tau_1 = \frac{M^2(x - \xi) - MR}{\beta^2} \qquad \tau_2 = \frac{M^2(x - \xi) + MR}{\beta^2}$$

Let

$$u(x,y,t) = \sum_{n=1}^{N} C_n u_n(x,y) e^{ikt} \qquad \text{for} \quad \begin{array}{l} 0 \le x \le 1 \\ -\frac{1}{2} \le y \le \frac{1}{2} \end{array}$$

$$= 0 \qquad \text{elsewhere} \tag{21}$$

where the u_n are specified functions. Then

$$\phi(x,y,t) = -\frac{b}{\pi a}\sum_{n=1}^{N} C_n \int_0^x e^{-iMK(x-\xi)} \int_{\zeta_1}^{\zeta_2} \left(\frac{\partial u_n}{\partial \xi} + ik u_n\right) \frac{\cos(KR)}{R}\, d\zeta\, d\xi\, e^{ikt}$$

$$= \sum_{n=1}^{N} C_n \Phi_n(x,y) e^{ikt} \tag{22}$$

$$\Phi_n(x,y) = -\frac{b}{\pi a}\int_0^x e^{-iMK(x-\xi)} \int_{\zeta_1}^{\zeta_2} \left(\frac{\partial u_n}{\partial \xi} + ik u_n\right) \frac{\cos(KR)}{R}\, d\zeta\, d\xi \tag{23}$$

Now ζ_1 or ζ_2 or both may lie off the panel (outside the unit square) in which case the inner integral of equation (23) cannot be readily evaluated. Kobett (ref. 8) circumvented this difficulty by expanding the spanwise part of u_n in a Fourier series valid over the entire range of ζ. One can also account for the presence of wind-tunnel walls by constructing an image system for the spanwise deflection and representing it as a Fourier series. Let

$$u_n(\xi,\zeta) = f_n(\xi)g(\zeta)$$

$$g(\zeta) = 0 \qquad \frac{1}{2} < \zeta < -\frac{1}{2}$$

and let $g_p(\zeta)$ be the periodic function obtained by reflecting $g(\zeta)$ and its images in walls $2p$ (dimensionless) apart where $p = B/2b$ and B is the dimensional distance between the walls. Then

$$\begin{aligned} g_p(\zeta) &= g(\zeta) && |\zeta| \leq p \\ &= g(-\zeta - 2p) && -2p < \zeta < -p \\ &= g(-\zeta + 2p) && p < \zeta < 2p \\ g_p(\zeta) &= g_p(\zeta + 4p) && \text{for all } \zeta \end{aligned}$$

and the Fourier series is

$$g_p(\zeta) = \sum_{j=0}^{\infty}\left(\varepsilon_j a_j \cos\frac{j\pi\zeta}{2p} + b_j \sin\frac{j\pi\zeta}{2p}\right) \tag{24}$$

$$\varepsilon_j = \begin{cases} \frac{1}{2} & j = 0 \\ 0 & j \neq 0 \end{cases}$$

$$a_j = \frac{1}{2p}\int_{-2p}^{2p} \cos\frac{j\pi\zeta}{2p}\, g_p(\zeta)d\zeta \tag{25}$$

$$b_j = \frac{1}{2p}\int_{-2p}^{2p} \sin\frac{j\pi\zeta}{2p}\, g_p(\zeta)d\zeta \tag{26}$$

Making the transformation

$$\zeta = y + \frac{x - \xi}{\beta \mathcal{R}} \cos\theta \tag{27}$$

in equation (23) results, after some manipulation, in

$$\Phi_n(x,y)$$

$$= -\frac{2}{\beta}\sum_{j=0}^{J}\left(\varepsilon_j a_j \cos\frac{j\pi y}{2p} + b_j \sin\frac{j\pi y}{2p}\right)\int_0^x [f_n'(\xi) + ikf_n(\xi)]e^{-ikM(x-\xi)} J_o[(x-\xi)\Gamma_j]d\xi \tag{28}$$

The integral in equation (28) is in essentially the same form as equation (12) for the two-dimensional case. From the two-dimensional result, the generalized force expressions are obtained as follows:

$$Q_{mn} = -\frac{1}{\beta}\sum_{j=0}^{J}(\varepsilon_j a_j c_j + b_j d_j)\frac{1}{L}\sum_{l=0}^{L-1} I_{mn_{jl}}$$

$$I_{mn_{jl}} = \frac{1}{(m^2-n^2)(B_{jl}^2-m^2\pi^2)(B_{jl}^2-n^2\pi^2)}\Big\{mn[1-(-1)^{m+n}](n^2\pi^2+2kB_{jl}+k^2)$$

$$+ mn(m^2-n^2)\pi^2(B_{jl}+k)^2[1-(-1)^m\cos B_{jl}]$$

$$- i(-1)^m mn(m^2-n^2)\pi^2(B_{jl}+k)^2\sin B_{jl}\Big\} \qquad m \neq n \tag{29}$$

$$I_{nn_{jl}} = \frac{1}{2(B_{jl}^2-n^2\pi^2)^2}\Big\{2n^2\pi^2(B_{jl}+k)^2[1-(-1)^n\cos B_{jl}]$$

$$+ i[(2kn^2\pi^2 + B_{jl}n^2\pi^2 + B_{jl}k^2)(B_{jl}^2-n^2\pi^2)$$

$$- (-1)^n 2n^2\pi^2(B_{jl}+k)^2\sin B_{jl}]\Big\}$$

$$B_{jl} = \Gamma_j\cos\left[\left(l+\frac{1}{2}\right)\frac{\pi}{L}\right] - KM$$

where

$$\Gamma_j = \left[\left(\frac{j\pi a}{2p\beta b}\right)^2 + K^2\right]^{1/2}$$

$$K = \frac{Mk}{\beta^2} \qquad P = \frac{B}{2b}$$

B = tunnel width

$$c_j = \int_{-1/2}^{1/2} \cos \frac{j\pi y}{2p} g(y)dy \qquad d_j = \int_{-1/2}^{1/2} \sin \frac{j\pi y}{2p} g(y)dy$$

As in the two-dimensional case, expressions (29) contain removable singularities that may be handled as previously discussed. The summation limits J and L are chosen to give the desired accuracy. The derivation given here is similar to that of reference 8. It should also be noted that three-dimensional generalized forces have also been calculated by the numerical integration technique known as the Box method. See references 9 and 10, for example.

RESULTS AND DISCUSSION

In figure 2 the absolute value of a typical diagonal generalized force component $|Q_{11}|$ is plotted as a function of Mach number for a square panel and a reduced frequency of 1.0 for each of the four theories. It is well known that the quasi-steady theory breaks down in the vicinity of $M = \sqrt{2}$, and the figure clearly shows this in a quantitative way. It is also of interest that, for $M > 1.3$, the simplest theory, Piston theory, gives the best results for this combination of parameters.

In figure 3 a typical off-diagonal component Q_{12} is plotted for the same parameters as in figure 2. The agreement is very good for Mach numbers above 1.3. Note that in this case Piston theory and quasi-steady theory yield identical results. In figure 4 Q_{12} is shown as a function of length-to-width ratio for $M = 1.6$ and $k = 1.0$. It is usually stated in the literature that Piston theory and quasi-steady theory should be restricted to Mach numbers above 1.6, but limitations on a/b are hardly ever given. It is apparent from the figure that some restriction on length-to-width ratio is also needed since the approximate theories are in error by about a factor of 3 at $a/b = 10$.

For $a/b > 1.0$ the Piston theory predictions are generally comparable to or better than those of either the quasi-steady theory or two-dimensional theory; therefore, if an approximate theory can be used, Piston theory is preferable because of its simplicity. For these reasons, in what follows only Piston theory results are compared to the three-dimensional results. Also, it is known from flutter studies that the off-diagonal components of the generalized force matrix dominate the diagonal components in the parameter range where Piston theory is applicable. Since each component of the Piston theory generalized force matrix in general has a different error, in what follows the maximum percent difference between Piston theory and three-dimensional theory for all off-diagonal components of a 6×6 matrix is used as a measure of the error. In figure 5 the percent difference is shown as a function of length-to-width ratio for several Mach numbers and a reduced frequency of 1.0. For a given Mach number the error rises sharply beyond a certain length-to-width ratio and the a/b at which the rise begins increases with increasing Mach number. In figures 6 and 7 contours of constant percent difference are

plotted in the $M - a/b$ plane for reduced frequencies of 0.2 and 2.0. From these figures the ranges of M and a/b for a given error can be conveniently obtained.

CONCLUDING REMARKS

On the basis of the results presented it appears that when Piston theory or quasi-steady theory is used, limitations should be placed on length-to-width ratio as well as Mach number, and to a lesser degree, the reduced frequency should be considered. The maximum acceptable error in the generalized forces depends on the particular problem in which they are used, but a convenient cutoff is indicated by the point where the rapid rise in error with increasing length-to-width ratio occurs.

REFERENCES

1. Ashley, H.; and Zartarian, G.: Piston Theory - A New Aerodynamic Tool for the Aeroelastician. J. Aero. Sci., vol. 23, no. 12, Dec. 1956, pp. 1109-1118.

2. Fung, Y. C.: The Flutter of a Buckled Plate in a Supersonic Flow. AFOSR TN 55-237, California Institute of Technology, July 1955.

3. Garrick, I. E.: Nonsteady Wing Characteristics. Vol. VII of High Speed Aerodynamics and Jet Propulsion. A. F. Donovan and H. R. Lawrence, eds., Princeton Univ. Press, Princeton, New Jersey, 1957.

4. Erdelyi, A., ed.: Higher Transcendental Functions. Vol. II, McGraw Hill Book Co., Inc., 1953, Formula 2, p. 81.

5. Fettis, H. E.: Numerical Calculation of Certain Definite Integrals by Poisson's Summation Formula. Mathematical Tables and Other Aids to Computation 9, July 1955.

6. Luke, Y. L.: Simple Formulas for the Evaluation of Some Higher Transcendental Functions. J. Math. Phys., vol. 34, Jan. 1956, pp. 298-307.

7. Luke, Y. L.; and St. John, A.: Supersonic Panel Flutter. WADC TR 57-252, July 1957.

8. Kobett, D. R.: Research on Panel Flutter. NASA CR-80, 1964.

9. Cunningham, Herbert J.: Flutter Analysis of Flat Rectangular Panels Based on Three-Dimensional Supersonic Unsteady Potential Flow. NASA TR R-256, 1967.

10. Dowell, E. H.; and Voss, H. M.: Theoretical and Experimental Panel Flutter Studies in the Mach Number Range 1.0 to 5.0. AIAA J., vol. 3, no. 12, Dec. 1965, pp. 2292-2304.

COORDINATE SYSTEM AND PANEL GEOMETRY

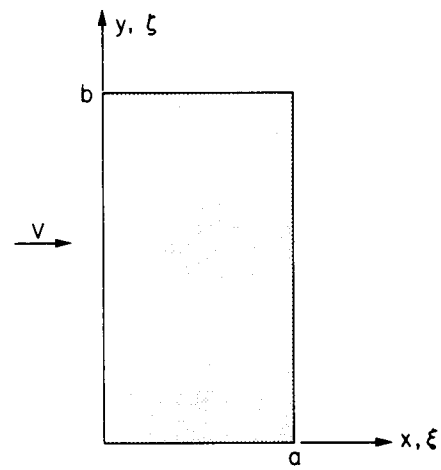

Figure 1

TYPICAL DIAGONAL GENERALIZED FORCE COMPONENT
AS FUNCTION OF MACH NUMBER

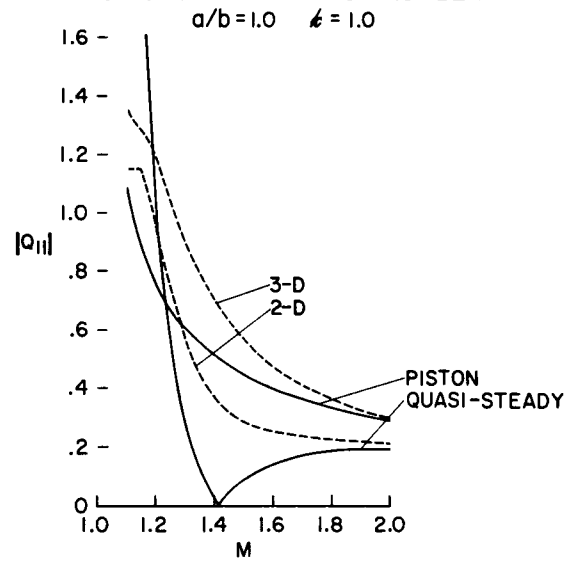

Figure 2

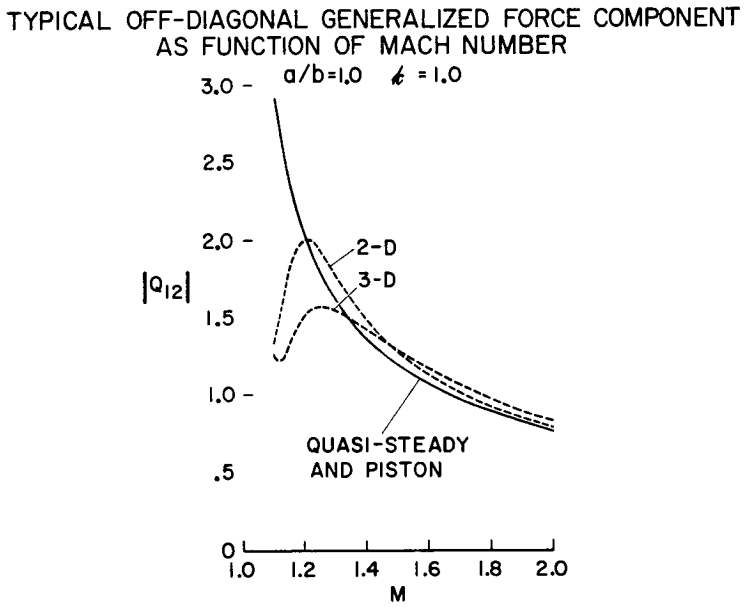

Figure 3

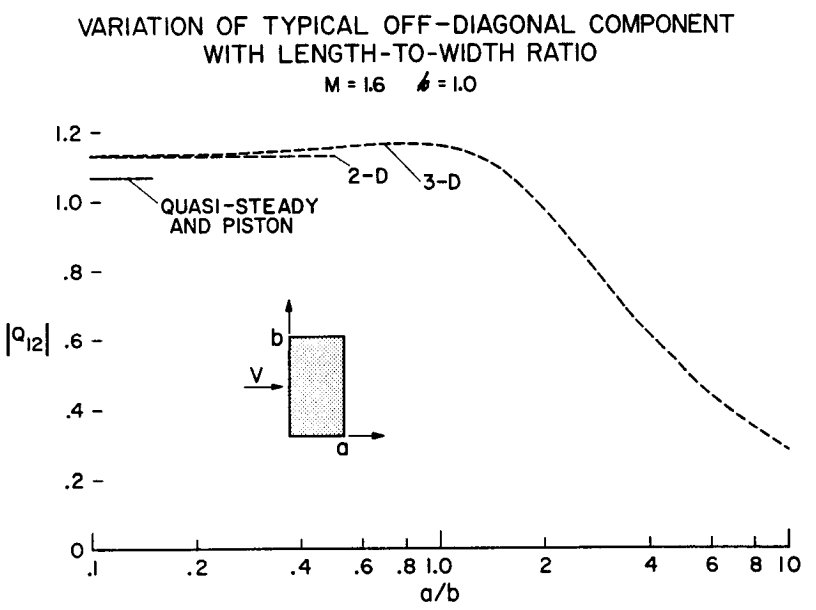

Figure 4

PERCENT DIFFERENCE BETWEEN PISTON AND 3-D THEORIES FOR OFF-DIAGONAL GENERALIZED FORCE COMPONENTS

$k = 1.0$

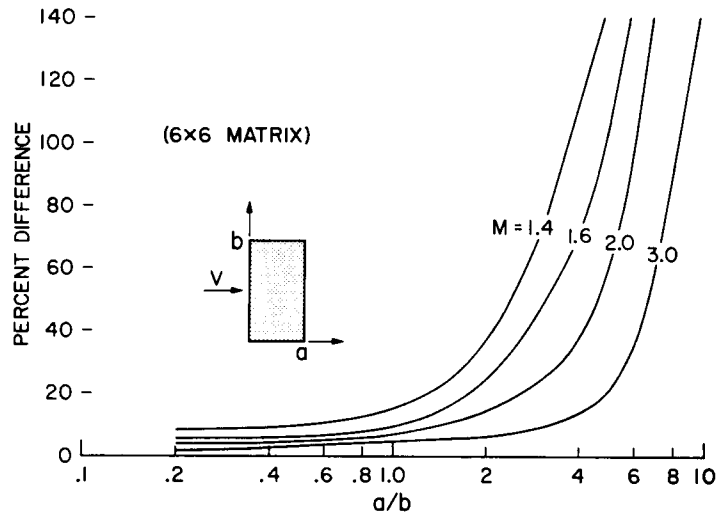

Figure 5

CONTOURS OF CONSTANT PERCENT DIFFERENCE BETWEEN PISTON THEORY AND 3-D THEORY FOR OFF-DIAGONAL COMPONENTS

$k = 0.2$

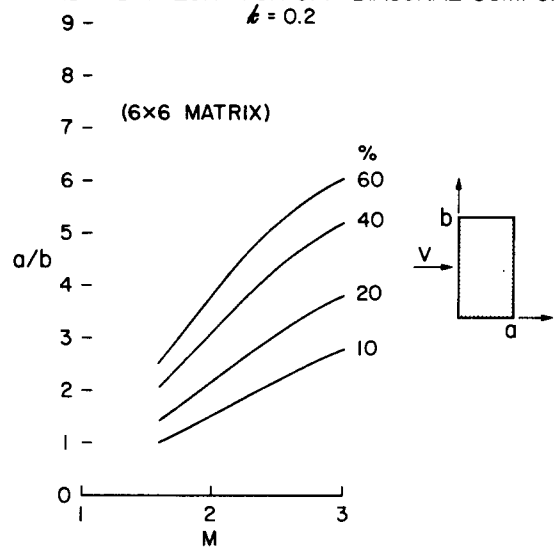

Figure 6

CONTOURS OF CONSTANT PERCENT DIFFERENCE BETWEEN PISTON THEORY AND 3-D THEORY FOR OFF-DIAGONAL COMPONENTS

$\ell = 2.0$

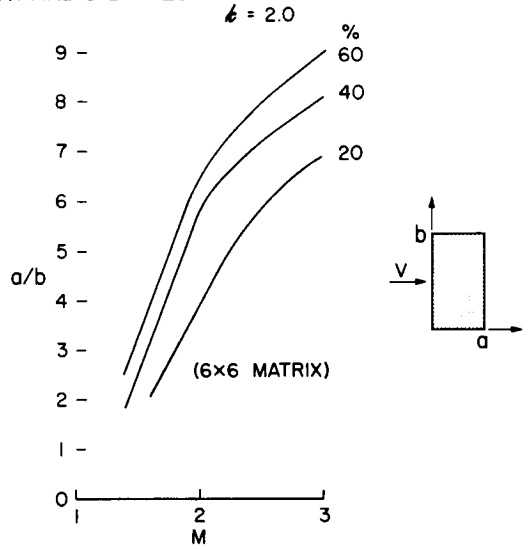

Figure 7

DISCUSSION

HOLT ASHLEY, Stanford University: I guess if Wally Hayes can knock the equivalence principle I can knock piston theory, although it is worth pointing out that the version Mr. Gaspers has been using in his paper was originally developed by Dr. Peter Jordan in Germany during World War II in its linearized form.

I think very wisely you didn't try to state any general conclusions about when that method can be used, but looking at the curves, one might conclude that for the relatively higher aspect ratio panel you can get away with taking piston theory down to a pretty low supersonic Mach number. I don't think that conclusions is incorrect for the higher aspect ratio panels that you described here. But for the benefit of those aero-elasticians that might not know too much about aerodynamic theory, I would like to issue a warning about the use of the piston theory generally at the lower Mach numbers. In our original paper on the subject (Ashley and Zartarian, J. A. S., 23, 12, Dec. 1956) we suggested that for wing flutter calculation probably a Mach number, normal to the leading edge, in excess of 2.5 is a fairly safe rule on the basis of practical calculations.

That brings in the fact that some panels and also a great many wings for supersonic aircraft are swept, and I think it would be very dangerous to draw a conclusion about even high aspect ratio swept wings and panels on the basis of calculations made essentially for what amounts to unswept wings.

A. R. GEORGE, Cornell University: I am not an aero-elastician at all, but it struck me that the fact that you can use narrower panels at higher Mach numbers is related perhaps to the fact that the Mach angle is narrower and I was wondering whether normalizing the aspect ratio by the tangent of the Mach angle would collapse these curves, such as in figure 11, to more nearly one curve?

GASPERS: I don't think there is any analytical way of doing what you suggest. The three-dimensional generalized forces are complicated functions of Mach number and aspect ratio and in addition the curves of figure 11 are envelopes of all the off-diagonal elements of a 6×6 generalized force matrix.

GEORGE: The theoretical reason is that the aerodynamic influence of a part of a panel is limited by its downstream Mach cone.

GASPERS: It might be possible to normalize the curves in an approximate manner, but I have not investigated this.

HARRY L. RUNYAN, JR., NASA Langley Reserach Center: I just might make one comment about piston theory. I think it is a very valuable tool, and we used it on the X-15 where we were worrying about the flutter of the vertical tail, and we wanted to clear the airplane for flutter for around Mach 6. We ran flutter tests of small wedges, since we had a tail with a cross-section wedge, and three-dimensional linear theory was 400 or 500 percent in error,

whereas piston theory agreed with the experiment, and this was because we could include the effect of thickness using piston theory.

GASPERS: You mean by including nonlinear term?

RUNYAN: Yes. We had more terms than you had. In piston theory you can expand the pressure expression to the number of terms you want, which brings in new nonlinear terms. It is really a very valuable theory from Mach 2 and higher.

RECENT ADVANCES IN RESEARCH ON COMPRESSIBLE TURBULENT BOUNDARY LAYERS

By Ivan E. Beckwith
Langley Research Center

N70-21369

SUMMARY

A review is given of significant developments since 1967 in methods for computing compressible turbulent boundary layers. Because of the indeterminate nature of relations between the fluctuating flow correlations and mean flow quantities, the theoretical predictions must be evaluated by comparisons with experimental data. Some limited comparisons are shown for the three main categories of theoretical approaches which are herein designated as (1) integral methods, (2) finite-difference solutions of the partial differential equations, and (3) correlation techniques. Selected methods from each category are described in some detail so that possible reasons for differences in predictions can be identified. New developments in experimental methods and results are also reviewed briefly.

Two principal conclusions are offered. First, the greatest need at the present time is for more detailed and more reliable experimental data for both mean and fluctuating flow properties within turbulent boundary layers for a wide range of Mach numbers, pressure gradients, and wall-temperature gradients. Measurements of surface shear stress and heat transfer should also be obtained when possible. Second, while the integral methods are of value for developing and assessing correlations of profile parameters and trends or "laws" for skin friction and heat transfer, the finite-difference methods appear to have significant advantages for future requirements.

One of the principal advantages of the finite-difference methods is the conceptual simplicity that can be utilized in the models of the turbulent-flux terms. Since detailed predictions of nonsimilar mean flow profiles, surface shear stress, and heating are obtained, the reasons for poor predictions of experimental results can be identified and appropriate modifications can be easily made. Through the use of this process which has been called "numerical experimentation," basic understanding of turbulent-flow mechanisms can be improved. Another advantage of the finite-difference methods is that they can be more easily extended to include detailed effects of normal pressure gradients, to account for unusual boundary conditions such as surface mass transfer and external vorticity, and to compute three-dimensional boundary layers.

18

INTRODUCTION

The purpose of this paper is to review briefly the more significant improvements and extensions, developed since 1967, of methods for predicting turbulent-boundary-layer

Preceding page blank

characteristics. The state-of-the-art for incompressible flows, at least for two-dimensional and zero-mass-transfer applications, has been extensively treated at the 1968 Stanford conference on turbulent boundary layers (see ref. 1). A principal conclusion of this conference was that (ref. 1, p. 479) "A considerable number of methods can now predict integral parameters for incompressible 2D flows nearly as well as we have any right to expect in view of the uncertainties indicated by the momentum imbalances in the data." This statement emphasizes that reliable experimental data for a broad range of flows and conditions are essential in both the development and evaluation of theoretical approaches. In order to assess the accuracy of the predictions, "standardized" sets of data are desirable such as were tabulated in reference 2 for the particular problem area treated at the 1968 Stanford conference. The objectives and principal results of this conference were reviewed by Morkovin and Kline at the 1968 Langley symposium on turbulent boundary layers (see paper no. 2 of ref. 3).

Several review papers are available that present some excellent discussion and assessments of theoretical developments up through 1967. Spalding reviewed theoretical methods in reference 4 and advocated the use of an effective-eddy-viscosity hypothesis and numerical solutions of the partial differential equations. Also available are three review papers by Bradshaw – a brief but general treatment of boundary-layer problems (ref. 5), a more complete review of turbulent boundary layers (ref. 6), and a review (ref. 7) of extensions to the method developed by Bradshaw, et al. (ref. 8) for utilizing the turbulent kinetic energy equation in numerical methods. Azzouz and Pratt (ref. 9) have reviewed the turbulent-mixing problem. This latter problem has also been treated recently (ref. 10) by a method which utilizes the turbulent-kinetic-energy equation. Earlier reviews of theoretical methods and experimental data have been given by Thompson (ref. 11), Rotta (ref. 12), and Hornung (ref. 13).

The aforementioned reviews, except references 5, 12, and 13, were concerned primarily with incompressible boundary layers. In references 5 and 12 some special problems and results for compressible turbulent boundary layers were considered briefly. The paper by Hornung (ref. 13) is one of the more complete and general reviews of theory and experiment for compressible boundary layers available up to 1966.

Several numerical methods that were developed originally for the calculation of incompressible turbulent boundary layers have been recently extended to adiabatic compressible flows (refs. 14 to 17). The present review is concerned with these and other more recent developments in the prediction of compressible turbulent boundary layers. Much of the material utilized in this review is available in the proceedings of the 1968 Langley symposium (ref. 3) and in papers presented at the AIAA Fluid and Plasma Dynamics Conference, San Francisco, California, June 16-18, 1969.

SYMBOLS

A^*	parameter in Van Driest's wall damping function (eq. (20d))
a	Mach number parameter (eq. (22))
A_2,b,C	parameters used in Pinckney's integral method
B	dimensionless blowing rate, $\frac{(\rho v)_w}{(\rho u)_e}$
C_f	skin-friction coefficient, $\frac{\tau_w}{\frac{1}{2}\rho_e u_e^2}$
c_p	specific heat at constant pressure
F_C,F_R	functions of M_e and T_w/T_e
$F = \frac{\bar{u}}{u_e}$	
f_1,f_2	mixing-length functions (eqs. (20a) and (20b))
G	any dependent variable
H	total enthalpy, $h + \left(u^2/2\right)$
H^*	form factor, δ^*/θ
H_i^*	kinematic form factor, δ_i^*/θ_i
h	static enthalpy
K	Prandtl's mixing-length constant, approximately 0.4
K^*	proportionality constant (eq. (36))
$\hat{K}$	laminarization parameter, $\frac{\nu_e}{u_e^2}\frac{du_e}{dx}$

k	molecular thermal conductivity
L	reference length
l	mixing length
l_c	modified mixing length to account for effect of curvature (eq. (40))
l_H	total-enthalpy mixing length (eqs. (18))
l_u	velocity mixing length (eqs. (17))
M	Mach number
N_{St}	Stanton number, $\frac{q_w}{\left(h_{aw} - h_w\right)\rho_e u_e}$
$\bar{n}$	exponent in equation (33)
N_{Pr}	molecular Prandtl number, $\frac{c_p \mu}{k}$
$N_{Pr,T}$	turbulent Prandtl number based on total enthalpy, $\frac{c_p \epsilon}{\kappa}$
$N_{Pr,t}$	turbulent Prandtl number based on static enthalpy
p	pressure
q	flux of total enthalpy
q_T	turbulent flux of total enthalpy (eq. (6b))
q'	magnitude of fluctuation in velocity vector, $\sqrt{u'^2 + v'^2 + w'^2}$
R_s	reference Reynolds number, $\frac{\rho_s \sqrt{2H_e} L}{\mu_s}$
R_x	Reynolds number based on x length, $\frac{\rho_e u_e x}{\mu_e}$

R_ϵ	eddy-viscosity Reynolds number, $\frac{\bar{\rho} u_e \delta_i^*}{\epsilon}$
R_θ	Reynolds number based on momentum thickness, $\frac{\rho_e u_e \theta}{\mu_e}$
R_∞	free-stream Reynolds number per foot, $\frac{\rho_\infty u_\infty}{\mu_\infty}$
r	lateral radius from axis of symmetry
r_c	longitudinal radius of curvature of body surface
$\bar{r}$	recovery factor, $\frac{h_{aw} - h_e}{H_e - h_e}$
T	temperature
T_t	stagnation temperature
u	velocity component in x-direction
v	velocity component in y-direction
$\tilde{v}$	effective normal velocity, $\bar{v} + \frac{\overline{\rho' u'}}{\bar{\rho}}$
w	velocity component normal to x- and y-directions
X	modified defect parameter of reference 15 (eq. (28))
x,y	boundary-layer coordinates, parallel and normal to surface, respectively
α	local wall angle with respect to body center line
β	function in modified mixing-length relation, taken herein as the constant 7
β_T	pressure-gradient parameter, $\frac{\delta^*}{\tau_w} \frac{dp}{dx}$
γ	ratio of specific heats
δ	boundary-layer thickness

δ^*	displacement thickness, $\int_0^\delta \left(1 - \frac{\bar{\rho}\bar{u}}{\rho_e u_e}\right)\frac{r}{r_w}\,dy$
δ_i^*	kinematic displacement thickness, $\int_0^\delta \left(1 - \frac{\bar{u}}{u_e}\right)\frac{r}{r_w}\,dy$
ϵ	eddy viscosity (eq. (9a))
Θ	total-enthalpy thickness, $\int_0^\delta \left(1 - \bar{\theta}\right)\frac{\bar{\rho}\bar{u}}{\rho_e u_e}\frac{r}{r_w}\,dy$
θ	momentum thickness, $\int_0^\delta \left(1 - \frac{\bar{u}}{u_e}\right)\frac{\bar{\rho}\bar{u}}{\rho_e u_e}\frac{r}{r_w}\,dy$
$\bar{\theta}$	normalized total-enthalpy parameter, $\frac{\bar{H} - H_w}{H_e - H_w}$
θ_i	kinematic momentum thickness, $\int_0^\delta \left(1 - \frac{\bar{u}}{u_e}\right)\frac{\bar{u}}{u_e}\frac{r}{r_w}\,dy$
κ	eddy conductivity of total enthalpy (eq. (9b))
μ	molecular viscosity
ν	molecular kinematic viscosity, μ/ρ
ξ,η	transformed coordinates (eqs. (33))
π	profile parameter in Coles' law of the wake
ρ	density
τ	shear stress
τ_T	turbulent shear stress (eq. (6a))
Φ	eddy-viscosity relations of reference 15 (eqs. (26) and (27))
χ	modified law-of-the-wall parameter of reference 15 (eq. (24))

Subscripts:

aw	adiabatic wall
e	local edge of boundary layer
exp	experimental
L	laminar
max	maximum
o	free-stream stagnation
s	reference conditions
theo	theoretical
w	wall or surface
∞	free stream ahead of bow shock

Superscript:

j	body shape index ($j = 0$ for two-dimensional flow; $j = 1$ for axisymmetric flow)

A bar over a symbol indicates a mean value except where otherwise noted. A prime denotes a fluctuating value.

ABBREVIATIONS

C.T.	correlation techniques
F.D.	finite-difference methods
I.M.	integral methods

AREAS WHERE SIGNIFICANT ADVANCES HAVE BEEN REPORTED

Experimental Methods and Results

The indeterminate nature of the turbulent-flow problem requires that experimental data be relied upon for validation of the prediction methods to a much greater extent than for laminar flows. Therefore, while the emphasis of the present compilation is on analytic methods, it is appropriate to begin with a few remarks on some recent experimental results.

For any given experimental situation, it is clearly mandatory to obtain as many independent measurements as possible of both mean and fluctuating flow properties. The direct measurement of surface skin friction with floating-element force balances has until recently been limited to adiabatic flows with zero pressure gradient. Improvements in the construction and calibration of these balances have now allowed their use under conditions with pressure gradients and large heat transfer. A description of two different balances is available in references 18 and 19, and results obtained with them are given in references 20 and 21, respectively. (Ref. 21 is essentially the same as paper no. 10 of ref. 3.)

In order to specify the mean flow profiles across a boundary layer, at least two independent measurements are required. Thus, for example, from measurements of pitot pressure and total temperature, all mean flow profile parameters such as Mach number, velocity, and density can be computed if the usual assumption of constant static pressure across the boundary layer is accepted. When the streamwise pressure gradients on a body in supersonic flow are large, the pressure gradients normal to the surface are appreciable and become larger as the Mach number increases. The local static pressures within the boundary layer should then be measured as in reference 22, for example. For flat-plate-type flows where the entire development of the boundary layer occurs with essentially zero pressure gradients, the assumption of negligible normal pressure gradient is usually justified. Recent experimental investigations on flows of this type where two independent sets of measurements were obtained are reported in references 23 to 27.

The turbulent boundary layers on the walls of hypersonic nozzles, while subject to the effects of upstream pressure and temperature gradients, are usually thicker than those on models at comparable unit Reynolds numbers. These boundary layers are therefore convenient for detailed probing. Recent examples of such detailed profile data, where again more than one profile parameter was measured, are available in references 20 and 28 to 37. When these data from nozzle-wall boundary layers are plotted in the form of $\bar{\theta}$ as a function of F (sometimes referred to as Crocco plots), a nearly quadratic variation is obtained (ref. 35). Most flat-plate-type data, on the other hand, show on the average a more nearly linear variation as would be expected for $dp/dx \approx 0$

and $N_{Pr,T} \approx 1.0$ for the entire boundary-layer development. Thus, even though most of the nozzle-wall data were obtained with small local pressure gradients, it seems that the effects of large upstream pressure and temperature gradients that are present in the nozzle flows may persist far downstream. Another possible cause of this difference between flat-plate-type flows and nozzle-wall flows has been identified in paper no. 12 of reference 3. In this paper, Jones has described a total-temperature deficiency found near the settling-chamber wall of a typical hypersonic facility and has indicated that such a deficiency could account for at least part of the quadratic trends of the variation of $\bar{\theta}$ with F.

Measurements of fluctuating flow quantities in compressible flows are needed in order to extend the present limited knowledge of relations between fluctuating-flow correlations and mean flow quantities. The investigation of reference 37 is therefore noteworthy because the fluctuations in density were measured for the first time in a turbulent boundary layer. An electron-beam probe was used to measure both mean and fluctuating density in the boundary layer on the wall of a shock tunnel at a free-stream Mach number of about 9. The wall- to total-temperature ratio varied from about 0.06 to 0.16. Mean and fluctuating pitot pressures were also obtained in this investigation. These data on the fluctuating density and pitot pressure were utilized in references 38 and 39 to obtain estimates of the root-mean-square intensity of longitudinal velocity fluctuations for these conditions. By comparison with previous data it was tentatively concluded (ref. 39) that the magnitude and distribution of the root-mean-square values of both the density and velocity fluctuations are not greatly affected by Mach number and heat transfer if appropriate normalizing parameters are used. One exception to this statement is that the viscous sublayer does appear to increase in thickness, relative to the total boundary-layer thickness, as the Mach number increases (see also refs. 33 and 40).

Another technique for measuring fluctuating flow properties is the crossed-beam correlation technique (ref. 41), which yields such data as relative turbulence intensities and integral scales of turbulence (ref. 42).

Another new instrument has recently been developed that is designed to provide direct measurements of all three components of fluctuating velocities (ref. 43). This technique depends on the Doppler principle applied to changes in frequency of scattered light from a laser beam by particles added to the flow. In order for the particles to follow the random motions of the flow with sufficient accuracy, the density of the liquid or gas flow must be high and the particles must be small. To date, the technique has therefore been used mostly in liquid or high-density gas flows, although preliminary data have been obtained in a supersonic jet at Mach number 3. (See ref. 44.)

A further experimental result of considerable significance is the accurate measurement of surface heat transfer on a flight vehicle with a turbulent boundary layer at

Mach 20 (ref. 45). Also of significance for flight applications is the correlation of turbulent heating on the windward and leeward sides of cones, swept plates, and delta wings at angle of attack (paper nos. 17 and 18 of ref. 3). The tests reported in these two papers were conducted at free-stream Mach numbers of 7.4 and 6.0, respectively, and for angles of attack up to 12° and 5°, respectively.

Analytic Approaches

Since the subject of the present compilation is analytic methods, the remainder of this paper is devoted to a discussion of the three principal approaches to the calculation of compressible turbulent boundary layers and comparisons between experimental data and predictions obtained from selected methods. For the present purposes these three approaches are categorized as (1) integral methods (I.M.), (2) finite-difference solutions of the partial differential equations (F.D.), and (3) correlation techniques (C.T.). Before proceeding to a description of these three categories and comparisons of typical theoretical results with data, the classes of problems that can now be treated with expectation of obtaining reasonable predictions are considered.

Before the development of high-speed computing machines, the methods used by the design engineer who required estimates of skin friction and heat transfer were limited primarily to the C.T. methods (category (3)). Such methods have been reviewed and classified by Spalding and Chi (ref. 46) and are directly applicable only to flat-plate-type flows with zero pressure gradients. These methods provide closed-form expressions (or working charts) for skin friction as a function of M_e, R_θ or R_x, and T_w/T_e. Hence, additional assumptions for the Reynolds analogy factor $2N_{St}/C_f$ and the recovery factor $\bar{r}$ are required to obtain the heat transfer. When both large heat transfer and large pressure gradients are present locally, the more recent I.M. and F.D. methods (categories (1) and (2)) provide more realistic predictions than the C.T. methods.

A somewhat different situation exists for nozzle-wall boundary layers where the boundary layer near the nozzle exit has been subjected to large pressure or wall-temperature gradients during its upstream development while local conditions are nearly uniform. The boundary layer is then in the process of "relaxing" or adjusting to the local uniform conditions, and the question arises as to how fast (or over how long a streamwise distance) the boundary-layer profiles, surface shear stress, and surface heating come into equilibrium with these local conditions. That is, does the boundary layer "remember" its upstream history? Comparisons of limited nozzle-wall and flat-plate data (ref. 47) indicate that the surface shear stress and heating may not be much influenced by upstream history. However, the profiles across the boundary layer, particularly the relation between $\bar{\theta}$ and F mentioned previously, may not relax to

equilibrium forms until downstream distances of many boundary-layer thicknesses have been reached. Experimental evidence of such effects are available in references 35 and 36. Theoretical studies of these effects are possible with the F.D. methods as shown in reference 34. The I.M. approaches that incorporate appropriate profile correlations and nonequilibrium control parameters, such as the method of reference 48, could also be applied to these relaxing flows.

Special problems in turbulent boundary layers that will not be considered in this review because they are treated in other papers of this compilation are as follows:

(1) Three-dimensional boundary layer with nonuniform (or nonequilibrium) surface mass transfer, large heat transfer, and large pressure gradients (This problem is treated by an F.D. method in paper no. 19.)

(2) Interaction between turbulent boundary layer and shock wave (A technique for computing the interaction is presented in paper no. 21 and utilizes the concept of an inviscid outer layer and a laminar viscous inner layer; the solution for this inner layer may be obtained by any of the methods reviewed in paper no. 20.)

(3) A separating turbulent boundary layer (The technique of paper no. 21 could presumably be applied to a separating turbulent boundary layer; the method of Fernandez and Lees (ref. 49) could also be applied to this type of problem, providing a suitable expression for the dissipation integral could be formulated.)

DESCRIPTION OF ANALYTIC METHODS

Basic Equations

Boundary-layer equations.- The boundary-layer equations for turbulent flow may be derived from the conservation equations for a viscous heat-conducting fluid by substituting mean and fluctuating parts for the instantaneous flow variables, applying the Reynolds time-averaging process, and finally neglecting higher-order terms. For two-dimensional or axisymmetric time-steady flow, the resulting equations for continuity, x-momentum, and y-momentum, respectively, are as follows:

$$\frac{\partial}{\partial x}\left(r^j\bar{\rho}\bar{u}\right) + \frac{\partial}{\partial y}\left(r^j\bar{\rho}\tilde{v}\right) = 0 \tag{1}$$

$$\bar{\rho}\bar{u}\frac{\partial\bar{u}}{\partial x} + \bar{\rho}\tilde{v}\frac{\partial\bar{u}}{\partial y} = -\frac{\partial\bar{p}}{\partial x} + \frac{1}{r^j}\frac{\partial}{\partial y}\left[r^j\left(\bar{\mu}\frac{\partial\bar{u}}{\partial y} - \bar{\rho}\overline{v'u'}\right)\right] \tag{2}$$

$$\pm\frac{\bar{\rho}\bar{u}^2}{r_c} = -\frac{\partial\bar{p}}{\partial y} - \frac{1}{r^j}\frac{\partial}{\partial y}\left(r^j\bar{\rho}\overline{v'^2}\right) \tag{3}$$

In equation (3) the upper and lower signs should be used for flows on bodies and in nozzles, respectively. (These sign conventions apply to flows with simple, or nonreflecting, Mach wave systems.)

The equation for total enthalpy is

$$\bar{\rho}\bar{u}\frac{\partial\bar{H}}{\partial x} + \bar{\rho}\tilde{u}\frac{\partial\bar{H}}{\partial y} = \frac{1}{r^j}\frac{\partial}{\partial y}\left\{r^j\left[\frac{\bar{k}}{c_p}\frac{\partial\bar{H}}{\partial y} - \bar{\rho}\overline{v'H'} + \bar{\mu}\left(1 - \frac{1}{N_{Pr}}\right)\bar{u}\frac{\partial\bar{u}}{\partial y}\right]\right\} \tag{4}$$

All terms of order δ or smaller have been neglected in equations (1) to (4), and the relative order of magnitude of the coordinates and flow variables is taken as

$$\left.\begin{aligned} x,r,r_c,\bar{u},\bar{\rho},\bar{H}&: \text{ Order of } 1 \\ y,\bar{v},\overline{(\ )'(\ )'}&: \text{ Order of } \delta \\ \bar{\mu},\bar{k}&: \text{ Order of } \delta^2 \end{aligned}\right\} \tag{5}$$

where $(\ )'$ denotes the fluctuating part of any flow variable except μ' and k' which are considered of order δ^3. In general, the radius to a point in the flow is given by

$$r = r_w \pm y \cos \alpha$$

where the upper and lower signs apply to external and internal flows, respectively. When $\delta \ll r_w$, this relation becomes

$$r = r_w(x)$$

and r^j drops from equations (2) to (4).

Turbulent-flux terms.- The terms which include correlations of fluctuating quantities

$$\tau_T = -\bar{\rho}\overline{v'u'} \tag{6a}$$

and

$$q_T = -\bar{\rho}\overline{v'H'} = -\bar{\rho}\overline{v'h'} - \bar{u}\bar{\rho}\overline{v'u'} \tag{6b}$$

have the effect of increasing the flux of momentum or total enthalpy due to the turbulence and are therefore known as the Reynolds shear stress and enthalpy flux. (In the

conventional sense, the term $-\frac{\bar{\rho}}{c_p}\overline{v'h'}$ would represent the turbulent flux of heat; however, for the present purpose, it is convenient to retain the total-enthalpy correlation $-\bar{\rho}\overline{v'H'}$.) Since there is no general relation between these correlations of fluctuating quantities and the mean flow variables, empirical models of the correlations must be used to solve equations (1) to (4).

Static-pressure variation.- It should be noted that the normal-momentum equation (eq. (3)) is generally not included in the system of equations to be solved because of the additional complications. (These complications are associated with the hyperbolic nature of the complete continuity and normal-momentum equations with higher-order terms included (see ref. 50). Presumably, when only the first-order terms for turbulent flows are retained in the normal-momentum equation, as in equation (3), the system of equations (1) to (4) is still parabolic and conventional solution techniques should be applicable.) When r_c is small, the normal pressure gradients are large and are presumably caused mainly by the wall curvature. For this situation, therefore, the pressure distribution across the boundary layer is nearly the same as for the inviscid flow, as shown in reference 51. The effect of normal pressure gradients can then be easily included in integral methods, as shown, for example, in references 52 and 53.

When r_c is large, the normal pressure gradients may still be appreciable. Their magnitude may then be evaluated from equation (3) which for two-dimensional flow and large r_c can be integrated to give

$$\bar{p} = \bar{p}_w - \bar{\rho}\overline{v'^2} \tag{7}$$

Then if $\overline{v'^2} \approx \frac{1}{4}\overline{q'^2}$ (ref. 54) and $\frac{\tau_T}{\bar{\rho}\overline{q'^2}} \approx 0.15$ (ref. 8), the following equation is obtained:

$$\frac{\bar{p}}{\bar{p}_w} \approx 1 - \frac{5}{3}\frac{\tau_T}{\bar{p}_w} \tag{8}$$

The variation in static pressure across the boundary layer caused by turbulent velocity fluctuations can then be estimated after formulation of a suitable model for turbulent shear stress.

Eddy-Diffusivity Concepts

General relations.- By analogy with the molecular shear stress and heat transfer, it is often assumed that eddy-diffusivity coefficients relate the turbulent correlations to

the corresponding mean flow gradients. From equations (6a) and (6b) the total shear stress and enthalpy flux then become

$$\tau = \tau_L + \tau_T = \bar{\mu}\frac{\partial \bar{u}}{\partial y} + \epsilon\frac{\partial \bar{u}}{\partial y} \tag{9a}$$

and

$$q = q_L + q_T = \frac{\bar{k}}{c_p}\frac{\partial \bar{H}}{\partial y} + \frac{\kappa}{c_p}\frac{\partial \bar{H}}{\partial y} \tag{9b}$$

Again by analogy with the molecular Prandtl number

$$N_{Pr} = \frac{c_p\bar{\mu}}{\bar{k}} \tag{10}$$

the turbulent Prandtl number is defined as

$$N_{Pr,T} = \frac{c_p\epsilon}{\kappa} \tag{11a}$$

or by the use of equations (6) and the definitions of ϵ and κ (eqs. (9a) and (9b))

$$N_{Pr,T} = \frac{\overline{v'u'}}{\overline{v'H'}}\frac{\partial \bar{H}/\partial y}{\partial \bar{u}/\partial y} \tag{11b}$$

Since this definition of $N_{Pr,T}$ is in terms of the total enthalpy rather than the static enthalpy, it corresponds to the "total" Prandtl number defined in reference 34. An elementary analysis and the results of finite-difference solutions presented in this reference indicated that values of $N_{Pr,T}$ may be as large as 2.0 for nozzle-wall boundary layers.

From the definitions of ϵ, κ, and $N_{Pr,T}$, equations (2) and (4) may be written as

$$\bar{\rho}\bar{u}\frac{\partial \bar{u}}{\partial x} + \bar{\rho}\tilde{v}\frac{\partial \bar{u}}{\partial y} = -\frac{\partial \bar{p}}{\partial x} + \frac{1}{r^j}\frac{\partial}{\partial y}\left[r^j(\mu + \epsilon)\frac{\partial \bar{u}}{\partial y}\right] \tag{12}$$

and

$$\bar{\rho}\bar{u}\frac{\partial \bar{H}}{\partial x} + \bar{\rho}\tilde{v}\frac{\partial \bar{H}}{\partial y} = \frac{1}{r^j}\frac{\partial}{\partial y}\left\{r^j\left[\left(\frac{\mu}{N_{Pr}} + \frac{\epsilon}{N_{Pr,T}}\right)\frac{\partial \bar{H}}{\partial y} + \mu\left(1 - \frac{1}{N_{Pr}}\right)\bar{u}\frac{\partial \bar{u}}{\partial y}\right]\right\} \tag{13}$$

Since the appropriate boundary conditions on $\bar{u}$ and $\bar{H}$ are

$$\left.\begin{aligned} \bar{u} = 0; \bar{H} = H_w(x) \qquad & (y = 0) \\ \bar{u} \rightarrow u_e(x); \bar{H} \rightarrow \bar{H}_e \qquad & (y \rightarrow \infty) \end{aligned}\right\} \tag{14}$$

it can be seen that for $\partial\bar{p}/\partial x = 0$, $N_{Pr} = 1.0$, and $N_{Pr,T} = 1.0$, a solution to equation (13) is the Crocco integral

$$\frac{\bar{H} - H_w}{H_e - H_w} = F \tag{15}$$

if H_w, u_e, and H_e are constants. From the definition of $N_{Pr,T}$ (eq. (11b)), the ratio of the streamwise-momentum and total-enthalpy flux correlations for an ideal gas under these conditions is then

$$\frac{\overline{v'u'}}{\overline{v'H'}} u_e = \frac{(\gamma - 1)M_e^2}{\left(1 + \frac{\gamma - 1}{2} M_e^2\right)\left(1 - \frac{T_w}{T_o}\right)} \tag{16}$$

Hence the assumption of $N_{Pr,T} \approx 1.0$ implies that the turbulent momentum flux and enthalpy flux are caused by the same or closely related mechanisms since their ratio is constant for given values of M_e, u_e, and T_w/T_o. It follows that when any of the aforementioned restrictions $\left(\frac{\partial\bar{p}}{\partial x} \approx 0,\ N_{Pr} \approx 1.0, \text{ and constant } T_w\right)$ are not satisfied, the assumption of $N_{Pr,T} \approx 1.0$ may not be applicable.

Mixing-length expressions.- One of the more successful models for eddy-diffusivity relations is based on Prandtl's mixing-length hypothesis, which states that $v' \approx u' \approx l_u \frac{\partial\bar{u}}{\partial y}$ and $G' \approx l_G \frac{\partial\bar{G}}{\partial y}$ where G is any quantity diffused or transferred by the action of turbulence. Application of the hypothesis to Reynolds stress or turbulent shear stress then gives (from eqs. (6) and (9))

$$\tau_T = -\bar{\rho}\overline{v'u'} = \bar{\rho} l_u^2 \left|\frac{\partial\bar{u}}{\partial y}\right| \frac{\partial\bar{u}}{\partial y} \tag{17a}$$

or

$$\epsilon = \bar{\rho} l_u^2 \left|\frac{\partial\bar{u}}{\partial y}\right| \tag{17b}$$

where the absolute sign is used to insure that the shear stress will have the same sign as the velocity gradient. Similarly, the flux of total enthalpy becomes

$$q_T = -\bar{\rho}\overline{v'H'} = \bar{\rho} l_u \left|\frac{\partial \bar{u}}{\partial y}\right| l_H \frac{\partial \bar{H}}{\partial y} \tag{18a}$$

or

$$\frac{\kappa}{c_p} = \bar{\rho} l_u l_H \left|\frac{\partial \bar{u}}{\partial y}\right| \tag{18b}$$

The turbulent Prandtl number (eq. (11a)) is then

$$N_{Pr,T} = \frac{l_u}{l_H} \tag{19}$$

When $N_{Pr,T} > 1.0$ (see ref. 34), equation (19) indicates a smaller mixing length for enthalpy than for velocity.

For direct application to the calculation of boundary layers, the velocity mixing length l_u in the outer part of the boundary layer is usually scaled to the boundary-layer thickness (ref. 4). That is,

$$\frac{l_u}{\delta} = f_1\left(\frac{y}{\delta}\right) \tag{20a}$$

where the function f_1 is based on experimental data such as those of references 55 and 56 for incompressible flows. Calculations by Maise and McDonald (ref. 57) and Patanker and Spalding (ref. 17) have shown that the same function is applicable to adiabatic compressible flows on flat plates (small values of dp/dx). Results obtained by Bushnell and Beckwith (ref. 34) indicate that for application to nonequilibrium compressible flows with pressure gradients, the mixing-length function may also depend on the incompressible form factor H_i^*; hence

$$\frac{l_u}{\delta} = f_2\left(\frac{y}{\delta}, H_i^*\right) \tag{20b}$$

These and other results (for example, ref. 39 and paper no. 15 of ref. 3) indicate that the turbulence properties of compressible turbulent boundary layers can be correlated on the basis of scale factors that depend only on the kinematics of the flow rather than the dynamics. Thus, the variations in density apparently have little effect on the empirical models of the turbulent flux terms which retain their basic kinematic character (see also refs. 58 and 59).

In the near-wall region of a boundary layer where the only length scale factor is the distance normal to the surface, the Prandtl mixing-length relation becomes

$$l_u = Ky \tag{20c}$$

Experimental data show that $K \approx 0.4$. Again, this value of K is found to be nearly a universal constant. When the boundary-layer equations are integrated all the way to the wall as in some of the F.D. methods (refs. 15, 16, and 34, for example), it is necessary to modify equation (20c) to provide the correct behavior of τ_T (or ϵ) as the wall is approached. Analysis of the basic equations shows that ϵ should vary as y^4 or y^3 as $y \to 0$ (see refs. 60 and 61). Van Driest's wall damping function provides this type of variation and also accounts for the effect of Reynolds number (or density level) on the sublayer thickness (ref. 62). Equation (20c) then becomes

$$l_u = K\left[1 - \exp\left(-\frac{\bar{\rho}y}{A^*\bar{\mu}}\sqrt{\frac{\tau_w}{\rho}}\right)\right]y \tag{20d}$$

where $A^* \approx 26$. This damping function has also been used in references 16 and 17. A different function was used for the same purpose in reference 15. For application to problems with wall blowing, A^* may be considered a function of the blowing parameter $2B/C_f$ as shown in reference 34.

Eddy viscosity in the outer part of the boundary layer.- Clauser introduced an alternate approach to the mixing-length formulation for eddy viscosity (ref. 63) with a Reynolds number parameter

$$R_\epsilon = \frac{\bar{\rho}u_e\delta_i^*}{\epsilon} \tag{21}$$

Clauser showed that for equilibrium flows the value of this parameter was nearly constant at $R_\epsilon \approx 60$ in the defect or "wake" portion of the boundary layer where the direct influence of the wall is negligible. When this formulation is applied to adiabatic compressible flows, the same constant value of $R_\epsilon \approx 60$ gives good results (refs. 15 and 16) if the scale factor δ_i^* is retained in the incompressible form. Hence, this is another example of how the characteristics of turbulence for compressible flow seem to depend only on the kinematics of the flow.

Category 1: Integral Methods (I.M.)

As is well known, the integral methods are based on solutions of various integral forms of the equations of motion. That is, the momentum and enthalpy equations (usually written as eqs. (12) and (13)) are combined with the continuity equation (eq. (1)) and integrated across the boundary layer to give two ordinary differential equations for the momentum thickness θ and total-enthalpy thickness Θ. These equations cannot be solved without additional information or assumptions for the form factor H^*, the surface

shear stress τ_w, and surface heat transfer q_w as functions of θ, Θ, and the boundary conditions of the problem such as wall temperature and pressure gradients. An additional difficulty for compressible flows is that H^* is a function of not only the velocity profile shapes but also the density (or temperature) profiles. Since general formulations for these functions are not yet possible, many different procedures based on various assumptions have been developed. Typical of these procedures is the technique of first multiplying equation (12) (combined with eq. (1)) by a weighting function and then integrating the new equation across the boundary layer. In this way, a new ordinary differential equation can be obtained for each weighting function used. Thus, for example, if the weighting functions are just y or $\bar{u}$, the resulting integral equations are known as the moment-of-momentum equation and the kinetic-energy equation, respectively. For turbulent boundary layers additional unknown integrals involving the turbulent shear stress then arise. With weighting functions y and $\bar{u}$, these unknown integrals are called the shear-stress integral and the dissipation integral, respectively. A large body of literature is concerned primarily with the development of correlations and expressions for these integral quantities.

Since about 1962 an improved method of integral relations has been developed wherein the weighting functions are linearly independent functions of $\bar{u}$ (see paper no. 14 of ref. 3; ref. 64; and ref. 1, pp. 16-29 and 46-53). The proponents of this method claim that, in principle, the solution of the resulting system of ordinary differential equations can approach the correct solution of the original partial differential equation if the weighting functions satisfy all boundary conditions and are chosen to avoid singularities. In this approach the unknown shear-stress integrals are evaluated by the use of conventional eddy-viscosity relations such as equations (17) to (21). Thus, one advantage of the simpler integral methods is lost since the detailed behavior of the turbulent shear stress or heat transfer across the boundary layer has to be specified.

Rather than to attempt a detailed discussion of the many different integral methods and the great variety of assumptions used in their formulation, the following discussion is limited to four methods that utilize $\bar{u}$ or y as weighting functions. Predictions from these four methods are compared with data and some of the assumptions used in each method are discussed briefly.

Reshotko-Tucker method (ref. 65).- The method of reference 65 was included herein mainly because it is representative of several of the early approaches. Also, as pointed out by McDonald (paper no. 6 of ref. 3), the method has been widely used and some simple modifications of the basic approach (for example, refs. 66 and 67) have provided much improved predictions. (The more important of these modifications was to the expressions for the shear-stress integral.) The method of reference 65 utilizes the momentum and moment-of-momentum integral boundary-layer equations which are solved directly in the transformed plane for the transformed momentum thickness and form factor.

Stewartson's coordinate transformation was used. The skin-friction relation was obtained by application of Eckert's reference-enthalpy expression (ref. 68) to the Ludwieg-Tillmann skin-friction equation for incompressible flow (ref. 69). In order to express the moment-of-momentum equation in terms of the form factor, power-law velocity profiles were used, a functional relation between the shear-stress integral and form factor was assumed, and integrals of the enthalpy profiles were assumed to have the same functional relation to the form factor as in laminar flows. All these functions and assumptions were applied in the transformed plane. Finally, to compute the heat transfer, the Reynolds analogy factor was modified to account for the effect of pressure gradient by analogy with a laminar-flow result. The results computed by this method and presented herein were taken directly from paper no. 6 of reference 3.

In retrospect, the many assumptions used in the Reshotko-Tucker method seem difficult to justify. For some flow conditions, the much simpler and straightforward method developed by Charles B. Johnson and described briefly in reference 35 would probably give predictions at least as good as the method of reference 65. This statement is based on the good results obtained from Johnson's method for a wide range of conditions (ref. 35). Also in Johnson's method the velocity and enthalpy profile correlations were based directly on experimental data, the calculations were carried out in the physical plane, and the Spalding-Chi skin-friction relation (ref. 46) was used.

Camarata-McDonald method (ref. 70).- The method of reference 70 has been included in the present review because the momentum and moment-of-momentum integral equations have been used just as in the Reshotko-Tucker method except that two significant modifications have been introduced which, on conceptual grounds, might be expected to improve the predictions. The procedure is described briefly in paper no. 6 of reference 3 and also in reference 1 (pp. 83-98) as applied to incompressible flows. The two significant modifications of the Reshotko-Tucker method are the procedure for evaluating the shear-stress integral and the use of Coles' transformation (ref. 71) for velocity profiles and skin friction. In order to evaluate the shear-stress integral, the "extended mixing-length hypothesis" was introduced wherein the value of the mixing length in the outer part of the boundary layer varied in the streamwise direction as governed by an integral form of the turbulence kinetic-energy equation. In this way the effect of the upstream history on the local turbulence properties (that is, on the mixing length) is accounted for. Consequently, this new method presumably represents a conceptual improvement over the previous methods of references 65 to 67 where the shear-stress integral was assumed to be a function of local conditions only $\left(H_i^* \text{ or a combination of } H_i^* \text{ and } C_f\right)$.

In order to compute heat transfer, a Reynolds analogy factor would be required. However, published results from this method have been limited to predictions of skin friction, momentum thickness, and form factor.

Alber-Coats method (ref. 48).- In the method of reference 48 the momentum and mean kinetic-energy integral equations are solved simultaneously in the physical plane for the dependent variables δ^* and π. The velocity profiles and a differential equation for skin friction were obtained from Coles' incompressible "law-of-the-wall" and "law-of-the-wake" forms (ref. 72) which were adapted to compressible flow by replacing the incompressible velocity by Van Driest's generalized velocity

$$u^* = u_e \frac{1}{a} \sin^{-1} a \frac{u}{u_e} \tag{22}$$

where $a = \sqrt{\left(\bar{r} \frac{\gamma - 1}{2} M_e^2\right) \Big/ \left(1 + \bar{r} \frac{\gamma - 1}{2} M_e^2\right)}$. For equilibrium flows, $d\pi/dx = 0$, and the dissipation integral is then an analytic function of the profile parameters, the skin-friction function, and the equilibrium pressure-gradient parameter $\beta_T = \frac{\delta^*}{\tau_w} \frac{dp}{dx}$. For application to nonequilibrium flows, the dissipation integral is "unhooked" from the local pressure gradient by assuming the empirical relation between β_T and π is the same as that found for incompressible flows (ref. 1, pp. 126-135). While the method has not yet been applied to compressible nonadiabatic flows, a procedure was derived and illustrated for incompressible flows (ref. 48). In this procedure, law-of-the-wall and defect solutions for the enthalpy profiles were used to derive a local heat-transfer law and a modified Reynolds analogy relation that incorporates the effects of wall temperature and pressure gradients. These results would then be used in conjunction with a two-parameter family of equilibrium enthalpy profiles as obtained from numerical solutions of the thermal-energy equation. An eddy-thermal-conductivity formulation similar to the eddy-viscosity expressions as given in equations (17b), (20c), and (21) was used to obtain these solutions. The only advantage in this approach is that the energy equation is an ordinary differential equation which, at least for incompressible flow, can be solved once for all for a given range of the equilibrium wall-temperature and pressure-gradient parameters.

Extension of this procedure to compressible flows, particularly for hypersonic conditions, may be fraught with unforeseen difficulties. While the general approach is obviously useful in the derivation and study of correlation parameters, the numerical advantages of solving ordinary differential equations, present in all I.M. approaches, may be outweighed by the conceptual problems.

Pinckney method.- A complete description and detailed derivation of the method of S. Z. Pinckney of NASA Langley Research Center has not yet been published but the main features of an earlier version of the method were described briefly by Henry in paper no. 19. of reference 3. In the method as applied herein, the momentum, moment-of-momentum, and total-energy integral equations are solved simultaneously in the physical

plane for the dependent variables δ, C, and A_2. The variable C is a coefficient in a modified Crocco relation between the velocity and static temperature. An iterative procedure at each station in the solution determines the local value of C which makes the integral of the total-energy profile consistent with the net heat transfer along the surface of the body up to the local station (see ref. 73). The variable A_2 is the coefficient of the term $\log y/\delta$ in a modified Coles' law-of-the-wall and law-of-the-wake velocity profile relation. The shear-stress integral in the moment-of-momentum equation was evaluated with a shear-stress profile of the form

$$\frac{\tau}{\tau_w} = 1 + \left(\frac{y}{\delta}\right)^b \tag{23}$$

where the exponent b is a correlated function of Mach number and of the y derivatives of velocity and temperature evaluated at $y/\delta = 0.95$ from adiabatic flat-plate profile data. Spalding-Chi skin friction and heat-transfer relations from reference 74 were used.

These brief synopses illustrate the conceptual and mathematical difficulties often encountered in the formulation of general I.M. approaches. The effects of the different assumptions on the final predictions are difficult to evaluate since usually they are not easily isolated or modified.

Category 2: Finite-Difference Solutions of Partial Differential Equations (F.D.)

In contrast with the I.M. approaches, the methods considered in this section are simple in both concept and mathematical manipulations. The computer programs required to execute the solutions are often more simple and straightforward than those required in some of the more complex I.M. approaches. However, longer computer times are generally required for the F.D. methods because of the large number of repetitive calculations that are required.

Since the partial differential equations are solved directly by numerical methods, subject to specified initial conditions and the boundary conditions of relations (14), only three aspects of the various F.D. methods can account for different predictions for the same problem. These three aspects are (1) the models of the turbulent-flux terms, (2) the basic numerical procedures for solving the equations, and (3) the interpolation or fairing procedures applied to the input information. The following discussion is limited to four methods selected to illustrate the effects of variations in some of these aspects.

One important approach not included in the following detailed descriptions utilizes independent partial differential equations for the turbulent-flux terms or related turbulence correlations. These equations are derived from basic principles and govern the

dynamics or detailed behavior of these correlation terms. The difficulty in this approach is that the problem of closing th system of equations is only moved up the hierarchy of unknowns from the second-order to the third-order correlations. For incompressible flows, the required relations can be satisfactorily modeled as indicated, for example, by the results of references 8, 75, and paper no. 7 of reference 3. For compressible flows, progress has been limited by the lack of knowledge of both second- and third-order correlations, some of which do not appear in the equations for incompressible flow. The only attempt published to date to solve the compressible-boundary-layer problem by this approach is that of Bradshaw (ref. 14) who has extended his method for incompressible flow directly to adiabatic flows with $M \lesssim 4$.

Herring-Mellor method (ref. 15).- The eddy viscosity used in the method of reference 15 for the wall or inner layer was (in the present notation)

$$\frac{\bar{\mu} + \epsilon}{\bar{\mu}} = 1 + \frac{\chi^4}{\chi^3 + (6.9)^3} \tag{24}$$

where

$$\chi = \frac{K\bar{\rho}y}{\bar{\mu}}\sqrt{\frac{\bar{\tau}}{\bar{\rho}}} \equiv \frac{K\bar{\rho}y}{\bar{\mu}}\sqrt{\frac{\bar{\mu} + \epsilon}{\bar{\rho}}\frac{\partial\bar{u}}{\partial y}}$$

For large values of χ,

$$\frac{\bar{\mu} + \epsilon}{\bar{\mu}} \rightarrow \chi$$

or

$$\bar{\mu} + \epsilon \rightarrow K^2\bar{\rho}y^2\frac{\partial\bar{u}}{\partial y} \tag{25}$$

For small values of χ or for $y \rightarrow 0$, ϵ varies as y^4 which, as noted previously, should be the correct trend.

In the outer or defect layer, Clauser's relation (ref. 63) was modified to give the forms

$$\Phi \equiv \frac{\bar{\mu} + \epsilon}{\bar{\rho}u_e\delta_i^*} = X \qquad (X < 0.016) \tag{26}$$

and

$$\Phi = 0.016 \qquad (X \geqq 0.016) \tag{27}$$

where

$$X = \frac{Ky}{u_e \delta_i^*}\sqrt{\frac{\bar{\tau}}{\bar{\rho}}} \equiv \frac{Ky}{u_e \delta_i^*}\sqrt{\frac{\bar{\mu} + \epsilon}{\bar{\rho}} \frac{\partial \bar{u}}{\partial y}} \tag{28}$$

Hence for $\Phi = 0.016$, Clauser's relation in the form of equation (21) is obtained if $\epsilon >> \bar{\mu}$. When $\Phi = X$,

$$\bar{\mu} + \epsilon = \bar{\rho} K^2 y^2 \frac{\partial \bar{u}}{\partial y} \tag{29}$$

Thus in the overlap region between the inner and outer layers (that is, for large χ and for $X < 0.016$), inner relation (25) is asymptotic to the outer relation evaluated for $X < 0.016$ (eq. (29)). Except for the appearance of the molecular viscosity $\bar{\mu}$, equation (29) is identical to the Prandtl wall mixing-length relation obtained by substituting equation (20c) into equation (17b). Since for most situations $\epsilon/\bar{\mu} >> 1.0$, the appearance of $\bar{\mu}$ in relations (24) to (29) should not cause any difficulty except when $\bar{\rho}$ is very small and ϵ is of the same order as $\bar{\mu}$. A tentative modification to equation (27) was introduced as

$$\Phi = 0.016\left[1 + \left(\frac{1100\bar{\mu}}{\bar{\rho} u_e \delta_i^*}\right)^2\right] \tag{30}$$

which would have the effect of increasing $\epsilon/\bar{\mu}$ in the outer part of the layer and would therefore suppress the effect of $\bar{\mu}$ in equation (27). The main purpose of this modification, however, was to maintain an overlap layer, which for $\Phi = 0.016$ tends to disappear when the local value of $\bar{\rho}$ in the sublayer becomes small.

The partial differential equations were solved in the x,η plane where $\eta = y/\delta^*$. (Some numerical problems would be expected when δ^* becomes very small, or even negative as for highly cooled walls.) All x derivatives were replaced with the finite-difference expressions

$$\frac{\partial G}{\partial x} = \frac{G_1 - G_o}{x_1 - x_o} = \frac{G_m - G_o}{x_m - x_o} \tag{31}$$

where G represents any of the dependent variables and x_m is an adjustable point intermediate between the initial station x_o and the downstream station x_1 where new profiles are required. The partial differential equations were then reduced to two ordinary differential equations in the variables G_m with all corresponding G_o values known or specified at station x_o. The new set of variables G_1 required at station x_1 are then determined by extrapolation from equation (31). A fourth-degree Runge-Kutta

method is used to solve the set of ordinary differential equations for G_m that are first written in a pseudolinear form. This procedure, together with the use of an asymptotic solution which assures the correct exponential behavior for large η, eliminated the numerical difficulties often encountered in the "shooting techniques" used previously, for example, by Smith and Clutter (ref. 76).

An operational procedure was available for computing the initial velocity and enthalpy profiles when they are not available at the input station. The boundary conditions of M_e, T_w $\left(\text{or } M_e, (\partial T/\partial y)_w\right)$ are read in at the discrete values of x_1 where profiles are to be computed and the location of the intermediate points x_m are specified. The solution of the ordinary differential equations for momentum and energy was carried out by an iterative procedure. In this procedure, the velocity profiles, enthalpy profiles, and effective diffusivities were computed in that order from the momentum, energy, and diffusivity relations by utilizing "updated" values for each successive step within the iteration loop. From two to seven iterations were required to obtain convergence. Note, finally, that the eddy diffusivity for heat was computed from a turbulent Prandtl number $N_{Pr,t}$ defined in terms of the static enthalpy. While $N_{Pr,t}$ could be specified as a function of y, $N_{Pr,t} = 1.0$ was used for all cases reported in reference 15.

Fish-McDonald method (ref. 77).- The method of reference 77 was described briefly by McDonald in paper no. 6 of reference 3. The predictions by this method, as given in the present review, were taken directly from reference 3. In these predictions the Herring-Mellor eddy-viscosity relation was used as just described in the previous paragraphs. Therefore, according to McDonald (paper no. 6 of ref. 3), "any differences which might arise between the predictions of the Herring procedure and the Fish-McDonald procedure can at this stage only be attributable to the differences in the numerical techniques employed."

The Fish-McDonald method uses essentially the same numerical technique as that of Cebeci, Smith, and Mosinskis (given in ref. 16 and described in more detail in ref. 78), except that the streamwise derivatives were replaced by four-point (least-squares) finite-difference formulas rather than the three-point formulas of reference 16. Five-point finite-difference formulas were used in the direction normal to the surface. The resulting system of algebraic equations are linearized and solved in the physical coordinates by a matrix-inversion method. The iteration procedure used provides a final solution which presumably has converged to the correct solution of the original nonlinear system of equations. The method is an implicit finite-difference procedure in the sense that the final values of the dependent variables calculated at each grid point depend on the previous values all the way across the boundary layer (in this case at the three upstream stations, since four-point finite-difference formulas are used in the x-direction) through the simultaneous solution of the system of equations and the iteration procedures used. In contrast

to this implicit procedure, the variables at each grid point in a simple explicit method depend only on the values at the three grid points just upstream of the point where values are being computed.

Bushnell-Beckwith method (ref. 34).- The eddy-viscosity model used in the present calculations by the method of reference 34 combined the outer and inner wall-region mixing-length relations given by equations (20b) and (20d), respectively. Thus, a single relation for eddy viscosity was applied to the entire boundary layer. This relation was

$$\epsilon = \bar{\rho} f_2^2 \left[1 - \exp\left(-\frac{\rho_w y}{A^* \mu_w}\sqrt{\frac{\tau_w}{\rho_w}}\right)\right]^2 \left|\frac{\partial \bar{u}}{\partial y}\right| \tag{32}$$

where the function f_2 (see eq. (20b)) is the same as that of reference 34. (The dependence on H_i^* was taken as variation (3) of fig. 2 in ref. 34.)

The numerical technique of reference 34 is also an implicit finite-difference procedure wherein the partial derivatives in the equations of motion are replaced by linear difference quotients. A two-point central differencing scheme is used in both the streamwise and normal directions as in reference 75. The result is a set of N-1 linear equations for each of the unknown variables (the mean velocity $\bar{u}$ and the enthalpy) at the N grid points for the next downstream station. The matrix for each of these sets of linear equations is tridiagonal, so an efficient algorithm is available for the solution of each matrix (ref. 79). Instead of solving the matrices for the momentum and energy equations simultaneously as in reference 80, they were solved separately and successively during each cycle of an iteration procedure. The transformed normal velocity is then obtained from the continuity equation. The iteration procedure applied successively to the sets of linear equations then provides a convergent solution to the nonlinear system of partial differential equations as in the methods of references 16 and 77.

Since the boundary conditions at the wall and outer edge are imposed on the sets of linear equations at each streamwise step and the equations in each set are solved simultaneously, the correct slopes of the velocity and enthalpy profiles at the wall are automatically obtained during each step of the iteration cycle. The sensitivity of the solutions to these wall slopes, which in previous methods (ref. 76, for example) had to be determined by direct iteration to satisfy the outer-edge boundary condition (the two-point boundary-value problem), is thereby eliminated completely.

The equations are solved in the transformed coordinates which are defined as

$$\left.\begin{aligned}\xi\left(\frac{x}{L}\right) &= R_s\int_0^{x/L}\frac{(\rho\mu)_e}{(\rho\mu)_s}\frac{u_e}{\sqrt{2H_e}}\,r_w^{2j}\,d\left(\frac{x}{L}\right)\\ \eta\left(\frac{x}{L},\frac{y}{L}\right) &= R_s\frac{u_e\Big/\sqrt{2H_e}}{(2\xi)^{\bar{n}}}\,r_w^{j}\int_0^{y/L}\frac{\rho}{\rho_s}\,d\left(\frac{y}{L}\right)\end{aligned}\right\} \tag{33}$$

where $\bar{n}$ is adjusted to obtain nearly a constant boundary-layer thickness in the ξ,η plane and thereby increase the computational efficiency. A variable step size in the η-direction also increases the computational efficiency, as in reference 75, by increasing the relative number of steps near the wall where finer detail is required. Tabular inputs are used for both the initial profiles and the wall and edge boundary conditions.

Harris method.- A complete description of the method of Julius E. Harris of NASA Langley Research Center has not yet been published. The eddy-viscosity relation used by Harris for the results given in this review is essentially the same as that of Cebeci, Smith, and Mosinskis (ref. 16). That is, the law for the inner region uses the Prandtl mixing-length relation (eq. (20c)) modified with the Van Driest damping function to give

$$\epsilon_{inner} = K^2y^2\left[1 - \exp\left(-\frac{\bar{\rho}y}{26\bar{\mu}}\sqrt{\frac{\tau}{\bar{\rho}}}\right)\right]^2\left|\frac{\partial\bar{u}}{\partial y}\right| \tag{34}$$

The law for the outer region is Clauser's relation (see eq. (21)), but the eddy viscosity is multiplied by an intermittency function similar to that of reference 54.

The numerical procedure for solving the equations is an implicit finite-difference procedure developed by Davis and Flügge-Lotz for solving the first- and second-order boundary-layer equations (ref. 50). In this procedure, a Levy-Lees type transformation is applied to the partial differential equations; then the derivatives in both the streamwise and normal directions are replaced with three-point finite-difference formulas. The finite-difference quotients are therefore accurate to the order of the square of the step sizes in both directions rather than in the normal direction only as in the method of reference 34. The resulting algebraic equations are linearized and solved in the same way as by Blottner (ref. 80) in that the matrices for the momentum and energy equations are solved simultaneously. The use of this procedure apparently reduces the number of iterations required to obtain convergence, as compared with methods in which these matrices are solved separately during each iteration cycle as in reference 34, for example. In the computer program developed by Harris, the initial and boundary conditions can be specified as either analytic or tabulated functions.

Category 3: Correlation Techniques (C.T.)

As mentioned in the section "Analytic Approaches," C.T. methods have been reviewed and classified by Spalding and Chi in reference 46 where the various assumptions and equations embodied in each of five types of C.T. methods are given in some detail. For the present purposes, it is therefore sufficient to list four main types of these methods with brief comments and a few representative references. Since these methods are primarily concerned with the prediction of skin friction, additional assumptions for the Reynolds analogy factor $2N_{St}/C_f$ and recovery factor $\bar{r}$ are required before heat-transfer predictions can be made. The predictions from these methods are strictly applicable to flat-plate-type flows only ($dp/dx \approx 0$); however, they have been widely used for parametric design studies of supersonic vehicles and will continue to be useful for preliminary design estimates. Consequently, in a subsequent section, predictions from one method representative of each of the following four main types are compared with recent experimental data for skin friction and heat transfer.

Reference temperature.- Reference-temperature methods utilize formulas developed for incompressible flow by evaluating all gas properties that appear in these formulas at some intermediate or reference temperature (or enthalpy). This reference temperature is generally a function of M_e, T_w, and T_{aw} as determined by empirical correlations with data. Typical methods in this group are those of Sommer and Short (ref. 81) and Eckert (ref. 68).

Assumed functional relations.- A universal function ψ is assumed of the form

$$C_f F_C = \psi\left(R_\theta F_R\right) \tag{35}$$

where F_C and F_R are functions of M_e and T_w/T_e. At least one of these functions $\left(F_C \text{ and/or } F_R\right)$ would be determined by empirical correlation methods. Since for flat-plate flows, relations between C_f, R_θ, and R_x can be specified (ref. 82, for example), the function ψ can be expressed also in terms of R_x. This method was developed by Spalding and Chi (ref. 46) and modified slightly by Komar (ref. 82).

Use of Prandtl or von Karman wall mixing-length relations.- Either the Prandtl mixing-length relation (eq. (20c)) or von Karman's assumption that

$$u' \approx v' = K^* \frac{\left(d\bar{u}/dy\right)^2}{d^2\bar{u}/dy^2} \tag{36}$$

is used to obtain the shear stress which is assumed constant across the boundary layer and equal to the wall value. The resulting differential equations for the velocity are

$$\tau \approx \frac{C_f}{2} \rho_e u_e^2 = \bar{\rho} K^2 y^2 \left(\frac{d\bar{u}}{dy}\right)^2 \tag{37}$$

and

$$\tau \approx \frac{C_f}{2} \rho_e u_e^2 = \bar{\rho} K^{*2} \frac{(d\bar{u}/dy)^4}{\left(d^2\bar{u}/dy^2\right)^2} \tag{38}$$

After the assumption of approximate relations for $\bar{\rho}(y)$ or $\bar{\rho}(\bar{u})$ (generally a Crocco relation), these equations are solved for $\bar{u}(y)$. Then with the use of the flat-plate momentum integral equation

$$\frac{d\theta}{dx} = \frac{C_f}{2} \tag{39}$$

closed-form expressions or charts are obtained for C_f in terms of M_e, T_w/T_e, T_{aw}/T_e, and parameters or constants used in the density function.

Typical methods in this group include those of Van Driest (ref. 83 with eq. (37); ref. 84 with eq. (38)), Wilson (ref. 85), and Rubesin, Maydew, and Varga (ref. 86). The last two methods were based on von Karman's mixing-length relation (eq. (38)).

Compressibility transformations.- The general objective of compressibility-transformation methods is to devise a set of analytic functions which relate or transform all quantities in an unknown compressible flow to a corresponding incompressible flow. In this way the larger amount of more reliable data for incompressible boundary layers can be utilized directly to provide predictions for the compressible counterparts. When large, arbitrary, streamwise pressure gradients are present, the companion incompressible flow must generally be calculated by suitable integral or finite-difference methods such as those of reference 1. Another advantage of the transformation methods is that no arbitrary assumptions for the behavior of the turbulent flux of momentum in the compressible flows are required. This advantage cannot generally be realized, however, unless the approach of Coles is used wherein the "transformation represents at every stage a genuine kinematic and dynamic correspondence between two real flows" (p. iii of ref. 87). It immediately becomes obvious from this statement and from the equations treated by Coles and others that when physical phenomena encountered in the compressible flow do not even exist in the corresponding incompressible flow, the transformation methods may not provide reliable predictions. Examples of this lack of correspondence of the transformed incompressible flow are as follows:

(1) When streamwise pressure gradients are large in a hypersonic boundary layer, then the normal pressure gradients are also large because of the inherent Mach wave structure of the flow. The corresponding normal pressure gradients in the

incompressible, low-speed flow do not exist (essentially because the $\bar{u}^2$ term in eq. (3) becomes a higher-order term). For the same reason, the tendency for the effects of upstream history to persist for large downstream distances in hypersonic flow (see paper no. 12 of ref. 3 and ref. 36) cannot be duplicated by the incompressible flow.

(2) When the Mach number is large, the last term in the bracket of equation (4) (viscous dissipation) may become important near the wall where the temperature and viscosity are large. Again the corresponding term in the low-speed flow is of higher order.

(3) If the energy equation for the static enthalpy is used, a first-order turbulent dissipation term $\bar{u}\bar{\rho}\overline{v'u'}$ arises (see eqs. (6)). This term is again of higher order in low-speed flows and hence is usually neglected in the energy equation for the transformed flow. This and the preceding limitation would apply mainly to the calculation of heat transfer.

(4) When the heat transfer is large in the compressible flow, $\partial\bar{T}/\partial y$ is large both in the compressible flow and in the corresponding incompressible flow which is, however, restricted by the conditions that $\frac{\partial\bar{p}}{\partial y} \approx 0$ and that $\bar{\rho}$ is constant. Hence, for any reasonable equation of state for gases, the requirements for correspondence between the two flows cannot be satisfied.

(5) Lastly, if the turbulent correlation terms containing ρ' are significant in low-density compressible flows (as indicated by tentative results of ref. 34), then the transformation again breaks down because of the constant-density limitation in the low-speed flow.

In view of these limitations, it should not be surprising that the transformation methods have so far yielded good results only for moderate Mach numbers $\left(M_e \lesssim 6.0\right)$, moderate heat transfer $\left(\frac{T_w}{T_o} \gtrsim 0.5\right)$, and moderate streamwise pressure gradients. Various modifications of the Coles approach have been developed and the resulting predictions are compared with data in references 88 to 91. In reference 91 the formal transformation theory for arbitrary pressure gradients was used to compute integral parameters for three different cases of adiabatic flows with large pressure gradients and $M_e \leqq 3.0$. (The results for one of these cases is discussed in a subsequent section.) This method (ref. 91) might be termed an integral method, since the corresponding incompressible flows were computed by an integral method which used the momentum and moment-of-momentum integral equations and a differential form of the skin-friction law based on Coles' law-of-the-wall and law-of-the-wake formulation (ref. 72).

COMPARISONS OF PREDICTIONS WITH EXPERIMENTAL DATA

A few comparisons of predictions from the I.M. and F.D. theories with experimental data are included in subsequent sections of this review to indicate in a limited way the scope and capability of these theoretical methods and their relative accuracy for only those particular cases shown. These comparisons are not intended to provide any general assessment of the absolute or relative accuracy or reliability of these theoretical methods. The reader is cautioned that any such assessment should not be attempted without reference to the original sources and the large number of comparisons available therein. Remarks in this section and elsewhere in this paper regarding the relative merits of the various I.M. and F.D. methods are based on a careful perusal of all available comparisons and some limited personal experience with the use of some of the methods.

On the other hand, predictions from the C.T. methods are compared with most of the available data obtained by direct measurements with surface-shear-stress balances on flat plates. The corresponding heat-transfer data are not as extensive, but include most of the recent data obtained for the same range of T_w/T_{aw} as that of the shear-stress data. The review of the C.T. methods is thus a reasonably current and general assessment of the four representative approaches considered. Since the C.T. methods are used widely for parametric design studies and even for final estimates of surface friction and heating, they are considered first.

C.T. Methods for Skin Friction and Heat Transfer on Flat Plates

One method from each of the four groups of C.T. methods listed in the preceding section has been selected for further assessment by detailed comparisons with data. The methods selected are those of Sommer and Short (ref. 81), Spalding and Chi (ref. 46), Van Driest (ref. 84), and Coles (ref. 71). The experimental data and calculations are taken from the detailed survey paper of C.T. methods by Hopkins, et al. (see ref. 21 or paper no. 10 of ref. 3), which includes new data obtained with surface shear-stress balances on flat plates at $M_e = 6.5$ and $M_e = 7.4$ for $0.31 \leqq \frac{T_w}{T_{aw}} \leqq 0.51$ and $2100 < R_\theta < 8400$. These data were compared with other data (also obtained with balances) for $M_e < 7.4$, $\frac{T_w}{T_{aw}} > 0.13$, and $2000 < R_\theta < 700\,000$.

The results are shown in figure 1(a) as percent deviations of data from predictions by the four methods. Both the predictions and data were used throughout as functions of R_θ rather than R_x to avoid the problem of defining a virtual origin of the turbulent boundary layer. The use of R_θ confers the further advantage of widening the applicability of the methods to flows with favorable and mild adverse pressure gradients, since

fairly simple integral methods (ref. 35, for example) can account for such effects on R_θ if the region of transition from laminar to turbulent flow is specified. Since all the original data points and their identification are available in reference 21, only shaded bands are used herein to represent the data.

The results shown in figure 1(a) indicate that none of the theories predict the correct trends with T_w/T_{aw} over the entire range of this temperature ratio, which is a direct index of the magnitude of surface heating. The Van Driest and Coles theories provide the best overall predictions; however, these predictions are somewhat below the data for the range $0.4 < \frac{T_w}{T_{aw}} < 1.0$ and considerably above the data for $\frac{T_w}{T_{aw}} < 0.2$. The Spalding-Chi theory underpredicts the data by 20 to 40 percent for $0.2 < \frac{T_w}{T_{aw}} < 0.6$, while the Sommer-Short theory gives the poorest indication of trends with T_w/T_{aw}, the predictions varying from 40 percent below to 20 percent above the data for a range of T_w/T_{aw} from 1.0 down to 0.15.

As mentioned previously, these theories can be used to predict heat-transfer rates if the Reynolds analogy factor $2N_{St}/C_f$ and recovery factor $\bar{r}$ are known or specified. Predictions of N_{St} from the same four theories are compared with heat-transfer measurements in figure 1(b) where the values assumed for these two factors were $\left(2N_{St}/C_f\right)_{theo} = 1.16$ and $\bar{r} = 0.9$. The experimental data were obtained on flat plates and cones for $4.9 \leqq M_e \leqq 7.4$ and $3000 < R_\theta < 5000$ by Mateer and Polek (first published in ref. 21) and Cary (ref. 92). The assumed value of $2N_{St}/C_f = 1.16$ is representative of subsonic and moderately supersonic data for $\frac{T_w}{T_{aw}} > 0.6$ as indicated by Cary's recent survey (ref. 93). The assumed value of the recovery factor is typical of data for turbulent boundary layers for a wide range of conditions.

The heat-transfer results (fig. 1(b)) indicate that predictions of the Van Driest and Coles theories are considerably above the data (by as much as 40 percent for the smaller values of T_w/T_{aw}). The Spalding-Chi theory predicts the trend with T_w/T_{aw} better than the other theories but generally underpredicts the mean of the data. The Sommer-Short theory gives good agreement with the mean of data down to $\frac{T_w}{T_{aw}} = 0.4$ and then increasingly overpredicts the data as T_w/T_{aw} is decreased further.

Comparison of figure 1(b) with figure 1(a) therefore indicates large inconsistencies in the predictions obtained by the same theories for heat transfer and skin friction. Recent direct measurements of both skin friction and heat transfer on a flat plate for $\frac{T_w}{T_{aw}} = 0.32$ and for $M_e = 6.8$ and $M_e = 7.4$ (ref. 21) indicate that the Reynolds analogy

factor may be more nearly 1.0 for these conditions. Measurements made on sharp slender cones at Mach 5 (ref. 94) indicate that for $\frac{T_w}{T_o} < 0.5$, the Reynolds analogy factor decreases below values of approximately 1.2 as the temperature ratio is decreased. Cary's recent survey (ref. 93) also indicates a possible trend, particularly for nozzle-wall flows, of the Reynolds analogy factor decreasing to values nearer 1.0 when T_w/T_{aw} is decreased and the Mach numbers are large. It is therefore of interest to determine if the heat-transfer predictions by the C.T. methods are improved by the use of a value for $\left(2N_{St}/C_f\right)_{theo}$ of 1.0 rather than 1.16, which was based primarily on low Mach number data with $\frac{T_w}{T_{aw}} > 0.8$. The resulting predictions for the heat-transfer data of figure 1(b) are shown in figure 1(c), where the skin-friction results of figure 1(a) are superimposed for comparison. The main conclusion from figure 1(c) is that the predictions of heat transfer and skin friction are now reasonably consistent for each of the four theories used. This consistent set of predictions favors the use of Reynolds analogy factors near 1.0 for these conditions. Two other results of interest should be noted. First, the Coles theory provides the best correlation of the data in terms of the minimum spread in deviation at a given T_w/T_{aw}. Second, the Spalding-Chi theory gives the best prediction of trends with T_w/T_{aw}, although the total spread in the percent deviations from this theory are large. Presumably this defect in the Spalding-Chi theory could be remedied by reevaluating the empirical function F_R (see eq. (35)) for the present data. On the other hand, the large discrepancies in the observed and predicted trends with T_w/T_{aw} for the Coles theory may not be easily corrected, in view of the basic limitations of transformation theory indicated in the previous section.

The relative simplicity of the C.T. theories as compared with more advanced methods insures their continued use for, at least, preliminary estimates of surface shear stress and heating. However, when more reliable values of these surface quantities are required, particularly for small values of T_w/T_{aw}, large local Mach numbers, and large pressure gradients, the I.M. and F.D. methods must be used. These latter methods must also be used when more detailed information is required (such as local boundary-layer thicknesses and profiles and the effects of large upstream gradients on these local characteristics). A typical situation where such detailed information is necessary is for inlet design problems as indicated in paper no. 19 of reference 3.

Other limitations of the C.T. methods are the difficulties encountered in their application to three-dimensional flows and flows with more complex boundary conditions such as external vorticity and surface mass transfer. The transformation methods have been extended to flows with mass transfer (refs. 89 and 90, for example), but the same limitations of moderate heat transfer, pressure gradients, and Mach number still apply.

In the F.D. methods discussed in the next section, none of these limitations apply. In the I.M. approaches, the limitation of moderate pressure gradients is not too significant, even when C.T. skin-friction laws or transformation theory are used.

I.M. and F.D. Methods Applied to Adiabatic Flows With Arbitrary Pressure Gradients

Predictions for C_f, θ, and H^* are compared with data from two experimental investigations that have been used as test cases for several theoretical methods. The two experimental investigations are by Winter, Rotta, and Smith (ref. 95) and by McLafferty and Barber (ref. 96). Predictions from nine different theories are compared with these data. The theories and line symbols to be used for the predictions are shown in figure 2.

Winter, Rotta, and Smith (ref. 95).- In reference 95 experimental data for velocity profiles and skin friction on a waisted body of revolution for values of M_∞ from 0.57 to 2.8 were obtained. The velocity profiles were based on pitot-pressure surveys, the measured wall static pressures with $\partial p/\partial y = 0$ apparently assumed, and an assumed quadratic relation between static temperature and velocity. Small razor blade "scoops" which functioned as Stanton tubes provided data for the skin friction. The free-stream test Reynolds number based on the 5-foot body length was maintained approximately constant at 10×10^6. Comparisons are shown herein only for the data at the highest free-stream Mach number of 2.8. For this test condition there was a favorable pressure gradient up to about the 24-inch station followed by an adverse pressure gradient to $x = 45$ inches; then the pressure was approximately constant to the end of the body.

The predictions and data are shown for skin friction in figure 3(a) and for θ and H^* in figure 3(b). Note the wide disparity between the various predictions for C_f. The F.D. results of reference 15 are generally the highest while the results of reference 91 (utilizing the formal transformation) are generally the lowest. The older I.M. approach of reference 65 fails in that separation was predicted on the aft portion of the body. The methods that are in the best overall agreement with the C_f data are the I.M. approaches of references 70 and 48 and the F.D. methods of Harris and reference 34.

The appreciable differences between the predictions for C_f by the F.D. methods of Herring and Mellor (ref. 15) and Fish and McDonald (ref. 77) are evidently due to the differences in numerical techniques since the eddy-viscosity relations are identical. According to previous discussion of these methods, the Fish-McDonald procedure should provide better accuracy because of the improved finite-difference expressions used for the x derivatives. Hence, it could be speculated that the Herring-Mellor procedure is more sensitive to the step size in the x-direction and if the Δx steps were too large,

the procedure would give erroneous results, particularly in the large favorable-pressure-gradient region for $x > 42$ inches. The large underprediction of the transformation-integral approach of reference 91 may be associated with the complete reliance in this method on the formal transformation, since the I.M. approaches of references 48 and 70 give fairly good predictions. On the other hand, the I.M. approach of Pinckney overpredicts C_f by a large amount except on the aft portion of the body. The precise reasons for this result would be difficult to determine because of the involved assumptions of this theory. Possibly the use of a flat-plate skin-friction relation or the formulation of the shear-stress integral could account partly for the erroneous predictions. All the results for C_f except those of references 34 and 91 are too high at the station $x = 24$ inches, which in many of the methods was used as an input station because the first experimental profile was obtained there and hence values of θ and H^* were available. (At this station, the experimental R_θ is 2140.)

It is of interest to note that the F.D. methods of reference 34 were started with both the experimental C_f and the outer part of the velocity profile as inputs so that the experimental values of θ and H^* were also matched reasonably at $x = 24$ inches (see fig. 3(b)). In spite of this forced match at $x = 24$ inches, the computed skin friction increased very rapidly up to the level of most of the other theoretical results. Apparently the mixing-length model in this theory as well as the effective turbulent-flux models present in most of the other theories result in predictions of skin friction that are inconsistent with the experimental velocity profile at $x = 24$ inches, which was generally matched as an input. These results suggest that some relaminarization effects may have been present in the boundary layer.

In an investigation of laminarization in a nozzle-wall turbulent boundary layer, Back, et al. (ref. 97) found that when values of the parameter $\hat{K} = \frac{\nu_e}{u_e^2}\frac{du_e}{dx}$ exceeded 2×10^{-6}, the heat transfer generally decreased to values below those typical of turbulent boundary layers. Also when $\hat{K} > 1.3 \times 10^{-6}$, noticeable changes in velocity profiles occurred in the law-of-the-wall region. Calculations by Julius E. Harris for the Winter-Rotta-Smith body showed that $\hat{K}$ exceeded this latter value from about $x = 17$ inches to $x = 23$ inches for the test at $M_\infty = 2.8$. The low observed values of skin friction as compared with predictions in this region may therefore be partly caused by laminarization of the boundary layer. Furthermore, this tendency towards laminarization may have persisted downstream of the 23-inch station. The authors of this experimental investigation (ref. 95) stated that the roughnesses (installed at 1.5 inches from the tip) were not fully effective above $M_\infty = 1.4$.

Other factors that could account for the disagreement between most of the predictions and the skin-friction data in the region $20 < x < 35$ inches are errors in the data

and effects of normal pressure gradients. This latter factor has not been accounted for in either the theories or (apparently) the data-reduction procedures.

In the F.D. solution by Harris, experimental velocity profiles were not used. Instead, the solution was started at the tip with a similar laminar solution as the input, and transition was initiated at $x = 1.8$ inches by "switching on" the eddy viscosity. However, through the use of an intermittency function of x, the full value of ϵ was not utilized in the solution until $x = 9$ inches, so only from this station on would fully developed turbulent profiles be computed. Consequently, the values of θ computed by Harris and shown in figure 3(b) are higher than the data, as would be expected if laminarization were present. These values of θ are also higher than the results of other theories which used the experimental θ at $x = 24$ inches as an input. On the other hand, possible reasons for the overprediction of θ by all the theories for $x > 35$ inches (fig. 3(b)) are not readily apparent. (The gross overprediction of H^* by the older I.M. method of ref. 65 again reflects a breakdown of that method.)

Another possible explanation for some of the discrepancy between predictions and data for C_f (fig. 3(a)) is the effect of curvature on the turbulent-shear-stress term. Bradshaw (ref. 98) and Rotta (ref. 99) have both indicated that this effect may be large. To investigate this possibility, the mixing-length modification of Bradshaw (ref. 98) was used to recompute the boundary layer for this test at $M_\infty = 2.8$ by the F.D. method of reference 34. All inputs and boundary conditions of the original solution were retained, but the mixing-length model of equation (20b) (as applied in eq. (32)) was modified according to the formula (see ref. 98)

$$l_c = \left(1 - 2\beta \frac{\bar{u}/r_c}{\partial\bar{u}/\partial y}\right) l_u \tag{40}$$

where l_c is the new mixing length which accounts for the effect of curvature. For very large longitudinal radius of curvature, l_c reduces to the previous l_u which is the same function of y/δ and H_1^* as described in reference 34. The quantity β is recommended as a constant by Bradshaw and was taken as 7 for the results shown in figure 3. Rotta (ref. 99) indicates that β should be a function of Mach number, but that function was not used herein.

In order to obtain physically realistic values of l_c from equation (40), the limitation that $0 \leqq l_c \leqq l_{c,e}$ was imposed, where $l_{c,e} = 0.1\delta$. The lower limit simply prohibits negative values of l_c, which would give improper behavior to the eddy viscosity for small positive values of r_c, corresponding to large convex curvature and large damping of turbulence. The upper limit avoids unrealistically large values of l_c that would otherwise be computed when r_c is negative and $\partial\bar{u}/\partial y \rightarrow 0$ near the outer edge of the boundary layer.

The results (fig. 3(a)) indicate that up to $x = 27$ inches, C_f was reduced only slightly by using equation (40), but from there on it was generally increased appreciably since the radius of curvature changed from positive to negative values (convex to concave curvature) at $x \approx 27$ inches and hence, the modified mixing length l_c was greater than l_u from that region downstream. The improved agreement with the data downstream of the minimum in C_f indicates that longitudinal curvature may have had some effect in this region. Of course, this statement must be regarded as speculative, since some of the other theories which did not explicitly include the curvature effect gave results in equally good agreement with data in the region downstream of $x \approx 44$ inches (notably the F.D. theory of Harris and the I.M. theories of refs. 70 and 48). The effects of longitudinal curvature on θ and H^* according to these calculations were very slight, as indicated by the results shown in figure 3(b). The effect of lateral curvature (not included in all theories as indicated in fig. 2) has been determined for this case by Harris and by Cebeci, et al., in reference 16. The effect of using $r = r_w + y \cos \alpha$ rather than $r = r_w$ increased C_f by, at most, 15 percent.

McLafferty and Barber (ref. 96).- In reference 96 wall static pressures and pitot pressures across the boundary layer and in the inviscid flow were measured on several curved ramps with large adverse pressure gradients. The curved ramps were mounted flush with the wall near the exit of a supersonic nozzle. No measurements of skin friction or static pressures across the boundary layer were made. However, the variation in local static pressure across the boundary layer was accounted for in the data-reduction procedure used to obtain the velocity and density distributions. (The stagnation temperature was assumed constant across the boundary layer.) This static pressure distribution was assumed to be a quartic curve which matched the measured wall static pressure and the local free-stream static pressure as determined from pitot-pressure measurements outside the boundary layer. The quartic curve also satisfied the requirements that $(\partial p/\partial y)_w = 0$ (see eq. (3)) and that the derivatives outside the boundary layer $\left(\left(\frac{\partial p}{\partial y}\right)_e\right.$ and $\left.\left(\frac{\partial^2 p}{\partial y^2}\right)_e\right)$ match the values obtained from the pitot-pressure distributions. The use of this procedure was presumably justified by improved values for the velocity and density, but these improvements may have been partly negated by the use of p_w rather than p_e to compute the reference velocity and density used in the evaluation of δ^* and θ.

One set of experimental data was chosen from several available in reference 96 for comparison with theoretical predictions. This set of data was obtained at $M_\infty = 3.0$ on a circular arc compression ramp with $r_c = -6$ inches. The point of tangency between the ramp and the flat floor of the wind tunnel was used as the input station for all the calculations except those of references 65, 70, and 77. The experimental values of the integral parameters at this station were $\theta = 0.0161$ inch, $H^* = 5.75$, and $R_\theta = 2540$.

The predictions for θ and H^* are compared with the data in figure 4. Again the older I.M. approach of reference 65 gives poor predictions. The values of H^* from the transformation-integral procedure of reference 91 also deviate considerably from the data for $x > 2$ inches because of a near separation predicted by this theory and the resulting effect on the form factor. Most of the other theories give good predictions (in view of the uncertainties in the data, as mentioned previously) except for the values of θ on the aft portion of the ramp as predicted by the I.M. approach of reference 70 and the F.D. method of reference 34.

The failure of the I.M. method of reference 65 in this and the previous example is believed to be caused primarily by the assumption used for the shear-stress integral and the use of the Stewartson coordinate transformation which cannot provide the correct transformation for the turbulent shear stress. This statement is supported by the much improved results of the transformation-integral theory of reference 91 which used the Coles transformation. This latter theory still fails to give satisfactory predictions, probably because of the inherent limitations of the transformation theory in large pressure gradients (see previous discussion of C.T. methods).

The method of reference 34 has been used to determine the effects of two mixing-length relations and different values of du_e/dx on θ, H^*, profiles of F, and C_f. The results are shown in figure 4 for three solutions identified by case number and symbol as follows: (1) closed triangle, (2) open triangle, and (3) cross (+).

For case (1), equation (40) was used for the mixing length, and all boundary conditions $\left(\text{namely, } u_e, \ du_e/dx, \text{ and } \rho_e\right)$ were obtained from the measured values of p_w as given in reference 96. This solution gave good agreement with data for θ and H^* (fig. 4(a)) and reasonable agreement with velocity profiles (fig. 4(b)); however, it predicted separation at $x \approx 2.7$ inches (fig. 4(c)).

Since separation did not occur in the experiment, case (2) was obtained with the input values of du_e/dx computed from p_e rather than p_w but with the same values used for u_e, and ρ_e (based on p_w). This solution gave considerably larger values of C_f with no separation (fig. 4(c)), but the values of θ were reduced (fig. 4(a)) and the velocity profiles (fig. 4(b)) were too full at all x stations.

Cases (1) and (2) were both computed with the mixing-length relation of equation (40) which, with the negative radius of curvature of -6 inches (ref. 96), increases the eddy viscosity. The limitation of $l_{c,e} = 0.1\delta$, which resulted in improved agreement for the data of reference 95 (shown in the preceding section), was also used for cases (1) and (2). Thus, in order to determine if the curvature modification to the mixing length was too large, case (3) was computed without this correction. The mixing-length relation of equation (20a) was used with $(l/\delta)_{max} = 0.1$. The values of C_f were lower than for case (2), but the velocity profiles, θ, and H^* were essentially the same. The effect of

the curvature modification is therefore limited primarily to the values of C_f. This result would be expected because the values of l/δ in the outer part of the boundary layer were the same in all these cases, since $\frac{l_{c,e}}{\delta} = 0.1$ or $(l/\delta)_{max} = 0.1$ was used.

Predicted values of C_f from two other methods are also shown in figure 4(c). These predictions are from the I.M. approach of reference 48 and the transformation-integral method of reference 91. The trends from all the methods are similar. The method of reference 91 predicts separation at about the same location as case (1) by the method of reference 34.

The main reason for including this rather lengthy presentation of results obtained with the method of reference 34 is to illustrate how various modifications to the eddy-viscosity model and to the boundary conditions can be easily incorporated in the procedure. The general objective of using these modifications would be to determine, by a trial and error process, the optimum models for the turbulent-flux terms. For this example, such a process is limited because of the lack of C_f data and because the correct effects of normal pressure gradient cannot, as yet, be obtained from the theory. Nevertheless, it can be tentatively concluded that the convex curvature increased the turbulence intensity and C_f in this experiment as compared with a flat-plate flow. Also the evaluation of du_e/dx from wall pressures rather than edge pressures gives better agreement with velocity profiles and momentum thickness, but causes premature separation. The prediction of premature separation will be corrected when the normal-momentum equation is included in the calculation. Obviously, further investigation of these matters is required before a complete or reliable assessment of the F.D. mixing-length methods can be made.

Profile Predictions for Nonsimilar Hypersonic Turbulent Boundary Layers

One further comparison is made as an example of the potential capabilities of the F.D. methods. As mentioned previously in the section "Areas Where Significant Advances Have Been Reported," experimental results and theoretical analyses (refs. 34 and 35) indicate that turbulent boundary layers near the exit of hypersonic nozzles are different in some respects from flat-plate turbulent boundary layers. One of these principal differences is the relation between total temperature and velocity. When the molecular and turbulent Prandtl numbers are 1.0, $\frac{d\bar{p}}{dx} = 0$, and $\frac{dT_w}{dx} = 0$, the linear Crocco integral

$$\bar{\theta} = F \tag{41}$$

is obtained (see eq. (15)). However, typical data obtained near the exit of hypersonic nozzles where locally $\frac{d\bar{p}}{dx} \approx 0$ give more nearly the quadratic relation

$$\bar{\theta} \approx F^2 \tag{42}$$

Two typical sets of data that exhibit this approximate relation are shown in figure 5. Pitot-pressure and total-temperature measurements with calibrated probes and the assumption of constant static pressures were used to compute the velocity ratio in both experimental investigations. The data of Harvey and Clark were obtained near the exit of a Mach 18 contoured nozzle and have been reported in references 34 and 35. The data of Perry and East were obtained in a conical nozzle (ref. 29), and therefore the local values of dp/dx are somewhat larger (negatively) than in the Mach 18 contoured nozzle.

Solutions by the F.D. methods of Harris and of Bushnell and Beckwith (ref. 34) were obtained for comparison with these data. The solution by Harris was obtained for a flat plate $\left(\frac{dp}{dx} = 0\right)$ with the boundary conditions along the entire plate taken the same as the local conditions at the survey station near the exit of the Mach 18 contoured nozzle. Since the value of the "static" Prandtl number $N_{Pr,t}$ was 0.9 (constant) for this solution, the resulting variation of $\bar{\theta}$ with F is somewhat below the linear variation. The reason for this result is immediately obvious when it is realized that for flat-plate profile relations like that of equation (41), a value of $N_{Pr,t} = 0.9$ corresponds to a value for the total Prandtl number $N_{Pr,T}$ of slightly greater than 1.0 over most of the boundary layer as shown in reference 34. The transport coefficient ϵ/Pr_T for $\bar{H}$ (or, in effect, $\bar{\theta}$) is then slightly less than the transport coefficient ϵ for $\bar{u}$. Consequently, by inspection of equations (12) and (13), it can be seen that with $\frac{dp}{dx} = 0$, $\frac{dT_w}{dx} = 0$, and $N_{Pr} = 1$, the y profiles for $\bar{\theta}$ must be somewhat less full than the y profiles for F at the same x station. It then follows that for the same y the value of $\bar{\theta}$ must be less than F. Therefore, the variation of $\bar{\theta}$ with F must be below the linear curve.

In the same way it can be seen that a negative pressure gradient has a direct effect in accelerating or "bulging" out the profile for F and it might be expected that F would then be much greater than $\bar{\theta}$ at the same y. However, the relative increase in the values of F over those of $\bar{\theta}$ is not very large because of the tendency for the $\bar{\theta}$ profile to "follow" the F profile as a result of the relation $\bar{\theta} = \frac{F^2 + \bar{h} - h_w}{H_e - h_w}$. Thus for turbulent Prandtl numbers near 1.0, the variation of $\bar{\theta}$ with F relaxes rapidly back towards the linear variation after the disturbing influence of a pressure gradient. (Results in ref. 34 showed that the effect of negative values of dT_w/dx on $\bar{\theta}$ are analogous to the effect of negative dp/dx on F.) Nevertheless, the experimental data for nozzle-wall boundary layers indicate that the effects of these large gradients, particularly in the outer part of the boundary layer, can persist far downstream.

For the first solution by the method of reference 34 (see solid curve in fig. 5), $N_{Pr,t} = 0.9$ was used and the complete upstream distributions of pressure and wall temperature for the nozzle flow (see ref. 34) were used as inputs. The results show that this nonsimilar F.D. method duplicates to a surprising extent the experimental findings. However, within the inner part of the boundary layer for $F \lesssim 0.7$, the theoretical values of $\bar{\theta}$ are still too large. The only way to correct this discrepancy is by the use of larger values of $N_{Pr,T}$ which reduce the transport coefficients for $\bar{H}$ relative to the values for F. Accordingly, when $N_{Pr,T}$ in the outer part of the boundary layer was increased to 1.5 $\left(\text{so that } N_{Pr,t} \approx 0.5\right)$, good agreement with data all the way across the boundary layer was obtained as shown in figure 5 by the second solution from the method of reference 34.

The distributions of turbulent Prandtl numbers as used in these solutions are shown in figure 6. Note that when $N_{Pr,T} = 1.5$ in the outer part of the boundary layer, the corresponding values of $N_{Pr,t}$ (the static turbulent Prandtl numbers) as computed back from results of the solution with the equation (obtained from ref. 34)

$$N_{Pr,t} = \frac{\left(1 - \dfrac{u_e^2/2H_e}{1 - \dfrac{T_w}{T_{t,e}}} \dfrac{\partial F^2/\partial y}{\partial \bar{\theta}/\partial y}\right) N_{Pr,T}}{1 - N_{Pr,T} \dfrac{u_e^2/2H_e}{1 - \dfrac{T_w}{T_{t,e}}} \dfrac{\partial F^2/\partial y}{\partial \bar{\theta}/\partial y}} \tag{43}$$

are approximately 0.6 ± 30 percent for $y/\delta > 0.05$. These values of $N_{Pr,t}$ are in agreement with incompressible data (ref. 100, for example). For the range of $0.02 < y/\delta < 0.05$, the values of $N_{Pr,t}$ are physically unrealistic because of the singular nature of equation (43) in this region. Apparently, this singular behavior can be avoided by using $N_{Pr,t}$ as the input function.

As indicated in previous discussion of the C.T. methods, the Reynolds analogy factor is required to obtain heat-transfer predictions with these methods. In view of the differences just noted in the profiles for nozzle walls and flat plates, it is of interest to compare values of Reynolds analogy factor $2N_{St}/C_f$ obtained from the F.D. solutions. From the solution for the flat plate (Harris) and the first and second solutions for the Mach 18 nozzle wall by the method of reference 34, these values of $2N_{St}/C_f$ were, respectively, 1.18, 1.09, and 0.92. The recovery factor used in all these solutions was $\bar{r} = 0.89$. Since the general relation for Reynolds analogy factor at a fixed x is (for constant c_l

$$\frac{2N_{St}}{C_f} = \frac{1}{N_{Pr,w}} \frac{1 + \frac{\gamma - 1}{2} M_e^2 - \frac{T_w}{T_e}}{1 + \bar{r}\frac{\gamma - 1}{2} M_e^2 - \frac{T_w}{T_e}} \left(\frac{d\bar{\theta}}{dF}\right)_w \tag{44}$$

it is clear from figure 5 that the decreasing values of $2N_{St}/C_f$ as just quoted are caused by the effects of pressure gradient and the increase in $N_{Pr,T}$ on the relation between $\bar{\theta}$ and F. Finally, the experimental values of $2N_{St}/C_f$ for nozzle-wall boundary layers might then be expected to be somewhat lower than the values for flat-plate flows. Although the scatter in the data is large, the survey by Cary (ref. 93) indicates that most of the values of $2N_{St}/C_f$ for the nozzle-wall data are somewhat smaller than the flat-plate data.

In this section some examples of how the F.D. methods can be utilized to provide a better understanding of observed phenomena in the development and relaxation of turbulent boundary layers under the influence of various upstream and local conditions have been given. The now well-known differences in the relation between total temperature and velocity that occur in nozzle-wall boundary layers and flat plates can be partly attributed to the upstream effects of pressure and wall-temperature gradients and the deviations of turbulent Prandtl numbers from unity. The same effects can cause smaller values of Reynolds analogy factor for nozzle-wall boundary layers than for flat plates.

CONCLUDING REMARKS

Comparisons of predictions with experimental data for supersonic and hypersonic turbulent boundary layers by three main categories of approaches have been given in this review. These three categories were designated herein as integral methods (I.M.), finite-difference solutions of the partial differential equations (F.D.), and correlation techniques (C.T.). Four typical methods in each category were described in sufficient detail to indicate some of the basic differences in the methods and to thereby provide a basis for the discussion of possible causes of differing predictions. The intent was also to illustrate briefly the wide diversity of assumptions that have been utilized to close the system of governing equations. This closure problem stems from the lack of basic knowledge concerning the relations between the turbulent-flux terms and the mean flow quantities.

Comparisons of experiment with predictions from the C.T. methods (such as the reference-temperature methods and the direct application of transformation theory) for skin friction and heat transfer on flat plates have shown that none of the methods give accurate predictions for the entire range of the ratio of wall temperature to adiabatic

wall temperature. The trends with this temperature ratio are perhaps better predicted by the Spalding-Chi method than by other methods considered in this category. Since these essentially empirical methods are severely limited in some respects (such as by the applicability to simple flat-plate-type flows only, the lack of information regarding the boundary-layer profiles, and remaining questions concerning the appropriate Reynolds analogy factor to use), the more advanced methods must be applied to flows with large arbitrary pressure and wall-temperature gradients, large heat transfer, and hypersonic Mach numbers.

For large arbitrary pressure gradients, the comparisons between theoretical results and experimental data for skin friction and integral thicknesses as shown herein and as available in the cited references have indicated that reasonable predictions can be obtained with some of the recently developed I.M. and F.D. methods. Possible reasons for the poor predictions of some methods have been suggested. For example, one of the earlier I.M. methods utilized a version of transformation theory that has since been shown to lack generality. In certain of the other I.M. methods, the assumptions used to evaluate the shear-stress integrals and other relations between integral quantities were not sufficiently general and may have contributed to the discrepancies obtained.

On the other hand, poor predictions by the F.D. methods could be traced directly to the finite-difference formulations and associated limits on step sizes or on the eddy-viscosity formulations. On balance, it appears that the F.D. methods offer significant advantages for future development and application. One of the main advantages of the F.D. methods is the conceptual simplicity that can be utilized in the formulation of the turbulent-flux terms. This conceptual simplicity eases the burden of identifying and adjusting the causes of poor predictions. By the use of this "numerical-experimentation" approach, the knowledge of basic turbulent mechanisms could ultimately be improved. One such mechanism considered in this review in a very preliminary fashion is the effect of longitudinal curvature on the turbulent shear stress. However, the preliminary results have indicated that a complete and reliable assessment of the F.D. methods is not yet possible because of limitations in the experimental data. Also, for application to flows with large adverse pressure gradients, the normal-momentum equation should be included in the theory.

Application of F.D. methods to hypersonic nozzle-wall boundary layers with large heat transfer and large gradients in pressure and wall temperature upstream of the local station of interest has shown that these "upstream history" effects can persist for large distances downstream. The local velocity and temperature profiles as well as Reynolds analogy factors can then be appreciably different from those in flat-plate-type boundary layers with no upstream history. Again, because of the conceptual simplicity of the F.D.

methods and the relative ease of incorporating modifications that are based on physical processes, the basic reasons for the different boundary-layer characteristics for these flows could be identified with some certainty.

REFERENCES

1. Kline, S. J.; Morkovin, M. V.; Sovran, G.; amd Cockrell, D. J., eds.: Computation of Turbulent Boundary Layers – 1968 AFOSR-IFP-Stanford Conference. Vol. I – Methods, Predictions, Evaluation and Flow Structure. Stanford Univ., c.1969.
2. Coles, D. E.; and Hirst, E. A., eds.: Computation of Turbulent Boundary Layers – 1968 AFOSR-IFP-Stanford Conference. Vol. II – Compiled Data. Stanford Univ., c.1969.
3. Anon.: Compressible Turbulent Boundary Layers. NASA SP-216, 1969.
4. Spalding, D. B.: Theories of the Turbulent Boundary Layer. Appl. Mech. Rev., vol. 20, no. 8, Aug. 1967, pp. 735-740.
5. Bradshaw, P.: Boundary-Layer Problems of 1967. NPL Aero Rep. 1253, Brit. A.R.C., Sept. 1967.
6. Bradshaw, P.: Turbulent Boundary Layers. Aeronaut. J., vol. 72, no. 689, May 1968, pp. 451-458.
7. Bradshaw, P.: Calculation of Boundary-Layer Development Using the Turbulent Energy Equation. IX: Summary. NPL Aero Rep. 1287, Brit. A.R.C., Jan. 30, 1969.
8. Bradshaw, P.; Ferriss, D. H.; and Atwell, N. P.: Calculation of Boundary-Layer Development Using the Turbulent Energy Equation. J. Fluid Mech., vol. 28, pt. 3, May 26, 1967, pp. 593-616.
9. Azzouz, D.; and Pratt, N. H.: Supersonic Turbulent Mixing. I – Literature Survey and Assessment of the State-of-the-Art. A.A.S.U. Rep. No. 281, Univ. of Southampton, May 1968.
10. Lee, S. C.; and Harsha, P. T.: The Use of Turbulent Kinetic Energy in Free Mixing Studies. AIAA Paper No. 69-683, June 1969.
11. Thompson, B. G. J.: A Critical Review of Existing Methods of Calculating the Turbulent Boundary Layer. Brit. A.R.C. 26 109, Aug. 7, 1964.
12. Rotta, J. C.: Recent Developments in Calculation Methods for Turbulent Boundary Layers With Pressure Gradients and Heat Transfer. Trans. ASME, Ser. E: J. Appl. Mech., vol. 33, no. 2, June 1966, pp. 429-437.
13. Hornung, H. G.: A Survey of Compressible Flow Boundary Layers – Theory and Experiment. Rep. ACA 67, Dep. Supply, Australian Aeronaut. Res. Comm., Feb. 1966.

14. Bradshaw, P.; and Ferriss, D. H.: Calculation of Boundary-Layer Development Using the Turbulent Energy Equation. II – Compressible Flow on Adiabatic Walls. NPL Aero Rep. 1217, British A.R.C., Nov. 24, 1966.

15. Herring, H. James; and Mellor, George L.: A Method of Calculating Compressible Turbulent Boundary Layers. NASA CR-1144, 1968.

16. Cebeci, Tuncer; Smith, A. M. O.; and Mosinskis, G.: Calculation of Compressible Adiabatic Turbulent Boundary Layers. AIAA Paper No. 69-687, June 1969.

17. Patankar, S. V.; and Spalding, D. B.: Heat and Mass Transfer in Boundary Layers. Morgan-Grampian (London), 1967.

18. Bruno, James R.; Yanta, William J.; and Risher, Donald B.: Balance for Measuring Skin Friction in the Presence of Heat Transfer. ICIASF '69 Record, IEEE Publ. 69 C 19-AES, pp. 173-177.

19. Keener, Earl R.; and Hopkins, Edward J.: Use of Preston Tubes for Measuring Hypersonic Turbulent Skin Friction. AIAA Paper No. 69-345, Apr. 1969.

20. Brott, David L.; Yanta, William J.; Voisinet, Robert L.; and Lee, Roland E.: An Experimental Investigation of the Compressible Turbulent Boundary Layer With a Favorable Pressure Gradient. AIAA Paper No. 69-685, June 1969.

21. Hopkins, Edward J.; Rubesin, Morris W.; Inouye, Mamoru; Keener, Earl R.; Mateer, George C.; and Polek, Thomas E.: Summary and Correlation of Skin-Friction and Heat-Tranfer Data for a Hypersonic Turbulent Boundary Layer on Simple Shapes. NASA TN D-5089, 1969.

22. Hoydysh, Walter G.; and Zakkay, Victor: An Experimental Investigation of Hypersonic Turbulent Boundary Layers in Adverse Pressure Gradient. AIAA J., vol. 7, no. 1, Jan. 1969, pp. 105-116.

23. Softley, Eric J.; and Sullivan, Robert J.: Theory and Experiment for the Structure of Some Hypersonic Boundary Layers. AGARD CP No. 30, May 1968, pp. 3-1 – 3-18.

24. Watson, E. C.; Gnos, A. V.; Gallo, W. F.; and Latham, E. A.: Boundary Layers and Hypersonic Inlet Flow Fields. AIAA Paper No. 66-606, June 1966.

25. Martellucci, A.; Rie, H.; and Sontowski, J. F.: Evaluation of Several Eddy Viscosity Models Through Comparison With Measurements in Hypersonic Flows. AIAA Paper No. 69-688, June 1969.

26. Danberg, James E.: Characteristics of the Turbulent Boundary Layer With Heat and Mass Transfer: Data Tabulation. NOLTR-67-6, U.S. Naval Ordnance Lab. (White Oak, Md.), Jan. 23, 1967. (Available from DDC as AD 650 272.)

27. Samuels, Richard D.; Peterson, John B., Jr.; and Adcock, Jerry B.: Experimental Investigation of the Turbulent Boundary Layer at a Mach Number of 6 With Heat Transfer at High Reynolds Numbers. NASA TN D-3858, 1967.

28. Bertram, Mitchel H.; and Neal, Luther, Jr.: Recent Experiments in Hypersonic Turbulent Boundary Layers. Presented at the AGARD Specialists' Meeting on Recent Developments in Boundary-Layer Research (Naples, Italy), May 10-14, 1965.

29. Perry, J. H.; and East, R. A.: Experimental Measurements of Cold Wall Turbulent Hypersonic Boundary Layers. AGARD CP No. 30, May 1968, pp. 2-1 – 2-19.

30. Scaggs, Norman E.: Boundary Layer Profile Measurements in Hypersonic Nozzles. ARL 66-0141, U.S. Air Force, July 1966.

31. Lee, Roland E.; Yanta, William J.; and Leonas, Annette C.: Velocity Profile, Skin Friction Balance and Heat Transfer Measurements of the Turbulent Boundary Layer at Mach 5. Proceedings of the 1968 Heat Transfer and Fluid Mechanics Institute, Ashley F. Emery and Creighton A. Depew, eds., Stanford Univ. Press, c.1968.

32. Matthews, R. K.; and Trimmer, L. L.: Nozzle Turbulent Boundary-Layer Measurements in the VKF 50-In. Hypersonic Tunnels. AEDC-TR-69-118, U.S. Air Force, June 1969.

33. Kemp, Joseph H., Jr.; and Sreekanth, A. K.: Preliminary Results From an Experimental Investigation of Nozzle Wall Boundary Layers at Mach Numbers Ranging From 27 to 47. AIAA Paper No. 69-686, June 1969.

34. Bushnell, Dennis M.; and Beckwith, Ivan E.: Calculation of Nonequilibrium Hypersonic Turbulent Boundary Layers and Comparisons With Experimental Data. AIAA Paper No. 69-684, June 1969.

35. Bushnell, Dennis M.; Johnson, Charles B.; Harvey, William D.; and Feller, William V.: Comparison of Prediction Methods and Studies of Relaxation in Hypersonic Turbulent Nozzle-Wall Boundary Layers. NASA TN D-5433, 1969.

36. Jones, Robert A.; and Feller, William V.: Preliminary Surveys of the Wall Boundary Layer in a Mach 6 Axisymmetric Tunnel. NASA TN D-5620, 1970.

37. Wallace, J. E.: Hypersonic Turbulent Boundary Layer Measurements Using an Electron Beam. CAL Rep. No. AN-2112-Y-1 (Contract No. NSR33-009-029), Cornell Aeronaut. Lab., Inc., Aug. 1968.

38. Harvey, William D.; and Bushnell, Dennis M.: Velocity Fluctuation Intensities in a Hypersonic Turbulent Boundary Layer. AIAA J. (Tech. Notes), vol. 7, no. 4, Apr. 1969, pp. 760-762.

39. Harvey, William D.; Bushnell, Dennis M.; and Beckwith, Ivan E.: Fluctuating Properties of Turbulent Boundary Layers for Mach Numbers up to 9. NASA TN D-5496, 1969.

40. Czarnecki, K. R.; and Monta, William J.: Effects of Compressibility and Heat Transfer on the Laminar Sublayer of the Turbulent Boundary Layer. NASA TN D-1998, 1964.

41. Fisher, M. J.; and Krause, F. R.: The Crossed-Beam Correlation Technique. J. Fluid Mech., vol. 28, pt. 4, June 22, 1967, pp. 705-717.

42. Fisher, M. J.; and Johnston, K. D.: Turbulence Measurements in Supersonic, Shock-Free Jets by the Optical Crossed-Beam Method. NASA TN D-5206, 1970.

43. Fridman, J. D.; Huffaker, R. M.; and Kinnard, R. F.: Laser Doppler System Measures Three-Dimensional Vector Velocity and Turbulence. Laser Focus, vol. 4, no. 21, Nov. 1968, pp. 34-38.

44. Huffaker, Robert M.; Fuller, Charles E.; and Lawrence, T. R.: Application of Laser Doppler Velocity Instrumentation to the Measurement of Jet Turbulence. [Preprint] 690266, Soc. Automot. Eng., Jan. 1969.

45. Rumsey, Charles B.; Carter, Howard S.; Hastings, Earl C., Jr.; Raper, James L.; and Zoby, Ernest V.: Initial Results From Flight Measurements of Turbulent Heat Transfer and Boundary-Layer Transition at Local Mach Numbers Near 15 (Reentry F). NASA TM X-1856, 1969.

46. Spalding, D. B.; and Chi, S. W.: The Drag of a Compressible Turbulent Boundary Layer on a Smooth Flat Plate With and Without Heat Transfer. J. Fluid Mech., vol. 18, pt. 1, Jan. 1964, pp. 117-143.

47. Wallace, J. E.: Hypersonic Turbulent Boundary-Layer Studies at Cold Wall Conditions. Proceedings of the 1967 Heat Transfer and Fluid Mechanics Institute, Paul A. Libby, Daniel B. Olfe, and Charles W. Van Atta, eds., Stanford Univ. Press, c.1967, pp. 427-451.

48. Alber, Irwin E.; and Coats, Douglas E.: Analytical Investigations of Equilibrium and Nonequilibrium Compressible Turbulent Boundary Layers. AIAA Paper No. 69-689, June 1969.

49. Fernandez, Fernando L.; and Lees, Lester: Effect of Finite Plate Length on Supersonic Turbulent Boundary Layer With Large Distributed Surface Injection. AIAA Paper No. 69-162, Jan. 1969.

50. Davis, R. T.; and Flügge-Lotz, I.: Laminar Compressible Flow Past Axisymmetric Blunt Bodies (Results of a Second-Order Theory). Tech. Rep. No. 143, (Grants AF-AFOSR-62-242 and AF-AFOSR-235-63), Div. Eng. Mech., Stanford Univ., Dec. 1963.

51. Myring, D. F.; and Young, A. D.: The Isobars in Boundary Layers at Supersonic Speeds. Aeronaut. Quart., vol. XIX, pt. 2, May 1968, pp. 105-126.

52. Miller, Leonard D.: Predicting Turbulent Compressible Boundary Layers in Strong Adverse Pressure Gradients. AIAA Paper No. 67-196, Jan. 1967.

53. Shamroth, Stephen J.; and McDonald, Henry: A New Solution to the Near-Wake Recompression Problem. Rep. G212237-2, Res. Lab., United Aircraft Corp., Sept. 1968.

54. Klebanoff, P. S.: Characteristics of Turbulence in a Boundary Layer With Zero Pressure Gradient. NACA Rep. 1247, 1955. (Supersedes NACA TN 3178.)

55. Escudier, M. P.: The Distribution of the Mixing Length in Turbulent Flows Near Walls. Rep. No. TWF/TN/1, Mech. Eng. Dep., Imp. Coll. Sci. Technol., Mar. 1965.

56. Goldberg, Perry: Upstream History and Apparent Stress in Turbulent Boundary Layers. Rep. No. 85 (Contract Nonr 1841(91)), Gas Turbine Lab., Massachusetts Inst. Technol., May 1966. (Available from DDC as AD 636323.)

57. Maise, George; and McDonald, Henry: Mixing Length and Kinematic Eddy Viscosity in a Compressible Boundary Layer. AIAA J., vol. 6, no. 1, Jan. 1968, pp. 73-80.

58. Morkovin, Mark V.: Effects of Compressibility on Turbulent Flows. The Mechanics of Turbulence. Gordon and Breach Sci. Publ., Inc., c.1964, pp. 367-380.

59. Bradshaw, P.: The Insensitivity of Turbulent Flow to Changes in Reynolds Number and Mach Number. NPL Aero Note 1057, Brit. A.R.C., May 1967.

60. Ohji, Michio: Statistical Theory of Wall Turbulence. Phys. Fluids Suppl., vol. 10, pt. II, no. 9, Sept. 1967, pp. S153-S154.

61. Meroney, Robert N.: Turbulent Sublayer Temperature Distribution Including Wall Injection and Dissipation. Int. J. Heat Mass Transfer, vol. 11, no. 9, Sept. 1968, pp. 1406-1408.

62. Van Driest, E. R.: On Turbulent Flow Near a Wall. J. Aeron. Sci., vol. 23, no. 11, Nov. 1956, pp. 1007-1011.

63. Clauser, Francis H.: The Turbulent Boundary Layer. Vol. IV of Advances in Applied Mechanics, H. L. Dryden and Th. von Kármán, eds., Academic Press, Inc., 1956, pp. 1-51.

64. Lynes, Larry L.; Nielsen, Jack N.; and Kuhn, Gary D.: Calculation of Compressible Turbulent Boundary Layers With Pressure Gradients and Heat Transfer. NASA CR-1303, 1969.

65. Reshotko, Eli; and Tucker, Maurice: Approximate Calculation of the Compressible Turbulent Boundary Layer With Heat Transfer and Arbitrary Pressure Gradient. NACA TN 4154, 1957.

66. Sasman, Philip K.; and Cresci, Robert J.: Compressible Turbulent Boundary Layer With Pressure Gradient and Heat Transfer. AIAA J., vol. 4, no. 1, Jan. 1966, pp. 19-25.

67. Flaherty, R. J.: A Method for Estimating Turbulent Boundary Layers and Heat Transfer in an Arbitrary Pressure Gradient. Rep. UAR-G51, United Aircraft Corp., Aug. 1968.

68. Eckert, E. R. G.: Engineering Relations for Friction and Heat Transfer to Surfaces in High Velocity Flow. J. Aeronaut. Sci. (Readers' Forum), vol. 22, no. 8, Aug. 1955, pp. 585-587.

69. Ludwieg, H., and Tillmann, W.: Investigations of the Wall-Shearing Stress in Turbulent Boundary Layers. NACA TM 1285, 1950.

70. Camarata, F. J.; and McDonald, H.: A Procedure for Predicting Characteristics of Compressible Turbulent Boundary Layers Which Includes the Treatment of Upstream History. Rep. G212238-3, Res. Lab., United Aircraft Corp., Aug. 1968.

71. Coles, Donald: The Turbulent Boundary Layer in a Compressible Fluid. Phys. Fluids, vol. 7, no. 9, Sept. 1964, pp. 1403-1423.

72. Coles, Donald: The Law of the Wake in the Turbulent Boundary Layer. J. Fluid Mech., vol. 1, pt. 2, July 1956, pp. 191-226.

73. Pinckney, S. Z.: Static-Temperature Distribution in a Flat-Plate Compressible Turbulent Boundary Layer With Heat Transfer. NASA TN D-4611, 1968.

74. Neal, Luther, Jr.; and Bertram, Mitchel H.: Turbulent-Skin-Friction and Heat-Transfer Charts Adapted From the Spalding and Chi Method. NASA TN D-3969, 1967.

75. Beckwith, Ivan E.; and Bushnell, Dennis M. (With appendix C by Carolyn C. Thomas): Detailed Description and Results of a Method for Computing Mean and Fluctuating Quantities in Turbulent Boundary Layers. NASA TN D-4815, 1968.

76. Smith, A. M. O.; and Clutter, Darwin W.: Machine Calculation of Compressible Laminar Boundary Layers. AIAA J., vol. 3, no. 4, Apr. 1965, pp. 639-647.

77. Fish, R. W.; and McDonald, H.: Practical Calculations of Transitional Boundary Layers. Rep. UAR-H48, United Aircraft Corp., Mar. 14, 1969.

78. Cebeci, Tuncer; Smith, A. M. O.; and Wang, L. C.: A Finite-Difference Method for Calculating Compressible Laminar and Turbulent Boundary Layers. Pt. I. Rep. No. DAC-67131, McDonnell Douglas Aircraft Co., Inc., Mar. 1969.

79. Richtmyer, Robert D.: Difference Methods for Initial-Value Problems. Interscience Pub. Inc., 1957.

80. Blottner, F. G.: Nonequilibrium Laminar Boundary-Layer Flow of Ionized Air. AIAA J., vol. 2, no. 11, Nov. 1964, pp. 1921-1927.

81. Sommer, Simon C.; and Short, Barbara J.: Free-Flight Measurements of Turbulent-Boundary-Layer Skin Friction in the Presence of Severe Aerodynamic Heating at Mach Numbers From 2.8 to 7.0. NACA TN 3391, 1955.

82. Komar, J. J.: Improved Turbulent Skin-Friction Coefficient Predictions Utilizing the Spalding-Chi Method. Rep. DAC-59801, Missile & Space Syst. Div., Douglas Aircraft Co., Inc., Nov. 1966.

83. Van Driest, E. R.: Turbulent Boundary Layer in Compressible Fluids. J. Aeron. Sci., vol. 18, no. 3, Mar. 1951, pp. 145-160, 216.

84. Van Driest, E. R.: The Turbulent Boundary Layer With Variable Prandtl Number. 50 Jahre Grenzschichtforschung (50 Years of Boundary Layer Research), H. Görtler and W. Tollmien, eds., Friedr. Viewg & Sohn (Braunschweig), 1955, pp. 257-271.

85. Wilson, Robert E.: Turbulent Boundary-Layer Characteristics at Supersonic Speeds – Theory and Experiment. J. Aeron. Sci., vol. 17, no. 9, Sept. 1950, pp. 585-594.

86. Rubesin, Morris W.; Maydew, Randall C.; and Varga, Steven A.: An Analytical and Experimental Investigation of the Skin Friction of the Turbulent Boundary Layer on a Flat Plate at Supersonic Speeds. NACA TN 2305, 1951.

87. Coles, D. E.: The Turbulent Boundary Layer in a Compressible Fluid. R-403-PR (Contract No. AF 49(638)-700), RAND Corp., Sept. 1962. (Available from DDC as AD 285 651.)

88. Baronti, Paulo O.; and Libby, Paul A.: Velocity Profiles in Turbulent Compressible Boundary Layers. AIAA J., vol. 4, no. 2, Feb. 1966, pp. 193-202.

89. Jeromin, L. O. F.: A Transformation for Compressible Turbulent Boundary Layers With Air Injection. J. Fluid Mech., vol. 31, pt. 1, Jan. 1968, pp. 65-94.

90. Economos, Constantino: A Transformation Theory for the Compressible Turbulent Boundary Layer With Mass Transfer. AIAA Paper No. 69-161, Jan. 1969.

91. Lewis, John E.; Kubota, Toshi; and Webb, Wilmot H.: Transformation Theory for the Compressible Turbulent Boundary Layer With Arbitrary Pressure Gradient. AIAA Paper No. 69-160, Jan. 1969.

92. Cary, Aubrey M., Jr.: Turbulent Boundary-Layer Heat Transfer and Transition Measurements for Cold-Wall Conditions at Mach 6. AIAA J., vol. 6, no. 5, May 1968, pp. 958-959.

93. Cary, Aubrey M., Jr.: Summary of Available Information on Reynolds Analogy for Zero-Pressure-Gradient, Compressible, Turbulent-Boundary-Layer Flow. NASA TN D-5560, 1970.

94. Wilson, Donald M.: A Correlation of Heat-Transfer and Skin-Friction Data and an Experimental Reynolds Analogy Factor for Highly Cooled Turbulent Boundary Layers at Mach 5.0. NOLTR-69-51, U.S. Navy, Mar. 5, 1969. (Available from DDC as AD 690 454.)

95. Winter, K. G.; Rotta, J. C.; and Smith, K. G. (Francesca Neffgen, Transl.): Turbulent Boundary Layer Studies on a "Waisted" Body of Revolution in Subsonic and Supersonic Flow. B-533, Boeing Co., Apr. 1969. (Translated from DLR-FB-65-52, Nov. 1965.)

96. McLafferty, George H.; and Barber, Robert E.: Turbulent Boundary Layer Characteristics in Supersonic Streams Having Adverse Pressure Gradients. Rep. R-1285-11 (Contract No. NOa(s) 55-133-c), Res. Dep., United Aircraft Corp., Sept. 1959.

97. Back, L. H.; Cuffel, R. F.; and Massier, P. F.: Laminarization of a Turbulent Boundary Layer in Nozzle Flow – Boundary Layer and Heat Transfer Measurements With Wall Cooling. Pap. No. 69-HT-56, Amer. Soc. Mech. Eng., Aug. 1969.

98. Bradshaw, P.: The Analogy Between Streamline Curvature and Buoyancy in Turbulent Shear Flow. J. Fluid Mech., vol. 36, pt. 1, Mar. 1969, pp. 177-191.

99. Rotta, J. C.: Effect of Streamwise Wall Curvature on Compressible Turbulent Boundary Layers. Phys. Fluids Suppl., vol. 10, Pt. II, no. 9, Sept. 1967, pp. S174-S180.

100. Johnson, Donald S.: Turbulent Heat Transfer in a Boundary Layer With Discontinuous Wall Temperature. Publ. No. 55 (OSR Tech. Note 55-289), Dep. Aeronaut., The Johns Hopkins Univ., Aug. 1955.

DIRECT MEASUREMENTS OF $C_{f\,exp}$: $M_e \leq 7.4$; $C_{f,exp}$ AND $C_{f,theo}$ FUNCTIONS OF R_θ

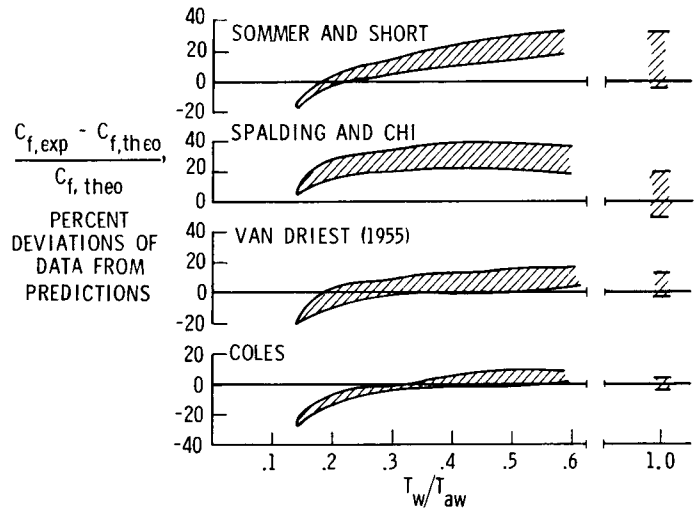

(a) Skin friction on flat plates.

$N_{St,exp}$ HEAT-TRANSFER DATA FOR $4.9 \leq M_e \leq 7.4$;
HEAT-TRANSFER PREDICTIONS FROM SKIN-FRICTION THEORIES

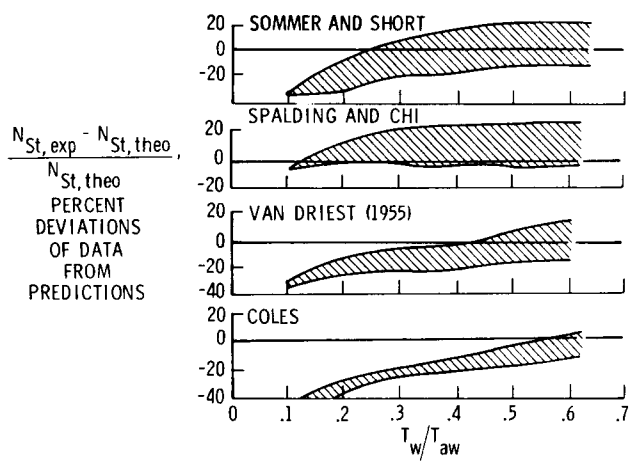

(b) Heat transfer on flat plates and cones with $\left(2N_{St}/C_f\right)_{theo} = 1.16$ and $\bar{r} = 0.9$.

Figure 1.- Comparisons of experimental data with predictions from correlation techniques (C.T.).

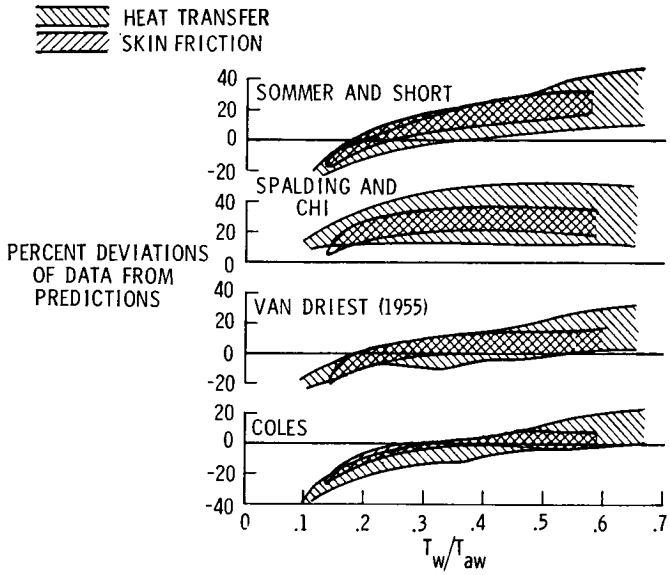

(c) Comparison of skin friction and heat transfer with $\left(2N_{St}/C_f\right)_{theo} = 1.0$ and $\bar{r} = 0.9$.

Figure 1.- Concluded.

	Authors	Source: Date	Ref. No.	Lateral curvature	Method
— — — — —	Reshotko and Tucker	1957	65	r_w	Integral
— - —	Camarata and McDonald	1968	70	r_w	Integral
—x—	Alber and Coats	1969	48	No	Integral
— - - - —	Pinckney	1969	Unpublished	r_w	Integral
———	Herring and Mellor	1968	15	r	Finite Difference
—•—	Fish and McDonald	1969	77	No	Finite Difference
—+—	Bushnell and Beckwith	1969	34	r_w	Finite Difference
—▽—	Bushnell and Beckwith (modified to use ℓ_c (eq. (40))	1969		r_w	Finite Difference
—○—	Harris	1969	Unpublished	r	Finite Difference
— - - —	Lewis, Kubota, and Webb	1969	91	No	Transformation-Integral

Figure 2.- Line key for theoretical predictions of figures 3 and 4.

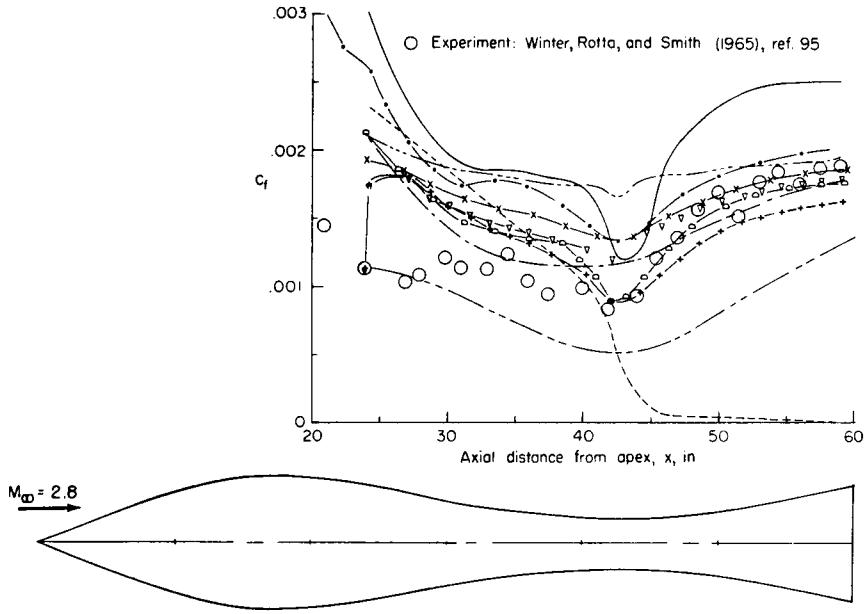

(a) Skin friction.

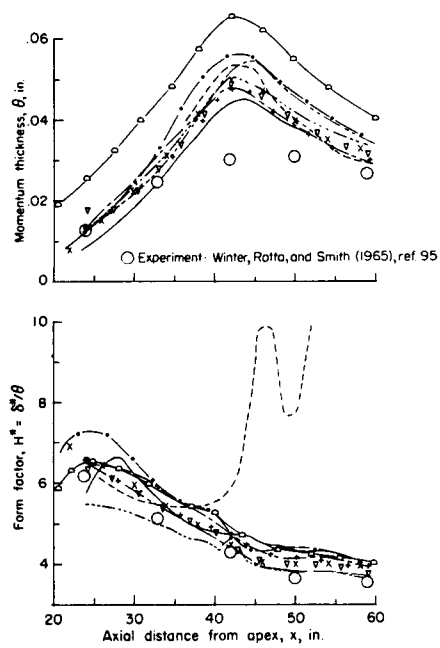

(b) Momentum thickness and form factor.

Figure 3.- Comparison of predicted values of integral parameters with experimental values on a body of revolution with favorable and adverse pressure gradients. $\frac{T_w}{T_{aw}} \approx 1.0$; $M_\infty = 2.8$; $R_\infty = 2.02 \times 10^6$. At input station $x = 24$ inches, $R_\theta = 2140$. (See fig. 2 for key to theoretical-prediction curves.)

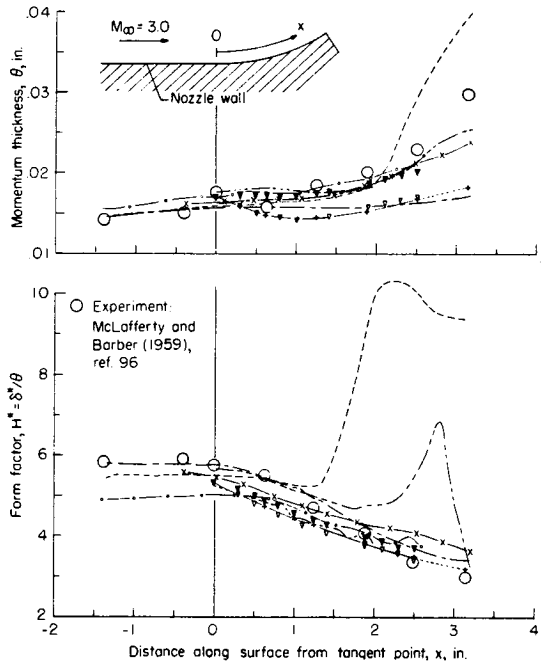

(a) Momentum thickness and form factor. (See figs. 2 and 4(b) for keys to theoretical-prediction curves.)

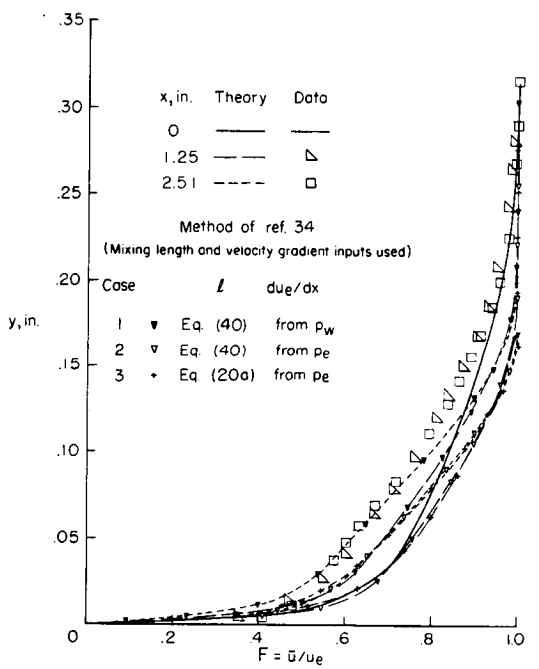

NOT REPRODUCIBLE

(b) Velocity profiles.

Figure 4.- Comparisons of theoretical predictions with experimental data on a curved plate with large adverse pressure gradients. $\frac{T_w}{T_{aw}} \approx 1.0$; $M_\infty = 3.0$; $R_\infty = 1.9 \times 10^6$. At input station $x = 0$, $R_\theta = 2540$.

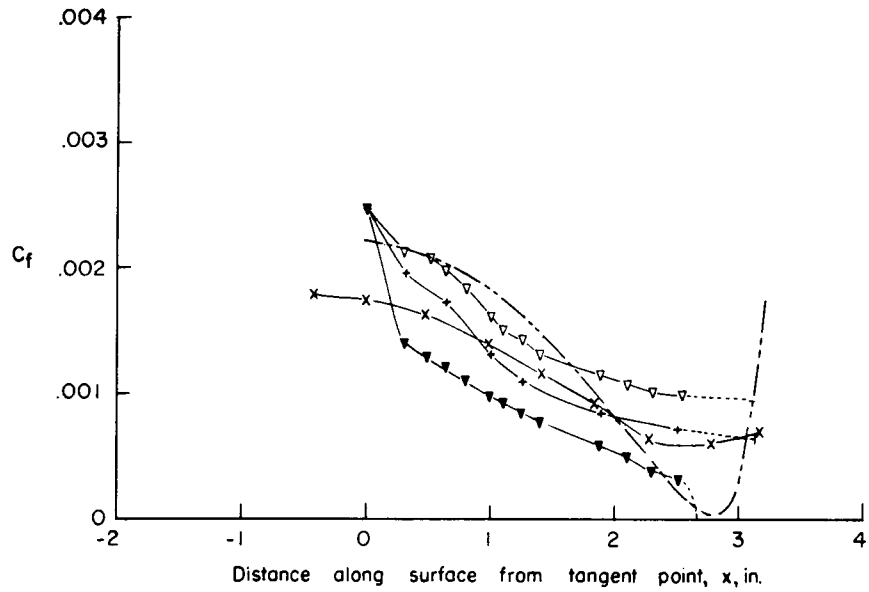

(c) Skin-friction predictions. (See figs. 2 and 4(b) for keys to theoretical-prediction curves.)

Figure 4.- Concluded.

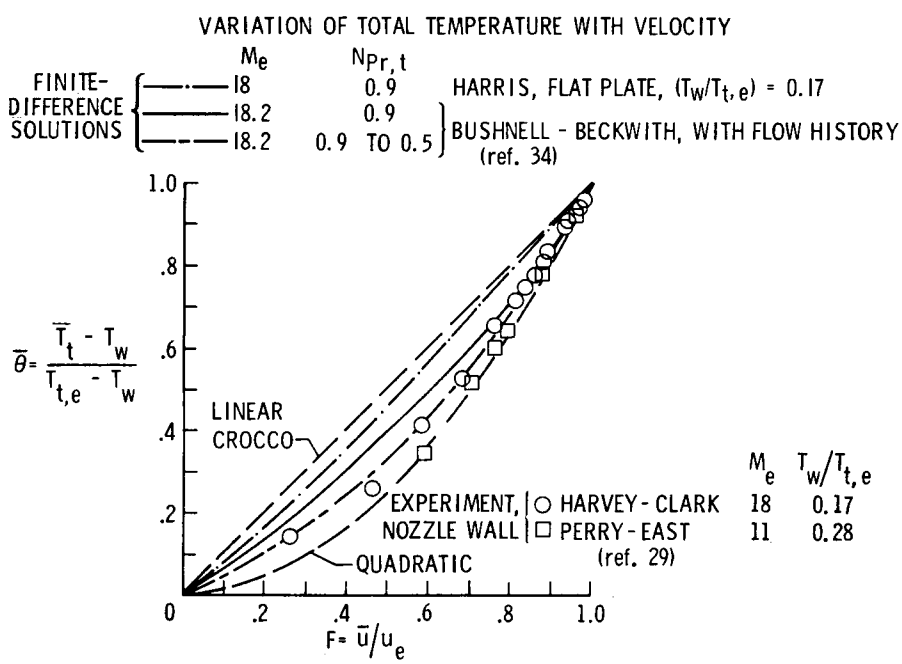

Figure 5.- Comparisons of predicted and experimental profile shapes in boundary layers on hypersonic nozzle walls.

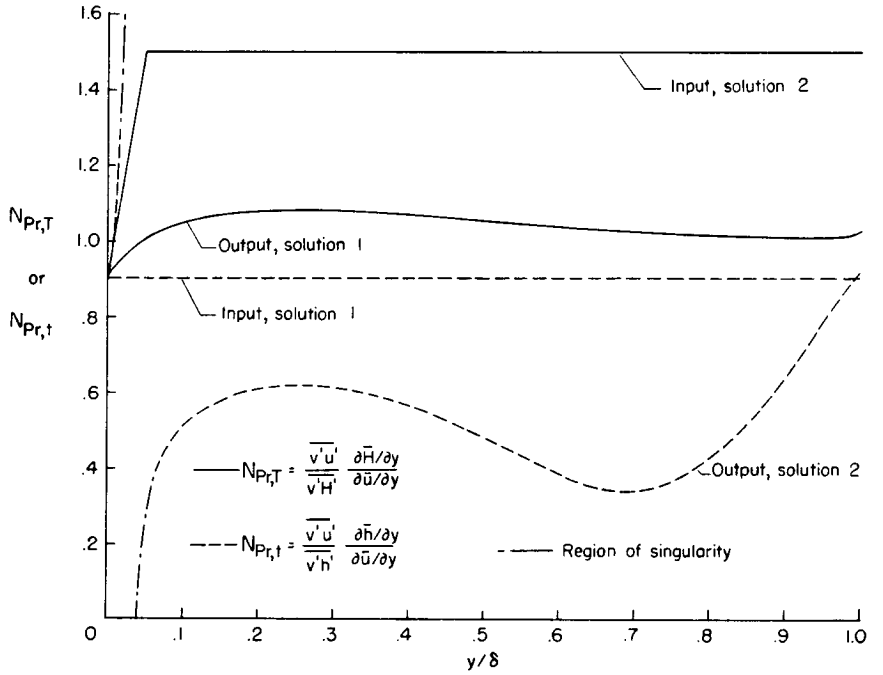

Figure 6.- Input and computed turbulent Prandtl numbers for finite-difference (F.D.) solutions of figure 5.

DISCUSSION

HARRY A. DWYER, University of California, Davis: You mentioned that you thought the eddy-viscosity terms might depend on normal pressure gradients somewhat, and I was wondering whether you were considering thin turbulent boundary layers, relatively thin?

BECKWITH: You may have misinterpreted my remarks there. I think the eddy viscosity, that is the model for turbulent correlations, will depend on the curvature of the streamlines, and this goes back essentially to the idea of stability of flow in concave and convex flows.

The normal pressure gradient would presumably be incorporated by means of a normal-momentum equation in one form or another.

STANLEY G. RUBIN, Polytechnic Institute of Brooklyn: I would like to comment on two things. First, it seems to me that the essence of this type of turbulence analysis lies in the model for the Reynolds stress and not in whether you use a finite difference or an integral technique. It seems to me that based on some of the incompressible theories that have been derived recently, for example, the invariant modeling of Donaldson or the energy-type analysis of Bradshaw, that other effects that have not been accounted for in the eddy-viscosity or mixing-length models that you have mentioned, like triple correlations, may have significant effects, and more sophisticated modeling techniques could account for some of the deviations shown in the results presented here. It may in fact be that this is the way that one has to go if significant improvements are to come about.

Secondly, you show some data for Mach numbers of 19, and it seems to me that once you get into the hypersonic range you really have to ask yourself the question whether or not density fluctuations and viscosity fluctuations are important. It seems to me that they would be very signficant in the hypersonic flow range.

BECKWITH: Let me consider your last comment first. We certainly have asked ourselves these questions. In fact, we have played around a little bit with modifying the mixing-length expressions to account for the density fluctuations (see AIAA Paper no. 69-684), but we felt that we were getting too far into the unknown there to be sure of what we were doing, so we haven't done much more with that, but they do have to be considered.

Now, as far as the use of the turbulent kinetic energy equation or some of the other more exotic approaches are concerned, again I feel here that there are so many unknown correlations like the third-order correlations you mentioned, particularly as far as compressible flow is concerned, that even though we can bring in these equations we just introduce more and more unknowns. Consequently, you are no better off than if you use modified mixing-length expressions, which can be done successfully at least in first order, and often can supply a good practical answer without all the difficulties of the more exotic approaches.

RAYMOND SEDNEY, Martin Company: In the written version of the discussion that was held after the Langley meeting of a year ago, there was a statement made concerning transformation methods. As I remember the statement (and I don't think it was challenged), it was that the transformation type of approaches can't possibly work above, say, roughly Mach 5. Do you have any comment on that?

BECKWITH: I think I would probably have to agree with it, primarily because in transformation techniques when you try to apply them to flow situations above Mach 5 you are getting into conditions where the heat transfer may be large, and where the normal pressure gradients as well as longitudinal pressure gradients could be large, and transformation theories as yet can't handle these matters very well, just because in the incompressible flow we don't have the same physical situation present. Now, somebody might take exception to that, but that is my own personal opinion.

ARTUR MAGER, Aerospace Corp.: I would like to take an issue with that last statement. I do not see any reason why an appropriate transformation could not be devised which would take into account all these effects which you just mentioned.

BECKWITH: Well, like I say, I think the basic difficulty is that in the typical incompressible flows you don't have a large heat transfer present, at least physically, and therefore you have a difficult time finding a suitable model to transform to.

Also, you may have to consider three-dimensional flows, wall blowing, separation, etc. The incompressible flows are there, at least in certain limited cases, but they may not always provide the range of variables that you are interested in, so the transformation methods are limited.

ALFRED GESSOW, NASA Headquarters, Washington, D.C.: You mentioned at the conclusion that you really couldn't evaluate the theories too well until we get better experimental data, and there is certainly a need for that. In view of my impression that the kind of experimental data that you get from the tunnels is dependent upon tunnel noise effects that come off the walls and could affect transition by the amount of turbulence you have, what kind of data do we now have that we could trust and use as a standard against which to compare theory?

BECKWITH: As far as the effects of tunnel noise itself are concerned, that is very important, as you know, on transition. I think when you are looking at an established turbulent boundary layer the effects are, hopefully, secondary on the structure of the turbulent boundary layer itself.

I think the emphasis, as far as getting data at the present time is concerned, needs to be on measuring the fluctuating properties of turbulent flow and how they relate to the mean flow and how the correlations behave, and we can do this in the wind tunnels better than anywhere else.

GESSOW: You say the correlations between various sources of experimental data are much better for turbulent skin friction than they are for the transition, so you do have a pretty good feeling, I would say, for the experimental data that you did use. You feel then that they can be used as a fair standard. Is this correct?

BECKWITH: You mean the direct measurements of skin friction — is that what you are referring to there?

GESSOW: Yes.

BECKWITH: No, I don't think I really meant to imply that. What I meant was, we can continue to get detailed measurements in the boundary layer on nozzle walls, for instance, that is of profiles as well as the skin friction and heat transfer, just as well as anywhere else, in fact, somewhat better in certain cases.

MAGER: I noticed in those comparisons between the various methods that you made, you have compared a number of transformation methods, for example, Reshotko and some of the newer ones. The issue that bothers me is that you have not really indicated the validity of the specific transformation because you have not mentioned the incompressible method which is used in each case. In other words, when the transformation of Reshotko and Tucker failed, it is not clear whether it failed because of the nature of the transformation or whether it failed because of the specific incompressible method that was used with it. After all, the incompressible method could conceivably mispredict the occurrence of separation.

BECKWITH: Wait a minute, maybe you misunderstood there. The older Reshotko-Tucker integral methods did not rely on any physical transformation. There was no physical transformation involved in the sense that Coles' method is physical as opposed to a Stewartson type transformation of independent variables. All they did was to assume a certain set of functions for the profiles of velocity and enthalpy in the Stewartson plane and use modified incompressible relations for skin friction and the shear-stress integral.

MAGER: I don't know which one you referred to, but the original Reshotko-Tucker method does employ transformation.

BECKWITH: Well, I'd have to look this up. A general transformation could have been involved if they do use Coles' transformation theory and integral methods, yes. I'm not sure at the moment just what transformation was involved there, so I can't answer the question.

MICHAEL S. HOLDEN, Cornell Aeronautical Laboratory, Inc.: In connection with the measurements on tunnel walls, have you established from the theoretical analysis a criterion for suggesting when these measurements are compatible with flat-plate measurements? Can this be expressed in terms of the boundary-layer thickness at the end of the nozzle?

BECKWITH: In figure 5, we were showing a situation where there were definitely differences between nozzle-wall boundary layers and flat-plate boundary layers. This is just one particular way of plotting the total temperature against the velocity, but actually the nozzle-wall boundary layer turns out to be a useful thing if you are interested in trying to compute the effect of previous history. If you have a nonsimilar method, which the finite-difference approach would be, this presumably would be and can be incorporated in the method. The thing we really need to know is what is the relation between the fluctuating quantities within the turbulent boundary layer itself and the mean flow, whether it be a nozzle-wall boundary layer or a flat-plate boundary layer.

HENRY McDONALD, United Aircraft Research Laboratories: I'd just like to answer Dr. Mager's comment on the method of Reshotko-Tucker. I believe the figure you presented was pulled from a Langley presentation*, and if that is true, then the calculation was performed using essentially the transformation of Mager, and in the same paper that you pulled that calculation from, there is another calculation which showed a very simple modification of the basic incompressible method which in conjunction with the tranformation of Mager performed much, much better. So, Dr. Mager's point was that perhaps the error was in the incompressible method, and that indeed was justified by subsequent calculations.

BECKWITH: A very good point. Actually, you have to remember, here, the situation we were comparing it with was adiabatic, no heat transfer, and that can be handled by the transformation.

WILLIAM J. EVANS, Grumman Aircraft Engineering Corp.: This question is a little bit outside the realm of theoretical work in boundary layers itself, but I would be very much interested if, based on the fact that some of your curves show a range of accuracy, whether one can on perhaps even simple wind-tunnel models estimate the range of accuracy to which we are currently estimating skin frictions, since we are putting together wave drag plus I don't know what else, and come up with a complete correlation of the drag force, and I have not seen this done.

When you don't exactly agree with wind-tunnel data, people will say that the method is no good, and yet the skin-friction estimate itself is a basic weakness in the elements we have to put together. Is anyone working on trying to estimate ranges of accuracy of the skin-friction estimate by complete models?

BECKWITH: Maybe someone would care to comment on that. I don't think I could add much to it. What about Ed Hopkins back there?

EDWARD J. HOPKINS, NASA Ames Research Center: I can say a few remarks with regard to our data which showed up in figure 1.

---

*Compressible Turbulent Boundary Layers. NASA SP-216, 1969.

We made direct measurements using a skin-friction balance. Beckwith, in his paper, gives reference to our skin-friction summary paper in which the accuracy that we estimate for skin friction is given as about ±5 percent.

The other broader question of when you combine airplane components how much effect does interaction and accuracy of skin-friction measurements have on the final configuration estimated drag is something I can't answer.

HOLDEN: I noticed measurements of skin friction up to Mach 8; was any of this the data obtained by Wallace at CAL?

BECKWITH: Yes, Wallace's flat-plate data was included.

HOLDEN: I just want to comment that the skin-friction gages Jim Wallace used to obtain his measurements are believed accurate to within 5 to 10 percent.

FINITE-DIFFERENCE ANALYSIS OF THE COMPRESSIBLE TURBULENT BOUNDARY LAYER ON A BLUNT SWEPT SLAB WITH LEADING-EDGE BLOWING

By James L. Hunt, Dennis M. Bushnell,
and Ivan E. Beckwith

Langley Research Center

N70-21370

SUMMARY

A finite-difference method has been developed to solve the equations for compressible turbulent boundary layers on swept infinite cylinders. Predictions by the method have been compared with experimental data on a 60° swept, blunt, slab configuration with and without leading-edge blowing. The test conditions were a stream Mach number of 8 and a range of stream Reynolds number based on leading-edge diameter $N_{Re,\infty}$ from 0.92×10^5 to 9.3×10^5.

Three different approaches to the formulation of eddy-viscosity models for three-dimensional boundary layers were considered. Two of these formulations were used in the numerical solutions. Nonsimilar solutions for laminar flow were obtained by setting the eddy viscosity equal to zero.

Comparisons of the resulting predictions for heat transfer, surface streamlines, Mach number profiles, and boundary-layer thickness with the experimental data have indicated that for $N_{Re,\infty} \geqq 2.6 \times 10^5$, the leading-edge boundary layer was turbulent and that laminarization apparently occurred as the flow expanded around the leading edge. At the higher test Reynolds number of 9.3×10^5, transition back to turbulent flow was observed on the downstream part of the slab. Both eddy-viscosity models gave satisfactory predictions of the turbulent flow provided the mixing length in the outer part of the boundary layer was taken as 0.05 of the boundary-layer thickness. This fraction is generally larger on flat-plate turbulent boundary layers where values up to 0.10 have been used. The smaller values of the ratio required to obtain agreement between theory and the present data suggest that the level of turbulence in the present three-dimensional boundary layers was small compared with flat-plate flows at high Reynolds numbers.

The presence of low turbulence levels in the leading-edge boundary layers of these tests was also consistent with the apparent laminarization phenomenon since the value of the parameter that characterizes the onset of laminarization was an order of magnitude below the critical levels observed for laminarization in two-dimensional flow. The small value of this parameter suggests that the turbulent boundary layer on the leading edge was highly susceptible to laminarization as would be expected if the initial turbulence levels

19

were small. The laminarization-like behavior and the subsequent transition were independent of leading-edge blowing.

INTRODUCTION

The boundary layers on large lifting vehicles are predominantly turbulent and three dimensional in nature. For supersonic cruise vehicles, the accurate prediction of frictional drag is essential. As the flight Mach numbers are increased above approximately 3, reliable predictions of heat transfer also become important. On windward and leading-edge regions where passive or active cooling systems are required, the accurate prediction of heating is critical.

Calculation procedures by both integral and finite-difference methods for two-dimensional, compressible, turbulent boundary layers are now well developed, and further advancements depend on more detailed and accurate data. (See paper 18 of this compilation.) The finite-difference procedures can be extended in a straightforward manner to a particular class of three-dimensional flows. This class of flows may be designated as quasi two dimensional, since the governing equations can be expressed in terms of only two independent variables. The turbulent boundary layers on sharp cones at angle of attack and on infinite cylinders at yaw belong to this class if transition from laminar flow has occurred far upstream of the region of interest. These flows may exhibit large three-dimensional effects since the velocity vector within the boundary layer may have large components normal to the external inviscid streamline. The boundary-layer velocity components in this direction are generally referred to as simply the cross flow.

Previous methods developed for the calculation of compressible turbulent boundary layers of this quasi-two-dimensional class, as well as more general three-dimensional flows, were integral methods in which the assumption of small (or zero) cross flow within the boundary layer was used (refs. 1 to 5). A finite-difference procedure for solving the general equations for incompressible turbulent boundary layers without the small-cross-flow assumption has been developed by Nash (ref. 6). The small-cross-flow assumption requires that the magnitude of the velocity normal to the inviscid streamlines and the derivatives in that direction are small. With this assumption, it follows that the component of the surface shear normal to the inviscid streamlines is small and can have no effect on the streamwise flow which develops independently of the cross flow (see ref. 7, for example). The Reynolds stress in the streamwise direction is then independent of the cross flow, and two-dimensional models of the Reynolds stress are directly applicable.

The assumption of small cross flow is more generally valid for turbulent flows than for laminar ones, as shown by the results of reference 5. However, for some conditions such as large streamline curvature in the cross-flow direction and large surface blowing,

the cross flow in turbulent boundary layers will be large. The critical problem is then the formulation of models for both components of Reynolds stress that will properly account for the three-dimensional nature of the flow.

In order to study this problem, the finite-difference procedure of reference 8 has been extended to include the spanwise momentum equation for swept infinite cylinders. The computational advantages of two independent variables are thereby retained, while the boundary layer may have large cross-flow components. Although the computations are not done in streamline coordinates, the flow is computed in complete detail and the only restrictions are those arising from the assumed models for the components of the Reynolds stress in the chordwise and spanwise directions and for the turbulent flux of enthalpy.

The purpose of the present paper is to evaluate this procedure by comparison with experimental data on a 60° swept slab with and without homogeneous blowing at the leading edge. The test conditions were a stream Mach number of 8 and stream Reynolds numbers, based on leading-edge diameter, from 0.92×10^5 to 9.3×10^5. Several solutions for test Reynolds numbers of 2.6×10^5 and 9.3×10^5 have been obtained with various combinations of two eddy-viscosity models and different mixing-length functions. The results are compared with measurements of wall heat transfer, oil flow lines (representing surface streamlines), Mach number profiles, and boundary-layer thickness. The region of special interest is just downstream of the blunt leading edge where the boundary-layer profiles are far from equilibrium because of the upstream conditions of blowing and large cross-flow pressure gradients.

SYMBOLS

A area

A^* function of blowing parameter (see ref. 8)

a_i,b_i,c_i,d_i,e_i,f_i temperature coefficients in heat-balance matrix (30)

B normalized blowing rate, $\frac{(\rho v)_w}{(\rho u)_e}$

c specific heat of model material

c_p specific heat at constant pressure

C_f skin-friction coefficient, $\frac{\tau_w}{\frac{1}{2}\rho_e u_e^2}$

D/Dt	substantial derivative for time steady flow, $\bar{u}\frac{\partial}{\partial x} + \tilde{v}\frac{\partial}{\partial y}$
d	leading-edge diameter
G	eddy-viscosity function defined by equation (19)
g_i	constants in heat-balance matrix (30)
H	total enthalpy, $h + \frac{u^2 + v^2}{2}$
h	static enthalpy
h^*	heat-transfer coefficient
k	molecular thermal conductivity
L	reference length
l	mixing length (eqs. (8) and (9))
M	Mach number
$\dot{m}$	mass flow rate per unit area
N_{Pr}	molecular Prandtl number, $\frac{c_p\mu}{k}$
$N_{Pr,T}$	turbulent Prandtl number based on static enthalpy, $\frac{\overline{v'u'}}{\overline{v'h'}}\frac{\partial\bar{h}/\partial y}{\partial\bar{u}/\partial y}$
$N_{Re,s}$	reference Reynolds number, $\frac{\rho_s\sqrt{2H_e}L}{\mu_s}$
$N_{Re,\infty}$	free-stream Reynolds number based on leading-edge diameter, $\frac{\rho_\infty u_\infty d}{\mu_\infty}$
N_{St}	Stanton number, $\frac{h^*}{\rho_e u_e(h_{aw} - h)}$
$\bar{n}$	exponent in transformation (eqs. (26))
p	pressure
$\dot{q}$	heat-transfer rate per unit area per unit time

q	local velocity vector, $\sqrt{u^2 + w^2}$
R	ideal gas constant
s	distance along an inviscid streamline
T	absolute temperature
t	time
u,v,w	velocity components in x-, y-, and z-directions (fig. 1)
$\tilde{v} = \bar{v} + \frac{\overline{\rho' v'}}{\bar{\rho}}$	
V	volume
x,y,z	Cartesian coordinate system (fig. 1), also coordinate system used in heat-conduction problem (see fig. 8)
α	permeability, ft^2
δ	boundary-layer thickness, usually evaluated at the point where $\frac{M}{M_e} \approx 0.995$
Δy	wall thickness at thermocouple stations on slab
ΔY	wall thickness of porous leading edge
ϵ	eddy viscosity
ϵ^*	emissivity
θ	angle between z-coordinate direction and local velocity vector
κ	eddy thermal conductivity
Λ	leading-edge sweep
μ	molecular viscosity

ξ,η	transformed coordinate system (eqs. (26))
ρ	mass density
σ	Boltzmann constant
τ	shear stress

Subscripts:

aw	adiabatic wall
c	coolant conditions inside porous leading edge before injection
e	local "edge" of boundary layer
g	gas
m	model material
max	maximum
min	minimum
n	direction parallel to surface and normal to local inviscid streamline
o	initial condition at time zero
p	direction parallel to the surface and parallel to the local inviscid streamline
r	local reference condition, may be either wall or edge
s	stagnation line
T	turbulent
t	total
w	wall or outside surface of model

x,y,z in the x-, y-, or z-directions

∞ free-stream flow in tunnel

A bar over a symbol indicates a mean quantity. A prime indicates a fluctuating quantity.

ANALYTIC METHOD

Numerical solutions to the partial differential equations for the boundary layer on swept infinite cylinders are obtained by an implicit finite-difference procedure. The method of reference 8 for two-dimensional and axisymmetric flows is extended to swept cylinders by including the spanwise momentum equation. The Reynolds stress terms in the momentum equations are formulated by the use of eddy-viscosity concepts. The turbulent flux of static enthalpy is related to the Reynolds stress by the turbulent Prandtl number.

The formulation of models for the eddy viscosity in three-dimensional boundary layers is of primary concern herein. Two different models for the eddy viscosity are utilized in the calculations: (1) the "invariant turbulence" model in which the total shear is treated as a vector and the eddy viscosity is assumed independent of direction and (2) Lettau's vorticity-transfer hypothesis (ref. 9) in which the change of vorticity along an eddy trajectory is expressed in a general vector form.

Boundary-Layer Equations

The coordinate system for the idealized flow model is shown in figure 1(a). The instantaneous flow variables in the general conservation equations are divided into mean and fluctuating parts and the Reynolds averaging process is applied. The following equations are then obtained after the higher order terms are neglected according to the usual order-of-magnitude analysis for thin boundary layers:

Continuity

$$\frac{\partial}{\partial x}(\bar{\rho}\bar{u}) + \frac{\partial}{\partial y}(\bar{\rho}\bar{v}) = 0 \tag{1}$$

Chordwise momentum

$$\bar{\rho}\,\frac{D\bar{u}}{Dt} = -\frac{\partial\bar{p}}{\partial x} + \frac{\partial}{\partial y}\left(\bar{\mu}\,\frac{\partial\bar{u}}{\partial y} - \bar{\rho}\,\overline{v'u'}\right) \tag{2}$$

Spanwise momentum

$$\bar{\rho}\,\frac{D\bar{w}}{Dt} = \frac{\partial}{\partial y}\left(\bar{\mu}\,\frac{\partial\bar{w}}{\partial y} - \bar{\rho}\,\overline{v'w'}\right) \tag{3}$$

Total enthalpy

This equation may be written in either of two forms which, to the first order, are equivalent. Written in terms of the total enthalpy flux, this equation is

$$\bar{\rho}\,\frac{D\overline{H}}{Dt} = \frac{\partial}{\partial y}\left[\frac{\bar{k}}{c_p}\,\frac{\partial\overline{H}}{\partial y} - \bar{\rho}\,\overline{v'H'} + \overline{\mu}\,\frac{N_{Pr} - 1}{N_{Pr}}\,\frac{\partial}{\partial y}\left(\frac{\bar{u}^2 + \overline{w}^2}{2}\right)\right] \tag{4a}$$

The alternate form is obtained by using the static enthalpy in the transport terms to give

$$\bar{\rho}\,\frac{D\overline{H}}{Dt} = \frac{\partial}{\partial y}\left[\frac{\bar{k}}{c_p}\,\frac{\partial\bar{h}}{\partial y} - \bar{\rho}\,\overline{v'h'} - \bar{\rho}\bar{u}\,\overline{v'u'} - \bar{\rho}\overline{w}\,\overline{v'w'} + \overline{\mu}\,\frac{\partial}{\partial y}\left(\frac{\bar{u}^2 + \overline{w}^2}{2}\right)\right] \tag{4b}$$

In this latter form, turbulent "dissipation" terms appear (the third and fourth terms within the brackets) which have no counterpart in low-speed flows. On the other hand, equation (4a) is directly analogous to the energy equation for low-speed flow if $\overline{H}$ is replaced by $\bar{h}$ and if the viscous dissipation term (the last term within the bracket) is neglected. Neglecting this term would be an acceptable approximation for turbulent boundary layers except near the wall.

Before equations (1) to (4) can be solved, expressions must be supplied for the Reynolds stress or turbulent shear terms in the momentum equations and the turbulent flux of enthalpy in the total-enthalpy equations. The approach used in the present method is to model these terms as functions of the mean-flow variables.

Eddy Diffusivity Coefficients

The concept that the Reynolds stress in turbulent flow is proportional to a momentum exchange coefficient times the mean-flow velocity gradient was first proposed by Boussinesq. This concept is based on an assumed analogy between eddy viscosity and molecular viscosity. The shear components in the chordwise and spanwise directions are then written as

$$\tau_x = \overline{\mu}\,\frac{\partial\bar{u}}{\partial y} - \bar{\rho}\,\overline{v'u'} \approx \overline{\mu}\,\frac{\partial\bar{u}}{\partial y} + \epsilon_x\,\frac{\partial\bar{u}}{\partial y} \tag{5a}$$

$$\tau_z = \overline{\mu}\,\frac{\partial\overline{w}}{\partial y} - \bar{\rho}\,\overline{v'w'} \approx \overline{\mu}\,\frac{\partial\overline{w}}{\partial y} + \epsilon_z\,\frac{\partial\overline{w}}{\partial y} \tag{5b}$$

where the eddy viscosities in the x- and z-directions might in general be different. Since the total resultant shear must be a vector quantity, its magnitude is written as

$$\tau = \left(\tau_x^{\,2} + \tau_y^{\,2}\right)^{1/2} = \left[\left(\overline{\mu} + \epsilon_x\right)^2\left(\frac{\partial\bar{u}}{\partial y}\right)^2 + \left(\overline{\mu} + \epsilon_z\right)^2\left(\frac{\partial\overline{w}}{\partial y}\right)^2\right]^{1/2} \tag{6}$$

In a similar manner the total heat flux in equation (4b) becomes

$$\dot{q} = \frac{\bar{k}}{c_p}\frac{\partial \bar{h}}{\partial y} - \bar{\rho}\,\overline{v'h'} \approx \frac{\bar{k}}{c_p}\frac{\partial \bar{h}}{\partial y} + \frac{\kappa}{c_p}\frac{\partial \bar{h}}{\partial y} \tag{7}$$

Eddy-Viscosity Models

The simplest approach to the formulation of models for the Reynolds stress is based on Prandtl's mixing-length hypothesis. For two-dimensional flow this hypothesis states that

$$\left.\begin{aligned} u' &\propto -l\frac{\partial \bar{u}}{\partial y} \\ v' &\propto l\left|\frac{\partial \bar{u}}{\partial y}\right| \end{aligned}\right\} \tag{8}$$

The turbulent shear and eddy viscosity are then

$$\tau_T \equiv -\bar{\rho}\,\overline{v'u'} = \bar{\rho}l^2\left|\frac{\partial \bar{u}}{\partial y}\right|\frac{\partial \bar{u}}{\partial y} \tag{9}$$

$$\epsilon = \bar{\rho}l^2\left|\frac{\partial \bar{u}}{\partial y}\right| \tag{10}$$

where the quantity l is some characteristic length related to the size or scales of eddies responsible for the flux of momentum in the y-direction. In the near-wall region of a boundary layer, l is assumed proportional to the distance from the wall. In the far-wall region or in free turbulence, l is assumed proportional to the width of the mixing layer, that is, to the boundary-layer thickness or the width of the mixing jet. Although the details of such a transfer mechanism are not well understood, the basic concept gives satisfactory results even at hypersonic Mach numbers in the presence of large heat transfer and large pressure gradients. (See ref. 8 and paper 18 of this compilation.) One purpose of the present paper is to determine whether the basic mixing-length concept can be extended to three-dimensional flows. Three different approaches to this problem will be considered.

Independence principle.- The chordwise development of the laminar, incompressible boundary layer on a swept infinite cylinder is independent of the spanwise flow. The application of this same principle to turbulent flow was first attempted by Young and Booth (ref. 10). Although the variable density in compressible flow couples the chordwise and spanwise momentum equations, it is of interest to consider whether a valid mixing-length expression for the Reynolds stress can be formulated from the independence principle.

Thus, if the chordwise flow is independent of the spanwise flow, the chordwise shear would have to be of the form

$$\tau_{x,T} = \bar{\rho} l_x^2 \left|\frac{\partial \bar{u}}{\partial y}\right| \frac{\partial \bar{u}}{\partial y} \tag{11}$$

The simplest expression for the spanwise shear that retains the correct form at the stagnation line is

$$\tau_{z,T} = \bar{\rho} l_z^2 \left|\frac{\partial \bar{w}}{\partial y}\right| \frac{\partial \bar{w}}{\partial y} \tag{12}$$

The resulting expressions for the eddy viscosities are

$$\left.\begin{aligned} \epsilon_x &= \bar{\rho} l_x^2 \left|\frac{\partial \bar{u}}{\partial y}\right| \\ \epsilon_z &= \bar{\rho} l_z^2 \left|\frac{\partial \bar{w}}{\partial y}\right| \end{aligned}\right\} \tag{13}$$

Hence the eddy viscosities are different in the two directions and behave as vector quantities. The turbulent Prandtl number would then presumably be based on the "total" eddy viscosity, with the result that

$$N_{Pr,T} = \frac{c_p}{\kappa}\sqrt{\epsilon_x^2 + \epsilon_z^2} \tag{14}$$

However, substitution of equation (13) into equation (6) gives

$$\tau = \left[\left(\bar{\mu} + \bar{\rho} l_x^2 \left|\frac{\partial \bar{u}}{\partial y}\right|\right)^2 \left(\frac{\partial \bar{u}}{\partial y}\right)^2 + \left(\bar{\mu} + \bar{\rho} l_z^2 \left|\frac{\partial \bar{w}}{\partial y}\right|\right)^2 \left(\frac{\partial \bar{w}}{\partial y}\right)^2\right]^{1/2} \tag{15}$$

and it is evident that a total eddy viscosity like that of equation (14) cannot be obtained in explicit form from equation (15). The requirement of the independence principle that the eddy viscosity should be a vector-like quantity, or should depend on coordinate direction, may therefore be erroneous. Experimental data of Ashkenas and Riddell (ref. 11) also indicate that the independence principle may not apply to turbulent flows. (See also discussion in ref. 12.) In view of these difficulties, the formulation of eddy viscosities from the independence principle will not be pursued further herein.

Invariant turbulence.- An alternate approach to the independence principle is based on the concept that the eddy viscosity should depend only on the properties of the turbulence and a local eddy scale as in the methods of Prandtl (ref. 13) and Glushko (ref. 14). The application of this concept to a mixing-length approach suggests that the eddy viscosity would be a scalar function independent of the coordinate direction. Accordingly, the components of Reynolds stress are written

$$\left.\begin{aligned} \tau_{x,T} &= \bar{\rho} l^2 \frac{\partial G}{\partial y} \frac{\partial \bar{u}}{\partial y} \\ \tau_{z,T} &= \bar{\rho} l^2 \frac{\partial G}{\partial y} \frac{\partial \bar{w}}{\partial y} \end{aligned}\right\} \tag{16}$$

and the eddy viscosity is then

$$\epsilon = \epsilon_x = \epsilon_z = \bar{\rho} l^2 \frac{\partial G}{\partial y} \tag{17}$$

To determine the scalar function G, equation (17) is substituted into equation (6) with the result

$$\tau = \left(\bar{\mu} + \bar{\rho} l^2 \frac{\partial G}{\partial y}\right)\left[\left(\frac{\partial \bar{u}}{\partial y}\right)^2 + \left(\frac{\partial \bar{w}}{\partial y}\right)^2\right]^{1/2} \tag{18}$$

Then by analogy with equations (9) and (10), where the velocity-gradient function for the shear component is repeated in the eddy viscosity, the expression for G is

$$\frac{\partial G}{\partial y} = \left[\left(\frac{\partial \bar{u}}{\partial y}\right)^2 + \left(\frac{\partial \bar{w}}{\partial y}\right)^2\right]^{1/2} \tag{19}$$

The final expression for the eddy viscosity then becomes

$$\epsilon = \bar{\rho} l^2 \left[\left(\frac{\partial \bar{u}}{\partial y}\right)^2 + \left(\frac{\partial \bar{w}}{\partial y}\right)^2\right]^{1/2} \tag{20}$$

Bradshaw (ref. 15) has derived a set of differential equations for the two components of shear stress based on the Navier-Stokes equations and several assumptions regarding the behavior and formulation of correlation terms for fluctuating pressure and velocity. These equations indicate that the directions of the shear stress components are not generally the same as the directions of the corresponding mean velocity gradients. However, in the near-wall region, Bradshaw's equations reduce to the same form as the present results (eqs. (18) and (19)).

Lettau's vorticity transfer hypothesis.- In reference 9, Lettau proposed a modification of Taylor's vorticity transfer theory that accounts for the combined action of conservation and adjustment of the vorticity of a fluid element as it is convected along an eddy trajectory. The resulting expressions for the three components of fluctuating velocity reduce to simple forms for the present application. That is, by the use of conventional order-of-magnitude analysis for a thin boundary layer on a swept infinite cylinder, these expressions for the fluctuating velocity components reduce to

$$\left.\begin{aligned} u' &= -l_y \frac{\partial \bar{u}}{\partial y} \\ v' &= l_x \frac{\partial \bar{u}}{\partial y} + l_z \frac{\partial \bar{w}}{\partial y} \\ w' &= -l_y \frac{\partial \bar{w}}{\partial y} \end{aligned}\right\} \tag{21}$$

For simplicity, the various components of an "eddy displacement vector," represented in equations (21) by l_x, l_y, and l_z, are assumed to be independent of direction. The components of Reynolds stress then become

$$\left.\begin{aligned} \tau_{x,T} &\equiv -\bar{\rho}\,\overline{v'u'} = \bar{\rho}l^2\left(\frac{\partial\bar{u}}{\partial y} + \frac{\partial\bar{w}}{\partial y}\right)\frac{\partial\bar{u}}{\partial y} \\ \tau_{z,T} &\equiv -\bar{\rho}\,\overline{v'w'} = \bar{\rho}l^2\left(\frac{\partial\bar{u}}{\partial y} + \frac{\partial\bar{w}}{\partial y}\right)\frac{\partial\bar{w}}{\partial y} \end{aligned}\right\} \tag{22}$$

The eddy viscosity is then given by

$$\epsilon = \bar{\rho}l^2\left(\frac{\partial\bar{u}}{\partial y} + \frac{\partial\bar{w}}{\partial y}\right) \tag{23}$$

which is the same for both shear components, but in contrast with the invariant-turbulence model of equation (20), this modification of Lettau's hypothesis is the scalar sum of two vector quantities. Recently, Lettau (ref. 16) has generalized his original hypothesis of reference 9 in an attempt to account for possible variations of his eddy displacement vector and has applied the results to a free-turbulence problem.

Mixing-Length Function

The mixing-length function used for the present calculations is

$$\frac{l}{\delta} = \left[1 - \exp\left(-\frac{\rho_w y}{A^*\mu_w}\sqrt{\frac{\tau_w}{\rho_w}}\right)\right]f\left(\frac{y}{\delta}\right) \tag{24}$$

This expression is the same as the function used in reference 8 except that the gas properties in the exponential are herein always evaluated at the surface, and the function $f(y/\delta)$ was modified to account for smaller levels of turbulence. That is, the f_1 function of reference 8 (see table I in ref. 8) was modified by reducing the maximum value of the function for $y/\delta > 0.1$ from the value of 0.09, to 0.07 or 0.05. The Prandtl slope in the near-wall region $\frac{df}{d(y/\delta)} = 0.4$ was retained. Also, the functional dependence of A^* on the blowing parameter $2B/C_f$ as given in figure 1 of reference 8 has been used in the present calculations.

Turbulent Prandtl Number Variation

The variation in turbulent Prandtl number through axisymmetric compressible boundary layers with large heat transfer and large favorable pressure gradients was treated extensively in reference 8. The results indicated that values of $N_{Pr,T} = \frac{c_p\epsilon}{\kappa}$

(the "static" turbulent Prandtl number) in the outer part of these boundary layers may be as small as 0.5. Values of $N_{Pr,T}$ obtained from experimental data on flat plates and reported in references 17 and 18 are generally greater than 1.0 near the wall and tend to decrease below 1.0, or in some cases to nearly 0.5, farther from the wall. On the basis of these results, the $N_{Pr,T}$ variation used in all solutions reported herein was taken as a simple ramp function of y/δ as given by the following relations:

$$\left.\begin{aligned} N_{Pr,T} &= 2.0 - 5\frac{y}{\delta} && \left(\frac{y}{\delta} \leqq 0.3\right) \\ N_{Pr,T} &= 0.5 && \left(\frac{y}{\delta} \geqq 0.3\right) \end{aligned}\right\} \tag{25}$$

Some check calculations with the alternate assumption of $N_{Pr,T} = 0.9$ reduced the predicted heat transfer by at most 15 percent, which was considered to be within the range of experimental uncertainties. For the present conditions, the choice of the $N_{Pr,T}$ function is apparently not critical.

Numerical Procedure

The Reynolds stress terms in equations (2) and (3) are replaced by the eddy-viscosity expressions (eqs. (17), (20), or (23)) with the mixing-length function given by equation (24). These eddy-viscosity and mixing-length expressions are also used in the energy equation (4b) after replacement of the turbulent heat flux by the eddy-conductivity relation of equation (7) and the introduction of $N_{Pr,T}$. The resulting equations are transformed to the coordinate system ξ,η defined by

$$\left.\begin{aligned} \xi\left(\frac{x}{L}\right) &= N_{Re,s}\int_0^{x/L}\frac{(\rho\mu)_r}{(\rho\mu)_s}\frac{u_e}{\sqrt{2H_e}}\,d\left(\frac{x}{L}\right) \\ \eta\left(\frac{x}{L},\frac{z}{L}\right) &= N_{Re,s}\frac{u_e/\sqrt{2H_e}}{(2\xi)^{\bar{n}}}\int_0^{z/L}\frac{\rho}{\rho_s}\,d\left(\frac{z}{L}\right) \end{aligned}\right\} \tag{26}$$

where $\bar{n}$ is adjusted to obtain a nearly constant boundary-layer thickness in the ξ,η plane in order to increase the computational efficiency.

The numerical procedure used to solve the transformed equations is an implicit finite-difference procedure similar to that of reference 19. The partial derivatives are replaced by linear-difference quotients. The result is a set of $N - 1$ linear algebraic equations for each of the unknown velocity components and enthalpy $(\bar{u}, \bar{w}, \text{and } \bar{H})$ at the N grid points for the next downstream station. The matrix for each set of these linear equations is tridiagonal, so that an efficient algorithm is used in their solution. After the solution for $\bar{u}$ and $\bar{w}$ is obtained from the momentum equations, the transformed

normal velocity is obtained from the continuity equation; then the enthalpy (at each grid point) is obtained by the same numerical method used for $\bar{u}$ and $\bar{w}$. This procedure is repeated with updated values used in all difference coefficients until convergence is obtained.

The solutions were started at a small but finite chordwise distance from the stagnation line with an assumed set of profiles for $\bar{u}/u_e$, $\bar{w}/w_e$, and $\frac{\bar{H} - H_w}{H_e - H_w}$. This procedure was used for the present solutions because the correct limiting forms of the equations at $x = 0$ had not yet been incorporated in the computer program. It was found that "unique" solutions for all variables could be obtained within a distance equivalent to 2 or 3 boundary-layer thicknesses by using a large number of small steps in the chordwise variable ξ. These unique solutions depended on the particular eddy-viscosity model used but were independent of the input profile shapes and input boundary-layer thicknesses, provided reasonable assumptions were used for these quantities.

EXPERIMENTAL METHODS

The implicit finite-difference procedure as just described can provide, for all practical purposes, nearly "exact" solutions to the partial differential equations since the method is numerically stable. Of course, the accuracy of the solutions depends on the step sizes, the convergence criteria for the iterative cycles, and the accurate specification of boundary conditions. Essentially by trial-and-error processes, these matters have been treated during the course of this and previous investigations (refs. 19 and 8) with the result that the present solutions are believed to be accurate to within 1 percent or better. Consequently, the comparison of theoretical predictions with data provides a direct evaluation of the eddy-viscosity models, the mixing-length functions, and turbulent Prandtl number distributions since for a given set of boundary conditions, these are the only ingredients in the theory that can account for different predictions. Thus, by using various eddy-viscosity models and mixing-length functions in the theory and comparing results over a range of Reynolds number and with as many different experimental measurements as possible, the optimum formulation of Reynolds stress and turbulent Prandtl number can be determined. Such a process may be considered as "numerical experimentation" to determine the best form and values of the Reynolds stress.

Experimental data have been obtained for this purpose on a 60° swept slab with and without blowing at the blunt leading edge. The surface heat transfer, Mach number profiles, boundary-layer thickness, and surface streamlines were obtained for the model without blowing. For the model with blowing at the leading edge, the only data available as yet are for surface heat transfer on the leading edge and downstream on the slab. The wind-tunnel facility and models will be described in detail in the following sections.

Facility

All the data presented herein were obtained in the Langley Mach 8 variable-density hypersonic tunnel. This blowdown-type facility has a contoured axisymmetric nozzle with an 18-inch-diameter test section. Transient testing techniques, that is, rapid exposure of models to established flow conditions, are accomplished by means of a model injection mechanism located directly beneath the test section. Windows are located on both sides and at the top of the test section for lighting and photographing models. The free-stream Mach number varies slightly with free-stream Reynolds number (ref. 20). Data will be presented herein for free-stream Reynolds numbers, based on leading-edge diameter, of 0.92×10^5, 2.6×10^5, and 9.3×10^5. The corresponding free-stream Mach numbers used in the data reduction are 7.81, 7.94, and 7.98, respectively.

Models

For this investigation the test configuration is a 60° swept slab with a leading-edge radius of 1/2 inch. One pressure model, three plastic heat-transfer models, and one porous-leading-edge model were used in the experimental tests. A sketch of the basic configuration used for the pressure model is shown in figure 1(b). The coordinate system used to locate the instrumentation on the various models is also given in this figure. The forward portion of all models (ahead of the dashed lines) was geometrically identical with the pressure model shown. The aft portion of the plastic models and the porous-leading-edge model were modified as indicated by the dashed lines in the figure. The mounting plate as shown in the sketch was used for the pressure model and the plastic heat-transfer models. The mounting plate for the porous-leading-edge model was modified, as will be shown subsequently; however, the leading edge of the plate was 1/4 inch ahead of the apex of all models.

Pressure model.- The pressure model was made of stainless steel and was provided with seven chordwise rows of pressure orifices over a 12-inch span as shown in figure 2. The distribution of these orifices in the three chordwise rows used in this investigation is given in table I. A boundary-layer pitot-tube rake is shown attached to the model in figure 2. Details of the rakes used will be given in a subsequent section.

Phase-change heat-transfer models.- A photograph of one of the three plastic models used with the phase-change coating technique is shown in figure 3. The model shown was cast from an epoxy resin with a silica base. One of the other plastic heat-transfer models was cast from a slightly different mixture of epoxy and silica, and for the third model, mica was used as the base material. Therefore, these three models had different thermophysical properties. The value of the combination of these properties required in the phase-change method is $\sqrt{\rho c k}$. The values of this quantity for the three models were 0.073, 0.075, and 0.034 Btu/ft^2 $^{\circ}$R sec$^{1/2}$, respectively.

Porous-leading-edge model.- A photograph of the porous-leading-edge model used in this investigation is shown in figure 4. The leading edge of this model consisted of a porous hemicylinder $10\frac{1}{8}$ inches long and approximately 3/32 inch thick. The hemicylinder was made of sintered stainless steel with a porosity of approximately 13 percent. The leading edge was electron-beam welded to the swept slab which consisted of a machined, ribbed structure with a thin skin. The mounting-plate configuration for this model is different from that shown in figures 1(b), 2, and 3. In particular, the forward section of the plate was machined into an elliptical planform which projected beyond the periphery of the model apex by 1/4 inch.

The coolant air was fed into a chamber just behind the porous leading edge. The chamber could be pressurized to 415 psia. The pressure and temperature of the coolant air were measured in this chamber.

Thermocouples were installed in the porous leading edge and attached to the thin skin of the slab. The locations of the thermocouples used in this investigation are given in table II. To install the thermocouples on the porous leading edge, 0.016-inch-diameter balls were formed at the thermocouple junctions. Teflon-coated chromel-alumel wires of 0.003-inch diameter were used. The thermocouple wires were then inserted into a 0.013-inch-diameter hole which was burned by an electric-arc technique through the porous leading edge at an angle of 45° to the surface. The axes of the holes were alined in spanwise planes which in turn were normal to the surface. The thermocouple junction (a 0.016-inch-diameter ball) was tapped into the 0.013-inch-diameter hole and finished flush with the outer surface. The hole was then filled with epoxy resin to prevent direct leaks of coolant air around the junction. This procedure resulted in a thermocouple junction within 0.004 inch of the external surface. Good thermal contact of the junction with the porous matrix was obtained.

On the slab portion of the model the thermocouples were welded to the back surface of the stainless-steel skin, which was 0.030 inch thick.

Boundary-Layer Pitot-Tube Rakes

One of the boundary-layer pitot-tube rakes used to obtain Mach number profiles is shown attached to the pressure model in figure 2. A photograph of these rakes showing the tube assembly is presented in figure 5(a). The rakes consisted of two rows of three pitot tubes each. Sketches of the pitot-tube configurations with pertinent dimensions are given in figure 5(b).

Test Techniques and Data Reduction

All data were obtained by using a transient testing technique in which the tunnel was started and brought to the desired operating conditions and then the model was rapidly

injected into the airstream by a pneumatic piston. An analog-to-digital data recording system with a maximum resolution of 40 points per second was used for thermocouple and static-pressure data.

Pressure data.- Strain-gage pressure transducers were used to measure the static pressures on the model shown in figure 2. The locations of the pressure orifices (0.040-inch diameter on the leading edge and 0.060-inch diameter on the slab) used in this investigation are given in table I. The output of the transducers was monitored to determine when time-steady pressures were reached, then the data were recorded on the readout system at the rate of 20 points per second.

The pitot-tube rakes shown in figure 5 were mounted on the pressure model as indicated in figure 2. Pitot pressure data were obtained at five chordwise locations on the slab portion of the model. The rakes were alined so that the pitot tubes were parallel to the free-stream flow direction. The plane of the pitot orifices was located approximately 1/4 inch behind a static-pressure orifice at each chordwise location. The y-location of the tube assembly was adjusted with shims between the rake and model. The pitot-pressure data were read from photographs of a mercury manometer board.

The ratios of the local surface static pressure to the pitot pressure were used to compute the Mach number distributions through the boundary layer. The boundary-layer thickness was taken as the distance from the surface where the Mach number became approximately constant.

Oil flow.- In order to obtain the direction of the wall streamlines and the overall flow pattern, small dots of a mixture of oil and lampblack were placed on the slab portion of the pressure model. The model was then rapidly injected into the airstream. After exposure to the flow of 3 to 8 seconds, depending on the Reynolds number, the model was retracted and the resultant patterns photographed.

Heat transfer for no blowing.- Heat-transfer-coefficient distributions on the plastic "stycast" models (fig. 3) were obtained with the phase-change coating technique (ref. 21). In this technique, a thin surface coating of material that undergoes a visible phase change at a known temperature is sprayed on the model. The model is then injected rapidly into the established flow and the phase-change patterns which develop as the model is heated are recorded by motion-picture photography. The patterns of isothermal lines so obtained may be transformed to lines of constant heat-transfer coefficient provided the distribution of adiabatic wall temperature is available and the thermophysical properties (ρck) of the model material are known. Exact solutions of the heat-conduction equation for the specific geometry are not generally practical; therefore, the local heat-transfer coefficients for the model are determined from the solution for a semi-infinite slab. The results obtained with this assumption are a good approximation to the solution for the actual body geometry when the depth of heat penetration is small compared with

pertinent model dimensions, as is the case for the present model. A detailed discussion of the accuracy limits due to the semi-infinite-slab assumption is presented in reference 20.

Measurement of mass injection rates.- The local mass injection rates on the porous leading edge were measured at several spanwise stations and chordwise distances over a range of internal pressures from 150 to 400 psig. These measurements were made with a plastic tip probe (0.096 inch inside diameter) which was pressed against the porous surface as shown in figure 6. The probe was connected with a butyl phthalate manometer and a pressure-sealed container of known volume. The total mass flow rate through the porous leading edge was set at the desired level by adjusting the internal pressure. This flow rate was measured with a floating ball-type flowmeter. The plastic tip probe was held in contact with the model for a measured period of time. At the end of this period ($\geqq 30$ sec) the system was sealed just downstream of the plastic tip probe. After equilibrium was established, the change in pressure and volume (the change in volume due to the change in level of the manometer fluid) of the isothermal system was recorded. The local mass flow rate through the contact area of 0.096-inch diameter could then be calculated. The pressure rise in the sealed volume was limited to less than 0.7 percent of the pressure inside the model. Therefore, the mass-flow distribution through the porous material was not altered by the measurement technique. The validity of this statement is evident from the relation for the mass flow rate through a uniformly porous material. This relation is given in reference 22 (eq. (7), p. 78) and, in the notation herein, is

$$\dot{m} \equiv \rho_w v_w = \frac{\alpha}{2R(\mu T)_w} \frac{p_c^2 - p_w^2}{\Delta Y} \tag{27}$$

Measurements were made at chordwise intervals of 10° around the leading edge and at spanwise intervals of 1 inch or less along the porous leading edge in the region $7.85 \leqq z/d \leqq 11.85$. Large spanwise and chordwise variations in mass flow rates were found to exist. The results are shown in figure 7 in the form of the permeability parameter α which would be constant if the material were perfectly uniform in porosity and thickness. The chordwise variation in permeability is shown in figure 7(a) for the spanwise location $z/d = 8.85$ and for the range of internal pressures shown. The spread of the data at a given x/d location in this figure gives an indication of the repeatability of the technique since the only variable was the internal pressure. The chordwise variation of the permeability for a range in span of 4 inches ($7.85 \leqq z/d \leqq 11.85$) and pressures of 250 and 300 psig is presented in figure 7(b). The data spread here is due primarily to the spanwise variation in the permeability.

Test procedure for heat transfer with blowing.- The porous-leading-edge model described previously and shown in figure 4 was instrumented to provide heat-transfer

data on both the porous leading edge and on the thin-skinned slab. The locations of the thermocouples used in the present investigation are given in table II.

For the wind-tunnel tests, the desired mass flow rate was established first with the model in the retracted position inside the sealed chamber below the tunnel test section. (See ref. 20.) During the tunnel startup process this chamber was evacuated to tunnel static pressure which was about 0.05 times the pressure on the stagnation line of the swept leading edge after the model was exposed to the flow. This sudden change in external pressure on the porous leading edge after model injection did not affect the preset mass flow because of the large pressures (150 to 400 psig) inside the model.

Heat-transfer data were used during the period from 0.2 to 1.5 seconds after the model first entered the airstream. Because of the short testing time, the model was practically isothermal; thus heat-conduction effects were minimized and any change in the injected mass flow rate which would occur with an increase in model temperature (see eq. (27)) was prevented. The thermocouple data were recorded at a rate of 20 points per second on the digital readout system.

Data reduction procedures for tests with blowing.- A numerical procedure was developed to reduce the temperature-time histories of each thermocouple within the porous wall to heating rates. The method provides an approximate solution of the two-dimensional heat-conduction problem in a porous matrix with one-dimensional (or radial) fluid flow and with temperature-dependent thermal properties. The temperature of the fluid is assumed the same as that of the porous matrix.

To illustrate the procedure, consider the finite slab shown divided into six blocks in figure 8. The initial temperature and time-dependent one-dimensional blowing rates for each block are known. At time $t = t_o$, the front face of the slab (the left side in the figure) is exposed to an unknown heating rate which may vary with time and block location. The upper and lower surfaces of the slab are insulated. In order to determine the temperature-time profiles of the remaining blocks, a heat balance is written for each block by assuming a linear temperature variation between blocks. The heat balance for block 1 is as follows:

Convection	Radiation	Stored	Gas absorbed	x conducted, material

$$\dot{q}_1 A_{\dot{q},1} - A_{\dot{q},1}\epsilon^*\sigma\left(T'_{A_{\dot{q},1}}\right)^4 - \rho_1 c_1 V_1 \frac{\left(T_1 - T'_1\right)}{\Delta t} - 2\dot{m}_3 A_{x,3} c_{p,1} \frac{x_1\left(T_1 - T_2\right)}{\left(x_1 + x_2\right)} - 2\bar{k}_{1,2} A_{x,1} \frac{\left(T_1 - T_2\right)}{\left(x_1 + x_2\right)}$$

x conducted, gas	y conducted, material	y conducted, gas

$$- 2\left(\bar{k}_g\right)_{1,2} A_{x,1} \frac{\left(T_1 - T_2\right)}{\left(x_1 + x_2\right)} - 2\left(\bar{k}_g\right)_{1,4} A_{y,1} \frac{\left(T_1 - T_4\right)}{\left(y_1 + y_4\right)} - 2\left(\bar{k}_g\right)_{1,4} A_{y,1} \frac{\left(T_1 - T_4\right)}{\left(y_1 + y_4\right)} = 0 \tag{28}$$

where the primes denote a temperature evaluated at the previous time step and the subscripts 1 to 6 refer to block numbers. The subscript $\dot{q}$ indicates the surface exposed to heating rate $\dot{q}$. Since the calculation starts at $t = t_o$, all the primed quantities are known. A similar heat balance is written for all blocks and the resulting system of linear equations are obtained:

$$\left.\begin{array}{llllllll}
a_1T_1 & + b_1T_2 & & + d_1T_4 & & & = -A_{\dot{q},1}\dot{q}_1 & + g_1 \\
a_2T_1 & + b_2T_2 & + c_2T_3 & & + e_2T_5 & & = & g_2 \\
 & b_3T_2 & + c_3T_3 & & & + f_3T_6 & = & g_3 \\
a_4T_1 & & & + d_4T_4 & + e_4T_5 & & = & g_4 - A_{\dot{q},4}\dot{q}_4 \\
 & b_5T_2 & & + d_5T_4 & + e_5T_5 & + f_5T_6 & = & g_5 \\
 & & + c_6T_3 & & + e_6T_5 & + f_6T_6 & = & g_6
\end{array}\right\} \tag{29}$$

The temperatures T_1 and T_4 are known; that is, they are obtained from the measured temperatures. Also, the temperature coefficients $a_i, b_i, \ldots, f_i$ and the constants g_i are calculated from the given inputs. The unknowns are then $\dot{q}_1$, $\dot{q}_4$, T_2, T_3, T_5, and T_6 which may be obtained from the solution of the following determinant system:

$$\left.\begin{array}{cccccc|l}
 & & \text{Unknowns} & & & & \\
\dot{q}_1 & T_2 & T_3 & \dot{q}_4 & T_5 & T_6 & \\
 & \text{Determinant elements} & & & & & \text{Constants for any } n \text{ time step} \\
A_{\dot{q},1} & b_1 & 0 & 0 & 0 & 0 & -a_1T_1 - d_1T_4 + g_1 \\
0 & b_2 & c_2 & 0 & e_2 & 0 & -a_2T_1 \qquad + g_2 \\
0 & b_3 & c_3 & 0 & 0 & f_3 & \qquad + g_3 \\
0 & 0 & 0 & A_{\dot{q},4} & e_4 & 0 & -a_4T_1 - d_4T_4 + g_4 \\
0 & b_5 & 0 & 0 & e_5 & 0 & - d_5T_4 + g_5 \\
0 & 0 & c_6 & 0 & e_6 & f_6 & \qquad + g_6
\end{array}\right\} \tag{30}$$

This system is solved successively at each n time step where $t = t_o + n\Delta t$. The values of the specific heats and thermal conductivities are "updated" at the new temperatures obtained after each time step. The coefficients and constants of the determinant can then

be updated, and the heating rates and temperature distributions obtained for the next time step. This procedure is repeated until a specified time interval $t_f = t_o + j\Delta t$ is reached. The surface heating rates for each block are thereby computed over this specified time interval with the time-dependent inputs T_1, T_4, $\dot{m}_6$, and $\dot{m}_3$ and the temperature-dependent material properties.

Two different block configurations were used for five spanwise stations on the porous leading edge as shown in figure 9. These block configurations were set up so that experimental thermocouple readings could be used as direct inputs to the computer program without smoothing techniques applied to the data. Hence, the chordwise thermocouple distributions at the spanwise stations as indicated in the figure determined the block configurations because the temperature-time history for one block in each column of blocks is required as an input to the program. In the 56-block configuration, the symmetry of the thermocouple locations about the $x/d = 0$ station allowed the use of the "surface" thermocouple readings at both the location of the thermocouple and its "mirror" image. This increase in the number of columns from four to seven was made in order to reduce the chordwise length of the blocks and still provide thermocouple data in the chordwise center of each column of blocks. Superposition of the thermocouple locations in this manner is strictly valid only if the chordwise distribution of permeability α is perfectly symmetrical. Deviations in α from symmetry can be obtained from figure 7 where the data for the x locations of 10°, 30°, 40°, and 70° are shown as flagged symbols. These deviations are small for most of the data and hence were neglected in the 56-block configuration.

The chordwise conduction errors are small, in spite of the relatively large block dimensions in the chordwise plane, because of the nearly isothermal conditions during the short test period. The surface block of each column was made 0.004 inch thick in accordance with the approximate depth of the thermocouple junction. The remaining thickness of approximately 0.090 inch was divided into seven blocks of equal thickness. The time step used herein for all solutions was 0.05 second.

Comparisons of results from calculations for one-dimensional heat-conduction problems with exact solutions from Carslaw and Jaeger (ref. 23) indicated that for the block thicknesses and time steps of the present computations, errors would have been negligible had only five equal-thickness blocks been used. To assess further the reliability of the heat-balance method, tests were conducted on the porous-leading-edge model with no mass injection at the same tunnel conditions for which the phase-change heat-transfer technique was used on the plastic models. The validity of the inverse heat-balance method was confirmed by comparisons of the resultant heat-transfer distributions. Description and verification of a one-dimensional inverse heat-balance solution without fluid flow is given in reference 24.

Downstream of the interface of the porous leading edge and the slab, the thermocouple wires were spotwelded to the inside surface of the thin stainless-steel skin which was 0.030 inch thick. Here, the heating rates were obtained by fitting a second-degree curve to the temperature-time data by the method of least squares, over a time interval of 1.0 second. The time derivatives of temperature were then computed from the slopes of these second-degree curves at the midpoint of the 1.0-second time interval. The heating rates, neglecting conduction, were then obtained from the equation

$$\dot{q}_w = (\rho c)_m \, \Delta y \, \frac{dT_w}{dt} \tag{31}$$

RESULTS AND DISCUSSION

Static Pressure Distribution

The experimental pressure distributions obtained with the model of figure 2 are shown in figure 10. The line faired through the data was used as the distribution of p_e from which u_e and ρ_e were computed for the input to all theoretical solutions included herein. An isentropic expansion from p_s to p_e was assumed for these computations of u_e and ρ_e.

Zero Blowing

Heat transfer.- The chordwise distribution of heat-transfer coefficient at the spanwise station $z/d = 10.6$ for $N_{Re,\infty} = 0.92 \times 10^5$ is presented in figure 11. The plastic models (fig. 3) were used to obtain these data with the phase-change technique. The width of the hatched band represents the scatter in 56 data points obtained with eight different phase-change coatings $\left(0.45 \leq T_w/T_t \leq 0.55\right)$ on the three models with different thermophysical properties. The theoretical laminar distribution (solid line) was obtained with the finite-difference procedure for $T_w/T_o = 0.4$ and $\epsilon = 0$. The good agreement between experimental data and the theoretical predictions indicates that the numerical procedure is satisfactory.

Heat-transfer-coefficient contours obtained for typical runs on the plastic models with the phase-change coating technique are shown in figures 12(a) and 12(b) for $N_{Re,\infty} = 2.6 \times 10^5$ and 9.3×10^5, respectively. In figure 12(a) the values of h^* decrease continuously along the chord at $z/d = 10.6$. The fact that the contours in this region are essentially parallel to the leading edge indicates that the interference disturbances between the mounting plate and the model are small; thus, the infinite-cylinder approximation is acceptable.

In contrast to the contours in figure 12(a), the contours at the larger Reynolds number (fig. 12(b)) are not parallel to the leading edge at any spanwise station for $x/d \gtrsim 1.2$.

On the leading edge for $x/d \lessapprox 1.1$ and along the chord $z/d = 10.6$, the contour lines are parallel to the stagnation line and the values of h^* decrease with increasing x/d. However, for $x/d \gtrapprox 1.3$ (at $z/d = 10.6$), the values of h^* increase from a minimum of 2.8×10^{-3} to a maximum of 4.3×10^{-3}. At $x/d \approx 2.2$, the values of h^* again began to decrease. The locations of these minimum and maximum contours in h^* are too far from the mounting plate to be caused by interference effects, as shown by the results of figure 12(a). Figure 12(a) also shows that the effects of the downstream end of the slab are not responsible for the contour behavior noted in figure 12(b).

Comparisons and discussion of these different results are best made by means of heat-transfer-coefficient distributions. The chordwise distributions of h^* along the chord $z/d = 10.6$ for the same test conditions of figure 12 are given in figure 13. Theoretical predictions for $T_w/T_t = 0.4$ and with the eddy-viscosity models described previously (invariant turbulence and Lettau's (ref. 9) vorticity-transfer hypothesis) for $(l/\delta)_{max}$ of 0.05 and 0.07 are shown as the dashed lines. The solid lines represent predictions of the laminar theory obtained with $\epsilon = 0$.

The data and theoretical results in figure 13(a) are for $N_{Re,\infty} = 2.6 \times 10^5$. The width of the hatched band represents the scatter in 97 data points obtained with six different phase-change coatings $\left(0.41 \leqq T_w/T_t \leqq 0.58\right)$ on the three models with different values of ρck. In the leading-edge region the theoretical turbulent distributions are within the spread of the data; however, the original density of data points indicated that the agreement is best with the $(l/\delta)_{max}$ value of 0.05.

On the forward portion of the slab $\left(0.785 \leqq x/d \lessapprox 1.5\right)$, the experimental values of h^* fall below the theoretical turbulent distribution and approach the laminar predictions. The experimental values of h^* remain somewhat above the laminar predictions over the remainder of the slab region to $x/d = 3.5$.

The experimental and theoretical results for $N_{Re,\infty} = 9.3 \times 10^5$ are shown in figure 13(b). On the leading edge the theoretical turbulent prediction with the invariant-turbulence assumption and $(l/\delta)_{max} = 0.05$ is in best agreement with the data. On the forward portion of the slab, the data again drop below the turbulent predictions and tend to approach the laminar prediction. However, in contrast with the experimental results at the lower Reynolds number (fig. 13(a)), the level of the data begins to increase at $x/d \approx 1.3$ until agreement with turbulent levels is obtained at $x/d \approx 2.0$.

These trends of the experimental data with x/d and Reynolds number (figs. 13(a) and 13(b)) as compared with the theoretical predictions suggest the possibility of laminarization of the initially turbulent boundary layer on the leading edge. The drop in experimental heat transfer just aft of the rapid expansion on the leading edge until nearly laminar values are reached could also be caused partly by the effect of streamline curvature on the

mixing length. (See ref. 25 and paper 18 of this compilation.) However, if the effects of curvature were the main cause of this drop in heating, it might be expected that the experimental levels of heating on the slab would rapidly approach turbulent values at both Reynolds numbers since the curvature on the slab is zero. The possibility of laminarization will be discussed further after additional data are presented that will confirm the experimental trends noted in figure 13.

Surface streamlines.- Oil flow patterns obtained on the slab portion of the pressure model at $N_{Re,\infty} = 2.6 \times 10^5$ and 9.3×10^5 are shown in figures 14(a) and 14(b), respectively. The streamlines at the wall computed from theoretical values of $\tau_{w,x}$ and $\tau_{w,z}$ for both laminar and turbulent flow are included in the figure for comparison. These results are referred to in the figures as "surface viscid" streamlines. Inviscid streamlines at the edge of the boundary layer as based on the pressure distribution of figure 10 and the infinite-cylinder assumption that $\overline{w}_e$ is constant are also shown. The large deviations between the viscid and inviscid streamlines indicate that large cross flows are present.

For the lower Reynolds number (fig. 14(a)) the oil flow patterns are essentially parallel to the laminar viscid streamline. This result is in agreement with the heat-transfer trends noted in figure 13(a). At $N_{Re,\infty} = 9.3 \times 10^5$ (fig. 14(b)), the oil flow patterns are nearly parallel (except just aft of the leading edge) to the theoretical viscid streamline for turbulent flow with the invariant-turbulence eddy-viscosity model. Again these results are in agreement with the corresponding results of figure 13(b). Surface oil flow patterns caused by the boundary-layer pitot-tube rake are evident in figure 14(b). Of course, these interference patterns and those near the mounting plate should be disregarded in the comparisons with theoretical predictions.

Velocity and Mach number profiles.- In order to illustrate the behavior of the velocity and stagnation-temperature profiles obtained from the finite-difference solutions, the profile parameters $\bar{u}/u_e$, $\overline{w}/w_e$, and $\dfrac{\overline{T}_t - T_w}{T_{t,e} - T_w}$ are plotted against y/δ in figure 15. These profiles are in the stagnation region ($x/d \approx 0.1$) for the two Reynolds numbers of 2.6×10^5 and 9.3×10^5.

The chordwise velocities "overshoot" the values of u_e appreciably for $y/\delta \gtrsim 0.3$. These results are qualitatively similar to those of reference 26, where exact solutions for the laminar compressible boundary layer on swept cylinders also resulted in overshoot of the chordwise velocity profiles. In reference 26 the overshoot phenomenon was attributed to the effects of compressibility. Comparison of the computed profiles with a power-law profile

$$\left.\begin{matrix}\dfrac{\bar{u}}{u_e} \\ \\ \dfrac{\bar{w}}{w_e}\end{matrix}\right\} = \left(\frac{y}{\delta}\right)^n \tag{32}$$

for $n = 1/4$ also shown in figure 15 indicates that the present results differ greatly from simple power-law profiles, as used for example in reference 3.

Experimental and theoretical Mach number profiles are shown in figures 16(a) and 16(b) for the test Reynolds numbers of 2.6×10^5 and 9.3×10^5. The experimental Mach number profiles were obtained from the ratios of measured pitot pressures and the local static pressures given by the faired line in figure 10. The theoretical profiles were computed for laminar ($\epsilon = 0$) and turbulent flow. The invariant-turbulence model with $(l/\delta)_{max} = 0.05$ was used in the turbulent calculations.

Although there is considerable scatter in the data, comparisons at the lower Reynolds number (fig. 16(a)) indicate good agreement between the experimental results and predicted profile shapes and boundary-layer thicknesses for laminar flow. At the higher Reynolds number (fig. 16(b)) the experimental results are in excellent agreement with the predictions for turbulent flow. The pitot pressure data are therefore consistent with the results of figures 13 and 14 which showed that for $x/d > 2.0$, the boundary layer was nearly laminar at the lower Reynolds number and turbulent at the higher Reynolds number.

Boundary-layer thickness.- The boundary-layer-thickness distributions with x/d for $N_{Re,\infty} = 2.6 \times 10^5$ and 9.3×10^5 are shown in figures 17(a) and 17(b). These values of boundary-layer thickness were obtained from the Mach number profiles as indicated for typical data in figure 16. In figure 17(a) the first datum point at $x/d = 1.41$ is between the lower turbulent prediction and the laminar prediction. As x/d increases, the experimental values of δ approach the laminar predictions up to $x/d \approx 3.2$, in agreement with the results of the heat-transfer and oil flow data (figs. 13(a) and 14(a)). The last two data points at $x/d = 4.16$ and 5.16 show a slight increase from the theoretical laminar values. Since the heat-transfer data of figure 13(a) only extended to $x/d = 3.5$, any trends for $x/d > 3.5$ in the heating data are not available. Close examination of the oil-flow data (fig. 14(a)) indicates a slight upward trend near the end of the slab ($x/d \approx 5$) toward the turbulent prediction. However, this trend may be caused partly by interference from the mounting plate.

At the larger value of $N_{Re,\infty}$ (fig. 17(b)), the first datum point ($x/d = 1.41$) is between the laminar and turbulent distributions. This result is again consistent with the corresponding heat-transfer and oil-flow results of figures 13(b) and 14(b). The remaining data points are on or slightly above the turbulent result with $(l/\delta)_{max} = 0.05$, and are also consistent with the heat-transfer and oil-flow data.

Laminarization.- The preceding comparisons of data and theory for heat transfer, oil flow, Mach number profiles, and boundary-layer thickness have all given consistent results regarding the apparent trends toward laminar or turbulent flow. To provide some further indication of whether these trends were caused by laminarization of the initially turbulent boundary layer as the flow expands around the leading edge, values of a laminarization parameter have been computed. This parameter is based on the form proposed in reference 27 but modified herein for application to three-dimensional flow.

The investigation in reference 27 for two-dimensional nozzle flow showed that laminarization effects become significant when

$$\frac{\mu_e}{\rho_e \bar{u}_e^{\,2}} \frac{d\bar{u}_e}{dx} \gtrapprox 2 \times 10^{-5} \tag{33}$$

This parameter can presumably be extended to three-dimensional flow by using streamline coordinates. That is, by replacing $\bar{u}_e$ with $\bar{q}_e$ and dx with ds, the value for the parameter of 2×10^{-5} would be applicable to three-dimensional flow. Thus, when

$$\frac{\mu_e}{\rho_e \bar{q}_e^{\,2}} \frac{d\bar{q}_e}{ds} \gtrapprox 2 \times 10^{-5} \tag{34}$$

laminarization in three-dimensional flows might be expected if the same mechanisms are responsible for the phenomenon as in two-dimensional flow. However, calculated values of the parameter in relation (34), for the present configuration, were at most nearly 2 orders of magnitude smaller than 2×10^{-5}. Apparently, if the tendency noted in the present results for the heat transfer to approach laminar values aft of the leading edge were caused by laminarization effects, the criteria of relation (34) would be much smaller. A possible explanation of a smaller criterion in three-dimensional flow is as follows: It has been established that three-dimensional laminar boundary layers with large cross flows are inherently unstable and therefore premature transition due to small disturbances is likely (ref. 28). For the present configuration, disturbances generated by the leading-edge portion of the mounting plate upstream of the model apex would be sufficient to cause transition to turbulent flow at small Reynolds numbers. (See refs. 29 and 30.) Consequently, the turbulent boundary layers observed on the leading edge in the present tests may have low levels of turbulence intensity and would therefore be highly susceptible to laminarization. The small values of $(l/\delta)_{max}$ used in the theory (0.05 compared with usual values of approximately 0.09) tend to support the possibility of low turbulence levels, since small values of the mixing length cause small values of eddy viscosity which imply low levels of turbulence.

Heat Transfer With Blowing

Application of theory for nonsimilar blowing rates.- The present finite-difference procedure can be applied directly to calculation of boundary layers with surface mass transfer if the chordwise distribution of the normal velocity v_w at the surface is known. The infinite-cylinder condition that spanwise derivatives of all mean-flow quantities are zero requires that $\frac{\partial v_w}{\partial z} = 0$. This requirement is not met in the present tests because of the large spanwise variations in the permeability α as shown by figure 7(b). Equation (27) shows that the spanwise variations in v_w are directly proportional to the α variations, since $\frac{\partial \rho_w}{\partial z} \approx 0$.

Consequently, a direct comparison of theoretical predictions with data is not possible. Instead, calculations for each of the two values of $N_{Re,\infty}$ have been carried out for two different blowing rates that represent the maximum and minimum range of α values over the span interval $7.85 \leqq z/d \leqq 12.85$. These results will then be compared with the experimental data over the same span interval. Thus, the general validity of the theoretical predictions can be assessed provided that the experimental values of heat transfer on both the porous leading edge and the downstream slab are affected mainly by leading-edge blowing rates within the same span interval.

The chordwise distributions of the maximum and minimum mass flow measured over the span interval $7.85 \leqq z/d \leqq 12.85$ are shown in figure 18 as the shaded bands for values of the internal chamber pressure of 212 and 405 psia. The chordwise distributions of v_w corresponding to these maximum and minimum mass flow rates were used as inputs for the computer program. Solutions for these input flow rates were then obtained for laminar flow ($\epsilon = 0$) and turbulent flow where the invariant-turbulence or the Lettau eddy-viscosity models with $(l/\delta)_{max} = 0.05$ were used. Comparisons with experimental data for the two test Reynolds numbers of 2.6×10^5 and 9.3×10^5 will be presented. The chamber pressures used for these tests were approximately 210 and 400 psia, respectively, and hence the injection flow rates correspond to those shown in figure 18.

Results for $N_{Re,\infty} = 2.6 \times 10^5$.- The predictions of heating rates and the experimental data for $N_{Re,\infty} = 2.6 \times 10^5$ are shown in figure 19(a). The hatched bands in the figure are bounded by the upper and lower limits of the predicted heat-transfer rates for the minimum and maximum limits in $\dot{m}$ obtained from the boundaries of the shaded bands of figure 18(a). Note that the lower limit of $\dot{m}$ gives the upper limit of heating rate and vice versa. The experimental data are shown as the vertical bars. The length of these bars represents the variation of heating rates measured within the same span interval $7.85 \leqq z/d \leqq 12.85$. Since measurements of recovery temperature with blowing were not available, all experimental data and theoretical results with blowing have been

normalized with the local theoretical heating rates for no blowing. These reference values of heating rates for no blowing were computed for the same local values of T_w that occurred in the test data or were used in the theory with blowing. All reference values of heating rate in this and subsequent figures were computed with the invariant-turbulence model and $(l/\delta)_{max} = 0.05$.

Comparison of the experimental and theoretical results in figure 19(a) indicates that the boundary layer on the leading edge was turbulent and that the data agree with predictions for minimum injection rates rather than those for maximum injection rates. Just upstream of the slab interface, the experimental heating rates decrease and are within the predicted laminar limits. The data on the slab agree with laminar predictions for the minimum injection rates. The negative heating rates predicted by the theory for laminar flow with maximum blowing rates in the vicinity of $x/d \approx 0.8$ are caused by the large expansion of the flow around the leading edge. This large expansion reduces the static temperature of the injected film of air near the surface below its temperature farther upstream (which would be nearly the wall temperature). Hence, when this surface film of air is convected downstream, its temperature is below the local surface temperature and heat is then conducted from the model to the flow.

The agreement of data on the leading edge with predictions for minimum flow rates rather than the maximum rates may be attributed partly to the thermocouple installation technique, which apparently caused some local blockage of coolant flow in the vicinity of the thermocouple junctions. That is, the measured mass flow rates at these thermocouple locations tended to be somewhat smaller than most of the other measured flow rates within the span interval $7.85 \leqq z/d \leqq 12.85$ as indicated in figure 18(a) where the data points obtained at the junction locations are shown as x. However, the agreement of data on the slab with predicted heat transfer for minimum leading-edge blowing could only be attributed to the reduced levels of injection rates as z/d is reduced. (Some of these smaller values of injection rates for $z/d < 7.85$ are shown in fig. 18(a).) That is, the streamlines on the forward portion of the slab at outboard z/d locations have originated farther inboard at smaller values of z/d on the leading edge. The flow along these streamlines has therefore been subjected to generally smaller blowing rates than measured at the outboard z/d locations (see fig. 18(a)) because of the spanwise variations in permeability. The reduction in blowing rates for $z/d \leqq 7.85$ may also affect measured heating rates on the leading edge for $z/d > 7.85$. That is, the local heating rates would tend to be larger because of the upstream history of small blowing rates along streamlines. The reduction in blowing rates for $z/d < 7.85$ is therefore another cause for the tendency of the data on the leading edge to agree with predictions for minimum blowing rates.

The results shown in figure 19(a) indicate the same laminarization trends noted for this value of $N_{Re,\infty}$ in the data for no blowing (figs. 13(a), 14(a), and 17(a)). It may therefore be concluded that leading-edge blowing had no significant effect on the laminarization phenomenon. Note also, by comparison of figures 19(a) and 13(a), that the leading-edge blowing did not move transition forward, at least for the region $x/d < 4.0$.

Results for $N_{Re,\infty} = 9.3 \times 10^5$.- The chamber pressure for the tests at $N_{Re,\infty} = 9.3 \times 10^5$ was held at $p_c \approx 400$ psia. The predictions and the experimental data are shown in figure 19(b) where the same format as that of figure 19(a) for data and theory has been used. The maximum injection rate for laminar flow caused "blowoff," or boundary-layer separation, so that no solution was obtained for this condition. The predicted ratios of heating rates for the minimum injection flow, with the Lettau eddy-viscosity model, exceed unity over most of the slab because the reference $\dot{q}_{m=0}$ is for the invariant-turbulence model.

Comparisons of data and predictions shown in figure 19(b) again indicate turbulent flow on the leading edge with measured heating levels near the predictions for minimum blowing. The large decrease in the measured heating just upstream of the slab is probably again caused by laminarization. Following this minimum, the heating on the slab increases rapidly toward the predicted turbulent levels for minimum blowing. The tendency of the data on the slab to agree with predictions for minimum blowing rates at the leading edge is again attributed to the reduction in blowing with decreasing z/d. (See fig. 18(b).) These results are therefore consistent in every respect with the no-blowing results at the same Reynolds number. (Compare figs. 13(b), 14(b), 16(b), and 17(b).) Apparently, the blowing has not significantly affected the laminarization effects or transition location. The tendency of the data on the leading edge to agree with predictions for minimum blowing rates is also consistent with the blowing data at the lower Reynolds number (fig. 19(a)) but is apparently caused mainly by the spanwise variations in blowing rather than by the partial blockage of the injected air at the thermocouples as indicated by comparisons of the data for the thermocouple locations and for $z/d < 7.85$ in figure 18(b). It is concluded that both eddy-viscosity models gave heating predictions within the spread of the data for $x/d \gtrsim 2.5$.

Effect of blowing in the stagnation region.- Solutions were obtained by the finite-difference procedure for several blowing rates in addition to those shown in figure 18. The heat-transfer predictions in the vicinity of the stagnation line from these solutions are shown in figure 20. The ratios of $N_{St}/N_{St,\dot{m}=0}$ are plotted against the blowing parameter B/N_{St}, where, as in reference 31, for both data and theory the recovery factor with blowing was taken as 0.9 of the recovery factor for no blowing.

The dashed line is a correlation of the computed values to within 1 percent for both test Reynolds numbers. The experimental data are in reasonable agreement with the theoretical prediction over the range of blowing rates available. The blowing rates used for the data points were taken as the measured values at the corresponding thermocouple locations.

Also shown for comparison in figure 20 is a correlation in terms of the same parameters for flat-plate and cone data. These data are for turbulent boundary layers and the correlation is obtained from reference 31. The blowing rates for the present data are too small to provide a reliable assessment of the prediction. However, comparison of the correlation lines indicates that blowing near the stagnation line of swept cylinders reduces the heating more than a comparable blowing rate on flat plates.

Cross-Flow Predictions

As mentioned in the Introduction, the use of an inviscid-streamline coordinate system and the assumption of small cross flow simplify the boundary-layer equations. That is, the momentum equation in the streamwise direction and the energy equation become independent of the cross flow. If the inviscid streamlines are known, the problem is therefore reduced to the solution of an equivalent two-dimensional flow.

In order for the assumption of small cross flow to be generally valid, the square of the ratio of the cross-flow velocity to the streamwise velocity must be small. The maximum value of this ratio occurs at the limit as $y \rightarrow 0$ (see refs. 5 and 7, for example). The small-cross-flow criterion is then

$$\left(\frac{\tau_n}{\tau_p}\right)_w^2 << 1.0 \tag{35}$$

In the present notation this shear-ratio parameter is

$$\frac{\tau_n}{\tau_p} = \tan\left(\theta_w - \theta_e\right) \tag{36}$$

where θ_e is the angle between the spanwise coordinate direction and the local inviscid streamline direction, and $\theta_w = \text{arc tan}\left(\frac{\tau_x}{\tau_z}\right)_w$.

The chordwise distributions of the small-cross-flow parameter $\left(\tau_n/\tau_p\right)_w^2$ from several of the same solutions used in previous figures are shown in figure 21. The maximum values in the curves occur near the interface of the leading edge and slab and range from 0.17 to 0.28 for turbulent flow with no blowing. These results are consistent with the location and magnitude of maximum values of the cross-flow parameter obtained by Bradley (ref. 5) for turbulent flow on a circular cylinder at higher Reynolds numbers. These peak values from reference 5 were approximately 0.12.

The distributions from the solutions for laminar flow with no blowing are essentially independent of Reynolds number and the maximum value is 0.44, which is in agreement with corresponding values obtained in reference 7. The results given in reference 7 are for laminar boundary layers on circular cylinders with the assumption of local similarity. Interpolation between the results of reference 7 gives a maximum value for the cross-flow parameter of about 0.4 for the present conditions.

The effect of blowing increases the values of the cross-flow parameter by as much as an order of magnitude when the maximum blowing rates are used. For these conditions, the assumption of small cross flow would not be applicable to the momentum characteristics of the boundary layer such as velocity profiles, skin friction, and surface streamlines. However, the results of reference 7 indicated that heat-transfer predictions from the small cross-flow theory for laminar boundary layers were within 15 percent of the correct values when the cross-flow parameter was as large as 3.0.

CONCLUSIONS

A finite-difference method has been developed to solve the equations for compressible turbulent boundary layers on swept infinite cylinders. Predictions of surface heat transfer by the method were compared with experimental data on a blunt-slab configuration with and without leading-edge blowing. The leading edge was a hemicylinder which was swept 60° with respect to the free-stream flow direction.

A numerical procedure for solving the two-dimensional heat conduction problem in a porous matrix with one-dimensional fluid flow was also developed. This procedure was used to reduce the temperature-time history of the thermocouples near the surface of the porous leading edge to surface heat-transfer rates.

Predictions from the finite-difference method for solving the boundary-layer equations were also compared with experimental values of surface streamlines, Mach number profiles, boundary-layer thickness, and heat transfer on a similar configuration but without blowing. The tests were conducted at a stream Mach number of 8 and over a range of stream Reynolds numbers based on leading-edge diameter $N_{Re,\infty}$ of 0.92×10^5 to 9.3×10^5.

Two eddy-viscosity models which utilized general mixing-length functions scaled to the boundary-layer thickness were used in the calculations. One was termed the "invariant turbulence" model and was a scalar function based on the assumption that eddy viscosity is independent of direction. The other model was based on Lettau's vorticity-transfer hypothesis (Journal of the Atmospheric Sciences, vol. 21, no. 4, July 1964) and was also independent of direction but contained the scalar sum of two velocity-gradient terms.

The main conclusions from the investigation are as follows:

1. The finite-difference method gave reasonable predictions for heat transfer, surface streamlines, Mach number profiles, and boundary-layer thickness on the test configuration without blowing for both laminar and turbulent flow. Reasonable predictions for heat transfer on both the leading edge and slab were also obtained with nonuniform, discontinuous blowing at the leading edge.

2. Just aft of the leading edge, the turbulent boundary layer was apparently laminarized. At $N_{Re,\infty} = 2.6 \times 10^5$, the boundary layer remained essentially laminar to the end of the slab (5 nose diameters along the chord from the leading edge). At $N_{Re,\infty} = 9.3 \times 10^5$, transition back to turbulent flow occurred at about 2 diameters from the leading edge. Predictions from both eddy-viscosity models for maximum values of the ratio of the mixing length to the boundary-layer thickness $(l/\delta)_{max}$ of 0.05 were then in reasonable agreement with data. These results were based on comparisons of theoretical predictions with all measured quantities mentioned above.

3. For the blowing rates used in this investigation, leading-edge blowing had no appreciable effect on either the laminarization phenomenon or transition.

4. Comparison of values for a laminarization criterion indicated that the turbulent boundary layer on the leading edge for these tests was much more susceptible to laminarization than a comparable two-dimensional flow.

5. This increased susceptibility to laminarization is tentatively attributed to the low turbulence levels of the boundary layer on the leading edge as evidenced by the relatively small values of $(l/\delta)_{max}$ required to obtain agreement of theory with experiment.

6. Measured heat-transfer rates on the leading edge over a 4-inch span interval agreed with values predicted for the minimum injection rates measured on the leading edge over the same 4-inch interval in span. This agreement with predictions for minimum injection was attributed mainly to the smaller injection rates near the apex of the leading edge. The influence of the partial blockage of injection at the thermocouple locations on the leading edge was considered minor.

7. Downstream of the leading edge on the thin-skinned slab, the measured heating rates were also generally in agreement with predictions for the minimum injection rates on the leading edge. These results are attributed to the smaller injection rates near the apex of the leading edge due to the spanwise distribution of permeability.

8. Blowing on the leading edge increased the magnitude of the cross-flow velocities by as much as an order of magnitude. Therefore, the assumption of small cross flow, which was not used in the present method, would not be expected to provide reliable predictions with large leading-edge blowing.

REFERENCES

1. Braun, Willis H.: Turbulent Boundary Layer on a Yawed Cone in a Supersonic Stream. NASA TR R-7, 1959. (Supersedes NACA TN 4208.)

2. Vaglio-Laurin, Roberto: Turbulent Heat Transfer on Blunt-Nosed Bodies in Two-Dimensional and General Three-Dimensional Hypersonic Flow. J. Aero/Space Sci., vol. 27, no. 1, Jan. 1960, pp. 27-36.

3. Beckwith, Ivan E.; and Gallagher, James J.: Local Heat Transfer and Recovery Temperatures on a Yawed Cylinder at a Mach Number of 4.15 and High Reynolds Numbers. NASA TR R-104, 1961. (Supersedes NASA MEMO 2-27-59L.)

4. Nagel, A. L.; Fitzsimmons, H. D.; and Doyle, L. B.: Analysis of Hypersonic Pressure and Heat Transfer Tests on Delta Wings With Laminar and Turbulent Boundary Layers. NASA CR-535, 1966.

5. Bradley, Richard G.: Approximate Solutions for Compressible Turbulent Boundary Layers in Three-Dimensional Flow. AIAA J., vol. 6, no. 5, May 1968, pp. 859-864.

6. Nash, J. F.: The Calculation of Three-Dimensional Turbulent Boundary Layers in Incompressible Flow. J. Fluid Mech., vol. 37, pt. 4, July 1969, pp. 625-642.

7. Beckwith, Ivan E.: Similarity Solutions for Small Cross Flows in Laminar Compressible Boundary Layers. NASA TR R-107, 1961.

8. Bushnell, Dennis M.; and Beckwith, Ivan E.: Calculation of Nonequilibrium Hypersonic Turbulent Boundary Layers and Comparisons With Experimental Data. AIAA Paper No. 69-684, June 1969.

9. Lettau, H.: A New Vorticity-Transfer Hypothesis of Turbulence Theory. J. Atmos. Sci., vol. 21, no. 4, July 1964, pp. 453-456.

10. Young, A. D.; and Booth, T. B.: The Profile Drag of Yawed Wings of Infinite Span. Aero. Quarterly, vol. III, pt. III, Nov. 1951, pp. 211-229.

11. Ashkenas, Harry; and Riddell, Frederick R.: Investigation of the Turbulent Boundary Layer on a Yawed Flat Plate. NACA TN 3383, 1955.

12. Turcotte, Donald Lawson: On Incompressible Turbulent Boundary Layer Theory Applied to Infinite Yawed Bodies. Graduate School Aero. Eng., Cornell Univ. (Contract AF 33 (038)-21406), Sept. 1955.

13. Prandtl, L. (Suppl. by K. Wieghardt): On a New Representation of Fully Developed Turbulence. Publ. No. 13, Jet Propulsion Lab., California Inst. Technol., Aug. 1952. (Translation of "Über ein neues Formelsystem für die ausgebildete Turbulenz." Nachrichten der Akademie der Wissenschaften, Göttingen, Mathematisch-Physikalische Klasse, 1945.)

14. Blushko, G. S.: Turbulent Boundary Layer on a Flat Plate in an Incompressible Fluid. Bull. Acad. Sci. USSR, Mech. Ser., no. 4, 1965, pp. 13-23.

15. Bradshaw, P.: Calculation of Boundary-Layer Development Using the Turbulent Energy Equation. VII: Three-Dimensional Flow. NPL Aero Rep. 1286, Brit. A.R.C., Jan. 30, 1969.

16. Lettau, Heinz H.: New Hypothesis for the Relationship Between Eddy and Mean States. Phys. Fluids Suppl., vol. 10, pt. II, no. 9, Sept. 1967, pp. S79-S83.

17. Rotta, J. C.: Heat Transfer and Temperature Distribution in Turbulent Boundary Layers at Supersonic and Hypersonic Flow. AGARDograph 97, Pt. I, May 1965, pp. 35-63.

18. Johnson, Donald S.: Turbulent Heat Transfer in a Boundary Layer With Discontinuous Wall Temperature. Publ. No. 55 (OSR Tech. Note 55-289), Dep. Aeronaut., The Johns Hopkins Univ., Aug., 1955.

19. Beckwith, Ivan E.; and Bushnell, Dennis M. (With appendix C by Carolyn C. Thomas): Detailed Description and Results of a Method for Computing Mean and Fluctuating Quantities in Turbulent Boundary Layers. NASA TN D-4815, 1968.

20. Stainback, P. Calvin: Heat-Transfer Measurements at a Mach Number of 8 in the Vicinity of a 90° Interior Corner Alined With the Free-Stream Velocity. NASA TN D-2417, 1964.

21. Jones, Robert A.; and Hunt, James L.: Use of Fusible Temperature Indicators for Obtaining Quantitative Aerodynamic Heat-Transfer Data. NASA TR R-230, 1966.

22. Muskat, J.: The Flow of Homogeneous Fluids Through Porous Media. First ed., second printing, J. W. Edwards, Inc., 1946.

23. Carslaw, H. S.; and Jaeger, J. C.: Conduction of Heat in Solids. Second ed., Oxford Univ. Press, Inc., 1959.

24. Howard, Floyd G.: Single-Thermocouple Method for Determining Heat Flux to a Thermally Thick Wall. NASA TN D-4737, 1968.

25. Bradshaw, P.: The Analogy Between Streamline Curvature and Buoyancy in Turbulent Shear Flow. J. Fluid Mech., vol. 36, pt. 1, Mar. 1969, pp. 177-191.

26. Reshotko, Eli; and Beckwith, Ivan E.: Compressible Laminar Boundary Layer Over a Yawed Infinite Cylinder With Heat Transfer and Arbitrary Prandtl Number. NACA TN 3986, 1957.

27. Back, L. H.; Cuffel, R. F.; and Massier, P. F.: Laminarization of a Turbulent Boundary Layer in Nozzle Flow – Boundary Layer and Heat Transfer With Wall Cooling. Pap. No. 69-HT-56, Amer. Soc. Mech. Eng., Aug. 1969.

28. Gregory, N.; Stuart, J. T.; and Walker, W. S.: On the Stability of Three-Dimensional Boundary Layers With Application to the Flow Due to a Rotating Disk. Phil. Trans. Roy. Soc. (London), ser. A., vol. 248, no. 943, July 14, 1955, pp. 155-199.

29. Bushnell, Dennis M.; and Huffman, Jarrett K.: Investigation of Heat Transfer to Leading Edge of a 76° Swept Fin With and Without Chordwise Slots and Correlations of Swept-Leading-Edge Transition Data for Mach 2 to 8. NASA TM X-1475, 1967.

30. Bushnell, Dennis M.: Effects of Shock Impingement and Other Factors on Leading-Edge Heat Transfer. NASA TN D-4543, 1968.

31. Baronti, Paolo; Fox, Herbert; and Soll, David: A Survey of the Compressible Turbulent Boundary Layer With Mass Transfer. Astronaut. Acta, vol. 13, no. 3 (May-June), 1967, pp. 239-249.

TABLE I.- LOCATIONS OF PRESSURE ORIFICES USED

Chordwise location x/d at spanwise location z/d of –		
9.18	11.18	13.18
-0.524	-----	-0.524
-----	-0.439	-----
-.175	-----	-.175
-----	0	-----
.087	-----	.087
-----	.262	-----
.349	-----	.349
-----	.611	-----
.698	-----	.698
.911	.911	.911
1.411	1.411	1.411
2.161	2.161	2.161
3.161	3.161	3.161
-----	4.161	4.161
-----	5.161	4.161

TABLE II.- LOCATIONS OF THERMOCOUPLES ON POROUS-LEADING-EDGE MODEL

Chordwise location x/d at spanwise location z/d of –								
8.85	9.35	9.85	10.35	10.85	11.35	11.85	12.35	12.85
-0.611	----	-----	----	-0.611	----	-----	----	-0.611
-----	----	-0.349	----	-----	----	-0.349	----	-----
-.262	----	-----	----	-.262	----	-----	----	-.262
-----	----	-.087	----	-----	----	-.087	----	-----
0	----	-----	----	0	----	-----	----	0
-----	----	.175	----	-----	----	.175	----	-----
.439	----	-----	----	.439	----	-----	----	.439
-----	----	.524	----	-----	----	.524	----	-----
1.223	1.223	-----	1.223	1.223	1.223	1.223	----	1.223
-----	1.650	-----	----	1.650	1.650	1.650	1.650	-----
2.150	----	-----	----	-----	2.150	2.150	----	-----
-----	----	-----	2.650	-----	----	-----	----	-----
-----	2.900	-----	----	-----	----	-----	----	-----
-----	----	3.150	----	3.150	----	-----	----	-----
-----	3.650	-----	3.650	-----	----	-----	----	-----
-----	----	4.150	----	-----	----	-----	----	-----

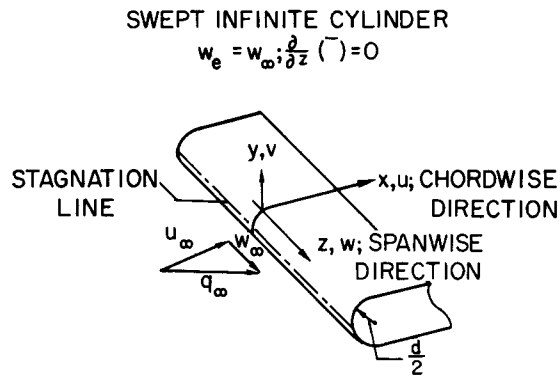

(a) Idealized flow model.

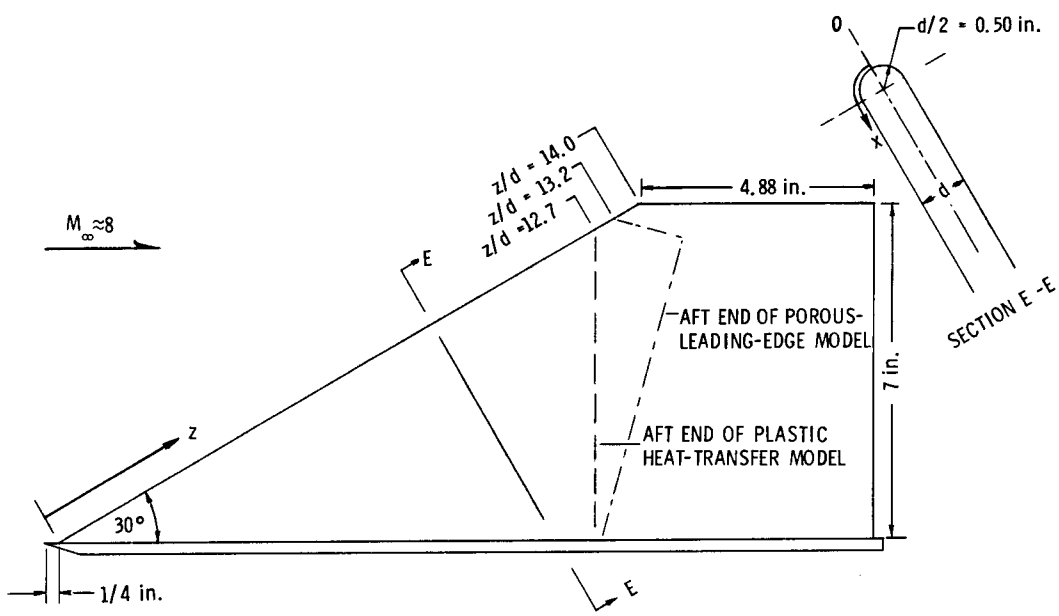

(b) Test model configurations.

Figure 1.- Basic model configuration and coordinate definitions.

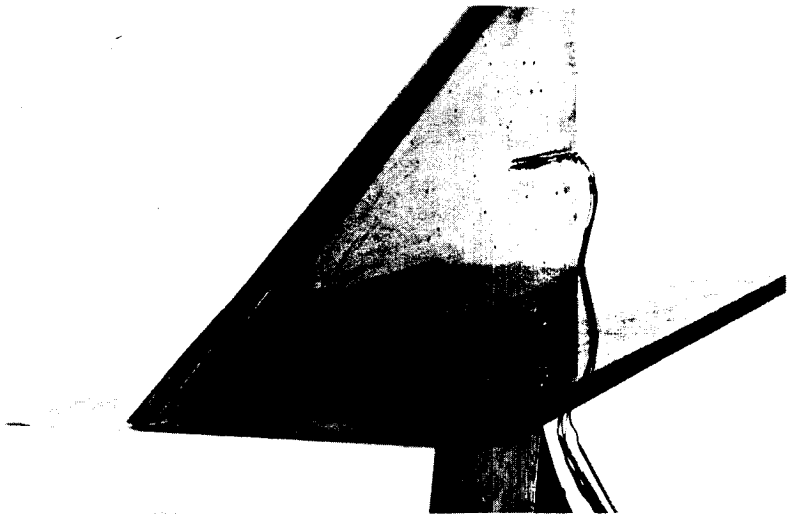

Figure 2.- Pressure model.

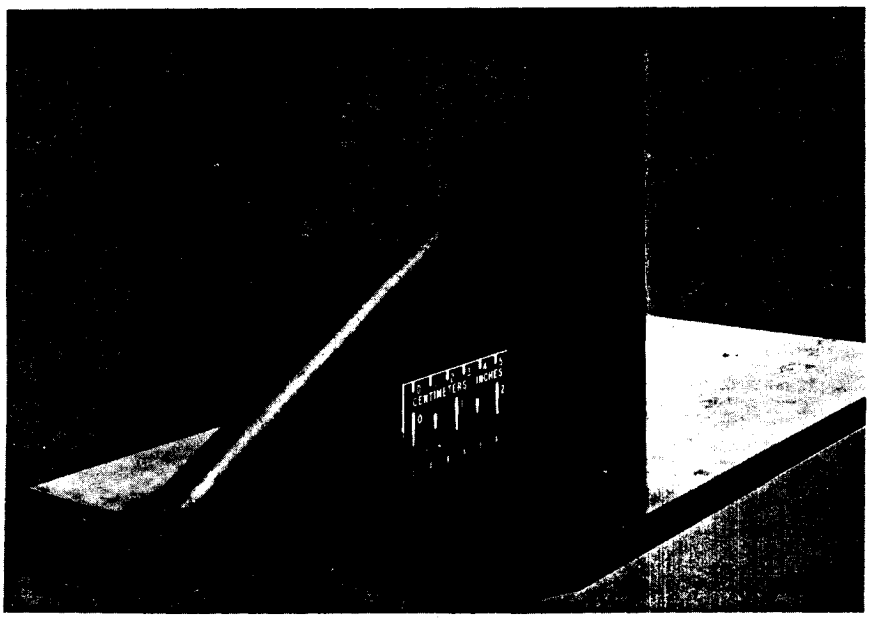

Figure 3.- Plastic model used with phase-change technique.

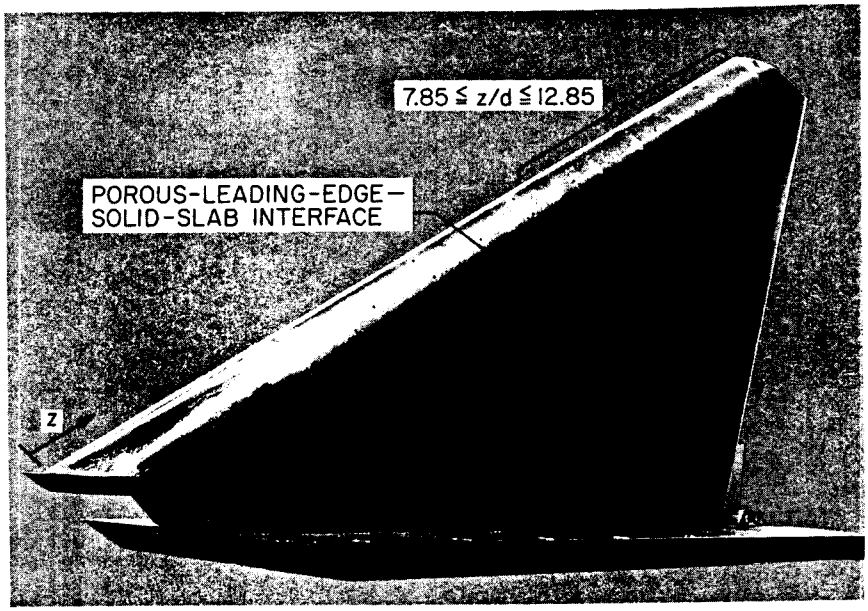

Figure 4.- Porous-leading-edge model.

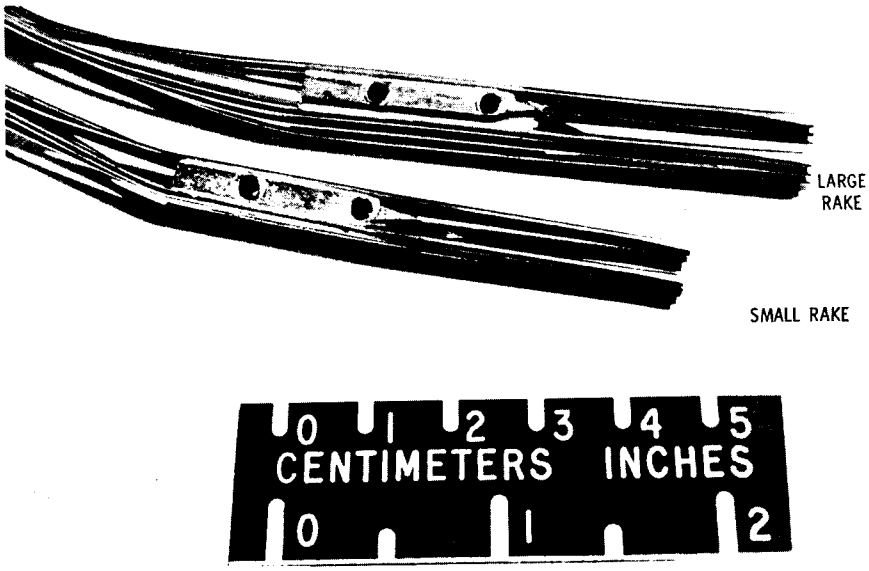

(a) Photographs of rakes.

Figure 5.- Pitot pressure rakes used for boundary-layer surveys.

SIZE OF ORIGINAL CIRCULAR TUBING

	I.D., in.	O.D., in.
SMALL RAKE	0.030	0.050
LARGE RAKE	.040	.060

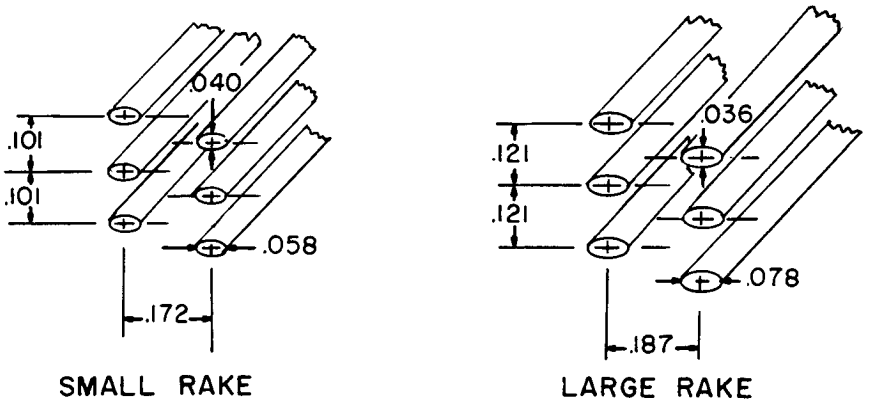

(b) Sketch of pitot tubes. Dimensions are in inches.

Figure 5.- Concluded.

Figure 6.- Plastic tip probe and alinement jig for measuring injection rates.

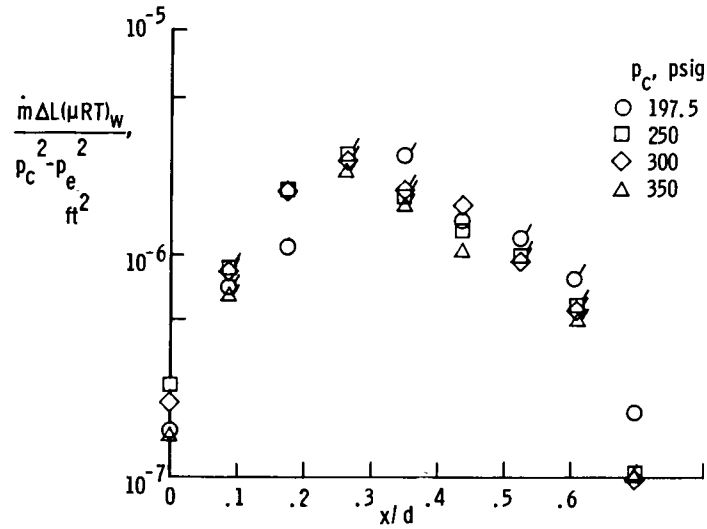

(a) z/d = 8.85 and various values of p_c.

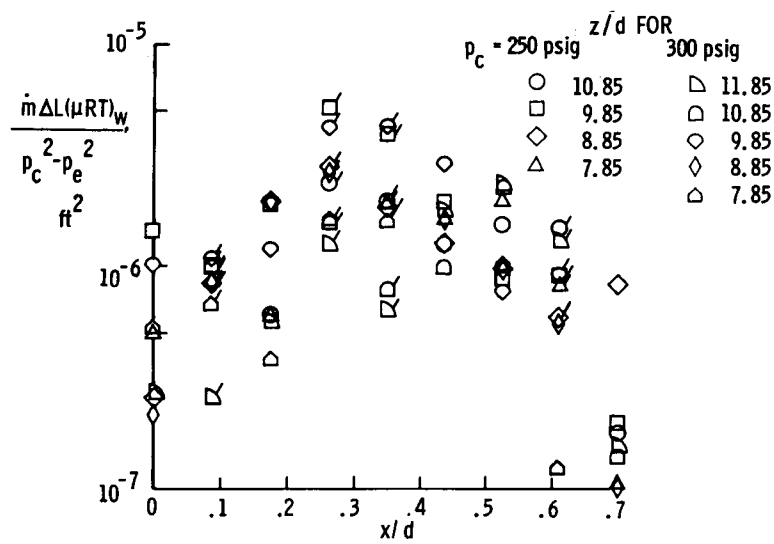

(b) 7.85 ≦ z/d ≦ 11.85. p_c = 250 and 300 psig.

Figure 7.- Chordwise distributions of permeability on porous leading edge. (Flagged symbols indicate data "folded" from negative x/d locations.)

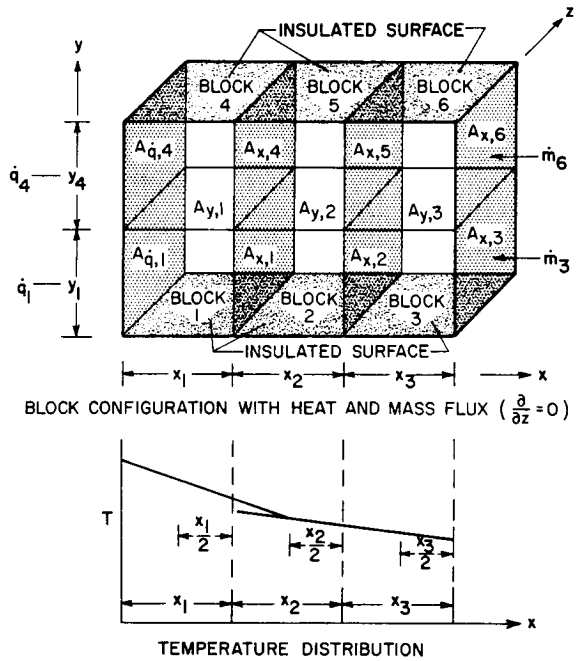

Figure 8.- Sketch of six-block heat-conduction model to illustrate method and notation. Model is assumed two dimensional; that is, derivatives of all quantities in z-direction are zero.

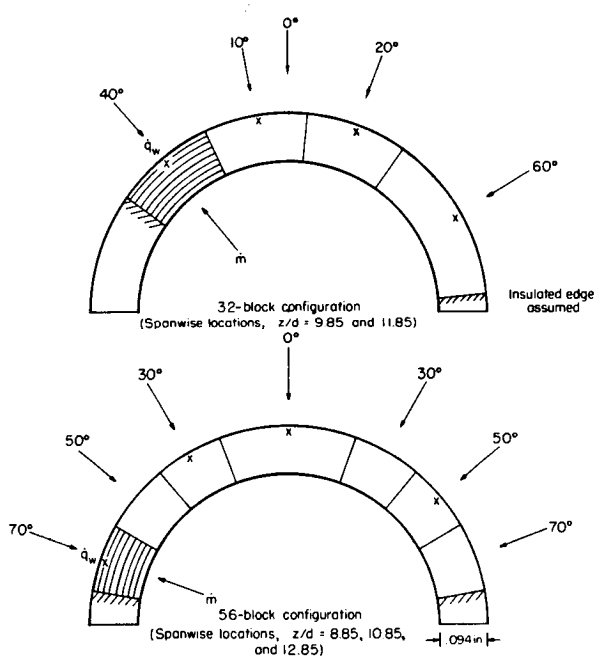

Figure 9.- Block configurations used to reduce data from porous leading edge. Thermocouple locations are given in table II and designated as x in sketch.

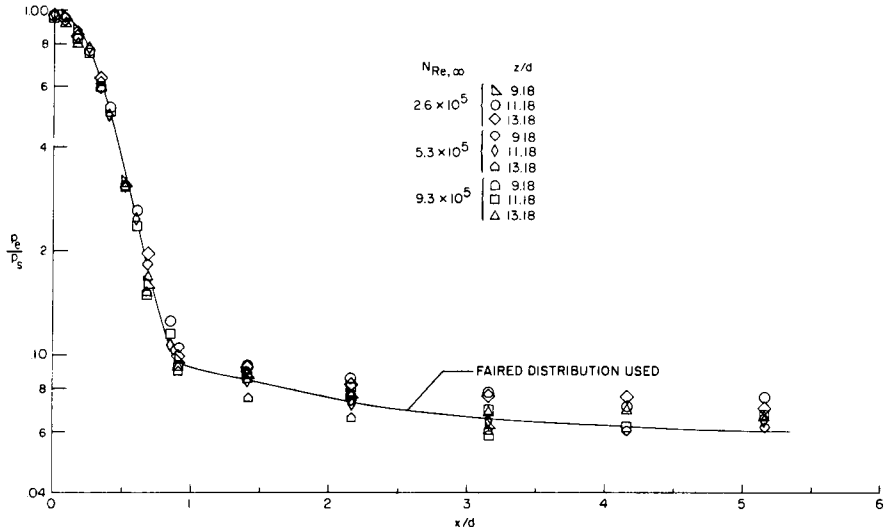

Figure 10.- Chordwise distribution of static pressures.

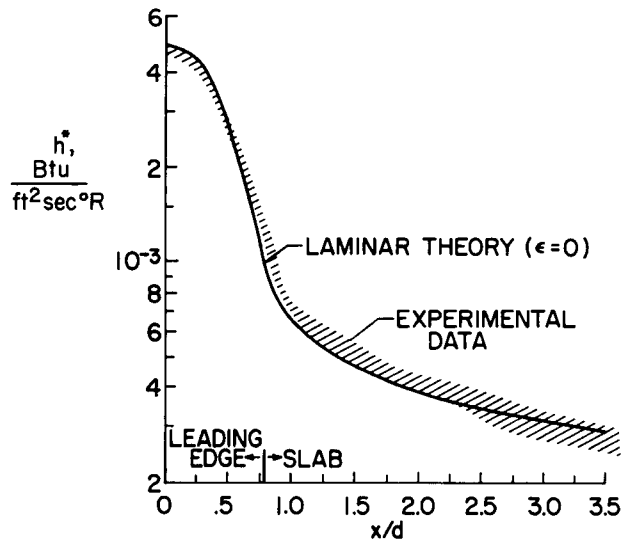

Figure 11.- Comparison of theory and data for laminar flow. $N_{Re,\infty} = 0.92 \times 10^5$; $\dot{m} = 0$; $z/d = 10.6$.

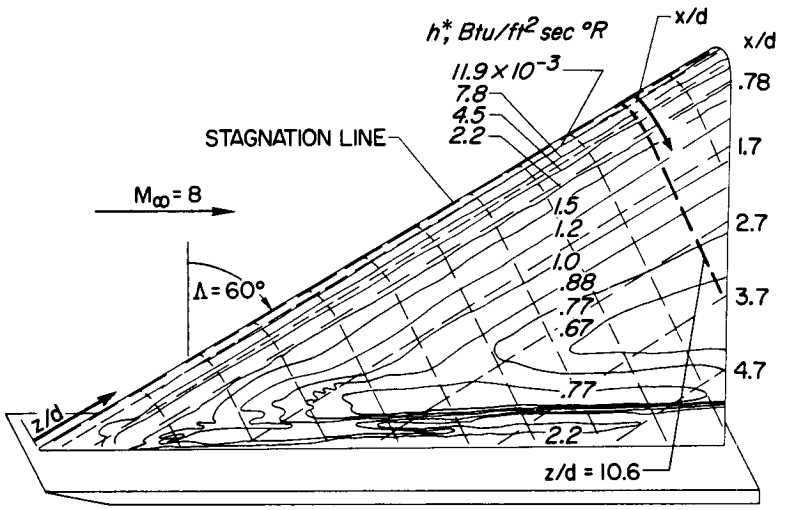

(a) $N_{Re,\infty} = 2.6 \times 10^5$.

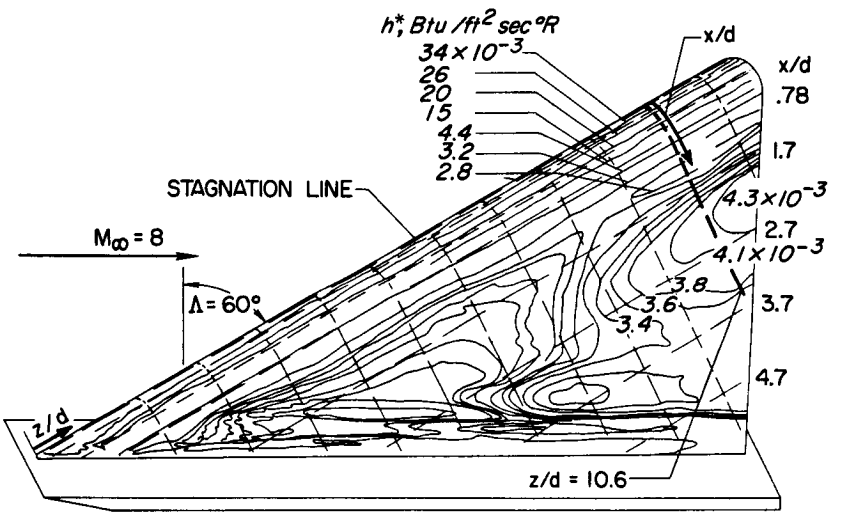

(b) $N_{Re,\infty} = 9.3 \times 10^5$.

Figure 12.- Test configuration showing heat-transfer-coefficient contours for $\dot{m} = 0$.

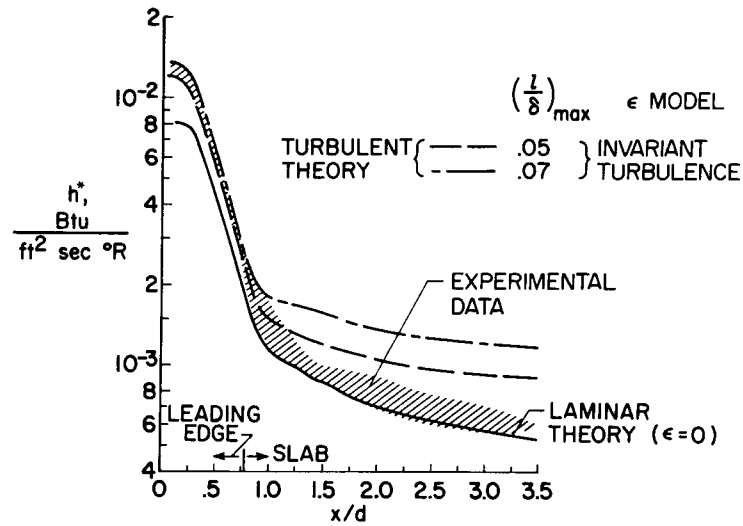

(a) $N_{Re,\infty} = 2.6 \times 10^5$.

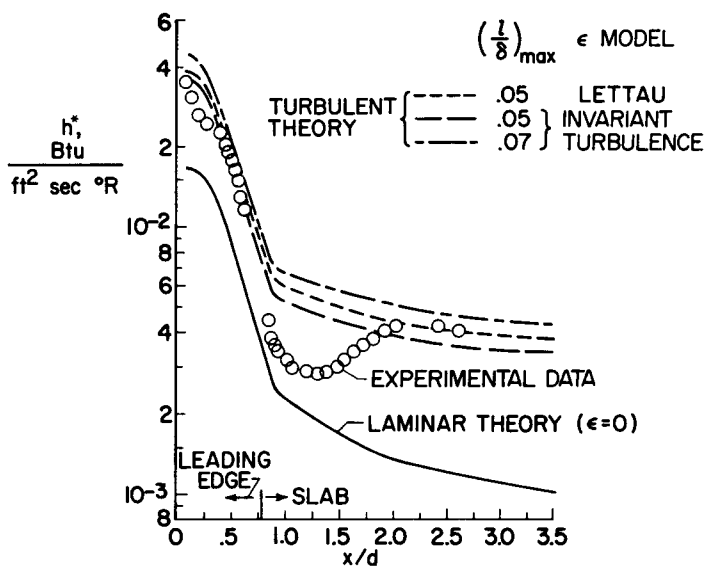

(b) $N_{R,\infty} = 9.3 \times 10^5$.

Figure 13.- Chordwise distribution of heat-transfer coefficient. $\dot{m} = 0$; $z/d = 10.6$.

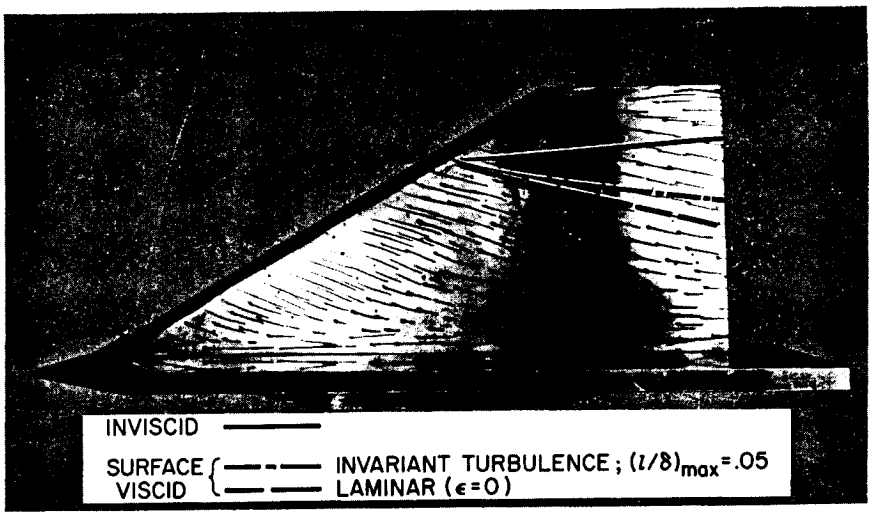

(a) $N_{Re,\infty} = 2.6 \times 10^5$.

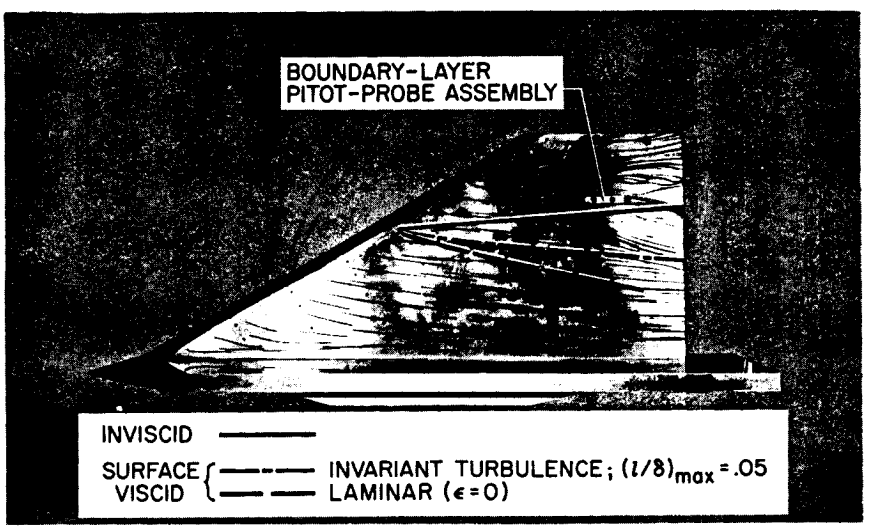

(b) $N_{Re,\infty} = 9.3 \times 10^5$.

Figure 14.- Comparisons of computed streamlines with surface oil flow lines for $\dot{m} = 0$.

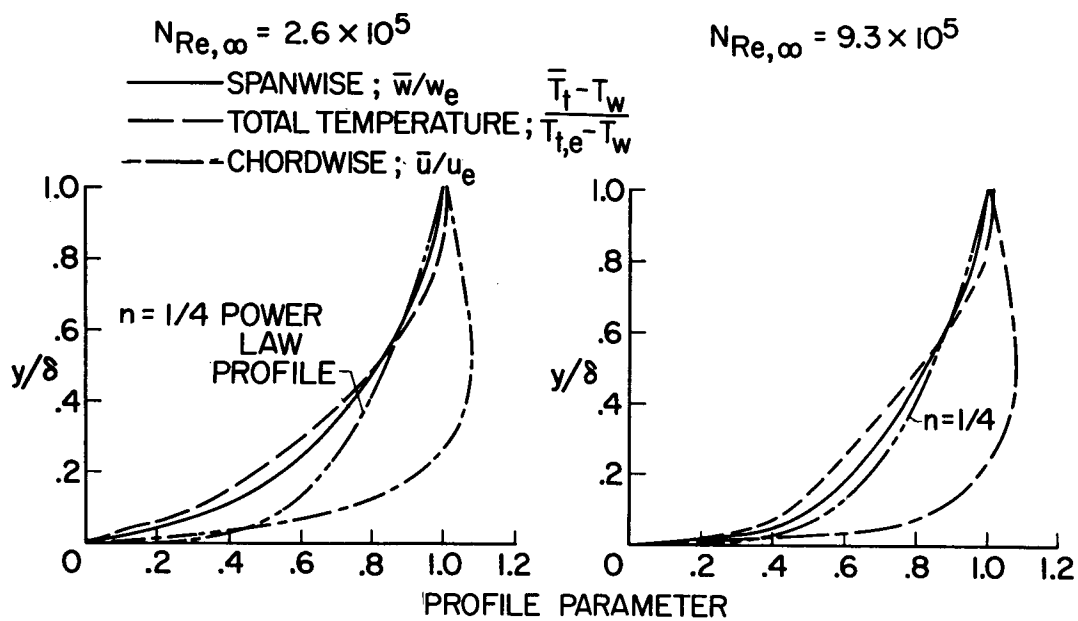

Figure 15.- Computed profiles in stagnation region $x/d \approx 0.1$. $\dot{m} = 0$.

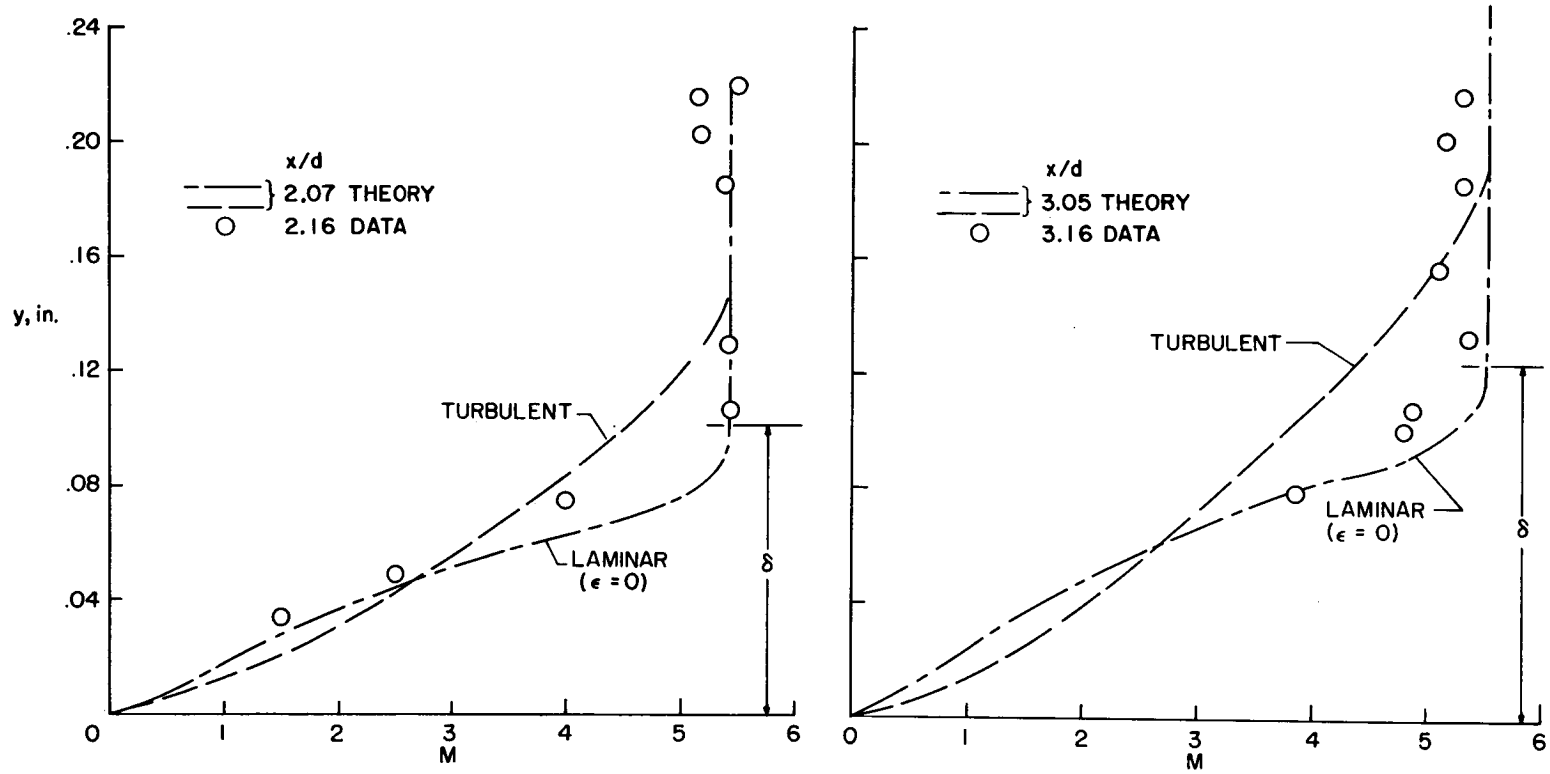

(a) $N_{Re,\infty} = 2.6 \times 10^5$.

Figure 16.- Mach number profiles. All computed profiles for turbulent flow were obtained with the invariant-turbulence model and $(\ell/\delta)_{max} = 0.05$. $\dot{m} = 0$.

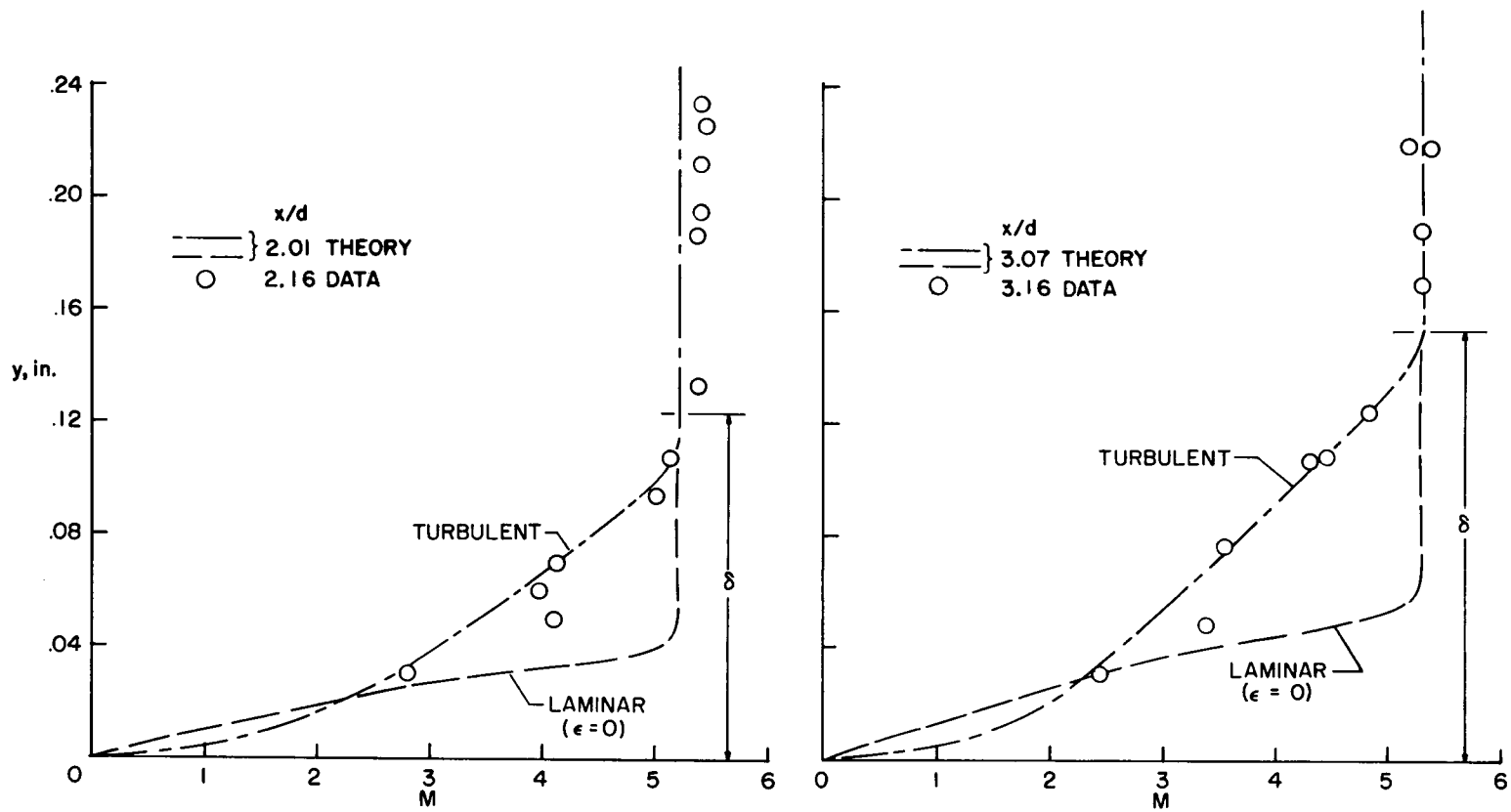

(b) $N_{Re,\infty} = 9.3 \times 10^5$.

Figure 16.- Concluded.

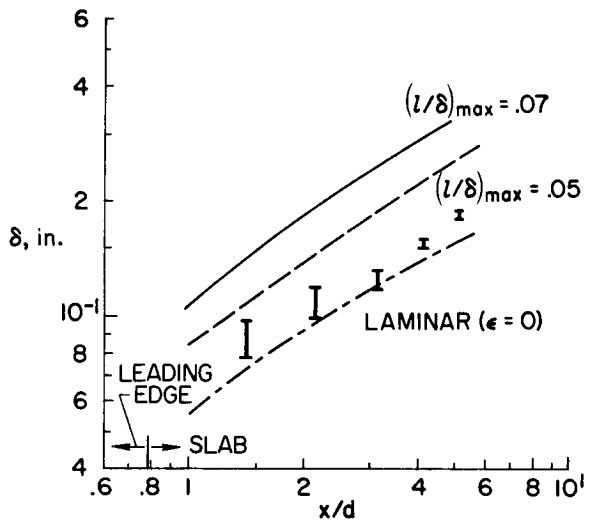

(a) $N_{Re,\infty} = 2.6 \times 10^5$.

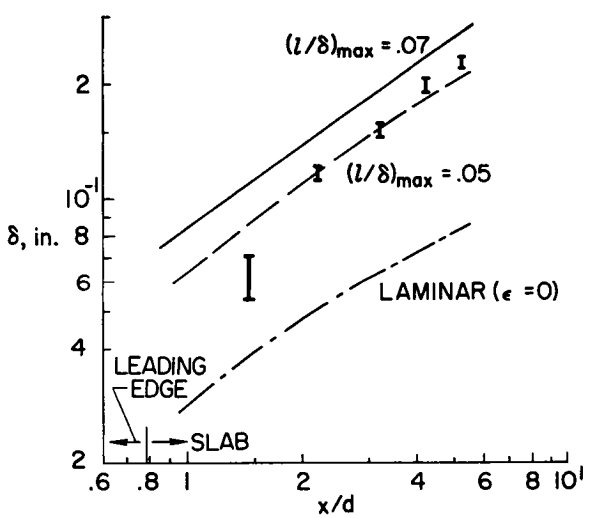

(b) $N_{Re,\infty} = 9.3 \times 10^5$.

Figure 17.- Chordwise distribution of boundary-layer thickness for $\dot{m} = 0$ and $z/d = 10.6$. Invariant-turbulence model used for the two upper lines.

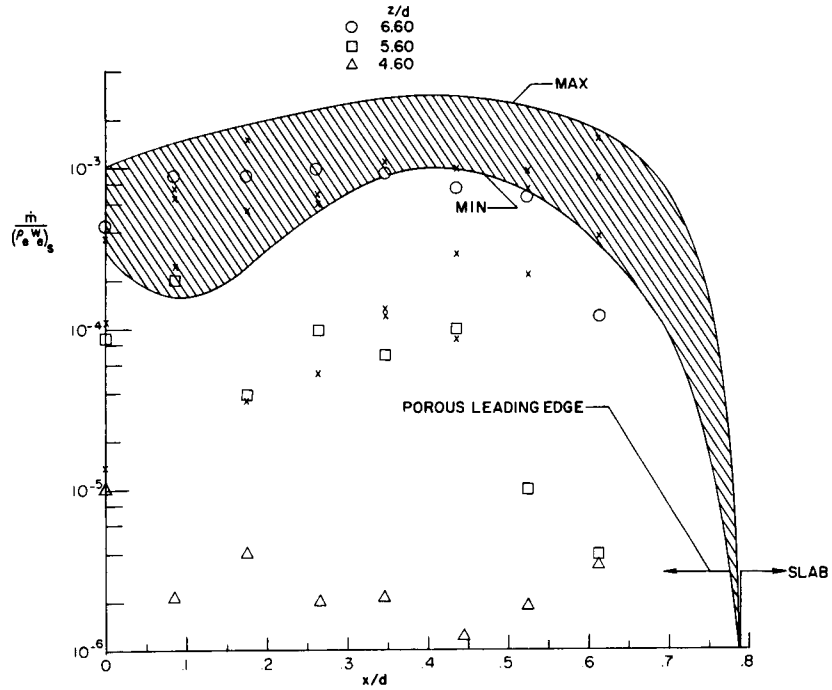

(a) p_c = 212 psia.

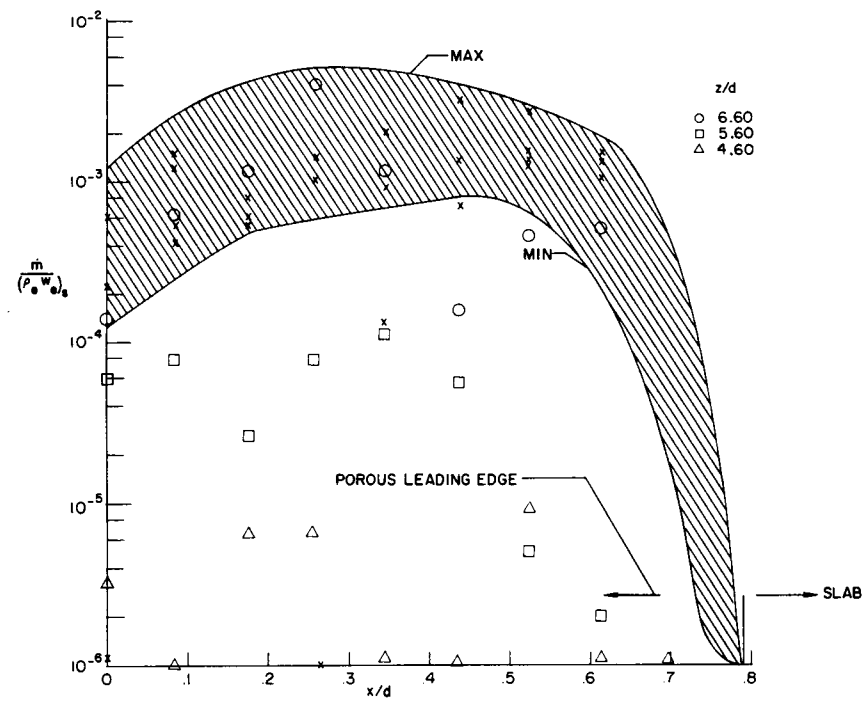

(b) p_c = 405 psia.

Figure 18.- Experimental chordwise variation of mass flow through porous leading edge. Shaded band is for $7.85 \leqq z/d \leqq 12.85$. The x symbols indicate values measured at locations of thermocouple junctions within the same z/d interval.

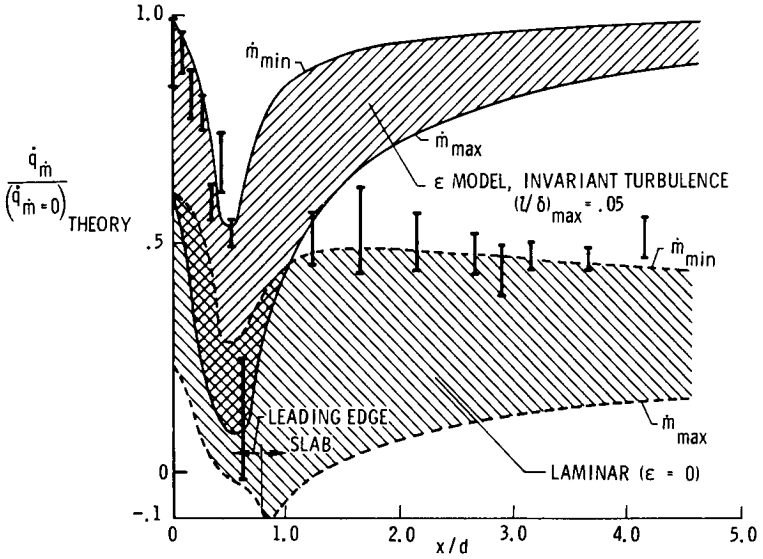

(a) $N_{Re,\infty} = 2.6 \times 10^5$ and $p_c \approx 210$ psia.

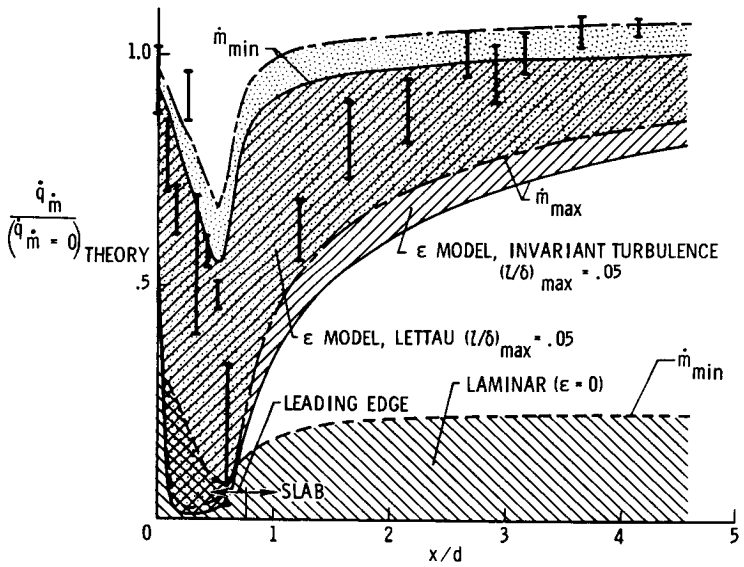

(b) $N_{Re,\infty} = 9.3 \times 10^5$ and $p_c \approx 400$ psia.

Figure 19.- Effect of blowing on chordwise heat-transfer distribution for $8.85 \leqq z/d \leqq 12.85$.

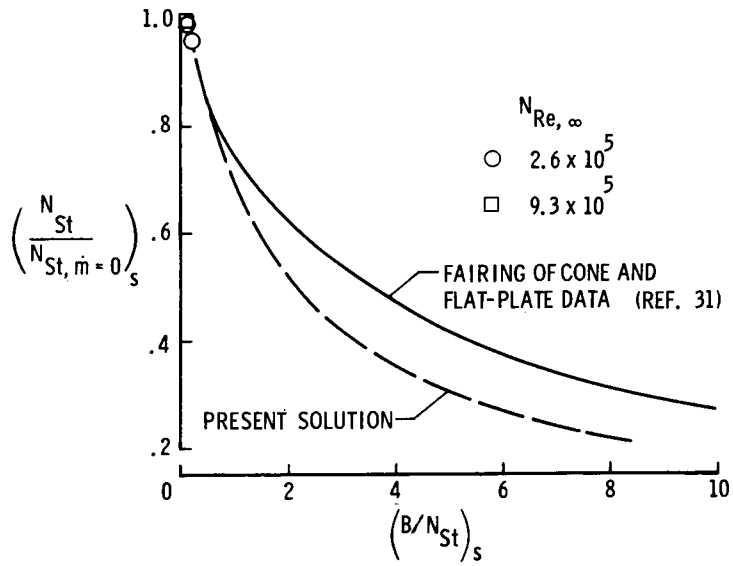

Figure 20.- Effect of blowing in the stagnation region $x/d \approx 0.1$.

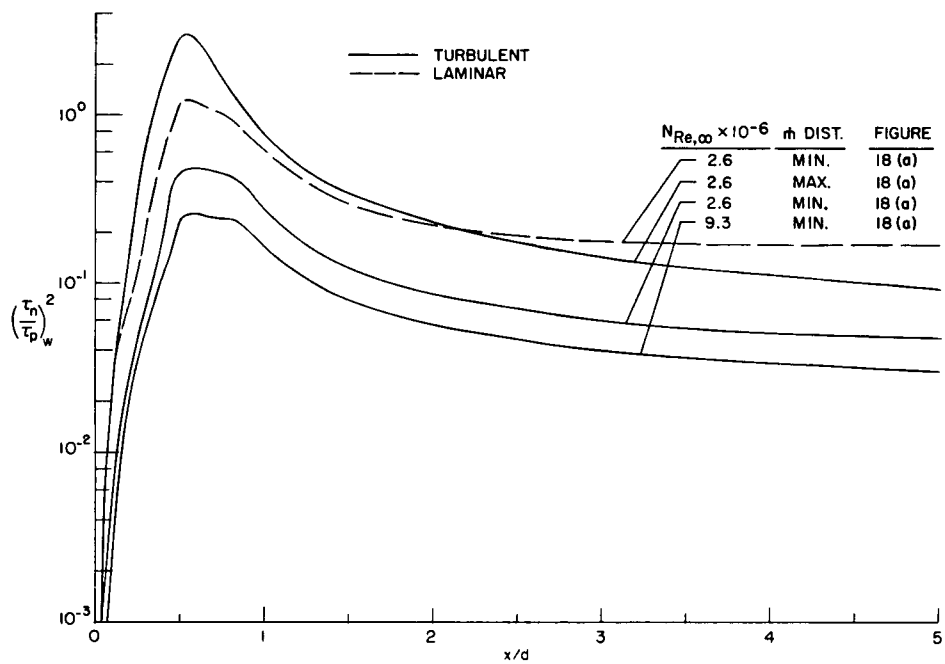

Figure 21.- Chordwise distribution of small-cross-flow parameter from theory. Invariant-turbulence model with $(\ell/\delta)_{max} = 0.05$ used for turbulent computations.

DISCUSSION

GEORGE R. INGER, McDonnell Douglas Corp.: I notice in your modeling of the eddy viscosity which is incorporated in your calculations, that in spite of rather large rates of mass transfer you ignored the explicit effect of mass transfer in the eddy model.

HUNT: It is true that the effect of mass transfer in the eddy models was not presented, but it wasn't ignored.

INGER: I'm sorry, I didn't see it on your slide.

HUNT: You are correct in mentioning that. Perhaps we should have presented it. The effect of mass transfer on the eddy viscosity was incorporated through the Van Driest damping function used in the near wall region of the mixing length model. A coefficient in the damping term was made a function of the blowing rate.

INGER: Then you incorporated it the same as the others?

HUNT: Yes.

WILBUR L. HANKEY, USAF, Aerospace Research Laboratory: I have a couple of questions. First, how did you start the calculations at the stagnation point, and did your analyses check with the classical stagnation-point solution? In particular, I thought at least in the simple turbulent theories, heating did not occur at the stagnation point but near the sonic point.

The other question is, what proof do you have that the flow was turbulent in the stagnation region? Looking at the data I might contend that the flow was laminar all the way to the slab and then becoming turbulent instead of relaminarizing as you contend.

HUNT: To answer your second question first, because I think I can answer that one better, we compared quite a few simple theories on the stagnation line with the experimental data and the agreement was acceptable. Everything we had indicated turbulent flow on the leading edge. Bushnell has made heat-transfer measurements on 60° swept cylinders with the same leading-edge radius at these Reynolds numbers and concluded that the flow was turbulent on and in the vicinity of the stagnation line.

I have to say I feel very strongly that the boundary layer is turbulent on the leading edge. The only thing that I have to verify this is that quite a number of theories indicate that it is turbulent there, not only this one. I tried simpler theories on the leading edge that Beckwith reported on earlier, and I am quite confident that in the vicinity of the stagnation line the flow is turbulent.

Now, as far as your first question, how do we start the procedure on the leading edge of the swept slab, I do know that we had to have a very small mesh size. Since

Beckwith is the program man, he probably should answer this. Do you want to say anything, Ivan?

BECKWITH: As far as starting the solution is concerned, what we had to do was just to take a number of very small steps, starting a finite distance away from the leading edge, and the solution would converge to unique profiles and unique boundary-layer thicknesses corresponding to whether you had zero eddy viscosity or finite values, that is, according to whether the flow was laminar or turbulent.

Now, I might just remark also on the other question as to whether or not the flow was really turbulent at the leading edge. I think the strongest item might be the fact that the heat transfer is above the laminar theory, and presumably the laminar theory is correct. Of course, the turbulent theory can be questioned, but the agreement over a range of Reynolds numbers is convincing.

RAYMOND SEDNEY, Martin Company: I find it very difficult to understand why you concluded you have relaminarization anywhere.

HUNT: I said relaminarization, but perhaps the term is laminarization.

SEDNEY: I want to use your term. I wonder if you have firm evidence for it.

HUNT: We have three different types of measurements and they all agree – boundary-layer thickness, wall-shear direction, and heat transfer. I know this is not answering your question, but the way I look at it, the data are your judge.

METHODS OF ANALYZING PROPELLER AND ROTOR BOUNDARY LAYERS WITH CROSSFLOW

W. J. McCroskey
U.S. Army Aeronautical Research Laboratory
Moffett Field, Calif.

and

H. A. Dwyer
University of California
Davis, Calif.

N70-21371

SUMMARY

Secondary effects in the boundary layers on propellers and helicopter rotor blades produce skin friction and separation characteristics that differ from those on classical two-dimensional airfoils. These effects can be analyzed and computed by the methods described in this paper, which include two approximate differential analyses and a finite difference numerical procedure. The combined numerical and analytical results demonstrate explicitly the detailed nature of laminar viscous flows on rotor blades and propellers.

INTRODUCTION

Rotating blades provide some of the most complex problems to be found in the field of fluid dynamics. For example, a typical helicopter rotor in high speed forward flight experiences centrifugal and Coriolis forces, separated flow and stall phenomena, turbulence, periodic variations in flow speed and direction, and compressibility effects. Furthermore, these phenomena occur in complex three-dimensional patterns, and the local flow field around one blade may be strongly influenced by the tip vortex and wake shed from another. Present analytical tools available to designers are incapable of analyzing these combined effects completely, partly because so little is known about the viscous phenomena that occur in rotating environments. In this paper we shall examine some of the complicating factors that occur in the boundary layer on rotating blades, and we shall discuss some methods of analysis that have been developed for treating laminar incompressible flows.

Basically, the flow around a propeller or helicopter blade section is similar to that about a classical airfoil. In figure 1 we have depicted the evolution of complications as one proceeds from the flows we know the most about, which are two-dimensional steady flows about classical airfoils, to the flows that we know the least about, which are the complex three-dimensional unsteady flows in the rotating environment of helicopter rotor blades in forward flight. We know from experience that the forces and moments produced

on rotating blades resemble those on their two-dimensional counterparts, but there are important differences also. Because of the similarity, we shall refer to the chordwise flow as the primary flow, and because of the differences caused by secondary effects, we shall refer to the flow in the spanwise direction as the crossflow.

This is illustrated in figure 2, where the x-direction is the chordwise direction and the z-coordinate signifies the spanwise direction. These moving, rotating coordinates are attached to the leading edge of the blade. If we consider a helicopter rotor in forward flight, then a relative wind with velocity V_1 approaches the blade in the plane of rotation. For a hovering rotor or conventional propeller, a relative wind with velocity V_2 approaches the blade along the axis of rotation. This velocity is generally small compared to Ωz for a helicopter in hover and is comparable to Ωz for a conventional propeller.

Most of the previous analytical work on rotating blades of these types was done by W. R. Sears and his co-workers (refs. 1-7) in the 1950's. Viscous problems involving pure rotation were treated within the framework of the small-crossflow approximation. Graham (ref. 7), Banks and Gadd (ref. 8), and Velkoff (ref. 9) performed integral analyses, the latter being the first attempt to include the translational velocity V_1. Recently, McCroskey and Yaggy (ref. 10) formulated regular perturbation expansions for forward flight, and this formulation provides the basis for the first main part of this paper. The basis for the numerical analysis used in this paper was developed by Dwyer (ref. 11) in connection with another problem. The most recent treatments of rotating blades are by Warsi (refs. 12, 13).

The methods of analysis considered herein include a perturbation analysis, an analysis of reduced or linearized equations, and direct numerical integration of the boundary-layer equations of motion. The perturbation analysis, which evolves from small-crossflow and quasi-steady approximations, allows us to reduce the number of independent variables from four to two, but the method is not useful in predicting separation characteristics. We shall display the results of this analysis for the flat plate case and use the derivations to demonstrate the role and importance of the various secondary terms. The linearized analysis is more relevant to problems involving separation and in giving the qualitative details of the flow field. With the numerical analysis, we examine the flow field without approximations and up to the point of separation. Also the numerical calculations are used to evaluate the significance of the approximations made in the other analyses.

We have only considered laminar incompressible flows; we have neglected the effects of the complex trailing vorticity in the inviscid flow; and we have not calculated the flow in the case of oscillating angle of attack. Within these limitations, however, the combination of the three methods of analysis gives us a complete theoretical understanding of the flow and detailed knowledge of the origin of the various secondary terms, their size, and their significance in affecting the primary flow.

NOMENCLATURE

a, b	constants
c	chord
C_L	lift coefficient
C_p	local pressure coefficient
f, F	chordwise flow velocity functions
g, G	spanwise flow velocity functions
i, m, n	indices
p	pressure
P, Q	inhomogeneous functions defined in the appendix
t	time
u	chordwise velocity in boundary layer
u_o	reference velocity, $\Omega z + V_1 \sin \Omega t$
U_e	chordwise velocity at outer edge of boundary layer
v	vertical velocity in boundary layer
V_1	translational velocity in plane of rotation
V_2	translational velocity along axis of rotation
w	spanwise velocity in boundary layer
W_e	spanwise velocity at outer edge of boundary layer
x	curvilinear chordwise coordinate
X	Cartesian chordwise coordinate
y	curvilinear coordinate normal to airfoil surface
Y	Cartesian coordinate along axis of rotation
z, Z	Cartesian spanwise coordinates
α	angle of attack
δ	boundary-layer thickness

ε	expansion parameter, $\frac{x}{z}$
ζ	spanwise coordinate, $\frac{z}{c}$
η	vertical boundary-layer coordinate, defined as used
μ	expansion parameter, $\frac{V_1}{\Omega z}$
ν	kinematic viscosity
ξ	chordwise coordinate, $\frac{x}{c}$
ρ	density
τ	dimensionless time, also shear stress
τ_B	local instantaneous Blasius shear stress (two-dimensional)
Φ	unit potential function
ψ	azimuthal angle
Ω	blade angular velocity

ANALYSES

General Formulation

Because of the slender planform of the rotating blades that we shall consider, it is advantageous to adopt Cartesian axes (X,Y,Z) fixed to the leading edge of the moving blade, as shown in figure 2. We have utilized a left-handed coordinate system, so that we may retain standard two-dimensional terminology for the primary flow and denote Z as the spanwise direction. Thus, the blade rotates about the Y-axis, and this axis may translate either along or perpendicular to itself.

In the case of translation along the Y-axis (i.e., a propeller), the translational velocity V_2 influences the boundary layer only by virtue of its effect on the contraction of the propeller slipstream, which produces an inviscid crossflow velocity, W_e.[1] This problem is essentially a steady, quasi-two-dimensional one in rotating coordinates. However, in the case of a helicopter rotor flying forward at velocity V_1, the translational velocity approaches the blade at a yaw angle $\psi = \Omega t$ relative to the leading edge; therefore, the problem is both highly three-dimensional and unsteady, even in the rotating system. We shall see shortly the magnitude of the complications introduced by V_1.

---

[1]This inviscid crossflow can be large for a hovering helicopter rotor, but it decreases rapidly with increasing V_2.

The appropriate laminar flow equations for the curvilinear boundary-layer coordinates shown in figure 2 have been presented in reference 10, and are the following:

continuity
$$\frac{\partial u}{\partial x} + \frac{\partial v}{\partial y} + \frac{\partial w}{\partial z} = 0 \tag{1}$$

x-momentum
$$\frac{\partial u}{\partial t} + u\frac{\partial u}{\partial x} + v\frac{\partial u}{\partial y} + w\frac{\partial u}{\partial z} - 2\Omega w \cos\alpha = \nu\frac{\partial^2 u}{\partial y^2} - \frac{1}{\rho}\frac{\partial p}{\partial x} + \Omega^2 X \tag{2}$$

z-momentum
$$\frac{\partial w}{\partial t} + u\frac{\partial w}{\partial x} + v\frac{\partial w}{\partial y} + w\frac{\partial w}{\partial z} + 2\Omega u \cos\alpha = \nu\frac{\partial^2 w}{\partial y^2} - \frac{1}{\rho}\frac{\partial p}{\partial z} + \Omega^2 Z \tag{3}$$

Here α is the angle between the x and X axes, and the pressure gradients are related to the potential flow as follows:

$$-\frac{1}{\rho}\frac{\partial p}{\partial x} = \frac{\partial U_e}{\partial t} + U_e\frac{\partial U_e}{\partial x} + W_e\frac{\partial U_e}{\partial z} - 2\Omega W_e - \Omega^2 X$$

$$= \frac{\partial U_e}{\partial t} + U_e\frac{\partial U_e}{\partial x} + W_e\frac{\partial W_e}{\partial x} - \Omega^2 X \tag{4}$$

$$-\frac{1}{\rho}\frac{\partial p}{\partial z} = \frac{\partial W_e}{\partial t} + U_e\frac{\partial W_e}{\partial x} + W_e\frac{\partial W_e}{\partial z} + 2\Omega U_e - \Omega^2 Z$$

$$= \frac{\partial W_e}{\partial t} + U_e\frac{\partial U_e}{\partial z} + W_e\frac{\partial W_e}{\partial z} - \Omega^2 Z \tag{5}$$

Mathematically, equations (1) - (3) can be classified as parabolic, with initial value problems posed in the x, z, and t directions, a boundary value problem posed in the y-direction, and inhomogeneous "forcing functions" given by equations (4) - (5).

The boundary conditions for equations (1) - (3) are no-slip at $y = 0$, and $u = U_e$, $w = W_e$ at $y = \delta$. In general, the determination of U_e and W_e is extremely difficult; in this paper, we shall use the solutions of reference 10 for infinite blades with constant circulation, given below.

$$U_e = (\Omega z + V_1 \sin \Omega t)\frac{\partial \Phi}{\partial X} \tag{6}$$

$$V_e = (\Omega z + V_1 \sin \Omega t)\frac{\partial \Phi}{\partial Y} = 0 \tag{7}$$

$$W_e = \Omega(\Phi - 2X) + V_1 \cos \Omega t \tag{8}$$

The use of $\Phi = \Phi\ (X, Y = 0,\ t)$, which is the potential solution for two-dimensional flow of unit mean speed past the airfoil section in question, is a direct extension of the solutions of Sears (refs. 1, 2).

The nonuniform thickness of the boundary layer can cause complications in obtaining solutions, and therefore, it is convenient to introduce a coordinate transformation that reduces the variation in boundary-layer thickness. The ones utilized in the present paper are

$$\xi = \frac{x}{c}, \qquad \eta = y\sqrt{\frac{\Omega z + V_1 \sin \Omega t}{2\nu x}}, \qquad \zeta = \frac{z}{c}, \qquad \tau = \Omega t$$

for the perturbation analysis and

$$\xi = \frac{x}{c}, \qquad \eta = y\sqrt{\frac{\Omega z + V_1 \sin \Omega t}{2\nu x}\left(\frac{\partial \Phi}{\partial x}\right)}, \qquad \zeta = \frac{z}{c}, \qquad \tau = \Omega t$$

for the numerical calculations. The latter case introduces an extra term into the transformed momentum equations, but this is accompanied by rendering the boundary-layer thickness more nearly constant.

Although the boundary conditions in the η-direction are obtained from the inviscid flow equations, the initial conditions in the t-, x-, and z-directions must be obtained by other means. Since we are only interested in the periodic solutions ultimately obtained at large t, we may start at $t = 0$ with any convenient set of velocity profiles, such as the two-dimensional solution. Along the leading edge, $x \to 0$, the boundary-layer equations reduce to a Blasius flow for sharp bodies and to a two-dimensional stagnation-point flow for blunt bodies; therefore, these classical solutions represent the proper initial conditions in the x-direction. In the z-direction, however, the crossflow in the boundary layer is both positive and negative, and there is no "starting position" for the numerical computations where w is either zero or known beforehand. Also, great care must be exercised when the crossflow velocity changes sign, lest numerical instabilities appear in the finite difference techniques.

The problem of negative crossflow was overcome by requiring that the finite difference operator $(u/\Delta x + w/\Delta z)$ in the momentum equations be positive. The lack of velocity profiles at an initial value of z was handled by an iterative technique described in the section "Direct Numerical Integration." As will be seen from the results, this iterative method of calculation proved to be very accurate in predicting the velocity profiles at a given z station.

Perturbation Analysis

Our basic procedure in this case is to perform a regular perturbation expansion of the unsteady, three-dimensional equations of motion, employing quasi-steady and small-crossflow approximations to determine the order of

magnitude of the various terms in equations (1) - (5). In this section only the main features of the analysis will be described; further details are given in the appendix.

Although the perturbation analysis is suspect near separation, it can be used to predict most of the boundary-layer flow on rotors and propellers. Furthermore, it is extremely useful in providing a basic theoretical understanding of the relative significance of various crossflow and unsteady effects and the mechanisms by which these effects influence the primary flow. From a computational standpoint, the perturbation analysis offers the advantages that, first, the equations are reduced from four to two independent variables, and second, all the equations except the lowest order primary flow equation are linear.

Implicit in equations (2) and (3) is the classical boundary-layer approximation, $\partial/\partial x \ll \partial/\partial y$, valid by virtue of the "thinness" of the viscous layer. The small-crossflow approximation that we invoke is actually a crossflow *derivative* approximation, expressed as $\partial/\partial z \ll \partial/\partial x$. This inequality is generally appropriate for propellers and helicopter blades by virtue of their "slenderness," or high aspect ratio. Likewise, the Coriolis and centrifugal forces in the x-momentum equation are relatively small, as shown in references 3 to 10, although they are relatively large in the z-momentum equation.

The quasi-steady approximation of neglecting partial derivatives with respect to time is based on the observation that the fundamental reduced frequency is $\Omega x/(\Omega z + V_1 \sin \Psi)$, which is generally small.[2] In reference 10, this reduced frequency was shown to be of the same order as $(\partial/\partial z)/(\partial/\partial x)$, so that the small crossflow and quasi-steady approximations are mutually consistent. Accordingly, these approximations should be employed only where $\Omega x/(\Omega z + V_1 \sin \Psi) \ll 1$.

From the criteria just described, it is clear that two ratios are vital: a length parameter, $\varepsilon = x/z$, and a velocity parameter, $\mu = V_1/\Omega z$. These are incorporated into the solutions as follows:

$$\frac{u}{\Omega z} = (1 + \mu \sin \tau)[f_o'(\xi,\eta) + \varepsilon f_1'(\xi,\eta,\tau) + \varepsilon^2 f_2'(\xi,\eta,\tau) + \ldots] \tag{9}$$

$$\frac{w}{\Omega z} = \mu \cos \tau \; g_o'(\xi,\eta) + \varepsilon g_1'(\eta,\xi,\tau) + \varepsilon^2 g_2'(\eta,\xi,\tau) + \ldots \tag{10}$$

where

$$\xi = \frac{x}{c} \qquad \eta = y\sqrt{\frac{\Omega z(1 + \mu \sin \Omega t)}{2\nu x}} \qquad \tau = \Omega t = \Psi \tag{11}$$

[2]We should mention that the dynamics of highly loaded rotors may introduce higher harmonics of blade motion, and the time derivative of angle of attack is an important parameter (cf. the recent paper by Harris, ref. 14).

and

$$f_1'(\xi,\eta,\tau) = \frac{\mu \cos \tau}{(1 + \mu \sin \tau)^2} F_{11}'(\xi,\eta) \tag{12}$$

$$f_2'(\xi,\eta,\tau) = \frac{F_{20}'(\xi,\eta)}{(1 + \mu \sin \tau)^2} + \frac{\mu \sin \tau}{(1 + \mu \sin \tau)^3} F_{21}'(\xi,\eta) + \frac{\mu^2 \cos^2 \tau \, F_{22}'(\xi,\eta)}{(1 + \mu \sin \tau)^4} \tag{13}$$

etc. Note that the F's are functions only of ξ and η. The appropriate differential equations are given in the appendix.

The special case of a flat plate blade, for which the F's are universal functions independent of ξ, was examined in reference 10. These results are shown in figure 3 and table 1, including corrected values for F_{21}' and F_{22}'. It should be mentioned that F_{11} has been split into a component F_{1u} due to unsteady effects, and a component of opposite sign F_{1y} due to yaw effects. The analogous universal functions for the crossflow are shown in figure 4.

It is interesting that the analysis outlined above for unsteady three-dimensional flows incorporates the physical and mathematical features of several previous studies for less complicated flows. Tan (ref. 4) outlined the perturbation expansion procedure for pure rotation, and Liu (ref. 5) calculated the expansions to second order in ε for both the flat plate and the "cubic airfoil," which has $U_e = 3u_o(\xi - \xi^3)$. Liu also generalized the geometry to include spanwise taper of the blade and cases where the axis of rotation is not at the leading edge. This offset of the axis of rotation produces a spanwise flow that, in a quasi-steady sense, is equivalent to the crossflow produced in forward flight by $V_1 \cos \Psi$. To first order in ε, this effect is represented by F_{1y}, equal to Liu's F_{11} for the flat plate, and it helps to delay separation when w is negative (i.e., $90° < \Psi < 270°$).

On the other hand, the sinusoidal variation in U_e is analogous to that for two-dimensional unsteady flows studied by Lighthill (ref. 15), Moore (ref. 16), and subsequent investigators. To order ε, this unsteady effect is represented by F_{1u}, equal to Moore's f_o for the flat plate, and it helps to delay separation when the blade is accelerating (e.g., when $(\partial/\partial t)(V_1 \sin \Omega t) > 0$). In the rotor case, this corresponds to the rear half of the rotor disc (i.e., $-90° < \Psi < 90°$).

Finally, we should mention briefly the limits of validity of the perturbation analysis. We shall return to this point in the Results and Discussion section, where we explicitly compare the results of the perturbation and numerical analyses, but here we make two observations. In the first place, the expansion parameter $\varepsilon = x/z$ enters to first order in the forward flight

case, while only to second order in the case of pure rotation with zero offset. Hence, the perturbation analysis should be valid for larger values of x/z for a propeller or hovering helicopter rotor than for a helicopter blade in forward flight. Secondly, each term in the expansions for forward flight contains a factor of the form

$$\frac{\varepsilon^n \mu^m}{(1 + \mu \sin \Psi)^{n+m}}$$

where $m \leq n$ and $\Psi = \tau$. These factors must be small with respect to one if the series expansions are to converge. Therefore, it is obvious that larger values of $\varepsilon = x/z$ are allowed when $0 < \Psi < 180°$ than when $180° < \Psi < 360°$, and that our analysis will break down first in the vicinity of $\Psi = 270°$.

Direct Numerical Integration

The most straightforward approach to rotor and propeller boundary-layer problems is direct numerical integration of the finite-difference equations. We mentioned earlier that we are faced with a set of parabolic equations which must be solved as a combined initial and boundary value problem. Therefore, the choice of our numerical method is based on its ability to model the diffusion and convection processes in the boundary layer by starting from the initial conditions and then marching forward in ξ, ζ, and τ, simultaneously satisfying all the boundary conditions in η. The method is an extension of the one described in reference 11, which, in turn, is a three-dimensional extension of the Crank-Nicolson implicit method frequently used in two-dimensional boundary-layer computations.

An essential feature of the set of parabolic equations is that second derivatives occur only in the η direction. When we evaluate derivatives along this diffusive coordinate in an implicit manner, the resulting set of simultaneous equations will have a tridiagonal matrix form and can be evaluated by the efficient algorithm developed for those types of simultaneous equations. The time-like derivatives, $\partial/\partial\xi$, $\partial/\partial\zeta$, and $\partial/\partial\tau$ are evaluated at the center of four grid points in either the ξ, ζ or ξ, τ planes,[3] with an averaging process directly analogous to the Crank-Nicolson method in ξ alone. To avoid the kinds of instabilities associated with "time reversals" when the crossflow becomes negative, it is necessary to choose the grid spacings such that $(u/\Delta\xi + w/\Delta\zeta) > 0$. The reasons for this requirement were pointed out by Krause (ref. 17), and it appears from numerous computations that if this criterion is satisfied, the step sizes in the ξ and ζ or the ξ and τ directions are not restricted by stability considerations.

The difficulty in starting the calculations at some initial z-station was mentioned earlier. This was handled by the following iterative technique. Starting conditions at a particular initial constant z were obtained by

[3]Reference 11 may be consulted for the specific details of the finite difference quotients.

first assuming the local primary flow to be the corresponding two-dimensional one and the crossflow to be zero. Then iterations from these profiles were calculated from the full three-dimensional equations and boundary conditions. The outer boundary conditions were kept constant at their local values and successive iterations were applied until the velocity profiles no longer changed.

The validity of this approach, which neglects the upstream history of the flow, was checked by comparing the results of marching in different directions, for the flat plate case. That is, the iteration technique was applied first at a large value of z, where the crossflow is small, and the boundary-layer flow was calculated inward from that station to a station near to the axis of rotation. Next, the iteration technique was started near the axis, where the actual crossflow is large, and the calculation proceeded outward. The results of these two different calculations are shown in figure 5, where the chordwise shear is normalized by the local Blasius, or two-dimensional, value. The agreement is better than 1 percent over the entire blade. As might be expected, the outside-in calculation is faster, because fewer iterations are required to relax from the two-dimensional solution to the correct three-dimensional flow.

The numerical scheme was originally programmed for three-dimensional steady (ξ, η, ζ) problems, and this was modified for two-dimensional unsteady (ξ, η, τ) problems by simply replacing $w(\partial/\partial z)$ by $\partial/\partial t$. At this writing the program has not yet been extended to the full three-dimensional, unsteady $(\zeta, \eta, \zeta, \tau)$ problem. Therefore, the calculations for such problems are best handled at present by an iterative scheme. Since the forward marching in the z-direction is performed after sufficient iterations on the assumed initial profiles, it seems natural to start the calculations as a two-dimensional unsteady problem with small crossflow, that is, first integrate the continuity equation and both unsteady momentum equations, neglecting all derivatives with respect to z. Then the z-derivatives are estimated and iterations are performed much in the same manner as in the perturbation analysis. A limited number of such calculations have been performed for the flat plate. The results agree well with the full perturbation solution, which is the only basis for comparison at the present time.

Finally, we should briefly compare the present implicit method with the recent investigation of Warsi (ref. 12). He employed an explicit scheme, based on the method of Der and Raetz (18), which seems to have a practical problem of slow convergence and requires very small step sizes near the leading edge. Warsi's results for the flat plate are also shown in figure 5. Much longer computation times are required, for example, 2-1/2 hours on an IBM 360 computer for each curve shown versus 1 to 2 minutes on an IBM 7044 computer required by the present method to carry the results to $x/z = 1.2$. Furthermore, Warsi's results appear deficient in two other important respects. First, he obtains two distinct curves for different values of z, whereas both the present calculations and the perturbation analysis show that τ/τ_B is uniquely determined by x/z. Secondly, Warsi's results disagree significantly with the perturbation analysis for virtually any finite value of x/z. Intuitively, one would tend to feel that disagreement at large x/z would constitute an indictment of the small crossflow assumption, but disagreement

at $0.002 < x/z < 0.02$ would seem to indicate fundamental errors in his numerical calculations. This conclusion is strengthened by the present numerical calculations, which agree with the perturbation analysis to much larger values of x/z.

Linearized Analysis

If we wish to analyze the boundary-layer flow in regions where the small crossflow and quasi-steady approximations fail, it may prove fruitful to look at another simplified set of equations. In this case, we retain the complete coupling between the primary and secondary flows, but we introduce two different assumptions that should considerably simplify the analysis without destroying the dominant features of the problem. Both assumptions are quite good in the case of a flat plate; their validity and utility for flows with strong adverse pressure gradients is currently under study.

The first assumption is that the crossflow derivatives are the same in the boundary layer as they are in the free stream, that is

$$\frac{\partial u}{\partial z} \approx \frac{\partial U_e}{\partial z} = \Omega \frac{\partial \Phi}{\partial x}$$

$$\frac{\partial w}{\partial z} \approx \frac{\partial W_e}{\partial z} = 0$$

The second assumption is similar to an Oseen-type linearization, that is,

$$u \frac{\partial u}{\partial x} + v \frac{\partial u}{\partial y} \approx a \frac{\partial u}{\partial x}$$

$$u \frac{\partial w}{\partial x} + v \frac{\partial w}{\partial y} \approx a \frac{\partial w}{\partial x}$$

where a is an arbitrary constant, say $U_e/2$.

Under the foregoing assumptions, equations (2) and (3) become

$$\frac{\partial u}{\partial t} + a \frac{\partial u}{\partial x} = \nu \frac{\partial^2 u}{\partial y^2} - \frac{1}{\rho} \frac{\partial p}{\partial x} + \Omega^2 X + \Omega\left(2 - \frac{\partial \Phi}{\partial x}\right) w \tag{14}$$

$$\frac{\partial w}{\partial t} + a \frac{\partial w}{\partial x} = \nu \frac{\partial^2 w}{\partial y^2} - \frac{1}{\rho} \frac{\partial p}{\partial z} + \Omega^2 Z - 2\Omega u \tag{15}$$

with the same boundary conditions as before. We observe that there are no z-derivatives in the equations; rather, z merely plays the role of a parameter influencing the inhomogeneous terms. Therefore, we are dealing with a coupled parabolic system, with linear equations of the form

$$u_{yy} - u_t - u_x = g(x)w + f_1(x,t;z) \tag{16}$$

$$w_{yy} - w_t - w_x = bu + f_2(x,t;z) \tag{17}$$

This set of equations resembles a pair of heat diffusion equations with heat sources (or sinks) in two time-like variables, t and x, and one space-like variable, y. Furthermore, the heat sources (or sinks) are comprised of f_1 and f_2, which are uniquely determined by the potential flow, and the coupling terms, $g(x)w$ and bu. The x-momentum coupling term, $g(x)w$, represents the net difference between the Coriolis force and the crossflow momentum flux. The z-momentum coupling, bu, is just the Coriolis force; if there were no Coriolis coupling between the x and z equations, the equation for the crossflow could be solved independently of the primary flow.

To date, attempts to solve equations (14) and (15) in closed form have not been successful. Hopefully, the large body of literature available on coupled parabolic systems will be helpful.

RESULTS AND DISCUSSION

Comparison of Perturbation and Numerical Analyses

The significance of the approximations employed in the perturbation analysis can be partially assessed by a detailed comparison with exact numerical calculations of the same flow field; for illustrative purposes, we shall consider the flat plate. Because the numerical scheme has been programmed in three independent variables, this evaluation will be done in two parts. First, we shall examine the small-crossflow assumption by considering the steady problem of pure rotation, corresponding to a propeller or hovering helicopter rotor. In the second part, we shall evaluate the quasi-steady approximation in the case of a sinusoidally-varying free stream velocity for a two-dimensional boundary layer.

Basic effects of rotation.- An essential result of the perturbation analysis for the flat plate in pure rotation is that the corrections to the basic Blasius primary flow profile are uniquely determined by x/z. As mentioned earlier in connection with figure 5, this result is verified by the exact numerical solutions.

Velocity profiles at small and large values of x/z are shown in figures 6 and 7. Considering first the crossflow profiles, we see that for $x/z \ll 1$, the centrifugal force pumps the fluid outward near the bottom of the boundary layer. However, the flow at the top of the boundary layer is pulled inward by W_e. This is a characteristic of the coordinates we have used; the potential flow for the flat plate follows circular arcs, and there is zero *radial* flow at the outer edge of the boundary layer. At large x/z, the Coriolis force in the crossflow direction becomes increasingly important, and the spanwise flow is inward throughout the boundary layer.

At the same time, the x-component of centrifugal force exerts a strong accelerating force on the primary flow at large x/z, increasing the wall shear and "stabilizing" the boundary layer, as shown in figure 7.

The perturbation solutions shown in figures 6 and 7 are carried out to order ε^2, and at $\varepsilon = x/z = 0.7$, which is hardly a small value to be using in a perturbation expansion, rather large errors obtain. The reason is that the effects of the crossflow derivatives, $\partial w/\partial z$ and $\partial u/\partial z$, have been overestimated. However, if we add the next term in the expansion for the primary flow, F''_{40}, that is,

$$\frac{\tau}{\tau_B} = 1 + 3.852\left(\frac{x}{z}\right)^2 - 5.412\left(\frac{x}{z}\right)^4 + \ldots \tag{18}$$

the agreement is better, as shown by the solid symbols in figure 5. Even so, we must conclude that $x/z = 0.7$ is too large to apply the perturbation analysis accurately.

The main conclusion that we may draw from this comparison of perturbation and numerical results is that the small crossflow perturbation analysis does, in fact, correctly order the relative magnitudes of the various terms in the boundary-layer equations. Furthermore, the perturbation solutions are surprisingly accurate, especially if the expansion is carried as far as the second correction term, F_{40}, (i.e., to order ε^4).

Basic unsteady velocity effect.- The effect of a sinusoidally-varying external flow is of considerable interest in general studies of unsteady boundary layers. Within the framework of the development in the Perturbation Analysis section, the expansion parameter $\varepsilon = x/z$ plays the role of a reduced frequency, $\Omega x/U$, where $U = \Omega z$, and $\mu = V_1/U$ represents the ratio of the fluctuation in free-stream velocity to the *average* free-stream velocity. We shall see in the succeeding paragraphs that even more important is the ratio of V_1 to the *instantaneous* free-stream velocity, $\Omega z + V_1 \sin \Omega t$.

As in the rotating case, the results can best be summarized by the wall shear; accordingly, figure 8 shows the local instantaneous shear normalized by the local instantaneous Blasius shear, for both the perturbation and numerical solutions. Considering first $\varepsilon = 0.1$, we see that the two agree well for all values of $\tau = \Omega t$, just as rotating solutions agree well for $\varepsilon << 1$, even though μ has the rather large value of 0.57.

However, for $\varepsilon = 0.29$ and $\mu = 0.57$, the perturbation analysis produces large errors in the vicinity of $\tau = 3\pi/2$, where the ratio of fluctuating velocity to instantaneous free-stream velocity is greater than unity. Even if more terms are added, for example,

$$\frac{\tau}{\tau_B} = 1 + \frac{2.555\ \varepsilon\mu \cos \tau}{(1 + \mu \sin \tau)^2} + \frac{1.414\ \varepsilon^2\mu \sin \tau}{(1 + \mu \sin \tau)^3} + \frac{0.8158\ \varepsilon^2\mu^2 \cos^2 \tau}{(1 + \mu \sin \tau)^4}$$

$$- \frac{1.107\ \varepsilon^3\mu \cos \tau}{(1 + \mu \sin \tau)^4} + \frac{2.112\ \varepsilon^3\mu^2 \sin \tau \cos \tau}{(1 + \mu \sin \tau)^5}$$

$$+ \frac{1.136\ \varepsilon^3\mu^3 \cos^3 \tau}{(1 + \mu \sin \tau)^6} + \ldots \tag{19}$$

(The first three terms are identical to the result of ref. 16.) The series converges so slowly at this large value of μ that poor results are obtained for $\pi < \tau < 2\pi$. On the other hand, the results are very good for $0 < \tau < \pi$, where $V_1/(\Omega z + V_1 \sin \tau)$ is small and the series converges rapidly.

Finally, we observe that the inertia effects tend to "stabilize" the boundary layer for $-\pi/2 < \tau < \pi/2$ and to "destabilize" the boundary layer for $\pi/2 < \tau < 3\pi/2$. For a helicopter, this corresponds to the rear and front halves of the rotor disc, respectively.

The main conclusions that we can draw from this discussion are, first, that the quasi-steady perturbation analysis correctly orders the inertia effects in the boundary layer, and second, the quasi-steady approximation implies that both ε and $\mu/(1 + \mu \sin \tau)$, that is, the ratio of the fluctuating free-stream velocity to the instantaneous free-stream velocity, are small. The latter implication is not present in the case of pure rotation.

Laminar Separation Characteristics of Airfoils

Detailed numerical analyses of the flow over an NACA 0012 airfoil section show that crossflow and oscillating velocities influence the separation characteristics of rotor blades and propellers. For the computations described below, the angle of attack was taken to be zero, where the crossflow and unsteady effects are greatest. The potential flow was calculated using Theodorsen's (ref. 19) method for the primary flow and equation (8) for the crossflow. It will be helpful to keep in mind that for steady, two-dimensional flow, laminar separation occurs theoretically at $x/c = 0.695$ for this airfoil at $\alpha = 0$. We should mention again that x is the curvilinear boundary coordinate along the surface of the airfoil.

Effect of rotation on separation.- The qualitative effects of rotation are very similar to those for the flat plate, as indicated by a comparison of figures 6 and 9, where the NACA 0012 crossflow profile at $x/c = 0.63$ and $z/c = 1$ is shown. The centrifugal pumping effect is evident at the bottom of the boundary layer, but the inviscid flow pulls the spanwise velocity inward in the outer 75 percent of the boundary layer.

The crossflow has a considerable effect on the primary flow at this large value of x/z, as shown in figure 10. Shown for comparison is the profile at the same chordwise station, but at $z \to \infty$ where the two-dimensional solution is approached.

The large change in "fullness" of the two profiles in figure 10 is reflected in the large change in wall shear, that is, the curve labeled "$x/c = 0.63$, varying z" in figure 11. On the other hand, near the leading edge where the chordwise pressure gradients are larger, the effect of rotation is much less, as indicated by the curve for $x/c = 0.186$ in figure 11.

If we consider a fixed value of z/c, say 1.0, and move along the blade in the chordwise direction, we see from the dashed curve in figure 11 that the wall shear rises to many times the local two-dimensional value, since the latter vanishes at $x/c \simeq 0.70$. The separation point in the rotating case is farther aft, as shown in figure 12, where we see that the rotational forces are particularly important for $z/c < 4$. This trend obtains in the analyses of Liu (ref. 5) and Banks and Gadd (ref. 8), and in the experiments of Himmelskamp (ref. 20).

Also shown in figure 12 is a line denoting the boundary between favorable and adverse chordwise pressure gradients. The shape of this boundary for $z/c < 2$ is purely an inviscid phenomenon that we shall discuss later. Here we merely observe that there is no adverse pressure gradient at sufficiently large values of x/z; therefore, the separation point moves completely off the airfoil somewhere between $z/c = 1.5$ and 2.

Effect of oscillating velocity on separation.- The unsteady effects on the NACA 0012 airfoil are also qualitatively similar to those on the flat plate. That is, the wall shear increases while the velocity is increasing and decreases while the velocity is decreasing. The separation characteristics are shown in figure 13 as a function of time. We should mention that $\Omega t = n\pi/2$ ($n = 1,3,5$, etc.) are the times when the acceleration of the free stream is zero. For this example, separation is advanced to $x/c = 0.59$ at $\Omega t \simeq 1.3\pi$, corresponding to $\psi \simeq 235°$ for a helicopter rotor, and delayed to $x/c = 0.80$ at $\Omega t \simeq 1.8\pi$, or $\psi \simeq 325°$.

Combined Rotation and Translation

We turn our attention now to the more specialized and more difficult problem of a helicopter rotor in forward flight. Here unsteady effects are important because of the oscillating velocities U_e and W_e; spanwise gradients are significant because of the linearly varying velocity Ωz; and the crossflow is larger than for a conventional propeller because of the spanwise component of V_1. First, let us consider the crossflow velocity profiles on a flat plate, shown in figure 14. In this and the next figure, the curves are drawn out to the point where $u/U_e = 0.99$, which is taken to be the edge of the boundary layer. From the locations of these outer points, we see the thinning of the boundary layer on the advancing side, where $\psi \to 90°$, and the thickening of the boundary layer on the retreating side, where $\psi \to 270°$.

A striking feature of these results is that the crossflow due to translation dominates the spanwise velocity over most of the rotor disc for the conditions indicated. For $\psi = 90°$ and $270°$, the crossflow is primarily that due to rotation, and the principal effect of the translational motion V_1 is to thin or thicken the boundary layer. However, for points only 45° away, the translational contribution clearly predominates. This effect is further magnified as the flight velocity is increased, or the distance from the leading edge decreased, but it is virtually independent of z.

The crossflow in the case of adverse pressure gradients is qualitatively the same, as indicated in figure 15. These profiles were obtained for linearly decelerating flow, $U_e \propto (1 - \xi)$. The scales of the ordinates and abscissas are the same in figures 14 and 15, and by comparing these figures closely, we see that the boundary layer is thicker for the adverse pressure gradients as would be expected. Also, the centrifugal pumping effect at the bottom of the boundary layer is slightly greater. The predominate effect over most of the rotor disc, however, is still the inviscid crossflow at the outer edge of the boundary layer, and the crossflow due to translation is generally large compared to the crossflow due to rotation. This important result was presented first in reference 10 and discussed there in somewhat greater detail.

The primary flow in cases with pressure gradients is subjected to the influences described under Laminar Separation Characteristics of Airfoils, except that there is a larger crossflow. Since separation results are not available at this time, we shall focus our attention now upon the individual factors that can be expected to alter the two-dimensional steady results for a given airfoil.

Discussion of Secondary Terms

If we are to understand fully the viscous flow on propellers and rotor blades, it is important to be able to identify the secondary effects and to determine the physical mechanisms by which they influence the primary flow around the blades. The continuity and chordwise momentum equations are

$$\frac{\partial u}{\partial x} + \frac{\partial v}{\partial y} = - \frac{\partial w}{\partial z} \tag{20}$$

$$u \frac{\partial u}{\partial x} + v \frac{\partial u}{\partial y} - \nu \frac{\partial^2 u}{\partial y^2} - U_e \frac{\partial U_e}{\partial x} = \frac{\partial}{\partial t} (U_e - u) - w \frac{\partial u}{\partial z} + 2\Omega w + W_e \frac{\partial W_e}{\partial x} \tag{21}$$

Using the perturbation analysis as a guide, we have written the dominant or primary terms on the left-hand side, and the secondary terms on the right-hand side of the equations.

Now let us look at the size of each individual term in these equations for flow conditions corresponding to that in figure 14. These terms are displayed in figures 16 to 18. Considering first figure 16, the primary

momentum terms, we can see the net effect of the secondary terms by comparing the dotted and solid lines. The secondary terms are plotted on the same scales in figure 17, with a sign convention such that a positive quantity exerts a favorable influence with regard to separation. We should mention that the signs and magnitudes of the various terms depend upon the value ψ (i.e., where the rotor blade is in the plane of the disc), and for the value of ψ as shown in the figure, they generally tend to be a maximum. It is interesting to note that for the conditions indicated, these secondary terms tend to be comparable in size to the primary terms in the x-momentum equation, even though their net effect is small. On the other hand, the crossflow derivative in the continuity equation shown in figure 18 is quite small compared to the primary flow derivatives.

Unsteady velocity effects.- We have observed earlier that the unsteady effects due to oscillating velocity and sweep angle first enter to order $\varepsilon\mu = (x/z)(V_1/\Omega z)$ and are designated by the function F_{1u}. Mathematically, they enter through the terms so designated in equations (A6) and (A8) in the appendix for the primary flow, and equation (A7) for the crossflow. The function F'_{1u} is modulated by $\cos\psi$ and is positive, so that it acts favorably on the rear half of a helicopter rotor disc. The unsteady contribution to F'_{21} comes from the time derivative of the crossflow and from $\partial F'_{11}/\partial t$. Its sign and phase are such that a favorable influence is exerted on the retreating blade. However, this is to order $\varepsilon^2\mu$ and hence less important than F'_{1u}. The unsteady contribution to F'_{22} is always destabilizing and comes from higher order unsteady effects in the chordwise flow.

Crossflow derivatives.- The crossflow derivative in the continuity equation, $\partial w/\partial z$, manifests itself in the primary flow momentum equation mostly through the vertical velocity v. The physical effect is one of bringing momentum from one strata of the boundary layer to another, and therefore it is favorable with regard to separation when the perturbation in v is negative, which occurs when $\partial w/\partial z$ is positive. In forward flight, this effect enters to order $\varepsilon\mu$ because the dominant crossflow is produced by $V_1 \cos\psi$. The gradient in the z-direction comes from the spanwise variation in the boundary-layer thickness (i.e., $\delta \propto (\Omega z + V_1 \sin\psi)^{-1/2}$). Separation is delayed on the front half of the rotor disc by this effect.

The crossflow momentum derivative, $w(\partial u/\partial z)$, also enters to order $\varepsilon\mu$. This is because the largest crossflow is due to $V_1 \cos\psi$, because u varies linearly with z, and because the boundary-layer thickness varies inversely with $\sqrt{z}$. The mathematical expression is indicated in equations (A6) and (A8) in the appendix. Physically, the effect of this term is to transfer momentum from one spanwise location on the blade to another. A spanwise inflow has a favorable effect with regard to separation, since the crossflow momentum flux brings momentum from farther out on the blade, where the velocity is greater, into the lower momentum regions closer to the hub.

Coriolis force.- The term $2\Omega w$ represents a well-known *rotational* effect in mechanics, but for a rotor in forward flight, most of the w term comes from the translational motion, since $V_1 \cos\psi$ is generally large compared to

the centrifugal pumping effect. The mathematical contribution is straightforward, and to all orders in ε the physical effect is a favorable one when w is positive.

Centrifugal force.- This purely rotational force affects the primary flow in two separate ways. In the first place, there is a direct contribution in the x-momentum equation through the term $\Omega^2 X$. This is an effect of order ε^2 and is expressed through the function F_{20}. It is favorable for all $x > 0$.

The second effect is one of centrifugal pumping, which contributes to order ε^2 to an outward component of the spanwise velocity w. This component of w, in turn, couples with the primary flow through the continuity equation, the crossflow momentum flux, and the Coriolis force. In the past, this has been considered probably an important effect; however, the present analysis shows that it is much weaker than generally or intuitively supposed. Compared to the other effects it is unimportant for most helicopter rotors, particularly in forward flight. However, it should be noted that the centrifugal pumping does increase as the adverse pressure gradient increases.

Crossflow-induced apparent pressure gradient.- The term $W_e(\partial W_e/\partial x)$ in equation (21) is one which has not been appreciated by most investigators of rotor boundary layers, but it represents an effect that can be important in influencing the separation characteristics. It arises as a combination of the coordinates which we have selected and the method we have used to evaluate the chordwise pressure gradient from the inviscid Bernoulli equation. An alternate expression is given by

$$W_e \frac{\partial W_e}{\partial x} = W_e\left(\frac{\partial U_e}{\partial z} - 2\Omega\right) \tag{22a}$$

$$= \Omega W_e\left(\frac{\partial \Phi}{\partial x} - 2\right) \tag{22b}$$

Equation (22a) is valid in general, but equation (22b) is derived from the constant-circulation solution of reference 10. In the special case of the flat plate, this term has the simple form

$$W_{e_{\text{translation}}}\left(\frac{\partial W_e}{\partial x}\right)_{\text{rotation}} = -\frac{\partial U_e}{\partial t} \tag{23a}$$

$$W_{e_{\text{rotation}}}\left(\frac{\partial W_e}{\partial x}\right)_{\text{rotation}} = \Omega^2 X \tag{23b}$$

with the result that the chordwise pressure gradient is zero, but in general this is not the case. As an example, we refer to figure 12. The dashed line in that figure indicates the boundary between favorable and adverse pressure gradients. The term $W_e(\partial W_e/\partial x)$ and the x-component of centrifugal force

are sufficiently large to create a region of entirely favorable pressure gradients sufficiently close to the axis of rotation.

This term exerts a favorable influence with regard to separation when it is positive. It is interesting to note from equation (22b) that $\partial W_e/\partial x$ is positive when $\partial\Phi/\partial x$ is greater than 2. This corresponds to a chordwise pressure coefficient $C_p < -3$ (i.e., for a blade that is developing rather large lift). Of course, it is also important whether W_e itself is positive or negative.

For actual rotors with complex induced flow fields, it may be difficult to establish the magnitude of this term precisely. However, it appears that for many practical problems we can evaluate it as follows: for a propeller or helicopter rotor in hover, W_e should perhaps be estimated from the geometry of the slipstream contraction and the expression $(\partial W_e/\partial x) \simeq \Omega[(\partial\Phi/\partial x) - 2]$ should be utilized. On the other hand, for a helicopter rotor in high speed forward flight, the largest contribution to W_e comes from $V_1 \cos\psi$, and again $\partial W_e/\partial x$ should be approximately $\Omega[(\partial\Phi/\partial x) - 2]$. It should be emphasized that this phenomenon is purely inviscid; hence, it has been called a crossflow-induced apparent pressure gradient.

Spanwise pressure gradients and crossflow boundary conditions.- The crossflow *within* the boundary layer is also strongly dependent upon the potential flow, by virtue of the spanwise pressure gradient serving as an inhomogeneous term in the z-momentum equation and by the potential velocity, W_e, serving as the outer boundary condition for w. We have seen in figures 6, 9, 14, and 15 how strongly the crossflow velocity profiles depend upon W_e; the remarks in the preceding paragraph apply insofar as evaluating W_e is concerned.

The spanwise pressure gradient is given by

$$-\frac{1}{\rho}\frac{\partial p}{\partial z} = \frac{\partial W_e}{\partial t} + U_e\frac{\partial U_e}{\partial z} + W_e\frac{\partial W_e}{\partial z} - \Omega^2 z \tag{5}$$

Intuitively, we would expect the spanwise pressure gradient to be negative in the important regions near and downstream of the suction peak on the airfoil sections, because the tip regions generally carry larger aerodynamic loads. In other words, the largest term in equation (5) is $U_e(\partial U_e/\partial z)$, which is always positive. This term should be given accurately by the McCroskey and Yaggy (ref. 10) solution, $\Omega u_o(\partial\Phi/\partial x)^2$, and $\partial W_e/\partial t$ approximately by $-\Omega V_1 \sin \Omega t$. The term $W_e(\partial W_e/\partial z)$ is positive for a *hovering* rotor developing lift. It is the most difficult term in equation (5) to estimate in forward flight, and its influence is probably the major reason that the largest spanwise pressure gradients seem to occur in the vicinity of $\Psi = 0$, as pointed out by Blaser (ref. 21).

Since the net result in any case is a negative spanwise pressure gradient, this term contributes a small positive value of w. In turn, this has an unfavorable effect upon primary flow separation by virtue of the coupling of the crossflow derivatives, and a favorable one through Coriolis coupling.

SUMMARY AND CONCLUSIONS

In our analysis of the boundary layers on rotors and propellers, we have demonstrated most of the essential features of the flow by means of relatively simple analytical solutions. The approximations used in the perturbation analysis have been investigated by direct numerical calculations. The numerical analysis has also provided the detailed structure of the flow near separation.

The limitations of the results obtained so far are threefold. In the first place the separation results have been obtained for rotating three-dimensional steady flows and for two-dimensional unsteady flows, but not for the complete helicopter problem of three-dimensional unsteady flows. Second, complete solutions for the potential flow, which serve as boundary conditions at the outer edge of the boundary layer, are not available at this time, and therefore the solutions for infinite blades with constant circulation of reference 10 had to be used. Third, we have not calculated the flow for blades with oscillating changes in angle of attack. Nevertheless, within these limitations, the role of the various physical effects has been identified, and the laminar flow on rotating blades is now well understood.

From the present investigation we can draw the following specific conclusions.

1. The small crossflow approximation is valid for the flow over rotating airfoil sections, provided the ratio of chordwise distance from the leading edge to the spanwise distance from the axis of rotation, x/z, is small. This conclusion applies to helicopter rotor blades and many classes of propellers. However, for the values of x/z appropriate to ship propellers, the small crossflow approximation does not hold.

2. The flow field on a rotating flat plate is uniquely determined by a Blasius-type boundary-layer coordinate and the length ratio x/z. For flows on rotating airfoils with pressure gradients, the differences from the two-dimensional solution can be correlated with x/z.

3. The effects of rotation can be important and beneficial with regard to separation of the primary flow in regions of adverse pressure gradients. Since these effects scale with $(x/z)^2$, the maximum benefits accrue closest to the axis of rotation.

4. The quasi-steady approximation for flows with oscillating chordwise velocities is valid, provided the parameter $\varepsilon\mu/(1 + \mu \sin \Omega t)$ is small.

5. The unsteady velocity effect has a favorable influence on separation when U_e is accelerating and an unfavorable one when U_e is decelerating. The effect is largest at small angles of attack. For a given blade geometry, the unsteady effect is larger than the effects of pure rotation. The ordering of these effects is ε and ε^2, respectively.

6. For a helicopter blade in forward flight, there is a substantial inviscid crossflow due to translation, $V_1 \cos \Omega t$, and therefore the boundary layer generally resembles the viscous flow over a swept wing. The perturbation analysis shows that this swept wing effect influences the primary flow to order ε and has a favorable effect with regard to separation on the front half of the rotor disc (i.e., $90° < \Psi < 270°$). If we add the second-order effects, the maximum benefits accrue in the third quadrant, $180° < \Psi < 270°$, where retreating blade stall is commonly presumed to begin. This may be one reason the actual rotors have been observed to perform better than would be expected on the basis of the steady-state two-dimensional section characteristics of the blade.

7. The secondary effects that influence the primary flow have been identified. Of these, the centrifugal force effect appears to be the least important for helicopter rotor blades and slender propellers. The most important effects appear to be time derivatives and crossflow derivatives. Also important are Coriolis forces and apparent pressure gradients that are induced by the potential crossflow. The latter effect has not been recognized by most previous investigators.

8. There are few experimental data available for comparison with the present investigation. Generally speaking, however, aerodynamic loads and separation patterns have been observed that agree qualitatively with the conclusions outlined above. Future experimental programs should be directed primarily at defining the locations and patterns of separated flows, at measuring the direction of streamlines and the magnitude of the local skin friction, and at developing a better physical model of turbulent crossflow.

9. For a more complete treatment of propellers and rotors, additional analytical efforts are needed in two main areas. The first is the development of methods to treat three-dimensional unsteady turbulent flows. Secondly, better potential flow solutions are needed to serve as outer boundary conditions for the viscous flows and to prescribe more accurately the chordwise and spanwise pressure gradients.

APPENDIX

PERTURBATION ANALYSIS FOR ARBITRARY PRESSURE GRADIENTS

As discussed in the Analysis, the equations governing the boundary-layer flow are

$$\frac{\partial u}{\partial x} + \frac{\partial v}{\partial y} + \frac{\partial w}{\partial z} = 0 \tag{A1}$$

$$\frac{Du}{Dt} - 2\Omega w \cos \alpha = \nu \frac{\partial^2 u}{\partial y^2} + \frac{\partial U_e}{\partial t} + U_e \frac{\partial U_e}{\partial x} + W_e \frac{\partial W_e}{\partial x} \tag{A2}$$

$$\frac{Dw}{Dt} + 2\Omega u \cos \alpha = \nu \frac{\partial^2 w}{\partial y^2} + \frac{\partial W_e}{\partial t} + U_e \frac{\partial U_e}{\partial z} + W_e \frac{\partial W_e}{\partial z} \tag{A3}$$

where

$$\alpha \simeq 0$$

$$U_e = \upsilon_o \frac{\partial \Phi(x)}{\partial x}$$

$$W_e = V_1 \cos \Omega t + \Omega[\Phi(x) - 2]$$

$$u_o = \Omega z + V_1 \sin \Omega t$$

Let

$$\frac{u}{u_o} = \sum_{m=o}^{\infty} \varepsilon^m \frac{\partial f_m}{\partial \eta} (\xi,\eta,\tau)$$

$$\frac{w}{\Omega z} = \mu \cos \tau \frac{\partial g_o}{\partial \eta} (\xi,\eta) + \sum_{n=1}^{\infty} \varepsilon^n \frac{\partial g_n}{\partial \eta} (\xi,\eta,\tau)$$

where

$$\varepsilon = \frac{x}{z}, \qquad \mu = \frac{V_1}{\Omega z}, \qquad \xi = \frac{x}{c},$$

$$\tau = \Omega t, \qquad \eta = y\left(\frac{\Omega z + V_1 \sin \Omega t}{2\nu x}\right)^{1/2}$$

The velocity v is determined from the integral of the continuity equation and is

$$v = -\left(\frac{2\nu u_o}{c\xi}\right)^{1/2}\left\{\sum_{m=o}^{\infty}\varepsilon^m\left[\left(m+\frac{1}{2}\right)f_m + \xi\frac{\partial f_m}{\partial\xi} - \frac{\eta}{2}\frac{\partial f_m}{\partial\eta}\right] + \left(\frac{\Omega z}{u_o}\right)\sum_{n=1}^{\infty}\varepsilon^{n+1}(1-n)g_n\right.$$

$$\left. + \frac{1}{2}\left(\frac{\Omega z}{u_o}\right)^2\left[\varepsilon\mu\cos\tau\left(\eta\frac{\partial g_o}{\partial\eta} - g_o\right) + \sum_{n=1}^{\infty}\varepsilon^{n+1}\left(\eta\frac{\partial g_n}{\partial\eta} - g_n\right)\right]\right\}$$

We can substitute these expressions into equations (A2) and (A3), equate like powers of ε, and derive the equations given below for f_m and g_n.

$$\frac{\partial^3 f_o}{\partial\eta^3} + f_o\frac{\partial^2 f_o}{\partial\eta^2} - 2\xi\left(\frac{\partial f_o}{\partial\eta}\frac{\partial^2 f_o}{\partial\eta\,\partial\xi} - \frac{\partial f_o}{\partial\xi}\frac{\partial^2 f_o}{\partial\eta^2}\right) = -\xi\frac{\partial\Phi}{\partial x}\frac{\partial^2\Phi}{\partial x\,\partial\xi} \tag{A4}$$

$$f_o = \frac{\partial f_o}{\partial\eta} = 0 \quad \text{at} \quad \eta = 0$$

$$\frac{\partial f_o}{\partial\eta} \to \frac{\partial\Phi}{\partial x} \quad \text{as} \quad \eta \to \infty$$

$$\frac{\partial^3 g_o}{\partial\eta^3} + f_o\frac{\partial^2 g_o}{\partial\eta^2} - 2\xi\left(\frac{\partial f_o}{\partial\eta}\frac{\partial^2 g_o}{\partial\eta\,\partial\xi} - \frac{\partial f_o}{\partial\xi}\frac{\partial^2 g_o}{\partial\eta^2}\right) = 0 \tag{A5}$$

$$g_o = \frac{\partial g_o}{\partial\eta} = 0 \quad \text{at} \quad \eta = 0$$

$$\frac{\partial g_o}{\partial\eta} \to 1 \quad \text{as} \quad \eta \to \infty$$

Equation (A4) is equivalent to the two-dimensional steady equation for the airfoil section in question, and equation (A5) is equivalent to the linear equation for the crossflow on an infinite swept wing with the same airfoil. Hence both f_o and g_o are functions of neither τ nor z. The higher order equations can be rendered independent of τ and z by the following substitutions:

$$f_1 = \frac{\mu \cos \tau}{(1 + \mu \sin \tau)^2} F_{11}(\xi,\eta)$$

$$g_1 = G_{10}(\xi,\eta) + \left(\frac{\mu \sin \tau}{1 + \mu \sin \tau}\right) G_{11}(\xi,\eta) + \left(\frac{\mu \cos \tau}{1 + \mu \sin \tau}\right)^2 G_{12}(\xi,\eta)$$

$$f_2 = \frac{1}{(1 + \mu \sin \tau)^2} F_{20}(\xi,\eta) + \frac{\mu \sin \tau}{(1 + \mu \sin \tau)^3} F_{21}(\xi,\eta)$$

$$+ \frac{\mu^2 \cos^2 \tau}{(1 + \mu \sin \tau)^4} F_{22}(\xi,\eta)$$

Then

$$\frac{\partial^3 F_{11}}{\partial \eta^3} + f_o \frac{\partial^2 F_{11}}{\partial \eta^2} - 2 \frac{\partial f_o}{\partial \eta} \frac{\partial F_{11}}{\partial \eta} + 3 \frac{\partial^2 f_o}{\partial \eta^2} F_{11}$$

$$- 2\xi \left[\frac{\partial f_o}{\partial \eta} \frac{\partial^2 F_{11}}{\partial \eta \, \partial \xi} + \frac{\partial^2 f_o}{\partial \eta \, \partial \xi} \frac{\partial F_{11}}{\partial \eta} - \frac{\partial f_o}{\partial \xi} \frac{\partial^2 F_{11}}{\partial \eta^2} - \frac{\partial^2 f_o}{\partial \eta^2} \frac{\partial F_{11}}{\partial \xi}\right]$$

$$= \underbrace{2 \frac{\partial f_o}{\partial \eta} + \eta \frac{\partial^2 f_o}{\partial \eta^2} - 2 \frac{\partial \Phi}{\partial x}}_{\text{(unsteady)}} + \underbrace{g_o \frac{\partial^2 f_o}{\partial \eta^2}}_{(vu_y)} + \underbrace{2 \frac{\partial g_o}{\partial \eta} \frac{\partial f_o}{\partial \eta}}_{(wu_z)} - \underbrace{4 \frac{\partial g_o}{\partial \eta}}_{\text{(Coriolis)}} - \underbrace{2 \frac{\partial \Phi}{\partial x} + 4}_{(W_e W_{e_x})} \qquad \text{(A6)}$$

$$F_{11} = \frac{\partial F_{11}}{\partial \eta} = 0 \qquad \text{at} \quad \eta = 0$$

$$\frac{\partial F_{11}}{\partial \eta} \to 0 \qquad \text{as} \quad \eta \to \infty$$

$$\frac{\partial^3 G_{1i}}{\partial \eta^3} + f_o \frac{\partial^2 G_{1i}}{\partial \eta^2} - 2 \frac{\partial f_o}{\partial \eta} \frac{\partial G_{1i}}{\partial \eta} - 2\xi\left(\frac{\partial f}{\partial \eta} \frac{\partial^2 G_{1i}}{\partial \eta\, \partial \xi} - \frac{\partial f_o}{\partial \xi} \frac{\partial^2 G_{1i}}{\partial \eta^2}\right) = P_i \qquad \text{(A7)}$$

$$i = 0, 1, 2$$

$$G_{1i} = \frac{\partial G_{1i}}{\partial \eta} = 0 \quad \text{at} \quad \eta = 0$$

$$\frac{\partial G_{10}}{\partial \eta} \to \left(\frac{\Phi}{x} - 2\right) \quad \text{as} \quad \eta \to \infty$$

$$\frac{\partial G_{11}}{\partial \eta} = \frac{\partial G_{12}}{\partial \eta} \to 0 \quad \text{as} \quad \eta \to \infty$$

where

$$P_0 = \underbrace{4 \frac{\partial f_o}{\partial \eta}}_{\text{(Coriolis)}} - \underbrace{2\left(\frac{\partial \Phi}{\partial x}\right)^2}_{(U_e U_{e_z})}$$

$$P_1 = \underbrace{2\left(1 - \frac{\partial g_o}{\partial \eta}\right)}_{\text{(unsteady)}}$$

$$P_2 = \underbrace{\eta \frac{\partial^2 g_o}{\partial \eta}}_{\text{(unsteady)}} + \underbrace{\left(g_o - 3F_{11} + 2\xi \frac{\partial F_{11}}{\partial \xi}\right) \frac{\partial^2 g_o}{\partial \eta^2}}_{(vw_y)} - \underbrace{2\xi \frac{\partial F_{11}}{\partial \eta} \frac{\partial^2 g_o}{\partial \eta\, \partial \xi}}_{(uw_x)}$$

$$\frac{\partial^3 F_{2i}}{\partial \eta^3} + f_o \frac{\partial^2 F_{2i}}{\partial \eta^2} - 4 \frac{\partial f_o}{\partial \eta} \frac{\partial F_{2i}}{\partial \eta} + 5 \frac{\partial^2 f_o}{\partial \eta^2} F_{2i}$$

$$- 2\xi\left(\frac{\partial f_o}{\partial \eta} \frac{\partial^2 F_{2i}}{\partial \eta\, \partial \xi} + \frac{\partial^2 f_o}{\partial \eta\, \partial \xi} \frac{\partial F_{2i}}{\partial \eta} - \frac{\partial f_o}{\partial \xi} \frac{\partial^2 F_{2i}}{\partial \eta^2} - \frac{\partial^2 f}{\partial \eta^2} \frac{\partial F_{2i}}{\partial \xi}\right) = Q_i \qquad \text{(A8)}$$

$$i = 0, 1, 2$$

$$F_{2i} = \frac{\partial F_{2i}}{\partial \eta} = 0 \qquad \text{at} \quad \eta = 0$$

$$\frac{\partial F_{2i}}{\partial \eta} \to 0 \qquad \text{as} \quad \eta \to \infty$$

where

$$Q_0 = \underbrace{G_{10} \frac{\partial^2 f_o}{\partial \eta^2}}_{(vu_y)} + \underbrace{2 \frac{\partial f_o}{\partial \eta} \frac{\partial G_{10}}{\partial \eta}}_{(wu_z)} - \underbrace{4 \frac{\partial G_{10}}{\partial \eta}}_{\text{(Coriolis)}} - \underbrace{2\left(\frac{\Phi - 2x}{x}\right)\left(\frac{\partial \Phi}{\partial x} - 2\right)}_{(W_e W_{e_x})}$$

$$Q_1 = \underbrace{-2 \frac{\partial F_{11}}{\partial \eta}}_{\text{(unsteady)}} + \underbrace{G_{11} \frac{\partial^2 f_o}{\partial \eta^2}}_{(vu_y)} + \underbrace{2 \frac{\partial f_o}{\partial \eta} \frac{\partial G_{11}}{\partial \eta}}_{(wu_z)} - \underbrace{4 \frac{\partial G_{11}}{\partial \eta}}_{\text{(Coriolis)}}$$

$$Q_2 = \underbrace{\eta \frac{\partial^2 F_{11}}{\partial \eta^2} - 2 \frac{\partial F_{11}}{\partial \eta}}_{\text{unsteady}} + \underbrace{2\left(\frac{\partial F_{11}}{\partial \eta}\right)^2 + 2\xi \frac{\partial F_{11}}{\partial \eta} \frac{\partial^2 F_{11}}{\partial \xi\, \partial \eta}}_{uu_x}$$

$$+ \underbrace{G_{12} \frac{\partial^2 f_o}{\partial \eta^2} - 3F_{11} \frac{\partial^2 F_{11}}{\partial \eta^2} + g_o \frac{\partial^2 F_{11}}{\partial \eta^2} - 2\xi \frac{\partial^2 F_{11}}{\partial \eta^2} \frac{\partial F_{11}}{\partial \xi}}_{vu_y}$$

$$+ \underbrace{2 \frac{\partial f_o}{\partial \eta} \frac{\partial G_{12}}{\partial \eta}}_{wu_z} - \underbrace{4 \frac{\partial G_{12}}{\partial \eta}}_{\text{Coriolis}}$$

For the special case of a flat plate blade, all derivatives with respect to ξ vanish, and $\Phi = x$ if the axis of rotation is located at the leading edge. Therefore, equations (A4) to (A8) become ordinary differential equations in η. The solutions are plotted in figures 3 and 4 and are tabulated in table 1. Errors in F'_{21} and F'_{22} reported in reference 10 have been corrected.

REFERENCES

1. Sears, W. R.: Potential Flow Around a Rotating Cylindrical Blade. J. Aero. Sci., vol. 17, no. 3, March 1950, p. 183.

2. Fogarty, L. E.; and Sears, W. R.: Potential Flow Around a Rotating Advancing Cylindrical Blade. J. Aero. Sci., vol. 17, no. 9, Sept. 1950, p. 599.

3. Fogarty, L. E.: The Laminar Boundary Layer on a Rotating Blade. J. Aero. Sci., vol. 18, no. 4, April 1951, pp. 247-252.

4. Tan, H. S.: On Laminar Boundary Layer Over a Rotating Blade. J. Aero. Sci., vol. 20, no. 11, Nov. 1953, p. 780.

5. Liu, S. W.: The Laminar Boundary Layer Flow on Rotating Cylinders. AFOSR TN 57-298, June 1957.

6. Rott, N.; and Smith, W. E.: Some Examples of Laminar Boundary Layer Flow on Rotating Blades. J. Aero. Sci., vol. 23, no. 11, Nov. 1956, pp. 991-996.

7. Graham, M. E.: Calculation of Laminar Boundary Layer Flow on Rotating Blades. Ph.D. Thesis, Cornell University, Ithaca, New York, 1954.

8. Banks, W. H. H.; and Gadd, G. E.: Delaying Effect of Rotation on Laminar Separation. AIAA J., vol. 1, no. 4, April 1963, pp. 941-942.

9. Velkoff, H. R.: A Preliminary Study of the Effect of a Radial Pressure Gradient on the Boundary Layer of a Rotor Blade. Proc. CAL/USAAVLABS Symposium on Aerodynamic Problems Associated With V/STOL Aircraft, vol. 3, 1966.

10. McCroskey, W. J.; and Yaggy, P. F.: Laminar Boundary Layers on Helicopter Rotors in Forward Flight. AIAA J., vol. 6, no. 10, Oct. 1968, pp. 1919-1926.

11. Dwyer, H. A.: Solution of a Three-Dimensional Boundary Layer Flow With Separation. AIAA J., vol. 6, no. 7, July 1968, pp. 1336-1342.

12. Warsi, Z. U. A.: A Numerical Method of Solving the Three-Dimensional Boundary Layer Equations With Application to a Rotating Flat Blade. Preprint 69-227, AIAA, 1969.

13. Warsi, Z. U. A.: Further Theoretical Investigation of the Laminar Boundary Layer Over Rotating Blades in Yawed Infinite Wings. AIAA J., vol. 7, no. 4, April 1969, pp. 687-693.

14. Harris, F. D.; Tarzanin, F. J., Jr.; and Fisher, R. K., Jr.: Rotor High Speed Performance - Theory Versus Test. Presented at the U.S. Air Force Flight Dynamics Laboratory V/STOL Technology and Planning Conference, Las Vegas, Nev., Sept. 1969.

15. Lighthill, M. J.: The Response of Laminar Skin Friction and Heat Transfer to Fluctuations in the Stream Velocity. Proc. Royal Soc., ser. A, vol. 224, 1954, p. 1.

16. Moore, F. K.: Unsteady Laminar Boundary Layer Flow. NACA TN 2471, 1951.

17. Krause, E.: Comment on Solution of a Three-Dimensional Boundary Layer Flow With Separation. AIAA J., vol. 7, no. 3, March 1969, p. 575.

18. Der, J., Jr.; and Raetz, G. S.: Solution of General Three-Dimensional Laminar Boundary Layer Problems by an Exact Numerical Method. IAS Paper 62-70, 1962.

19. Theodorsen, T.; and Garrick, I. E.: General Potential Theory of Arbitrary Wing Sections. NACA Rep. 452, 1933.

20. Himmelskamp, H.: Profiluntersuchungen an einem umlaufenden Propeller. Mitteilungen der Mas-Planck Institut, no. 2, 1950.

21. Blaser, D. A.: A Study of the Possible Effects of Pressure Gradients on the Stall and Boundary Layers of Helicopter Rotor Blades. M. S. Thesis, Ohio State University, 1966.

TABLE 1. WALL DERIVATIVES OF FLAT PLATE UNIVERSAL FUNCTIONS

$f_o''(0)$	0.469599	$g_o''(0)$	0.469599
$F_{1y}''(0)$[a]	-1.2959	$G_{10}''(0)$	0.4711
$F_{1u}''(0)$[a]	1.2000	$G_{11}''(0)$	-1.2383
$F_{20}''(0)$	1.8090	$G_{12}''(0)$	-0.3935
$F_{21}''(0)$	-1.2257	$G_{20}''(0)$	0
$F_{22}''(0)$	-0.8132	$G_{30}''(0)$	-1.6975
$F_{30}''(0)$	0		
$F_{40}''(0)$	-2.5414		

[a]Subscripts y and u denote solutions due to yawed wing and unsteady effects, respectively.

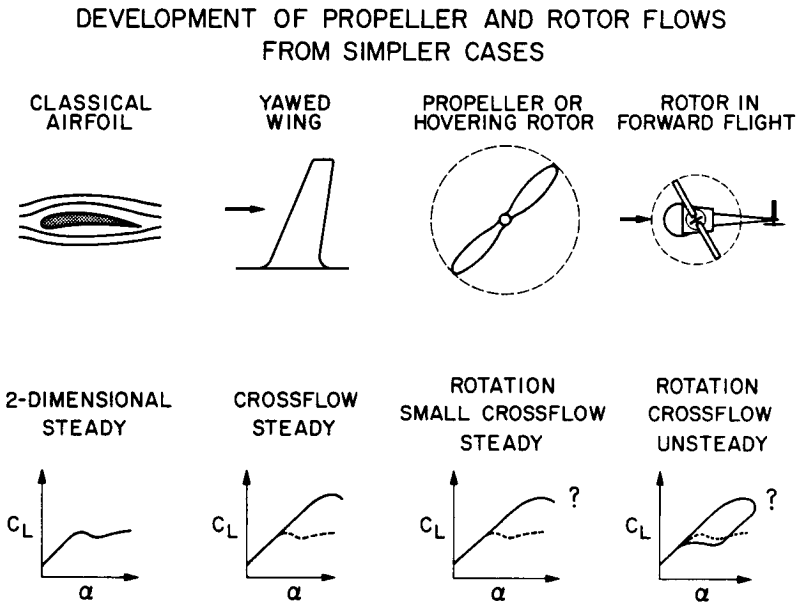

Figure 1

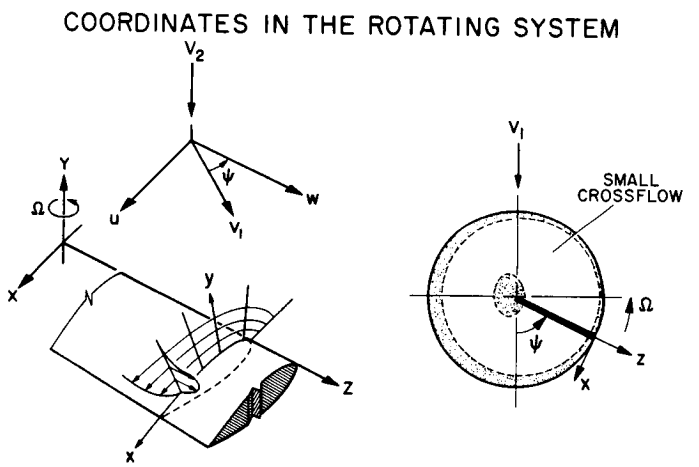

Figure 2

UNIVERSAL VELOCITY FUNCTIONS FOR PRIMARY FLOW
OVER A FLAT PLATE BLADE

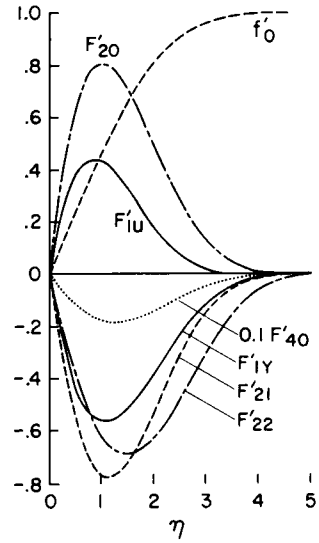

Figure 3

UNIVERSAL VELOCITY FUNCTIONS FOR CROSSFLOW
OVER A FLAT PLATE BLADE

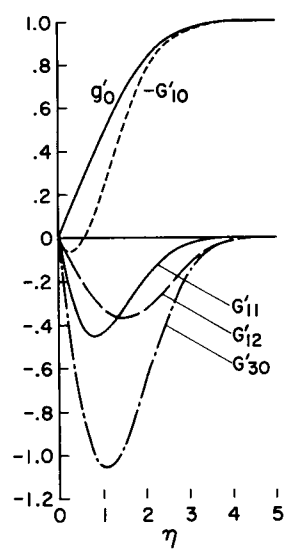

Figure 4

COMPARISON OF RESULTS FOR PRIMARY SHEAR STRESS ON A STEADILY ROTATING FLAT PLATE BLADE

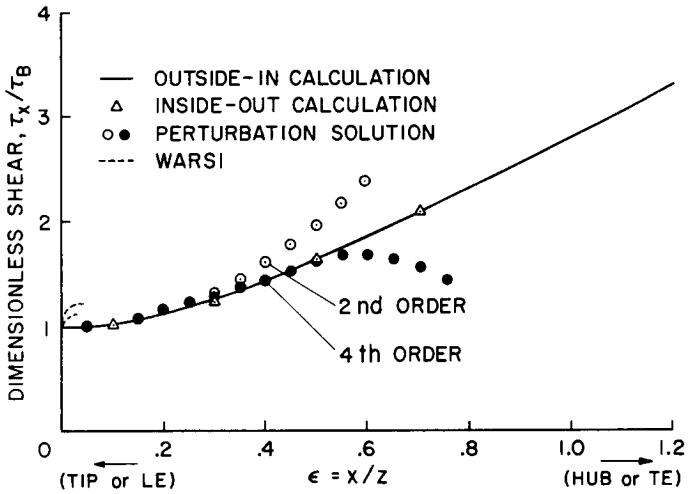

Figure 5

CROSSFLOW VELOCITY PROFILES ON A ROTATING FLAT PLATE

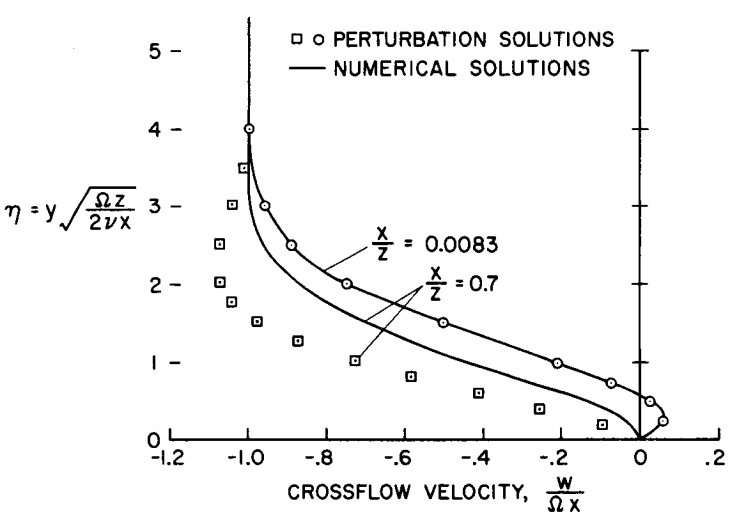

Figure 6

PRIMARY VELOCITY PROFILES ON A ROTATING FLAT PLATE

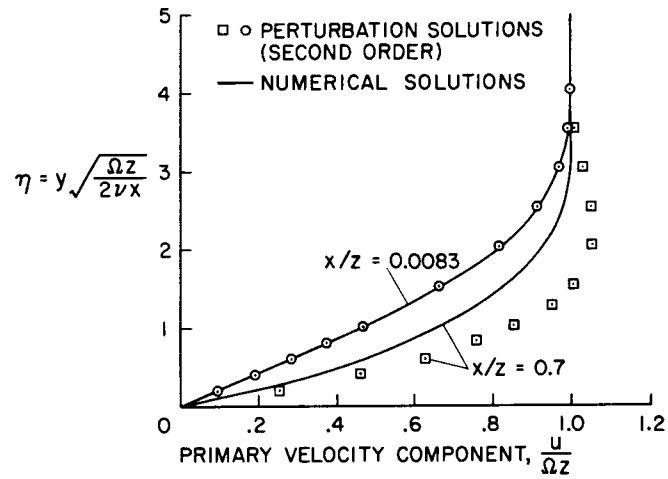

Figure 7

COMPARISON OF RESULTS FOR SHEAR STRESS FOR A 2-D UNSTEADY FLAT PLATE

$U_e = 1 + 0.57 \sin \Omega t$

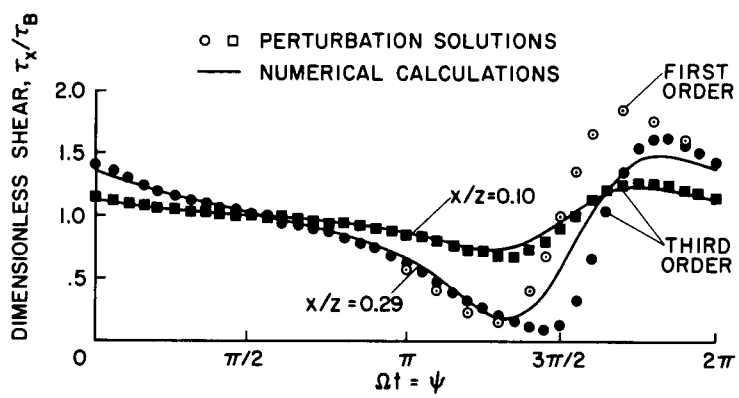

Figure 8

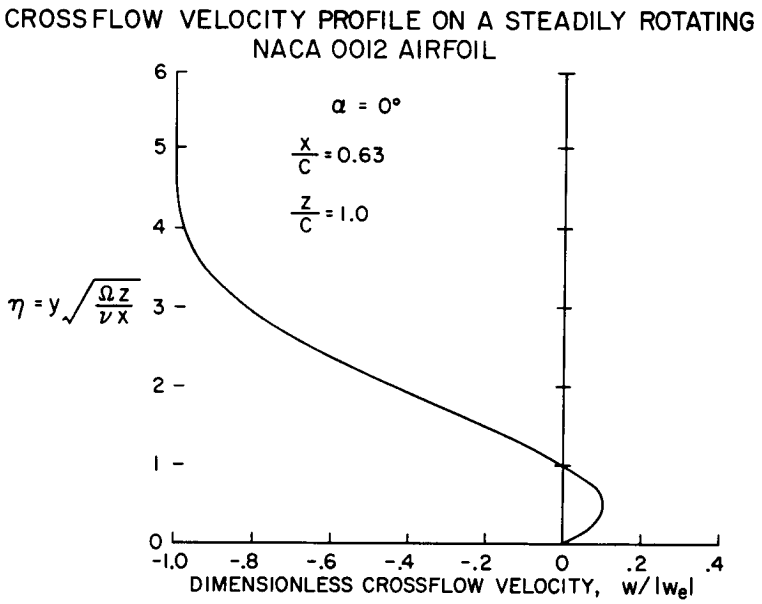

Figure 9

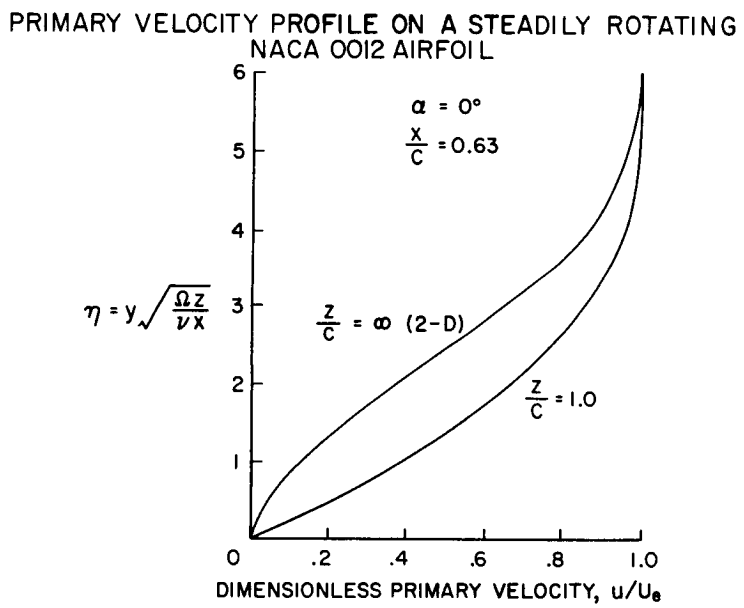

Figure 10

DISTRIBUTION OF PRIMARY SHEAR ON A ROTATING NACA 0012 AIRFOIL

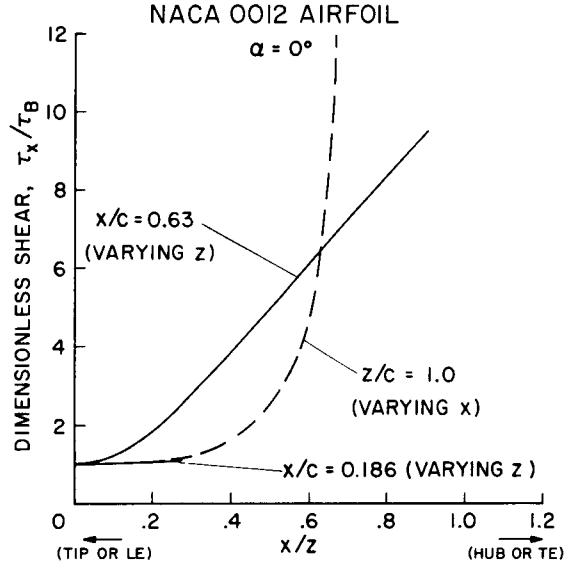

Figure 11

EFFECT OF ROTATION UPON POSITION OF PRIMARY FLOW SEPARATION FOR NACA 0012 AIRFOIL

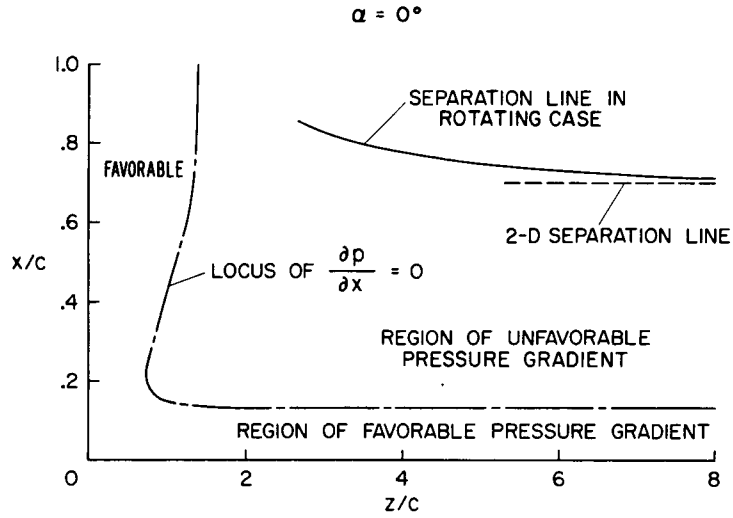

Figure 12

EFFECT OF UNSTEADY VELOCITY UPON SEPARATION
NACA 0012 AIRFOIL
$\alpha = 0°$

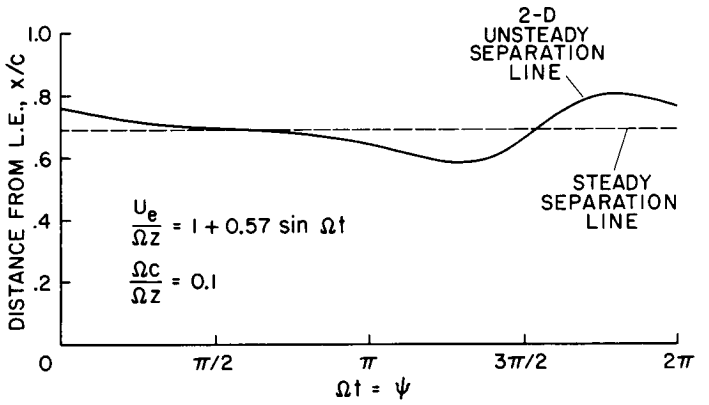

Figure 13

CROSSFLOW VELOCITY PROFILES ON A FLAT PLATE
BLADE IN FORWARD FLIGHT

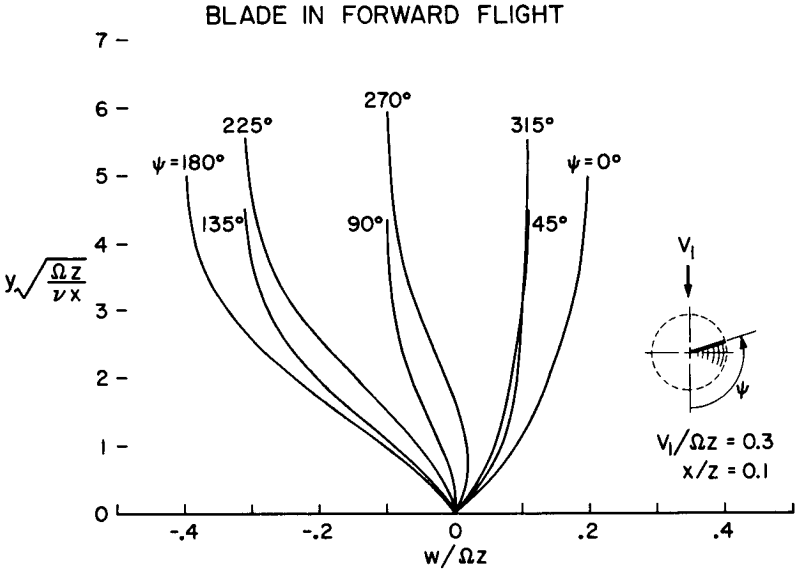

Figure 14

CROSSFLOW VELOCITY PROFILES IN FORWARD FLIGHT
FOR A FLOW WITH ADVERSE PRESSURE GRADIENT
$U_e \propto (1-\xi)$

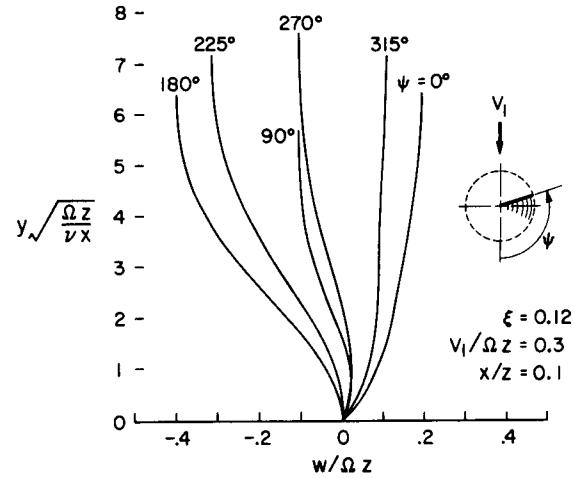

Figure 15

INDIVIDUAL PRIMARY TERMS IN X-MOMENTUM EQUATION
FOR A FLAT PLATE IN FORWARD FLIGHT
ψ = 225°
$V_1/\Omega z = 0.3$

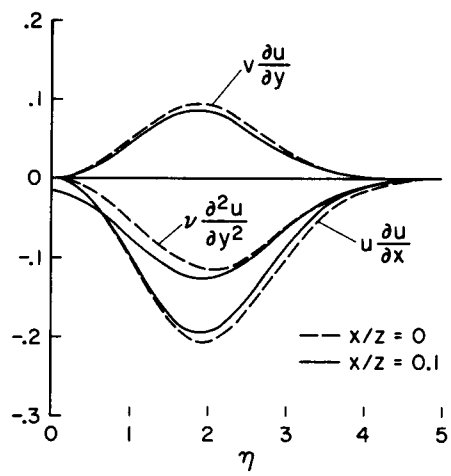

Figure 16

INDIVIDUAL SECONDARY MOMENTUM TERMS IN X-MOMENTUM EQUATION FOR A FLAT PLATE IN FORWARD FLIGHT

$\psi = 225°$
$V_1/\Omega z = 0.3$
$x/z = 0.1$

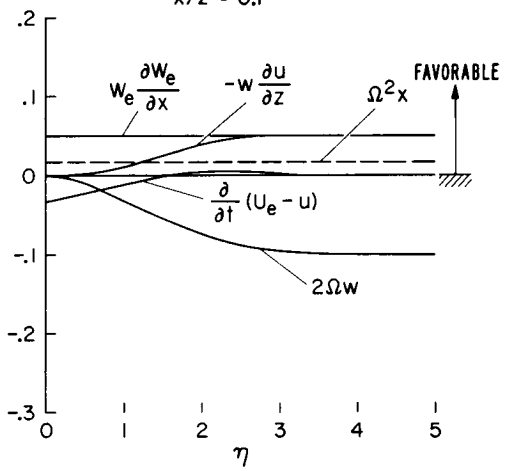

Figure 17

INDIVIDUAL CONTINUITY DERIVATIVES FOR A FLAT PLATE IN FORWARD FLIGHT

$\psi = 225°$
$V_1/\Omega z = 0.3$
$x/z = 0.1$

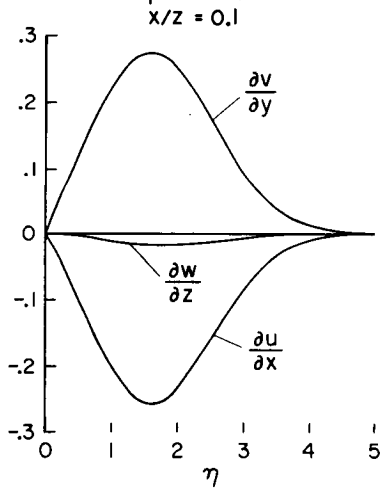

Figure 18

DISCUSSION

G. J. SISSINGH, Lockheed-California Company: My comments refer to the application of the theory to rotors in forward flight. The crossflow angles are zero for hovering and increase with speed or, more accurately, with the advance ratio. Obviously, the largest crossflow angles occur when the blade is in the fore or aft position. However, your Fig. 2 shows the maximum effect in the retreating sector of the rotor disk. Will you please explain why this is the case. Also, what is the criterion for the shaded area of Fig. 2?

McCROSKEY: The shaded region represents the regions where I would very much suspect a small perturbation analysis. That is, there are important regions near the tip where strong trailing vorticity is generated, which introduces a strong crossflow as well as upwash. At this time it is difficult to explicitly say what it is or to say in what manner it actually would affect the flow.

I think I know better now than I did when I first drew the slide up how to treat it, but I still don't know what the effects are, and I don't know anyone who knows how to predict the strong potential crossflow near the tip. It is largest, probably, in the fourth quadrant.

The inner region, the little circle in the middle, corresponds to the reverse flow region, where just because V_1 is larger than the local value of Ωz, the flow is coming at the blade from the trailing edge.

SISSINGH: Next, the crossflow, somehow, changes the lift and drag coefficients of the blade elements. Are you able to predict the overall effect of the crossflow on the rotor characteristics? I am especially thinking of the effects on the blade dynamic response.

McCROSKEY: Well, I hope that in not too much longer I can bring a lot of solid evidence to bear on the effects of crossflow on lift and drag. You realize, of course, at this stage we are trying to be as basic as possible, which has hardly ever been done before in this area, and build up on a solid theoretical understanding.

Now, with regard to what it all means and how it all affects performance, I would refer you to a very recent paper by Frank Harris, presented at the Air Force V/STOL Planning and Technology meeting in Las Vegas in September, in which he has used some empirical corrections to modify the aerodynamic coefficients, such as C_L, C_D, and C_m, on the basis of first of all, a swept-wing correction, which is just taken from static swept-wing wind-tunnel data, and then secondly, an oscillating airfoil correction, which is taken from 2-D oscillating wind-tunnel tests. In an empirical manner he has shown how to formulate these into performance calculations which are very much better in agreement with actual test data than anyone has ever done in the past, and this is extended into the regime where there is lots of blade stall. Now, he has identified the source of the most important contributions. He has done it empirically, and fairly well.

GEORGE R. INGER, McDonnell Douglas Corp.: I want to congratulate you on your presentation because it adds a note and a well-needed one at this conference, I think, that analytical studies are still very much necessary before we trust computer program approaches too much, and I think your slide no. 6 brings this out dramatically. We cannot necessarily trust numerical solutions as a wind-tunnel experiment. The Warsi numerical results, I think, would be suspicious because of the apparently very large slopes that they imply.

McCROSKEY: Well, when he plotted them in the presentation in Atlanta, they didn't show up that way because he used different scales. One has to be very careful presenting and interpreting numerical results.

INGER: In any case, we ought to remember that we need analytical solutions to check the computer programs out, and again, I think this was well brought out by your paper.

ARTUR MAGER, Aerospace Corp.: One of the points which you raised was the separation of the boundary layer caused by the rotation and I was wondering what type of separation criteria did you use? I mean, the separation criteria do change in three-dimensional boundary layers.

McCROSKEY: Well, it would be easy to be flippant and say we called the flow "separated" when we found the computer program going insane, but what it really boils down to is the criterion of the chordwise velocity gradient $\partial u/\partial y$ vanishing. Now, this occurred in such a way that there was almost no build-up of spanwise flow upstream of this. In any event, it is the point where the implicit finite difference technique blows up.

I wish we could look more into the detail of what happens in those little fluid elements right in the neighborhood of separation.

GEORGE R. BARTÉ, JR., General Electric Company: First, let me add my compliments on a very excellent paper, and in particular for having added a word to my vocabulary. "Microsonic" is beautiful. Some might prefer "minisonic" but that is a little too topical.

In listening to and trying to understand the historical and evolutionary manner in which your proceeded from, one of the things that struck me was your comment that ships' propellers or water screws, because they have a relatively low ratio of the x/c parameter, thus require more attention in attempting to come up with some meaningful analysis or theoretical result that you could apply to some real design.

It occurred to me that it needn't be a water screw. It could also be a relatively large aspect ratio wing with ambient twist, and even variable section. I particularly appreciate your comment on possible applications of the thinking and creativity that went into what you have done to a problem so far divorced in concern with low-power fields from the primary intent of your paper.

HARRY A. DWYER, University of California, Davis: I did the numerical part of the paper, and I want to comment on the comment about numerical analysis.

I think if you combine the numerical method with a little bit of analysis you can save a lot of time. We can do a rotating NACA 0012 airfoil in less than two minutes of 7044 computer time, so if you pick your coordinate system right and use the analysis you can really save a lot of time.

ALFRED GESSOW, NASA Headquarters, Washington, D. C.: This delay of separation is a very interesting thing to me because for many years of the problem or anomaly of using two-dimensional airfoil data to calculate rotor characteristics in the stall condition. For example, when calculating the thrust of a rotor at high angles of attack where stall exists, two-dimensional theory indicates that the thrust levels off as the angle of attack goes up, and you predict a lot of stall. But here, by putting your analysis into the performance equations you might show that the thrust continues to go up if stall is delayed sufficiently.

McCROSKEY: Yes, that is exactly what I would expect, and I think some measurements of pressure distributions on helicopter rotors done here at Ames in the full-scale wind tunnel indicate this is, in fact, the case. One develops higher lift coefficients than you should ever be able to expect to get no matter what the angle of attack was in 2-D steady flow. That is, a real airfoil should not develop that high a C_L, and yet it does. There are clear indications of this from some of the pressure measurements, as well as the thrust going in excess of what one should expect on the basis of 2-D section characteristics and strip theory. That is comforting because at least the experimental evidence that we have, although quite meager, does not contradict the trends and conclusions that we would draw from this preliminary study.

A CRITICAL EVALUATION OF ANALYTIC METHODS FOR PREDICTING LAMINAR-BOUNDARY-LAYER SHOCK-WAVE INTERACTION

By John D. Murphy

Ames Research Center

N70-21372

SUMMARY

The present paper is a status report on the existing analytic capability for the prediction of boundary-layer and flow-field characteristics in the presence of a shock-wave—boundary-layer interaction.

Methods for analyzing such interactions have technological application in determining inlet performance and control surface effectiveness at supersonic and hypersonic speeds.

A discussion of three completely analytical methods for describing the observed interaction phenomena is given, and results obtained with these methods are compared with selected experimental data. It is shown that the presently available theoretical methods are in essential agreement with each other at all flow conditions considered and in agreement with experimental data at low Mach numbers for weak shock waves but do not agree with experimental observations for stronger shock waves at hypersonic velocities.

INTRODUCTION

The present paper reports on the status of existing analytic methods for predicting laminar-boundary-layer parameters in the presence of an oblique impinging shock wave.

The scope of this study is restricted to completely analytic methods in which both the boundary-layer parameters and the pressure distribution are computed, for the entire interaction, as part of the solution. As a result of this restriction, only three basic methods were considered. The methods differ only in their mathematical structure and are virtually identical in their underlying physical assumptions. The three analytic methods considered are the method of Lees and Reeves (ref. 1) and its extension to nonadiabatic flows by Klineberg (ref. 2), the method of Nielson, Lynes, and Goodwin (refs. 3 and 4), and the method of Reyhner and Flügge-Lotz (ref. 5). The methods are compared with each other and with carefully selected experimental data.

The experimental data that are compared with the theories cover a range of Mach numbers from 2 to 9.7, wall cooling ratios (T_w/T_{aw}) from 0.2 to 1.0, and unit Reynolds numbers from 0.72×10^6 to 4.4×10^6 ft^{-1}.

SYMBOLS

A	$\frac{1 - M^2}{M^2}$
a	velocity profile parameter employed by Lees and Reeves and by Klineberg
a_e, a_∞	acoustic velocity evaluated at subscript conditions
B	$\frac{h}{pu}\left[\frac{1}{u}\frac{\partial}{\partial y}\frac{\mu\,\partial u}{\partial y} - \frac{1}{Pr^2 h}\frac{\partial}{\partial y}\frac{\mu\,\partial h}{\partial y} - (\gamma - 1)M_\infty{}^2\frac{\mu}{h}\left(\frac{\partial u}{\partial y}\right)^2\right]$
b	enthalpy profile parameter employed by Klineberg
C	Chapman-Rubesin constant
$C_i(x)$	parameter of the inverse shear profile employed by Nielsen et al.
C_f	skin-friction coefficient
D	denominator of the right-hand side of moment equations of Lees and Reeves or of Klineberg
f	dimensionless stream function
H	total enthalpy
h	static enthalpy or flow parameter employed by Lees and Reeves and by Klineberg
M	Mach number
N_i	numerator of the right-hand side of the ith moment equation of Lees and Reeves or of Klineberg
Pr	Prandtl number
p	pressure
Re	Reynolds number based on subscript length
S	$\frac{H}{H_e} - 1$

T	absolute temperature
u	streamwise component of velocity
v	cross-stream component of velocity
x	streamwise space variable
y	cross-stream space variable
α_s	$\frac{\partial u}{\partial \eta}$ on zero velocity streamline in separated region
$\overline{\beta}$	Stewartson transformation coefficient
γ	isentropic exponent
δ	boundary-layer thickness
δ^*	boundary-layer displacement thickness
δ_i^*	transformed boundary-layer displacement thickness
η	transformed y variable
μ	dynamic viscosity
ρ	density
ϕ	flow turning angle across incident shock

Subscripts

aw	evaluated at adiabatic wall conditions
e	evaluated at boundary-layer edge
f	evaluated downstream of interaction
i	evaluated at shock impingement point
o	evaluated at beginning of interaction
s	evaluated on zero velocity streamline
w	evaluated at wall
∞	evaluated at undisturbed free-stream conditions

DESCRIPTION OF THE ANALYTICAL METHODS

General

The analytic methods for predicting laminar boundary-layer—shock-wave interactions will be described in two stages. First, the analytic model together with the governing equations will be described, and second, the mathematical procedures employed in each of the methods will be discussed.

Analytic Model and Governing Equations

The description of the analytic model and the governing equations is relatively straightforward since all the methods considered employ essentially the same model. The equations are those of the conservation of mass, momentum, and energy to the boundary-layer approximation, plus an equation of state and a so-called "free-interaction" relation which couples the local viscous and inviscid flows. The equations can be written as

$$\frac{\partial(\rho u)}{\partial x} + \frac{\partial(\rho v)}{\partial y} = 0 \tag{1}$$

$$\rho u \frac{\partial u}{\partial x} + \rho v \frac{\partial u}{\partial y} = - \frac{dp}{dx} + \frac{\partial}{\partial y}\left(\mu \frac{\partial u}{\partial y}\right) \tag{2}$$

$$\rho u \frac{\partial H}{\partial x} + \rho v \frac{\partial H}{\partial y} = \frac{\partial}{\partial y}\left(\frac{\mu}{Pr} \frac{\partial H}{\partial y}\right) - \frac{\partial}{\partial y}\left[\mu\left(\frac{1}{Pr} - 1\right)u \frac{\partial u}{\partial y}\right] \tag{3}$$

$$p = p(\rho, T) \tag{4}$$

$$\frac{dp}{dx} = f\left(\frac{v_e}{u_e}\right) \quad \text{or} \quad f\left(\frac{d\delta^*}{dx}\right) \tag{5}$$

Each theoretical method discussed employs some form of the above equations in the common procedure described below. Initial conditions are prescribed at the assumed beginning of interaction, x_o, and the interaction is initiated by one of the following procedures: The methods of Lees and Reeves, Klineberg, and Nielsen et al., employ a small positive pulse in surface pressure which causes an outward displacement of the local boundary-layer-edge streamline or the displacement thickness line;[1] in the method of Reyhner and

[1]A discussion of the sign of $d\delta^*/dp$ in laminar boundary layers is presented in a later section of this report.

Flügge-Lotz the initial portion of the calculation is carried out in a weak prescribed adverse distribution. This outward displacement in turn increases the pressure through the free-interaction relation (eq. (5)), and the process amplifies in the streamwise direction until the shock impingement point, x_i, is reached (see sketch (a)). At this point, the boundary-layer edge or displacement thickness line is turned through an angle ϕ:

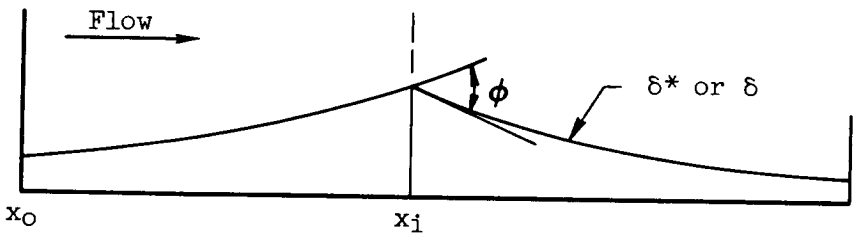

Sketch (a)

The angle ϕ is chosen in the methods of Lees and Reeves and of Klineberg such that an isentropic turn back to the free-stream direction will provide the desired final pressure, and either x_o or x_i is employed as an iteration parameter; whereas in the methods of Reyhner and Flügge-Lotz and of Nielsen et al., the angle ϕ itself is employed as an iteration parameter. For the value of ϕ chosen, the calculation procedure employed upstream of shock impingement is resumed and carried on until some downstream conditions are satisfied or until it becomes obvious that they cannot be satisfied. The downstream compatibility condition in the methods of Reyhner and Flügge-Lotz and of Nielsen et al., is $dp/dx = d^2p/dx^2 = 0$, while in the methods of Lees and Reeves and of Klineberg, it is assumed that the solution must pass through the Crocco-Lees point and approach the flat-plate solution far downstream. An illustration of this iteration process is shown in the computed pressure distributions of sketch (b). Depending on the direction of divergence of the

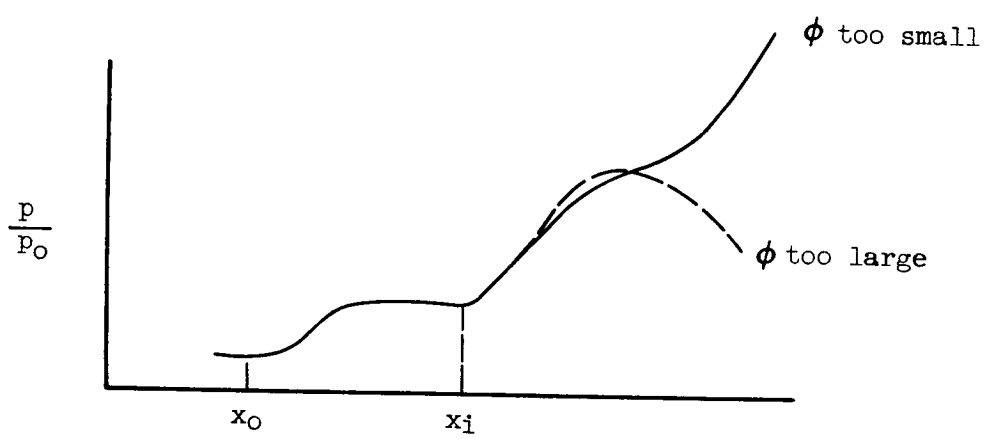

Sketch (b)

solution, ϕ is either increased or decreased until the solution is bracketed. At this point the increment of ϕ is successively halved until the desired convergence criteria are satisfied. As a result of imposing the downstream boundary condition on the system of parabolic equations, the physically elliptic problem is solved as a two-point boundary-value problem rather than the initial value problem of classical boundary-layer theory. The three parameters of the solution are x_o, the beginning of interaction, x_i, the shock impingement point, and ϕ, the flow turning angle or shock strength. Once any two of these parameters is chosen, the third parameter is uniquely specified.

Mathematical Procedures

As noted above, the physical models employed by the various analytic methods are virtually indistinguishable. As a result, differences in the predicted results of the several methods must be attributed to the differing mathematical techniques employed in the solution of the governing equations. These differences arise primarily from the manner in which the system of partial differential equations (eqs. (1)-(5)) is reduced to a system of equations amenable to computer solution.

Moment methods.- The methods employed by Lees and Reeves, Klineberg, and Nielsen et al., fit into the broad category of moment methods. In these methods some functional or tabulated form is assumed to describe the y dependence of the unknowns in terms of an x dependent parameter or parameters. This assumed form is then substituted into the partial differential equations and the resulting equations are multiplied by some weighting function (e.g., u^i, $i = 0, n$) and integrated with respect to y. The result is a system of ordinary differential equations describing the variation of the x dependent profile parameters. The accuracy of these methods then depends on the choice of the approximating functions (i.e., the assumed profiles) and on the weighting functions chosen (cf. ref. 6).

The method of Lees and Reeves employs the continuity, momentum, and first moment of momentum equations for flow over adiabatic walls. The momentum and first moment of momentum equations are obtained by choosing the weighting functions 1 and u. The approximating function for the velocity profiles is represented by the Falkner-Skan family of profiles, for attached flow and by the Stewartson reverse-flow family of profiles (ref. 7) for separated flow. The dependence of these profiles on the pressure gradient parameter β is neglected in favor of a new parameter a defined as

$$a = \eta_\delta f''_w \qquad \text{attached flow}$$

$$a = \frac{\eta_{f'=o}}{\eta_\delta} \qquad \text{separated flow}$$

where

$$f''_w = \left.\frac{\partial u/u_e}{\partial \eta}\right|_{\eta=0}$$

η is the cross-stream variable (transformed y) under the Stewartson transformation and $\eta_{f'=0}$ is the value of this variable on the zero velocity streamline between the forward and reverse flow.

When these assumptions and definitions are introduced into the transformed continuity, momentum, and moment of momentum equations, they can be integrated with respect to y to yield the system of ordinary differential equations:

$$\frac{\delta_i^*}{M_e}\frac{dM_e}{dx} = \frac{\overline{\beta}C}{Re_{\delta_i^*}}\frac{M_\infty}{M_e}\frac{N_1(M_e,a,h)}{D(M_e,a)} \tag{6}$$

$$\frac{d\delta_i^*}{dx} = \frac{\overline{\beta}C}{Re_{\delta_i^*}}\frac{M_\infty}{M_e}\frac{N_2(M_e,a,h)}{D(M_e,a)} \tag{7}$$

$$\delta_i^*\frac{da}{dx} = \frac{\overline{\beta}C}{Re_{\delta_i^*}}\frac{M_\infty}{M_e}\frac{N_3(M_e,a,h)}{D(M_e,a)} \tag{8}$$

where $\overline{\beta} = a_e p_e/a_\infty p_\infty$, and here a is the acoustic velocity, C is the Chapman-Rubesin constant, N_i and D are complicated functions of the arguments noted, and h is a parameter of both the viscous and inviscid flow. The streamwise integration is carried out in an iterative fashion until the downstream compatibility relation is satisfied. The integration is conceptually straightforward, but in its practical application is quite complicated. Readers interested in the iteration procedure are referred to references 1 and 2.

The method of Klineberg (ref. 2) is an extension of the method of reference 1 to the more general case of nonadiabatic flow with initial conditions characteristic of flow in a region of weak interaction. An extension of the method of Lees and Reeves to nonadiabatic flows was carried out by Holden (ref. 8) but is not considered separately here since it is essentially contained within the method of Klineberg. The velocity and enthalpy profiles employed by Klineberg are those of Cohen and Reshotko (ref. 9). The addition of the enthalpy profile as an unknown in the analysis requires an additional equation (the energy equation) and a parameter b proportional to the enthalpy gradient at the wall. The system of equations becomes:

$$\frac{\delta_i^*}{M_e}\frac{dM_e}{dx} = \frac{\overline{\beta}C}{Re_{\delta_i^*}}\frac{M_\infty}{M_e}\frac{N_1(M_e,a,b,h)}{D(M_e,a,b)} \tag{9}$$

$$\frac{d\delta_i^*}{dx} = \frac{\overline{\beta}C}{Re_{\delta_i^*}}\frac{M_\infty}{M_e}\frac{N_2(M_e,a,b,h)}{D(M_e,a,b)} \tag{10}$$

$$\delta_i^*\frac{da}{dx} = \frac{\overline{\beta}C}{Re_{\delta_i^*}}\frac{M_\infty}{M_e}\frac{N_3(M_e,a,b,h)}{D(M_e,a,b)} \tag{11}$$

$$\delta_i^*\frac{db}{dx} = \frac{\overline{\beta}C}{Re_{\delta_i^*}}\frac{M_\infty}{M_e}\frac{N_4(M_e,a,b,h)}{D(M_e,a,b)} \tag{12}$$

Again streamwise integration is conceptually straightforward. In the case of flow over cooled walls, however, additional difficulties are encountered in the streamwise integration. These difficulties are associated with the behavior of so-called "supercritical" boundary layers. This concept and the related concept of a critical temperature ratio as proposed by Nielsen et al., are discussed in a later section of this report.

Nielsen, Lynes, and Goodwin in their method employ a "Crocco like" coordinate system and for attached flow approximate the shear profile as:

$$\frac{\partial u}{\partial \eta} = \frac{(1 - u)\sqrt{u + C_4(x)}}{C_1(x) + C_2(x)u + C_3(x)u^2}$$

and the enthalpy profile as:

$$S = S_w(1 - u) + E_1(1 - u)\left[\sqrt{C_4(x)} - \sqrt{u + C_4(x)}\right]$$

In the separated flow regime the above equations are employed above the zero velocity streamline. Below this line the velocity is assumed to have the form:

$$u = -\alpha_s\eta\left(1 - \frac{\eta}{\eta_s}\right)$$

and the enthalpy profile is taken as:

$$S = S_w + (S_s - S_w)\frac{\eta}{\eta_s}$$

Conditions are imposed so that the first and second derivatives of the velocity profile and the first derivative of the enthalpy profile are continuous across the $u = 0$ line. The equations employed are the first four moments of the momentum equation and the first moment of the total energy equation, giving a system of five ordinary differential equations in the five unknowns $C_i(x)$, $i = 1, 4$, and $E_1(x)$. Streamwise integration is carried out by a standard fourth-order Adams-Moulton routine.

Finite difference method.- The method of Reyhner and Flügge-Lotz is the only method considered that applies a full finite difference technique to equations (1)-(5). This procedure represents derivatives in the cross-stream direction by a finite difference approximation and results in a system of equations which can be solved as ordinary differential equations in the streamwise direction. The y dependent problem is solved iteratively at each x location and the streamwise integration is carried out by the Crank-Nicolson method. This procedure provides an exact numerical solution to equations (1)-(5) in the attached flow region, and in the region of separated flow, it provides an exact numerical solution to these equations under the additional assumption that $u(\partial u/\partial x) = u(\partial H/\partial x) = 0$ below the zero velocity streamline. This last assumption was made necessary by the appearance of nondamping eigenvalues in this flow region which results in an inherently unstable system of equations. The streamwise integration is subject to the conditions described in the preceding section. Initial velocity and temperature profiles may be input in tabular form or, alternatively, provision is made within the program to compute a flat plate initial profile. Wall temperature and/or mass transfer distributions may be input as functions of the streamwise variable. As a result, the Reyhner Flügge-Lotz method is the most accurate and general of the methods considered here.

SUBCRITICAL AND SUPERCRITICAL BOUNDARY LAYERS AND THE CRITICAL TEMPERATURE RATIO

As noted earlier, in the description of the analytic model employed in all the methods considered here, it is required that the boundary layer respond to an adverse pressure gradient by thickening. The resulting outward displacement of the inviscid flow causes an increasing pressure through the free-interaction relation (eq. (5)), and feeds back into the boundary-layer equations such that the whole process is self-supporting in the downstream direction.

In 1955, Crocco (ref. 10) described an extension of the Crocco-Lees mixing theory to the problem of shock-wave—boundary-layer interaction. From his analysis he deduced that the displacement of the boundary-layer edge under a positive pressure gradient $(d\delta/dx)/(dp/dx) = d\delta/dp$ can be either positive or negative, depending on the details of the velocity and density profiles, the magnitude of the edge velocity and the choice of the boundary-layer edge, δ. Boundary layers for which $d\delta/dp$ was greater than zero were termed subcritical and boundary layers for which $d\delta/dp$ was less than zero were termed supercritical. The net result of this finding is that only subcritical boundary layers are consistent with the free-interaction model employed by the methods considered here.

In applying their method to flows over a cooled wall, Nielsen et al., (ref. 3) found that if the wall cooling ratio was reduced below some critical value, no free interaction could be induced by a pressure pulse (i.e.,

$(d\delta^*/dp) \leq 0)$ or supercritical behavior. Fleeman (ref. 11) used this program to map the locus of the critical temperature ratio as a function of Mach number.

Lees and Reeves (ref. 1) provide an extensive discussion of the general theory of the application of moment methods to the prediction of shock-wave—boundary-layer interaction and discuss the criticality concept in detail. Problems of supercritical-subcritical transition did not arise, however, in their treatment of adiabatic flows. When Klineberg (ref. 2) attempted to extend the Lees and Reeves procedure to flows with heat transfer, he found that for cold walls, the initial profiles were supercritical. To circumvent this difficulty, Klineberg introduced a discontinuous jump from the supercritical to the subcritical state to permit free interaction when the boundary layer is initially supercritical. Many other investigators have carried out analyses of various degrees of approximation to determine when supercritical behavior is to be expected. One of the most interesting and complete of these analyses is by Weinbaum (ref. 12) who derived from the boundary-layer equations an expression of the form:

$$\frac{dp}{dx} = \frac{p\left(\frac{v_e}{u_e}\right) + \int_0^\delta B\ dy}{\frac{1}{\gamma}\int_0^\delta A\ dy}$$

where B is a function of the velocity and temperature profiles and

$$A = \frac{1 - M^2}{M^2}$$

It is clear from this expression that when $\int_0^\delta A\ dy = 0$, no finite value of dp/dx is consistent with the boundary equations unless the numerator goes to zero at the same rate. This is equivalent to the condition employed by Klineberg that N_i and D must simultaneously approach zero in order to pass through the downstream critical or Crocco-Lees point.

The zeros of the integral $\int_0^\delta A\ dy$ are interpreted as the streamwise locations where the boundary layer passes from supercritical to subcritical or vice versa. Since the integrand $(1 - M^2)/M^2$ is a strong function of the velocity and temperature profiles, it is not surprising that methods employing different approximate representations of the velocity and temperature profiles, provide conflicting testimony regarding the criticality of a given flow. In order to avoid the effects of the assumed velocity and temperature profile forms, the method of Reyhner and Flügge-Lotz was employed in conjunction with the numerical integration of the Cohen and Reshotko Mach number profiles to deduce the criticality of perturbations on zero pressure gradient flows for several Mach numbers $\leq M_\infty \leq 10$ and wall cooling ratios $0.03 \leq T_w/T_{aw} \leq 1.0$. It was found that while initially zero pressure gradient boundary layers frequently exhibit supercritical characteristics for high

cooling rates even at moderate Mach numbers, they can undergo a smooth supercritical-subcritical transition as a result of a short streamwise exposure to a mild adverse pressure gradient. This transition can occur because the flow near the wall, having very little momentum, reacts rapidly to small adverse pressure gradients and yields a large positive contribution to the integral. The resulting condition is such that computing methods employing a small pulse in surface pressure to induce the interaction will not generate adverse pressure gradients unless specific allowance is provided for a supercritical-subcritical jump. The method of Reyhner and Flügge-Lotz, which induces the interaction by prescribing some initial region of small adverse pressure gradient, effectively bypasses the problem. With regard to the other analytic methods considered, only the method of Nielsen et al., is limited to initially subcritical flows. In the present application, however, this does not constitute a serious shortcoming since the condition occurs only for $T_w/T_{aw} \leq 0.2$ at $M = 10$, and at even lower wall temperature ratios for Mach numbers less than 10.

COMPUTER PROGRAMS

Each theoretical method discussed in the present study is embodied in a computer program. In each case the program employed in the comparisons was provided by the respective authors. However, certain modifications were required to make the program compatible with the NASA-Ames DCS 7040-7094 computer. These modifications were made with reasonable care to prevent any loss of accuracy; however, the program for the method of Reyhner and Flügge-Lotz was written for the CDC 6600 employing 15 significant figures, and the 7040-7094 employs only 9 significant figures. Since double precision was not used in the program conversion, for some conditions the convergence criteria employed in this program had to be relaxed somewhat.

In terms of the generality of the programs, the method of Reyhner and Flügge-Lotz is clearly superior to the others because of the transport property options (see table 1) and the capability of employing tabulated initial profiles as well as nonisothermal walls with or without mass transfer. The transport properties employed by the remaining methods are $Pr = 1$ and the Chapman-Rubesin viscosity law. The boundary conditions imposed at the wall are $u_w = v_w = 0$ and $T_w/T_{aw} = \text{const}$. Initial conditions employed by these methods are either flat-plate similarity profiles, employed by Nielsen et al., and by Lees and Reeves or the hypersonic strong- or weak-interaction solutions employed by Klineberg.

In terms of user convenience, the method of Nielsen et al. is superior to the other methods considered. Only three input cards are required, and all setup and iteration procedures are carried out internally. Of the four methods comsidered, Klineberg's is the most difficult to use for two reasons: First the program was written as a research program and as such was never intended for "batch" calculations. The second reason is directly associated with the underlying theory. Since the approximating functions for velocity and enthalpy are tabulated functions of a and b the functions appearing on the right-hand side of equations (9) through (12) must be generated

externally and curve fitted. A separate subroutine must be written employing these curve fits for each value of wall cooling ratio, T_w/T_{aw}, considered. At the present time these subroutines are available only for $T_w/T_{aw} = 0.2$.

EXPERIMENTAL DATA

In choosing the experimental data for comparison with the analytic methods the following criteria were employed:

1. In addition to presenting the pressure distribution throughout the interaction region, the data source should provide supplementary information, such as schlieren photographs, skin-friction distributions, or heat-transfer distributions.

2. The flow should be two-dimensional and laminar throughout the interaction. These criteria are necessarily qualitative in most cases. When experimental data did not provide downstream profiles or skin-friction distributions, the flow was considered laminar if a well-defined edge white line on the schlieren photograph could be traced throughout the interaction. A flow was considered to be two-dimensional if the predicted downstream mass flow profiles matched those obtained experimentally or, lacking measured downstream profiles, if the aspect ratio (i.e., model width divided by distance from the leading edge to shock impingement) was of the order of unity or greater (cf. ref. 13).

COMPARISON OF EXPERIMENTAL AND ANALYTIC RESULTS

General

Before the results of the analytic methods are compared with experimental data, a few words are necessary to describe the manner in which the comparisons were made. As noted earlier, specifying any two of the three parameters x_o, x_i, and ϕ or the shock strength is sufficient to provide a unique solution to the analytic problem. Unfortunately, none of these parameters can be determined very precisely even when experimental data are available, so that a certain lack of uniqueness exists in the application of these analytic methods to the prediction of experimental data. In the present study each analytic method was employed in an iterative fashion to obtain a reasonably good match to the pressure distribution over the entire interaction regime. For flow at high Mach numbers (i.e., $M_\infty \geq 7.4$) it was found that this procedure could not be followed except for very weak impinging shock waves. When the entire pressure distribution could not be matched it was decided to match the pressure distribution upstream of shock impingement (i.e., $x_o \leq x \leq x_i$). When this procedure was followed, the final pressure ratio was generally underpredicted.

Comparison With the Data of Hakkinen et al.

Figures 1(a) through 1(c) show comparisons of the three analytic methods with the data of Hakkinen et al. (ref. 14). An experimental measure of skin friction was obtained for these data employing the pitot probe as a Preston tube. It can be seen from these figures that the predicted pressure distributions are indistinguishable from each other and agree well with the experimental data. The predicted skin-friction distributions also agree closely with each other but only qualitatively with the data. It can be seen in each of the three sets of data for this series (figs. 1(a) through 1(c)), that the analytic methods have a common tendency to overpredict the extent of separation relative to that observed experimentally.

Comparison With the Data of Lewis

In figures 2(a) and 2(b) the three analytic methods are compared with the data of Lewis (ref. 13). For these experiments, only surface pressure distributions were reported in reference 13. In figure 2, predicted skin friction is plotted for intercomparison among the theories even though experimental results are lacking. In figure 2(a) excellent agreement is found for surface pressures both among the theories and between theory and data. Some difficulty was experienced with the 7094 (single precision) version of the Reyhner and Flügge-Lotz program. In particular, convergence difficulties were encountered immediately downstream of shock impingement. The results shown for this program were obtain by Dr. Reyhner on the Boeing CDC 6600 using, what would be on the 7094, double precision calculations.

Figure 2(b) provides the first and only comparison, in the present study, of the method of Klineberg with other methods and with data primarily because of the wall cooling ratio limitations implicit in Klineberg's method. Of particular interest in this figure is the discontinuity in both predicted surface pressure and skin friction in Klineberg's method which is brought about by the supercritical-subcritical jump mentioned earlier. The cause of the discrepancy in surface pressure distributions among the several theories in this case is difficult to pinpoint since slightly different values of x_o and x_i were employed in each method in addition to the different profile descriptions, etc., described earlier. In any case, none of the theoretical methods departs from the data by more than 20 percent, which may be considered acceptable for many applications.

Comparison With the Data of Needham

In figures 3(a) through 3(c) the methods of Reyhner and Flügge-Lotz and of Nielsen et al., are compared with the data of Needham (ref. 15). The Mach number for these tests was 7.4. The only variable parameter in this series of data is the shock strength. At high Mach numbers discrepancies between theories and the data begin to appear, even for relatively weak shocks. In figure 3(a), for example, the predicted pressure distributions display a well-defined kink, or plateau, while no such behavior is noted in the data. This

is consistent with the previously noted tendency to overpredict the extent of separation. A comparison of the measured and predicted heat transfer, however, indicates a more serious shortcoming in the analytic methods. Downstream of the shock-impingement point very large errors in predicted heat transfer are apparent. In figures 3(b) and 3(c), for increasing shock strength, the errors in predicted heat transfer become even larger. Furthermore, it is found that one can no longer match the final downstream pressure level if the pressure distribution upstream of shock impingement is to be matched.

Figures 4(a) and 4(b) show comparisons of the method of Nielsen et al., and Reyhner and Flügge-Lotz with additional data of Needham obtained at a Mach number of 9.7. The difference between these two sets of data is shock strength. Intercomparisons between the theories and comparison of theory with data are qualitatively the same as those discussed for figures 3(a) through 3(c). Again, for a weak shock, the pressure distribution throughout the interaction is reasonably well predicted, and the heat-transfer distribution is rather poorly predicted downstream of shock impingement. At somewhat higher shock strengths imposing x_o and x_i inferred from the data results in a substantial underprediction of the final pressure ratio.

CONCLUDING REMARKS

When all of the foregoing comparisons of theory and data are considered, the following general observations can be made. First, all of the theoretical predictions agree surprisingly well with each other considering the differences in the mathematical procedures employed. Second, for very weak shock waves, all the methods provide an adequate representation of the observed pressure distribution but have a uniform tendency to overpredict the extent of separation and underpredict heat-transfer rates. Third, for strong shocks when x_o, the beginning of interaction, and x_i, the shock impingement point, are determined from the data, all of the methods substantially underpredict the final pressure ratio. It is worth remarking that the second and third observations represent different manifestations of the same fundamental behavior of the analytic methods. In order to demonstrate this behavior, another comparison of the method of Nielsen et al., was made with the experimental data of figure 1(c). This method was employed because of the efficiency of the program and the demonstrated similarity of the results. In this case, however, the procedure used was to match the experimentally determined separation point. The results are presented in figure 5. It can be seen in this comparison that the predicted pressure distribution is poorer than that obtained for the same data in figure 1(c) and, as before, an underprediction of the final pressure rise results from this matching procedure.

Whether the discrepancy cited above results from a lack of two dimensionality in the experimental flows or from some basic shortcoming in the underlying physical model cannot be unequivocally determined from the present study. While reasonably convincing arguments can be marshalled in favor of either of the above possibilities, it is the author's opinion that

the inability of the methods to predict the experimental results is not wholly associated with shortcomings in the experimental data. As mentioned earlier, care was exercised to insure that all data considered was obtained in pure laminar interactions and on models of relatively large aspect ratio. (The aspect ratio employed here is the model span divided by the distance from the leading edge to the shock impingement point, i.e., span/x_i.) For the data of Needham at Mach number 9.7, the aspect ratio was 0.83 while for the data of Hakkinen et al., at Mach number 2, it was approximately 4. While, in the absence of side plates, a large but finite aspect ratio does not guarantee two-dimensionality, it is felt that the uniformity of the behavior of the experimental results over a wide range of parameters militates against random discrepancies in the data.

In order to determine how the existing physical model should be modified to provide a better quantitative description of the details of the flow, it is useful to reconsider the validity of the underlying assumptions. The first assumption is that the boundary-layer equations are valid. Implicit in this assumption is the condition $\partial p/\partial y = 0$. This condition together with the second assumption that the viscous and inviscid flows interact only along some line at or near the boundary-layer edge imposes the physically unrealistic condition that the supersonic inviscid flow cannot respond to perturbations in the boundary layer except insofar as these perturbations affect the inclination of the local edge streamline or the displacement thickness line. Only by carrying out an analysis wherein these assumptions have not been made can the validity of these assumptions be tested. Some efforts in this direction have been made by Rose (ref. 16). The third and last assumption is that the so-called downstream compatibility conditions are meaningful and correct. Since the location of a downstream critical point is related to the specific assumptions made for velocity and enthalpy profiles and to the choice of the line along which the viscous and inviscid flows are coupled, the condition that the solution pass smoothly through this point, as in the methods of Lees and Reeves and of Klineberg, while consistent with the boundary-layer approximation, seems somewhat artificial physically. The alternate condition employed by Reyhner and Flügge-Lotz and by Nielsen et al., is unfortunately equally artificial in that the simultaneous satisfaction of the conditions $dp/dx = d^2p/dx^2 = 0$ is inconsistent with the free interaction model, and it is this inconsistency which prevents continued downstream integration in these latter methods. It is clear that some downstream boundary condition is required to provide a relation between upstream influence and shock strength if nonelliptic equations are to be employed, but as to which, if either, of the above downstream conditions is valid, remains to be demonstrated.

REFERENCES

1. Lees, L.; and Reeves, B. L.: Supersonic Separated and Reattaching Laminar Flows: I. General Theory and Application to Adiabatic Boundary-Layer/Shock-Wave Interactions. AIAA J., vol. 2, no. 11, Nov. 1964, pp. 1907-1920.

2. Klineberg, J. M.: Theory of Laminar Viscous-Inviscid Interactions in Supersonic Flow. Ph.D. Thesis, Calif. Inst. Tech., June 1968.

3. Nielsen, J. N.; Lynes, L. L.; and Goodwin, F. K.: Calculation of Laminar Separation with Free Interaction by the Method of Integral Relations. (AFFDL TR 65-107). Part I: Two-Dimensional Supersonic Adiabatic Flow. Oct. 1965. Part II: Two-Dimensional Supersonic Nonadiabatic Flow and Axisymmetric Supersonic Adiabatic and Nonadiabatic Flows. Jan. 1966.

4. Goodwin, F. K.; Nielsen, J. N.; and Lynes, L. L.: Calculation of Laminar Boundary Layer-Shock Wave Interaction by the Method of Integral Relations. Nielsen Engineering and Research, Inc., NEAR Rep. TR 2, July 25, 1967.

5. Reyhner, T. A.; and Flügge-Lotz, I.: The Interaction of a Shock Wave with a Laminar Boundary Layer. Tech. Rep. 163, Div. Engin. Mech., Stanford Univ., Nov. 1966, published in abbreviated form in Int. J. Non-Linear Mech., vol. 3, no. 2, June 1968, pp. 173-199.

6. Murphy, John D.; and Rose, William C.: Application of the Method of Integral Relations to the Calculation of Incompressible Turbulent Boundary Layers. Proc. Computation of Turbulent Boundary Layers, 1968, AFOSR-IFP Stanford Symp., vol. 1, S. J. Kline, G. Sovran, M. V. Morkovin, D. J. Cockrell, eds., Aug. 1968.

7. Stewartson, K.: Further Solutions of the Falkner-Skan Equation. Proc. Cambridge Phil. Soc., 50, pt. 3, 1954, pp. 454-465.

8. Holden, M. S.: An analytical Study of Separated Flows Induced by Shock Wave Boundary Layer Interaction. NASA CR 600, Oct. 1966.

9. Cohen, Clarence B.; and Reshotko, Eli: Similar Solutions for the Compressible Laminar Boundary Layer With Heat Transfer and Pressure Gradient. NACA Rep. 1293, 1956.

10. Crocco, L.: Considerations on the Shock-Boundary Layer Interaction. Proceedings of the Conference on High-Speed Aeronautics, A. Ferri, N. J. Hoff, P. A. Libby, eds., Polytechnic Inst. of Brooklyn, Jan. 20-22, 1955, pp. 75-112.

11. Fleeman, Eugene L.: Incipient Separation for Highly-Cooled Walls in a Hypersonic Free Stream. FDCC TM 66-13, Air Force Flight Dyn. Lab., Dec. 1966.

12. Weinbaum, Sheldon: Near Wake Uniqueness and a Re-examination of the Throat Concept in Laminar Mixing Theory. Preprint 67-65, AIAA, Jan. 1967.

13. Lewis, John E.: Experimental Investigation of Supersonic Laminar, Two-Dimensional Boundary Layer Separation in a Compression Corner With and Without Cooling. Ph.D. Thesis, Calif. Inst. Tech., 1967.

14. Hakkinen, R. J.; Greber, I.; Trilling, L.; and Abarbanel, S. S.: The Interaction of an Oblique Shock Wave With a Laminar Boundary Layer. NASA MEMO 2-18-59W, 1959.

15. Needham, D. A.: Laminar Separation in Hypersonic Flow. Ph.D. Thesis, Univ. of London, 1965.

16. Rose, W. C.: A Method for Analyzing the Interaction of an Oblique Shock Wave and a Boundary Layer. Paper presented at NASA Symposium on Analytic Methods in Aircraft Aerodynamics, Oct. 28-30, 1969.

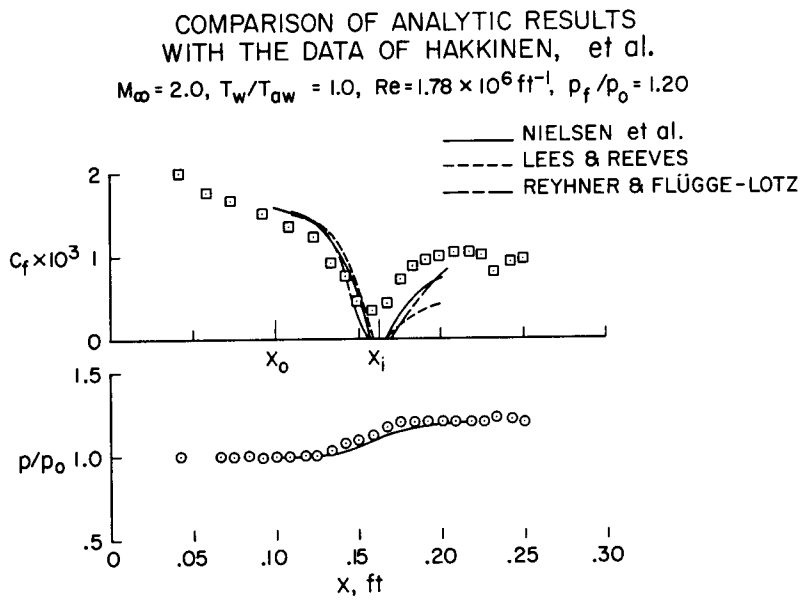

Figure 1(a)

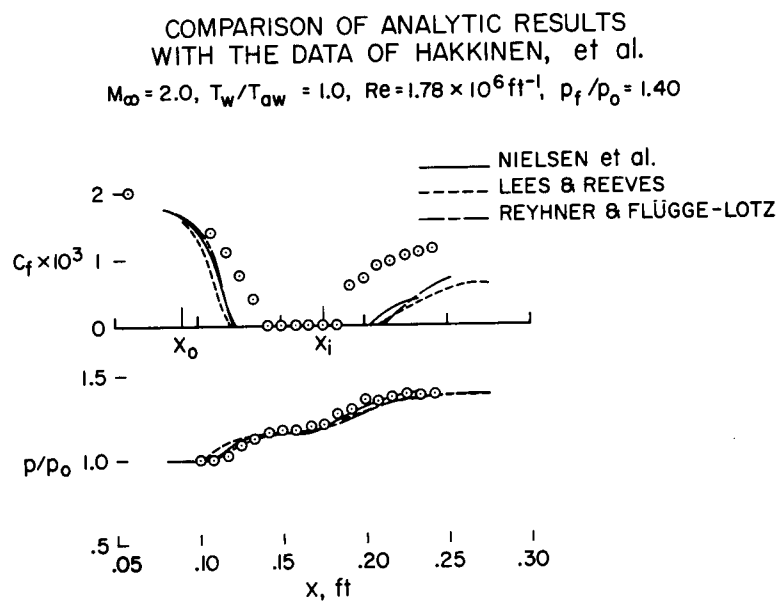

Figure 1(b)

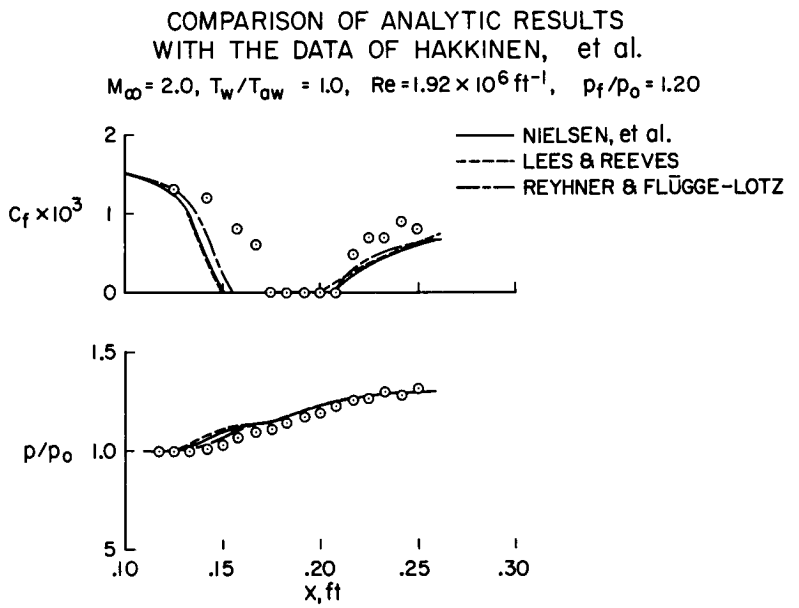

Figure 1(c)

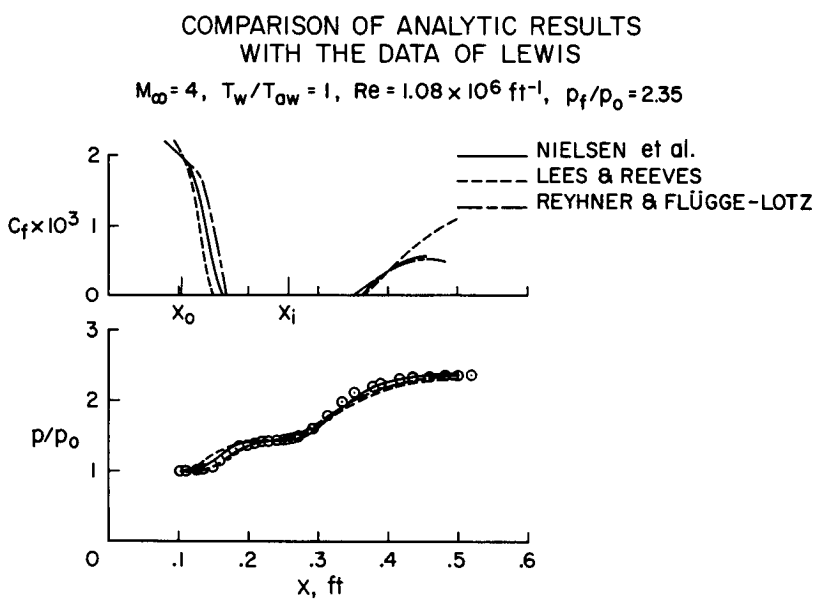

Figure 2(a)

COMPARISON OF ANALYTIC RESULTS WITH THE DATA OF LEWIS

$M_\infty = 6.06$, $T_w/T_{aw} = 0.2$, $Re = 0.72 \times 10^6\ ft^{-1}$, $p_f/p_o = 3.20$

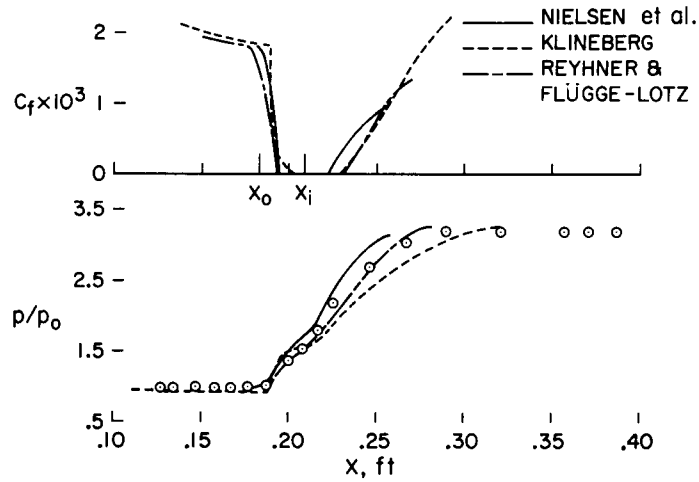

Figure 2(b)

COMPARISON OF ANALYTIC RESULTS WITH THE DATA OF NEEDHAM

$M_\infty = 7.4$, $T_w/T_{aw} = 0.264$, $Re = 4.4 \times 10^6\ ft^{-1}$, $p_f/p_o = 2.50$

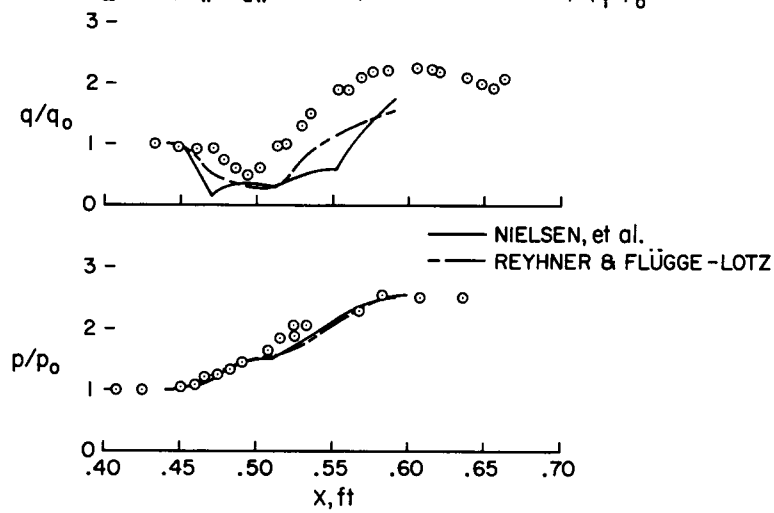

Figure 3(a)

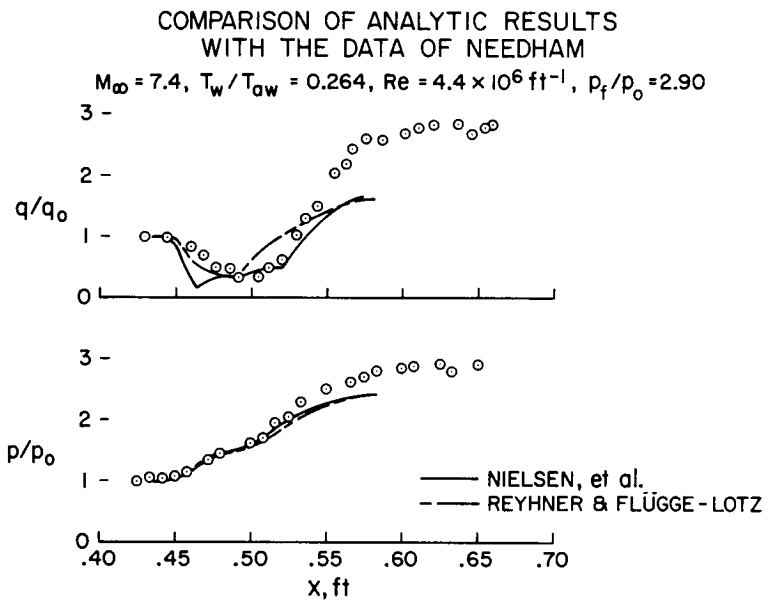

Figure 3(b)

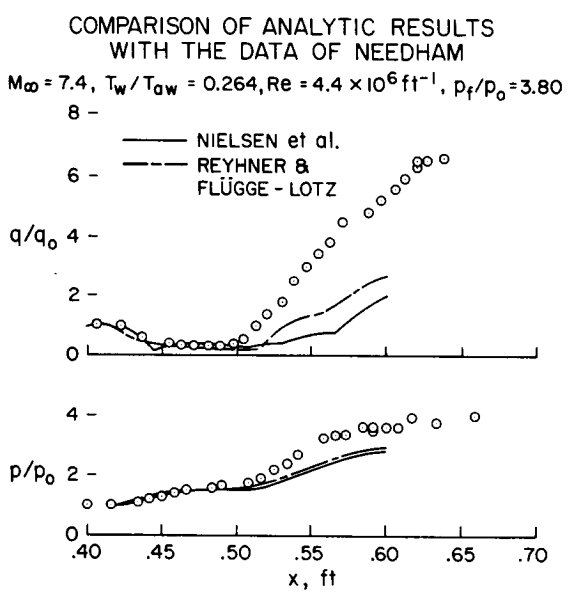

Figure 3(c)

COMPARISON OF ANALYTIC RESULTS
WITH THE DATA OF NEEDHAM

$M_\infty = 9.7$, $T_w/T_{aw} = 0.223$, $Re = 1.91 \times 10^6\ ft^{-1}$, $p_f/p_o = 2.90$

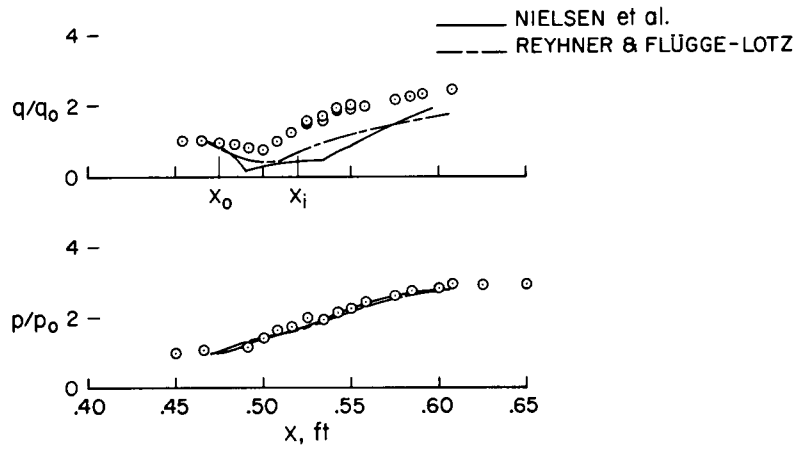

Figure 4(a)

COMPARISON OF ANALYTIC RESULTS
WITH THE DATA OF NEEDHAM

$M_\infty = 9.7$, $T_w/T_{aw} = 0.223$, $Re = 1.91 \times 10^6\ ft^{-1}$, $p_f/p_o = 4.0$,

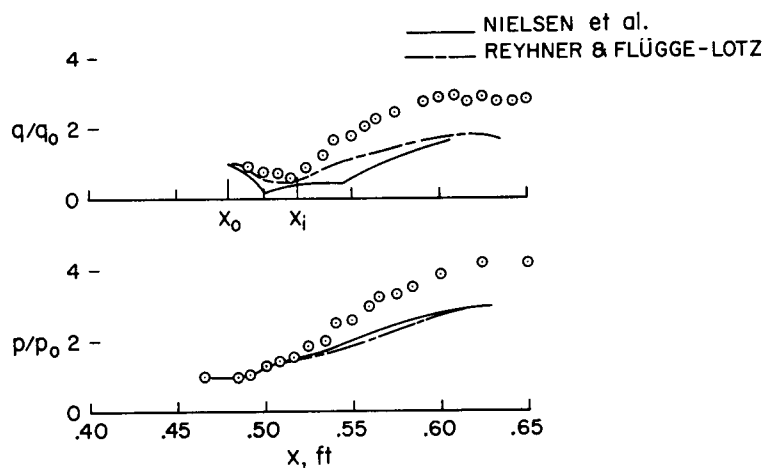

Figure 4(b)

COMPARISON OF THE METHOD OF NIELSEN et al. WITH THE DATA OF HAKKINEN et al.; SEPARATION POINT MATCHED

$M_\infty = 2.0$, $T_w/T_{aw} = 1.0$, $Re = 1.78 \times 10^6\ ft^{-1}$, $p_f/p_o = 1.40$

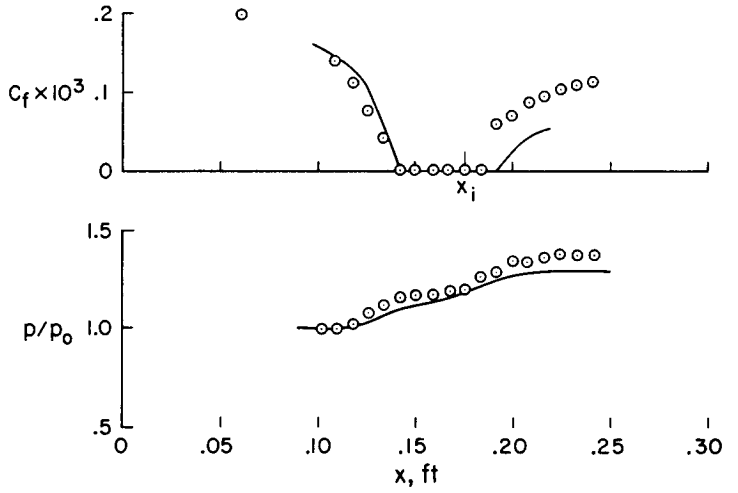

Figure 5

DISCUSSION

JAMES J. DER, General Dynamics, Pomona Division: You show the skin friction being zero in the reverse flow region. Is that right?

MURPHY: Since I did not have any experimental data showing negative skin friction, the output of the computer program was simply not plotted in the separated region. It does go negative in these regions, but since the present paper was an attempt to compare with experimental data, there didn't seem to be much point in plotting the theories alone.

JACK N. NIELSEN, Nielsen Engineering and Research, Inc.: I am very happy to see some party finally take these theories and compare them so as to show what the state of the art is at present.

I would like to suggest why the theories do not agree with the data at hypersonic speeds. I think the data for which the theories did not apply were ones for $\bar{x}$ greater than 1, so they have displacement-dominated pressure gradients near the leading edge, and highly favorable gradients which give initial conditions which are not Blasius initial conditions.

Now, I think probably you used Blasius velocity initial conditions in the theory for those two cases.

MURPHY: That is correct.

NIELSEN: Now, we have made some studies to determine the sensitivity of the extent of separation to slight changes in the initial profile, trying to calculate it for these favorable pressure gradients. We found that the extent of separation is sensitive, that small changes in the actual velocity profile can have a significant effect on this extent of separation. Now, this may be also associated with normal gradients. I can't say it isn't. But I know that the leading-edge effects can change the initial conditions enough to have a significant effect on the extent of separation.

MURPHY: Well, this is certainly quite possible. We haven't looked into perturbing the initial conditions at this point, but one can infer from the written version that initial profiles tending toward criticality will impose large effects on the solution.

MICHAEL S. HOLDEN, Cornell Aeronautical Laboratory, Inc.: I know the data of Needham; there is a weak interaction up to the beginning of separation. The free-stream Mach number is 10 and the Mach number at the beginning of interaction is 9.7, so I don't believe that the profiles in the boundary layer differ significantly from the Blasius profiles.

How do you determine the beginning of the interaction, x_o? Do you define this in terms of either pressure or heat transfer?

MURPHY: Well, the procedure that was followed was essentially a data matching procedure. We simply proceeded to guess x_o and x_i until the data

went through the pressure data. In a data matching procedure you can do this. As a design tool, one would have to, say, obtain the shock strength and the impingement point from some of the inviscid calculations, and then iterate on x_o to find an appropriate downstream pressure level.

HOLDEN: So you didn't match x_i minus x_o, you matched the plateau pressure.

MURPHY: Yes, we matched the pressure distribution, in effect, from x_o to x_i.

HOLDEN: Not explicitly $x_i - x_o$.

MURPHY: Not explicitly, no.

JAMES S. KEITH, General Electric Company: Would you care to comment about the relative computer times between the methods?

MURPHY: That's a little unfair. I don't mean the question, I mean my commenting on it. It depends to a great extent on how familiar you are with the programs and on the particular way in which the programs were designed.

We had the programs furnished to us by the several authors. The method of Klineberg was certainly the slowest, and it was difficult to use. However, it was a program that was not designed for batch calculations, so this has to be borne in mind.

The program of Rehner and Flügge-Lotz took about 10 minutes for, say, three iterations, and Nielsen's program would take on the order of 3 minutes. However, if one were to make some judgment as to which program to use in a given application he would have to examine your particular problem, look at the constraints that are imposed by the theory, and then make judgment on the basis of either efficiency, generality, or peripheral considerations rather than accuracy alone. Clearly for flow on a flat plate with impermeable, isothermal walls, Nielsen's method is the fastest.

A METHOD FOR ANALYZING THE INTERACTION OF AN OBLIQUE SHOCK WAVE AND A BOUNDARY LAYER

By William C. Rose

Ames Research Center

22

N70-21373

SUMMARY

A method is presented for predicting the characteristics of an interaction between an externally generated, oblique shock wave that impinges on either laminar or turbulent boundary layers. The basis of the method is the assumption that the boundary layer in the interaction region may be divided into two layers: the outer layer, an essentially inviscid but rotational layer, and the inner layer, an essentially viscous layer. Coupling of the inner and outer flows throughout the interaction region is discussed. The only empirical information required for using the method is the extent of upsteam propagation of the pressure rise. Correlations for the length of upstream influence, based on parameters consistent with the two-layer hypothesis, are presented in the appendix. Results predicted by the method are compared with experimental results in terms of surface pressure distributions, heat transfer, and flow-field configuration (i.e., shock-wave structure and regions of compression and expansion).

INTRODUCTION

For aircraft intended to fly at supersonic and hypersonic Mach numbers, interactions between oblique shock waves and boundary layers must be properly accounted for to predict adequately the external aerodynamic performance as well as the internal aerodynamics of engine inlets. Assessing aerodynamic performance requires knowledge of the details of the interaction of a shock wave and a boundary layer, such as the manner in which the boundary layer develops throughout an interaction, and how the flow external to the boundary layer is modified as a result of the interaction. For the boundary layer itself, it is important to know whether or not it will separate when subjected to the shock-induced pressure rise. Modifications of the external flow field include regions of compression and expansion induced by the interaction. These modifications are of paramount importance in internal flows, since the characteristics of the reflected compression and expansion regions originating at an interaction on one wall of a hypersonic inlet must be known to obtain the character of the flow field that interacts with the boundary layer on the opposite wall.

A method for analyzing the flow resulting from an oblique shock wave impinging on a turbulent boundary layer was presented in reference 1. This method was based on Lighthill's assumption (ref. 2) that a portion of a supersonic boundary layer on the interaction region could be treated as a

Preceding page blank

rotational but inviscid flow. This portion of the boundary-layer flow was solved in reference 1 by a method-of-characteristics computing program. The effects of viscosity were assumed to be confined to a thin layer near the wall and, therefore, were neglected in the analysis. Neglecting them, however, led to some rather serious shortcomings such as the inability to predict surface quantities such as skin friction and heat transfer. In spite of these shortcomings, fairly good agreement with surface pressure data and the location of incident and reflected shock waves was obtained for shock strengths below that which produced extensive separated regions. The analysis of reference 1 treated the interaction essentially as an inviscid problem, whereas other analytical methods use the boundary-layer equations. For example, the methods of references 3, 4, 5, and 6 describe the behavior of a laminar boundary layer in an interaction. However, a critical evaluation (ref. 7) indicated deficiencies in all four methods for interactions having large pressure rises. For turbulent boundary-layer interactions, no reliable modeling of the turbulent transport processes in an interaction region has been developed. Consequently, methods for treating these interactions are based on "control volume" models (e.g., refs. 8 and 9) or on semiempirical techniques, such as that of reference 10, rather than on analytical solutions of the governing differential equations. All of these methods treat the interaction as a boundary-layer problem, neglecting the external flow, per se, and consequently, yield little or none of the external flow-field information required for analyzing internal flows.

The purpose of this paper is to extend the analysis of reference 1 to include the effects of viscosity. The extension is accomplished by employing the two-layer approach of reference 1, and by assuming that the viscous layer is a laminar boundary layer coupled to the outer inviscid layer. The method by which the viscous and inviscid flows are coupled is discussed. The only empirical information required to complete the analysis of the interaction is a correlation for the extent of the upstream influence of the interacting shock wave. The correlation is discussed in the appendix.

The proposed method of analysis yields a self-consistent two-layer model of the interaction that provides boundary-layer profiles, skin friction, heat transfer, and surface pressure distributions throughout the interaction. The method also provides means for calculating the strength and location of the reflected expansion and compression regions. Results obtained by the proposed method are compared with experimental data for shock-wave—boundary-layer interactions for both laminar and turbulent entering boundary layers.

SYMBOLS

C_f	skin-friction coefficient
M	Mach number
M_o	Mach number at boundary-layer edge at onset of pressure rise
p	local pressure

q	heat-transfer rate
R	radius of leading edge
Re	Reynolds number
T	temperature
u	velocity
x	distance along surface from leading edge
y	distance normal to surface
$y_{viscous}$	distance defined in figure 2
α_L	local flow turning angle across incident shock wave
δ	boundary-layer thickness
δ^*	boundary-layer displacement thickness, $\delta\int_0^1\left(1 - \frac{\rho u}{\rho_\delta u_\delta}\right)d\,\frac{y}{\delta}$

Subscripts

final	downstream of interaction
i	station where incident shock intersects viscous layer (see figs. 12 and 13)
o	conditions at onset of pressure rise
P	plateau
t	total
δ	boundary-layer edge

DISCUSSION OF ANALYTICAL METHOD

Background

Subsequent to the publication of reference 1, the method presented therein has been applied to additional interactions of oblique shock waves with turbulent boundary layers. Examination of these analytical results indicated that further investigation of the fundamental concept of the two-layer model of the boundary layer in the interaction region was warranted.

Two important results obtained from the method of reference 1, but not discussed therein, can be described by the use of figure 1. The first, which is associated with the interaction of the incident shock wave and the vortical (or rotational) layer, is that as the incident shock passes through the vortical layer, a large expansion region is formed that propagates into the downstream flow. The expansion region has been observed in schlieren photographs and is evident in the photographs presented in figures 5, 17, and 18 of reference 11. This expansion region is quite evident in high Mach number, turbulent boundary-layer interactions. On the basis of analytical solutions of the flow obtained during the present study, it can be stated that the magnitude of the expansion decreases as both the Mach number and the shock strength decrease. This expansion is important as it affects the resulting external flow and the configuration of the reflected shock wave passing into the expansion region. Methods for analyzing a turbulent, boundary-layer—shock-wave interaction, other than reference 1, do not account for the presence of the expansion region.

The second result is that downstream of the interaction a region of vorticity exists external to the streamline that contains all the vortical flow ahead of the interaction. This region can be seen in the downstream Mach number and total temperature profiles in figure 1. The height to the outer limit of the predicted vortical layer is identified by the term "induced δ." This terminology has been selected to indicate that some of the vorticity downstream of the reflected shock wave is induced by inviscid effects alone. The "no mass addition δ" shown in figure 1 is the height where the streamline containing all the vorticity ahead of the interaction emerges from the reflected shock wave. The difference between these two heights represents the thickness of the induced vortical layer. It is evident in the solution presented in figure 1 that there would be an apparent increase in the mass flow contained in the total vortical layer downstream of the reflected shock (i.e., below the height indicated by "induced δ"). An increase of 200 to 300 percent over that in the entering boundary-layer mass flow is inferred. The predicted Mach number profile is in general agreement with the experimental profile data obtained slightly downstream of the predicted profile. The data were obtained in the study of reference 11. The experimental total-temperature profile at the same station is also shown and indicates that the outer edge of the region of temperature gradient is at about the same height as that indicated by the "no mass addition δ." This behavior of the experimental data supports the prediction of an inviscidly induced region of vorticity, since no total-temperature gradient exists above the no mass addition δ in the region of flow where a large Mach number (or total pressure) gradient exists. It should be emphasized that the additional vorticity was predicted solely from inviscid effects, neglecting any viscous mixing phenomenon.

In view of the above, it is evident that analytical methods based only on the usual boundary-layer equations have no means of accounting for the existence of induced vorticity in interactions. Furthermore, analyses based on control volume models (e.g., refs. 8 and 9) specifically exclude the possibility of mass addition in the region of pressure rise. The pressure distribution predicted by the method of reference 1 is shown in figure 1 for

comparison with the experimental pressure distribution; the pressure data are shown to be the same scale and properly alined with the flow-field sketch. It is apparent that the mass addition produced by the induced vorticity occurs within the region of the pressure rise. Therefore, it is apparent that excluding mass addition in that region is inconsistent with experimental observation and is consequently a shortcoming of control volume methods. Further examination of figure 1 shows a discrepancy in the predicted and experimental pressure distributions in the vicinity of the shock impingement point. Since, as noted previously, viscous effects were neglected, skin-friction and heat-transfer results were not obtained from the method.

It is thus apparent that the method of reference 1 can be used to predict many of the observable interaction features, but that it yields no information regarding viscous effects, such as skin friction and heat transfer. Furthermore, it yields no information as to the character of the expansion and compression regions that arise from the mutual interaction of the viscous and inviscid portions of the boundary-layer flow and that have been observed in schlieren pictures.

The Coupled, Two-Layer Model

An extension of the method of reference 1 was undertaken to correct the shortcomings noted in the preceding section. The interaction model proposed in the present study is shown schematically in figure 2. Although the entering Mach number profile, shown at the upper left of the figure, is typical of that for a turbulent boundary layer, the model described below is the same whether the boundary layer is turbulent or laminar. The present model differs from that considered in reference 1 in some features, but retains the basic hypothesis that the boundary layer in the interaction region may be divided into two distinct regions. The outer layer is considered to be an inviscid, rotational, isoenergetic region in which normal (i.e., transverse) pressure gradients may exist and in which any effects of viscosity and turbulent mixing are neglected. The inner layer is considered to be a laminar, viscous layer. It is also assumed that the entering Mach number profile may be used to determine the relative extent of the outer, or inviscid, layer, and the inner, or viscous, layer (i.e., the height $y_{viscous}$ indicated in fig. 2).

The primary difference between the presently proposed model and that of reference 1 is that in reference 1 it was assumed that once $y_{viscous}$ had been chosen, the inner layer could be neglected; the effect of the inner layer on the outer layer, and, conversely, that of the outer layer on the inner layer, was ignored. The significant feature of the present method is that it contains a procedure by which the interplay between the viscous and inviscid flows throughout the interaction may be included.

In order to proceed with the analysis, the division between the inner and outer flows must be made. Before the present procedure is described, that employed in reference 1 will be reviewed. In that study, the height to the line dividing the inner and outer flows, $y_{viscous}$, was chosen as that where a "break" or sudden change occurred in the slope of the entering Mach

number profile. This height was also subject to the condition that it be sufficiently large that the flow in the outer layer would remain supersonic downstream of the reflected shock wave. This latter condition was invoked so that a method-of-characteristics computing program could be used to obtain solutions in the outer layer.

This technique is quite subjective and lacks any quantitative procedure for determining the height $y_{viscous}$. Therefore, in the present study, a procedure for determining $y_{viscous}$ has been developed that is consistent with the two-layer hypothesis; that is, the portion of the entering boundary-layer flow above $y_{viscous}$ is assumed to be inviscid. Therefore, the portion of the entering profile that will not significantly deform in the absence of viscous effects as the solution moves downstream is sought. The procedure can be illustrated by the use of figure 3. A typical turbulent boundary-layer profile entering an interaction region is shown by the solid line. Three profiles, each obtained after computation over a distance of five boundary-layer thicknesses downstream of the entering profile, are shown by the dashed curves. Each profile represents a different choice of $y_{viscous}$. It is clear that the choice of 0.031 inch is too low since the profile deforms excessively from the entering profile. This behavior is characteristic of a $y_{viscous}$ low enough to encompass a portion of the profile that maintains its shape primarily through the effects of viscosity. A $y_{viscous}$ of 0.040 inch is slightly better than 0.031 inch but still is considered unacceptable for present purposes. On the other hand, $y_{viscous}$ = 0.062 inch is considered acceptable because the profile has not deformed significantly from the entering profile. As in reference 1, $y_{viscous}$ must still be chosen so that the flow downstream of the reflected shock remains supersonic. For the data examined in this study, the value of $y_{viscous}$, determined as outlined above, was sufficiently large that no problem with subsonic flow downstream was encountered for turbulent boundary-layer flows with an edge Mach number as low as 3.0. This, of course, depends on the shock strength, but for reasonable shock strengths (e.g., those not excessively above that required for incipient separation) no problem would be anticipated. The procedure described above for determining $y_{viscous}$ is much more quantitative than that proposed in reference 1 and has the esthetically pleasing feature of providing a division between the inner and outer layers, consistent with the two-layer concept. For the turbulent flows studied herein, the value of $y_{viscous}$ chosen as above corresponded to values of the law-of-the-wall parameter, y^+, ranging from 20 to 100 (based on a reference temperature). These values are consistent with those obtained for the edge of the laminar sublayer in a law-of-the wall analysis. Therefore, the assumption discussed below, that the inner layer of the present method is laminar, is not inconsistent with experimental observations of the thickness of the laminar sublayer.

The above discussion was concerned with a turbulent entering boundary layer. An identical procedure may be applied for an entering laminar boundary-layer profile. A typical turbulent profile with its appropriately chosen $y_{viscous}$ and a typical laminar profile with its $y_{viscous}$ are compared in figure 4. The profiles are shown as y/δ versus Mach number to indicate the relative portion of the boundary layer (independent of its absolute thickness) that may be considered essentially inviscid. It can be

seen that the percentage of the turbulent boundary-layer thickness in which viscous effects are neglected is much larger than that of the laminar layer. Note that, even though the inviscid portion of the laminar layer is small, the two-layer analysis may be applied.

Subsequent to determining $y_{viscous}$, the combined inviscid and viscous entering profile to be used in the computation of the combined flows must be determined. For a laminar boundary layer this is quite simple. The viscous portion is just the portion of the entering boundary below $y_{viscous}$, and the outer inviscid layer is taken to be the remainder of the profile above $y_{viscous}$ plus a portion of the flow external to the boundary layer. The combined entering profile for a typical laminar boundary layer is shown in figure 5(a). Both the Mach number and total-temperature profiles are considered. The Mach number profile is matched identically, while the assumed total-temperature profile has a slight discontinuity at $y_{viscous}$ because of the assumed isoenergetic outer layer.

The case of a turbulent entering profile is slightly more involved. For purposes of the present study, it is assumed that the entire viscous mixing phenomenon important in the interaction region can be represented by a laminar, viscous layer. This assumption leads to the following technique for obtaining the assumed entering profile. The entering profiles, obtained in the experimental investigation of reference 11, are shown in figure 5(b) to illustrate the procedure. The largest portion of the turbulent entering profile is above $y_{viscous}$; therefore, the Mach number profile is matched exactly. The viscous layer is assumed to be a zero-axial-pressure-gradient, laminar boundary layer with the same value of $y_{viscous}$ as the entering turbulent profile, and at $y_{viscous}$ the value of the local Mach number is set equal to that of the turbulent profiles as indicated in figure 5(b). The assumed Mach number profile differs slightly from the experimental entering profile. Therefore, below $y_{viscous}$, the gradients in the two profiles are generally not matched. This matching procedure yields the assumed total temperature profile shown in figure 5(b). The slight deviation of the assumed Mach number profile in the viscous layer from the experimental profile is probably within the experimental accuracy of determining profiles near the wall. The assumed total-temperature profile, however, is considerably in error. No means of estimating the errors introduced by this seemingly large discrepancy were investigated in this study other than those specifically discussed in the Results section.

For further discussion, it is convenient to divide the interaction into upstream and downstream portions. The division is made at station x_i in figure 2, the point where the incident shock wave impinges on the outer edge of the viscous layer. The manner of selecting the outer edge of the viscous layer is discussed next; a more detailed description of determining x_i is given in the appendix.

It is assumed that upstream of x_i, the viscous layer, constituted as described above, may be solved by any of the analytic computing programs described in references 3, 4, 5, or 6. These methods, in essence, require the specification of the length, l_o, which is the distance from the onset of

the pressure rise, x_o, to the station x_i (fig. 2), in order to initiate the interaction at the proper location. The extent of upstream influence, l_o, can be obtained from experimental data by the procedure outlined in the appendix. For the comparisons between experiment and analytical results presented herein, the extent of upstream influence employed in the viscous solution was determined from the specific data under consideration. These data, together with additional data covering a wide range of Mach numbers, Reynolds numbers, and shock strengths were used to formulate correlations for the extent of upstream influence presented in the appendix. The correlations, which are presented for both laminar and turbulent entering boundary layers, may be used to predict the length, l_o.

After the length of upstream influence is determined, a solution of the viscous, inner layer is obtained from which the lower boundary of the outer layer is then taken. Many possible boundaries can be taken from the inner solution; three are the displacement thickness line, the boundary-layer edge line, and some appropriately chosen streamline. The latter was chosen for the present study since the method-of-characteristics computing program employed has a streamline as its lower boundary. Therefore, if the dividing line taken from the viscous-layer solution is a streamline, the mass flow will be conserved from the wall to any streamline in the outer flow. There is a slight inconsistency in choosing a streamline for the boundary since, in the inviscid outer flow, the total pressure is constant along a streamline while the total pressure decreases slightly along a streamline in the viscous flow. The streamline chosen in the present study passes through a point that is the same distance from the wall as the height, $y_{viscous}$, at station x_o. (See fig. 2.) The shape of this line determines the configuration of the induced compression wave and, hence, the predicted surface-pressure distribution. As pointed out in reference 7, two methods (refs. 3 and 4), one employing the displacement thickness line as the coupling line and the other employing the local boundary-layer edge, give essentially the same pressure distribution and hence must produce essentially the same turning of the inviscid flow. The streamline chosen in this study was between the displacement thickness line and the boundary-layer edge for the viscous layer in all cases considered. Hence, the turning produced in the outer flow by this streamline, is essentially the same. In summary, it should be noted that upstream of x_i, the viscous layer turns the outer flow and the outer layer has no effect on the solution of the inner layer.

When one considers the flow downstream of x_i, the interaction between the inner and outer flows requires a slight modification from that outlined for the flow upstream of x_i. This can be demonstrated by the following two results: the first is for the case of a relatively weak shock wave interacting with a laminar boundary layer, and the second is for a stronger shock interacting with the same boundary layer. Figure 6 shows the surface-pressure distribution data obtained from reference 12 for a weak interaction between a laminar boundary layer and a shock wave. The predicted surface-pressure distribution obtained from the method of reference 3 by matching x_o and x_i is indicated by the dashed curve. The streamline through $y_{viscous}$ at x_o was obtained from this solution and was used as the lower boundary of the outer flow. The outer flow was then solved with the method-of-characteristics program. The pressure distribution obtained from this solution is shown by the

solid curve in figure 6. The agreement between the predicted pressures and the data both upstream and downstream of x_i is quite good, but this is not the case when the shock strength is increased, as is shown in figure 7. The upstream influence length is matched in the viscous solution (shown by the dashed curve labeled 1) and the resultant final pressure level underpredicts the data, a behavior discussed in detail in reference 7. In order to determine the reason for this failure and suggest a possible remedy, the following procedure was followed. The streamline for the lower boundary of the inviscid solution was taken as before. The resulting surface-pressure distribution from the outer layer (shown by the solid curve labeled 2) agrees reasonably well with the data and the inner solution only up to the shock impingement point. At shock impingement a discontinuity in the outer layer pressure distribution is evident. This discontinuity is similar to that shown for the solid curve labeled 1, the solution given by the method of reference 1. Comparison of the inner and outer solutions revealed that the flow angles immediately downstream of x_i on the matching streamline were not the same. The flow turning angle in the inner solution is not as large as that given by the outer flow solution. This causes the reflection of a discrete shock wave and the resulting pressure discontinuity, both of which are inconsistent with physical observation. To surmount this difficulty in the present study, it was hypothesized that the correct, coupled solution must have the same flow angles in the inner and outer layers immediately downstream of shock impingement. An iterative procedure between the inner and outer solutions was required to obtain this consistency in flow angle. The broken curve labeled 2 in figure 7 is the result of imposing on the inner solution the flow angle taken from the second outer solution. The inner and, hence, the outer solutions upstream of x_i are not changed by this modification. The matching streamline is then taken from this inner solution as the lower boundary for the next outer solution. The procedure is seen to be convergent and may be continued until the pressures from the inner and outer solutions agree. A converged solution is shown by the curve labeled 3. One difficulty with this procedure is that, in general, the inner solution does not satisfy the imposed downstream boundary condition (refs. 3 and 4) nor does it pass through the downstream saddle point (refs. 5 and 6). The solution is therefore prevented from advancing farther downstream; thus the inner solution stops short of both the final pressure level and the end of the interaction region, but continues at least to the reattachment point. The exact nature of this difficulty is not fully understood at present; however, it is almost certain that the solution of the viscous flow downstream of shock impingement requires additional conditions other than those contained in the weak-interaction technique now employed. In any event, the results obtained from the viscous programs with the modified downstream turning angle stop short of the end of interaction. Therefore, the matching streamline stops short of the end of interaction. In the present study, in order to obtain a lower boundary for the outer solution beyond the point where the program stopped, the slope of the matching streamline was smoothly extrapolated from its value at the end of computation to a value of zero at the station where the final surface pressure is realized in the outer flow solution.

It appears that the proposed analytical method accounts for most of the observed interaction phenomena, but it should be noted that the method is

in a research state. For example, the coupling between the inner and outer layers and the iterative procedure discussed above must be done externally.

COMPARISON OF ANALYTICAL AND EXPERIMENTAL RESULTS

Some preliminary results obtained by the present method are compared in the following sections with experimental results obtained for interactions with laminar and turbulent boundary layers.

Flow-Field Characteristics

Flow-field characteristics obtained by the present method for an interaction with a laminar boundary layer are presented in figure 8. Also shown for comparison is the schlieren photograph of the interaction taken from reference 12. The interaction considered here is the same as that for which the surface-pressure distribution was given in figure 6. The predicted isobars (p/p_o = constant) from the coupled analysis are shown in the sketch of figure 8. The formation of the induced compression wave, expansion region, and reflected wave are in good qualitative agreement with the observable features of the schlieren photograph. The predictions of the surface-pressure distribution throughout the interaction region are also in good quantitative agreement as shown in figure 6.

The flow-field predictions for the interaction corresponding to those conditions given in figure 7 are compared with the schlieren photograph in figure 9. The analytical results also indicate good qualitative agreement with the observed features. The iterative procedure outlined in the discussion was needed to establish the downstream flow angle for the interaction presented in figure 9, whereas in figure 8, no iteration was required. Without the iterative procedure, the analytical results would have shown a discrete reflected shock rather than the broad compression region seen in both the schlieren photograph and converged analytic solutions.

Surface Phenomena

Comparisons between surface-pressure data for laminar flow and predicted pressures from the coupled method are shown in figures 6 and 7. For a turbulent flow case the interaction data considered in figure 1 are compared in figure 10 with the prediction of the present method. The previously discussed iterative procedure was required to obtain the converged solution shown. A small separated region is predicted, but the spacing of the experimental data precluded any assessment of the validity of this prediction.

The results of heat-transfer predictions compared with the laminar boundary-layer data considered in figures 7 and 9 are presented in figure 11. The results obtained from the computing program of reference 3 are shown in

figure 11(a). The curve labeled 1 is the solution without iteration on the downstream flow angle, while the curve labeled 2 is the result from the second iteration, and the curve labeled 3 is the result from the converged solution. The iterative procedure brings both the magnitude and gradient of the predicted heat-transfer rate into better agreement with experimental data. Similar results, shown in figure 11(b), were obtained by the method of reference 4. The heat-transfer predictions obtained with the method of reference 4 agree somewhat better with the data than those obtained with the method of reference 3. No comparisons have been made in the present study of heat-transfer rates in a turbulent-boundary-layer—shock-wave interaction.

Skin-friction results are easily obtained from the present method; but since it is difficult to obtain C_f experimentally in interaction regions, no demonstrably reliable data are available for comparison. However, a qualitative note concerning skin-friction behavior and the inferred separation length can be made on the basis of results obtained from the present method. The iteration procedure tends to shorten the distance from x_i to the point where the boundary layer reattaches, thus shortening the predicted length of separation. This shortening would bring the predictions of the viscous methods (refs. 3 and 4) into better agreement with experimentally observed separation lengths (see ref. 7), but no quantitative comparisons have been made at present.

CONCLUDING REMARKS

An effort was made to develop an improved analytical method for describing the details of the flow in the vicinity of a shock wave interacting with either a laminar or turbulent boundary layer. A method was developed which is, at present, useful as a research tool in the study of the interaction of a shock wave and a boundary layer.

The analytical method employs the hypothesis that the boundary layer in an interaction consists of two distinct layers, one inviscid and the other viscous, and proposes a method of coupling the two layers. This method adequately described the characteristics of the flow field in the vicinity of a shock-wave—boundary-layer interaction as well as surface-pressure and heat-transfer distributions at least up to the reattachment point.

APPENDIX

THE EXTENT OF UPSTREAM INFLUENCE

General

The spreading of the pressure rise over several boundary-layer thicknesses upstream and downstream of the shock impingement location is a well-known feature of shock-wave—boundary-layer interactions. As noted in the text, information regarding the extent of upstream influence is required in order to use any of the existing analytical methods (refs. 3-6) to obtain a solution of the inner viscous layer as proposed in the present method. In order to make the comparisons between theory and data presented in the main text, a detailed examination of the specific data used was required. In particular, the extent of upstream influence taken from experimental data was used in the analysis. These data, together with additional data from several sources, were used to formulate correlations for the extent of upstream influence for both laminar and turbulent entering flows. These correlations, presented herein, may be used to obtain the length, l_o, when an analytical solution is desired but no experimental data are available.

Chapman, Kuehn, and Larson (ref. 13) used a weak-interation analysis in studying the interaction of a shock wave and a boundary layer. When their analysis is used to determine the extent of upstream influence, a functional dependence of the form

$$\frac{l_o}{\delta_o} = f\left(C_{f_o}, M_o, \frac{p_p - p_o}{p_o}\right) \tag{A1}$$

is indicated. Attempts have been made to correlate existing data using equation (A1). Popinski and Ehrlich (ref. 14) considered wedge-induced interactions for both laminar and turbulent entering boundary-layer flows, and Popinski (ref. 15) considered externally generated shock waves interacting with turbulent boundary layers. Satisfactory correlations were not obtained in these studies since the deviation of some of the data from the recommended correlation curves is over 300 percent of the value given by the curves. Difficulty is encountered in employing the relation implied by equation (A1) because the plateau pressure p_p is, within experimental accuracy, constant for a given entering boundary layer. The extent of the upstream influence therefore cannot increase with increasing shock strength, a behavior that is inconsistent with experimental observation. To circumvent this difficulty in the present study, the functional form relating the important parameters of the problem is taken to be

$$\frac{l_o}{y} = f\left(C_{f_o}, M_o, \frac{p_{final} - p_o}{p_o}\right) \tag{A2}$$

where the reference length y is defined differently for laminar and turbulent flow as follows.

Laminar Boundary Layer

The correlation results for an interaction with an entering laminar boundary layer are presented in figure 12. The data shown were obtained from the interaction studies of references 11, 12, 13, and 16. The reference length, y, in equation (A2) is taken to be δ_o, the boundary-layer thickness at the onset of the pressure rise as indicated in the sketch of figure 12. The length, l_o, is the distance from the onset of the pressure rise to the station where the incident shock wave impinges on the edge of the boundary layer. The choice of this impingement point can be made with reasonable certainty with the aid of a schlieren photograph of the interaction. In connection with determining the impingement point, x_i, it is interesting to note that, within the experimental accuracy of the data examined, the end of the pressure plateau and the impingement point occurred at the same station. Note that, in general, this impingement point cannot be obtained analytically from inviscid considerations alone, since the physical configuration of the incident shock wave is modified by the induced compression region ahead of shock impingement. However, using the coupled technique presented in the body of this report, one can analytically obtain the point x_i and, then through the suggested correlation, obtain the length l_o (and, hence, x_o). This is done by the iterative process outlined below. First, the outer layer is solved without any sublayer considerations as was done in reference 1. This process yields a first approximation to x_i. Next, a value for l_o is obtained from the correlation by assuming that the value of Re_{x_o} is that of Re_{x_i}. The sublayer is then computed from one of the viscous interaction programs suggested in the main text. The resulting streamline through $y_{viscous}$ is employed as the lower boundary for the outer layer solution, as outlined in the main text. A different x_i results and the entire process is repeated until little or no change in the value of x_i is obtained from two successive calculations.

The functional form of the term involving C_{f_o} in equation (A2) is taken as $\sqrt{C_{f_o}}$ in agreement with the weak interaction analysis. For convenience the term $Re_{x_o}^{-1/4}$ has been substituted for $\sqrt{C_{f_o}}$ for the laminar case; M_o is the boundary-layer-edge Mach number at the onset of the pressure rise.

It can be seen from figure 12 that these parameters adequately correlate the data for both separated and unseparated interactions over a wide range of Mach numbers and shock strengths for a range of Re_{x_o} from about 10^5 to 10^6. The largest deviation of the data from the recommended correlation equation

$$\frac{l_o M_o^{2.4}}{\delta_o Re_{x_o}^{1/4}} = 13.7\left(\frac{p_{final} - p_o}{p_o}\right)^{0.73} \tag{A3}$$

is about 30 percent, while most of the data are within 10 percent of the value given by the curve. Perhaps using the actual value of $\sqrt{C_{f_o}}$ instead of $Re_{x_o}^{-1/4}$ would reduce these deviations.

Turbulent Boundary Layer

The thesis of the present work has been employed to develop a set of parameters that give an adequate correlation for the extent of shock-induced upstream influence for turbulent layers. The reasoning that was used to select the parameters that might best describe the physical mechanism involved in the upstream propagation of the pressure rise is as follows. The forward propagation of the downstream disturbance must have its primary path in the subsonic flow adjacent to the wall. The effects of viscosity limit the extent of the upstream influence. The correct reference length in equation (A2), therefore, should be some height that encompasses the subsonic flow and above which the effects of viscosity may be neglected. Thus, in the present study, the height, $y_{viscous}$, obtained by the procedure outlined in the main text is taken as the reference length, since below $y_{viscous}$ the flow is primarily viscous and contains the subsonic region. For turbulent flow, x_i is taken as the station where the incident shock impinges on the local edge of the viscous sublayer, a procedure that is consistent with the laminar case. Experimental determination of this station is somewhat subjective, since no physical dividing line exists in the actual flow; however, schlieren photographs of the interaction can be employed to obtain the station x_i. For the purposes of the present study, the impingement point was taken from schlieren photographs at the position where the incident shock disappears within the lower portion of the boundary layer. This station is indicated in the sketch of figure 13.

Analytical determination of the shock impingement station is possible by employing the iterative technique outlined for the laminar boundary layer in the previous section of this appendix. Note that in contrast to the laminar case, the term $\sqrt{C_{f_o}}$ is not replaced by its corresponding Reynolds number for the reasons outlined by Watson et al. (ref. 17). The values of C_{f_o} are obtained by employing a reference temperature method with the law-of-the-wall exactly as done in reference 17.

The data (from references 11, 17, and 18) are well correlated by the relation

$$\frac{l_o\sqrt{C_{f_o}}\,M_o^{5.0}}{y_{viscous}} = 10.7\left(\frac{p_{final} - p_o}{p_o}\right)^{2.72} \tag{A4}$$

The maximum deviation of a data point from the recommended curve is about 50 percent while most of the data are within 20 percent of the curve. This latter deviation of the data from the correlation curve is probably within the accuracy that the correlation parameters may be obtained, but might be reduced if, instead of the actual edge Mach number, the Mach number at the edge of the viscous sublayer were used. Equation (A4) appears to represent a substantial improvement over previously existing correlation relationships.

REFERENCES

1. Rose, W. C.; Murphy, J. D.; and Watson, E. C.: Interaction of an Oblique Shock Wave With a Turbulent Boundary Layer. AIAA J., vol. 6, no. 9, Sept. 1968, pp. 1792-1793.

2. Lighthill, M. J.: Reflection at a Laminar Boundary Layer of a Weak Steady Disturbance to a Supersonic Stream, Neglecting Viscosity and Heat Conduction. Quart. J. Mech. Appl. Math., vol. III, pt. 3, 1950, pp. 303-325.

3. Goodwin, F. K.; Nielsen, J. N.; and Lynes, L. L.: Calculation of Laminar Boundary Layer-Shock Wave Interaction by the Method of Integral Relations. NEAR Rept. TR 2, Nielsen Engineering and Research, Inc., July 25, 1967.

4. Reyhner, T. A.; and Flügge-Lotz, I.: The Interaction of a Shock Wave With a Laminar Boundary Layer. Tech. Rep. 163, Div. Eng. Mech., Stanford Univ., November 1966, published in abbreviated form in Int. J. Non-Linear Mech., vol. 3, no. 2, June 1968, pp. 173-199.

5. Lees, L.; and Reeves, B. L.: Supersonic Separated and Reattaching Laminar Flows: I. General Theory and Application to Adiabatic Boundary-Layer/Shock-Wave Interactions. AIAA J., vol. 2, no. 11, Nov. 1964, pp. 1907-1920.

6. Klineberg, J. M.: Theory of Laminar Viscous-Inviscid Interactions in Supersonic Flow. Ph.D. Thesis, Calif. Inst. Tech., June 1968.

7. Murphy, John D.: A Critical Evaluation of Analytic Methods for Predicting Laminar-Boundary-Layer Shock-Wave Interaction. Paper presented at the NASA Symposium on Analytic Methods in Aircraft Aerodynamics, Oct. 28-30, 1969.

8. Reshotko, Eli; and Tucker, Maurice.: Effect of a Discontinuity on Turbulent Boundary-Layer-Thickness Parameters With Applications to Shock-Induced Separation. NACA TN 3454, 1955.

9. Seebaugh, William R.; Paynter, Girard C.; and Childs, Marvin E.: Shock-Wave Reflection From a Turbulent Boundary Layer With Mass Bleed. J. Aircraft, vol. 5, Sept.-Oct. 1968, pp. 461-467.

10. Pinckney, S. Z.: Semiempirical Method for Predicting Effects of Incident-Reflecting Shocks on the Turbulent Boundary Layer. NASA TN D-3029, 1965.

11. Watson, Earl C.; Murphy, John D.; and Rose, William C.: Shock-Wave Boundary-Layer Interactions in Hypersonic Inlets. Conference on Hypersonic Aircraft Technology. NASA SP-148, 1967, Paper no. 22.

12. Needham, D. A.: Laminar Separation in Hypersonic Flow. Ph.D. Thesis, Univ. of London, 1965.

13. Chapman, Dean R.; Kuehn, Donald M.; Larson, Howard K.: Investigation of Separated Flows in Supersonic and Subsonic Streams With Emphasis on the Effect of Transition. NACA Rep. 1356, 1958.

14. Popinski, Z.; and Ehrlich, C. F.: Development Design Methods for Predicting Hypersonic Aerodynamic Control Characteristics. (AFFDL TR-66-85), Lockheed California Co., Sept. 1966.

15. Popinski, Z.: Shock-Wave Boundary-Layer Interaction. Rep. LR 18307, Lockheed California Co., 29 June 1965.

16. Hakkinen, R. J.; Greber, I.; Trilling, L.; and Abarbanel, S. S.: The Interaction of an Oblique Shock Wave With a Laminar Boundary Layer. NASA MEMO 2-18-59W, 1959.

17. Watson, E. C.; Rose, W. C.; Morris, S. J.; and Gallo, W. F.: Studies of the Interaction of a Turbulent Boundary Layer and a Shock Wave at Mach Numbers Between About 2 and 10. Compressible Turbulent Boundary Layers. NASA SP-216, 1969, Paper no. 20.

18. Pinckney, S. L.: Data on Effects of Incident-Reflecting Shocks on the Turbulent Boundary Layer. NASA TM X-1221, 1966.

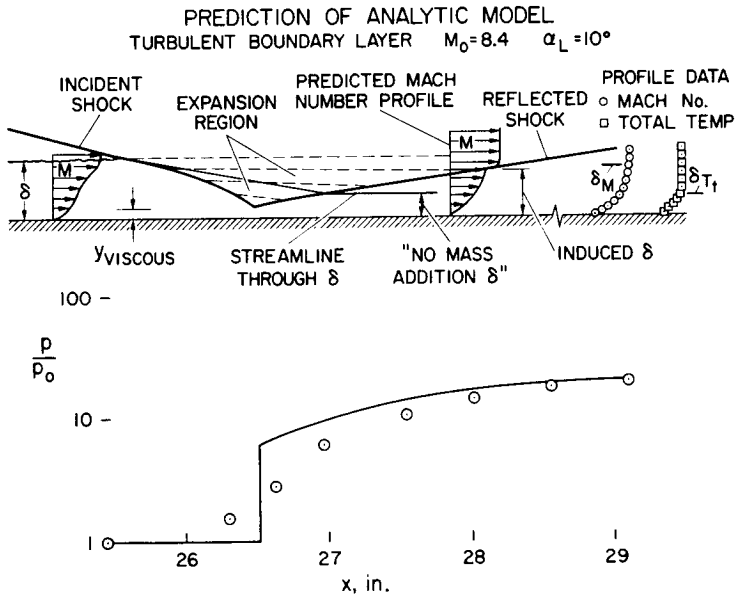

Figure 1

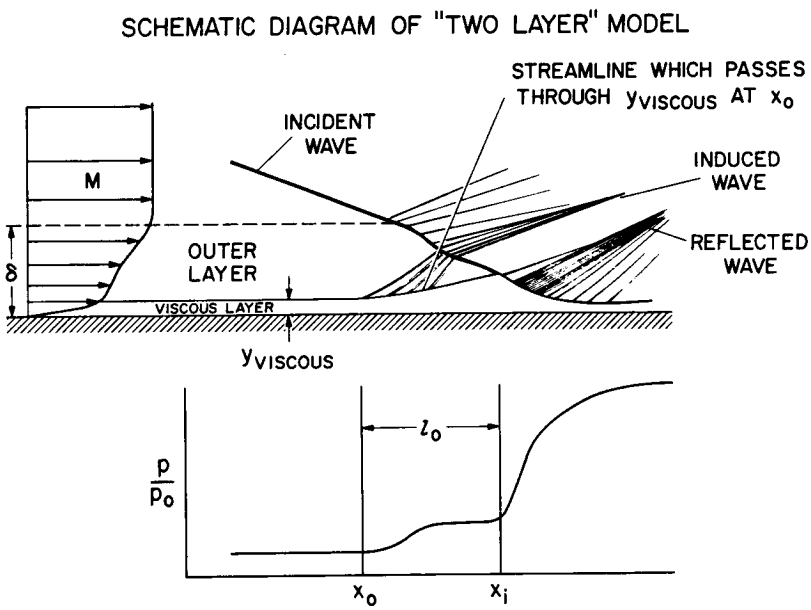

Figure 2

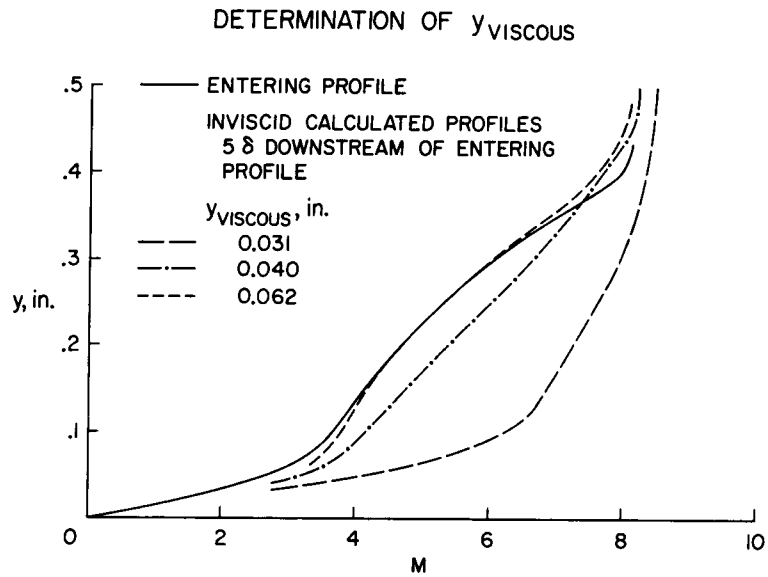

Figure 3

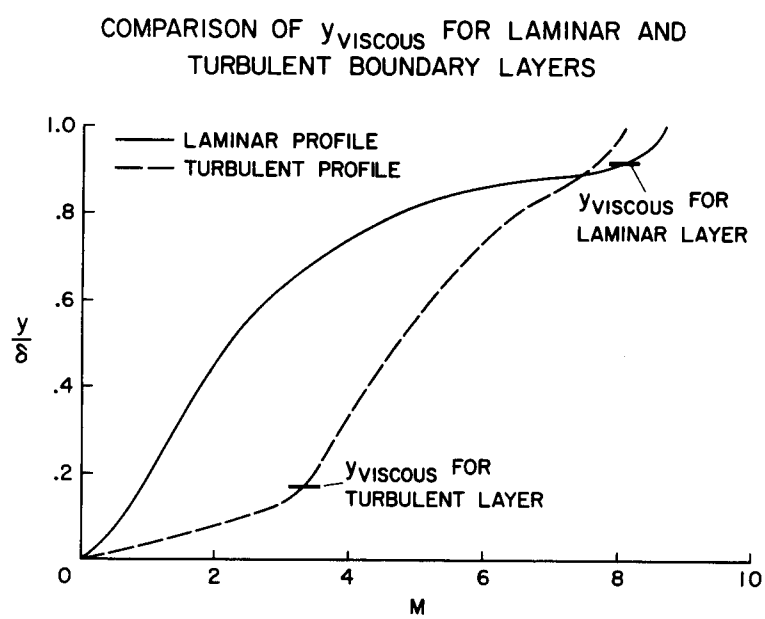

Figure 4

COMPOSITE ENTERING PROFILES
(a) LAMINAR BOUNDARY LAYER

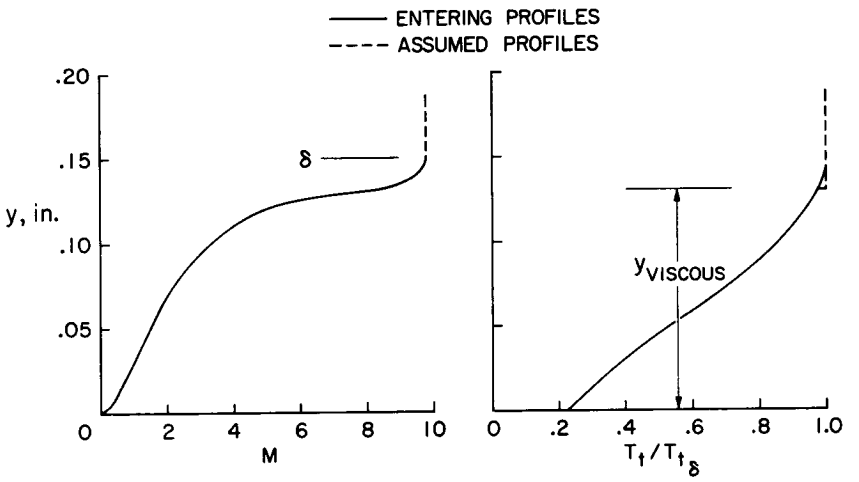

Figure 5(a)

COMPOSITE ENTERING PROFILES
(b) TURBULENT BOUNDARY LAYER

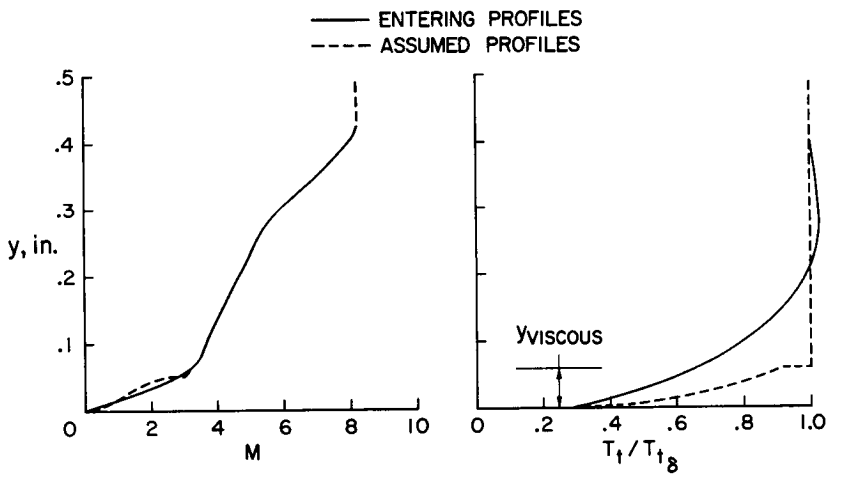

Figure 5(b)

COMPARISON OF PREDICTED AND EXPERIMENTAL SURFACE PRESSURE DISTRIBUTIONS

$M_0 = 9.7 \qquad \alpha_L = 2.2°$

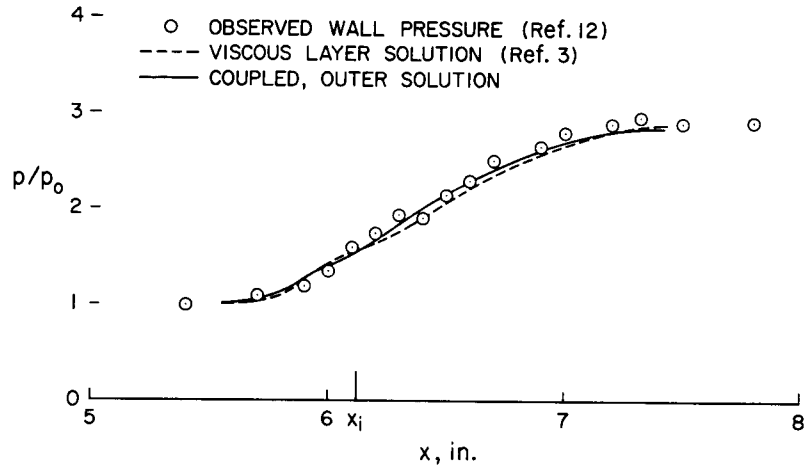

Figure 6

COMPARISON OF PREDICTED AND EXPERIMENTAL SURFACE PRESSURE DISTRIBUTIONS

$M_0 = 9.7 \qquad \alpha_L = 3.2°$

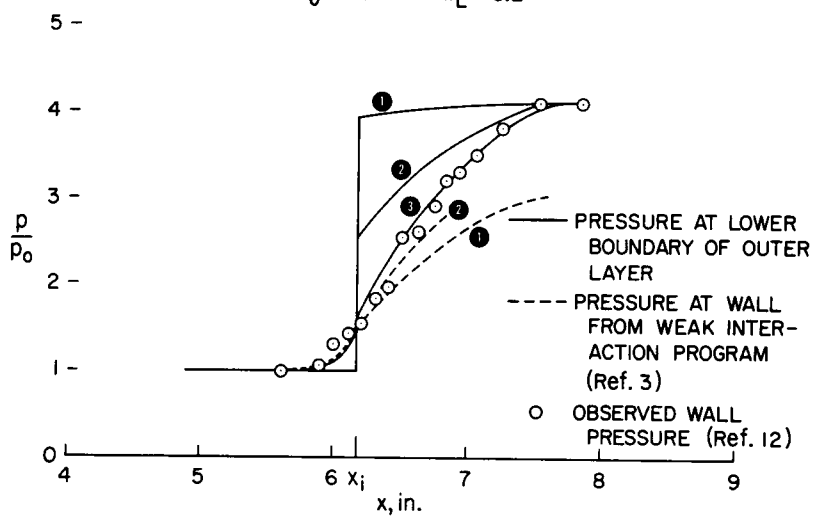

Figure 7

COMPARISON OF PREDICTED AND EXPERIMENTAL SHOCK WAVE CONFIGURATION FOR LAMINAR FLOW (REFERENCE 12)

$M_0 = 9.7 \qquad \alpha_L = 2.2°$

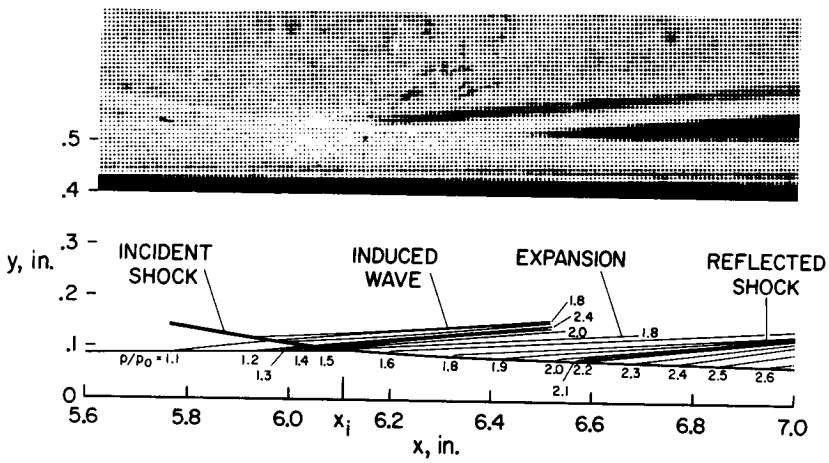

Figure 8

COMPARISON OF PREDICTED AND EXPERIMENTAL SHOCK WAVE CONFIGURATION FOR LAMINAR FLOW (REFERENCE 12)

$M_0 = 9.7 \qquad \alpha_L = 3.2°$

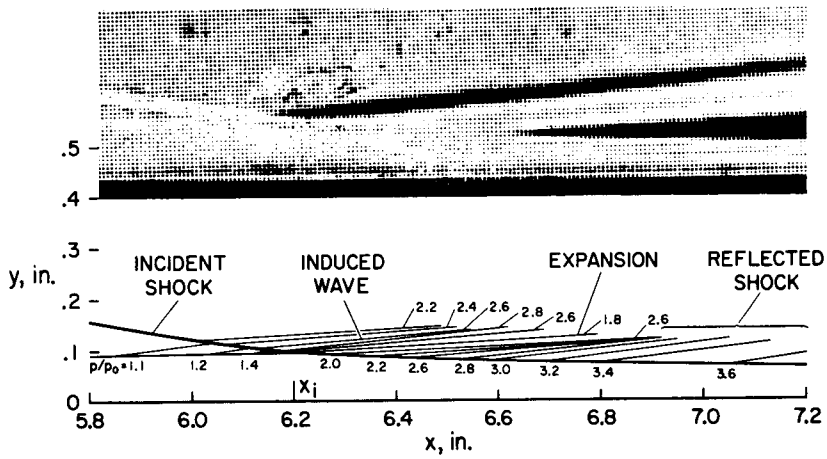

Figure 9

COMPARISON OF PREDICTED AND EXPERIMENTAL PRESSURE DISTRIBUTION FOR TURBULENT FLOW, DATA OF REFERENCE 11

$M_0 = 8.4 \qquad \alpha_L = 10°$

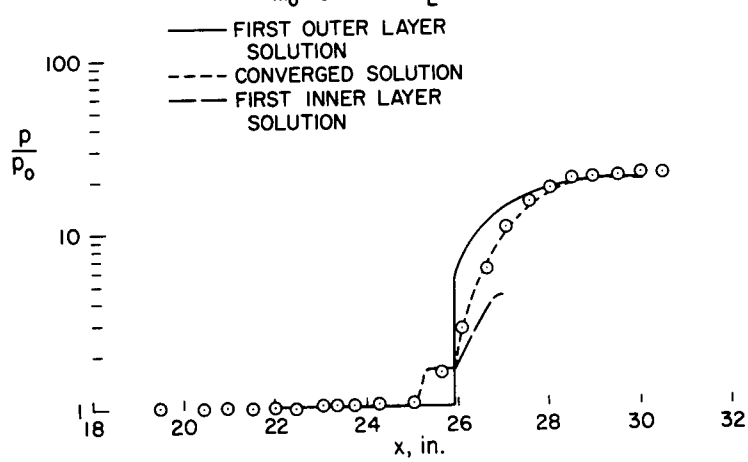

Figure 10

COMPARISON OF PREDICTED AND EXPERIMENTAL HEAT TRANSFER RATES FOR LAMINAR FLOW

$M_0 = 9.7 \quad \alpha_L = 3.2°$

(a) METHOD OF Ref. 3

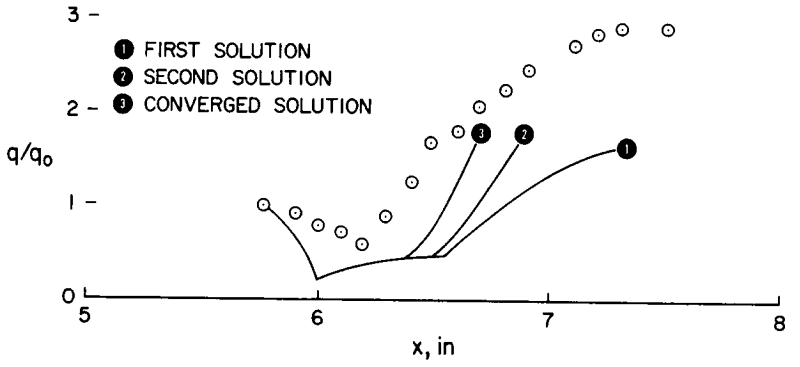

Figure 11(a)

COMPARISON OF PREDICTED AND EXPERIMENTAL HEAT TRANSFER RATES FOR LAMINAR FLOW

$M_0 = 9.7 \quad \alpha_L = 3.2°$

(b) METHOD OF Ref. 4

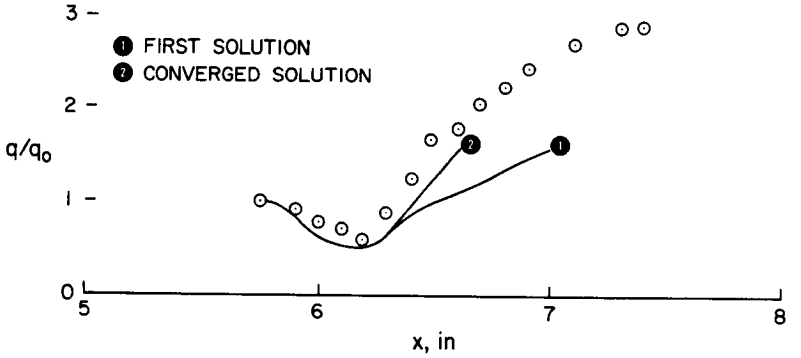

Figure 11(b)

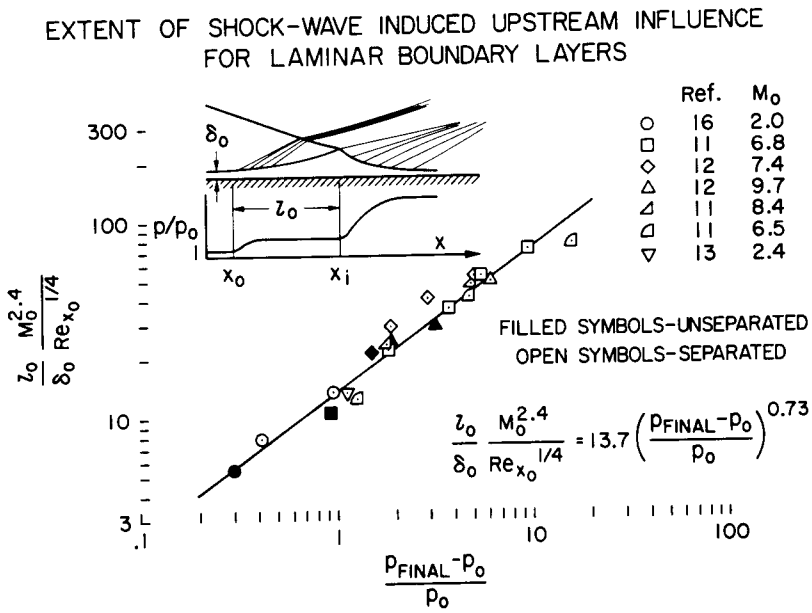

Figure 12

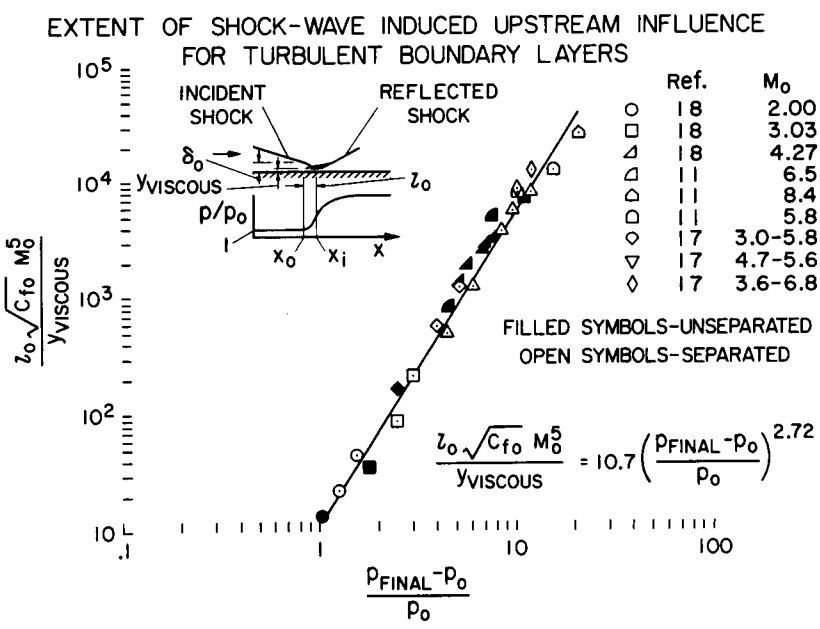

Figure 13

DISCUSSION

FERNANDO L. FERNANDEZ, Aerospace Corp.: I wonder if you could clarify one point. For the range of conditions for which you have obtained solutions is there some specific procedure that you use to determine $y_{viscous}$?

ROSE: Just the one I used here.

FERNANDEZ: Do I understand that you take an initial profile, given experimentally, and you change $y_{viscous}$ until five boundary-layer thicknesses downstream you haven't changed the external profile, or something like that?

ROSE: Yes, that is essentially correct; however, five boundary-layer thicknesses is just a length that is commensurate with the length of the interaction.

FERNANDEZ: But the answer is very sensitive to what you pick for $y_{viscous}$?

ROSE: Yes, although once above a certain height it doesn't seem to make very much difference.

GEORGE R. INGER, McDonnell Douglas Corp.: Let me pursue this point a little further. I notice from your figure 6 that your $y_{viscous}$ is, in effect, nothing more than the edge of the laminar sublayer.

ROSE: You can see that from the figure?

INGER: Yes. Indeed, that is exactly what you would expect by virtue of the definition you used to define $y_{viscous}$ in the first place. It is defined essentially as that part of the profile which is significantly influenced by viscosity, and that is essentially the laminar sublayer for a turbulent boundary layer.

So I would suggest that as a first approximation perhaps one could employ the definition of the laminar sublayer criteria which you find in the literature, to replace this.

ROSE: Yes, you can. Just a note on that. For the flows that I have looked at, if you do a law-of-the-wall analysis based on a reference temperature, the values of y plus at the edge of the sublayer range from around 20 to 100 corresponding to the chosen value of $y_{viscous}$.

INGER: Okay, now I have a second question. What relationship does your $y_{viscous}$ bear to the so-called Lighthill sublayer thickness which would contain the actual upstream influences of small disturbances? Do you know what I am speaking of?

ROSE: Yes. Just generally larger.

INGER: Well, can you give us some feel for . . .

ROSE: Well, for a turbulent boundary layer it is an order of magnitude larger. My familiarity with the Lighthill sublayer method is that it is generally very low in the turbulent boundary layer, simply because of the shape of the profile.

INGER: A final question, if I may. I was wondering if in your analysis there wasn't some element of semi-empiricism. I wasn't quite clear upon that point.

ROSE: Yes, I have taken the value of l_0, the upstream influence on the value, from the data. However, I have looked at an awful lot of other data during the course of this . . .

INGER: But l_0 is your free parameter?

ROSE: Yes. I was going to say I have looked at a lot of other data, and I do present in the written version some correlations for l_0. Using these correlations, my method requires no additional empirical information.

MICHAEL S. HOLDEN, Cornell Aeronautical Laboratory, Inc.: I wonder if you would comment on whether the method you give here would predict a supercritical response in some cases of high Mach number flows over highly cooled walls.

ROSE: The only thing I can say is that when I use the weak interaction program, I am low enough in the boundary layer that I have obtained a subcritical response to the pressure pulse. It is conceivable you could get, for example, a distorted turbulent boundary-layer profile, or if you jump the edge Mach number up to 50 you could probably obtain a viscous layer that would respond supercritically, but I haven't encountered that.

JACK N. NIELSEN, Nielsen Engineering and Research, Inc.: Did you have any separated turbulent boundary layers?

ROSE: I haven't compared with any data that are obviously separated. I should have noted on the last slide that the viscous interaction program predicted a small region of separation here, but the spacing of the data is obviously so large that you can't possibly determine, at least from the pressure distribution, whether separation is there or not. I haven't applied the method as it stands now to any interaction strong enough to produce a large separated region.

RAYMOND SEDNEY, Martin Company: I had two questions. One, is it correct, then, to say, in light of your answer to the previous question, that you didn't really use Lighthill's model except in the qualitative sense?

ROSE: That is correct, I used only his idea of the two-layer model.

SEDNEY: Can I ask, in the viscous layer do you still use the boundary-layer equations?

ROSE: The inner layer is exactly the laminar boundary layer, solved by one of the methods that Murphy just described. He only had the continuity, x momentum and total energy equations and the weak interaction equation.

SEDNEY: You shouldn't get reverse flow then.

ROSE: Yes you can. There is nothing in the weak interaction analysis that excludes that.

ROBERT E. MELNIK, Grumman Aircraft Engineering Corp.: I think there is one element that you probably overlooked in applying the viscous interaction theory, and that is if you want to apply the boundary layer to the viscous sublayer, you really have to match to a shear flow outside.

ROSE: I didn't overlook it in the sense of forgetting it. It is, however, neglected in the analysis as pointed out in the written version.

OPTIMIZATION OF SUPERSONIC INLETS USING THE METHOD OF CHARACTERISTICS

By Bernhard H. Anderson

Lewis Research Center

N70-21374

INTRODUCTION

One of the limiting factors for high-speed computer evaluation of the design and off-design potential of mixed compression supersonic inlets is the extensive trial and error procedures needed to arrive at optimum designs. The trial and error procedures encountered in on-design optimization stem partially from the fact that the primary input quantities to the computer program are only indirectly related to the important design parameters such as average throat Mach number, average flow angle, and throat Mach number distortion. The computations for optimum inlet performance over a Mach number range can become very estensive since the choice of inlet contours is partially dictated by the off-design performance requirements of the inlet.

The type of boundary data which must be prescribed to have a well-set problem is fundamental in establishing a numerical solution to the characteristic equations. However, with a proper formulation of the boundary data, the engineering design parameters (such as throat Mach number, nominal throat flow angle, and internal compression rate) can be introduced directly as boundary conditions. This permits more direct computations of optimum inlet contours with minimized Mach number distortion at the inlet throat.

Once the design contours have been established, computations have to be performed at lower Mach numbers to establish the off-design performance of the inlet. If the inlet performs unsatisfactorily, the original boundary contours must be modified and the calculations must be repeated at design as well as lower Mach numbers. Thus, multiple iterations are encountered in off-design when inlet optimizing performance. However, some properties of the inlet operating on-design can be re-

Preceding page blank

lated to desirable off-design characteristics. When these properties are incorporated at design conditions, a reasonable starting configuration can be obtained, and satisfactory performance can be achieved more rapidly both at design and at lower Mach numbers.

The object of this paper is to report on a characteristic program (ref. 1) formulated to incorporate directly the inlet design parameters of internal compression rate, throat Mach number, and flow angle and to discuss some of the traits of on-design operation which are indicative of acceptable off-design performance.

SYMBOLS

M	Mach number
q	velocity
X, Y	coordinates ratioed to cowl lip radius
μ	local Mach angle with respect to local flow angle
ρ	density
ϑ	local flow angle
ψ	stream function

Subscripts:

C	cowl surface
CB	centerbody surface

FORMULATION OF BOUNDARY DATA

Consider the supersonic portion of the inlet flow field within the cowling to be constrained between two arbitrary boundaries, one of which may be

undefined (see fig. 1). To have a well-set problem, initial data must be provided and two additional boundary conditions must be prescribed. However, there are four available boundary data from which the necessary pair may be chosen. These would include (1) the cowl surface contour $Y = Y_C(X)$, (2) the Mach number distribution along the cowl surface $M = M_C(X)$, (3) the centerbody surface $Y = Y_{CB}(X)$, and (4) the Mach number distribution along the centerbody surface $M = M_{CB}(X)$. Thus, the possible combinations of boundary data that could be prescribed are as follows:

(1) Two boundary curves (fixed boundary problem)

(2) One boundary curve and one Mach number distribution (free boundary problem)

(3) Two Mach number distributions (doubly free boundary problem)

It is not possible, however, to choose both the surface contour and the corresponding Mach number distribution if the downstream leading characteristic from the initial data line intersects the boundary.

Fixed Boundary Problem

The conventional characteristic program prescribes both boundaries, and thus the equations of the bounding surfaces become the program input variables. The calculation of the inlet flow field proceeds downstream from the initial data line to the solid boundary (fig. 2). When the flow field of one boundary is completed, the calculations continue downstream along the opposite characteristic from the previous flow field. If a particular flow field must be established, a trial and error iteration for the surface contours must be used.

Free Boundary Problem

The most desirable free boundary problem is obtained prescribing the centerbody surface and the corresponding Mach number distribution along that surface. The cowl contour that provides this Mach number distribution

is then calculated by the characteristic program. Since the centerbody surface contour and Mach number distribution are prescribed, the calculations proceed upstream from the centerbody surface to the unspecified cowl surface (fig. 3). For this free boundary problem, the establishment of the unknown cowl surface $Y = Y_C(X)$ essentially reduces to finding the streamline which passes through the specified cowl lip. In any inviscid flow, the streamlines (by definition) form surfaces across which there is no flow and consequently they may be replaced by a solid surface. The streamlines can either be determined by constructing them piecewise or by integrating the mass flux from a known boundary. This latter course was chosen and proceeds as follows. The inlet mass flow is first established by the integration of the mass flux along the initial characteristic or data line. This inlet mass flow is used as the stream function normalizing factor. The inlet flow field is constructed by successive field point calculations in the upstream direction as shown in figure 3. Simultaneously with the field point calculation, a mass flux integration is performed. When the normalized stream function exceeds unity, an iteration is performed to locate the streamline $\psi = 1.0$. The internal flow field calculations continue in a similar manner until all the boundary data are used.

To minimize the Mach number distortion at the inlet throat, the desired centerbody surface contour and the corresponding Mach number distribution are specified to the throat conditions. Downstream of this location on the centerbody, the throat Mach number and centerbody surface angle are held constant until the flow field calculations indicate that a uniform Mach number distribution has been established across the inlet throat. The position where uniform flow is achieved is the geometric throat of the inlet.

Equations for Streamline Tracing

The equations used for tracing the inlet streamlines are obtained by integration of the continuity relation along either a C+ or C- characteristic; thus,

$$\psi_B = \psi_A + \int_{Y_A}^{Y_B} \frac{\rho q y \, dy}{M \sin(\mu \pm \vartheta)} \tag{1}$$

where the + or - is used for integration along a C+ or C- characteristic, respectively. The integral on the right side of equation (1) represents the accumulation of mass flow between Y_A and Y_B in the flow field. If the interval AB is used as the distance between successive points on the characteristic net (along the appropriate characteristic), it may be assumed that the flow field properties take on the average values at the points A and B. Thus, for axisymmetric flow,

$$\psi_B = \psi_A + \frac{1}{4}\left\{\left[\frac{\rho q}{M \sin(\mu \pm \vartheta)}\right]_A + \left[\frac{\rho q}{M \sin(\mu \pm \vartheta)}\right]_B\right\}\left(Y_B^2 - Y_A^2\right) \tag{2}$$

For two-dimensional flow, equation (2) reduces to the expression

$$\psi_B = \psi_A + \frac{1}{2}\left\{\left[\frac{\rho q}{M \sin(\mu \pm \vartheta)}\right]_A + \left[\frac{\rho q}{M \sin(\mu \pm \vartheta)}\right]_B\right\}\left(Y_B - Y_A\right) \tag{3}$$

For a simple wave region the integration of equation (1) takes on a particularly simple form since the flow field properties are constant along either a C+ or C- characteristic; hence,

$$\psi_B = \psi_A + \frac{\rho q}{M \sin(\mu \pm \vartheta)}\left(Y_B - Y_A\right) \tag{4}$$

The derivation of the equations used for streamline tracing appeared first in reference 2.

In principle, the establishment of one physical boundary by means of a mass flux integration does not preclude flows where shock waves are pre-

sent. Under these conditions, however, the integration must account for changes in entropy experienced across the shock waves.

OFF-DESIGN INLET CALCULATIONS

Theoretical calculations for the inlet design study presented herein were made using the computer program described in reference 1. The on-design configuration was established by prescribing the internal centerbody surface contour and its Mach number distribution and then solving for the cowl contour. Downstream of the compression region, the Mach number was held fixed at the throat value in addition to keeping the centerbody surface angle constant. Once the inlet contours were established, off-design calculations were performed based on the design point contours and the variable geometry features of the inlet.

Bicone Mixed Compression Inlet with Cowl Lip Angle of 5.0°

Figure 4 shows a bicone mixed compression inlet designed for a free-stream Mach number of 2.5. The inlet forebody was composed of a 10.0° and 18.5° bicone configuration. The initial internal cowl lip angle was set at 5.0° and the resulting cowl lip shock was cancelled by an expansion corner at the centerbody shoulder, while subsequent compression was achieved isentropically. With a design throat Mach number of 1.3, the theoretical total pressure recovery behind the terminal shock was 0.968. For the inlet configuration shown in figure 4, the throat was located at about $X = 3.2$.

The inlet was designed to have a collapsing second cone to allow the inlet to operate at off-design conditions. For off-design operation, the second cone was collapsed with a fixed forward hinge-point location such that the cowl oblique shock intersected the centerbody shoulder. Thus, for the calculations presented, the second cone angle was dictated by the shock-on-shoulder condition, while the spike tip remained fixed relative

to the cowl lip. Consequently, hinge joints were located at the junction of the first and second cone and at the centerbody shoulder. The centerbody surface downstream of the shoulder hinge joint was considered to remain parallel to the design point surface during the collapsing process. The design centerbody position is indicated in figure 4 by the solid line, while the Mach 2.0 position is represented by the dashed line.

An inherent trait of this type of inlet at off-design conditions is the appearance of an expansion just downstream of the shoulder as indicated by the Mach number distribution computed for Mach 2.0 operation (fig. 4). At design point operation, the compressive turning of the cowl oblique shock was cancelled by the abrupt turning at the centerbody shoulder point. Collapsing the centerbody to permit operation at lower Mach numbers decreased the deflection angle of the cowl lip shock faster than the shoulder angle was reduced. As a result, an expansion occurred just behind the shoulder point. This, in general, caused flow distortion at the inlet throat which tended to increase the average throat Mach number and to produce alternating expansion and compression regions on both the centerbody and cowl surfaces. In general, the compression following the expansion tended to amplify the downstream direction causing high local compression rates. High compression rates on the cowl surface resulting from a cowl inflection point upstream of the inlet throat generally aggravated local compression rates at off-design conditions. This permitted the compression waves to prematurely coalesce and contributed to higher distortion levels and lower local Mach numbers ahead of the inlet throat. This would suggest that the angular surface distribution along the cowl contour is a sufficiently sensitive index to evaluate off-design performance prior to performing the calculations. The theoretical results presented in references 3 and 4 substantiate this conclusion. In general, it was concluded in these references that overall off-design improvements can be realized by decreasing the compressive turning rate along the cowl surface, and this compression rate appears to be limited by off-design considerations. It was also found that matched compression rates on the cowl and centerbody during on-design operation, appeared to provide good off-design flow.

Bicone Mixed Compression Inlet with Cowl Lip Angle of 2.0°

Figure 5 shows the same bicone forebody inlet configuration as does figure 4, but with the cowl angle reduced from 5.0° to 2.0° and the inlet increased about 6 percent. This decrease in the cowl lip angle reduced the theoretical total pressure recovery from 0.968 to 0.959. The Mach number distribution on the centerbody surface was chosen such that no inflection point occurred on the cowl contour upstream of the inlet throat. When this condition was satisfied, the Mach number gradients on both the cowl and centerbody surfaces internal to the inlet became nearly equal at design operation (fig. 5). Consequently, at a free-stream Mach number of 1.8, the high local compression rates that were prominant in the previous inlet example were greatly reduced. In addition, the Mach number distortion at the inlet throat was greatly improved.

CONCLUDING REMARKS

Previous inlet characteristic programs have required that the inlet surfaces be specified to obtain a numerical flow field solution. The inlet design parameters, such as internal compression rate, throat Mach number, and flow angle, were introduced as direct input data to the computer program by a reformulation of the boundary conditions necessary to achieve a solution to the characteristic equations. Specifying these flow parameters provides a direct method of obtaining optimum inlet contours with low throat distortion. Near-optimum inlet performance was nearly assured at off-design conditions by requiring a low compressive turning rate along the cowl surface. This requirement on the inlet contours for design operation directly provided a very good initial configuration from which further modifications could be made.

REFERENCES

1. Anderson, Bernhard H.: Design of Supersonic Inlets by a Computer Program Incorporating the Method of Characteristics. NASA TN D-5960, 1969.
2. Evvard, John C.; and Maslen, Stephen H.: Three-Dimensional Supersonic Nozzles and Inlets of Arbitrary Exit Cross Section. NACA TN 2688, 1952.
3. Anderson, Bernhard H.: Characteristics Study of a Bicone Mixed-Compression Inlet for Mach 1.8 to 2.5. NASA TN D-5084, 1969.
4. Anderson, Bernhard H.: Characteristic Design Study of Mixed-Compression Two-Dimensional Inlets with Low-Angle Cowls for the Mach Number Range 2.70 to 1.80. NASA TN D-5330, 1969.

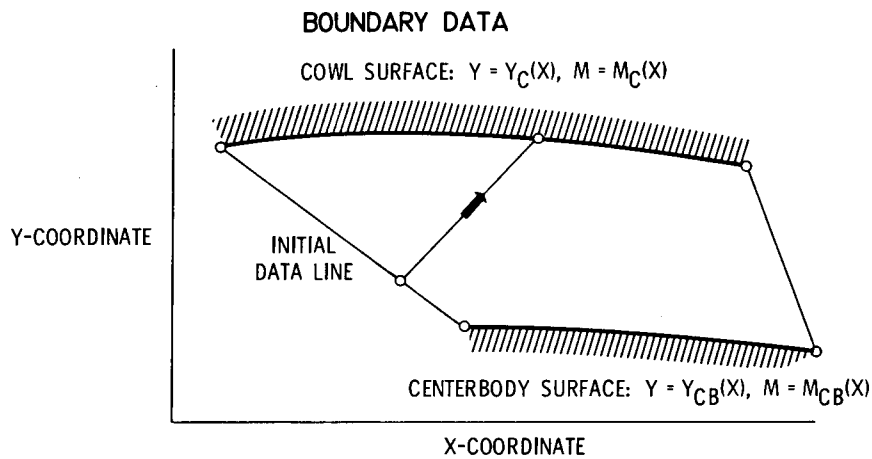

Figure 1

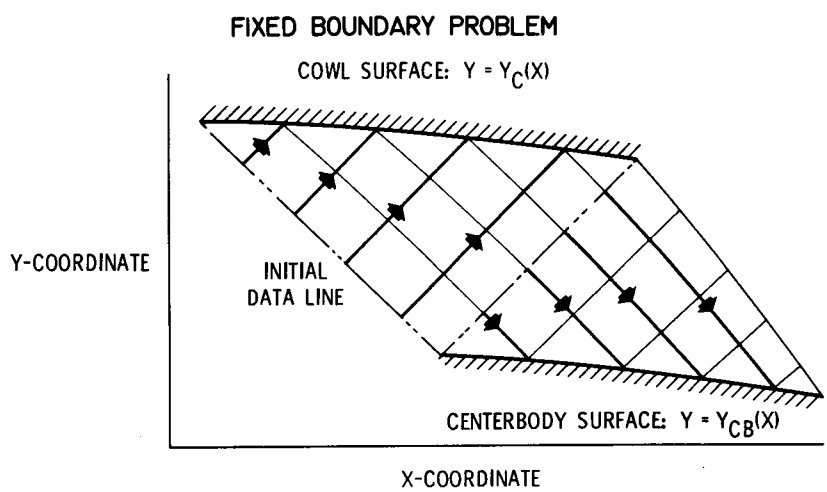

Figure 2

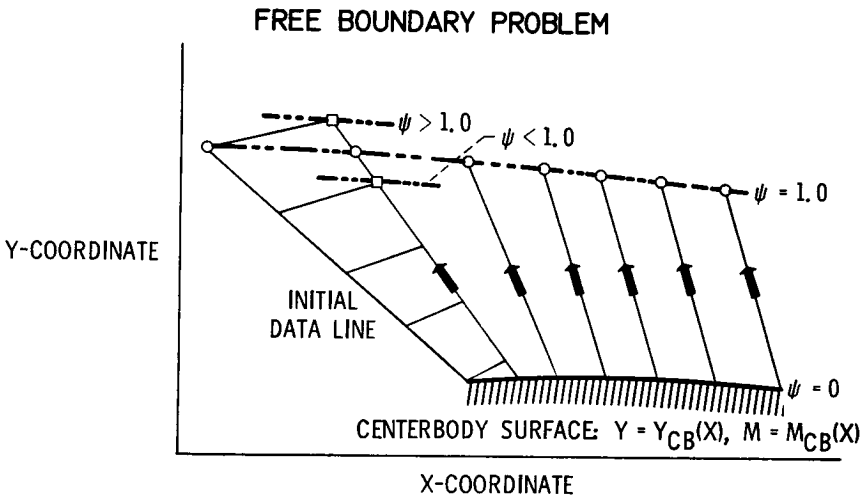

Figure 3

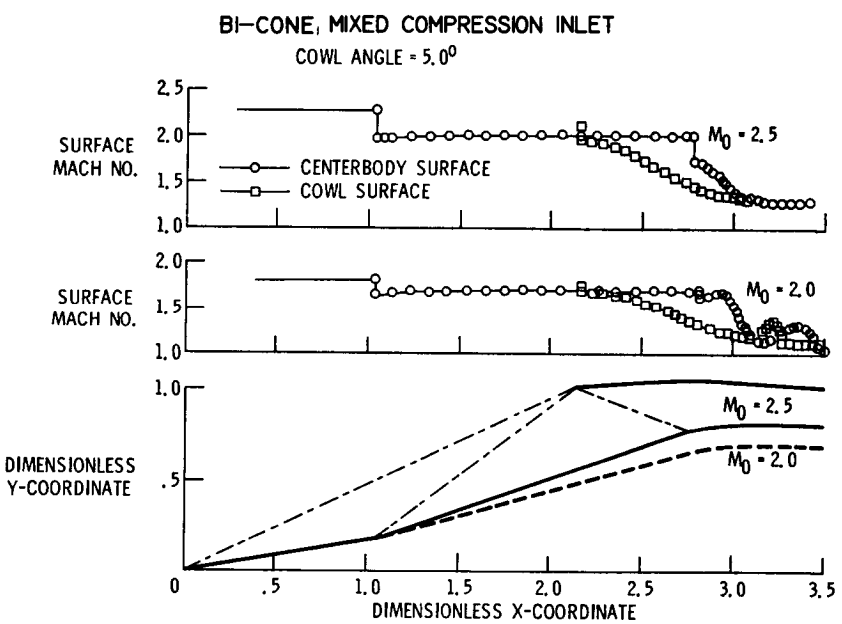

Figure 4

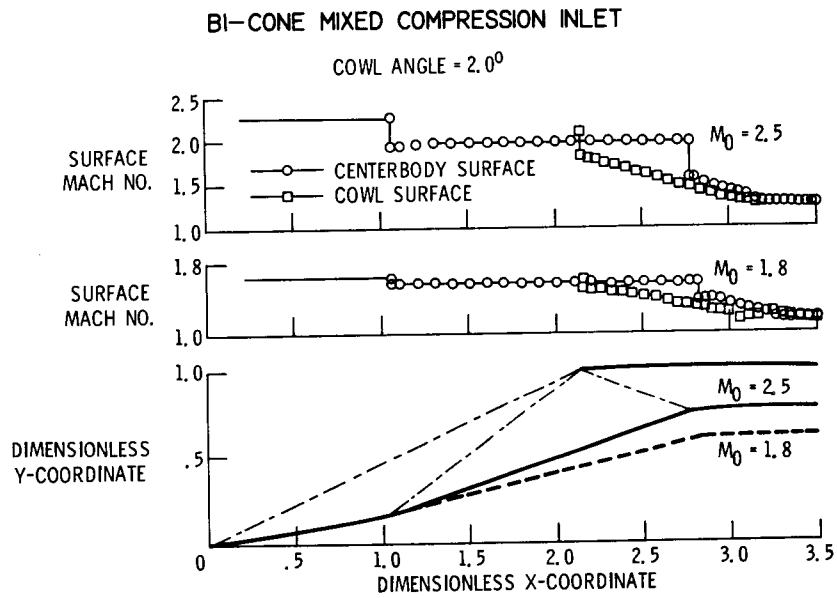
BI-CONE MIXED COMPRESSION INLET
COWL ANGLE = 2.0°
SURFACE MACH NO.
2.5
2.0
1.5
1.0
CENTERBODY SURFACE
COWL SURFACE
M_0 = 2.5
SURFACE MACH NO.
1.8
1.0
M_0 = 1.8
DIMENSIONLESS Y-COORDINATE
1.0
.5
0
M_0 = 2.5
M_0 = 1.8
.5
1.0
1.5
2.0
2.5
3.0
3.5
DIMENSIONLESS X-COORDINATE

Figure 5

DISCUSSION

C. R. LIMAGE, LTV Aerospace Corp.: I want to know if your conclusion of the improvement in off-design performance through the use of reduced cowl angle holds for translating spikes also?

ANDERSON: I don't know, but the thing I do believe is that the on-design properties of inlets can often give clues to the off-design performance. This depends on the type of inlet you are using and also the type of variable geometry mechanisms. I believe one should always take advantage of any properties like this, if one is going to go through an optimization study. It saves time, and that is the only point I am really trying to make.

Preceding page blank

PREDICTION OF SUPERSONIC AND HYPERSONIC INLET FLOW FIELDS

By Norman E. Sorensen, Eldon A. Latham,
and Shelby J. Morris

Ames Research Center

N70-21375

SUMMARY

Two computer programs are currently available that predict the flow field properties in supersonic and hypersonic inlets. One is termed an inviscid program that does not take the boundary layer into account. The other is termed a viscous program and takes into account the boundary layer and the interactions between the shock wave and the boundary layer. Neither program accounts for boundary-layer bleed which may be required to prevent boundary-layer separation. Experimental data have demonstrated the degree of confidence that can be placed in these methods of predicting the flow fields.

The major objectives of the present paper are to assess the adequacy of both prediction techniques and to indicate what modifications are required to improve the accuracy of the predictions. The inviscid program is considered adequate for supersonic inlets with boundary-layer bleed, but inadequate for hypersonic inlets where relatively thick boundary layers develop. For hypersonic inlets that incorporate boundary-layer bleed the viscous program is considered to be marginally adequate in its present form. In addition, the turbulent boundary-layer and shock-wave boundary-layer interaction models employed in the program are not considered adequate and should be improved if boundary-layer bleed is to be accounted for effectively.

INTRODUCTION

The development of suitable inlets for propulsion systems of supersonic and hypersonic vehicles depends on theoretical as well as experimental techniques. Once the basic inlet performance requirements for a particular vehicle mission have been defined, the designer must determine, among other things, suitable contours for the supersonic or hypersonic inlet diffuser of the complete inlet system. For cruising flight at high Mach numbers, the most likely inlet appears to be the mixed-compression type with high theoretical performance capabilities. The successful development of this type of inlet requires accurate knowledge of the compression flow fluid properties to avoid flow separation and to attain uniform flow in the inlet throat. Computer programs are currently available that predict the viscous as well as the inviscid flow field properties. These programs do not account for boundary-layer bleed, which may be required to control separation of the boundary layer. Such programs have allowed wind-tunnel testing of large-scale inlet models to proceed with varying degrees of confidence. Experimental data from these tests have demonstrated the degree of confidence that can be placed in the current methods of predicting the viscous and inviscid portions of the flow field.

The major objectives of this paper are to show how accurately supersonic and hypersonic inlet flow fields can be predicted without including boundary-layer bleed effects and to indicate what modifications are required to improve the accuracy of the predictions.

SYMBOLS

h	height above the surface, in.
M_∞	free-stream Mach number
$\frac{p}{p_\infty}$	static pressure ratio
$\frac{p_{t_p}}{p_{t_\infty}}$	pitot pressure ratio
R	capture radius, in.
Re	Reynolds number
$\frac{x}{R}$	$\frac{\text{axial distance}}{\text{capture radius}}$
α	angle of attack, deg
δ	boundary-layer height

PROGRAMS

Two types of computer programs have been used to calculate the inlet flow fields. One is a program that does not account for the presence of the boundary layer. For convenience it will be referred to as the inviscid program and is fully described in reference 1. This type of program has also been described by Mr. Anderson in a previous paper. The second program solves both the boundary layer and the inviscid flow. It will be referred to as the viscous program and is described in references 2 and 3. The major features of the viscous program are shown in figure 1. The program uses the local similarity method to solve numerically the classical laminar boundary-layer equations. The turbulent solution employed in this program is a first-order integral parameter solution in which a power law velocity profile and the skin friction law of Sivells and Payne are used with a reference enthalpy procedure to account for the effects of compressibility. Boundary-layer transition from laminar to turbulent is assumed to occur instantaneously at some chosen input point, and continuity of displacement thickness is imposed at the transition point to avoid large excursions in the computed pressure. The accuracy of the

laminar boundary-layer predictions is adequate when edge vorticity and normal pressure gradient effects are small. The turbulent predictions, however, are in serious question because of the crudeness of the model employed and the requirements imposed by inlet designs. In brief this comes about because there are no demonstrably accurate methods for predicting turbulent boundary layers in adverse pressure gradients, and inlets by their very nature impose severe adverse pressure gradients. The viscous program also accounts for shock-wave boundary-layer interaction. The procedure for simulating the interaction analytically is to treat the viscous interaction region as a discontinuous control volume. The continuity and momentum equations then are satisfied across the control volume, while the details of the flow in the interaction region itself are neglected. Efforts to improve the modeling of this phenomenon were outlined in previous papers by Messrs. Rose and Murphy.

The viscous program can be used to calculate flow fields for either sharp or blunt leading edges on the cowl and centerbody. The blunt body solution of Lomax provides accurate solutions for free-stream Mach numbers greater than 4. However, this paper will consider only axisymmetric inlets with sharp leading edges. Finally, the program is versatile being applicable to two-dimensional or axisymmetric inlets, real or perfect gases, and cooled or uncooled walls for inlets designed for a wide range of Mach numbers.

Supersonic Inlets

Currently, supersonic inlets for Mach numbers of at least 3.5 are successfully designed solely by inviscid programs (ref. 4). The boundary layer can be ignored primarily because the usual amount of bleed required to control it compensates very closely for the effective contour displacement that would result from its presence. This is illustrated with the aid of figures 2 and 3. Figure 2 shows the shock-wave structure for the portion of the inlet system shown in the inset. The shock-wave structure shown was calculated by the two programs for a mixed-compression inlet with a 10-inch capture radius designed for a Mach number of 3.5 and a Reynolds number of approximately 2.5×10^6 per foot and 0° angle of attack. The predicted boundary-layer height is also indicated. For these inlet contours including the boundary layer reduces the throat Mach number. This is indicated by the foreshortened shock-wave structure predicted by the viscous program compared to that predicted by the inviscid program. In fact the viscous program stopped computing at a point just upstream of the throat because the flow became subsonic. Without boundary-layer removal, the theoretical effective contraction at this point was great enough to choke the flow. Figure 3 compares the predicted pressure distributions on the centerbody and cowl calculated by the two programs with experimental data for the same inlet and test conditions of figure 2. Surface static pressure ratio is plotted as a function of axial distance. The model from which the experimental data were obtained provided for boundary-layer bleed which permitted the centerbody to be retracted to the design postion. The data, therefore, include the effects of 8-percent bleed. The viscous and inviscid predictions agree with the data up to the throat station. The highest pressure ratio of 32 in the throat was

predicted better with the inviscid program. Tests of many other supersonic inlet designs have shown similar agreement with the predictions. The main conclusion here is that if a viscous program is to be more accurate than an inviscid program for supersonic inlets with boundary-layer bleed, the effect of bleed in reducing the effective contour displacement of the boundary layer must be accounted for. In addition, the theoretical understanding of what is required to optimize the bleed could be enhanced.

Hypersonic Inlets

The prediction of flow fields for hypersonic inlets is not as well in hand as for supersonic inlets. Neither the present inviscid or viscous program can be relied on to predict hypersonic flow fields as accurately as supesonic flow fields. The various reasons for this situation are illustrated in figures 4, 5, and 6. Figure 4 shows the shock-wave structures predicted by the two types of programs for a mixed-compression inlet with a 5-inch capture radius designed for a Mach number of 5.2 at a Reynolds number of 2.5×10^6 per foot and 0° angle of attack. The predicted boundary-layer height is also shown. A comparison of this figure with figure 2 for the supersonic inlet shows what appear to be similar differences in the shock-wave structures predicted by the inviscid and viscous programs. However, the incremental differences in the average Mach numbers in the throats predicted by the two programs are approximately three times as large for the hypersonic inlet as for the supersonic inlet. More specifically, the incremental differences are 0.75 Mach number between the viscid and inviscid predictions for the hypersonic inlet and 0.25 for the supersonic inlet. The reason is that the boundary layer occupies a greater percentage of the flow area in the throat of the hypersonic inlet causing a greater incremental difference in predicted Mach number. Thus the inherent demands for accuracy become much greater for the hypersonic inlet designs. The inviscid program by itself is inadequate for predicting flow fields in inlets at hypersonic speeds.

Comparison of results predicted by the viscous program with experimental results has revealed additional problems. Figure 5 compares the predicted pressure distributions calculated by the two programs with the experimental distribution for the same inlet and conditions of figure 4. Surface static pressure ratio is plotted as a function of axial distance for the centerbody and cowl. When 11 percent of the capture mass flow is removed through the boundary-layer bleed areas indicated in the figure, the agreement of the viscous predictions with experimental results is better than for the inviscid predictions. However, the highest level of compression at the throat is underpredicted by both programs. That is, the bleed, required to achieve the high experimental compression ratio of approximately 120, has not compensated for inaccuracies in the viscous program as was the case for the supersonic inlet, and the inviscid predictions are simply more inaccurate. An indication as to the reason for the underprediction is shown in figure 6. Experimental boundary-layer profiles for the same inlet and test conditions as those of figure 5 are compared with the predicted profiles. Pitot pressure ratio is plotted as a function of the height above the surface for two longitudinal stations on both the cowl and centerbody. Comparisons show that at the survey

stations upstream of the boundary-layer bleed areas on the cowl side (station 2), the boundary-layer thickness is reasonably well predicted. On the centerbody side (station 1), the predicted thickness is much greater than measured. Measurements made downstream of the bleed areas in the locations near the throat show that on the centerbody side (station 3), theory and experiment agree. However, it should be noted that the theory does not include effects of bleed and since, in addition, the upstream profile does not agree with the theory the conclusion is that the profile agreement in this case is rather fortuitous. On the cowl side (station 4), the profile agreement is poor with the predicted height only about 50 percent of the experimentally measured height. This greater height or, more importantly, the effective contour displacement, particularly in the throat region, increases the effective contraction and leads to a higher pressure ratio than predicted by the viscous program as shown in figure 5.

Status of Programs

The adequacy of the available programs and requirements for improved accuracy are summarized in figure 7. The inviscid program is considered adequate for the prediction of flow fields for supersonic inlets in which boundary-layer bleed is employed because bleed fortuitously compensates for the effective displacement of the inlet contours caused by the boundary layer. The program, however, is inadequate for predicting hypersonic inlet flow fields even with bleed because the relatively large amounts of boundary layer, particularly in the throat region, cause enough effective displacement of the contours that the usual amounts of boundary-layer bleed required for performance do not adequately compensate.

The viscous program is believed to be marginally adequate in its present form for predicting flow fields for hypersonic inlets requiring boundary-layer bleed. It is considered less adequate than the inviscid program for supersonic inlets requiring bleed because the reduction of the effective contour displacement of the boundary layer caused by bleed is not accounted for. For this and other previously mentioned reasons, the viscous program requires several modifications for greater accuracy. For inlets in which boundary-layer bleed is required the effective change in the inlet contours must be taken into account in the calculations to properly account for the effects of the boundary layer on the inlet compression field. The present turbulent boundary-layer and shock-wave boundary-layer interaction models employed in the program are not considered adequate and should be improved if boundary-layer bleed is to be accounted for effectively.

REFERENCES

1. Sorensen, Virginia L.: Computer Program for Calculating Flow Fields in Supersonic Inlets. NASA TN D-2897, 1965.

2. Maslowe, S. A.; and Benson, John L.: Computer Program for the Design and Analysis of Hypersonic Inlets. Lockheed Report No. 18079, Aug. 1964.

3. Benson, J. L.; and Maslowe, S. A.: Bluntness and Boundary-layer Displacement Effects on Hypersonic Inlet Flow Fields. J. Spacecraft and Rockets, vol. 3, no. 9, Sept. 1966, pp. 1394-1401.

4. Sorensen, Norman E.; Smeltzer, Donald B.; and Cubbison, Robert W.: Study of a Family of Supersonic Inlet Systems. J. Aircraft, vol. 6, no. 3, May-June 1969, pp. 184-188.

VISCOUS PROGRAM

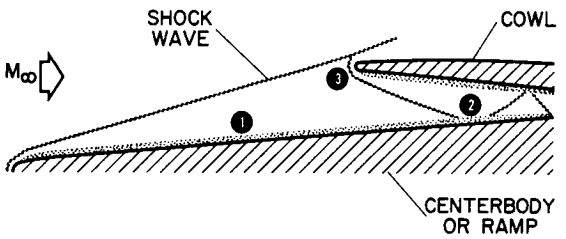

CALCULATIONS

1. LAMINAR AND TURBULENT BOUNDARY LAYER
2. BOUNDARY-LAYER SHOCK-WAVE INTERACTION
3. BLUNT OR SHARP LIPS

VERSATILITY

- AXISYMMETRIC OR 2-DIMENSIONAL FLOW
- REAL OR PERFECT GAS
- COOLED WALLS
- $M_\infty > 2$

Figure 1

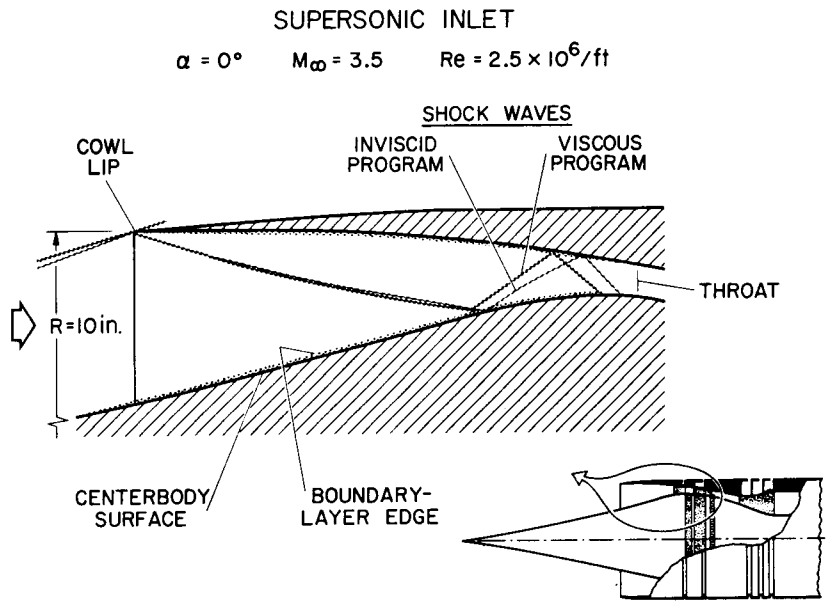

Figure 2

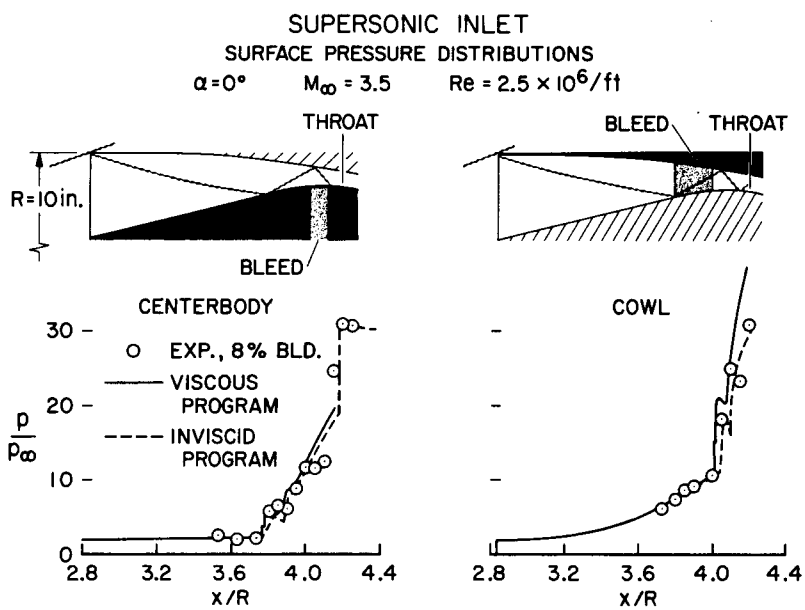

Figure 3

HYPERSONIC INLET

$\alpha = 0°$ $M_\infty = 5.2$ $Re = 2.5 \times 10^6/ft$

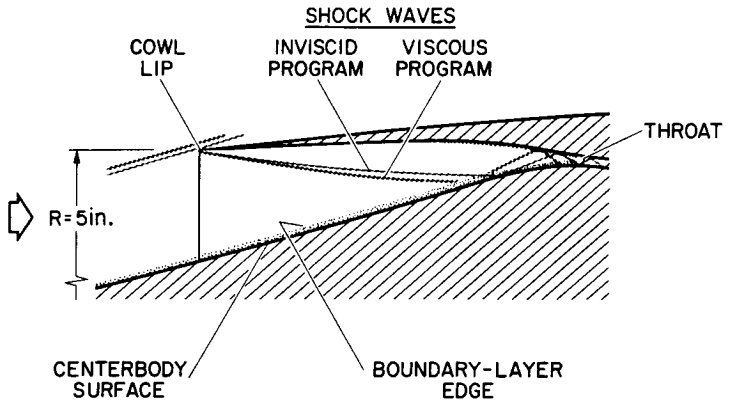

Figure 4

HYPERSONIC INLET

SURFACE PRESSURE DISTRIBUTIONS

$\alpha = 0°$ $M_\infty = 5.3$ $Re = 2.5 \times 10^6/ft$

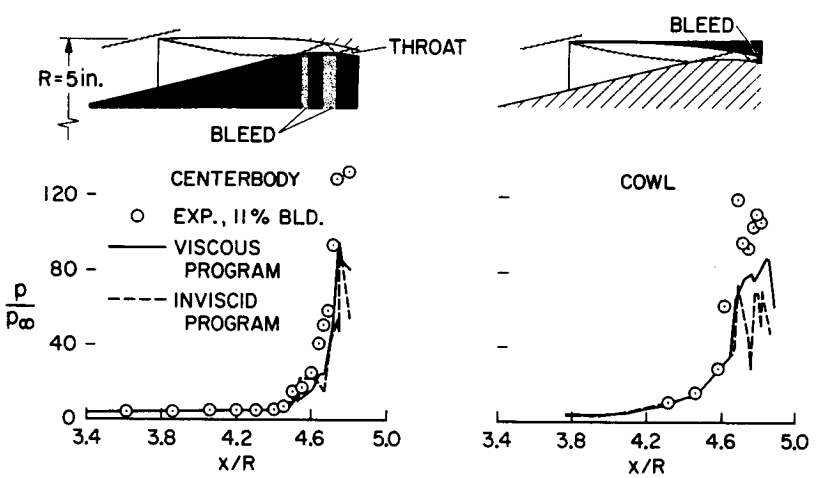

Figure 5

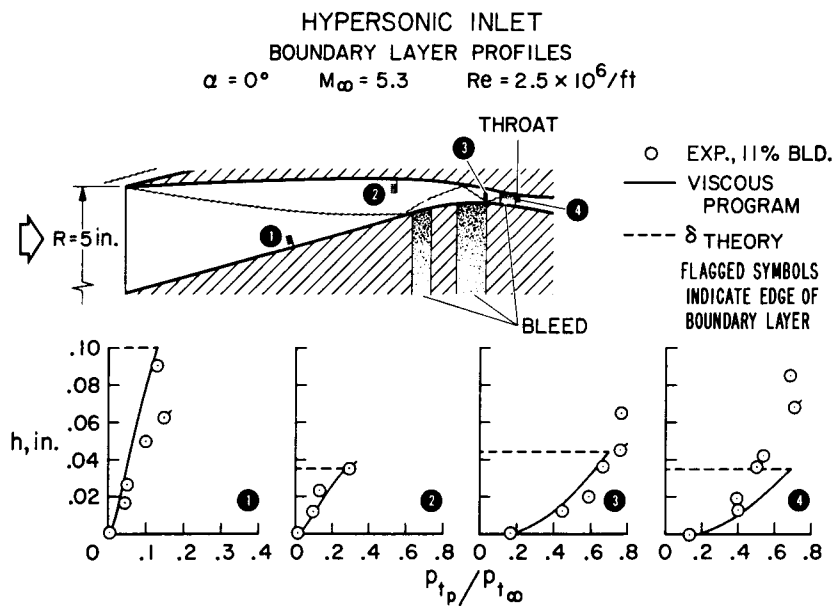

Figure 6

PROGRAM STATUS

INVISCID PROGRAM

- ADEQUATE FOR SUPERSONIC INLETS WITH NORMAL AMOUNT OF BLEED
- INADEQUATE FOR HYPERSONIC INLETS WITH OR WITHOUT BLEED

VISCOUS PROGRAM

- MARGINALLY ADEQUATE FOR HYPERSONIC INLETS WITH BLEED
- LESS ADEQUATE THAN INVISCID PROGRAM FOR SUPERSONIC INLETS
- MODIFICATIONS REQUIRED FOR GREATER ACCURACY
  - ACCOUNT FOR BLEED
  - BETTER TURBULENT B. L. THEORY
  - BETTER SHOCK WAVE B. L. INTERACTION MODEL

Figure 7

DISCUSSION

HOLT ASHLEY, Stanford University: I'd be very interested in hearing either of the last speakers, or anybody else that wants to speak up, tell us what is being done theoretically these days about another parameter which hasn't been mentioned in either of these papers, that is the very important effect of angle of attack on inlets with axisymmetric geometry.

SORENSEN: You are asking a question about another difficult problem. Admittedly, it is one that we would like to solve theoretically, but there doesn't seem to be anything on the horizon, to my mind, other than - I see Mr. Rakich has his hand up over here.

JOHN V. RAKICH, NASA, Ames Research Center: I'm glad you asked that question. I presented a paper on the first day of the conference on the method of characteristics for three-dimensional flow and the applications to date have all been to external flows. However, there should be no reason why we couldn't apply it directly to these more difficult problems of inlets simply by putting a solid boundary condition at the outer portion of the flows instead of a shock wave. However, it is more complicated because we have to consider the reflected shocks.

JOHN KURZROCK, General Motors Corp., Allison Div.: My first question I think you answered in your summary, but it appears that you don't take care of the bleed with your boundary-layer calculation at all. If there is a bleed or if there isn't, it doesn't really matter.

SORENSEN: No, we don't account for it, that's true, but it certainly does matter.

KURZROCK: I mean theoretically. Experimentally, of course, it shows some effect, but analytically you haven't taken account of that boundary condition in your boundary-layer calculation.

SORENSEN: That's right.

KURZROCK: My other question is: How do you account for your boundary conditions for your inviscid characteristics solution and your boundary-layer displacement effect? Is there an interaction between the two? Do you calculate displacement thickness and then this forms the boundary for your characteristics program, or do you iterate back and forth? Could you say a few words about these?

SORENSEN: This program simultaneously computes both the inviscid and viscous flow field. The shock wave normally emanates from the displacement thickness of the boundary layer, but it is done simultaneously. It is not the kind of program that calculates the inviscid solution and then calculates the boundary layer and goes back and puts it in as a displacement thickness. It does it all at one time.

GINO MORETTI, Polytechnic Institute of Brooklyn: I would just like to make a brief comment on Mr. Rakich's comment. I am very pleased with his optimism. Unfortunately, I don't share it completely because of personal experience with the method of characteristics in three dimensions. I think it is not very adequate for internal flows, and personally I would very much rather like the finite difference technique, which, incidentally, has been attempted for three-dimensional internal flow by Ricardo Bastianon and myself four years ago, I think, and presented at the AIAA meeting in New York in 1967. At that time we made a very sketchy example of a three-dimensional intake with a shock building up into part of the intake.

Now, that was far from being a finished program, but anyway, it showed the possibility of applying the technique to three-dimensional intakes for inviscid flow. It seems to me that the amount of work involved in making the inviscid flow computation with the finite difference is by far smaller than the amount of work involved if you work with the method of characteristics.

EDWARD W. PERKINS, NASA, Ames Research Center: I think that over the years we have made a considerable improvement in our ability to design inlet systems through the development of theoretical techniques which are available, as poor as they are at the present time. But one of the things that we really lack is a good theoretical framework for looking at the effects of angle of attack on the inlet performances, and we certainly feel that is an area we would like people to consider.

EARLL MURMAN, Boeing Scientific Research Laboratories: Does either the inviscid or the viscous program for the supersonic inlet predict the flow field distortion very well at the throat?

SORENSEN: The inviscid solution does not, but the viscous solution does give you a boundary layer with some representation of the true throat distortion. We presented a paper here at Ames two years ago at the Hypersonic Aircraft Technology conference that showed some comparisons. The paper showed a reasonably good comparison with the experiments using the viscous program, but it was not perfect.

MURMAN: The viscous wasn't better?

SORENSEN: The viscous wasn't - The inviscid turned out to be better because the boundary-layer bleed just compensates for the displacement of the boundary layer. We have worked with it long enough now, and we have enough experience that we feel pretty confident in making judgments in what the computer program tells us and what will happen in the wind tunnel.

SIDNEY A. POWERS, Northrop Corp.: I'd like to add a little oil to the troubled fires over here, replying to Professor Moretti. In a paper in a session that he chaired at Denver in 1966, we attacked a problem for Marshall of intereaction of local eddy in exhaust fumes by a three-dimensional method of characteristics. The San Diego Convair people - Thommen, I think it was - attacked the identical problem with the finite difference method.

Now, both of us were less than completely satisfactory, but in a situation where shocks are so terribly important as inlets, the finite

difference method smooths out so badly that you have a hard time telling what is error build-up and what is shock. So I agree with John Rakich. I think the three-dimensional method of characteristics is probably the way to go for inlets at angle of attack.

RAYMOND SEDNEY, Martin Company: I'm curious both with respect to your paper and the previous one. Can you give us some idea of how much computer time the programs take, and also (I can't remember whether it was you or the previous speaker who mentioned the possibility of taking into account real gas effects) are nonequilibrium real gas effects important, and is there any need to take them into account?

SORENSEN: The first part of your question about the time, the inviscid programs generally run under a minute on the 7094. The present version of the viscous program that we have can take up to an hour on a computer. However, we have an improved version which we will be obtaining, which should run about 20 minutes for a typical case on the IBM 360-65.

About the real gas effects up to Mach 5 at least, compressing down to nearly a sonic throat, even there the effects are not very significant, and when you go above Mach 5, we are talking about supersonic burning in those designs where the Mach number comes down to somewhere around, say, half of the free-stream Mach number, and there again, since there isn't too much compression, real gas effects are not really too important.

PERKINS: With respect to the question of equilibrium, they are all equilibrium calculations.

Dr. Moretti, would you like to have one more word?

MORETTI: All right. Of course, by now everybody knows what my comment is going to be.

My firm opinion is that the method of characteristics is a finite difference technique as much as any other finite difference technique, so that the same kind of criticism and objection can be raised to both techniques. Therefore, I think that one should be very careful in making statements which are so general, such as "finite difference techniques smear out bumps or discontinuities and the method of characteristics doesn't." That's not true at all. I can show you examples in which the relative errors are easily reduced to less than one tenth of one percent when the calculation is performed by a finite difference technique. But of course you have to use a good technique!

A NEW METHOD FOR ANALYSIS OF TRANSONIC FLOW

By Theodore Katsanis

Lewis Research Center

N70-21376

SUMMARY

A method has been developed to obtain a transonic flow solution in a partially guided passage. This method is based on extending a strictly subsonic finite-difference stream-function solution to the case where there is locally supersonic flow. This extension involves the use of a velocity-gradient equation which must be satisfied together with continuity. It is assumed that shock losses are negligible. A numerical example for flow through an axial stator is compared with experimental results. A technique is suggested for using this method for exterior flow problems.

INTRODUCTION

There are several useful techniques for calculating fluid velocities through a passage. Two of these are the finite-difference solution of the stream-function equation and the velocity-gradient (stream-filament) method. Each has advantages and limitations. In particular, the finite-difference solution of the stream-function equation (e.g., ref. 1) is limited to strictly subsonic flows. The velocity-gradient methods are not limited in this way (e.g., ref. 2). On the other hand, a simple velocity-gradient method is limited to a well-guided channel. The purpose of this paper is to explain how these two methods have been combined to extend the range of cases which can be solved so that locally supersonic (transonic) solutions can be obtained even in a poorly guided channel.

This method has been programmed for turbomachinery applications. The program, called TSONIC, is available and is fully described in reference 3. TSONIC obtains the numerical solution for ideal, transonic, compressible flow

Preceding page blank

for axial, radial, or mixed-flow cascades of turbomachine blades. The blades may be fixed or rotating. In this paper, a numerical example using this program is given.

Finally, there is a possibility of extending this method to exterior flow problems. Such a method is suggested in the concluding section.

SYMBOLS

b	stream-channel thickness, meters
c_p	specific heat at constant pressure, J/(kg)(K)
d	stream-channel width (fig. 3), meters
p	pressure, N/meter^2
q	blade pitch, meters
R	radius of boundary surface, meters
r	radius, meters
s	distance along a streamline, meters
T	temperature, K
t	time, sec
u	stream function
u_x	$\partial u/\partial x$
u_y	$\partial u/\partial y$
u_{xx}	$\partial^2 u/\partial x^2$
u_{xy}	$\partial^2 u/\partial x\, \partial y$
u_{yy}	$\partial^2 u/\partial y^2$
V	velocity, meters/sec
w	weight flow, kg/sec
x	x-coordinate
y	y-coordinate

β streamline flow angle from x-axis, rad

γ specific heat ratio

η outer normal to region

θ polar coordinate, rad

ρ density, kg/meter^3

Subscripts:

in inlet

out outlet

x x-component

y y-component

1 first point

2 last point

Superscripts:

' stagnation condition

$\bar{}$ vector quantity

METHOD OF ANALYSIS

The method described here is based on a combination of two other methods: a finite-difference stream-function analysis and a velocity-gradient analysis. For a well-guided passage, transonic solutions can be obtained directly by a velocity-gradient analysis because the direction and curvature of the flow are accurately known from the shape of the passage. However, for a wider passage without close wall guidance, the streamline curvatures cannot be estimated with sufficient accuracy. In this case, a subsonic solution is obtained at a reduced flow first in order to locate streamlines. The assumption is then made that the direction and curvature of the streamlines do not change significantly in passing from high subsonic to locally supersonic flows. After a subsonic solution is obtained, therefore, a transonic solution can be obtained by using the subsonic streamline directions and curvatures with the velocity-gradient methods.

Subsonic Solution

The weight flow through the passage is reduced in order to allow a totally subsonic solution (no locally supersonic regions) to be obtained. This subsonic solution yields information necessary for the velocity-gradient solution. This information consists of three items, each a function of the x, y coordinates. These three functions are

(1) β, the angle of the streamlines with respect to the x-axis

(2) $d\beta/ds$, the streamline curvature

(3) $\partial V/\partial x$, the gradient of the velocity in the x-direction

These three functions, β, $d\beta/ds$, and $\partial V/\partial x$ can be obtained from subsonic solutions, such as the following:

(1) Solution of the stream-function equation

(2) Solution of the potential-function equation

In order for a stream function to be defined, the weight flow crossing a line between two points must be independent of path. This requires that the flow be either incompressible or steady, and also, of course, that the flow be two-dimensional (i.e., on a surface, although not necessarily on a plane). A potential function, on the other hand, exists only if the flow is irrotational relative to the coordinate system used. These restrictions are summarized in the following table:

Function	Restrictions
Stream	(1) Incompressible <u>or</u> steady (2) Two-dimensional
Potential	Irrotational

Since the method is to be applied to stream surfaces in a turbomachine with varying radius and a rotating coordinate system, the flow would not be irrotational with respect to the rotating coordinate system. For this reason, the stream function was used instead of the potential function. For other applications, the potential function may be more suitable.

In references 1 and 4, this method is applied to rotating turbomachine blades of either axial, radial, or mixed flow. To illustrate the principles of the method, it will be adequate to consider a two-dimensional cascade in

the x-y plane. If the flow is assumed to be absolutely irrotational, the stream function u will satisfy the following equation (ref. 5):

$$\frac{\partial^2 u}{\partial x^2} + \frac{\partial^2 u}{\partial y^2} - \frac{1}{\rho}\left(\frac{\partial \rho}{\partial x}\frac{\partial u}{\partial x} + \frac{\partial \rho}{\partial y}\frac{\partial u}{\partial y}\right) = 0 \tag{1}$$

For the solution of equation (1), a finite region is considered (as indicated in fig. 1). The stream function u can be normalized so that u is zero on the upper surface of the lower blade, and 1 on the lower surface of the upper blade. Then the derivatives of the stream function satisfy

$$\frac{\partial u}{\partial x} = -\frac{b\rho}{w} V_y \tag{2}$$

$$\frac{\partial u}{\partial y} = \frac{b\rho}{w} V_x \tag{3}$$

When the flow is entirely subsonic, equation (1) is elliptic. (It must be remembered that ρ is a function of the derivatives of u; see ref. 5.) Boundary conditions for the entire boundary ABCDEFGHA of figure 1 will determine a unique solution for u. These boundary conditions are given in the following table:

Boundary segment	Boundary condition
AB	u is 1 less than the value of u on GH at the same x-coordinate
BC	$u = 0$
CD	u is less than the value of u on EF at the same x-coordinate
DE	$\left(\frac{\partial u}{\partial \eta}\right)_{out} = -\frac{\tan \beta_{out}}{q}$
EF	u is 1 greater than the value of u on CD at the same x-coordinate
FG	$u = 1$
GH	u is 1 greater than the value of u on AB at the same x-coordinate
AH	$\left(\frac{\partial u}{\partial \eta}\right)_{in} = \frac{\tan \beta_{in}}{q}$

Equation (1), subject to these boundary conditions, can be solved numerically by a finite-difference method. In this case, a uniform mesh was used, as illustrated in figure 2. A finite-difference equation is written at each mesh point, resulting in a large number of equations, with the same number of unknowns. The numerical solution of these equations involves two levels of iteration because equation (1) is nonlinear. The inner iteration is required to solve equation (1) when it is linearized, and the nonlinear solution is approached by the outer iteration.

After computing a numerical solution to equation (1) in a given flow region, the velocity at any point can be computed from equations (2) and (3) by using numerical differentiation. The three functions (β, $d\beta/ds$, and $\partial V/\partial x$) can also be calculated. The angle β is known since the velocity components

are known from equations (2) and (3). The curvature $d\beta/ds$ is not obtained directly. Along blade surfaces, $d\beta/ds$ is determined by the blade shape. Within the passage, it can be expressed as a function of the first and second partial derivatives of the stream function (see appendix). Finally, $\partial V/\partial x$ is approximately proportional to the weight flow and can be calculated by numerical differentiation. Therefore, at the full weight flow, $\partial V/\partial x$ is obtained by increasing $\partial V/\partial x$ in direct proportion to the increase in weight flow.

For the case where there is locally supersonic flow, equation (1) is no longer elliptic in the entire region, but is hyperbolic in the region of supersonic flow. (This is discussed in chapter 14 and appendix A of ref. 5.) With a mixed type problem like this, an analytical solution to equation (1) probably does not exist, as discussed in reference 8. This means that there is probably a shock loss. Equation (1) cannot be satisfied at the shock if there is a shock loss. However, the shock loss may be so small as to be negligible in a numerical solution. In this case, looking for a numerical solution to equation (1) can be justified.

At first one may think that equation (1) could be solved by a finite-difference method even when there is locally supersonic flow. There are, however, difficulties with this approach. The difficulty has to do with the fact that there are two velocities, one subsonic and one supersonic, which will give the same value for the weight flow parameter ρV. If a stream-function solution is obtained, the stream-function derivatives can be calculated to obtain values of ρV using equations (2) and (3). However, if there is locally supersonic flow, there is no easy way of telling which points should use the subsonic velocity and which points should use the supersonic velocity. This is further complicated by the fact that equation (1) is nonlinear and requires iteration to obtain the coefficients involving the density ρ. In the initial iteration, the predicted values of ρV near the supersonic region usually turn out to be too large, so that no velocity V can be found to correspond to the predicted value of ρV. Because of these difficulties, an alternative method was developed.

Transonic Solution

For well-guided flow, the velocity-gradient method works very well. Because this method is not very well known, the basic idea is first explained.

This method of analysis is sometimes called a stream-filament method, because the velocity-gradient equation normally involves the streamline (or stream filament) curvature.

Example of velocity-gradient method. - The idea of a velocity-gradient method can be demonstrated by considering a simple case. Suppose there is two-dimensional flow through a narrow passage, as shown in figure 3. Assume the height of the passage to be b and the width d. If the weight flow w is known, the velocity can be calculated approximately from continuity by

$$V = \frac{w}{\rho b d} \tag{4}$$

For compressible flow, iteration may be required since ρ depends on V. However, there is a variation in velocity across the width of the passage, so that the velocity V obtained by equation (4) is not correct at every point across the width. And, in turbomachinery, it is this velocity difference that is of interest. The velocity difference can be determined by balancing centrifugal force against the pressure gradient.

For a small volume of fluid moving along a curved path with radius of curvature r, the centrifugal force is equal to its mass times the centrifugal acceleration. In polar coordinates, then (assuming a unit height normal to the x-y plane)

$$\text{Mass} = \rho \, dr \, r \, d\theta$$

$$\text{Centrifugal acceleration} = \frac{V^2}{r}$$

The centrifugal force must be balanced by the pressure force in the direction normal to the direction of motion:

$$\text{Pressure force} = \frac{dp}{dr} \, dr \, r \, d\theta$$

Since the pressure force is equal to the centrifugal force,

$$\frac{dp}{dr} = \rho \frac{V^2}{r} \tag{5}$$

With the assumption of steady, nonviscous, and irrotational flow, the pressure gradient is directly related to the velocity gradient by

$$\frac{dp}{\rho} + V\,dV = 0 \tag{6}$$

Eliminating dp between equations (5) and (6) results in

$$\frac{dV}{dr} = -\frac{V}{r} \tag{7}$$

This is the velocity-gradient equation for this example.

Note that equation (7) could be obtained directly by assuming a free vortex; that is, rV = constant. However, this derivation illustrates the principle that a velocity-gradient equation can always be derived from the force equation.

Equation (7) can be integrated to obtain

$$\frac{V}{V_1} = \frac{R_1}{r} \tag{8}$$

where V_1 is the velocity at the wall with radius R_1. The value of V_1 can be determined by satisfying continuity:

$$w = \int \rho V\,dA \tag{9}$$

Substituting equation (8) in (9) results in

$$w = \int_{R_1}^{R_2} \rho V_1 R_1 b \frac{dr}{r} \tag{10}$$

Equation (10) gives a relation between V_1 and w. This relation is known if ρ is known as a function of r. Now it is assumed that the fluid is a perfect gas (constant c_p) and that the flow is isentropic. Then,

$$\frac{\rho}{\rho'} = \left(\frac{T}{T'}\right)^{1/(\gamma-1)} \tag{11}$$

where

$$T' = T + \frac{V^2}{2c_p} \tag{12}$$

Combining equations (8), (11), and (12) gives

$$\rho = \rho' \left(1 - \frac{R_1^2 V_1^2}{2r^2 c_p T'}\right)^{1/(\gamma-1)} \tag{13}$$

This value of ρ can be used in equation (10) to calculate the weight flow w:

$$w = \rho' V_1 R_1 b \int_{R_1}^{R_2} \left(1 - \frac{R_1^2 V_1^2}{2r^2 c_p T'}\right)^{1/(\gamma-1)} \frac{dr}{r} \tag{14}$$

The integral in this equation can be readily evaluated numerically for any given value of V_1. Therefore, w can be plotted as a function of V_1. For an example, let the constants in equation (14) have the following values:

$$c_p = 1000 \text{ J/(kg)(K)}$$

$$\gamma = 1.4$$

$$\rho' = 1 \text{ kg/meter}^3$$

$$T' = 1000 \text{ K}$$

$$b = 1 \text{ meter}$$

$$R_1 = 1 \text{ meter}$$

$$R_2 = 2 \text{ meters}$$

For this example, equation (14) becomes

$$w = V_1 \int_1^2 \left(1 - \frac{V_1^2}{2\times10^6\, r^2}\right)^{2.5} \frac{dr}{r} \tag{15}$$

The values of w for given values of V_1 were calculated and plotted in figure 4. The maximum value of V_1 (corresponding to a static temperature of absolute zero) is 1414 meters per second. The maximum (choking) weight flow is 349 kilograms per second with V_1 = 805 meters per second. The velocity distribution at choking weight flow is plotted in figure 5. While V_1 is supersonic, the velocity on the other wall is subsonic. From figure 4 it can be seen that, for a weight flow slightly less than choking, there are two solutions for V_1. For example, suppose that w = 325 kilograms per second. Then V_1 = 610 and V_1 = 1010 meters per second will both give the desired weight flows. The velocity distribution for these two solutions is plotted in figure 5. Both solutions have both subsonic and supersonic velocities, so to distinguish between the two solutions one is called the "subsonic" solution, and the other the "supersonic" solution. The "subsonic" solution is characterized by the fact that the velocity distribution curve is always below the choking velocity; the "supersonic" velocity is always greater than the choking velocity.

The "subsonic" solution would be used if the flow is subsonic upstream, and the passage is not choked. If the passage is choked, either solution is possible downstream of the throat. Whether the "subsonic" or the "supersonic" solution, or neither (with a strong shock) is correct would depend on the downstream static pressure, similar to a converging-diverging nozzle. The examples that have been analyzed so far have always used the "subsonic" solution.

Velocity gradient equation for a general two-dimensional passage. - The ideas just discussed can be applied to a general two-dimensional passage. First an equation is presented for the velocity gradient in the y-direction in the x-y plane. Then it will be apparent what information is needed from a subsonic solution. And it will be shown how this information can be calculated.

The velocity gradient in the y-direction is given by

$$\frac{\partial V}{\partial y} = \frac{V}{\cos\beta}\frac{d\beta}{ds} + \tan\beta\,\frac{\partial V}{\partial x} \tag{16}$$

The curvature $d\beta/ds$ may be calculated by either

$$\frac{d\beta}{ds} = \cos^3\beta \frac{d^2y}{dx^2} \qquad \text{(on the blade surface)} \tag{17}$$

or

$$\frac{d\beta}{ds} = \cos\beta \sin^2\beta\left(2\frac{u_{xy}}{u_x} - \frac{u_y u_{xx}}{u_x^2} - \frac{u_{yy}}{u_y}\right) \qquad \text{(at interior points)} \tag{18}$$

Equations (16) to (18) are derived in the appendix from the force equation. The quantitues in equation (16) are known if a solution to equation (1) is known. The transonic solution, of course, is not known. But, these quantities, that is, β, $d\beta/ds$ (streamline curvature), and $\partial V/\partial x$ may be estimated fairly accurately from a solution at a reduced weight flow with completely subsonic velocities. The streamline positions will shift with the increase to the full weight flow, but β and $d\beta/ds$ will change only slightly, depending on how well guided the flow is. For incompressible flow, $\partial V/\partial x$ is proportional to the weight flow. For compressible flow, $\partial V/\partial x$ will not be strictly proportional to the weight flow. However, for many cases it is sufficiently accurate to assume that $\partial V/\partial x$ is proportional to the weight flow. Then, at the full weight flow, $\partial V/\partial x$ is obtained by increasing $\partial V/\partial x$ in direct proportion to the increase in weight flow. And if β is small, the value of $\partial V/\partial x$ is not important in equation (16).

With reasonable estimates for β, $d\beta/ds$, and $\partial V/\partial x$, equation (16) can be solved numerically along a vertical line. As discussed previously, velocity V_1 on the lower boundary is determined by continuity. It is required that

$$\int_{y_1}^{y_2} \rho V \cos\beta b \, dy = w \tag{19}$$

where y_1 is the value of y at the lower boundary and y_2 is the value of y at the upper boundary. The technique for satisfying equation (19) is similar to that already discussed for a curved passage. Equation (16) is solved for some estimated initial value of V_1 on the lower boundary, using a simplified

Runge-Kutta method for numerical integration (ref. 9, p. 235). This gives values of V to use in equation (19). Then the value of the integral can be calculated numerically to obtain w for the given value of V_1. This can be done for a number of values of V_1 to obtain w as a function of V_1, similar to that shown in figure 4. Normally there will be two values of V_1 which will result in the correct weight flow in equation (19), corresponding to the "subsonic" and "supersonic" solutions. Usually the "subsonic" solution is chosen. This value of V_1 used with equation (16) gives the velocity distribution along the entire vertical line.

This procedure can be repeated along a large number of vertical lines to obtain the velocity distribution for the entire region, including both blade surfaces. Since a finite-difference mesh is established for the subsonic solution, it is convenient to use the same mesh points for the transonic velocity-gradient solution. The velocity gradient is then solved along each vertical line of mesh points.

NUMERICAL EXAMPLE

This method has been programmed to analyze a general turbomachine blade. The program, called TSONIC, is given in reference 3. TSONIC obtains the "subsonic" solution of the velocity-gradient equation. An example is given here of the results obtained with the program.

This example is a stator mean blade section (fig. 6) for a turbine built at the Lewis Research Center (ref. 6). Satisfactory results were obtained by using the TSONIC program. The stream-function solution was obtained first with 80 percent of the desired weight flow. Then the velocity-gradient method was used to obtain the velocities at the desired weight flow.

The blade surface velocities calculated by the program are plotted against blade surface length in figure 7. Also shown in figure 7 are experimental data obtained from the investigation described in reference 6. These are calculated from the pressure ratios plotted in figure 12 of reference 6. Most of the velocities are in close agreement.

CONCLUDING REMARKS

A method has been developed to obtain a transonic flow solution in a partially guided passage. This method is based on extending a strictly subsonic stream-function solution to the case where there is locally supersonic flow. This extension involves the use of a velocity-gradient equation which must be satisfied together with continuity.

The idea of combining the stream-function and velocity-gradient solutions is not necessarily limited to guided passages. For example, suppose it was desired to calculate transonic velocities over the surface of a two-dimensional airfoil immersed in a subsonic free stream. The velocity-gradient and curvature equations (16) to (18) would apply. And β, $d\beta/ds$, and $\partial V/\partial x$ could be obtained from a subsonic solution. However, the continuity equation (19), would be of no help. The condition now is that

$$\lim_{y \to \infty} V = V_\infty \tag{20}$$

where V_∞ is the free stream velocity. Practically, equation (16) would have to be solved for several values of velocity V_1 on the surface. For each value of V_1, equation (16) would be solved for increasing y until V reached an asymptotic value. When the asymptotic value for V is equal to V_∞, equation (20) has been satisfied, and the corresponding solution for equation (16) is the correct one.

APPENDIX - DERIVATION OF VELOCITY-GRADIENT EQUATION

Euler's force equation for a nonviscous fluid is

$$\frac{d\overline{V}}{dt} = -\frac{1}{\rho}\nabla p \tag{A1}$$

where the differentiation is with respect to a moving particle. The y-component of this equation is

$$\frac{dV_y}{dt} = -\frac{1}{\rho}\frac{\partial p}{\partial y} \tag{A2}$$

With the assumption of steady, nonviscous, and irrotational flow,

$$\frac{dp}{\rho} + V\,dV = 0 \tag{A3}$$

This holds throughout the flow field, not just along streamlines; therefore,

$$\frac{\partial p}{\rho\,\partial y} = -V\frac{\partial V}{\partial y} \tag{A4}$$

Combining equations (A2) and (A4) results in

$$\frac{\partial V}{\partial y} = \frac{1}{V}\frac{dV_y}{dt} \tag{A5}$$

The following relations (see fig. 8) are useful in the calculations:

$$V_x = V\cos\beta \tag{A6}$$

$$V_y = V\sin\beta \tag{A7}$$

$$\frac{dx}{dt} = V_x \tag{A8}$$

$$\frac{dy}{dt} = V_y \tag{A9}$$

$$\frac{ds}{dt} = V \tag{A10}$$

$$\frac{d\beta}{dt} = V \frac{d\beta}{ds} \tag{A11}$$

$$\frac{dV}{dt} = V_x \frac{\partial V}{\partial x} + V_y \frac{\partial V}{\partial y} \tag{A12}$$

The indicated differentiation of the right side of equation (A5) can be performed, and then the preceding relations may be used. Then the solution for $\partial V/\partial y$ (which appears on both sides of the equation) is obtained:

$$\frac{\partial V}{\partial y} = \frac{V}{\cos \beta} \frac{d\beta}{ds} + \tan \beta \frac{\partial V}{\partial x} \tag{A13}$$

It is desired to calculate the curvature $d\beta/ds$ either on a blade surface or from the stream-function solution. Along a streamline,

$$\tan \beta = \frac{dy}{dx} \tag{A14}$$

and

$$\cos \beta = \frac{dx}{ds} \tag{A15}$$

Now differentiate equation (A14) and use equation (A15) to obtain

$$\frac{d\beta}{ds} = \cos^3 \beta \frac{d^2y}{dx^2} \tag{A16}$$

Along a surface, d^2y/dx^2 can be calculated when y is given as an analytical function of x. However, in the passage, d^2y/dx^2 is given indirectly by the stream function. Hence, an expression is needed for d^2y/dx^2 in terms of the partial derivatives of the stream function.

Since $\tan \beta = V_y/V_x$, equations (2) and (3) can be used to obtain

$$\tan \beta = - \frac{u_x}{u_y} \tag{A17}$$

Using equation (A14) results in

$$\frac{dy}{dx} = - \frac{u_x}{u_y} \tag{A18}$$

Now equation (A18) can be differentiated to obtain

$$\frac{d^2y}{dx^2} = \frac{\partial}{\partial x}\left(\frac{dy}{dx}\right) + \frac{\partial}{\partial y}\left(\frac{dy}{dx}\right)\frac{dy}{dx} = \frac{2u_y u_x u_{xy} - u_y^2 u_{xx} - u_x^2 u_{yy}}{u_y^3} \tag{A19}$$

Using equation (A17) in equation (A19) results in

$$\frac{d^2y}{dx^2} = \tan^2\beta\left(2\frac{u_{xy}}{u_x} - \frac{u_y u_{xx}}{u_x^2} - \frac{u_{yy}}{u_y}\right) \tag{A20}$$

Finally, substituting equation (A20) into equation (A16) yields

$$\frac{d\beta}{ds} = \cos \beta \sin^2\beta\left(2\frac{u_{xy}}{u_x} - \frac{u_y u_{xx}}{u_x^2} - \frac{u_{yy}}{u_y}\right) \tag{A21}$$

The velocity-gradient equation is equation (A13), where $d\beta/ds$ is calculated by equation (A16) along the surface and by equation (A21) at interior points.

REFERENCES

1. Katsanis, Theodore; and McNally, William D.: FORTRAN Program for Calculating Velocities and Streamlines on a Blade-to-Blade Stream Surface of a Tandem Blade Turbomachine. NASA TN D-5044, 1969.
2. Katsanis, Theodore; and Dellner, Lois T.: A Quasi-Three-Dimensional Method for Calculating Blade Surface Velocities for an Axial Flow Turbine Blade. NASA TM X-1394, 1967.
3. Katsanis, Theodore: FORTRAN Program for Calculating Transonic Velocities on a Blade-to-Blade Stream Surface of a Turbomachine. NASA TN D-5427, 1969.
4. Katsanis, Theodore; and McNally, William D.: Revised FORTRAN Program for Calculating Velocities and Streamlines on a Blade-to-Blade Stream Surface of a Turbomachine. NASA TM X-1764, 1969.
5. Shapiro, Ascher H.: The Dynamics and Thermodynamics of Compressible Fluid Flow. Vol. 1. The Ronald Press Co., 1953.
6. Whitney, Warren J.; Szanca, Edward M.; Moffitt, Thomas P.; and Monroe, Daniel E.: Cold-Air Investigation of a Turbine for High-Temperature-Engine Application. I. Turbine Design and Overall Stator Performance. NASA TN D-3751, 1967.
7. Katsanis, Theodore: Use of Arbitrary Quasi-Orthogonals for Calculating Flow Distribution in the Meridional Plane of a Turbomachine. NASA TN D-2546, 1964.
8. Bers, Lipman: Mathematical Aspects of Subsonic and Transonic Gas Dynamics. John Wiley & Sons, Inc., 1958.
9. Hildebrand, Francis B.: Introduction to Numerical Analysis. McGraw-Hill Book Co., Inc., 1956.

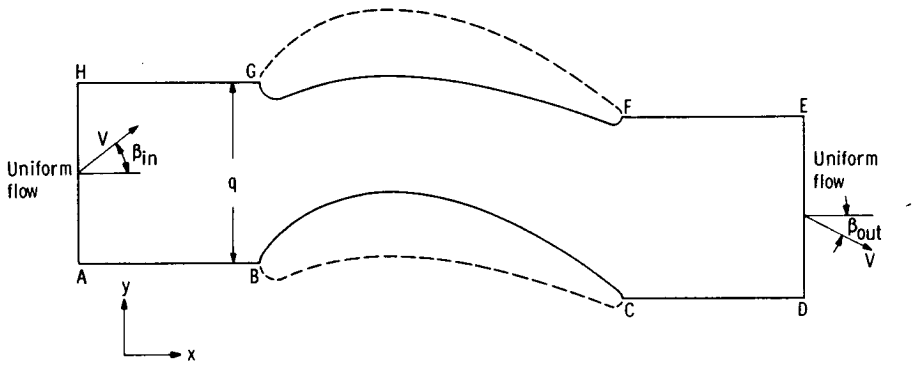

Figure 1. - Finite flow region.

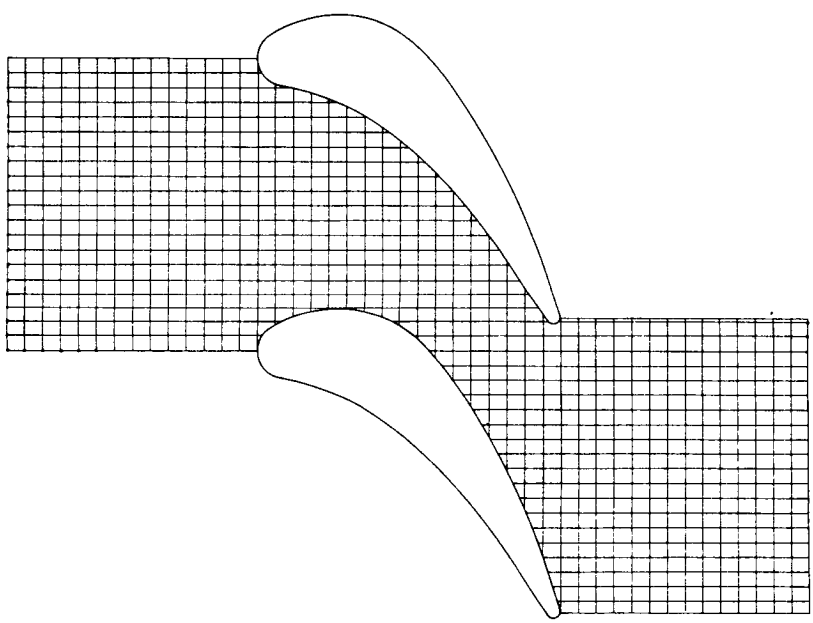

Figure 2. - Typical mesh in blade-to-blade solution region

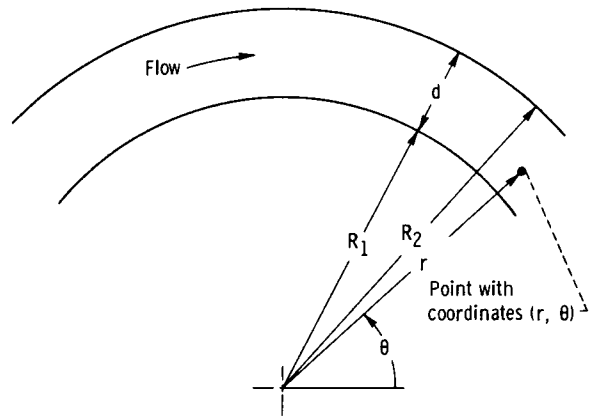

Figure 3. - Curved passage.

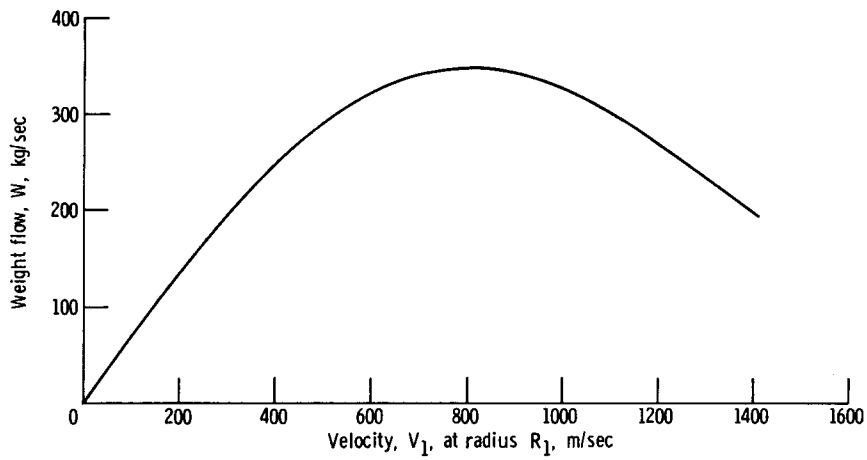

Figure 4. - Weight flow as a function of V_1.

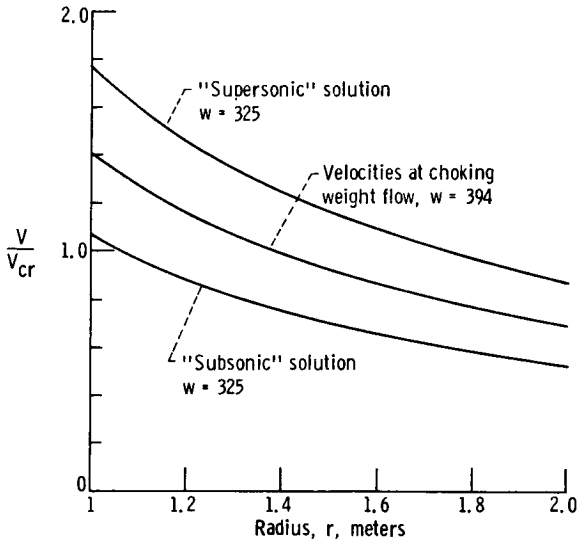

Figure 5. - Velocity distribution at various weight flows.

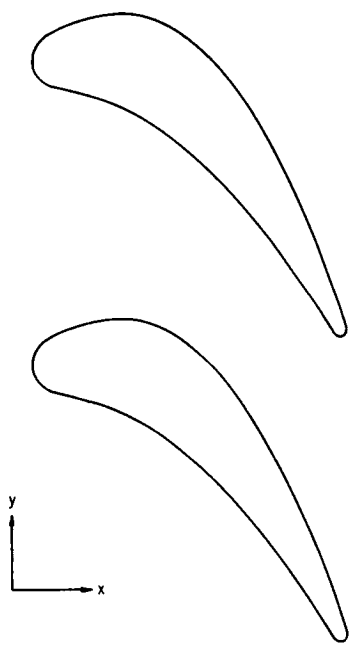

Figure 6. - Axial stator blade for numerical example.

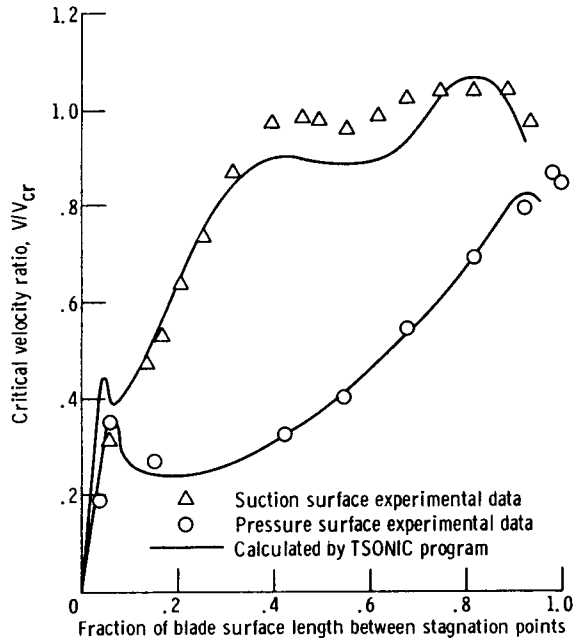

Figure 7. - Blade surface velocities for axial stator mean section compared with experimental data.

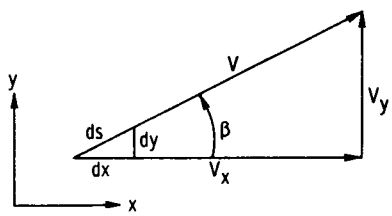

Figure 8. - Velocity components.

DISCUSSION

PIERRE G. SCHWAAR, AVCO/Lycoming Division: I have been working on the same problem for some time, and there are many questions which I would like to ask. I shall restrict myself to two.

First, you have shown a solution which is only slightly transonic, with a maximum suction side Mach number of 1.05 approximately. Under these conditions, the channel certainly is not choked. Is this the highest Mach level you have obtained with your method?

KATSANIS: I believe you could go a little higher than 1.05. I don't have any experimental comparisons for any higher Mach numbers. I would expect it to get up to 1.2 or 1.4. It also depends on how large the region is. One of the basic assumptions is that the shocks are negligible, so this would determine partially whether a satisfactory solution could be obtained.

SCHWAAR: I am specifically talking about a turbine rotor cascade similar to yours, but with a higher turning angle, where I have obtained a maximum suction side Mach number of 1.18, which corresponds to choked cascade flow conditions.

The second question is: How do you determine the radius of curvature of the streamlines? Do you make use of spline fits?

KATSANIS: The streamlines are not actually laid out, but I get the radius of curvature in terms of first and second derivatives of the stream function, which is calculated using a finite difference approximation. This is included in the written version of the paper.

SCHWAAR: This does not involve a spline fit, then?

KATSANIS: Not for calculating the curvature of the streamline. I use this for the blade surface definition, but not for this calculated first and second derivatives of the stream function.

SCHWAAR: If I understand correctly, you first obtain a subsonic solution and streamline pattern, and then use that streamline geometry without modification to get a transonic solution. My contention is that the streamline configuration changes substantially in the supersonic domain, and that a solution according to your method, for transonic conditions with suction side Mach number larger than say, 1.1, would not represent a good approximation. It is necessary to carry out the streamline analysis in the transonic domain in order to obtain a valid solution.

KATSANIS: All I can say is I have worked with velocity gradient equations more generally, and I have found this approach seems to be better. For example, when you have very low solidity, the velocity gradient method just doesn't seem to be very satisfactory.

MAURICE S. CAHN, Northrop Corp.: I'd like to make a general comment on the network calculation doctrine. It looks like the results in this paper were very good; however, the point I want to make is one which has to do with the theme set at this meeting.

The point I'd like to make is that computers don't stay awake at night and worry about their job. In a lot of papers I have seen, people have seemed to ignore this fact and to have taken advantage of the computer's tremendous capability. They quit worrying about their jobs and assume computers are going to solve all the problems. I particularly make this point for the problem of transonic flow. I think there is a solution to this problem that can use complex function analysis by making a simple transformation to get an equivalent incompressible flow. We have done this at Northrop, and have solved the problem for external flow around an airfoil. The same concept, I think, could be applied to this problem.

KATSANIS: This is applicable even to transonic flow?

CAHN: Right. Now, if you look at the basic equation system you are trying to satisfy, you have a network of ϕ and ψ lines which is an orthogonal network that satisfies a pretty simple equation: $d\phi/ds$, which is along the streamline, is equal to $1/\rho(d\psi/dn)$. It seems we have solved this problem in a simple manner. I will have to admit we have used a computer for the problem. But on the large computers it takes about 10 seconds.

KATSANIS: I'll have to obtain more information about your method.

CAHN: We welcome anyone to take a look at what we are doing. I think it is an exact solution to compressible isotropic flow. But a computer is not going to worry about whether this is an exact method or not, and I would welcome people who want to stay awake at night to talk to us and give further understanding to our approach.

KATSANIS: Well, I'd like to talk to you.

CAHN: Well, we welcome it. Anyway, my comment is that using the computer as a crowbar is going a little too far. A lot of solutions can be obtained with computers in a more efficient way if we look at the basic equations and think of more elegant ways to solve them.

STEPHEN STARCH, Boeing Co., Wichita: First of all, I would like to ask you what are the criteria for negligible shock? How would you know when you are dealing with this?

Second, how do you reconcile your comment that you must have a well-guided passage with your feeling that this method could be used for wings and airplanes?

KATSANIS: The idea of the method is that it is not limited to a well-guided passage. The velocity gradient method must be used in a well-guided passage, but by obtaining additional information from a subsonic solution, then you can extend this to a case where you don't have a well-guided passage.

This hasn't been actually tried out for a wing, so I don't know how well it is going to work, but it seems to me you should be able to get some results.

Then the question about the shock strength, well, if you have such a weak shock that it couldn't be picked up with a finite difference, then for all practical purposes it's going to be an exact solution. There's not much more to say.

LARS E. ERICSSON, Lockheed Missiles and Space Co.: I think a very good criterion for a negligible shock would be one that doesn't cause any flow separation in your duct.

PREDICTION OF HEAT-TRANSFER CHARACTERISTICS FOR EJECTOR EXHAUST NOZZLES

By Francis C. Chenoweth and Arthur Lieberman

Lewis Research Center

N70-21377

SUMMARY

A method is proposed for predicting the surface temperatures of the shroud of an ejector exhaust nozzle at afterburning conditions. These surface temperatures were obtained by applying a heat-balance equation employing radiation and convection heat transfer of the shroud with the jet and ambient surroundings. Conventional methods were used to predict all terms except the convective heat transfer between the film and the nozzle. This term was evaluated using the Hatch and Papell film-cooling correlation to predict an adiabatic wall temperature which was used as the driving temperature for heat transfer between the film and the wall.

Results from this analytical procedure are compared with experimental data obtained for the shroud of a cylindrical ejector nozzle tested with a nacelle-mounted afterburning turbojet engine in an altitude facility.

The analytical method yielded good results for cases of separated, impingement and smoothly attached flow conditions if the convective heat-transfer coefficient was calculated based on secondary-flow conditions rather than the more conventional primary-flow conditions. Maximum variation between experimental and predicted temperatures was 200° R (111 K).

INTRODUCTION

Many current aircraft jet propulsion systems make use of an ejector to provide a cooling film of air over the engine tailpipe. Thus film cooling of the ejector shroud is obtained by the secondary air providing an insulating layer of cool air between the hot gas jet and the shroud. To evaluate film cooling, several experimental investigations (refs. 1 to 6), have been made

Preceding page blank

of film cooling an insulated surface. There are, however, few reported investigations of applying this work to an environment where hot gas radiation and heat transfer to ambient conditions must also be evaluated to determine a wall temperature.

The method of predicting wall temperatures in a radiation and uninsulated environment has been investigated herein. This method utilizes a wall heat balance which includes radiant and convective heat transfer with the primary and secondary flows and the ambient environment. Conventional methods are used for predicting all the terms but the forced convection between the shroud and the internal flow. To evaluate this forced convection term, the Hatch and Papell film-cooling correlation (ref. 1) is used in combination with an estimated heat-transfer coefficient.

Results of the analytical method are compared with experimental data which were obtained using a nacelle-mounted afterburning turbojet engine with a cylindrical ejector nozzle in an altitude test facility. The internal thrust, secondary flow pumping characteristics, secondary flow total-pressure drop and temperature-rise characteristics through the nacelle are reported in reference 7. For the present comparisons, the engine was operated at the maximum afterburning setting providing an ejector secondary to primary diameter ratio of about 1.28. The maximum exhaust gas temperature was 3500° R (1940 K). The corrected secondary weight flow ratio was varied from approximately 0.03 to 0.09 over a range of exhaust nozzle pressure ratios from 2.0 to 6.3.

APPARATUS AND PROCEDURE

Details of the altitude facility, research hardware, installation and instrumentation are presented in reference 7. A schematic of a typical ejector is shown in figure 1. The experimental data included in the report is from ejector 4, reference 7. Some of the pertinent dimensional characteristics are as follows: the calibrated primary areas, A_{PRI}, averaged 181 square inches (1160 cm^2), the external shroud diameter, D_{SH}, was 19.6 inches (49.6 cm), and the length of the cylindrical portion of the ejector downstream of the primary nozzle was 24.8 inches (63.0 cm). The ejector was constructed of Inconel 600 having a nominal wall thickness of 0.063 inch (0.16 cm).

The nozzle pressure ratio was obtained by keeping the primary jet total pressure constant and varying the ambient pressure.

SYMBOLS

A	area
C_p	specific heat at constant pressure
D	diameter
$\mathscr{F}$	radiation configuration factor
Gr	Grashoff number
h	heat-transfer coefficient
k	thermal conductivity
M	Mach number
P	total pressure
p	static pressure
Pr	Prandtl number
Q	heat rate per unit area
R	gas constant
Re	Reynolds number
S	slot width
T	total temperature
t	static temperature
V	velocity
w	weight flow
x	distance
α	thermal diffusivity
γ	ratio of specific heats
σ	Stefen-Boltzman constant

τ temperature ratio T_{SEC}/T_{PRI}

ω weight flow ratio w_{SEC}/w_{PRI}

Subscripts:

AMB ambient

BL length of boundary-layer growth

C convection

D diameter

EX exit

f film

PRI primary

R radiation

r recovery

SEC secondary

SH shroud

W wall

x distance

ANALYSIS PROCEDURE

The model is shown in figure 2. It is assumed that both the temperature gradient across the wall and the axial heat-conduction rate in the wall are negligible.

A heat balance on the wall element shown in figure 2 is:

$$Q_{R,PRI} = Q_{C,SEC} + Q_{R,EX} + Q_{R,AMB} + Q_{C,AMB}$$

The first subscript defines the mechanism of heat transfer, either radiation or convection. All energy exchange is between the wall and another body. The second subscript defines this body.

Rewriting the heat-balance equation in terms of a heat-transfer coeffi-

cient and a temperature difference, we obtain:

$$h_{R,PRI}(t_{PRI} - T_W) = h_{C,SEC}(T_W - T'_W)$$
$$+ (h_{R,EX} + h_{R,AMB} + h_{C,AMB})(T_W - T_{AMB}) \qquad (1)$$

The components of heat transfer between the surface and the ambient surroundings are combined to simplify the equations. The heat-transfer areas are assumed to be equal for all components. Thus equation (1) is solved for the diabatic wall temperature T_W. Evaluation of the heat-transfer coefficients and gas temperatures utilized the experimental measurements of axial wall static-pressure distribution, the total pressures, total temperatures, weight flow rates and specific heat ratios of the primary and secondary streams, ambient pressure and temperature, and the geometry of the ejector. Standard one-dimensional flow equations and the static pressure distribution are combined to determine the primary flow conditions and areas. The secondary flow is assumed to fill the remaining area between the primary jet and the shroud wall.

The radiation components of heat transfer are defined by:

$$Q = \mathscr{F}_{ij}\sigma\left(T_i^4 - T_j^4\right) = h\left(T_i - T_j\right)$$

Thus the effective heat-transfer coefficients $h_{R,PRI}$, $h_{R,EX}$, and $h_{R,AMB}$, are described by:

$$h_R = \frac{\mathscr{F}_{ij}\sigma\left(T_i^4 - T_j^4\right)}{T_i - T_j}$$

The emissivity of the internal and external surfaces was assumed to be 0.65 based on data obtained from reference 8. Configuration factors for radiation out the exit were determined using data in reference 9. Hot-gas radiation configuration factors and emissivities were obtained as outlined in reference 10 for nearly black bodies.

The heat-transfer coefficient between the wall and the surroundings, $h_{C,AMB}$, was obtained using the standard free-convection coefficient for a horizontal cylinder (ref. 11).

$$h_{C,AMB} = 0.53 \frac{k}{D} \left(Gr_D Pr\right)^{1/4}$$

Properties are obtained at the arithmetic mean between the surface temperature and ambient temperature.

A similar method to that proposed in reference 12 was used to determine the heat-transfer characteristics between the wall and the secondary stream. This component of heat transfer was evaluated by assuming the potential for heat transfer was the difference between the adiabatic recovery temperature of the film and the wall temperature. The adiabatic recovery temperature, T'_w, was determined from the adiabatic wall film-cooling model proposed in reference 1. The correlation is repeated below:

$$\frac{T_{r,PRI} - T'_w}{T_{r,PRI} - t_{SEC}} = -\left(\frac{\pi D_{SH} h_f x}{w_{SEC} C_{P,SEC}} - 0.04\right)\left(\frac{S V_{PRI}}{\alpha_{SEC}}\right)^{0.125}\left[1 + 0.4 \tan^{-1}\left(\frac{V_{PRI}}{V_{SEC}} - 1\right)\right]$$

The primary flow field was dete ined by assuming one-dimensional isentropic flow and assuming that the measured wall static pressures were applicable across the ejector cross section. The local hot-gas recovery temperature, $T_{r,PRI}$, was determined at distance x downstream of the throat and was defined by

$$T_{r,PRI} = \left[1 + Pr_{PRI}^{1/3}\left(\frac{\gamma_{PRI} - 1}{2}\right) M_{PRI}^2\right] t_{PRI}$$

All secondary flow parameters (t_{SEC}, w_{SEC}, $C_{P,SEC}$, α_{SEC}, and V_{SEC}) are taken at slot inlet conditions. V_{PRI} represents the primary throat velocity. The local heat-transfer coefficient, h_f, is defined by

$$h_f = 0.265 \frac{k_f}{D_{SH}} Re^{0.8} Pr_f^{0.3}$$

where the fluid properties are evaluated at an average of the local primary static temperature and secondary slot inlet static temperature.

In reference 12 the heat-transfer coefficient between the wall and the film was determined for the hot-gas stream. However, for the configuration in reference 12 (a flat plate with an uncooled section upstream of the injection slot), the boundary-layer height was large compared to the injection slot height. For the case of an ejector, the height of the secondary flow passage at the primary exit is large compared to the primary stream boundary-layer height and so use of a different heat-transfer coefficient might be expected. Values of heat-transfer coefficient obtained from primary flow conditions provided more heat transfer than was observed in test. Coefficients based on the secondary stream conditions (assuming that the secondary flow boundary layer originated at the beginning of the cylindrical portion of the nozzle) were smaller and provided good agreement with the observed data. These heat-transfer coefficients were obtained using the standard flat-plate correlation for turbulent flow (ref. 13) as follows:

$$h_{C,SEC} = 0.0296 \frac{k}{x_{BL}} Re_x^{0.8} Pr^{1/3}$$

where the fluid properties are evaluated at an average of the adiabatic wall temperature T'_W and the wall temperature. The local velocity required for the secondary stream Reynolds number, was determined by using the adiabatic recovery temperature T'_W and the area of the secondary stream as shown below:

$$\frac{Pr_{SEC}^{1/3}}{2C_{P,SEC}} V_{SEC}^2 + \frac{p_{SEC} A_{SEC}}{w_{SEC} R_{SEC}} V_{SEC} - T_{r,SEC} = 0$$

Since the heat-transfer coefficients in equation (1) are either directly or indirectly a function of the wall temperature, the Newton-Raphson method of iteration was used for solution of the wall temperature value.

RESULTS AND DISCUSSION

Comparisons of the experimental and predicted wall temperatures are shown for three distinctly different flow conditions which were a function of the nozzle pressure ratio, and secondary flow. Completely separated flow was obtained at low nozzle pressure ratios. High pressure ratios yielded smoothly attached flow at high corrected secondary weight-flow and impinging-attached flow at low corrected secondary weight-flow.

A comparison of experimental and predicted wall temperatures for a typical attached-flow condition is shown in figure 3(a). The flow field for this condition is shown in figure 1. The dashed line represents an approximate boundary between the secondary and primary streams. The mixing between the two streams then forms a wake which overlaps this boundary. The decrease in primary flow area near the ejector exit is due to a separation and recompression of the over-expanded primary stream. The separation shock which occurs will move upstream as the nozzle pressure ratio decreases.

The scatter in experimental temperatures (fig. 3(a)), is due to nonuniform flow distribution. As would be expected this effect diminishes with length along the ejector. The dashed line is the adiabatic surface temperature calculated using the Hatch-Papell semiempirical film-cooling correlation. The solid line is the surface temperatures predicted using the analysis procedure outlined herein.

As can be seen, good agreement between the experimental and predicted data is obtained except near the ejector exit where the maximum error obtained is approximately 200° R (111 K). This increase in predicted wall temperature near the end of the ejector is due to the recompression of the over-expanded primary flow. The flat portion of the adiabatic surface temperature represents the distance downstream of the injection point the gas travels before the heat diffuses through the coolant stream to raise the adiabatic surface temperature.

A distribution of the various components of heat transfer are shown in figure 3(b). These curves represent an accumulative total of the heat-in and heat-out of the wall. The heat-transfer term between the wall and the secondary stream, $Q_{C,SEC}$, changes from a heat-out term near the entrance of the ejector to a heat-in term near the exit and appears to be responsible for the high predicted wall temperature near the ejector exit.

For most of the ejector it is evident that the radiation heat transfer between the primary stream and the surface is the most significant heating term. The most significant cooling term changes from the secondary convection heat transfer term to the combined ambient radiation terms. The convection heat transfer between the surface and ambient, $Q_{C,AMB}$, is pratically negligible over the entire length of the ejector since external flow was not present for these test conditions. The solid angle between a point on the surface and the opening in the exit of the ejector increases as x/D_{PRI} increases toward the exit. As a result of this the radiation from the surface to ambient through the exit of the ejector becomes a significant cooling heat-transfer component near the exit of the ejector.

The next flow condition to be considered is that of a separated primary. The flow field is shown in figure 1. This flow condition is that of a low nozzle pressure ratio, $P_{PRI}/P_{AMB} = 2.0$. The pressure ratio was reduced by increasing backpressure at constant inlet conditions so that the pressure environment of the nozzle is higher than at larger pressure ratios. The primary jet was separated from the shroud with the secondary flow adjusting at the exit to the local ambient pressure. The secondary flow along the entire length of the ejector is subsonic. The primary flow, in effect, is not significantly influenced by the shroud.

The predicted wall temperature, indicated by the solid line of figure 4(a), is approximately 200° R (111 K) higher than the experimental data over the length of the ejector. This is believed due to either a high estimate of radiation heat transfer between the primary stream and the surface or a high prediction of the adiabatic surface temperature by the film-cooling correlation. Due to the higher primary static pressures, its radiation term is greater than that for the attached flow condition by a factor of almost two over the entire length of the ejector.

As expected from the steep increase of the predicted adiabatic surface temperatures (fig. 4(a)) the convection between the surface and the secondary stream increases rapidly (fig. 4(b)). As in the attached flow condition the radiation term between the primary stream and the surface is the most significant. However, the primary cause of the excessive temperature prediction appears to be due to premature heating of the secondary stream.

The third flow condition to be discussed is that of impingement flow. The flow field, shown in figure 1, indicates the primary flow stream impinges

on the shroud a short distance downstream from the point of injection. A shock is created at this point. The secondary flow is due strictly to entrainment by the primary flow. The mixing of the secondary stream into the primary would be complete. This impingement flow condition is a combined effect of low corrected weight flow ratio and high nozzle pressure ratio.

A comparison of experimental and predicted temperature profiles is given in figure 5(a). Even though the model for the film-cooling correlation is somewhat different than an ejector flow system, it successfully predicts the very high adiabatic surface temperatures, necessary for good agreement with experiment. The maximum deviation from experiment is $\pm 100^{\circ}$ R (± 55 K).

Figure 5(b) shows a considerably different picture than for the previous two flow conditions. The convection heat transfer between the secondary and the surface is much more significant than the radiation between the primary and the surface. Most of the heat load to the surface, therefore, comes from mixing rather than radiation.

For this flow condition the cooling is provided entirely by the radiation from the surface to ambient. It should be pointed out that if the ejector were covered, such that $Q_{R,AMB}$ is decreased, the surface temperature would increase significantly.

CONCLUDING REMARKS

The measured wall temperatures of ejector nozzles for afterburning turtojet engines were compared with results of predicted data. The predicted data was obtained by combining an evaluation of the heat-transfer losses due to radiation and convection with an existing film-cooling correlation.

The prediction yielded good results for the three flow conditions considered. This was particularly true for the case where the predominant heat load was due to convection with the mixed secondary and primary streams (impingement flow). For the attached and for the separated flow conditions the primary heating component was radiation between the primary stream and the ejector shroud surface. For these cases it is evident the film-cooling correlation predicted somewhat excessive adiabatic surface temperature resulting in predicted surface temperatures being about 200° R (111 K) higher than were experimentally observed.

To improve the analysis presented, minor adjustments may be obtained by replacing the one-dimensional flow analysis with an axisymmetric method of characteristics, and by improving the techniques for calculating the radiation heat-transfer components. However, major improvements should be obtained by better estimating the heat transfer between the surface and the film. These adjustments would be made by replacing the present film-cooling correlation for calculating the adiabatic wall temperature of the film, with a similar correlation obtained for a geometry similar to an ejector. The heat-transfer coefficient for this component is also critical and needs further study.

REFERENCES

1. Hatch, James E.; and Papell, S. Stephen: Use of a Theoretical Flow Model to Correlate Data for Film Cooling or Heating an Adiabatic Wall by Tangential Injection of Gases ot Different Fluid Properties. NASA TN D-130, 1959.
2. Wieghardt, K.: Hot-Air Discharge for De-Icing. Translation F-TS-919-RE, Air Material Command, December 1946.
3. Chin, J. H.; Shirvin, S. C.; Hayes, L. E.; and Silver, A. H.: Adiabatic Wall Temperature Downstream of a Single Tangential Injection Slot. Paper 58-A-107, ASME, 1958.
4. Seban, R. A.; Chan, H. W.; and Scesa, S.: Heat Transfer to a Turbulent Boundary Layer Downstream of an Injection Slot. Paper No. 58-A-107, ASME, 1958.
5. Goldstein, R. J.; Eckert, E. R. G.; Tsou, F. K.; and Haji-Sheikh, A.: Film Cooling With Air and Helium Injection Through a Rearward-Facing Slot Into a Supersonic Air Flow. HTL TR No. 60, University of Minnesota, February 1965.
6. Lucas, James G.; and Golladay, Richard L.: Gaseous-Film Cooling of a Rocket Motor With Injection Near the Throat. NASA TN D-3836, 1967.
7. Samanich, Nick E.; and Huntley, Sidney C.: Thrust and Pumping Characteristics of Cylindrical Ejectors Using Afterburning Turbojet Gas Generator. NASA TMX-52565, 1969.

8. Wolf, J.: Aerospace Structural Metals Handbook, Vol. IIA, AFML-TR-68-115, 1968.

9. Sparrow, E. M.; Albers, L. U.; and Eckert, E. R. G.: Thermal Radiation Characteristics of Cylindrical Enclosures. Journal of Heat Transfer, Vol. 84, No. 1, 1962, pp. 73-81.

10. McAdams, William H.: Heat Transmission. Third Ed. McGraw-Hill Book Co., Inc., 1954.

11. Kreith, Frank: Principles of Heat Transfer. Holt, Rinehard and Winston, Inc., 1966.

12. Hartnett, J. P.; Birkebak, Richard C.; and Eckert, E. R. G.: Velocity Distributions, Temperature Distributions, Effectiveness and Heat Transfer for Air Injected Through a Tangential Slot Into a Turbulent Boundary Layer. ASME Paper No. 60-HT-31, 1960.

13. Rohsenow, Warren M.; and Choi, Harry: Heat, Mass, and Momentum Transfer. Prentice-Hall, Inc., 1961.

SCHEMATIC OF EJECTOR EXHAUST NOZZLE

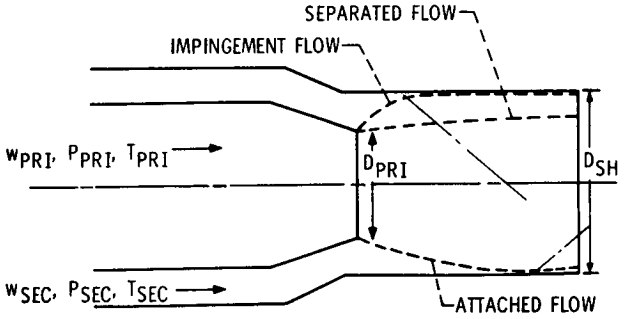

Figure 1

MODEL FOR APPLYING FILM-COOLING CORRELATIONS TO EJECTORS

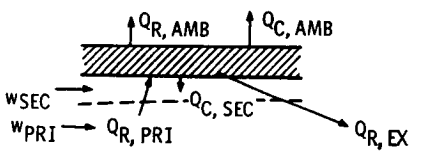

Figure 2

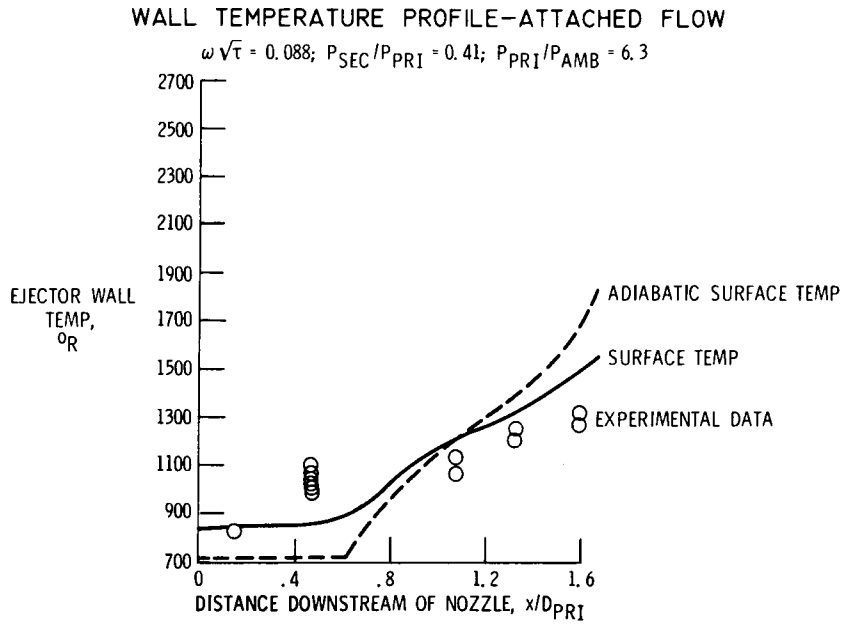

Figure 3(a)

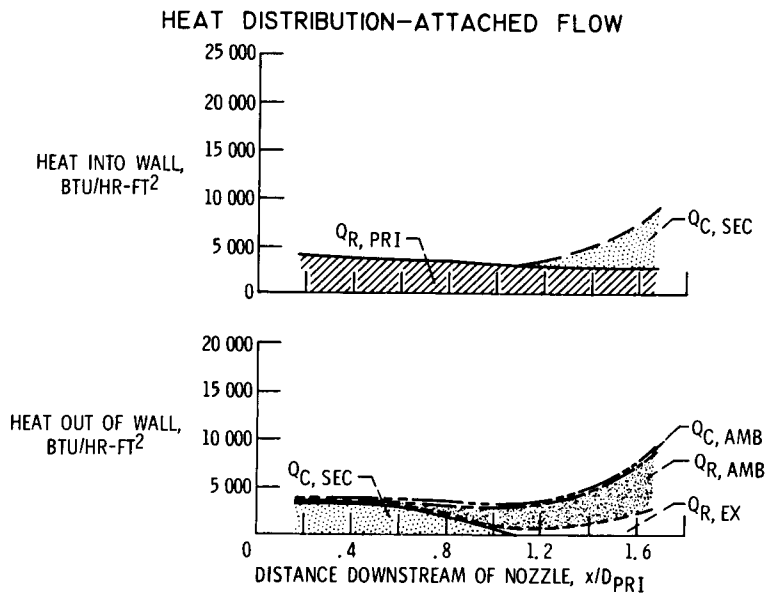

Figure 3(b)

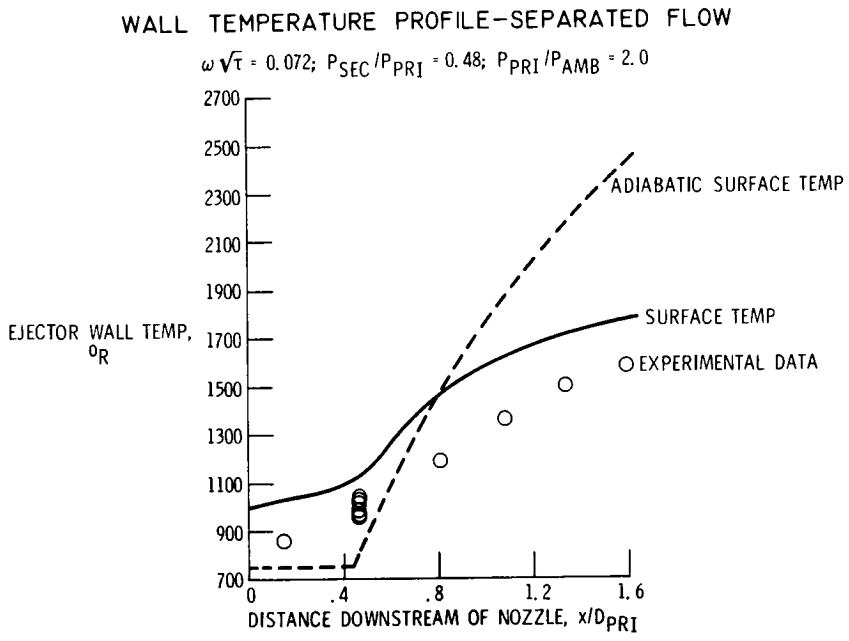

Figure 4(a)

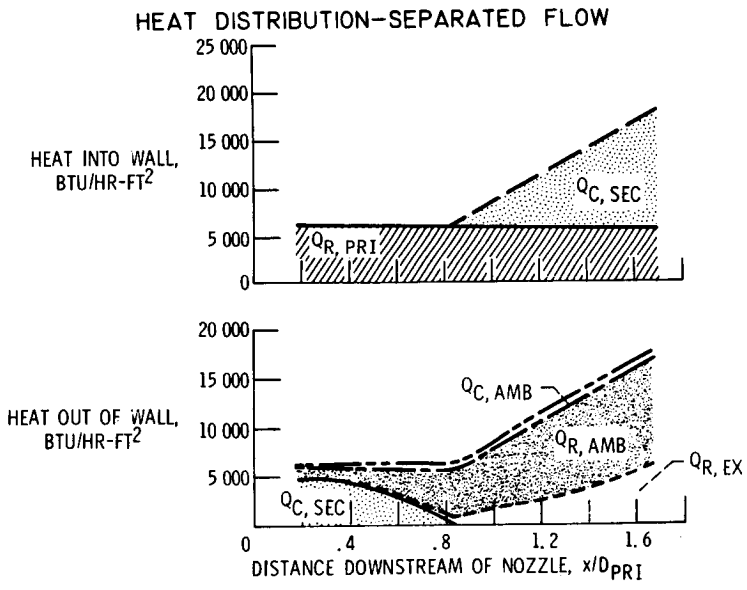

Figure 4(b)

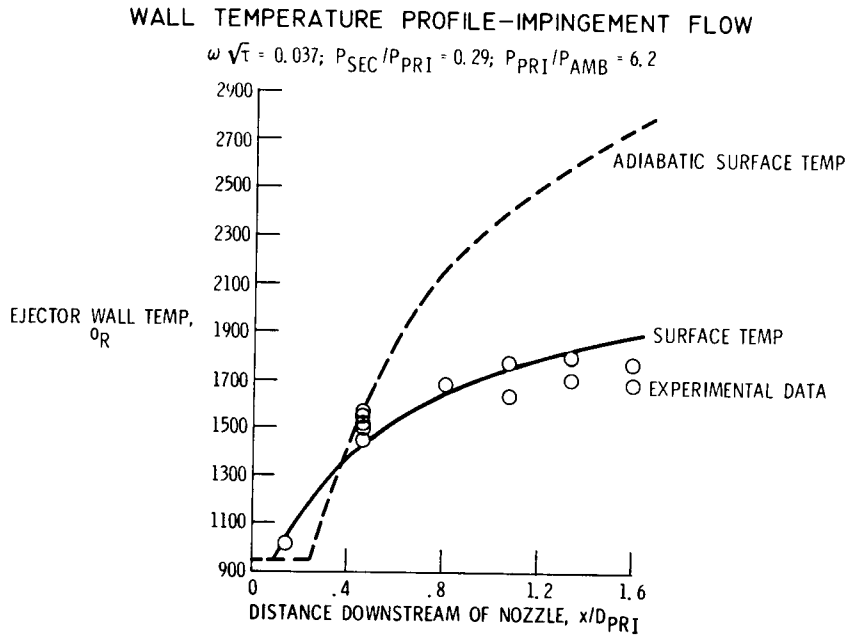

Figure 5(a)

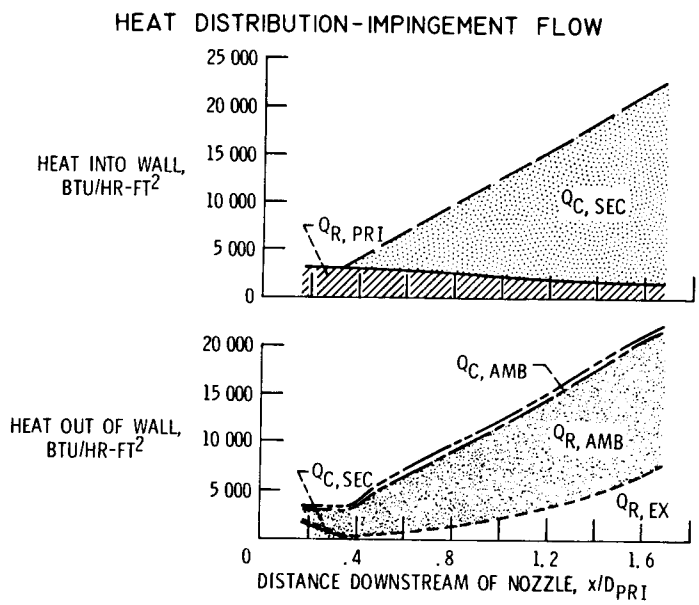

Figure 5(b)

A UNIFIED SYSTEM OF SUPERSONIC AERODYNAMIC ANALYSIS

By Harry W. Carlson and Roy V. Harris, Jr.

Langley Research Center

N70-21378

SUMMARY

The design and development of efficient aircraft is critically dependent on the availability of rapid and accurate theoretical methods for aerodynamic analysis to supplement wind-tunnel data so that aerodynamic factors can exert their proper influence early and often in the configuration selection process. In this paper a discussion is presented of the analytic methods developed at the Langley Research Center which provide not only for the estimation of forces and moments on supersonic airplane configurations but which also have certain design features for component shaping to minimize drag. The methods are based on linear-theory numerical solutions which have been implemented by programing of high-speed digital computers. The methods are described and examples are shown to indicate their applicability to aerodynamic estimation and optimization, to stability and control studies, and to sonic-boom predictions.

INTRODUCTION

The design and development of efficient aircraft are critically dependent on the availability of rapid and accurate theoretical methods for aerodynamic analysis to supplement wind-tunnel data so that aerodynamic factors can exert their proper influence early and often in the configuration selection process. For conventional subsonic airplanes, these requirements are satisfied by methods which consider the wing aspect ratio and span-efficiency factor in evaluation of lift-induced drag and by methods based on exposed surface areas and local skin-friction coefficients for the estimation of viscous drag. At supersonic speeds, however, the problem becomes more complex because of a drag component, not present at subsonic speeds, which is due to the longitudinal distribution of airplane volume and lift. This supersonic pressure drag, or wave drag, is responsible for the large differences in airplane shape that may be observed by comparing typical supersonic and subsonic airplanes. Efforts to keep the wave-drag contribution within acceptable bounds have resulted in relatively thinner airplane components and in greatly reduced wing span and aspect ratio in comparison with good subsonic designs. Thus, in the development of analytic methods applicable at supersonic speeds, a considerable amount of attention must be devoted to the treatment of wave drag – that associated with the lift distribution, as well as that dependent on the volume.

In this paper a discussion is presented of analytic methods developed at the Langley Research Center which provide not only for the estimation of forces and moments on supersonic airplane configurations but which also have certain design features for component shaping to minimize drag. The methods are based on linear-theory numerical solutions which have been implemented by programing of high-speed digital computers. The discussion will begin with an examination of some basic theoretical approaches to the evaluation of drag at supersonic speeds. Then a composite system of analysis that combines selected features of each approach will be outlined. This system provides predictions of drag characteristics of complete airplane configurations and certain design information. Elements of the numerical solutions used to adapt the theory to digital computer implementation are illustrated, and the resultant complex of computer programs is described. A set of examples is shown to indicate the applicability of the methods to aerodynamic estimation and optimization problems, to stability and control studies, and to sonic-boom predictions. Finally, some brief comments are made relative to possible future development of the system.

SYMBOLS

A_B	area of equivalent body
C_D	drag coefficient, $\frac{\text{Drag}}{qS_W}$
C_L	lift coefficient, $\frac{\text{Lift}}{qS_W}$
C_m	pitching-moment coefficient
C_p	pressure coefficient
D	drag
l	model length
M	Mach number
Δp	incremental pressure
q	dynamic pressure

S	surface area
S_a	surface area of aircraft
S_c	surface area of cylinder
S_d	surface area of disk
S_w	surface area of wing
U	free-stream velocity
u	perturbation velocity
x,r,θ	cylindrical coordinates
δ_c	canard deflection
δ_t	tail deflection
λ	surface slope
μ	Mach angle
ρ	density

BASIC THEORETICAL APPROACHES

At the present time, airplane wave drag is evaluated almost exclusively by application of the familiar linear theory of supersonic flow. More exact methods have not yet been developed to the point where they are broad enough in scope to be applicable to complete airplane configurations. Within the linear theory, there are two fundamental approaches to drag evaluation. (See fig. 1.) In the more direct approach, which might be termed the near-field method, pressures are evaluated at a sufficient number of control points on the airplane surface to assure that an integration of local panel forces will yield lift and drag values representative of the complete airplane. The usual linear-theory sources, sinks, doublets, and vortices are used to represent the airplane volume and the lift-generated flow fields which determine the influence of one part of the airplane on another. This near-field method in conjunction with a viscous, or skin-friction,

analysis can account for all the major airplane aerodynamic forces. Advantages of this approach are the consideration of the interaction between volume and lift effects, the surface-loading information obtained, and the opportunity afforded to minimize drag due to lift by the design of wing surfaces. The prime disadvantage of the method is its complexity. Numerical solutions are rather cumbersome and even when implemented by the most modern high-speed computers require relatively long running times. However, remarkable progress in adapting the technique to nearly complete airplane configurations has been accomplished. (See refs. 1, 2, 3, and papers no. 2 and 12 presented at this symposium.)

An alternate approach which might be termed the far-field method is based on the relationship between the forces on the airplane and the momentum transport through the boundaries of a surface completely surrounding the airplane. For convenience, this surface is assumed to be that of a cylinder whose axis passes through the airplane. When a cylinder with a sufficiently large diameter is chosen, the total airplane drag is represented by two concentrations of the momentum transport. In the airplane wake, near the center of the rear disk, is concentrated the momentum loss associated with the airplane skin-friction drag and with the vortex drag due to the lateral distribution of lift. In the vicinity of the Mach cone originating from the airplane nose is the momentum loss associated with the airplane wave drag which results from the longitudinal distribution of airplane volume and lift. No way is known to evaluate the skin-friction, or viscous, drag without consideration of airplane surface conditions; thus, the far-field approach is not applicable for this drag contribution. Surface conditions also must be considered in obtaining knowledge of lift distribution required for vortex-drag evaluation, and again the far-field approach is inapplicable. However, for airplane wave drag which is so critical to the development of a workable supersonic analysis technique, the far-field analysis provides, in a somewhat devious fashion, a remarkably simple analysis method for this complex problem. This method, known as the supersonic area rule, was advanced and developed by Hayes, Whitcomb, Jones, Lomax, and Ward (refs. 4 to 8).

Practical application of the far-field analysis to the evaluation of wave drag is based on the observation made by Hayes that on a control cylinder of infinitely large diameter, the effect of an airplane-created disturbance is not altered by a translation of the disturbance within a plane surface tangent to a Mach cone originating on the airplane axis. Thus, at large distances for any given azimuthal location, the flow field created by the airplane is indistinguishable from that of a particular body of revolution defined by cross-sectional areas of the airplane intercepted by Mach cutting planes. When this equivalent-body concept is accepted, airplane wave-drag evaluation is reduced to evaluation, by well-known methods, of the wave drag of a series of bodies of revolution, each accounting for a specific but narrow range of azimuthal angles.

The influence of the lift distribution on wave drag may be introduced into the equivalent-body theory by conversion of local forces to equivalent areas by use of a method set forth by Hayes (ref. 4), but this first requires an independent near-field evaluation of lift distribution. Thus, it is more convenient to resort to lifting-surface theory for the drag associated with lift – both the wave drag and the induced drag – and to treat only the thickness, or zero-lift, wave drag by the far-field method. The prime advantages of the equivalent-body wave-drag estimation system are that it is relatively simple, that it is applicable to any airplane configuration, no matter how complex, and that, as will be discussed later, provision can be made for direct optimization of airplane-component shapes for drag minimization.

A COMPOSITE SYSTEM OF ANALYSIS

Application of elements of both the near-field and far-field approaches to a composite analysis system for supersonic airplanes may be illustrated with the aid of the lift-drag curve of figure 2. The two contributions to drag due to lift, the wave drag and the vortex drag, are best handled simultaneously by the application of simplified near-field approaches to a wing of zero thickness with relatively small departures from a horizontal plane. Zero-lift wave drag due to the airplane volume may be found by the application of far-field supersonic-area-rule techniques. The assumptions of zero volume in the drag-due-to-lift analysis and of zero lift in the wave-drag analysis prevent consideration of mutual interaction between volume and lift, a factor which appears to be negligible for slender supersonic-transport configurations but which may be significant for supersonic-dash vehicles. Selection of these methods does, however, preserve the opportunities for design of a twisted and cambered wing surface for drag-due-to-lift minimization by near-field means and for component shaping for wave-drag minimization by far-field means. The only practical means of evaluating the skin-friction drag is the conventional manner based on exposed surface panels and average skin-friction coefficients determined by a representative local Reynolds number. Numerical techniques for evaluation of all three drag contributions have been developed and have seen extensive use in the national supersonic-transport program and in various military aircraft development projects.

FEATURES OF NUMERICAL SOLUTIONS

Some of the key elements in the zero-lift wave-drag and drag-due-to-lift numerical solutions are illustrated in figure 3. The complex geometrical calculations required to generate the equivalent-body-area developments for complete and rather arbitrarily shaped airplane configurations have been programed. The frontal projection of an

airplane section intercepted by a supersonic-area-rule cutting plane for a given supersonic Mach number and for a typical azimuth angle is shown at the upper left of figure 3. Also shown in this figure is a curve showing the distribution of frontal-projection cross-sectional area defining, for a typical azimuth angle, one of the many required equivalent bodies. Indispensable elements of the program-drag solution for the equivalent bodies are the minimum-drag fairing between successive points which assures convergent solutions and the techniques for drag evaluation provided by the work of Eminton (ref. 9) and Eminton and Lord (ref. 10). The airplane wave drag is taken to be the sum of the sector drags of a series of bodies of revolution, each of which represents a sector of the flow field (a specified range of azimuth angles). When the azimuthal spacing is uniform, as in this example, the airplane drag becomes simply the average drag of the series of equivalent bodies. In practice, many more points are used than are shown in this simple illustration.

For the evaluation of drag due to lift, the wing is divided into a large number of rectangular elements, and the influence of one element on another is found by the application of linear theory vortex-flow equations. Local element lifting forces are summed to find overall forces and moments. The drag due to lift for a range of lift coefficients is found by combining solutions for the warped surface and a flat surface of the same planform and by accounting for the effects of the mutual interaction of loadings and surfaces. Numerical solutions of the theory and computer-program inplementation allow consideration of arbitrary wing planforms which may have arbitrarily twisted and cambered surfaces. A planform which includes the fuselage and a mean camber surface defined by both the wing and fuselage has been found to provide improved accuracy for most airplane configurations. In addition to the program which provides for the estimation of aerodynamic characteristics of a given wing, a separate program is used in the design of minimum-drag wing surfaces by means of an optimum combination of specified loadings.

COMPLEX OF COMPUTER PROGRAMS

A chart depicting a complex of computer programs for aerodynamic analysis developed at the Langley Research Center is presented in figure 4. The task of aerodynamic analysis of an airplane configuration begins with the preparation of numerical-model data for machine program input. This process is aided by an electromechanical device, called a digitizer, which is useful in the direct conversion of model drawing geometry to a set of numerical coordinates. Each of the drag-evaluation programs makes use of a geometry section which provides fairings of input data, converts data to program units, and, in the wave-drag program, computes the equivalent-body areas.

Geometry programs also provide tapes for use in the preparation of machine-made drawings of the numerical model and for use in controlling machine-tool operations in the construction of model components. Three of the main aerodynamic programs, shown near the center of the figure, have been discussed. The fourth program computes an additional drag term due to the interference produced by nacelles or stores in the vicinity of a wing surface. Results from these programs when assembled provide a theoretical estimate of the aerodynamic characteristics of the configuration which may be used in evaluation of specific aircraft proposals or in selection among candidate configurations of a design study.

It is important to note the program optimization or design features. The wing program for an optimum camber-surface definition has already been mentioned. In addition, a version of the wave-drag program now has provision for the selection of a minimum-drag fuselage shape subject to appropriate restraints, such as specified minimum diameters. The interference program has a provision for designing a reflex wing surface in the vicinity of the nacelle for drag minimization or for moment control.

A sonic-boom program to compute near-field pressure signatures (the general case) is also a part of the computer-program complex. The aerodynamic analysis systems, as herein described, are well suited to sonic-boom analysis; and, in fact, three of the aerodynamic programs provide the input area and lift distributions required for sonic-boom solutions.

The form of the mathematical models used to represent the airplane may be seen in the drawings of figure 5. These machine-made drawings, generated by the geometric parts of the aerodynamic programs, illustrate the detail of the program solutions. They are quite useful in assessing the adequacy of the airplane representation and checking for obivous errors in the input data.

More complete descriptions of the computational techniques employed in the key programs and further discussions of program usage for the estimation and optimization of supersonic aircraft aerodynamic performance are given in references 11 to 20. The Computer Software Management and Information Center established through the Technology Utilization Office of the National Aeronautics and Space Administration can supply documentation, listings, and tapes or card decks for some of the more basic programs. Information on availability and costs may be obtained from

COSMIC
Computer Center
University of Georgia
Athens, Georgia 30601

APPLICABILITY AND LIMITATIONS

The applicability of the computer techniques has been demonstrated in numerous correlations of experiment and theory, such as that shown in figure 6. The theoretical lift-drag curves for a supersonic-transport configuration and for a fighter configuration employ shading to show the relative contribution of the three major drag components. The skin-friction component corresponds to the wind-tunnel test Reynolds numbers and, thus, indicates a larger relative contribution to the total drag than that for a full-scale airplane. For the more slender supersonic-transport configuration, there is an excellent agreement between experimental data and theoretical results. Similar agreement has been observed for slender configurations at Mach numbers as high as 3. As is often observed with figher aircraft configurations, particularly those with little symmetry about a horizontal plane, the prediction is somewhat less accurate. Other comparisons of the fighter aircraft data with theoretical results indicate that the discrepancy is due more to the vertical displacement of airplane components than to component thicknesses. This observation leads to the suggestion that improved accuracy may result from a consideration of mutual interaction between lift and volume effects in refinement of the calculative procedures. Processing time on a Control Data 6600 computer system for the programs employed totals about 6 minutes for a typical configuration at a given Mach number.

Application of the aerodynamic design features of the computing programs may be illustrated with the aid of figure 7. Theoretical and experimental data are shown for an optimized complete supersonic-transport configuration employing fuselage shaping, nacelle placement, wing design, and reflex treatment as specified by computer solutions. The effectiveness of the design procedures is demonstrated by the fact that this optimized configuration has the highest aerodynamic efficiency for a supersonic cruise vehicle yet attained (a value of about 9 for the full-scale airplane). For the estimated cruise-lift coefficient, it is seen that the complete configuration has no more drag than the corresponding flat wing-body configuration without nacelles or fins. Furthermore, the wing twist and camber allows the complete configuration to be trimmed with little or no drag penalty in contrast to a large penalty which would be incurred with the flat wing-body configuration.

A more recent addition to the assemblage of programs is a version of the wing program which, as illustrated in figure 8, allows for the calculation of lift, drag, and moments produced by wing-tail or wing-canard combinations. This capability which is achieved by introducing a zero-lift membrane between the two lifting surfaces is proving to be useful in the analysis of stability and control and trim-drag aspects of aerodynamic performance. In the drag and moment data shown for both a horizontal-tail and a canard

configuration, the theory displays a quite reasonable agreement with the experimental data. The configurations shown here have relatively little vertical displacement between the two lifting surfaces. In configurations where the displacement becomes appreciable, the ability of the program to provide valid results is somewhat impaired; thus, further study and development work is required.

The remaining member of the family of computer programs which provides a means of calculating the pressure field surrounding an airplane in supersonic flight, is used primarily for sonic-boom predictions. The flow-field analysis is directly related to the lift and drag analysis previously discussed, and in fact, the equivalent-body-area distributions obtained in the aerodynamic-performance programs provide the first steps in the sonic-boom analysis. With the area and lift distributions as input data, the sonic boom program implements the Whitham theory (ref. 21) to provide for the calculation of complete pressure signatures, including shock location and strength. An example of pressure-signature calculations and a comparison with wind-tunnel experimental data is shown in figure 9. It is clear that, at least for the relatively slender supersonic-transport configuration, the theory is in good agreement with the experimental data in all sectors of the flow field, even for a relatively small radius of $2\frac{1}{2}$ body lengths. Note that although negative areas are shown in the equivalent-body representation for the flow above the model, no difficulty is encountered in obtaining the theoretical signature. For airplane sonic-boom predictions, it has been the practice to modify the uniform-atmosphere solution given by the program by use of atmospheric correction factors derived from the work of Friedman, Kane, and Sigalla (ref. 22). Now, with the development of a method for computation of the complete signature in its propagation through a nonuniform atmosphere by Hayes, Haefeli, and Kulsrud (ref. 23), the program can be expected to serve as a source for the required airplane "F function" (ref. 21).

POSSIBLE FUTURE DEVELOPMENT

The present utility of a complex of related computer programs for supersonic aerodynamic and sonic-boom analysis has been shown in the preceeding discussions. It would now seem appropriate to discuss some steps that may be taken to make the system more useful in application to a greater variety of supersonic aircraft configurations and a greater variety of problem areas.

To make use of this system more convenient, plans call for an effort to provide for more computer handling of interprogram steps and an effort to provide for program consolidation so that a single standardized set of numerical data will serve all the aerodynamic programs. First steps toward this end are being made for a unified sonic-boom program which will have the airplane geometry as an input and the pressure signature as an output.

In order to provide a more accurate representation of the aerodynamic characteristics of certain categories of fighter airplanes, consideration has been given to the inclusion of lift interference in wave-drag evaluations and thickness influence in lift determination. A program has been developed to handle the lift-interference effect; but it is believed that the thickness influence is equally important and that further efforts to provide a means of estimating its effect on lift distributions are required.

It is sometimes difficult to realize that a method which has been so useful in the analysis of twisted and cambered wings is based on a seemingly unrealistic assumption that vertical displacements of lifting elements are small. Removal of that limitation should provide for more accurate theoretical solutions. It is also clear that the Mach line propagation paths assumed in the theories are not realistic, and accordingly, consideration is being given to incorporation of the Whitham correction (ref. 21) in a wing program.

Eventually, it is hoped that consideration of detached-flow phenomena and the wing-leading-edge vortex flow fields can be included in theoretical treatment of complete airplane configurations. That development appears to be out of reach for the present, but a semiempirical treatment may be of use in accounting for the primary influence of these factors on the overall airplane performance.

CONCLUDING REMARKS

The analytic techniques for the estimation and optimization of airplane supersonic aerodynamic characteristics discussed in this paper have been shown to be applicable to speeds up to a Mach number of about 3 for configurations employing slender bodies and thin moderately cambered wings. Thus, if a configuration meets the requirements for efficient supersonic cruise (a necessity for supersonic transport designs), the methods may be used with confidence. With configurations for which supersonic-cruise efficiency is not a major concern (for example, supersonic dash vehicles), there may be some question as to the complete applicability of methods based on linear theory.

REFERENCES

1. Woodward, F. A.; Tinoco, E. N.; and Larsen, J. W.: Analysis and Design of Supersonic Wing-Body Combinations, Including Flow Properties in the Near Field. Part I – Theory and Application. NASA CR-73106, 1967.
2. LaRowe, E.; and Love, J. E.: Analysis and Design of Supersonic Wing-Body Combinations, Including Flow Properties in the Near Field. Part II – Digital Computer Program Description. NASA CR-73107, 1967.
3. Carmichael, Ralph L.: A Critical Evaluation of Methods for Computing Wing-Body Interference at Supersonic Speeds. ICAS Paper No. 68-08, Sept. 1968.
4. Hayes, Wallace D.: Linearized Supersonic Flow. Rep. No. AL-222, N. Amer. Aviat., Inc., June 18, 1947.
5. Whitcomb, Richard T.: A Study of the Zero-Lift Drag-Rise Characteristics of Wing-Body Combinations Near the Speed of Sound. NACA Rep. 1273, 1956. (Supersedes NACA RM L52H08.)
6. Jones, Robert T.: Theory of Wing-Body Drag at Supersonic Speeds. NACA Rep. 1284, 1956. (Supersedes NACA RM A53H18a.)
7. Lomax, Harvard: The Wave Drag of Arbitrary Configurations in Linearized Flow as Determined by Areas and Forces in Oblique Planes. NACA RM A55A18, 1955.
8. Ward, G. N.: The Drag of Source Distributions in Linearized Supersonic Flow. Rep. No. 88, Coll. of Aeronaut., Cranfield (Engl.), Feb. 1955.
9. Eminton, E.: On the Minimisation and Numerical Evaluation of Wave Drag. Rep. No. Aero.2564, Brit. R.A.E., Nov. 1955.
10. Eminton, E.; and Lord, W. T.: Note on the Numerical Evaluation of the Wave Drag of Smooth Slender Bodies Using Optimum Area Distributions for Minimum Wave Drag. J. R.A.S., vol. 60, no. 541, Jan. 1956, pp. 61-63.
11. Harris, Roy V., Jr.: An Analysis and Correlation of Aircraft Wave Drag. NASA TM X-947, 1964.
12. Harris, Roy V., Jr.: A Numerical Technique for Analysis of Wave Drag at Lifting Conditions. NASA TN D-3586, 1966.
13. Carlson, Harry W.; and Middleton, Wilbur D.: A Numerical Method for the Design of Camber Surfaces of Supersonic Wings With Arbitrary Planforms. NASA TN D-2341, 1964.

14. Middleton, Wilbur D.; and Carlson, Harry W.: Numerical Method of Estimating and Optimizing Supersonic Aerodynamic Characteristics of Arbitrary Planform Wings. J. Aircraft, vol. 2, no. 4, July-Aug. 1965, pp. 261-265.

15. Mack, Robert J.: A Numerical Method for Evaluation and Utilization of Supersonic Nacelle-Wing Interference. NASA TN D-5057, 1969.

16. Robins, A. Warner; Morris, Odell A.; and Harris, Roy V., Jr.: Recent Research Results in the Aerodynamics of Supersonic Vehicles. J. Aircraft, vol. 3, no. 6, Nov.-Dec. 1966, pp. 573-577.

17. Baals, Donald D.; Robins, A. Warner; and Harris, Roy V., Jr.: Aerodynamic Design Integration of Supersonic Aircraft. AIAA Paper No. 68-1018, Oct. 1968.

18. Carlson, Harry W.: Correlation of Sonic-Boom Theory With Wind-Tunnel and Flight Measurements. NASA TR R-213, 1964.

19. Middleton, Wilbur D.; and Carlson, Harry W.: A Numerical Method for Calculating Near-Field Sonic-Boom Pressure Signatures. NASA TN D-3082, 1965.

20. Seebass, A. R., ed.: Sonic Boom Research. NASA SP-147, 1967.

21. Whitham, G. B.: The Flow Pattern of a Supersonic Projectile. Comm. Pure Appl. Math., vol. V, no. 3, Aug. 1952, pp. 301-348.

22. Friedman, Manfred P.; Kane, Edward J.; and Sigalla, Armand: Effects of Atmosphere and Aircraft Motion on the Location and Intensity of a Sonic Boom. AIAA J., vol. 1, no. 6, June 1963, pp. 1327-1335.

23. Hayes, Wallace D.; Haefeli, Rudolph C.; and Kulsrud, H. E.: Sonic Boom Propagation in a Stratified Atmosphere, With Computer Program. NASA CR-1299, 1969.

APPROACHES TO SUPERSONIC DRAG ANALYSIS

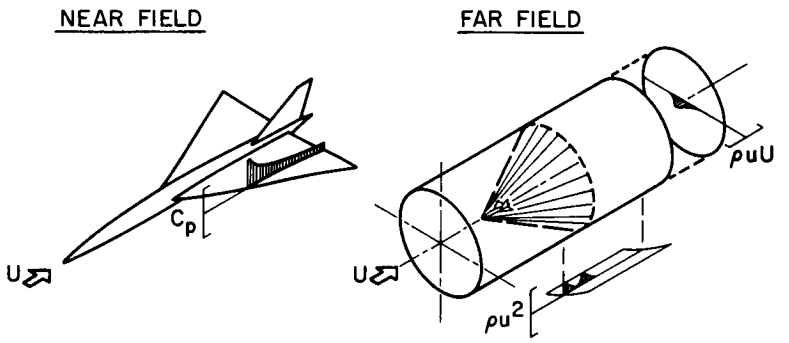

$$D = \frac{1}{2}\rho U^2 \int_{S_a} \lambda\, C_p \, dS$$

$$D = \int_{S_c} \rho u^2 \, dS - \int_{S_d} \rho u U \, dS$$

Figure 1

A COMPOSITE SYSTEM OF SUPERSONIC DRAG ANALYSIS

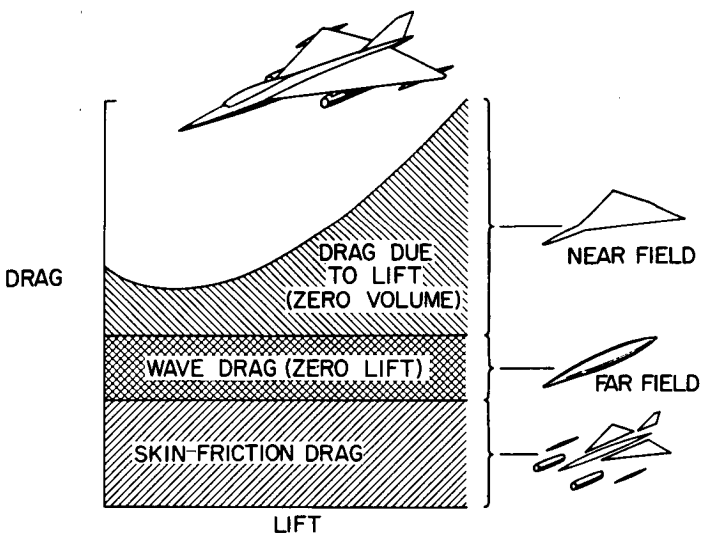

Figure 2

14. Middleton, Wilbur D.; and Carlson, Harry W.: Numerical Method of Estimating and Optimizing Supersonic Aerodynamic Characteristics of Arbitrary Planform Wings. J. Aircraft, vol. 2, no. 4, July-Aug. 1965, pp. 261-265.

15. Mack, Robert J.: A Numerical Method for Evaluation and Utilization of Supersonic Nacelle-Wing Interference. NASA TN D-5057, 1969.

16. Robins, A. Warner; Morris, Odell A.; and Harris, Roy V., Jr.: Recent Research Results in the Aerodynamics of Supersonic Vehicles. J. Aircraft, vol. 3, no. 6, Nov.-Dec. 1966, pp. 573-577.

17. Baals, Donald D.; Robins, A. Warner; and Harris, Roy V., Jr.: Aerodynamic Design Integration of Supersonic Aircraft. AIAA Paper No. 68-1018, Oct. 1968.

18. Carlson, Harry W.: Correlation of Sonic-Boom Theory With Wind-Tunnel and Flight Measurements. NASA TR R-213, 1964.

19. Middleton, Wilbur D.; and Carlson, Harry W.: A Numerical Method for Calculating Near-Field Sonic-Boom Pressure Signatures. NASA TN D-3082, 1965.

20. Seebass, A. R., ed.: Sonic Boom Research. NASA SP-147, 1967.

21. Whitham, G. B.: The Flow Pattern of a Supersonic Projectile. Comm. Pure Appl. Math., vol. V, no. 3, Aug. 1952, pp. 301-348.

22. Friedman, Manfred P.; Kane, Edward J.; and Sigalla, Armand: Effects of Atmosphere and Aircraft Motion on the Location and Intensity of a Sonic Boom. AIAA J., vol. 1, no. 6, June 1963, pp. 1327-1335.

23. Hayes, Wallace D.; Haefeli, Rudolph C.; and Kulsrud, H. E.: Sonic Boom Propagation in a Stratified Atmosphere, with Computer Program. NASA CR-1299, 1969.

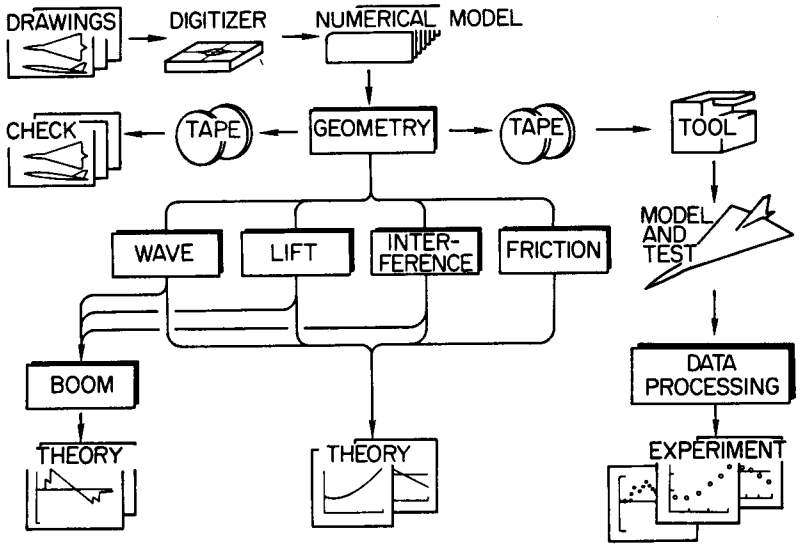

Figure 4

COMPUTER GRAPHICS

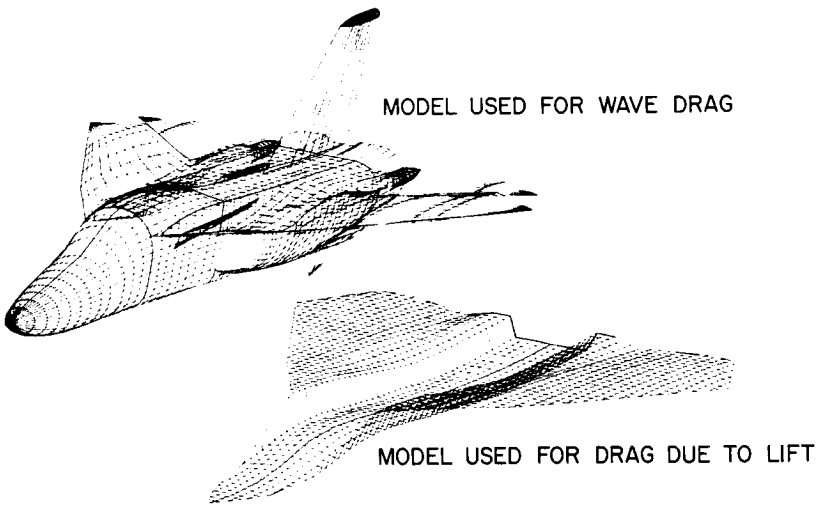

Figure 5

COMPUTER PROGRAM AERODYNAMIC PERFORMANCE EVALUATION

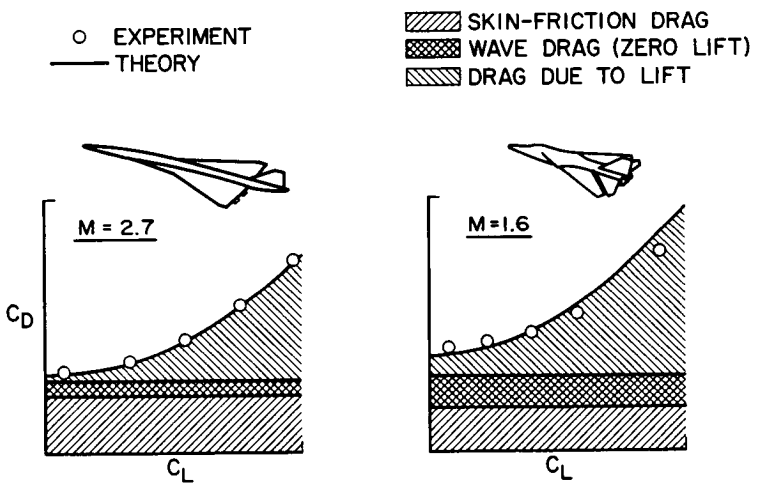

Figure 6

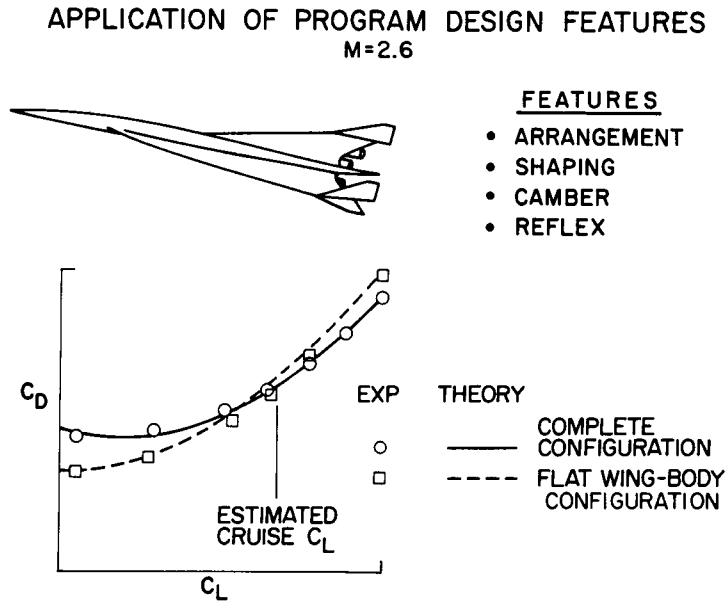

Figure 7

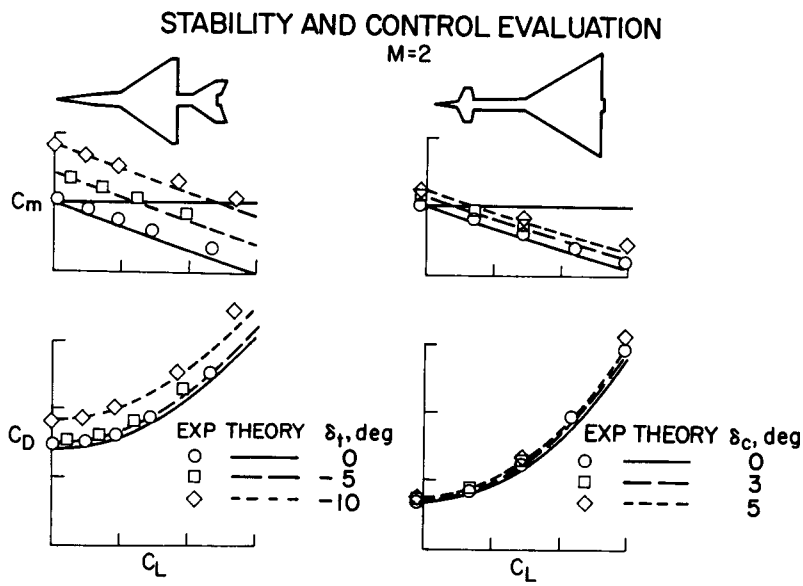

Figure 8

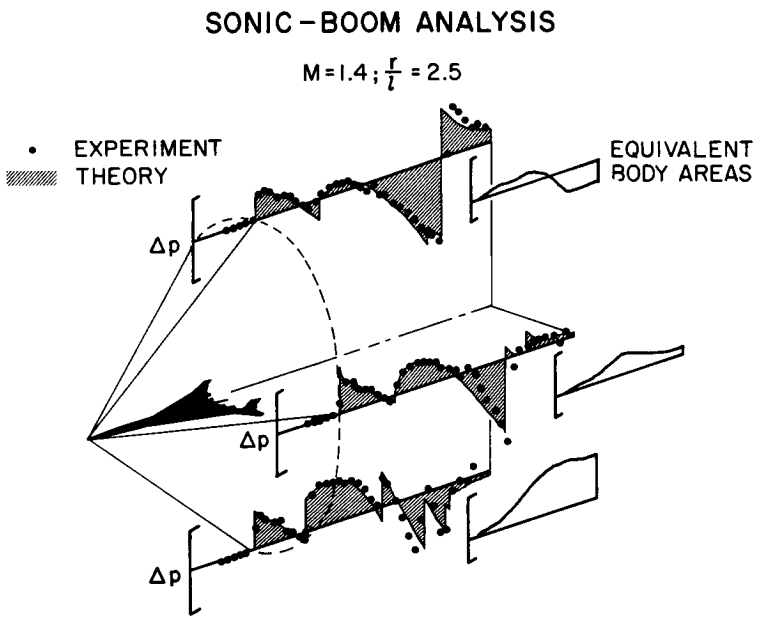
SONIC-BOOM ANALYSIS
M=1.4 ; r/l = 2.5
EXPERIMENT
THEORY
EQUIVALENT
BODY AREAS
Δp
Δp
Δp

Figure 9

GEORGE R. BARTÉ, JR., General Electric Co.: First, I would like to compliment the speaker on an extremely interesting presentation, and one that from a comparison of theoretical and experimental data appears, as the speaker suggested, to be a very useful tool in high performance laboratory work.

However, in the presentation there were a few points that bother me because I didn't understand what the speaker meant. I get disturbed from time to time when I hear people talk about conventional techniques, because I frankly don't think there are very many conventional techniques. It seems that most of the jobs I wind up doing are unconventional. So from that point of view, I'd like to first find out what you meant by "conventional techniques" in terms of skin friction analysis. What method do you use for skin friction?

CARLSON: Well, I would say that the Sommer and Short T' method with the Kármán-Schoenherr incompressible formula was used to find the skin friction coefficients, and the rest of the system simply employs what might be called strip theory, where the flat-plate skin friction coefficients are applied to panels of the airplane, and the values of the skin friction coefficients are dependent on local Reynolds numbers as defined by the length of these panels.

BARTÉ: I understand that. Thank you.

Going on to another point, you mentioned that in the modeling for the drag-due-to-lift computations you used essentially a mean camber distribution for the entire configuration, and you further stated that the agreement of the theory and the experiment was good. Yet when we refer to figure 6 and compare that to the tactical fighter versus the supersonic transport configuration, we find a departure in the drag-due-to-lift that is more pronounced for the fighter than for the SST.

CARLSON: Yes, this is such a complicated configuration that it is very difficult to assess in just which of the drag components the errors would lie.

Now, when I say that experimental data have shown that this mean camber surface concept provides an improved prediction of moments, I'm talking about data for other simplified configurations - simple wing-body shapes. For example, one of the cases was a delta wing with a wedge below it, to create an interference effect. We found that the analysis was improved by consideration of the mean camber surface, and could account for the major part of the interference lift.

BARTÉ: Would you perhaps suggest in terms of your summary comments that part of the departure might be due to an exclusion of the thickness distribution or relevant items?

CARLSON: Yes. For the fighter configuration shown in figure 6, one of the important features not considered is the influence of the thickness of the fuselage which lies mainly below the wing plane, in altering the lift distribution on the wing and, of course, influencing the drag-due-to-lift factors, and we at present have no way of accounting for this. This is just one of the items that are not considered.

BARTÉ: Finally, because I think I have outlived my usefulness as interrogator here, I'd just like to comment in terms of the presentations earlier this week. One of the questions that did not get an adequate answer was the question of what difference does it really make in terms of overall configuration performance to assess, let's say, skin friction at a greater degree of precision than 5 or 10 percent? The configuration dependency shown here (SST and Tactical Fighter in figure 6) indicates that the predictive importance of skin-friction values is about half that for total drag at flight conditions because the total drag values at some reasonable cruise lift coefficient are about twice what the skin-friction component is. A further observation is that the higher the lift-to-drag ratio and the higher the altitude of flight, the more important it is to accurately assess the skin-friction component.

LELAND M. NICOLAI, U.S. Air Force Academy: Considering a supersonic interceptor, pulling a 3- or 4-g turn, would he be operating at an angle of attack that is likely to violate any of the assumptions inherent in your program?

CARLSON: It violates just about everything. But from what information we have seen, it is very surprising that the percentage errors in the matter of drag for those high lift coefficient regions still remain quite small, within 10 percent, say. It doesn't completely fall apart.

NICOLAI: Okay, a second question. I presume that you can determine aerodynamic center locations. Can you also put in an estimate for a c.g. location and determine trim drags, and perhaps find an optimum position for c.g. that would minimize trim drag through a variety of Mach numbers?

CARLSON: There is quite a bit of that work done in the various groups at Langley. This is an important consideration.

HANS W. GRELLMANN, Northrop Corp.: The comparison with experimental data that you showed us was for high Mach numbers. How does your theory predict the wave drag at Mach numbers between, say, 1.2 and 2?

CARLSON: These techniques are based on supersonic linearized theory and, of course, are not really applicable in the transonic range. Now, how far down the transonic range you can apply them depends on the configuration. Normally we can expect these techniques to work reasonably well down to about from Mach 1.2 to 1.4. We don't expect them to cover the transonic range.

GRELLMANN: Have you actually predicted wave drag at those Mach numbers and found good agreement?

CARLSON: For some configurations it is good down to Mach 1.4. For a supersonic transport configuration, you can apply it down to about 1.2.

GRELLMANN: How about configurations with relatively low-sweep wings?

CARLSON: I can't give you any hard and fast numbers, but the Mach numbers at which these systems would apply would be higher, in all probability, for those cases. That's about all I can say, because it depends on the configurations, and we yet haven't done a thorough study of applicability to a large number of fighter configurations.

GRELLMANN: Well, there are several limitations in the way the configurations are represented in the supersonic area rule and one is the assumption that the wing is transparent, that is, that pressures are transmitted right through the wing.

CARLSON: That's right.

GRELLMANN: The other question I have is whether the equivalent body is really a good representation. It's probably quite good for a highly swept wing, but for a wing of less sweep, say 30° or 40°, I have some questions as to whether the equivalent body would really give you the same pressures, or the same drag.

CARLSON: It is surprising, it will. The main test that we have is how well we can correlate with measured data, and it seems to work out pretty well for relatively low-sweep wings.

POTENTIAL FLOW SOLUTIONS FOR INLETS OF VTOL LIFT FANS AND ENGINES

by Norbert O. Stockman

Lewis Research Center

N70-21379

SUMMARY

An axisymmetric incompressible potential flow method of solution is applied to the inflow problems associated with shallow VTOL inlets in static and crossflow operation. The basic approach of the method is described, and ways of applying it to compressible flow and to nonaxisymmetric inlets are presented. Several comparisons with experiment are presented, including cases of compressible flow and of unsymmetrical inlets, to demonstrate the applicability of the method in predicting the flow for VTOL inlets in static or crossflow operation.

INTRODUCTION

Several different types of propulsion systems have been proposed for achieving vertical flight. Among the more promising are lift fans and lift engines. For both types, since thrust for vertical lift-off is required, the propulsion system should be as light and compact as possible. Minimum engine volume is also desired to minimize drag if the lift propulsion system is carried along in pods during normal cruise flight. In the case of a lift fan installed in a wing, the inlet depth may be further restricted by the available maximum thickness of the wing section.

One of the factors involved in achieving minimum weight and volume for a lift fan or lift engine is the design of an efficient shallow inlet. A shallow fan or engine inlet, however, presents two major aerodynamic problems: (1) unfavorable velocity gradients on the bellmouth surface may lead to excessive boundary-layer growth and separation, and (2) large radial variations in velocity across the passage may make the design of the fan or compressor

28

more difficult or the operation less efficient. Such effects may appear when a VTOL aircraft is operating in either the landing, takeoff, or hover mode, for which the inlet is operating statically with no significant free-stream velocity relative to the airplane (fig. 1, upper left). The satisfactory solution to these problems will depend on reasonably accurate methods for estimating the surface velocity distributions and passage velocity profiles induced by various inlet configurations.

When the inlet is operating in a crossflow, that is, a free stream approximately normal to the inlet axis (fig. 1, lower left), the two problems just mentioned are aggravated and a further problem arises - that of circumferential distortion of the flow pattern at the rotor inlet or engine entrance planes. This distortion consists of a deviation from axial symmetry of the flow angle and velocity caused by the condition that the inlet is not deep enough for the flow to straighten out or the velocity to become uniform. This distortion is aggravated relative to the rotor, since the rotor is advancing into the flow on one side and retreating on the other, as shown in figure 1 (lower right). The changes in flow angle and velocity produce changes in the relative Mach number and the incidence angle at the fan or engine compressor. The rotor incidence angle varies from negative to positive, as shown on figure 1 (upper right). These changes from the design values could result in severe performance losses and blade vibration. Therefore, an analysis of the flow in inlets under crossflow conditions is necessary at least to obtain a knowledge of the severity of the distortion and to aid in controlling or eliminating it when necessary.

This paper presents a theoretical potential flow method for the calculation of flow in VTOL inlets in both static and crossflow operations. (An analysis of flow in static inlets based on this method has been presented in ref. 1.) First, the essentials of the method are described. Then sample results, including comparisons with experiments, are given to indicate the applicability of the method.

SYMBOLS

A, B, C	combination coefficients, eq. (1)
Δi	change in rotor incidence angle from design to transition
$\bar{n}_o$	unit vector in axial direction
$\bar{n}_{90}$	unit vector in direction perpendicular to axis
P_s	static pressure
P_t	total pressure
q	dynamic pressure
R	radius from inlet axis
R_H	hub radius
R_S	shroud radius
S	distance along profile of inlet surface
U_T	rotor tip speed
$\bar{V}$	velocity vector of combined solution
$\bar{V}_i$	velocity vectors of basic solution, where $i = 1, 2, 3$
Z	axial coordinate
α	direction of free-stream velocity relative to inlet axis
θ	circumferential coordinate

Subscripts:

a	bulk conditions of inlet flow at control station
c	average axial component at control station
∞	free-stream conditions

METHOD OF SOLUTION

The method used to calculate the flow in VTOL inlets is based on the Douglas incompressible potential flow computer program for axisymmetric

bodies. Only the bodies are assumed to be axisymmetric; the flow itself need not be. The details of the Douglas method are covered extensively in references 2 to 4; the highlights will be outlined herein.

1. Bodies are represented by a distribution of sources and sinks of initially unknown strengths.

2. An integral equation in the unknown source strength is derived from the potential flow equations and boundary conditions.

3. At discrete points on the bodies, the integral equation is approximated by a set of linear algebraic equations.

4. These equations are solved for the source strength by matrix methods.

5. Velocities are calculated on the surface and at other points of interest in the flow field from the source distribution obtained in step 4.

The program is basically for closed bodies in a free stream, and the method is exact for such cases. However, inlets are idealized for simplicity in applying the method. The idealization of a VTOL inlet is shown in figure 2. The real inlet may consist of a centerbody and a bellmouth installed in a body such as a wing, pod, or fuselage. For the ideal inlet, the actual body (dashed line in fig. 2) is replaced by a straight line extending from a point on the inlet far out into the free stream. This point is usually chosen where the bellmouth is tangent to the actual body. Also, the inlet duct is extended far downstream, as shown in figure 3. This method of idealizing a VTOL inlet is based on the procedure recommended for conventional inlets in reference 5.

Basic Solutions

The Douglas program is used to obtain three basic solutions for the idealized inlet profile and certain free-stream conditions, as shown in figure 3. The basic solutions are simple ones that provide a convenient basis for generating the combined solutions that are of physical interest. Basic solutions are represented by their general velocity vectors $\overline{V}_i$ (where $i = 1, 2,$ or 3). Basic solutions with a free-stream velocity of zero (static case) cannot be obtained; therefore, two basic axisymmetric solutions are needed: $\overline{V}_1$ with the inlet duct extension closed and $\overline{V}_2$ with the duct open. With these two solutions, a combined solution having any combination of free-stream velocity and

mass flow through the inlet can be obtained. For VTOL inlets, usually the only axisymmetric case of interest is the static case.

For inlets in crossflow operation, a third basic solution is needed: the pure crossflow solution $\overline{V}_3$. In this case, the free-stream velocity is perpendicular to the axis. The duct extension is made long enough so that the flow in the region of interest is not affected by the condition of the downstream end (open or closed).

The control station shown in figure 3 is a set of points spanning the passage (like a pressure rake). The function of the control station is to control the flow rate of the combined solution. The control station points are not needed to get basic solutions; however, since they are needed to get combined solutions, they must be specified along with the profile so that basic solution velocities are obtained at the control-station points. Any other points or stations where data are desired must also be specified along with the basic solution profile.

Combined Solutions

Since the governing equations of incompressible potential flow are linear, the basic solutions can be linearly combined to form solutions of interest for the given configuration:

$$\overline{V} = A\overline{V}_1 + B\overline{V}_2 + C\overline{V}_3 \tag{1}$$

where $\overline{V}$ is the velocity vector at any point of the combined solution and A, B, and C are the combination coefficients that are determined by writing equation (1) in terms of three specified quantities of the combined solution, as shown in figure 4. These quantities are: the average axial velocity at the control station V_c; the magnitude V_∞ and the direction α of the free-stream velocity.

Control station. - The average axial velocity V_c at the control station is defined by

$$V_c = \frac{\int_{R=R_H}^{R_S} \int_{\theta=0}^{2\pi} \overline{V} \cdot \overline{n}_o R \, d\theta \, dR}{\pi\left(R_S^2 - R_H^2\right)} \tag{2}$$

where R is the radius from the inlet axis, R_S is the shroud radius, R_H is the hub radius, $\overline{n}_o$ is the unit vector in the axial direction, and θ is the circumferential coordinate. Substituting equation (1) into equation (2) yields

$$V_c = \frac{\int_R \int_\theta (A\overline{V}_1 \cdot \overline{n}_o + B\overline{V}_2 \cdot \overline{n}_o + C\overline{V}_3 \cdot \overline{n}_o) R \, d\theta \, dR}{\pi\left(R_S^2 - R_H^2\right)} \tag{3}$$

Let the average axial control station velocity of basic solution i be represented by $V_{c,i}$. Then,

$$V_{c,i} = \frac{\int_R \int_\theta \overline{V}_i \cdot \overline{n}_o R \, d\theta \, dR}{\pi\left(R_S^2 - R_H^2\right)} \tag{4}$$

Since the $\overline{V}_i$ are known, $V_{c,i}$ can be obtained by numerical integration. The values of $V_{c,1}$ and $V_{c,2}$ will, in general, not be zero; however, $V_{c,3}$ is always zero, since $\overline{V}_3 \cdot \overline{n}_o$ is equal to $(\overline{V}_3 \cdot \overline{n}_o)_{\theta=0} \cos\theta$ and

$$\int_R \int_{\partial=0}^{2\pi} (\overline{V}_3 \cdot \overline{n}_o)_{\theta=0} \cos\theta R \, d\theta \, dR = \int_R (\overline{V}_3 \cdot \overline{n}_o)_{\theta=0} R \, dR \int_{\theta=0}^{2\pi} \cos\theta \, d\theta = 0$$

where $(\overline{V}_3 \cdot \overline{n}_o)_{\theta=0}$ is a function of R, only. Substituting equation (4) for $i = 1$ and 2 into equation (3) then yields

$$V_c = AV_{c,1} + BV_{c,2} \tag{5}$$

where V_c is prescribed and $V_{c,1}$ and $V_{c,2}$ are obtained by numerical integration of equation (4).

Free stream. - Two equations are obtained for the undisturbed free-stream conditions: one for the component of the free-stream velocity in the axial direction $\overline{n}_o$ and the other for the component in the direction 90° to the axial. In the axial direction,

$$\overline{V}_\infty \overline{n}_o = A\overline{V}_{\infty,1} \cdot \overline{n}_o + B\overline{V}_{\infty,2} \cdot \overline{n}_o + C\overline{V}_{\infty,3} \cdot \overline{n}_o \tag{6}$$

Now, in the Douglas program, the magnitude of $\overline{V}_\infty$ is always 1.0, and the directions for the three basic solutions are as shown in figure 3. Thus,

$$\overline{V}_{\infty,1} \cdot \overline{n}_o = \overline{V}_{\infty,2} \cdot \overline{n}_o = 1.0 \tag{7}$$

and

$$\overline{V}_{\infty,3} \cdot \overline{n}_o = 0 \tag{8}$$

The prescribed $\overline{V}_\infty$ is at some angle α with the axial direction so that

$$\overline{V}_\infty \cdot \overline{n}_o = V_\infty \cos \alpha \tag{9}$$

where α is the angle of attack in the Douglas program. (For combined solutions for VTOL inlets, α is usually near 90°.)

Then, putting equations (7) to (9) into equation (6) yields

$$V_\infty \cos \alpha = A + B \tag{10}$$

where V_∞ and α are known.

In the crossflow or $\overline{n}_{90}$ direction,

$$\overline{V}_\infty \cdot \overline{n}_{90} = A\overline{V}_{\infty,1} \cdot \overline{n}_{90} + B\overline{V}_{\infty,2} \cdot \overline{n}_{90} + C\overline{V}_{\infty,3} \cdot \overline{n}_{90} \tag{11}$$

where

$$\overline{V}_{\infty,1} \cdot \overline{n}_{90} = \overline{V}_{\infty,2} \cdot \overline{n}_{90} = 0 \tag{12}$$

$$\overline{V}_{\infty,3} \cdot \overline{n}_{90} = 1.0 \tag{13}$$

and

$$\overline{V}_{\infty} \cdot \overline{n}_{90} = V_{\infty} \sin \alpha \tag{14}$$

Combining equations (11) to (14) yields

$$V_{\infty} \sin \alpha = C \tag{15}$$

Equations (5), (10), and (15) are three equations in the three unknowns A, B, and C. Solving for A, B, and C yields

$$A = \frac{-V_c}{V_{c,2} - V_{c,1}} + V_{\infty} \cos \alpha \left(\frac{V_{c,2}}{V_{c,2} - V_{c,1}} \right) \tag{16}$$

$$B = \frac{V_c}{V_{c,2} - V_{c,1}} - V_{\infty} \cos \alpha \left(\frac{V_{c,1}}{V_{c,2} - V_{c,1}} \right) \tag{17}$$

$$C = V_{\infty} \sin \alpha \tag{18}$$

For an inlet in static operation ($V_{\infty} = 0$), equations (16) to (18) and (1) simplify to

$$A = \frac{-V_c}{V_{c,2} - V_{c,1}}$$

and

$$\overline{V} = A(\overline{V}_2 - \overline{V}_1)$$

From the four equations ((16) to (18) and (1)), the basic solutions ($\overline{V}_1$, $\overline{V}_2$, and $\overline{V}_3$), and the prescribed parameters (V_c, V_∞, and α), the velocity of the combined solution can be obtained at any point (R, Z) originally specified for the basic solutions. Velocities can also be obtained at any value of θ and the given R and Z; however, velocities at additional R or Z values can be obtained only by interpolation or by rerunning the basic solutions with the additional points. The velocities are actually given in terms of their components in cylindrical coordinates and from these components, any flow angles can be obtained as well as components in any other coordinate system. Also, pressures or pressure coefficients can be obtained from the velocities. Further, if enough measuring stations are included, streamlines can be obtained by numerically integrating the velocity across each station to get the local flow rate. Also, lift and drag forces on the inlet surfaces and the consequent pitching moment can be calculated by integrating the pressures over the surfaces.

Application to Compressible Flow and Asymmetric Inlets

As was stated previously, the method of solution is based on the assumptions that the flow is incompressible and the configuration is axisymmetric. However, in the case of real inlets, either one or both of these assumptions may not be satisfied. However, the method can be applied to compressible flow and to unsymmetrical inlets.

Compressibility. - In the real compressible flow, local variations in density may exist in the axial, radial, and circumferential directions, which are not accounted for in the incompressible solution. However, several techniques can be used to minimize the effects of these variations when applying the method to practical cases.

First, the control station is located in the region of interest (e.g., at the rotor inlet) rather than far downstream to minimize the effect of axial density

gradients. Second, the prescribed velocity at the control station V_c is determined from compressible flow relations; that is, V_c is calculated from the given weight flow and the average compressible static density corresponding to V_c. This ensures that there will be good agreement between the actual compressible flow and the theoretical incompressible flow at the control station, provided that the radial and circumferential density variations are not too large. In general, reasonable correspondence between real and incompressible solution values is to be expected wherever the Mach number does not differ greatly from the average Mach number at the control station.

Third, as a further refinement, if greater accuracy is desired at stations where the local Mach number is substantially different from that at the control station, additional calculations can be made with minor variations in the magnitude of the control station velocity such that one-dimensional compressible continuity is satisfied at all axial stations in the inlet. However, this approach cannot compensate for the effect of radial or circumferential variations of density in the real flow.

In addition, surface or stream pressures are determined from the solution velocities and compressible flow equations rather than from incompressible flow in order to more closely represent the local pressures of the real case.

Unsymmetrical inlets. - An approximate solution for unsymmetrical inlets can be obtained from a succession of solutions based on several discrete profiles at key circumferential locations. For example, a fan-in-wing inlet may be adequately represented by profiles 90° apart: the foreward (0°), the aft (180°), and the spanwise (90° and 270°) profiles. A solution is obtained for each of the profiles by assuming that the inlet is axisymmetric with the given profile. This solution is assumed to hold exactly only at the circumferential location of its profile. Solutions at the intermediate locations are obtained by averaging the solution at the key location or by fairing a plot of the flow parameter of interest against circumferential angle.

The averaging technique is briefly described. Each key profile is used to obtain solutions at several circumferential locations (say, every 15°) between it and the next key profile. This results in two solutions at each location. These two solutions are averaged, with the solution of the nearer key

profile given a greater weight. Thus, a complete circumferential distribution of the flow can be obtained from only a few profiles.

This method of constructing a solution for a nonsymmetrical inlet by using several axisymmetric profiles neglects the circumferential gradients in flow parameters caused by the asymmetry. Its accuracy will thus depend on the magnitude of these neglected gradients compared with the axial and radial gradients. In general, the radial and axial gradients on a bellmouth are usually relatively large; therefore, the accuracy should be adequate except in cases of extreme asymmetry.

COMPARISON WITH EXPERIMENTAL DATA

Several comparisons of theory with experiment are given in order to demonstrate the reliability of the method of calculation in predicting the real compressible flow in VTOL inlets.

Static Operation

The surface pressure distribution on an inlet operating statically is given on figure 5. The test inlet shown in the inset is a simple circular arc axisymmetric inlet set in a flat plate, so that it is almost identical to an ideal inlet. This case was chosen because it has a very high inlet Mach number. The static-to-total pressure ratio is plotted against the normalized surface distance on the shroud and on the hub. Distances are measured on the shroud and on the hub as shown in the inset. Even though there is a region of supersonic flow, theory and experiment are still in reasonably good agreement. Additional comparisons of theory and experiment for static inlets are given in reference 1.

Crossflow Operation

Several comparisons with experiment for inlets operating in crossflow are given.

In figure 6 is shown the surface pressure distribution in a chordwise cut of a fan-in-wing inlet. The static pressure coefficient is plotted against the surface distance in percent chord. Four surfaces are shown in the plot, and the distance on the abscissa corresponds to the numbers indicated on each surface in the inset: the forward surface of the bellmouth, forward surface of the centerbody, the aft surface of the centerbody, and the aft surface of the bellmouth. The agreement is extremely good everywhere on the inlet. For the surface forward of S equal to about 10, the real flow is two-dimensional wing flow, whereas the theoretical results are for flow on the axisymmetric idealization of the inlet. The experimental results are from the National Research Council of Canada and are given in either references 6 or 7.

In figure 7 are shown velocity contours for the same inlet as that in figure 6. These contours are for data taken in the plane shown as the $S = 0$ station in figure 6. The data of figure 7 are for a crossflow ratio of 0.837, whereas the data of figure 6 are for a crossflow ratio of 0.285. This case was chosen for presentation because, at this high crossflow ratio, the real flow ordinarily separates from the forward boundary. However, in this test, boundary-layer suction was distributed over the forward half of the bellmouth. The agreement between theory and experiment is reasonably good in the forward portion. The agreement breaks down in the aft region because the boundary layer has separated from the aft side of the centerbody.

The theoretical results of figure 7 were obtained from the solutions of three profiles: forward (0°), spanwise (90°), and aft (180°). Velocities at intermediate locations (every 15°) were obtained by the averaging technique mentioned in the section Unsymmetrical inlets. Experimental contours were obtained from the National Research Council of Canada (ref. 8).

In figure 8, a comparison is given for a severely nonsymmetrical inlet, the Lockheed XV-4B lift engine inlet. The four profiles used for the theoretical calculations are shown in the figure. The forward profile is a circular arc; the other three profiles are all different lemniscates. Theoretical results were obtained from each of these profiles; in addition, results were obtained in the immediate vicinity ($\pm 30^{\circ}$) of each profile as an aid in fairing the curve.

Experimental data were obtained from static pressure probes located as shown in the inset of figure 8. The plot shows static pressure coefficient as a function of circumferential location. The agreement is reasonably good except in the 90° outboard region where the greatest deviation from axial symmetry occurs.

APPLICATIONS

The capability of the method in adequately predicting the real flow in VTOL inlets makes it extremely useful for several applications:

1. It provides trial and error solutions for the design of a bellmouth for best performance in static and crossflow operation.
2. It provides surface velocity distributions for boundary-layer calculations for determining limiting decelerations to prevent separation.
3. It provides surface pressure distribution for calculation of inlet surface lift and drag forces and pitching moment.
4. It provides rotor inlet conditions in static and crossflow operation for rotor design and analysis.

An example of rotor inlet calculations is given in figure 9, which illustrates the effect of transition crossflow on rotor incidence angle for a fan-in-wing inlet also shown in the figure. The rotor of the fan and the inlet were both designed for static operation with a ratio of tip speed to fan axial velocity of 1.67. If this inlet is operated at a ratio of transition crossflow velocity to fan axial velocity of around 0.4, the flow incidence angle relative to the rotor blades will deviate from the design value, as indicated by the contours in figure 9. It can be seen that, in the plane of the rotor inlet, the incidence angle distortion due to the potential flow alone can be severe. (Incidence angle distortion does not include inlet total pressure variations or the modification of the potential flow due to the presence of the rotor.) Similar results can be obtained to study the effect of different design parameters such as inlet depth, transition velocity, inlet profile, and rotor conditions.

CONCLUDING REMARKS

A theoretical method based on incompressible potential flow in axisymmetric inlets was described. Several sample calculations and comparisons with experiments were presented to demonstrate the reliability of the method, and further applications were indicated. The method should be a very useful and powerful tool in both the design and analysis of VTOL inlets.

REFERENCES

1. Stockman, Norbert O.; and Lieblein, Seymour: Theoretical Analysis of Flow in VTOL Lift Fan Inlets Without Crossflow. NASA TN D-5065, 1969.
2. Smith, A. M. O.; and Pierce, Jesse: Exact Solution of the Neumann Problem. Calculation of Non-Circulatory Plane and Axially Symmetric Flows about or within Arbitrary Boundaries. Rep. ES-26988, Douglas Aircraft Co., Apr. 25, 1958.
3. Hess, J. L.; and Smith, A. M. O.: Calculation of Potential Flow about Arbitrary Bodies. Progress in Aeronautical Sciences. Vol. 8. D. Kuchemann, ed., Pergamon Press, 1967, pp. 1-138.
4. Hess, John L.: Calculation of Potential Flow about Bodies of Revolution Having Axes Perpendicular to the Free—Stream Direction. J. Aerospace Sci., v. 29, no. 6, June 1962, pp. 726-742.
5. Hess, John L.; and Smith, A. M. O.: A General Method for Calculating Low Speed Flow about Inlets. Aerodynamics of Power Plant Installation, part 1. AGARDograph 103, pt. 1, 1965, pp. 345-372.
6. Schaub, U. W.: Fan-in-Wing Aerodynamics - Experimental Assessment of Several Inlet Geometries. Paper No. 67-746, AIAA, Oct. 1967.

7. Schaub, U. W.: Experimental Investigation of Flow Distortion in Fan-in-Wing Inlets. J. Aircraft, vol. 5, no. 5, Sept.-Oct. 1968, pp. 473-478.

8. Schaub, W. W.: Experimental Studies of VTOL Fan-in-Wing Inlets. Aerodynamics of Power Plant Installation, part 2. AGARD ograph 103, pt. 2, 1965, pp. 715-747.

LIFT FAN INFLOW

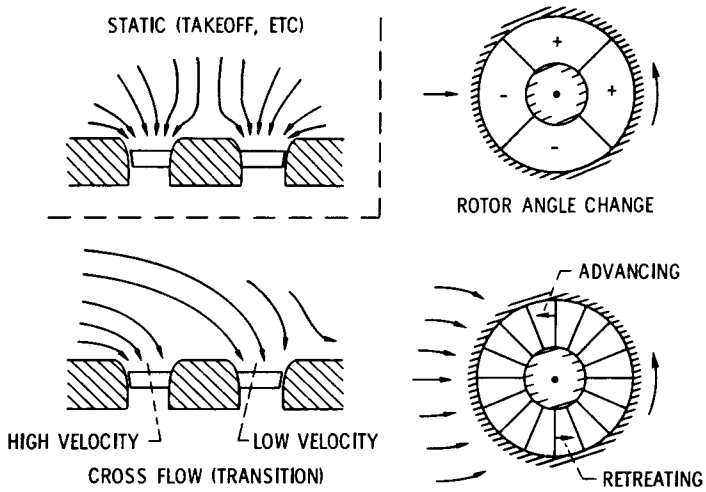

Figure 1

IDEALIZED PROFILE OF VTOL INLET

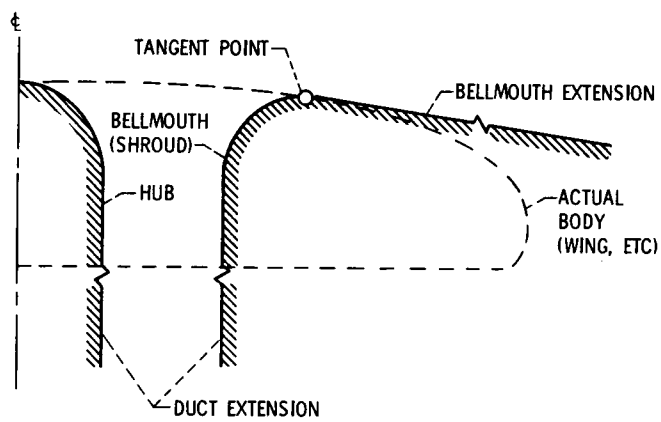

Figure 2

BASIC SOLUTIONS, $\bar{V}_i$

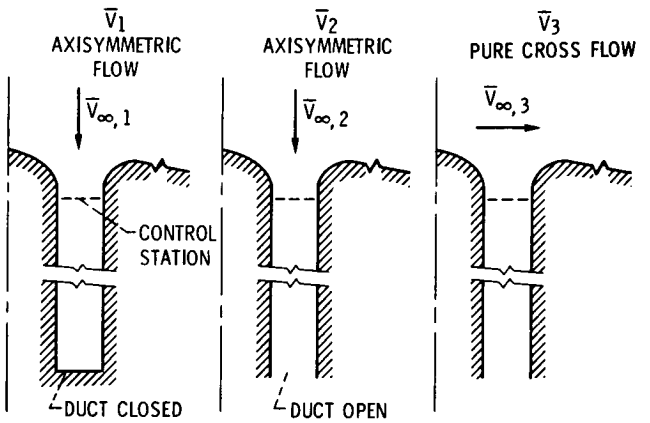

Figure 3

COMBINED SOLUTION, $\bar{V}$

AT ANY POINT, $\bar{V} = A\bar{V}_1 + B\bar{V}_2 + C\bar{V}_3$

A, B, AND C ARE DETERMINED BY SPECIFYING VALUES OF:

V_c AVERAGE AXIAL VELOCITY AT CONTROL STATION

V_∞ MAGNITUDE OF FREE STREAM VELOCITY

α DIRECTION OF FREE STREAM VELOCITY

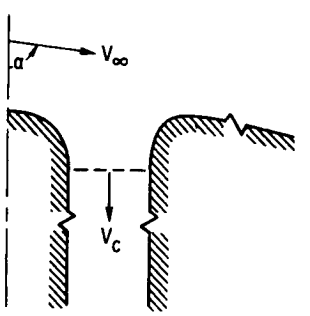

Figure 4

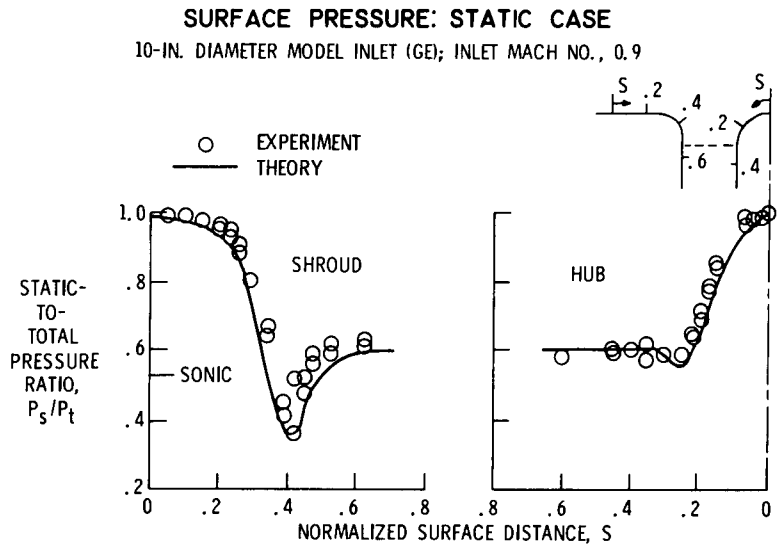

Figure 5

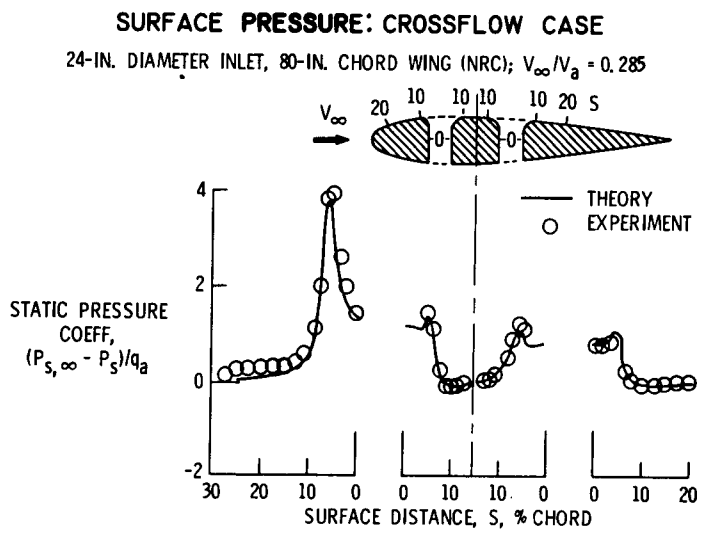

Figure 6

VELOCITY CONTOURS: CROSSFLOW CASE

$V_\infty/V_a = 0.837$ (WITH BOUNDARY LAYER SUCTION)

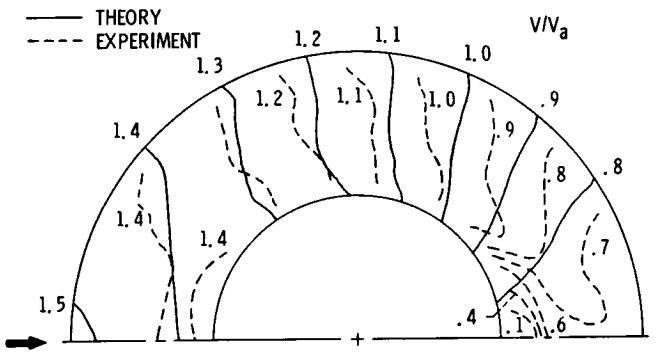

Figure 7

CIRCUMFERENTIAL VARIATION OF STATIC PRESSURE IN CROSSFLOW

LOCKHEED XV-4B INLET; $V_\infty/V_a = 0.52$

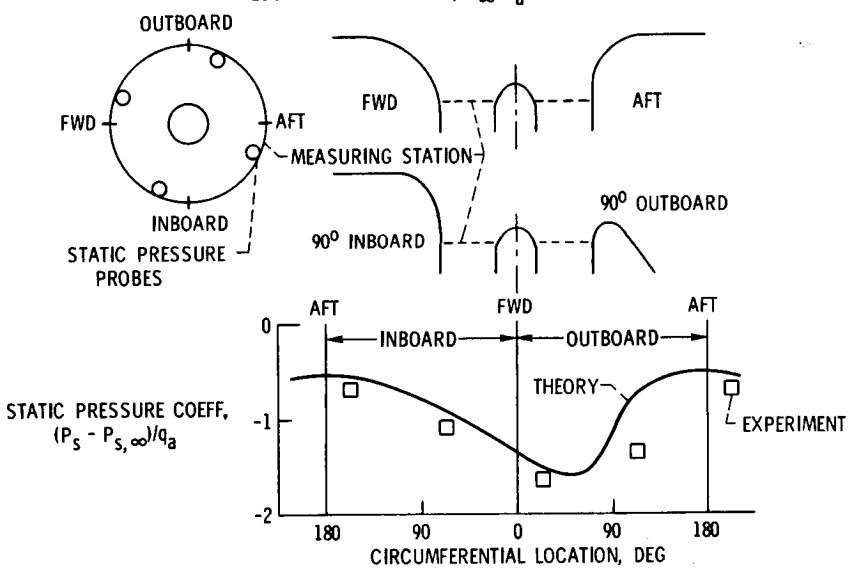

Figure 8

CHANGE IN ROTOR INCIDENCE AT TRANSITION

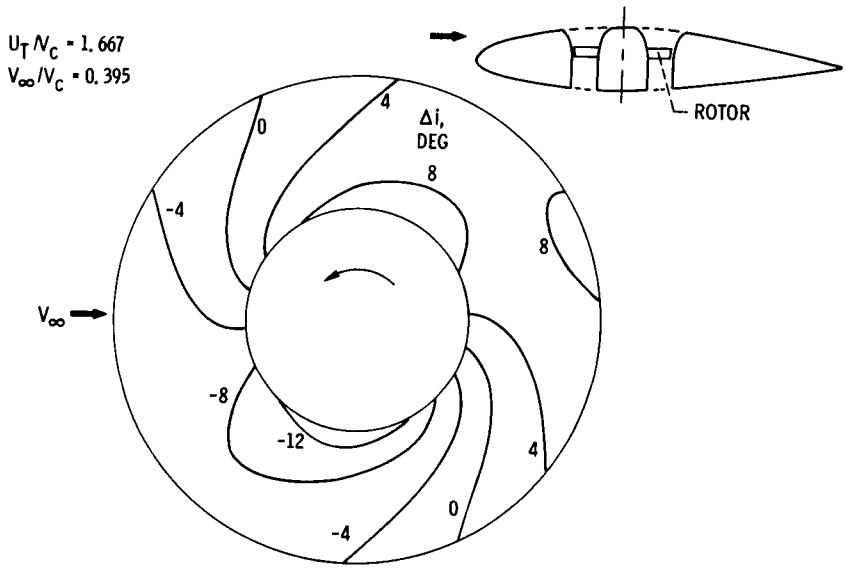

Figure 9

DISCUSSION

MAURICE S. CAHN, Northrop Corp.: Boy, that is good agreement!

On figure 6 you showed an axisymmetrical inlet in a 2-dimensional wing, is that right?

STOCKMAN: Yes. Well, the inlet isn't really axisymmetrical.

CAHN: I see.

STOCKMAN: At least, not in the region where the bellmouth approaches the wing upper surface.

CAHN: Now, the data you show are in the plane of symmetry.

STOCKMAN: Right, those results are in the chordwise plane, the forward profile and the aft profile, as shown in the inset of figure 6.

CAHN: How is the agreement, say, at 90° to that?

STOCKMAN: I don't have any experimental data for that. I am trying to compare all the experimental data I can find.

CAHN: You do expect good agreement, don't you? All the other data you showed was a lot tougher test than this. This is excellent agreement, and if it also agreed in the 90° plane, it would look like almost the whole answer to the problem.

STOCKMAN: What I do have on figure 7 are velocity contours which include the effect of the 90° profile.

CAHN: Yes, but that had a lot of separation, I believe you said.

STOCKMAN: Yes, but I do have some experimental data at lower crossflow ratios where it hasn't separated, but I haven't worked this up yet. I don't have surface pressures for the 90° profile, but I have velocity contours in the measuring plane.

JACK N. NIELSEN, Nielsen Engineering and Research, Inc.: I am amazed at the excellence of your agreement, but I am concerned about why it is so good. Because if I understand properly, you calculated the velocity field on incompressible grounds, and then put the velocities into the compressible Bernoulli equation. Did you put transformations on the inlet . . .

STOCKMAN: No. I should say that the only one that was really highly compressible was the first one (fig. 5). The one on figure 6 with the very good agreement was a low Mach number case.

NIELSEN: Okay, then let me ask you specifically, why did you really get such excellent agreement with the highly compressible one considering the

basis on which it was calculated? Is there something that is happening? You wouldn't expect good agreement, would you, on a priori grounds?

STOCKMAN: I think it is the fact that you can specify the velocity at the control station which is right in the region of interest, rather than far downstream, say. So I specify the velocity there based on compressible flow, and that kind of forces the agreement, at least there.

NIELSEN: You match the mass flows? Maybe that is the secret.

STOCKMAN: Yes, just at the one station, and then, if the variations in density aren't too great, you should get fairly good agreement throughout the region of interest.

JAMES S. KEITH, General Electric Company: I am concerned about the problem of the pumping characteristics of the fan influencing the boundary conditions. It appears to me that your boundary conditions are straight, parallel flow down low in the duct.

STOCKMAN: Well, let me think. No. The only boundary conditions are those three conditions that I am using to combine the basic solutions.

KEITH: Well, the fan tends to have its own flow rate distribution. A general rule is that the fan will "suck" constant flow per unit area. The incidence will change so that this condition will be met - not exactly, of course.

STOCKMAN: I should have pointed out on the last slide that those contours showing change in incidence were strictly potential flow. No effect was taken of that attenuation due to the fan itself. Also, for the experimental data, that is, the two for the NRC fan-in-wing inlet (figs. 6 and 7), there was no fan installed. The test flow was produced by suction.

However, in reference 1 of the paper, which is a TN on just static flow, in one of the comparisons shown there was a fan in the inlet, and the agreement is better than that first one shown here (fig. 5) at the high Mach number.

ROGER W. GALLINGTON, U. S. Air Force Academy: You have already commented on the compressibility. Why do you think the agreement is good in spite of the compressibility? What about some kind of geometric parameter? Why do you have good agreement without the axisymmetric condition being met? Do you have a feel for that?

STOCKMAN: Well, what I think we are doing when we get this three-dimensional solution by assuming that it is locally axisymmetric, is that we are neglecting the circumferential gradients caused by the geometry. Now, usually these gradients are small compared to the radial and axial gradients, so I think that this doesn't show up significantly unless they get severe, like they did on figure 8, in the region of severe deviation from axial symmetry.

BARNES W. McCORMICK, JR., Pennsylvania State University: Your assumed model must break down as the diameter of the fan gets large in comparison with the chord of the wing. Have you done anything on this? Have you looked at this to see what the limitations are?

STOCKMAN: No, I haven't. I'm inclined to agree with you that the model might break down in crossflow and I think this should be looked into.

PETER B. S. LISSAMAN, Northrop Corp.: I'd like to compliment the speaker, too. I think that is an excellent correlation, and I think that there is no reason to go any further, at least with the model that he assumes, because you can't expect any better accuracy.

In terms of this nonreality of the boundary conditions which McCormick pointed out, I think what you have actually done is something in terms of a perturbation solution of the inner part of the flow, and what you have shown numerically is something of great interest to me, which is that it is probably the local conditions that count, and the far distant conditions, both away from the fan on the outer surface and what goes on inside the duct after that, apparently don't grossly affect the flow around the lip, because your next step after this would be a very hard one. The next development would be either placing a constant head, actuator disk, in the position of the fan, in which case you have got to answer the whole mess of what goes on on the other side of the actuator disk, or the point that McCormick made of what about the leading edge and what about the trailing edge, and what about the perturbation in the neighboring fields. What I think is particularly interesting is one of these things that so often seems to happen with perturbation analysis, which is that infinity is darn close to your model, and things which look to us to be quite nearby physically are not affecting the flow field.

STOCKMAN: Well, I have found that it depends on what you are interested in in the flow field. For example, if you are interested in the surface distribution on the forward lip of the bellmouth, it is sensitive to the length of that extension which replaces the wing. When I first started out with the configuration that has the very good agreement (fig. 6), I had a length, that is, the outermost radius of the extension, that was 2-1/2 times the fan radius because I found that for static cases this was good enough. But I didn't get very good agreement in crossflow, so I kept increasing that length. The plot you saw there (fig. 6) I think was five times, and I did it at 10 and 15, after the figure was made, and the agreement did keep getting better, but, not very significantly.

One other point, when I want to do boundary-layer calculations on the inlet, I use the Douglas 2-dimensional program to get the flow around the wing and fair that into the results from the axisymmetric program, so I get a velocity distribution all the way from the stagnation point on up the wing and down into the inlet.

ANALYSIS OF THE FLOW FIELD OF A JET IN A SUBSONIC CROSSWIND

By Richard J. Margason

Langley Research Center

N70-21380

SUMMARY

The trends of the jet-induced effects on a turbojet or turbofan V/STOL aircraft in transition flight are discussed. A detailed qualitative description of the flow in the vicinity of the jet is presented to illustrate the blockage by the jet, the separation of the free stream, the rollup, and entrainment of the jet. Then a method for computing the cross section of the jet wake is developed. The pressure distribution induced in the plane of the jet exit is considered. The scatter among three sets of experimental data is illustrated. Finally, two different methods for computing the pressure distribution are described.

INTRODUCTION

The flight regime between hover and wingborne flight is unique to V/STOL aircraft. The lift force is obtained entirely from the engine in hover and entirely from the aerodynamic lift of the wing in conventional flight. As illustrated in figure 1 for a turbojet or turbofan V/STOL aircraft, this flight regime is characterized by a strong interaction between the high-speed jet and the low-speed free stream. The jet issuing from the aircraft is swept rearward by the free-stream flow and rapidly rolled up in a pair of vortices. This wake induces suction pressures on the fuselage and a distribution of downwash over the aircraft. This downwash is effectively an induced twist on the wing and tail and an induced camber over the length of the aircraft.

Figure 2 presents the general trend of jet-induced effects using experimental data (refs. 1 to 6). Data are presented for the increment of lift and the increment of pitching moment due to the interference between the jet and the free stream. There is usually a loss in lift which tends to increase with increasing forward velocity. The loss in lift is about the same with the tail off of the vehicle as with the tail on. There is an increment of pitching moment in transition flight which tends to increase nose-up with increasing velocity. Because of the change in downwash in the vicinity of the tail, there is an additional increment of pitching moment induced when the tail is on. The purpose of this paper is to examine the character of the jet wake and to evaluate some methods of representing this wake. Several other investigations of this problem are presented in references 7 and 8.

Preceding page blank

SYMBOLS

C_p	pressure coefficient, $\frac{\text{Local pressure - Free-stream static pressure}}{\text{Free-stream dynamic pressure}}$
d	jet diameter, ft (m)
ΔL	increment of lift caused by flow from jet, lb (N)
ΔM	increment of pitching moment caused by flow from jet, ft-lb (m-N)
n	sequence number of vortex filament around circular exit, counting clockwise from windward side
N	number of vortex filaments used to describe jet cross section
$\vec{r}$	path element vector, ft (m)
r_c	radius of curvature of jet-path center line, ft (m)
r_j	jet radius, ft (m)
T	thrust, lb (N)
$\vec{V}$	velocity vector, fps (m/s)
V_∞	free-stream velocity, fps (m/s)
V_j	jet velocity, fps (m/s)
x,y	Cartesian coordinates, ft (m)
z	complex plane coordinate, ft (m)
Γ	circulation strength, ft^2/sec (m^2/sec)
θ	cylindrical angular coordinate
ξ	natural jet coordinate along axis of jet, ft (m)

Φ complex velocity potential

Subscript:

n vortex filament sequence number

QUALITATIVE DESCRIPTION OF A JET IN A CROSSWIND

The following qualitative description of the flow phenomena associated with a jet in a crosswind is based primarily on flow visualization done by ONERA. (The following material is taken from Office National D'Études et de Recherches Aérospatiale film no. 575 entitled "Flows With Large Velocity Fluctuations," 1968.) Figure 3 is a schematic of a photograph taken in a water tunnel. The sketch shows a jet exhausting vertically from a flat plate into a free stream moving from left to right. Near the leading edge of the flat plate is a row of orifices through which colored milk is emitted. Figure 4 is the photograph of the flow-visualization experiment where the filaments (colored milk) show how the streamlines in the free-stream flow are influenced by the jet efflux. Consider two of these filaments, the one on the center line and the one just outboard. First, the streamline on the jet center line divides upstream of the jet exit and flows around it; this indicates that there is a stagnation point on the upstream face of the jet. Second, the filament outboard of the center line passes beside the jet and is then induced upward into the turbulent wake region behind the jet. This filament forms a saddle-shaped region immediately downstream from the jet which indicates another stagnation point. A portion of the filament from the saddle is induced upstream into the jet. The visible portion of the jet indicates flow from the colored filament which has been entrained into the jet. The rest of the filament from the saddle passes downstream and mixes with the wake region.

CALCULATION OF THE ROLLUP IN THE JET WAKE

Calculation of the rollup of the jet wake can be made by using information from Chang-Lu (ref. 9). This paper was concerned with the discharge of sewage into a river. The method is two dimensional and is described as follows. The cross section of the jet is described by filaments of vorticity. The sketch shows the jet exit and the free stream from the left. A discrete number of filaments parallel to the direction of the jet velocity are spaced around the jet exit. The

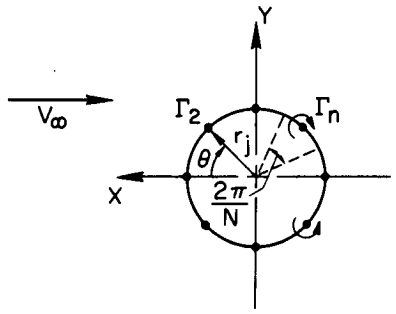

circulation strengths of these vortex filaments are defined by the complex potential function which describes flow about a circular cylinder perpendicular to a uniform stream; this function is written

$$\Phi = V_\infty\left(z + \frac{r_j^2}{z}\right)$$

The total derivative of this complex potential function yields the velocity vector induced by the presence of the cylinder; thus

$$\vec{V} = \frac{d\Phi}{dz}$$

Then, this velocity vector is integrated along a path to determine the circulation strength of the discrete vortex filaments, which is

$$\Gamma = \oint \vec{V} \cdot d\vec{r}$$

Integration over a sector of the circle gives the circulation strength for a single vortex filament as

$$\Gamma_n = 4V_\infty r_j \sin\frac{\pi}{N} \sin\left[\frac{2\pi}{N}(n - 1)\right]$$

These discrete vortex filaments are used to determine the change in the cross section of the jet as the flow passes downstream. This is done by a series of computations where the cross-section deformation is treated in two dimensions – x and y. Each of the vortex filaments is influenced for a small increment of time by the other filaments in the cross section. Since these filaments lie on a free surface, they must move to assume new positions where the net force induced by the other filaments is zero. This process is repeated many times as the flow moves away from the jet exit. As a result, the wake cross section changes shape. This computation procedure has been simplified and interpreted in figure 5 to represent a three-dimensional jet in a crosswind. The cross section is represented with 12 vortex filaments. The circular cross section in section A-A flattens on the downstream face to form the cross section labeled section B-B. Then, farther down the wake at section C-C, the characteristic kidney shape is formed. In section D-D and farther downstream, this evolves toward a very tightly wound pair of vortices. To form the surface of the wake boundary, a three-dimensional lattice of vorticity is constructed around the jet path by connecting these cross sections with filaments of vorticity. The jet path has been obtained from an empirical equation.

This series of computations represents one feature of the jet, the rollup into a pair of vortices.

Figure 6 shows the deformation as plotted by a computer. The cross section is described by straight-line segments which connect 96 vortex filaments spaced around the jet perimeter. This larger number of vortices is used to get a better description of the changes in shape. The cross sections are presented at 1-diameter increments along the jet axis starting at the circular jet exit and moving down the jet path for a distance of 7 jet diameters. They represent the rollup of the wake where the effective velocity ratio is 0.25. The overlapping lines occur near the spiral because the computer used straight lines to fair between the vortices. The evolution of the wake into a pair of vortices is clearly shown. Previous attempts at using this procedure to describe the rollup have failed to form the spiral pattern because of truncation error in the computation. The last three cross sections show the beginning of these errors by the presence of several inflections in the curvature of the spiral.

The similarity of this representation to the experimentally observed shape is indicated in figure 7. This photograph shows the cross section of a jet wake in a water tunnel at a point approximately 6 nozzle diameters along the jet-path axis.

FLOW INDUCED BY THE JET

An adequate mathematical model of a jet in a crosswind should describe all the major features of the flow field. One measure of adequacy is the estimation of pressure distribution on a flat plate in the plane of the jet exit. To obtain a standard for comparison, consider a portion of the pressure distribution. Data obtained from three experimental investigations (refs. 10 to 12) at an effective velocity ratio of 0.125 is presented in figure 8 for two sets of constant pressure contours. The data at a pressure coefficient of -0.2 show that two investigations yield similar contours. The third investigation gives results which cover a much larger area. Examination of the test conditions indicates that the boundary layer on the plate was very thin for the first two sets of data and was extremely thick for the third set of data. However, there must be other factors involved because all three contours are quite similar for the second pressure coefficient, -0.3. Yet, even here, noticeable differences exist in the downstream wake region. These data are presented to describe the experimental results and to indicate the type of scatter present in available data. The data obtained by McMahon and Mosher will be used for comparisons later in this paper.

The usefulness of the three-dimensional vortex-lattice model of the jet described previously was examined by computing the pressure distribution induced on a flat plate. Figure 9 presents this computed pressure distribution. It is entirely different from the

experimental data, a result which is not unexpected because this model describes only the effect of the free stream on the jet. The large positive pressure ahead of the jet indicates too large a blockage effect. The large positive pressure region downstream indicates that the flow separation is not represented. Finally, the negative pressure regions are too small because the entrainment is not adequately represented. As a result, this model does not adequately represent the influence of the jet wake on the induced pressure distribution.

There are, however, two other models which only represent the effect of the jet and do not accurately describe the detailed features of the jet. These models were developed by P. T. Wooler (refs. 13 to 15). The first is a vortex-sheet model shown in figure 10. This model uses a series of horseshoe vortices laid along an empirical jet path. The circulation strengths of the vortices are determined by the diameter of the jet, the local radius of curvature of the jet path, and the square of the inverse of the effective velocity ratio. The second model, shown in figure 11, uses sinks and doublets to represent the effect of the jet. This model calculates the jet path from a simplified set of the equations of motion. The solution of these equations requires that several constants describing the strengths of the sinks and doublets be determined empirically so that the computed path agrees with the experimentally determined path. This representation of the jet uses doublets located uniformly along the jet axis. The jet cross section is simplified. It is assumed to vary from a circle at the exit to an ellipse at some distance down the jet path. Then, at intervals of 1 jet-exit diameter, lines of sinks are placed across the jet path along the major axes of the elliptic cross sections.

Figure 12 presents a comparison of the pressure distributions from one set of experimental data with calculated results from the vortex-sheet model and the sink-doublet model. Data are presented for a pressure coefficient of -0.2. This comparison indicates that both models give reasonable results outside of the wake region at distances of 2 or more diameters from the jet exit.

This agreement indicates that these last two models may represent, to a large degree, the effect of the jet even though they do not describe the jet or the induced flow close to the jet. Further work is needed to develop a single mathematical model which describes both the jet characteristics and the induced flow field. This development will require more detailed experimental data on the jet as well as additional analytic work.

CONCLUDING REMARKS

The analysis of the flow field of a jet in a subsonic crosswind provides an understanding of the jet-induced effects on a turbojet or turbofan V/STOL aircraft in transition flight.

The complex character of the flow in the vicinity of the jet has been described. The primary features are the blockage of the free stream and its separation as it flows around the jet, the rollup by the jet into a pair of trailing vortices, and the entrainment of free-stream fluid into the jet. The entrainment can be considered in two parts: the fluid induced into the wake region by the swirling flow associated with the vortex pair and the fluid entrained by viscous mixing on the periphery of the jet surface. At the present time, there is very little quantitative experimental data available to provide detailed understanding of the relative importance of these features.

A method for computing the rollup of the jet wake into a pair of vortices has been developed and described. The pressure distribution induced by the jet in the plane of the jet exit has been considered. Several sets of experimental data were presented and two methods for computing the pressure distribution were presented and compared with experimental data.

Although the jet rollup and the pressure distribution in the plane of the exit can be computed by different methods, further work is needed to develop a single mathematical model which describes both the jet characteristics and the induced flow field. This development will require more detailed experimental data on the jet as well as additional analytic work.

REFERENCES

1. Williams, John; and Wood, Maurice N.: Aerodynamic Interference Effects With Jet-Lift V/STOL Aircraft Under Static and Forward-Speed Conditions. Tech. Rep. No.66403, Brit. R.A.E., Dec. 1966.
2. Vogler, Raymond D.: Interference Effects of Single and Multiple Round or Slotted Jets on a VTOL Model in Transition. NASA TN D-2380, 1964.
3. Hickey, David H.; Kirk, Jerry V.; and Hall, Leo P.: Aerodynamic Characteristics of a V/STOL Transport Model With Lift and Lift-Cruise Fan Power Plants. Conference on V/STOL and STOL Aircraft, NASA SP-116, 1966, pp. 81-96.
4. Margason, Richard J.; and Gentry, Garl L., Jr.: Aerodynamic Characteristics of a Five-Jet VTOL Configuration in the Transition Speed Range. NASA TN D-4812, 1968.
5. Barrack, Jerry P.; and Kirk, Jerry V.: Low-Speed Characteristics of High-Performance Lift-Engine V/STOL Aircraft. [Preprint] 680644, Soc. Automot. Eng., Oct. 1968.
6. Carter, Arthur W.: Effects of Jet-Exhaust Location on the Longitudinal Aerodynamic Characteristics of a Jet V/STOL Model. NASA TN D-5333, 1969.
7. Anon.: Analysis of a Jet in a Subsonic Crosswind. NASA SP-218, 1969.
8. Platten, J. L.; and Keffer, J. F.: Entrainment in Deflected Axisymmetric Jets at Various Angles to the Stream. UTME-TP 6808, Dep. Mech. Eng., Univ. of Toronto, June 1968.
9. Chang-Lu, Hsiu-Chen: Aufrollung eines zylindrischen Strahles durch Querwind (Rollup of a Cylindrical Jet in a Crosswind). Doctorial Dissertation, Univ. of Göttingen, 1942.
10. Bradbury, L. J. S.; and Wood, M. N.: The Static Pressure Distribution Around a Circular Jet Exhausting Normally From a Plane Wall Into an Airstream. C.P. No. 822, Brit. A.R.C., 1965.
11. McMahon, Howard M.; and Mosher, David K.: Experimental Investigation of Pressures Induced on a Flat Plate by a Jet Issuing Into a Subsonic Crosswind. Analysis of a Jet in a Subsonic Crosswind, NASA SP-218, 1969, pp. 49-62.
12. Gelb, G. H.; and Martin, W. A.: An Experimental Investigation of the Flow Field About a Subsonic Jet Exhausting Into a Quiescent and a Low Velocity Air Stream. Can. Aeronaut. Space J., vol. 12, no. 8, Oct. 1966, pp. 333-342.

13. Wooler, P. T.; Burghart, G. H.; Gallagher, J. T.: Pressure Distribution on a Rectangular Wing With a Jet Exhausting Normally Into an Airstream. J. Aircraft, vol. 4, no. 6, Nov.-Dec. 1967, pp. 537-543.

14. Wooler, P. T.: On the Flow Past a Circular Jet Exhausting at Right Angles From a Flat Plate or Wing. J. Roy. Aeronaut. Soc., vol. 71, Mar. 1967, pp. 216-218.

15. Wooler, P. T.: Development of an Analytical Model for the Flow of a Jet Into a Subsonic Crosswind. Analysis of a Jet in a Subsonic Crosswind, NASA SP-218, 1969, pp. 101-118.

LIFT-JET V/STOL AIRCRAFT IN TRANSITION FLIGHT

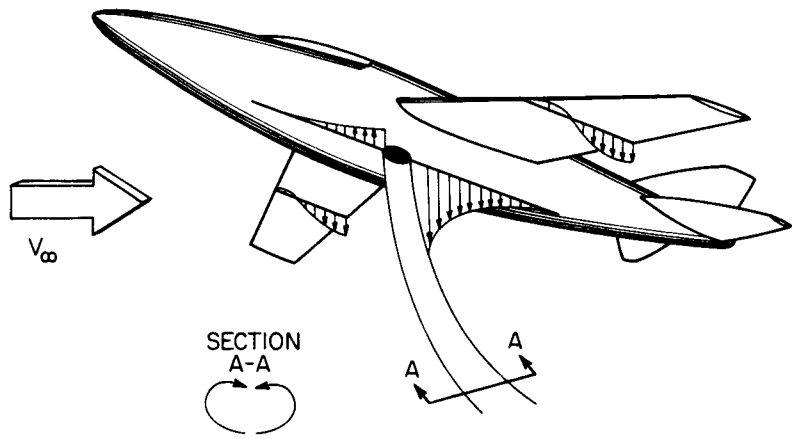

Figure 1

TYPICAL INDUCED LIFT AND PITCHING-MOMENT INTERFERENCE CAUSED BY THE JET

TRANSITION FLIGHT

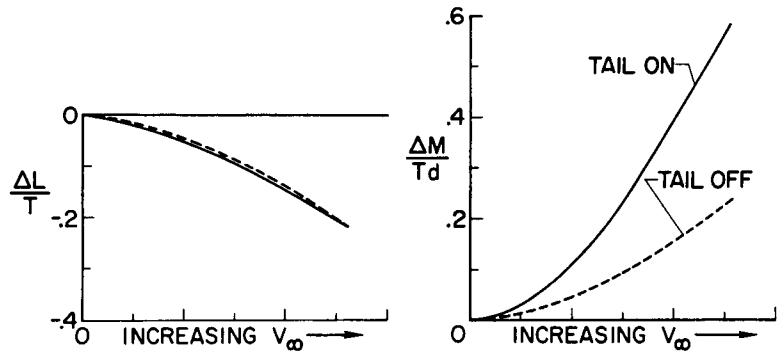

Figure 2

SCHEMATIC OF JET IN CROSSWIND

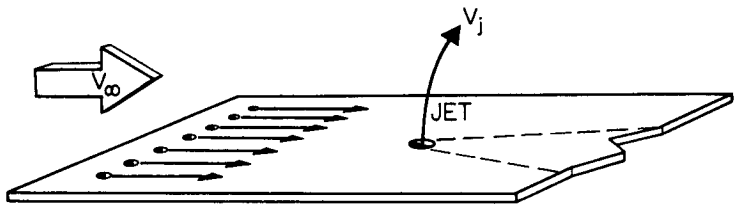

Figure 3

PHOTOGRAPH OF JET IN CROSSWIND
ONERA WATER TUNNEL VISUALIZATION

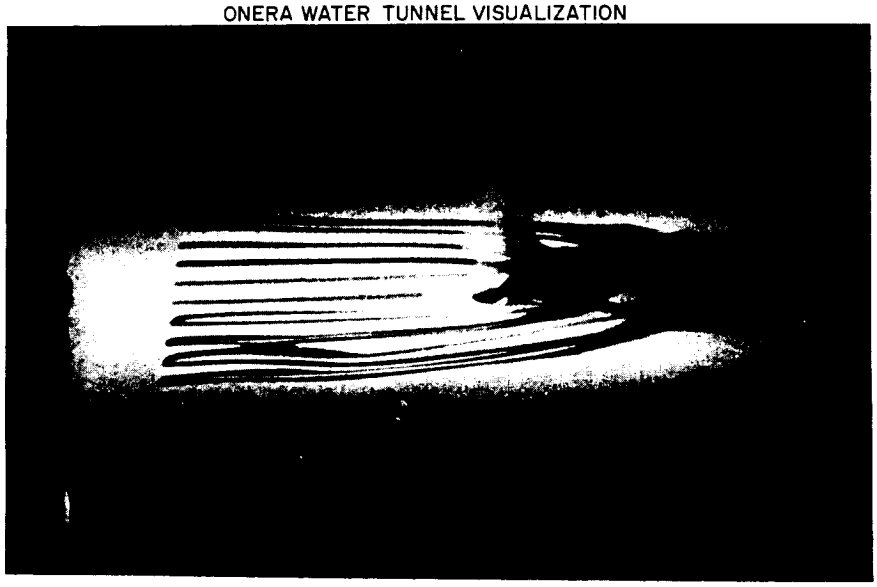

Figure 4

This page is reproduced at the back of the report by a different reproduction method to provide better detail.

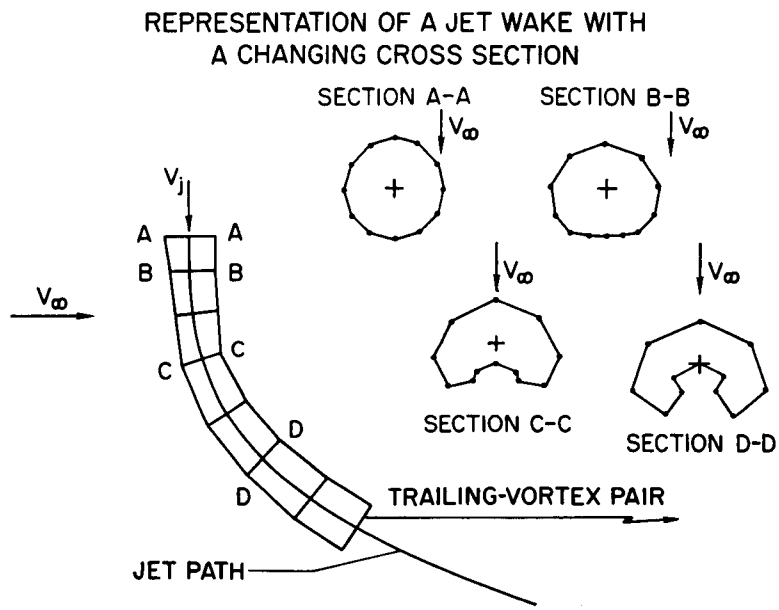
REPRESENTATION OF A JET WAKE WITH
A CHANGING CROSS SECTION
SECTION A-A
SECTION B-B
SECTION C-C
SECTION D-D
V_∞
V_j
A
B
C
D
TRAILING-VORTEX PAIR
JET PATH

Figure 5

WAKE CROSS SECTIONS SHOWING ROLLUP INTO PAIR OF VORTICES ($V_\infty / V_j = 0.25$)

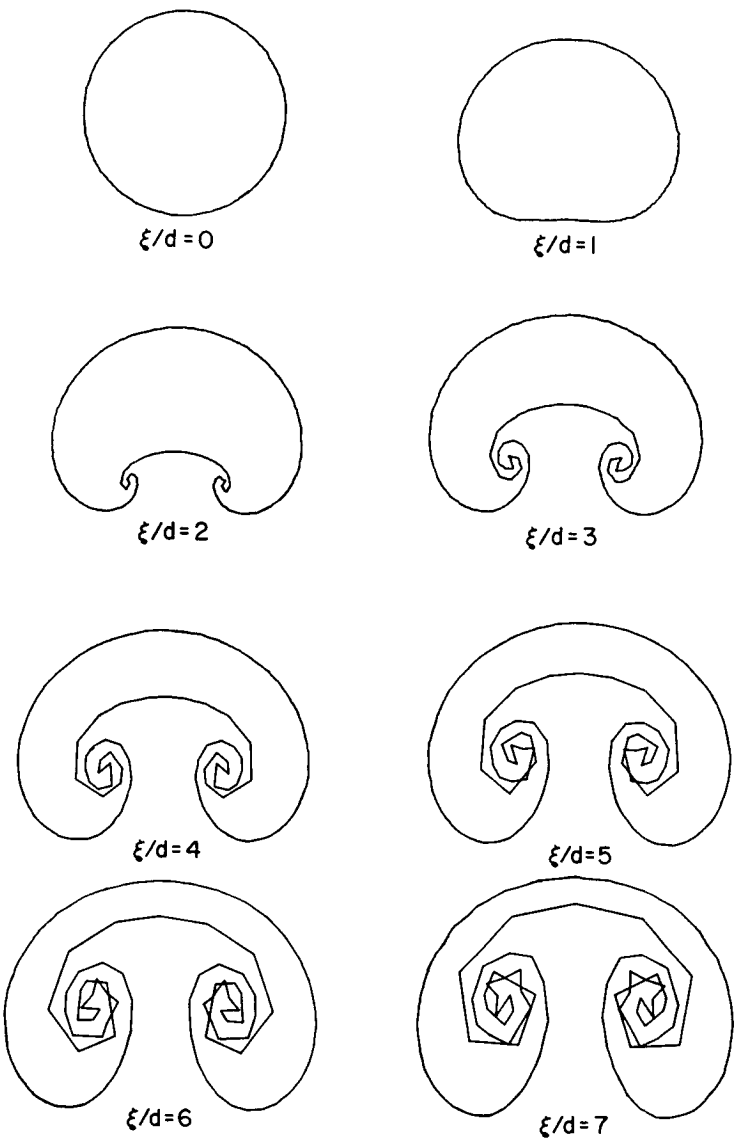

Figure 6

JET CROSS SECTION
ONERA WATER TUNNEL VISUALIZATION

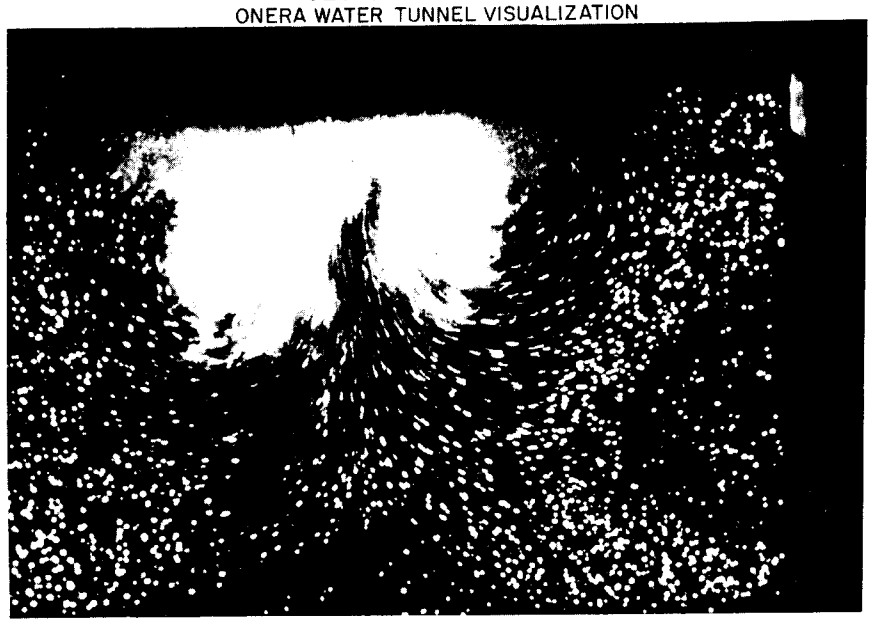

Figure 7

PRESSURE DISTRIBUTION AROUND A CIRCULAR JET
EXPERIMENTAL DATA; $V_\infty/V_j = 0.125$

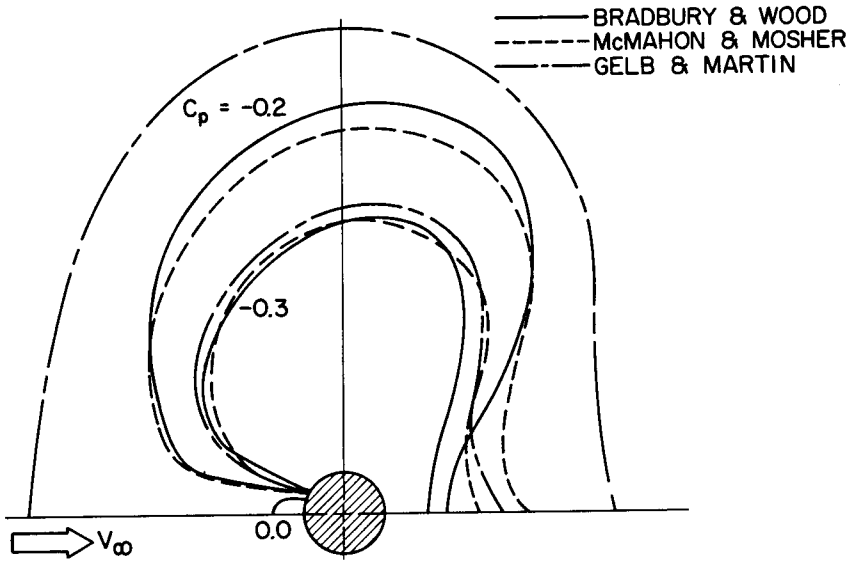

Figure 8

PRESSURE DISTRIBUTION AROUND A CIRCULAR JET

CALCULATED USING VORTEX-LATTICE MODEL; $V_\infty/V_j = 0.125$

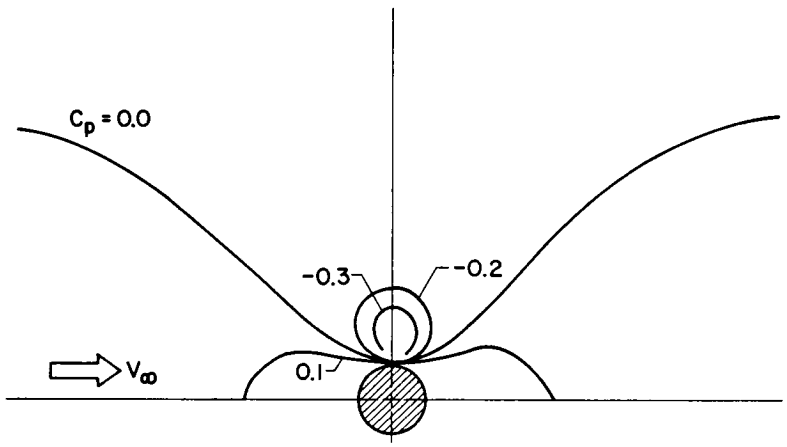

Figure 9

VORTEX-SHEET MODEL

DEVELOPED BY P.T. WOOLER

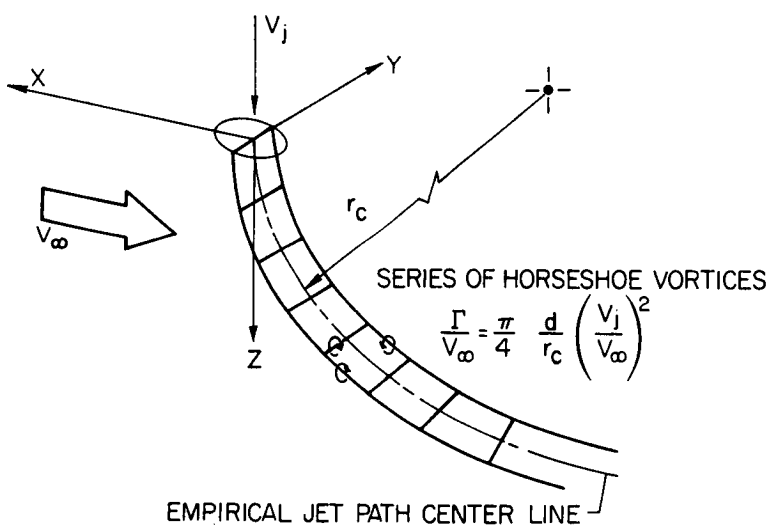

Figure 10

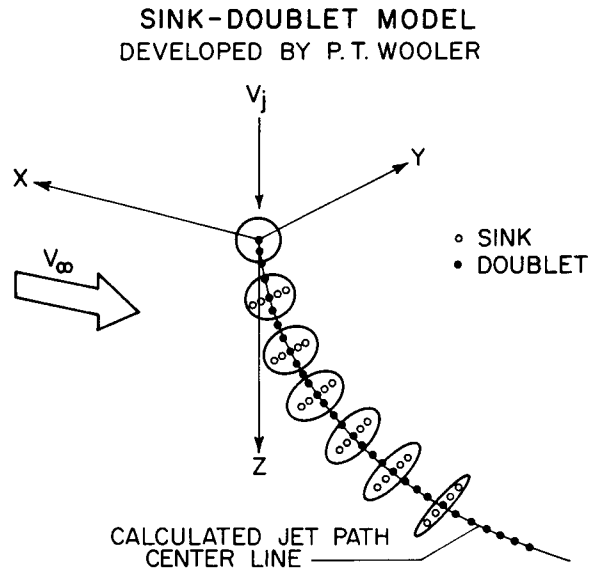

Figure 11

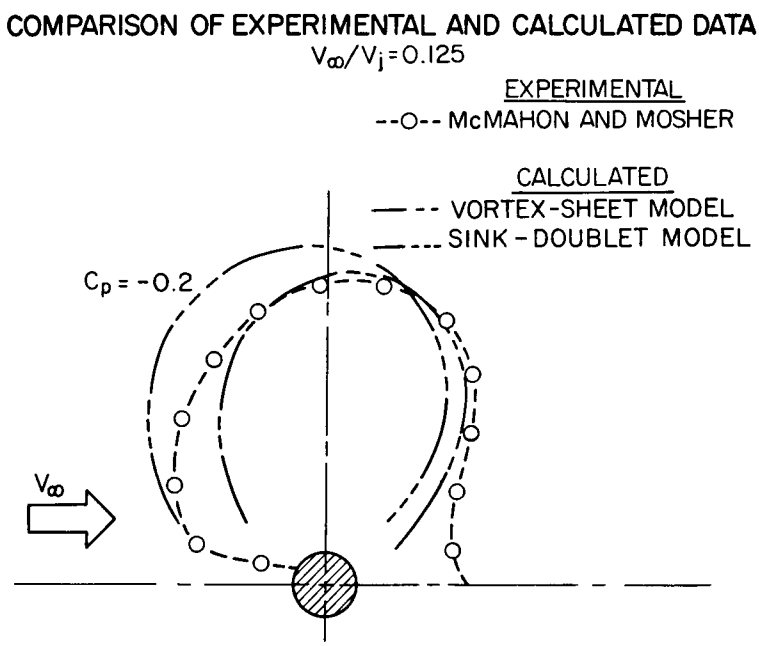

Figure 12

DISCUSSION

DAVID FINKLEMAN, U.S. Air Force Academy: One check on your truncation error might be in keeping track of the centroid of one-half of your symmetric vortex distribution. Do you have any idea how well that was preserved?

MARGASON: I made no check of that.

FINKLEMAN: Also, how many vortices are appropriate to describe the development of the weight properly? Is 12 the magic number?

MARGASON: Oh, no. Usually I try to get a number which is a multiple of 4 for symmetry purposes. I have tried anywhere from 8 to 96. It just depends on how much detail you want to obtain in the cross-section shape. I have found no difficulty at 96, and I suspect more vortices could be used.

FINKLEMAN: Also, with regard to your pressure distribution near the jet exit, perhaps you are aware of the paper by Westwater (F. L. Westwater, "Rolling Up of the Surface of Discontinuity Behind an Aerofoil of Finite Span," British ARC R and M No. 1692, August 1935), even older than the ones you cited, in which he tried to trace the roll-up of a vortex sheet behind an elliptically loaded wing. He was able to show that, since this is a slender body theory, the theory really should apply only several spans downstream. Trying to get the influence near the jet exit might be a misapplication of this particular two-dimensional theory. The two-dimensional theory presented here describes only the roll-up of the jet efflux.

MARGASON: It will take additional experimental information on the characteristics of the jet to determine how to describe the additional features needed. This is being worked on at the present time. Some computations have been done with a line of sinks added. These results look encouraging, but they are not ready to be presented at this meeting.

GEORGE R. BARTÉ, JR., General Electric Co.: You made a rather brief observation to some current work on the application of the material in Slide 5 to the problem of sewage discharge into a river. Now, since this is an interface area between hydrospace and aerospace, as well as having some immediate interest in some problems that we are currently working on, would you care to comment a little more on this particular work, who is doing it, and so forth? (Slide 5 is incorporated in the text as the sketch and the equations.)

MARGASON: The work I referred to was done in 1942, so of course it is not current. There is a fair amount of interest in this problem for another application: a smokestack discharging into the atmosphere with a crosswind. Keffer at the University of Toronto has done quite a bit with this.

Aside from that particular example, most investigators are interested in the problem for the aeronautical applications.

BARTÉ: Have you cited the reference to the 1942 work in your paper?

MARGASON: Yes. Also we had a symposium on this subject at Langley in September where there were 12 papers presented on the subject. This is available as NASA Special Publication 218. There are quite a few references in that document.

RAYMOND SEDNEY, Martin Co.: I wanted to get one thing cleared up about these very nice movies from the ONERA water tunnel. The water tunnel work there that I am familiar with is all extremely low Reynolds number, and it is always laminar flow. You mentioned turbulent flow. Is the Reynolds number high enough in these results for turbulent flow?

MARGASON: No, this is still quite low Reynolds number compared to aircraft applications. The primary purpose of the film was to indicate the character of the flow, to give a qualitative feel for it, and it is not necessarily a precise representation of airplane applications.

SEDNEY: Yes. Now, the other point I wondered about concerned the actual application. You mentioned that from the water tunnel visualization downstream on the flat plate there are two streamwise vortices.

MARGASON: Yes.

SEDNEY: Do you have any idea whether the presence of those vortices in a real case is important?

MARGASON: The strength of these is quite weak, but they are on the surface of the body, and the only configuration where we have any quantitative information is for the case of a jet coming out of a flat plate. For three-dimensional bodies we do not have any precise information. There are several experimental investigations under way which may give us some information on that, but they are not complete at the present time.

JOSEPH P. GIESING, Douglas Aircraft Co.: I just want to get one thing straight on the roll-up of your jet. Evidently you assume a vorticity distribution and then let it roll up without any change in vorticity strength?

MARGASON: That's correct.

GIESING: This isn't really the case is it? I mean, in a jet you have a bound vorticity which continuously feeds in shed vorticity down the jet. This process keeps building up the shed vorticity to a final value, does it not?

MARGASON: The representation of the jet presented in this talk includes only the effect of the crossflow on the jet. The mixing between the jet and the free stream are certainly not accounted for. These would get involved in your comment on the dissipation or shedding of vorticity. At the present time we do not know how these factors influence the variation of vorticity along the jet.

Last summer we did a few experiments where we tried to measure the vorticity in the jet. We found at a cross section of about 6 diameters

downstream from the nozzle (measured along the jet path) the vorticity was approximately twice the vorticity which this roll-up model gives you. This indicates that we are not considering all of the sources of vorticity.

Those measurements also indicated that the flow is spreading and that the vorticity certainly is dispersing over a fairly wide area as the jet efflux moves on downstream, so exactly what is going on in the flow is not completely clear at the present time. We hope to get a little better understanding of the flow in future experimental investigations so that we can do a better job of modeling it.

GIESING: I was just wondering if you maybe adopted some simplified or experimental curve of the jet trajectory to base your calculation of bound vorticity on, like one of the models you showed. It would give you a kind of idea of what the shedding vorticity strengths were as you progressed downstream. You could possibly build that into your jet roll-up program.

MARGASON: This is a possibility.

SELDEN B. SPANGLER, Nielsen Engineering and Research, Inc.: Rich, if you can characterize the wake, say three or four diameters downstream of the exit, like a rolled-up pair, and if you could somehow calculate the proper strength of that pair, what success do you think you would have in predicting the downwash over the tail of that aircraft?

MARGASON: The vortex-pair model of Wooler might be useful. Also the calculation for vortex roll-up has been modified by Hackett of Lockheed-Georgia Co. to handle this problem. He presented his results last July at an AIAA-CASI Meeting in Ottawa (J. E. Hackett and M. R. Evans, "Vortex Wakes Behind High-Lift Wings," AIAA Paper No. 69-740, July 1969). They provide a detailed description of the wing wake roll-up. This should provide a basis for estimating wake effects at the tail of an aircraft.

LEON E. RING, ARO, Inc.: Could you comment on how important it may be to get the right jet curvature, say in this vortex lattice model. That is, how much is fed back into the pressures on the wing?

MARGASON: You have to locate the fluid from the jet at the proper point in space to get its influence on a wing or other surface. From this point of view you certainly need to have a fairly adequate representation of the path of the jet.

J. ROSKAM, University of Kansas: It has been found that you can get some pretty fierce rolling moments when you put that situation in crossflow. Is your model suitable to predict those?

MARGASON: I assume you mean crossflow which is at a sideslip angle?

ROSKAM: Yes.

MARGASON: It would be a matter of predicting the pressure distribution over the region and integrating it properly, and you would find it is skewed

off to the side of the original centerline. Another application where you introduce some rather violent rolling moments is when you use reaction jets on the wing tips for roll control. Here you have the same sort of pressure fields induced in the vicinity of the jet and reduce the net thrust. This in turn reduces the net rolling moment produced by the reaction jets.

THEORETICAL INVESTIGATION OF DUCTED FAN INTERFERENCE FOR TRANSPORT-TYPE AIRCRAFT

By S. B. Spangler, M. R. Mendenhall,
and M. F. E. Dillenius

Nielsen Engineering and Research, Inc.

N70-21381

SUMMARY

A method has been developed for analyzing the aerodynamic interference effects associated with a wing-pylon-engine configuration typical of a modern high-speed transport aircraft. In order to perform the analysis, it was necessary to develop two new flow models. The first is a nonplanar lifting surface method, using a vortex lattice approach, capable of treating wing-pylon configurations. Provision was made in this model for modification of the pylon tip loading distribution to account for the force carryover effect caused by the engine at the pylon tip. The second model is that for a high-bypass-ratio turbofan engine. The essential characteristics modeled are the fan and core engine ducts, and the thrusts and resulting wakes of both the fan and core engine. These flow models are used in an iterative fashion to solve for the interference effects, including detailed load distribution and critical Mach number.

Comparison of the methods with data and other theories for load distribution and induced velocities for a wing alone, wing-pylon, and wing-pylon-engine indicate good agreement.

INTRODUCTION

This paper is directed towards the problem of aerodynamic interference between the wing, pylon, and engine of a modern subsonic transport-type aircraft at small angles of attack. Because of the complexity of the problem, most of the work in this area has been experimental (ref. 1). An analysis has been done treating the flow between the wing and engine cowl on one side of the pylon as a channel flow (ref. 2). No theoretical investigation has been reported in which the components have been treated as aerodynamically loaded surfaces in an external flow with interference between components. The purpose of this paper is to describe such an investigation. The work is being sponsored by the Ames Research Center, NASA.

The problem of interest is illustrated in figure 1. The configuration is a swept wing under which a pair of high-bypass-ratio turbofan engines is mounted on swept pylons. The three main aspects of interest are the overall interference characteristics (i.e., favorable or unfavorable), the detailed load distribution on the wing, pylon, and engine cowl, and the critical Mach

number. In order to compute these characteristics, flow models must be derived for each of the major components, interference flow fields must be determined, and component load distributions computed for the locally perturbed flow. In this paper, the general approach and methods will be described, followed by a presentation of some results obtained to date.

NOTATION

$\mathcal{AR}$ aspect ratio

b span

c chord

C_L wing lift coefficient

c_l section lift coefficient

M Mach number

s_p pylon span

V free-stream velocity

x chordwise distance

y spanwise distance

α aircraft angle of attack

α_w wing angle of attack

γ_{D_e} axisymmetric bound vorticity on engine duct

γ_{D_f} axisymmetric bound vorticity on fan duct

γ_e wake vorticity trailing from engine duct

γ_f wake vorticity trailing from fan duct

γ_{α_e} bound vorticity on engine duct due to angle of attack

γ_{α_f} bound vorticity on fan duct due to angle of attack

η dimensionless spanwise distance, $\frac{y}{b/2}$

Λ sweep angle

DISCUSSION

General Approach

The elements of the general approach are shown in figure 2. The analysis is based on the use of potential flow methods. It is necessary first to obtain a singularity flow model for each major component. The flow model in general consists of a distribution of bound and trailing vorticity placed on the mean surface of the component. The strength distribution of the vorticity is determined by satisfying the boundary condition of flow tangency to the mean surface at selected points on the configuration. The loading distribution on the component is then obtained from the product of the strength of the local vorticity and the local velocity acting on the element of vorticity. Furthermore, the known vorticity strength distribution can then be used to predict the flow field distortion in the vicinity of the component.

The manner in which the flow models of each of the components are combined to obtain interference effects is as follows. Component A (for instance, the wing) is assumed to act in a uniform onset flow and its vorticity strength distributuion is determined. Using this known distribution, the perturbations on the uniform flow over component B (for instance, the engine) are computed. The vorticity strength distribution representing component B is then determined with B acting in the perturbed flow. Using the vorticity distribution of B (which now includes interference), the flow perturbations induced by B on A are computed and superimposed on the uniform flow over A. The vorticity strength distribution on A is recomputed, accounting for the perturbed flow from B. This process can be continued in an iterative fashion until the strength of the vorticity distribution for a given component changes less than a prescribed amount between iterations, at which time the detailed load distributions and surface pressure may be determined. In practice, with the configurations examined to date, one complete iteration is sufficient.

Component Flow Models

Wing-pylon.- The wings of modern, high-speed, transport-type aircraft are swept, have a relatively high aspect ratio and some dihedral, and are twisted and cambered. The pylons are highly swept forward, may have a toe-in angle, and have a root chord which is an appreciable fraction of the local wing chord. With these characteristics, the pylon should be considered an integral part of the wing for purposes of developing a flow model, because there is no simple combination of separate wing and pylon models that will properly represent the mutual interference effects, particularly in the wing-pylon junction region.

Since no general method exists for handling a wing-pylon combination that will yield chordwise load distributions, a nonplanar lifting surface method was developed. The flow model selected is basically a vortex lattice

scheme, as illustrated in figure 3. The wing and pylons are divided into area elements, on each of which is placed a horseshoe vortex with the (yawed) bound leg along the element quarter chord and the trailing legs along the streamwise sides of the element. The flow tangency condition is applied at the midpoint of the three-quarter chord line of the element (control point).

The vortex layout on the wing and pylons is arbitrary but is governed by the following considerations. The spanwise widths of the area elements in a given chordwise row must be identical, but the widths of two adjacent rows need not be the same. In this way, smaller width vortices may be used in regions where the load is changing rapidly. The pylon is treated in identically the same fashion as the wing. Both pylon and wing are required to have the same number of vortices in the chordwise direction. The area elements in the region of the wing-pylon junction are arranged so that the trailing legs from the two wing rows and the upper pylon row all coincide at the junction. The total number of vortices is limited by the storage capacity of the digital computer used, and for the IBM 7094 this limit is 100 vortices on the semispan and one pylon. In the work done to date, four chordwise rows of vortices have proven to be sufficient to get chordwise loading information.

The flow tangency boundary condition and the load distributions are calculated in much the same manner as in Margason and Lamar's planar vortex lattice computer program. (Margason and Lamar's work is unpublished; however, the program may be obtained from them at Langley Research Center.) The Prandtl-Glauert transformation is used to account for compressible flow effects.

The vortex lattice flow model has a number of advantages for the present nonplanar problem. The use of several vortices along the chord permits chordwise loading variations to be obtained, an important consideration when engines and swept pylons are involved. The use of a discrete vortex model rather than a continuous vorticity distribution permits the velocities induced off the wing to be readily evaluated. The method is readily adaptable to inclusion of engine-induced velocities at the control points for calculation of interference effects. The use of yawed rather than rectangular vortices permits somewhat fewer vortices to be used, particularly on highly swept surfaces. The use of variable width vortices permits a concentration of vortices in areas where the loading is changing rapidly. Finally, the discrete vortex approach is amenable to inclusion of a pylon tip loading correction, as discussed below.

Pylon tip model.- The addition of an engine to the tip of a pylon in a sidewash has the effect of causing a nonzero loading at the pylon tip and some force carryover onto the engine. As a consequence, it is necessary to modify the pylon vortex model near the tip. An approximate method is used for this purpose, based on the wing-tip tank method of Robinson and Zlotnick (ref. 3), as illustrated in figure 4. An infinite cylinder alined with the engine axis is considered to exist at the pylon tip, and the horseshoe vortices on the pylon are imaged within the cylinder. In this manner, the boundary condition for cancelling the flow induced by the pylon vortices

through the "engine" is satisfied exactly in the plane of the pylon and at large distances upstream and downstream of the pylon and satisfied approximately elsewhere on the cylinder. The image vortices represent the "lift carryover" onto the engine and serve to modify the strengths of the pylon vortices because of the additional velocities induced at the pylon control points.

Engine model.- The engines of interest are high-bypass-ratio turbofan engines which tend to resemble high-pressure-ratio, single-stage fans driven by a core engine within an airbreathing centerbody. For purposes of examining the flow interference between the engine and the wing-pylon, the significant features in an engine model are the representation of the fan and engine ducts and the fan and engine thrusts together with their resulting wakes. The model used herein is an extension of earlier theoretical work done on ducted fans at Nielsen Engineering and Research, Inc. (ref. 4), and is shown in figure 5. The engine and fan wakes are represented by semi-infinite concentric, constant-diameter vortex cylinders entending downstream coaxial with the engine centerline. The fan and engine ducts are considered to be thin cylinders which may have camber and taper. The fan and engine thrusts are considered to be produced by uniformly loaded actuator disks within the ducts. A bound vorticity distribution is used on the fan and engine ducts to cause the local flow to be tangent to the mean surface of the ducts.

The engine model flow parameters are determined from gross engine performance characteristics which are assumed known from the flight condition. The information required is bypass ratio, air weight flow, thrust, and thrust division. These quantities are used to determine the wake velocities and strength of the wake vortex cylinders (γ). The axisymmetric portions of the duct-bound vorticities (γ_D) are then computed by simultaneously requiring flow tangency on the fan and core engine ducts due to the wake-induced flow and the free stream. If the engine is in an upwash field, the upwash is averaged over the fan duct chord and the core engine duct chord, and an additional duct-bound vorticity (γ_α) is used to cause flow tangency in the upwash flow. A sidewash flow over the engine is treated in the same manner as the upwash flow. The final engine flow model is then the superposition of the axisymmetric and crossflow solutions. Once the bound and trailing vorticity distributions on the engine are known, the flow field in the vicinity of the engine may be determined for the purpose of making interference calculations.

Combination of flow models.- A solution for a given wing-pylon-engine case makes use of the above noted flow models in the following manner. A solution for the wing-pylon in a uniform flow is calculated initially, and wing-pylon induced velocities at a number of points at the engine location are determined. The engine vorticity distribution is then determined for an onset flow consisting of the free-stream axial and upwash components plus wing-pylon induced upwash and sidewash velocities. The engine-induced velocities at the wing and pylon control points are computed, and the wing-pylon performance recomputed. Experience has shown that the interference effects

do not change significantly if a second iteration is carried out, so the computation is stopped here. With closely coupled engines, additional iterations would probably be required.

The final step consists of computing total forces and moments, load distributions, and chordwise pressure distributions on the configuration. The chordwise pressure distribution on the wing and pylon are obtained by fitting a Glauert series to the several chordwise circulation values computed by the vortex lattice method to get a continuous chordwise vorticity variation. The latter is then related to the discontinuous velocity over the airfoil section. The velocities due to all components and the free stream are summed and augmented by a two-dimensional thickness correction. The Bernoulli equation is then used to obtain pressure coefficients.

RESULTS

Several sets of results are shown in this paper to illustrate the relative importance of interference effects and the degree of correlation with data and other theoretical results. The wing-alone case is considered first, followed by results for a wing-pylon and a wing-pylon-engine configuration.

The first set of results, figure 6, shows correlations with data for downwash and sidewash velocities induced below a wing in a uniform onset flow. The location is typical of an engine-pylon intersection on a transport aircraft. These velocities must be accurately predicted to determine flow interference effects. The data in figure 6 were taken from reference 5. The configuration is a wing-body having a diameter-to-span ratio of 0.15 and a 45° swept, flat, uncambered wing of aspect ratio 4. Wing thickness effects were removed by subtracting from the velocities at $C_L = 0.49$ the appropriate velocities at $C_L = 0$. The predicted curves were obtained by neglecting any body effects and fitting the wing with a uniform spacing of 4 chordwise rows and 19 spanwise rows of horseshoe vortices. The abscissa represents distance aft of the section leading edge, as a fraction of the section chord. The agreement between theory and experiment is quite good and is representative of the results obtained at all locations examined except those close to the underside of the wing, where the peaks in wash velocities near the leading edge tend to be overpredicted. These results verify the capability of the vortex lattice method to predict off-wing velocities with sufficient accuracy to obtain proper interference effects.

It is interesting to note from figure 6 that relatively high sidewash angles are indicated in the region where an engine and pylon would be located. The pylon interference could be nearly eliminated by toe-in, twist, and camber of the pylon to make its mean surface conform to the wing-alone streamlines. However, the pylon would be matched to the local flow at only one angle of attack, and interference would still exist at other wing angles of attack.

The second set of results, figure 7, shows the spanwise variation of the additional span load coefficients for a swept wing with relatively large, swept forward pylons. Since there are few data available for loadings on wing-pylon combinations, a comparison is shown with theoretical results obtained by Blackwell (ref. 6). The Blackwell theory replaces the wing and pylons with a distribution of rectangular horseshoe vortices of uniform width with their bound legs located at the section quarter chord. With this approach, spanwise variations of loading can be predicted, but no chordwise loading distributions can be obtained because only one chordwise vortex is used. The Blackwell results in figure 7 were obtained using 1 chordwise by 40 spanwise vortices on the wing and 1 by 8 on the pylon, whereas the nonplanar vortex lattice results were obtained using 4 chordwise by 20 spanwise on the wing and 4 by 2 on the pylon. The results in figure 7 illustrate excellent agreement between the two theories, with the Blackwell theory showing a slightly larger discontinuity in loading across the pylon than the nonplanar vortex lattice method.

The third set of results (figs. 8 and 9) illustrates the importance of the various interference effects on the C-5A wing at a Mach number of 0.7 with only the outboard engines and pylons present. The pylons are swept forward about 70°, have a span of 0.15 of the local wing chord, and are toed in 1°. The engines have a negative incidence with respect to the wing root chord of 4.5°. The results shown are spanwise variation of dimensionless section lift coefficient for zero wing angle of attack (fig. 8) and the additional loading at 4° angle of attack, which approximates a cruise angle of attack. The results were obtained using 20 spanwise and 4 chordwise rows of vortices on the wing semispan and 2 spanwise by 4 chordwise rows on the pylon.

For the zero angle case, figure 8 shows that the wing-alone and wing-pylon results are very similar. The small discontinuity in loading at the pylon is due primarily to the toe-in angle of the pylon. The addition of the engine with its negative incidence causes an upwash over the wing which increases the section lift coefficients in the region of the pylon.

For the additional loading, figure 9 indicates that the addition of a pylon to the wing produces a discontinuity in loading at the pylon which is larger than that for the zero angle case because of the wing-induced sidewash over the pylon. The engine at positive angle of attack induces a downwash over the wing which decreases the wing section lift coefficients in the region of the pylon.

The total section lift at 4° angle of attack is the sum of the zero angle and additional loading curves given in figures 8 and 9. For the wing-pylon, it is of interest to note that the toe-in effect shown in figure 8 compensates in part for the pylon-induced interference due to additional loading, thereby reducing the overall pylon-induced interference. For the wing-pylon-engine combination, the pylon-engine induced effects for zero angle and additional loading tend largely to cancel because of the negative engine incidence angle, leaving little net interference at this angle of attack. At higher angles of attack, the interference effects associated with the additional loading would dominate.

The final set of results, figure 10, illustrates a comparison between predicted and measured section lift coefficients at two span stations on the C-5A. These unpublished data were obtained at the Langley Research Center on an 0.057 scale model with inboard engines and pylons removed. The tests are similar to those of reference 1 and make use of the same engine model. For the inboard station (η = 0.365), where the inboard engine would normally be located, the theory and data are in good agreement. For the outboard engine station, the theory and data are in reasonable agreement, although the theoretical lift-curve slope for the section just inboard of the pylon appears somewhat low. Both the theory and data show the station inboard of the pylon to have a higher lift-curve slope than the outboard station. The wing exhibits an extensive region of supersonic flow at $\alpha_W = 8.5°$, and the theory would not necessarily be expected to agree with the data at this angle.

CONCLUDING REMARKS

A method of analysis has been developed for analyzing the aerodynamic interference effects associated with a wing-pylon-engine configuration typical of a modern high-speed transport aircraft. In order to perform the analysis, it was necessary to develop a new nonplanar lifting surface method yielding chordwise loading distributions and a new high-bypass-ratio turbofan engine model describing the engine and wake flow characteristics important to the interference problem. Comparisons of the methods with wing-alone, wing-pylon, and wing-pylon-engine data and other theories indicate good agreement.

To date, the methods have been applied only to the C-5A configuration with one engine-pylon per wing panel. The methods include prediction of chordwise pressure distribution on the wing, pylon, and fan cowl, although no comparisons with such data have been made to date. The methods can be readily extended to include multiple engines per panel and pylons with camber and twist. Through use of the methods, parameters can be examined such as axial and vertical location of the engine relative to the wing, engine incidence relative to the wing, pylon incidence, camber and twist, and spacing of two engines along the span.

REFERENCES

1. Patterson, J. C.: A Wind Tunnel Investigation of Jet Wake Effect of a High-Bypass Engine on Wing-Nacelle Interference Drag of a Subsonic Transport. NASA TN D-4693, 1968.

2. Kutney, J. T.; and Piszkin, S. P.: Reduction of Drag Rise on the Convair 990 Airplane. J. Aircraft, vol. 1, no. 1, Jan.-Feb. 1964.

3. Robinson, S. W.; and Zlotnick, M.: A Method for Calculating the Aerodynamic Loading on Wing-Tip-Tank Combination in Subsonic Flow. NACA RM L53B18, 1953.

4. Mendenhall, M. R.; and Spangler, S. B.: A Computer Program for the Prediction of Ducted Fan Performance. Nielsen Engineering and Research, Inc., TR 16, June 1969. Prepared under NASA contract NAS 2-4953.

5. Alford, W. J.: Theoretical and Experimental Investigation of the Subsonic-Flow Fields Beneath Swept and Unswept Wings With Tables of Vortex-Induced Velocities. NACA Rep. 1327, 1957.

6. Blackwell, J. A.: A Finite-Step Method for Calculation of Theoretical Load Distributions for Arbitrary Lifting-Surface Arrangements at Subsonic Speeds. NASA TN D-5335, 1969.

WING-PYLON-ENGINE INTERFERENCE

- OVERALL INTERFERENCE
- DETAILED LOAD DISTRIBUTION
- CRITICAL MACH NUMBER

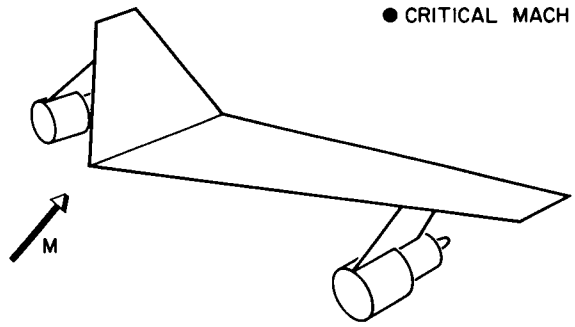

Figure 1

GENERAL APPROACH

- POTENTIAL FLOW METHODS
- SINGULARITY MODEL FOR EACH COMPONENT
- PREDICT FLOW FIELDS IN VICINITY OF EACH COMPONENT
- IMPOSE FLOW FIELD "A" ON COMPONENT "B" TO GET INTERFERENCE
- ITERATE

Figure 2

WING-PYLON MODEL

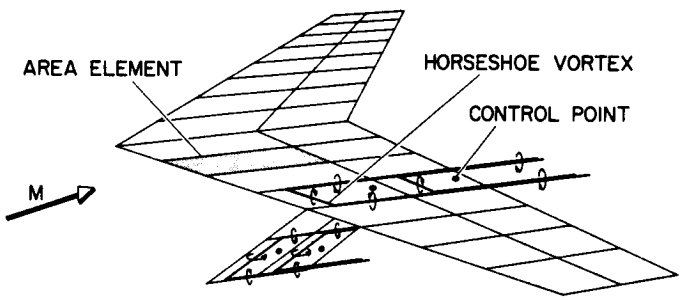

Figure 3

APPROXIMATE PYLON TIP MODEL

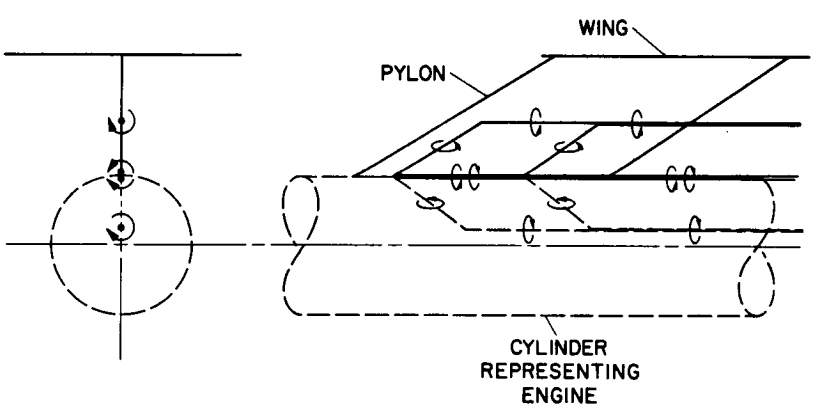

Figure 4

ENGINE MODEL

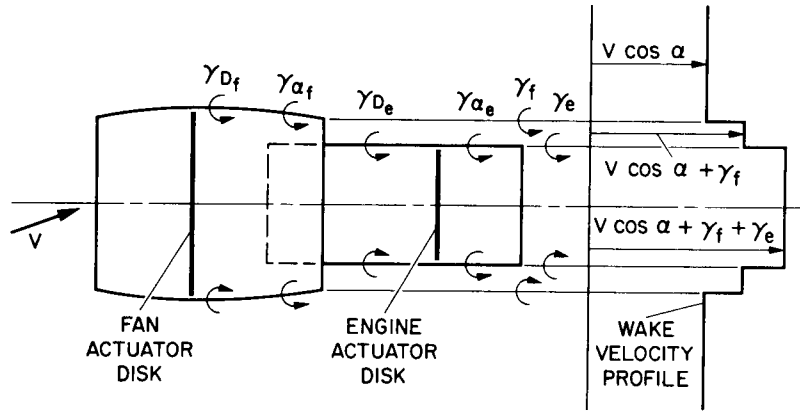

Figure 5

FLOW ANGLES BENEATH SWEPT WING
MID SEMISPAN LOCATION 0.2 CHORD BELOW WING

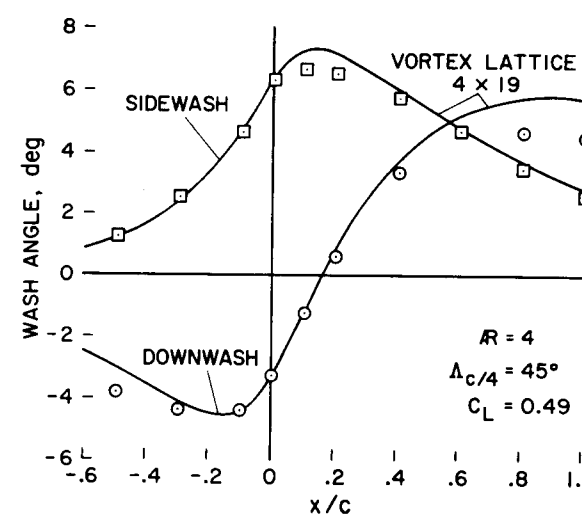

Figure 6

COMPARISON WITH BLACKWELL THEORY FOR WING-PYLON

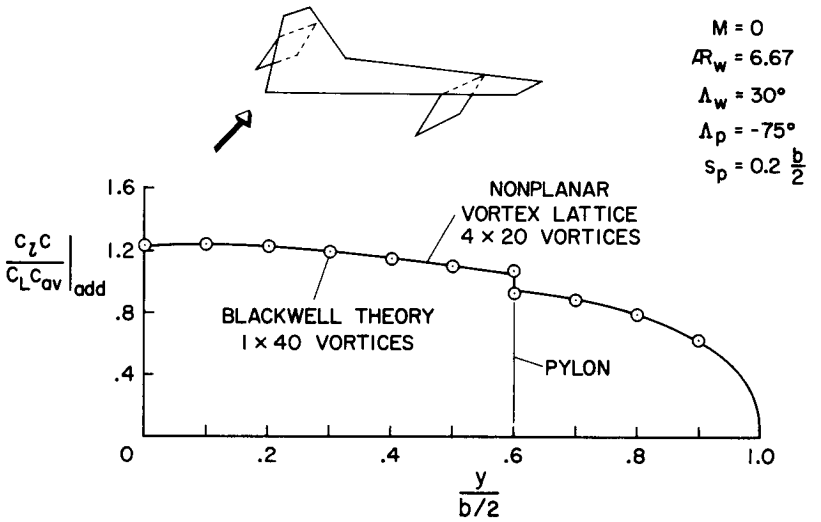

Figure 7

INTERFERENCE BUILD-UP ON C-5A WING

LOADING AT $\alpha_w = 0°$

M = 0.7

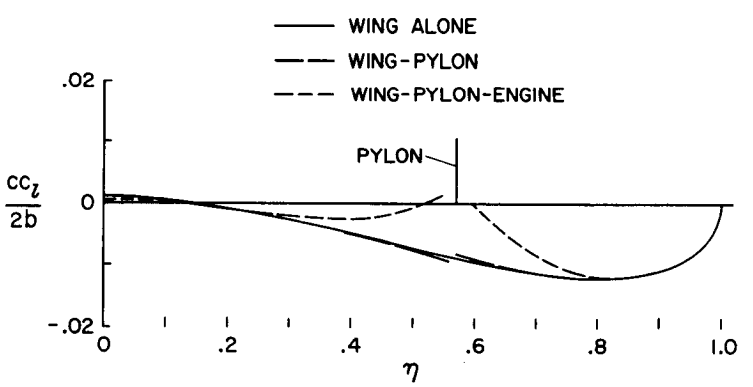

Figure 8

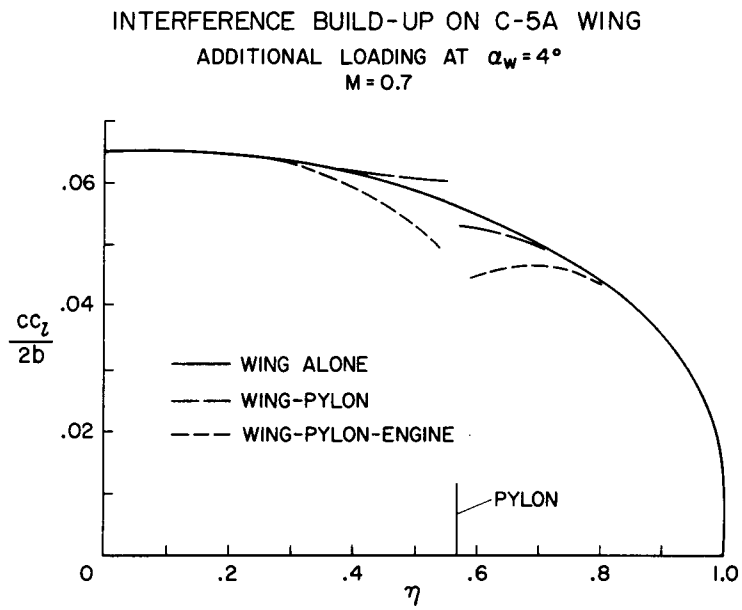

Figure 9

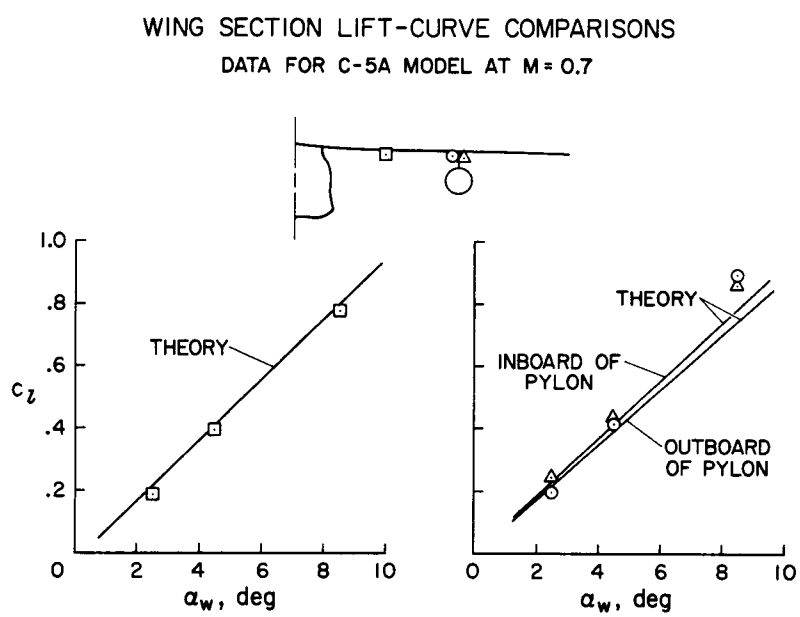

Figure 10

DISCUSSION

STEPHEN STARCH, Boeing Co., Wichita: How do you handle compressibility?

SPANGLER: We use a Prandtl-Glauert transformation and stretch the x coordinates on the wing and pylon.

TED DANSBY, Lockheed-Georgia Co.: On your nacelle model, did you try putting the vortex plates around, rather than an image system like you used? In other words, put vortex plates all around the cylinder that you used to simulate your nacelle.

SPANGLER: I am not sure what you mean by vortex plates.

DANSBY: Well, I mean a series of plates, that is, a plate with a bound vortex (lattice network).

SPANGLER: Are you thinking now of the slide I showed with the infinite cylinder?

DANSBY: Yes.

SPANGLER: This was done just for purposes of modifying the load distribution on the pylon due to the presence of the engine. Now, when the engine model is calculated, then we do have ring vortices . . .

DANSBY: Yes. I realize that, but I was wondering about the effect on the wing. In other words, you iterate. We have about the same approach, but we do not iterate. We describe the engine by using a series of these plates or lattice arrangements. Some of our results are quite consistent with yours. But I was wondering whether you actually tried the image versus the plate.

SPANGLER: Well, we do consider the interference effect induced by the engine on both the pylon and the wing. We take our engine loading, which has interference in it due to the wing and the pylon, and then compute the induced velocities on both the pylon and the wing to obtain the engine-induced interference. It's important that all of the boundary conditions for each of the various models which are added up to get the interference effects are all satisfied properly.

DANSBY: One more. Why do you iterate? Couldn't you combine this all into one large matrix?

SPANGLER: Yes, you could, if you had a big enough computer.

DANSBY: We have the same problem.

Oh, and one other thing. Of course, you will extend this to the case of thickness of the pylon?

SPANGLER: Yes. I didn't mention this in the talk. Just recently, in order to get pressure distributions, we have taken the mean-surface loadings, which give the discontinuous part of the loading on both the pylon and the wing, and added in the continuous velocities and profile thickness effects on both the pylon and the wing. This approach gives us a continuous chordwise pressure distribution on the pylon and the wing including thickness effects.

DANSBY: What was the incremental effect of power? Had you evaluated that separately?

SPANGLER: No, I can't tell you. We did not evaluate that separately.

JACK N. NIELSEN, Nielsen Engineering and Research, Inc.: I think it is true that there are many ways in which you can satisfy the boundary conditions on the engine. One of them is to place singularities on the surface of the engine. Another one is to place them on the axis. Now, I think the way we did it is still a third way. Even though we didn't satisfy the boundary conditions precisely by the vortex image system, we can still take the residue and throw it in with the interference velocities and cancel the sum, so that with our image system precise solution is possible.

I agree that iteration is unnecessary. It is a question of computer size and how many simultaneous equations you want to put into your matrix.

BRADFORD H. WICK, NASA, Ames Research Center: I would like to ask Mr. Joseph P. Giesing how did you like the location of his control point, 75 percent?

JOSEPH P. GIESING, Douglas Aircraft Co.: That's pretty well established. There has been no question as far as the vortex lattice method is concerned as to where to put the control point, in my estimation. This location is well established by two-dimensional analysis.

I would like to say that we have compared putting plates on a fuselage or some sort of body attached to a lifting surface and compared it to the image system approach which we also have had implemented. There does seem to be just a slight discrepancy right at the wing-fuselage intersection.

We also tried simulating a symmetry plane by putting a large number of vortices on a plane wall and attaching a wing to it. The loading always came out lower than the symmetry loading, which would be an exact solution. We found the same results when we attached a lifting surface to a fuselage with vortex elements on it. So I do believe that this relatively simple image system works out fairly well, especially if you couple it with an axial singularity system to take care of the residue that is left over from the image system.

I would also like to comment on your statement that "there are no other nonplanar methods." I'd like to call your attention to Albano and Rodden. Although their method is called unsteady double lattice, you can always set the frequency to zero, and it is a steady nonplanar method. Also some work in Russia by Belotserkovskii uses the vortex lattic system for nonplanar

configurations, and there are a lot of other planar type methods around. I am sure you are familiar with them.

NIELSEN: I just have one more comment. You have infinite sidewash and downwash around the tip of the pylon, and by putting the vortex images in, you get rid of that singularity. This is hard to do if you just use surface distributions. So I think the image approach is a simple way of doing it, which is better than just pure surface distributions.

ATLEE M. CUNNINGHAM, JR., General Dynamics, Fort Worth Div.: I didn't quite understand, when you were talking about the ring vortices, whether or not you account for circumferential variation in these and, if you do, how do you do it?

SPANGLER: We have two types of vortex rings. One is an axisymmetric ring which takes account only of the axisymmetric velocities induced through the duct surface by the wake cylinders, which are axisymmetric, and the $V \cos \alpha$, which is also axisymmetric.

The second type of ring has a cosine variation around the periphery, and this is the kind of ring you need to cancel a uniform crossflow across the duct. We have one harmonic, in essence, in the nonaxisymmetric ring distributions.

CUNNINGHAM: Does this work well whenever your nacelle gets very, very close to the wing?

SPANGLER: No. It, of course, gets worse as you bring the wing and the engine together. Now, in our method we average the upwash distribution over the length of the fan duct chord and over the length of the engine duct chord and treat them separately. To the extent that the upwash distribution varies considerably over either of these lengths then the engine vorticity model really should be more complex.

However, the engine effects on the wing loading for a C-5A configuration are fairly small, so I think for the configuration we have we are doing a pretty good job on modeling the interference effects. Now, if you bring the engine up closer to the wing, you will have to take more harmonics into effect.

THE ANALYSIS OF PROPELLER-WING FLOW INTERACTION

By Antony Jameson

Grumman Aircraft Engineering Corp.

N70-21382

SUMMARY

Theoretical methods are developed for calculating the interaction of a wing both with a circular slipstream and with a wide slipstream such as might be produced if the slipstreams of several propellers merged. To simplify the analysis rectangular and elliptic jets are used as models for wide slipstreams. Standard imaging techniques are used to develop a lifting surface theory for a static wing in a rectangular jet. The effect of forward speed is analyzed for a lifting line in an elliptic jet, and a closed form solution is found in the case when the wing just spans the foci of the ellipse. A continuous wide jet is found to provide a substantially greater augmentation of lift than multiple separate jets because of the elimination of edge effects at the gaps. Calculations based on these methods show good correlation with experimental data for wings without flaps, but deflection of flaps seems to result in a greater turning effectiveness than might be expected from the theory.

INTRODUCTION

The need for V/STOL aircraft to relieve air traffic congestion is becoming increasingly apparent. Interest therefore has been renewed in predicting the influence of propeller-wing flow interaction on the aerodynamic characteristics of deflected slipstream and tilt wing aircraft.

The lift of a wing spanning a single circular slipstream has been quite extensively studied. Early investigators used lifting line theory (refs. 1, 2). Later slender body theory was introduced to treat the case when the aspect ratio of the immersed part of the wing is small (refs. 3, 4). Neither of these theories agreed well with experimental results. Lifting surface theories were developed by Rethorst (ref. 5), using an analytical approach, and Ribner and Ellis (ref. 6), using a numerical approach. These give better agreement at the expense of lengthy computations. Only Sowydra (ref. 7) has attempted to allow for the deflection of the slipstream boundary.

Rethorst's method has been extended to treat approximately a wing in several separate slipstreams (ref. 8). None of these investigations, however, has allowed for the possibility of the slipstreams from several propellers merging to form a single wide jet. It can be expected that the elimination of the gaps would lead to an increase in efficiency by allowing the circulation to be maintained continuously across the span. Studies of wide jets were initiated by De Young (ref. 9), and have been continued by the present author. Results of calculations both for circular slipstreams from isolated propellers and for wide slipstreams are presented in this paper.

Preceding page blank

FORMULATION

The general case to be considered is a wing in a slipstream generated by one or more propellers with an external flow due to forward motion of the wing. The following simplifications are made:

(1) The fluid is inviscid and incompressible.

(2) Rotation in the slipstream is ignored and it is treated as a uniform jet.

(3) The jet boundary is assumed to extend back in a parallel direction.

Under these assumptions the perturbation velocity due to the wing can be represented as the gradient of a velocity potential which satisfies Laplace's equation (fig. 1). At the boundary it is necessary to maintain continuity of both pressure and the transverse flow angle. Let V_j and V_o be the undisturbed velocities in the slipstream and the external flow. Then if Bernoulli's equation is linearized, the boundary conditions can be expressed as

$$\phi_j = \mu\phi_o \tag{1}$$

$$\mu \frac{\partial\phi_j}{\partial n} = \frac{\partial\phi_o}{\partial n} \tag{2}$$

where ϕ_j is the interior potential, ϕ_o is the exterior potential, and μ is the velocity ratio

$$\mu = \frac{V_o}{V_j} \tag{3}$$

ANALYTIC METHODS

To restrict the complexity of the calculations it is desirable to use the simplest possible analytical models. Two models of wide slipstreams have been found to be amenable to analysis. In the first the slipstream is represented as a rectangular jet. A lifting surface theory can then be developed which is exact only in the static case. In the second the slipstream is represented by an elliptic jet. A quite simple lifting line theory can then be developed which is valid for the entire speed range. A simplified lifting surface theory for a circular slipstream can also be developed with the aid of calculations for a square jet.

Lifting Surface Theory for a Rectangular Jet

In the static case ($V_o = 0$) only the first boundary condition (1) remains to be satisfied. A rectangular jet can then be treated by the method of images as in the theory for an open wind tunnel (ref. 10). Since the wing

is large compared with the jet, it is necessary to allow for the nonuniformity of the additional downwash due to the jet boundary. When the wing spans the jet, the influence of the jet dimensions can be conveniently represented by the single parameter jet aspect ratio

$$AR_j = \frac{B}{H} \tag{4}$$

where B and H are the jet width and height.

The wing is represented by a distribution of horseshoe vortices (fig. 2). For each horseshoe vortex the boundary condition can be satisfied over the whole jet surface in three dimensions by introducing a doubly infinite set of images into a lattice formed by extending the rectangle containing the jet (fig. 3). The images thus give the correct longitudinal variation of the downwash, and a lifting surface theory can be developed. It is expedient to use Weissinger's simplified method in which the bound vorticity is concentrated at the 1/4 chord line, and the boundary condition that the flow must be tangential to the surface is satisfied only at the 3/4 chord line. If a finite number of vortices are used to represent the wing, the determination of the lift can be reduced to the solution of a set of algebraic equations. The downwash angle at the nth spanwise control point due to unit circulation at the mth spanwise station can be represented as an influence coefficient $A_{nm} + R_{nm}$, where A_{nm} is the contribution of the original vortex and R_{nm} is the contribution of the images. If Γ_m is the circulation at the mth station, the total induced angle at the nth control point is then

$$\alpha_n = \sum (A_{nm} + R_{nm})\Gamma_m \tag{5}$$

When one applies the boundary condition that the induced angle must equal the wing surface angle, equation (5) becomes a set of equations for the circulation.

It is convenient to distribute the horseshoe vortices so that their lateral limits are at the span fractions $\cos[(2m-1)\pi/2N]$ and their strengths represent the circulation at the points $\cos(m\pi/n)$. This permits previously developed methods (ref. 11) to be used for determining the free-stream influence coefficients A_{nm}. The interference influence coefficients R_{nm} have then each to be determined by summing a double series. The summation can be simplified by evaluating the interference downwash w_{jo} and its slope dw_j/dx at the 1/4 chord line and using the approximation

$$w_j = w_{jo}\left\{1 + \frac{x}{\sqrt{[w_{jo}/(dw_j/dx)]^2 + x^2}}\right\} \tag{6}$$

When the aircraft has a forward speed, it is unfortunately not possible to satisfy the two boundary conditions (1) and (2) by introducing images. The effect of forward speed may be treated approximately, however, by

multiplying the interference downwash distribution and therefore the influence coefficients R_{nm} in equation (5) by a scalar strength factor P. The correct answers are obtained for the static case and the free stream by setting $P = 1$ and $P = 0$ at these limits. At intermediate velocity ratios, it appears from an examination of the results of lifting line theory for an elliptic jet that a suitable strength factor is

$$P = \frac{1 - \mu^2}{1 + AR_j\mu^2} \tag{7}$$

Lifting Line Theory for an Elliptic Jet

For the purpose of developing a lifting line theory a single horseshoe vortex may be resolved into a pair of infinite line vortices and an antisymmetric pair of horseshoe vortices (fig. 4). The antisymmetric part produces no downwash at the lifting line, and it is therefore only necessary to represent the two-dimensional part of the potential. Let ϕ_v represent the potential of a vortex distribution in the absence of the jet boundary, and let $\Delta\phi_j$ and $\Delta\phi_o$ be the interior and exterior perturbation potentials due to the boundary, so that

$$\phi_j = \phi_v + \Delta\phi_j \tag{8}$$

$$\phi_o = \phi_v + \Delta\phi_o \tag{9}$$

These potentials can be represented as series

$$\phi_v = \sum A_n e^{-n\xi} \sin n\eta \tag{10}$$

$$\Delta\phi_j = \sum B_n \sinh n\xi \sin n\eta \tag{11}$$

$$\Delta\phi_o = \sum C_n e^{-n\xi} \sin n\eta \tag{12}$$

where ξ and η are elliptic coordinates

$$y + iz = a \cosh(\xi + i\eta) \tag{13}$$

and the boundary is at $\xi = \xi_o$ (fig. 5). Then introducing the boundary conditions (1) and (2), and equating coefficients, it is possible to solve for B_n and C_n in terms of A_n as

$$B_n = -\frac{1 - \mu^2}{1 + \mu^2 F_n(\lambda)} \frac{2A_n}{[(\lambda + 1)/(\lambda - 1)]^n - 1} \tag{14}$$

$$C_n = -\frac{(1 - \mu)[1 - \mu F_n(\lambda)]}{1 + \mu^2 F_n(\lambda)} A_n \tag{15}$$

where the ratio of width to height of the ellipse is

$$\lambda = \coth \xi_o \tag{16}$$

and

$$F_n(\lambda) = \coth n\xi_o = \frac{[(\lambda + 1)/(\lambda - 1)]^n + 1}{[(\lambda + 1)/(\lambda - 1)]^n - 1} \tag{17}$$

For a pair of vortices at (ξ_1, η_1) and $(\xi_1, -\eta_1)$ Tani and Sanuki (ref. 12) found that

$$A_n = \frac{2}{\pi n} \cosh n\xi_1 \cos n\eta_1 \tag{18}$$

The influence of forward speed on the interior potential is represented by the factor $(1 - \mu^2)/[1 + \mu^2 F_n(\lambda)]$ which reduces to $(1 - \mu^2)/(1 + \lambda\mu^2)$ for the first term.

When the wing extends exactly between the foci of the ellipse (fig. 6), a simple closed form solution can be obtained. The first term of the series represents a uniform downwash between the foci, and thus for a wing with an elliptic lift distribution only this term remains. For a given lift the effect of the jet is then simply to increase the induced downwash by the factor

$$\frac{\lambda + \mu^2}{1 + \lambda\mu^2} \tag{19}$$

The wing thus behaves as if its aspect ratio were divided by this factor. This is a generalization of a result obtained by Glauert (ref. 13) for open wind tunnels.

It is also possible to develop a slender-body theory for a wing in an elliptic jet (ref. 14). An extension to a lifting surface theory would require the representation of the antisymmetric part of the potential as an expansion in Mathieu functions.

Approximate Lifting Surface Theory For Circular Jets

For a circular jet the two-dimensional part of the interference potential due to a horseshoe vortex can be represented by images at the inverse points. The antisymmetric part can be represented as an expansion in Bessel functions (ref. 5). The results of wind-tunnel theory, however, indicate that the ratio of the slope of the downwash to the downwash at the load line is nearly the same for circular and square jets. Thus the slope can be approximated by multiplying the downwash at the load line for the circular jet by the ratio for the square jet. Then the longitudinal variation of downwash can be estimated by equation (6). Thus the need to determine the antisymmetric potential is obviated and the calculations can be simplified.

Results of Computer Calculations

Calculations for rectangular wings spanning rectangular jets have been made by computer, using 8 vortices per semispan to represent the wing. Typical results are shown in figures 7 to 9.

Figure 7 shows the effect of jet aspect ratio on lift and induced drag over the speed range for wings of aspect ratio 2 and 4. Forward speed is represented by the velocity ratio μ. In order to obtain meaningful values in the static case the lift and drag coefficients are referred to the jet velocity. With this convention the lift slope decreases as μ decreases because of the reduction in the external flow. Also for a given lift the induced drag increases. The wing is assumed to span the jet so that an increase in jet aspect ratio represents a decrease in jet height. It can be seen that the jet effects are accentuated as the jet becomes shallower.

When the angle of attack α is small and the aircraft is static, the jet deflection angle θ equals the ratio of lift to thrust. Figure 8 shows the static turning effectiveness $\theta/\alpha = L_\alpha/T$. For a given jet aspect ratio the turning effectiveness increases toward a limiting value as the wing chord is increased or its aspect ratio reduced. There is not much of a fall-off from this limiting value until $AR > AR_j$, or the wing chord is less than the jet height. The turning effectiveness also increases as the jet aspect ratio is increased and the jet becomes shallower: it is easier to deflect a flow which is close to the wing.

Figure 9 illustrates the influence which these trends could have on a design. The static performance of a wing in a large square jet is compared with its performance in a single wide jet of aspect ratio 4. In the large jet $L_\alpha/T = 0.365$. In the wide jet it is increased to 0.835. Since the disc loading of the wide jet is four times that of the large jet, the thrust for a given power input would be reduced. According to ideal actuator theory it would be a fraction $(1/4)^{1/3} = 0.630$ of the thrust of the large jet. Despite this the lift in the wide shallow jet would still be greater. It thus appears that it might well be advantageous to use several small propellers of high disc loading on each semispan, provided they could be placed close enough for their slipstreams to merge without incurring too large a loss of efficiency.

USE OF APPARENT MASS ARGUMENTS TO DERIVE SIMPLE APPROXIMATE FORMULAS

The form of the solution for a wing spanning the foci of a elliptic jet suggests a general approach to obtaining quick approximate answers. In a free stream an elliptic wing acts as if it deflected an apparent mass equal to that captured by a circle containing its tips through a uniform downwash angle. In a jet the reduction in the exterior velocity below the jet velocity causes the wing to encounter a smaller mass flow, so it can be expected to deflect a smaller apparent mass through a larger downwash angle. This is equivalent to a reduction in the effective aspect ratio from AR to

$$AR_\mu = \frac{AR}{1 + p}$$

where p is the fractional increase in downwash. Then according to lifting line theory the ratio of the lift slope to the lift slope in a free stream would be

$$\frac{C_{L_{\alpha_\mu}}}{C_{L_{\alpha_1}}} = \frac{2\pi/[1 + (2/AR)]}{2\pi/\{1 + [2(1 + p)/AR]\}} = \frac{AR + 2}{AR + 2(1 + p)}$$

It has been found that the results of detailed calculations for rectangular wings just spanning the slipstream can in fact be closely approximated by formulas of this type. If the free stream, the static case, and intermediate velocity ratios are denoted by subscripts 0, 1, and μ, the following formulas may be used for rectangular jets:

$$\frac{C_{L_{\alpha_o}}}{C_{L_{\alpha_1}}} = \frac{AR + 2}{AR + 2AR_j + [2.5/(1 + AR)]} \tag{20}$$

$$\frac{C_{L_{\alpha_\mu}}}{C_{L_{\alpha_1}}} = \frac{1}{1 + [(C_{L_{\alpha_1}}/C_{L_{\alpha_o}}) - 1][(1 - \mu^2)/(1 + AR_j\mu^2)]} \tag{21}$$

Also if r denotes the induced drag factor $C_D/C_L{}^2$

$$\frac{r_o}{r_1} = 0.76(AR_j + e^{-AR_j}) + 0.53 \tag{22}$$

$$\frac{r_\mu}{r_1} = \frac{(r_o/r_1) + [1 + AR_j - (r_o/r_1)]\mu^2}{1 + AR_j\mu^2} \tag{23}$$

These formulas are valid in the range $AR > (1/2)AR_j$, or wing chord less than twice the jet height. Similarly, for a rectangular wing spanning a circular jet the following formulas closely approximate the results of detailed calculations:

$$\frac{C_{L_{\alpha_o}}}{C_{L_{\alpha_1}}} = \frac{AR + 2}{AR + 3.54} \tag{24}$$

$$\frac{C_{L_{\alpha_\mu}}}{C_{L_{\alpha_1}}} = \frac{1}{1 + [(C_{L_{\alpha_1}}/C_{L_{\alpha_o}}) - 1][(1 - \mu^2)/(1 + \mu^2)]} \tag{25}$$

$$\frac{r_o}{r_1} = 1.68 \tag{26}$$

$$\frac{r_\mu}{r_1} = \frac{1.68 + 0.32\mu^2}{1 + \mu^2} \tag{27}$$

PREDICTION OF CHARACTERISTICS OF PRACTICAL CONFIGURATIONS

In order to estimate the lift of a propeller-wing combination at an angle of attack it is necessary to allow for the direct contribution of the propeller thrust, the propeller normal force due to the inclined inflow, and the change in the wing lift due to the propeller. The propeller slipstream has three principal effects on the wing: it increases the dynamic pressure, it alters the angle of attack, and it decreases the lift slope. All three effects must be estimated. The preceding analysis yields an insight into the last effect, but strictly only applies to wings completely contained in a jet. Assuming that the effect of a jet is small on the part of the wing outside the jet, it is, however, possible to make an estimate by using superposition. The increase in lift of the blown part of the wing, treated as if it were an independent planform, is added to the lift of the whole wing in a free stream. Along these lines a practical method has been developed for quick estimation of the characteristics of propeller-wing combinations, which gives good correlation with published experimental data. Two examples are shown in figures 10 and 11. All the aerodynamic coefficients are referred to the slipstream velocity, so that the static case is represented by CT = 1.0, and the lift coefficient decreases as the thrust coefficient increases and the velocity ratio decreases. The profile drag was not calculated, so that the theoretical drag curves should be to the left of the experimental points. At high thrust coeffcients the apparent profile drag coefficient is reduced because the drag coefficient of sections outside the slipstream is referred to the higher velocity in the slipstream. It should also be noted that rotation of the slipstream has been ignored. Provided that the wing completely spans the jet, the increase in angle of attack on one side of the jet should be compensated by the decrease on the other side, so the total lift should be about the same, although its distribution is altered.

DIVERGENCE BETWEEN THEORY AND OBSERVED DEFLECTION OF SLIPSTREAMS BY FLAPS

An exact calculation by potential theory of the lift of flapped wings would require the use of a model with multiple lifting lines. If, however, the effect of deflecting flaps through an angle δ is regarded as equivalent to an increase in the effective wing angle of attack α, the present method may be used, given suitable information about the effect of the jet on the

flap effectiveness α/δ. Tests have generally been made of wings with propellers attached to them, so that the angle of attack of the wing in the jet was fixed, and only the flap angle was varied. As a result the flap effectiveness cannot be directly determined, but if theoretical values of C_{L_α} are assumed for the wing, it is possible to impute values of α/δ.

In the static case the jet deflection angle θ is a convenient measure of performance. It has been shown that the turning effectiveness θ/α of a wing is close to a limiting value for a wing of infinite chord when the chord is about equal to the jet height (fig. 7). This limiting value is plotted as a function of jet aspect ratio in figure 12. It is less than unity because of edge effects illustrated in figure 13. The absence of a pressure differential at the jet boundary causes an inward spanwise pressure gradient above the wing and an outward gradient below it, so that the streamlines in the cross plane converge above the wing and diverge below it. The average downwash is less than the downwash in the plane of the wing, and the jet deflection angle is therefore less than the wing angle of attack. As the jet width is increased, the edge effects become less important, and the maximum turning effectiveness θ/α for an infinitely wide jet is predicted to be unity in agreement with the Coanda effect. For a circular jet the limiting turning effectiveness of a wing of large chord is found by slender-body theory (ref. 3) to be

$$\theta/\alpha_{max} = 1 - (4/\pi^2) = 0.595$$

For a pair of propellers producing a wide slipstream figure 12 indicates that the limiting turning ratio should be about 0.73.

Figure 14 is taken from Kuhn's summary of the results of tests of propeller-wing-flap combinations (ref. 15). It shows the turning effectiveness of flaps measured in static tests as a function of flap chord. Figures 15 and 16 show the results of several series of tests in greater detail. It can be seen that for some flap configurations θ/δ has been measured to be as high as 0.75. If the theoretical maximum value of θ/α is substituted in the relation

$$\theta/\delta = (\theta/\alpha)(\alpha/\delta)$$

these results indicate values of α/δ close to or even greater than unity.

The value imputed by the theory to θ/α_{max} depends on the application of the boundary condition without regard for jet deflection and distortion. Nevertheless, the edge effects should prevent a jet from being deflected through the full wing angle of attack. Assuming, therefore, that the theory is not grossly underpredicting the turning effectiveness of a complete wing, it appears that the flap effectiveness must be substantially greater in a jet than in a free stream. In fact the result of slender-body theory that the trailing-edge deflection angle is equivalent to wing angle of attack may be close to the truth.

CONCLUSION

The methods described in this paper provide a basis for engineering calculations which show good correlation with published experimental data for wings without flaps. In the light of the theory the jet deflection angles measured in tests of flapped wings are surprisingly large. There is a need for tests in which the jet producing device is removed from the wing so that the effect of changing the wing and flap angles can be measured separately to give an exact value of flap effectiveness. It would also lead to a better insight into the problem if the final shape and location of the jet could be determined. If jet distortion and deflection have an important influence on the interaction, it would be possible to allow for their effect by representing the slipstream boundary by a freely convecting vortex layer, and using a direct numerical approach, but massive computations would be needed to carry it through.

REFERENCES

1. Koning, C.: Influence of the Propeller on Other Parts of the Airplane Structure. Vol. IV of Aerodynamic Theory, W. F. Durand, ed., Julius Springer (Berlin), 1935, pp. 361-430.

2. Franke, A.; and Weinig, F.: The Effect of the Slipstream on an Airplane Wing. NACA TM 920, 1939.

3. Graham, E. W.; Lagerstrom, P. A.; Licher, R. M.; and Beane, B. J.: A Preliminary Theoretical Investigation of the Effects of Propeller Slipstream on Wing Lift. Douglas Rep. SM 14991, 1953.

4. Butler, Lawrence; Goland, Leonard; and Huang, Kuo P.: An Investigation of Propeller Slipstream Effects on V/STOL Aircraft Performance and Stability. Dynascience Rep. DCR 174, 1966.

5. Rethorst, S.: Aerodynamics of Nonuniform Flows as Related to an Airfoil Extending Through a Circular Jet. J. Aero. Sci., vol. 25, no. 1, Jan. 1958, pp. 11-28.

6. Ribner, H. S.; and Ellis, N. D.: Theory and Computer Study of a Wing in a Slipstream. Preprint 66-466, AIAA, 1966.

7. Sowydra, A.: Aerodynamics of Deflected Slipstreams. Part 1, Formulation of the Integral Equations. Cornell Aero. Lab. Rep. AI-1190-A-6, 1961.

8. Wu, T. Yao-tsu; and Talmadge, Richard B.: A Lifting Surface Theory for Wings Extending Through Multiple Jets. Vehicle Res. Corp. Rep. 8. 19 1.

9. DeYoung, John: Symmetric Loading of a Wing in a Wide Slipstream. Grumman Rep. ADR 01-04-66.1, 1966.

10. Theodorsen, Theodore: Interference on an Airfoil of Finite Span in an Open Rectangular Wind Tunnel. NACA TR 461, 1933.

11. DeYoung, John; and Harper, Charles W.: Theoretical Symmetric Span Loading at Subsonic Speeds of Wings Having Arbitrary Plan Form. NACA Rep. 921, 1948.

12. Tani, Itiro; and Sanuki, Matao: The Wall Interference of a Wing Tunnel of Elliptic Cross Section. NACA TM 1075, 1944.

13. Glauert, H.: Some General Theorems Concerning Wind Tunnel Interference on Aerofoils. R and M no. 1470, British A.R.C., 1932.

14. Jameson, A.: Preliminary Investigation of the Lift of a Wing in an Elliptic Slipstream. Grumman Aero. Rep. 393-68-2, 1968.

15. Kuhn, R. E.: Semiempirical Procedure for Estimating Lift and Drag Characteristics of Propeller-Wing-Flap Configurations for Vertical- and Short-Take-Off-and-Landing Airplanes. NASA MEMO 1-16-59L, 1959.

WING IN A WIDE SLIPSTREAM

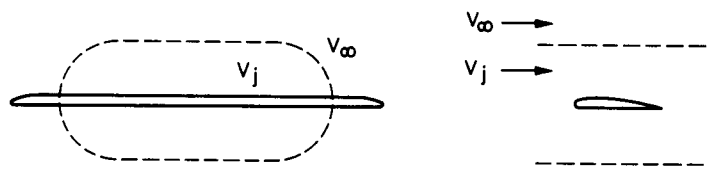

Figure 1

WING SPANNING A RECTANGULAR JET

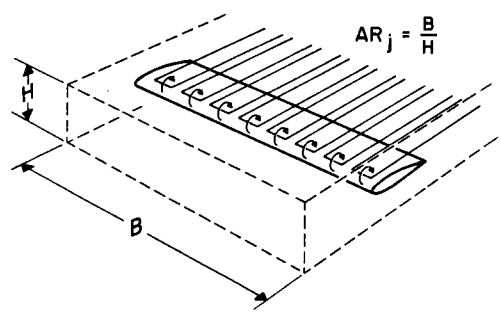

Figure 2

IMAGES FOR A HORSESHOE VORTEX

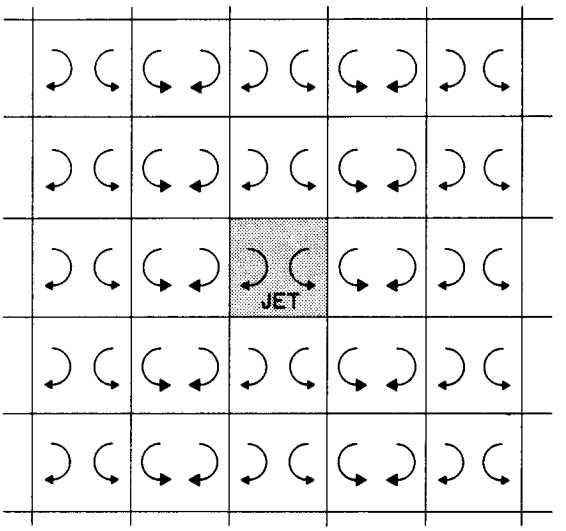

Figure 3

DECOMPOSITION OF A HORSESHOE VORTEX INTO TWO DIMENSIONAL AND ANTISYMMETRIC PARTS

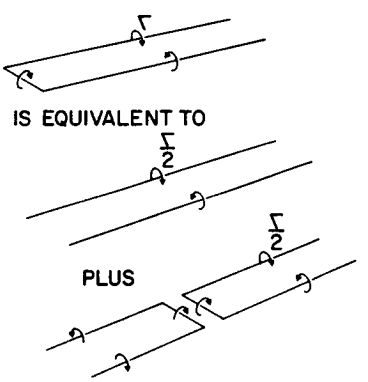

Figure 4

VORTEX PAIR IN AN ELLIPTIC SLIPSTREAM

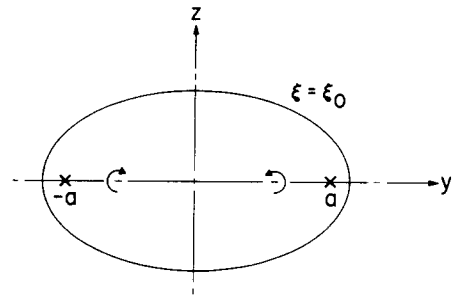

Figure 5

WING SPANNING FOCI OF ELLIPTIC SLIPSTREAM

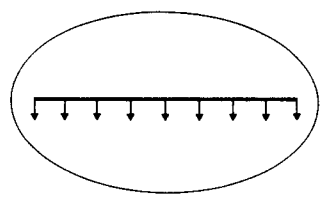

Figure 6

OPERATIONAL CURVES FOR A RECTANGULAR WING

AR = 2

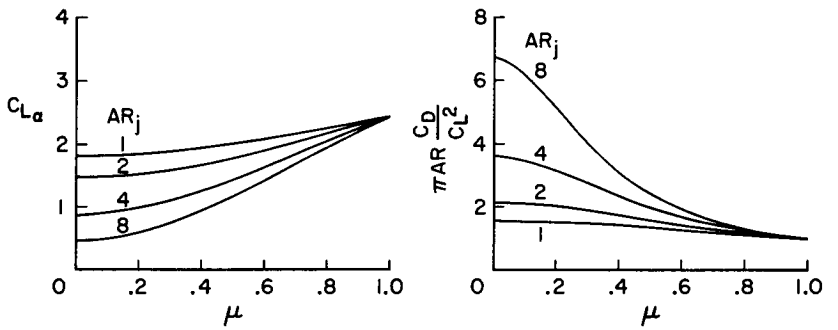

Figure 7(a)

OPERATIONAL CURVES FOR A RECTANGULAR WING

AR = 4

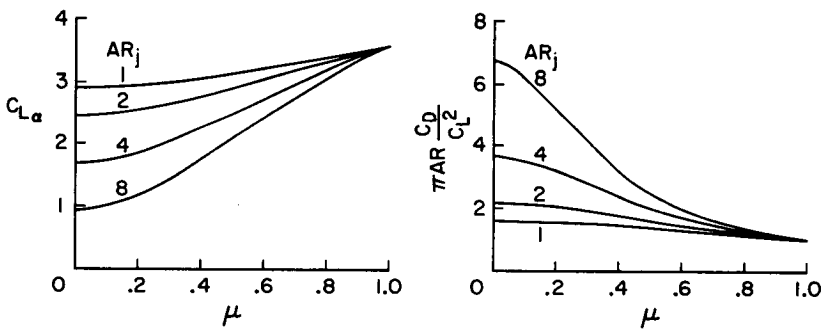

Figure 7(b)

TURNING EFFECTIVENESS OF RECTANGULAR WINGS IN STATIC JETS

$\mu = 0$

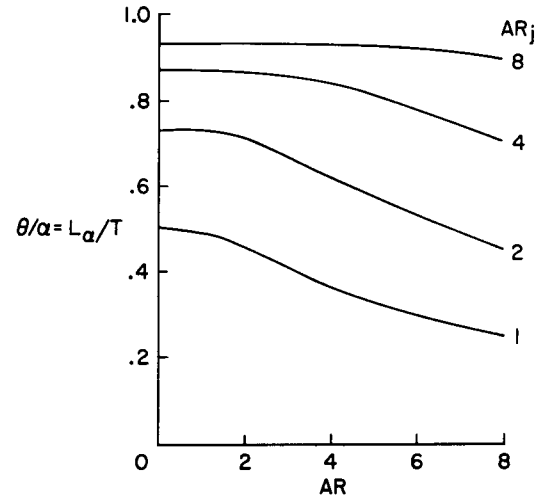

Figure 8

EFFECT OF DISPOSITION OF JETS ON THE STATIC TURNING EFFECTIVENESS OF A RECTANGULAR WING OF ASPECT RATIO 4

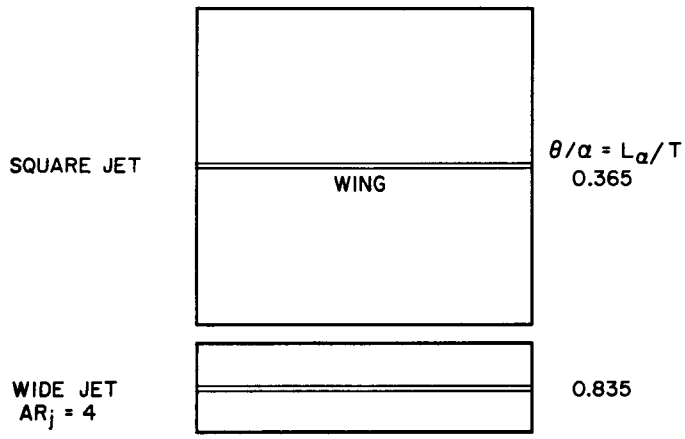

Figure 9

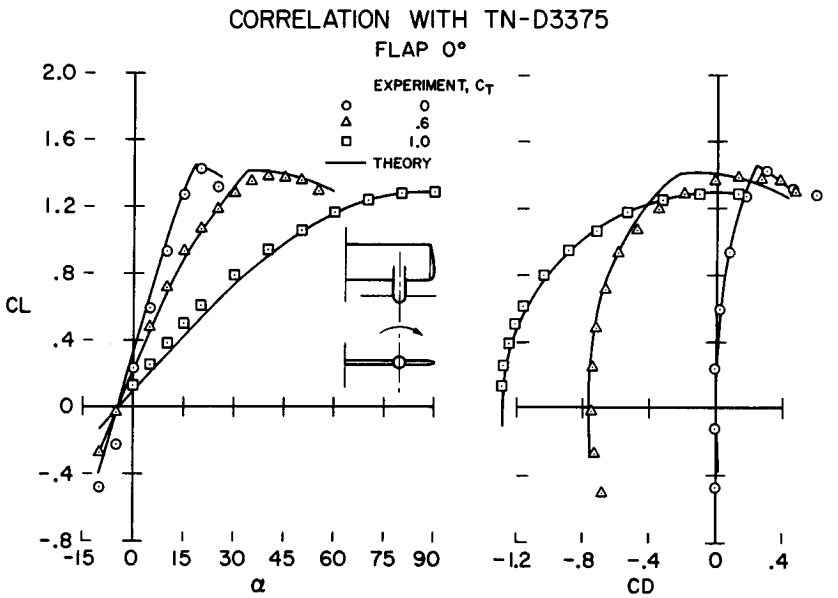

Figure 10

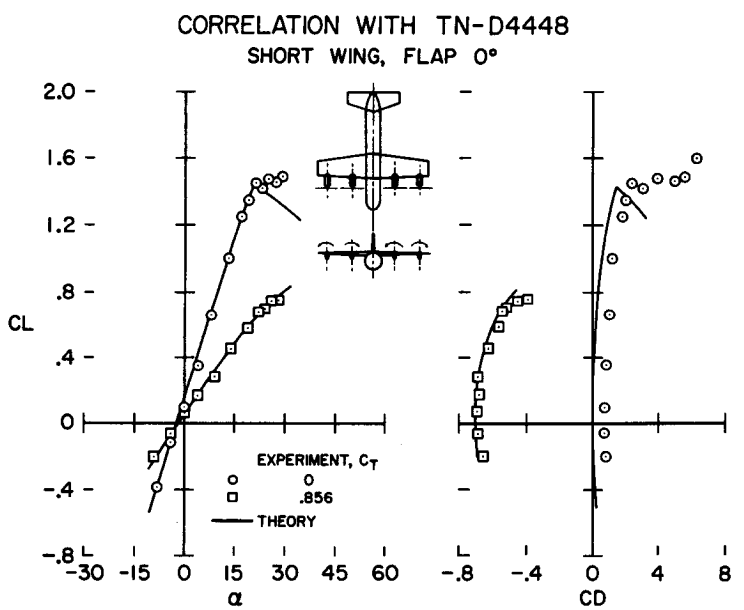

Figure 11

FLOW IN THE CROSS PLANE OF A JET OVER A WING

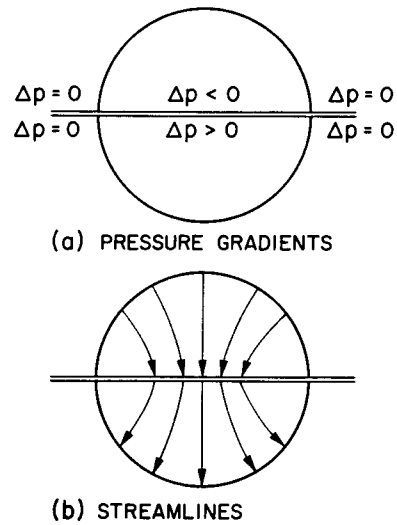

Figure 12

EFFECT OF JET WIDTH ON LIMITING TURNING RATIO

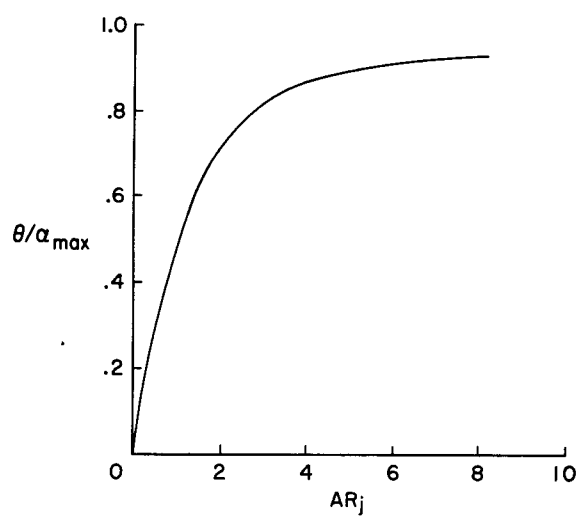

Figure 13

VARIATION OF TURNING ANGLE WITH THE RATIO OF TOTAL FLAP CHORD TO PROPELLER DIAMETER FOR VARIOUS FLAP CONFIGURATIONS IN HOVERING OUT OF GROUND-EFFECT REGION

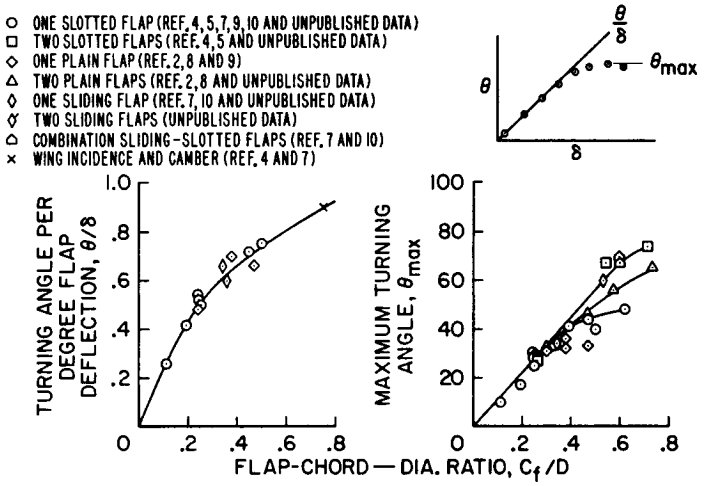

(REPRODUCED FROM NASA MEMORANDUM 1-16-59L)

Figure 14

FLAP DATA FROM TN 3307
TWO PROPELLERS PER SEMISPAN

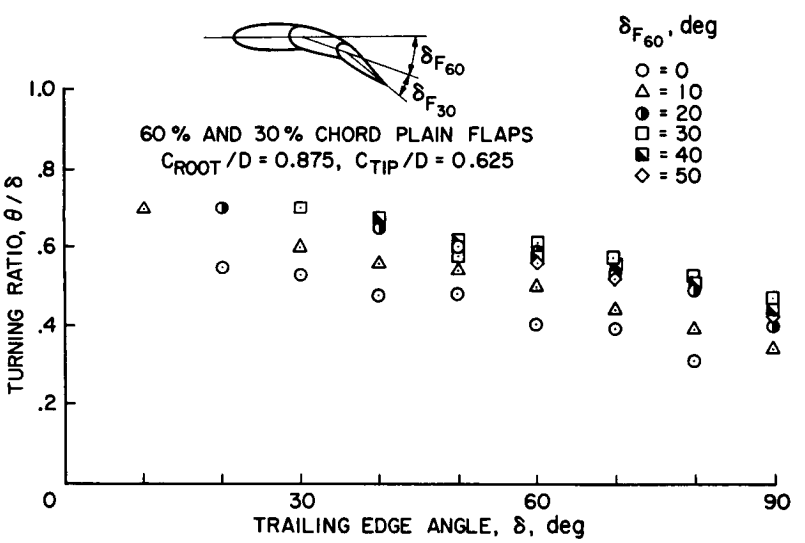

Figure 15

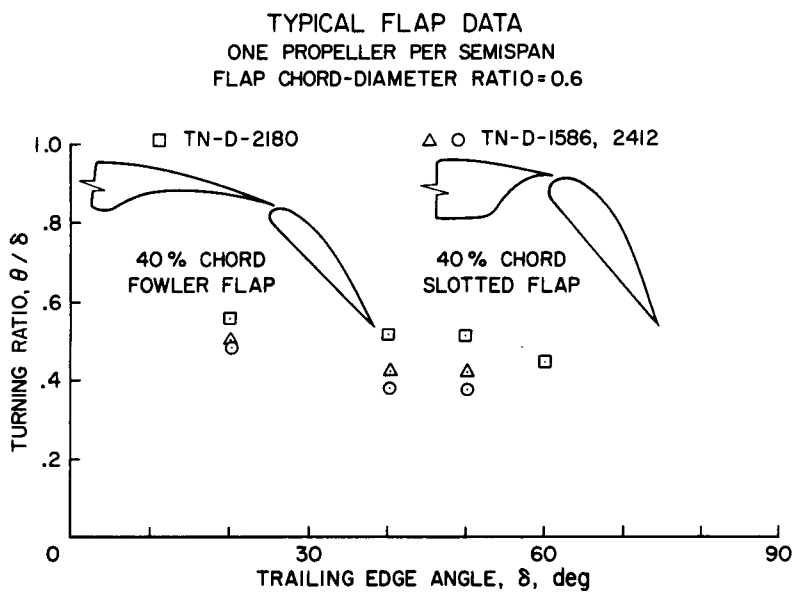
TYPICAL FLAP DATA
ONE PROPELLER PER SEMISPAN
FLAP CHORD-DIAMETER RATIO = 0.6
□ TN-D-2180
△ ○ TN-D-1586, 2412
40% CHORD
FOWLER FLAP
40% CHORD
SLOTTED FLAP
TURNING RATIO, θ / δ
1.0
.8
.6
.4
.2
0
30
60
90
TRAILING EDGE ANGLE, δ, deg

Figure 16

DISCUSSION

ELY S. LEVINSKY, Air Vehicle Corp.: Is the propeller slipstream tilted or untilted when the wing is tilted?

JAMESON: In the correlations I showed you, the propeller was fixed to the wing so they were tilted together. When there is a forward speed, of course, there would be some variation between the tilt of the slipstream and the wing, because of the interaction with the external flow, but statically the wing has a fixed angle of attack in the slipstream.

LEVINSKY: Well, at forward speed does the theory account for tilt of the propellers?

JAMESON: Well, this is one of the problems in the correlation. With this theory we are attempting to concentrate on the slipstream-wing interaction, but in order to correlate with available experiments, you are obliged to estimate the normal force of the propeller and the angle of the flow behind it. Therefore, when I showed you the correlation up there for that configuration, there was a procedure for estimating these. I would be happier to have tests in which you could separate all these factors. I think it would be easier to pin down whether you are really getting a good agreement or not.

LEVINSKY: I might mention that a while back Air Vehicle Corp. had done some work in this area under Army sponsorship. We treated the propeller-slipstream-wing interaction using essentially Ribner's method that you mentioned. Professor Hans Thomann, who participated in the program, developed an inclined actuator disk theory which was incorporated into the method so we could treat inclined propellers and wing angle of attack. We dealt with one, two and four propellers, but their slipstreams were separated, not merged, like you treated. Also, we included effects of slipstream rotation.

But I am in complete accord with you on the matter of test data. We got into the problem where we didn't really have adequate test data with which to evaluate the theory, and it was left at that. I might mention there are some very nice test data that were obtained by Stüper in Germany in 1938 (NACA TM-874). We have a hard time locating any better test data.

JAMESON: Yes, I agree with you completely. I think Stüper's tests are the sort of thing we would like to see renewed.

LEVINSKY: Because he did take out the swirl.

JAMESON: Yes, I know.

LEVINSKY: One further question. One of your slides showed a sharp corner on it, in the theory. This was when you looked at C_L versus α, and I was wondering . . .

JAMESON: Oh, yes, I am sorry about that. In the practical method - slide 12, please. I really ought to have deleted that. When dealing with

this practical correlation, I introduced an allowance for stall angle which is empirical. That has really nothing to do with the theory, but in trying to carry large angles of attack, you may get the wing outside the slipstream stalled and the wing inside the slipstream not stalled, so in order to carry it through, you've got to do something about estimating the stall. But that is not a theoretical stall estimate.

DAVID BEVAN, Boeing Company, Vertol Div.: First of all, let me say that you seem to have done very well with a very difficult subject, and after looking at perhaps 14 years of wind-tunnel data from Langley, we at Boeing do some computer work, but we have also spent something like 1,400 hours of wind tunnel time on this problem this past year, and we are looking forward to following your results.

It is very difficult to handle the stall problem, which you have drawn empirically there. As the man from Air Vehicle Corporation said, a propeller alone is very difficult to calculate and is often calculated wrong. It isn't that the force contribution is a very large part of the lift; it is that it suppresses the leading-edge angle of attack.

JAMESON: Yes, exactly.

BEVAN: And between that and the upgoing and outgoing size of the props, you've got a very difficult wing loading distribution problem. So you certainly are embarked on a very difficult course.

JAMESON: Yes. I would like to have a simple test of a wing in two flows and see if we can agree with that as a first step.

NASA-Langley, 1970 —— 1